UCRL-50021-79

Laser Program Annual Report ~ 1979

Volume 2

UCRL-50021-79
Distribution Category
UC-21,22

Laser Program Annual Report - 1979

Volume 2

Scientific Editor: Lamar W. Coleman
Publication Editor: John R. Strack
MS date: March 1980

Lawrence Livermore National Laboratory
University of California • Livermore, California • 94550

Available from: National Technical Information Service • U.S. Department of Commerce
5285 Port Royal Road • Springfield, VA 22161 • $18.00 per copy • (Microfiche $3.50)

Contents

Volume 1

Volume 2

Volume 3

Target Design

3

Target Design 3

Contents

Target Design

3

Introduction

The Target Design program at LLL combines the efforts of the plasma, code development, and design groups, in

- Developing theories of beam-plasma interaction, implosions, and thermonuclear microexplosions.
- Building plasma and implosion-burn computer codes.
- Using these theoretical and computational tools to design targets and simulate experiments.

In late 1979 a prototype of our high-density target design was irradiated at Shiva, and achieved sufficiently high neutron yield to enable an experimental determination of density. Preliminary measurements indicated that this target reached our prediction of approximately 100 to 200 times liquid density—a several-fold increase over the 50 to 100 times density achieved earlier in the year. We have thus increased achieved density by two of the three orders of magnitude (from normal density to 1000 times liquid density) required for high-performance ICF-reactor targets. Inferred thermonuclear parameters associated with this record density are $n\tau \approx 5 \times 10^{14}$ cm^{-3}-s and an ion temperature of 0.5 keV.

During the last year we attained a record thermonuclear ion temperature of 13 keV with an unusual type of exploding-pusher target irradiated at Shiva; with another type of exploding pusher we equaled our record exploding-pusher neutron yield of 3×10^{10}, achieved in 1978. The discrepancy between this neutron yield and our 1977–78 prediction of 10^{12} is due primarily to our anticipation of a higher implosion symmetry and laser-light absorption efficiency than actually occurred, and secondarily to the effects of less laser power and a longer pulse length that we assumed.

Advances in our modeling of energy transport and suprathermal electrons have greatly improved the agreement between LASNEX calculations and our high-density experimental data (x-ray microscope images, argon line images, and radiochemical measurements). Several of our laser-plasma theoretical predictions have been confirmed experimentally, including the behavior of Raman scattering in 2-ns disk experiments, improved coupling in short-wavelength disk experiments, and delayed suprathermal electron generation in high-density experiments, all of which play a key role in many of our ICF targets. On the other hand, analysis of our gold disk data has turned up small discrepancies which might be due to neglect of significant physical processes; experiments with more sophisticated diagnostics (for measuring the density profile, for example) are required to explore these discrepancies. Our plasma theorists have also formulated important nonlinear corrections to inverse bremsstrahlung, and improved our understanding of resonant absorption, filamentation, and Brillouin scattering.

The newly developed Cray-1 version of our primary target design code LASNEX has twice the computing capability of the old CDC 7600 version. LASNEX atomic physics, Brillouin scattering, and multigroup diffusion physics have all been improved, and a Monte Carlo photon-transport option has been added.

We have made advances in the design of targets for achieving 100 to 1000 times liquid density with Shiva, for ignition with Nova, and for high gain with reactor drivers. Scaling laws and analytic approximations for a number of critical phenomena are in good agreement with the detailed experimental results.

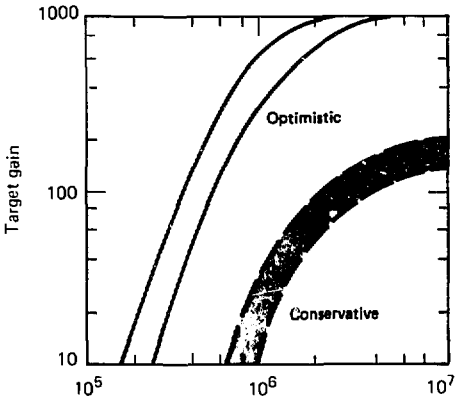

Fig. 3-1

Parameter	Conservative	Optimistic
Driver efficiency, %	≥ 6	≥ 1
Wavelength (or ion voltage)	≤ 0.3 μm 10 GeV U/5 MeVp	≤ 2 μm 20 GeV U/20 MeVp
Energy, MJ	3-5	>1
Peak power, TW	200	>100
Pulse rate, per second	8	4

Our predictions of fusion-reactor driver requirements have not changed since last year, nor did our calculated target gain curves change in 1979 (Fig. 3-1). We expect to achieve the conservative levels initially and then follow a learning curve leading toward the more optimistic levels. The "conservative" estimate in the figure is based on conservative assumptions about implosion instabilities and thermonuclear ignition and burn, and assumes efficient beam-target coupling (with ions or short-wavelength lasers). Target designs based on these conservative assumptions will achieve ignition at the LLL Nova laser facility (including frequency doubling) and at the Sandia Proton Beam Fusion Accelerator (PBFA II). Ignition is defined as energy deposited in D-T by thermonuclear heating, which equals thermal energy in D-T due to implosive heating.

Author: J. H. Nuckolls

High-Z Disk Modeling

In the past year we have continued our efforts at achieving classical (inverse bremsstrahlung) absorption of laser light incident on disk targets. "Shiva 2-ns Disk Experiments" in Section 6 of this annual report describes in detail the highly successful results of this effort, which has achieved 80% absorptions with gold disks both at Argus (using 0.53-μm light, 600-ps pulses, and mid-10^{14} W cm^2 intensities) and at Shiva (using 1.06-μm light, 2-ns pulses, and mid-10^{13} W/cm^2 intensities). Thus we have moved deep into the efficient inverse-bremsstrahlung absorption regime.

These experimental data supplement basic theoretical progress made in the past year on the process of inverse bremsstrahlung and on its competition with stimulated Brillouin scattering. (The theory is described in detail in several articles in this section that deal with laser-plasma theory and simulation.) Some aspects of this theoretical work were incorporated into our LASNEX modeling[1] of the disk experiments, and the improved model has been tested by comparing its predictions with previous disk experiments[1] and with the abovementioned Argus and Shiva data. The data present a formidable test for the model, as the experimental parameters involve factors of 2 in laser wavelength, 10 in pulse length and spot size, 20 in target Z, and 100 in intensity.

In this article we describe the effects of our various additions to the modeling and show comparisons with our experimental data. We find the model's absorption predictions to be below the experimental results, implying less severe inhibited electron transport or additional absorption mechanisms such as ion acoustic turbulence. In addition, we consider some simple models of inverse bremsstrahlung absorption and compare their scaling predictions with the LASNEX simulations and experimental data.

The Simulation Model. Before describing additions to the model, we briefly review the elements of the standard disk calculational model, which has

been shown to give good agreement with previous data.[1]

- A portion of the incident energy is completely discarded from the model's calculations, to account for stimulated scattering. The amount discarded is determined from previous experiments; theoretical arguments are used to scale from one experiment to another.
- The light is absorbed by inverse bremsstrahlung on its way to the critical-density surface, where some 20% of what remains is absorbed into a hot-electron spectrum to simulate resonance absorption.
- The thermal-electron heat conduction from critical and below (the regions where the light is absorbed) to the overdense plasma is inhibited by the 2-stream mechanism: the inhibition factor varies from 1 to 0.02 as ZT_e/T_i varies from 3 to 30; above 30 the factor remains at 0.02.
- Since conduction is inhibited, steep temperature and density gradients form at critical. An atom moving rapidly across these steep gradients is out of equilibrium, so the model must use non-LTE calculations of the mean atomic population levels and of the equation of state.

One of the major improvements in this model is the "Langdon factor" that reduces the classical absorption due to nonlinear effects.[2] In inverse bremsstrahlung the electrons oscillating coherently in the laser's E-field collide with an ion and become isotropic. Since collision frequency scales as v^{-3}, the slowest electrons absorb most efficiently, thus heating up and speeding up, depleting the distribution of the slow, efficient absorbers. Usually electron–electron collisions will restore a Maxwellian distribution, thus repopulating the depleted low-energy portions of the field. For high-Z targets, however, electron–ion collisions (inverse bremsstrahlung) occur Z times faster than the electron–electron collisions, so the depletion of the slow, efficient absorbers continues, thus reducing the net absorption. The figure of merit for this process is $\alpha \equiv Z(v_{osc}^2/v_{th}^2)$. Calculations by Langdon show that for $\alpha \geq 10$, the inverse bremsstrahlung absorption opacity should be reduced by half.[2] For $\alpha \leq 0.1$ there is no correction (the nonlinear effect is negligible) and for intermediate values of α the multiplier varies smoothly from 1 to 0.5.

We have also changed the way a one-dimensional problem is set up. Instead of a pure disk (rectangular LASNEX zoning) we now use a portion of a sphere whose radius of curvature equals the illuminated spot-size diameter. The spherical divergence of the underdense plasma then mocks up, in one dimension, the two-dimensional effect of large plasma blow-off. Comparisons with two-dimensional runs show that this one-dimensional method of running the code indeed mimics major two-dimensional features.

Although considerable progress has been made in understanding the competition between inverse bremsstrahlung and stimulated scattering in large underdense plasmas, the need for more sophisticated research remains an area for major improvement in the model. Many physical effects determine the amount of scatter, including reinforcing effects (such as light reflecting back off the critical surface) and weakening effects (such as convective damping of the scattering in the presence of a density gradient). These effects and others are still being studied theoretically before they can be incorporated into the LASNEX code. The Brillouin scattering model currently incorporated into LASNEX (discussed later in this section in "Brillouin Backscattering Model in LASNEX") has shown great promise. Since this addition to the basic model is still undergoing vigorous development, however, the work referred to in the remainder of this article does not include this addition.

Simulation Results. On our first set of runs we reinvestigated results for Au disks irradiated at Argus for 1 ns with 1.06-μm light. Figure 3-2 shows absorption predictions vs intensity for these shots, for two different inhibition models: classical conduction, and 2-stream inhibition of thermal electrons. Recall that these results are not corrected for scattering losses. As intensity increases the background temperature rises, lowering collision frequencies and thereby reducing inverse bremsstrahlung. The classical conduction model transports more energy into the overdense plasma and blows out more plasma into a shallow gradient, thus increasing the absorption as compared to the inhibited model. In addition, the inhibited model bottles up the energy in the absorption region, increasing its temperature, which reduces the inverse bremsstrahlung as compared to the classical model.

Figure 3-2 also shows the absorption predictions with a correction for stimulated scattering,

Fig. 3-2. Absorption predictions (for either classical or inhibited conduction models) vs laser intensity. Dotted lines are the same curves corrected for stimulated scattering losses. Experimental points (marked with an E) are from 1.06-μm Argus laser light on Au disks with 1-ns pulses.

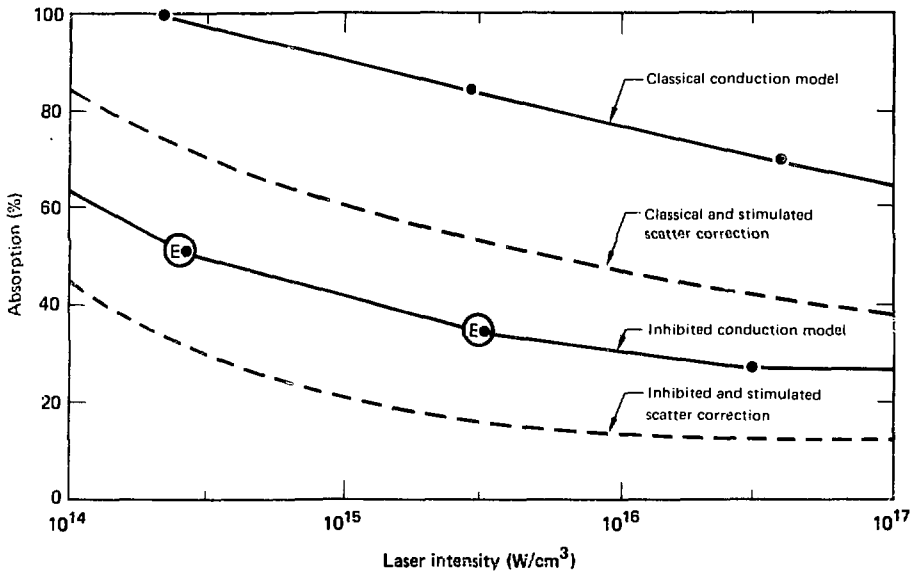

deduced from experiments. Note that the experimental points lie between the two corrected predictions; since previous modeling did not include the Langdon factor, absorption predictions were higher, thus making the inhibited model match the experiment. The possible implications of these new results are either that the 0.02 inhibition factor is too severe, or that we have not modeled other absorption processes (such as ion turbulence) which would increase the absorption prediction and bring the inhibited model back into agreement with experimental data. Despite the new absorption results, though, the inhibited model does predict the correct amount of energy that is radiated (in the range from 100 to 1500 eV) from the disk, whereas the classical conduction model predicts too much. This effect is due to the fact that the radiation is produced most efficiently in denser material, which is heated more efficiently under classical conduction conditions.

As mentioned earlier, we now have a broader data base with which to compare the model. Figure 3-3 also shows absorption predictions vs intensity

Fig. 3-3. Same as Fig. 3-2, but for 1.06-μm Shiva laser light at 2 ns. No corrections were made for stimulated Brillouin scattering due to uncertainties in the actual amount of scatter.

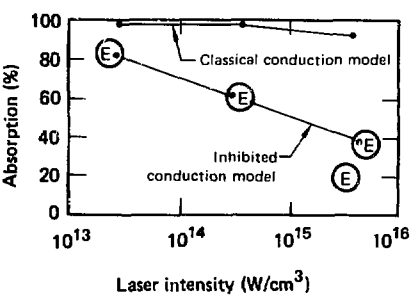

for the classical and inhibited model, but for 2-ns experiments at Shiva. Corrections for scattering have not been made and cannot be experimentally estimated at this time. It appears, as before, that the uncorrected inhibited model matches the experi-

Fig. 3-4. Same as Fig. 3-3, but for CH disk targets.

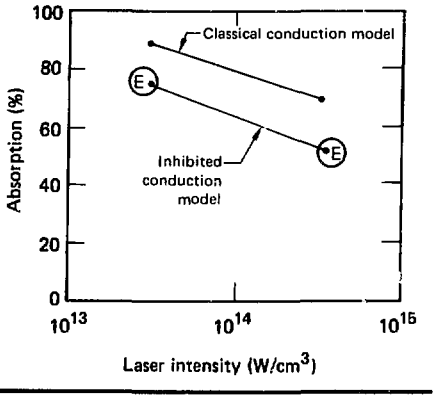

Fig. 3-5. Absorption vs material, for Argus 600-ps laser light at 0.53 μm incident on Au or CH; I = 3 × 10¹⁴ W/cm².

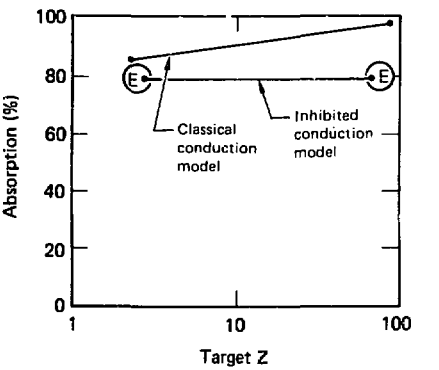

ments quite well, with the probable outcome that a stimulated scattering correction would result in the experimental point's lying squarely between the two models' predictions. Figure 3-4 shows precisely the same behavior for CH.

Figure 3-5 shows green-light results with CH and Au at 3 × 10^{14} W/cm² for 600 ps. The LASNEX curves are uncorrected for stimulated scattering. However, in this case there was experimental evidence that such scattering was negligible. Thus, the inhibited model fits these data better.

There are two surprises in these 2-ns data. First, the longer pulse and scale length (compared to the 1-ns data) slightly increased inverse bremsstrahlung at lower intensities (as expected) but apparently did not increase the stimulated scattering. Secondly, the parylene with much lower Z absorbed nearly as well as the gold. These questions will be dealt with shortly.

Scaling Laws. As we sweep from low to high intensity we pass from the very strong inverse bremsstrahlung regime to the weak one (with Brillouin scattering increasing all the way along). In this section we present results of scaling laws for inverse bremsstrahlung (and stimulated scattering) in both limits, by setting (f_{abs}, I) equal to $nT^{3/2}$.

The weak absorption limit, in which $f_{abs} = 1 - \exp(-\epsilon) \approx \epsilon \sim \nu_{ei}(n_c)(n/n_c)^2 L$, yields

$$f_{abs} \sim (Z\tau)^{0.6} I^{-0.4} \lambda^{-2.0} \qquad (1)$$

and

$$T_e \sim (I\tau Z)^{0.4} . \qquad (2)$$

These equations (and those that follow) were derived assuming that the density scale length, L, scales as $C_s \tau \sim T_e^{1/2}$. This assumption is somewhat questionable for at least two reasons. First, for very long pulses spherical divergence disturbs this relation. Second, for high intensity there is a steepening of the critical surface and a shortening of scale lengths.

Since the quality factor Q (a measure of the amount of stimulated scattering) scales as $(v_{osc}/v_e)^2 (L/\lambda)$, using Eqs. (1) and (2) we find

$$Q_{SBS} \sim \lambda (I\tau)^{0.8} Z^{-0.2} . \qquad (3)$$

In the strong absorption limit[3] $f_{abs} = 1$ and the absorption occurs at lower density [$n_a = n_c L_a/L_n$, where L_a is defined as $c^{-1} \int_0^{L_a} \nu_{ei}(n_c)(n/n_c)^2 d\lambda = 1$]. We find

$$T_e \sim (Z\tau I^3 \lambda^4)^{0.2} \qquad (4)$$

and

$$Q_{SBS} \sim I\tau^{0.3} \lambda^{2.5} Z^{-0.6} . \qquad (5)$$

We now consider the scaling with each parameter individually. Shorter wavelengths lead to greatly increased inverse bremsstrahlung [Eq. (1)] and decreased scattering [Eqs. (3) or (5)]. These

scalings were reflected in the high absorption results in the green light experiments. Lower intensity leads to higher inverse bremsstrahlung [Eq. (1)] and decreased scattering [Eqs. (3) or (5)]. This was also seen in the low-intensity 2-ns Shiva data. In the low intensity-high absorption regime, scattering depends only weakly on pulse length [Eq. (5)]. In the high intensity-low absorption regime, however, both inverse bremsstrahlung [Eq. (1)] and stimulated scattering [Eq. (3)] are strongly dependent on pulse length, with stimulated scattering actually scaling slightly stronger with τ. Indeed, there are experimental indications of this: for mid-10^{14} W/cm^2 irradiations, the 2-ns result on Au (60% absorption) is barely above the 1-ns result (50% absorption), while for mid-10^{15} W/cm^2 irradiations, the 2-ns result (25% absorption) is actually below the 1-ns result (36% absorption). The lesson to be learned is that if we wish to absorb efficiently at long pulse lengths by avoiding stimulated scattering, we must be sure to be in the strong inverse bremsstrahlung regime (by having low I and/or short λ) where Q_{SBS} scales weakly with τ.

The only mystery that remains is in the Z scaling. Equations (1) through (5) show that inverse bremsstrahlung should increase with Z, while SBS should decrease with Z, resulting in a higher-Z target absorbing better. The experiments, however, showed comparable CH and Au absorptions, as did the LASNEX code model. Study of this problem is underway, including the possibility that

- The Langdon factor acts more strongly on Au ($\alpha \equiv Z\, v_{osc}^2/v_e^2$) than on CH, thus reducing the inverse bremsstrahlung for Au.
- Two-stream inhibition is less effective for low Z (figure of merit ZT_e/T_i), which would render the CH "uninhibited"; it would then absorb more efficiently than in the inhibited situation (which holds for Au).

Since both the experiments and simulations run the full range from low to high inverse bremsstrahlung, we take as a global scaling law the geometric mean of the two limits, resulting in

$$T_e \sim \lambda^{0.4} I^{0.5} Z^{0.3} \tau^{0.3} . \qquad (6)$$

This scaling has been compared to LASNEX runs for which we find

$$T_e\,(\text{LASNEX}) \sim \lambda^{0.4} I^{0.4} Z^{0.3} \tau^{0.4} , \qquad (7)$$

in reasonable agreement with Eq. (6).

Conclusion. Our improved LASNEX model tracks many of the experimental trends which now cover a wide parameter range. An improved stimulated scattering package will help determine how well the model really stands up quantitatively. The nonlinear inverse bremsstrahlung correction lowers absorption which under many conditions implies the need for somewhat less inhibition or for invoking additional absorption mechanisms such as ion turbulence. On the other hand, LASNEX may be underestimating the absorption due to its including the average temperature (suprathermals and thermals) in the basically nonlinear inverse bremsstrahlung phenomenon. T_{AV} is thus too high, and reduces the calculated absorption. An experimental determination of density and temperature profiles would be extremely useful in specifying the correct physics to apply to the model. Finally, our simple scaling rules help to elucidate the experimental and code results.

Author: M. D. Rosen

References

1. M. D. Rosen, D. W. Phillion, V. C. Rupert, W. C. Mead, W. L. Kruer, J. J. Thomson, H. N. Kornblum, V. W. Slivinsky, G. J. Caporaso, M. J. Boyle, and K. G. Tirsell, "The Interaction of 1.06 μm Laser Radiation with High Z Disk Target," *Phys. Fluids* **22**, 2020 (1979).
2. A. B. Langdon, *Nonlinear Inverse Bremsstrahlung and Heated Electron Distribution*, Lawrence Livermore Laboratory, Livermore, Calif., UCRL-82353 (1979).
3. C. E. Max and K. G. Estabrook, *Wavelength Scaling in Laser Fusion from a Plasma Physics Point of View*, Lawrence Livermore Laboratory, Livermore, Calif., UCRL-82671 (1979).

Electron Transport and Preheat

One of the key requirements in the design of a high-gain target is keeping the fuel at a low adiabat in order to facilitate very high compressions. When laser light impinges on the outside of a pusher two physical processes (diagramed in Fig. 3-6) may occur that could raise the adiabat and significantly degrade the implosion:

- Laser-generated suprathermal electrons penetrating deep into the pusher may cause the preheated inside surface of the pusher to explode inward, sending a shock wave ahead that preheats the fuel.
- The large ablation pressure set up near the outside of the pusher (which will ultimately implode

Fig. 3-6. Two effects may set the fuel adiabat: First, preheat may cause the inner part of the pusher to explode into the fuel, sending a shock wave ahead of it that heats the fuel. Secondly, large ablation driven shock may arrive in the fuel too early and raise the adiabat.

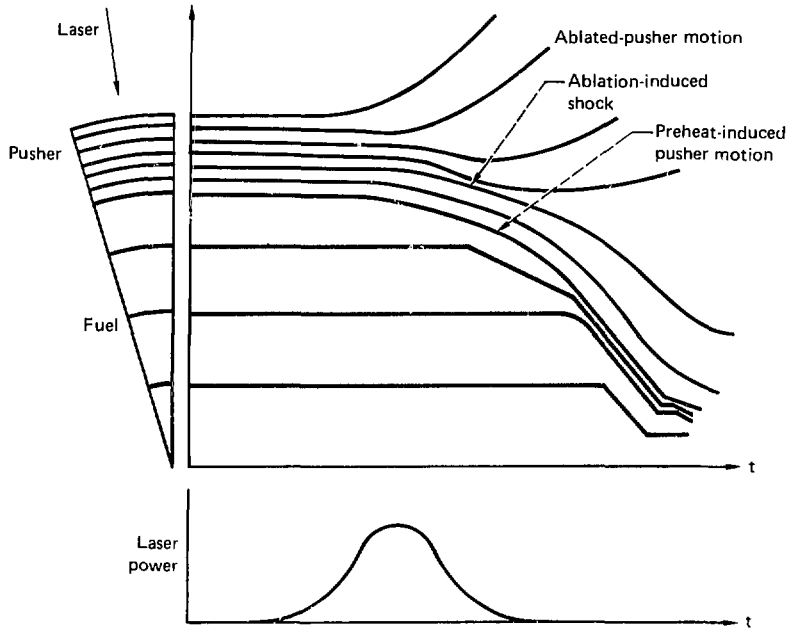

the capsule) sends a shock wave through the pusher that propagates through the fuel as well. If the timing of this shock is premature, the fuel temperature will be raised too soon, thus making high compression more difficult.

While our LASNEX code models these two phenomena (both temporally and spatially) quite accurately, it would nevertheless be useful to have simple analytic expressions for these effects. Such expressions would enable the target designer to pick the right place in parameter space without spending computer resources in a trial-and-error search for a low-adiabat implosion. In this article we develop such simple formulas, both for suprathermal preheat temperatures and for adiabat settings due to shocks generated by the ablation process.

Suprathermal Preheat and Transport. In laser-target experiments we usually monitor the high-energy (20 to 100 keV) x rays produced when hot electrons slow down in dense material and emit bremsstrahlung. From the slope of that distribution we deduce T_H, the suprathermal electron temperature, and from its magnitude we find E_H, the amount of energy in the hot electrons. Along with actual measurements we can appeal to theoretical predictions, since T_H can be related to laser intensity through particle codes[4] and simple heories.[5] For conditions in which inverse bremsstrahlung absorpton plays only a minor role (high intensity, a short pulse, and a low-Z pusher), E_H has been measured[6] (and theoretically predicted[7]) to be in the range of 25 to 30% of the incident energy (100% of the absorbed energy). For longer-pulse, lower-intensity irradiations we must rely on past experiments[8] and LASNEX simulations which show E_H to be only a few percent of the incident energy.

How does a suprathermal distribution (characterized by T_H and E_H) transport energy through and

deposit energy in a slab of material? What temperature, T_{ev}, does that material reach? Assuming an ideal gas and applying the simplification $A \approx 10\rho$ (valid for glass and gold), we find that

$$T_{ev}(Z+1) \approx 7 \times 10^5\, e(J/cm^3) \ , \qquad (8)$$

where e is the internal energy per unit volume. Taking ionization energy into account would slightly lower T: the ionization state Z can be approximated for gold as $Z \approx 1.6\, T_{ev}^{1/2}$ and for glass as $Z \approx 0.8\, T_{ev}^{1/2}$. To find T we need to know

$$e(x) = \frac{i}{A}\left.\frac{dE}{dx}\right|_{\lambda} \ , \qquad (9)$$

where A is the irradiated area. Thus, finding the preheat temperature at a distance x within a suprathermally bombarded slab requires an expression for dE/dx as a function of x.

We begin by hypothesizing an expression for the average dE/dx,

$$\frac{dE}{dx} = \frac{-E}{\lambda(E)} \ , \qquad (10)$$

where λ is the range[9] of an electron. (This equation is analogous to a conventional energy loss, where λ would be a mean free path along the direction of motion.) For energies between 10 and 100 keV, for solid material,

$$\lambda(E) \approx \lambda_H\left(\frac{E}{T_H}\right)^2 \approx 0.4\left(\frac{T_H}{Z_N}\right)^2\sqrt{Z_N}\left(\frac{E}{T_H}\right)^2 (\mu m) \ . \qquad (11)$$

This expression fits the energy scaling and coefficient presented for aluminum data in Ref. 9. The scaling of the expression with nuclear charge, Z_N, includes the transport effect of multiple-pitch-angle scattering in high-Z material, which changes the direction of the electron without changing its energy. Thus the electron is taking a random walk, scattering randomly Z times before losing its energy to a collision with another electron. This is the origin of $\sqrt{Z_N}$ in Eq. (11), since in a random walk the distance moved is the random step size times the square root of the number of steps.

Substituting Eq. (11) into Eq. (10) yields the Thomson-Whiddington law,

$$E(x) = E_0\left[1 - \left(\frac{2x}{\lambda(E_0)}\right)\right]^{1/2} \ , \qquad (12)$$

which gives the energy of a sample electron (which had energy E_0 at x = 0) as it proceeds through the slab. In order to consider an entire distribution of electrons, we define the following quantities:

$$T_H \equiv \frac{1}{2}(mv_H)^2 \ ,$$

$$f_M(v) \equiv N_H\left(\sqrt{\pi}v_H\right)^{-3}\exp\left[-\left(\frac{v}{v_H}\right)^2\right] \ ,$$

and

$$\langle g(v)\rangle \equiv \int_0^\infty \left(4\pi v_0^2\right) f_M(v_0)\, g(v_0)\, d(v_0) \ ,$$

giving, for $N = N_H$,

$$E_H = \langle E_{Tot}\rangle = \left\langle \frac{mv_0^2}{2}\right\rangle = \left(\frac{3}{2}\right)N_H T_H \ ; \qquad (13)$$

thus, from Eq. (12),

$$\langle E(x)\rangle = \int_0^\infty 4\pi v_0^2 f_M(v_0)\left(\frac{mv_0^2}{2}\right)\left[1 - \left(\frac{2 \times v_H^4}{\lambda_H v_0^4}\right)\right]^{1/2} dv_0 \ . \qquad (14)$$

This gives an expression for the energy at some distance x within the slab when a suprathermal distribution has impinged on the slab at x = 0. For convenience we define $Y \equiv v/v_H$ and $L \equiv 2x/\lambda_H$. Recall from Eq. (9) that we need to know dE/dx, so performing the differentiation of Eq. (14) yields

$$\left\langle\frac{dE}{dx}\right\rangle = \frac{3E_H}{2\lambda_H}\int_{L^{1/4}}^\infty y^2 e^{-y}(y^4 - L)^{-1/2} e^{-y^2} \ . \qquad (15)$$

We have evaluated the integral analytically (using the method of steepest descent) and checked the results numerically. For $1 \leq L \leq 100$, a simple fit to the integral yields the elegant result,

$$\frac{dE}{dx} = \frac{E_H}{(3\lambda_H)\lfloor \log_{10} L} . \qquad (16)$$

For thin samples ($L \ll 1$) the right-hand side should be $E_H/2\lambda_H$. Substituting Eq. (16) into Eq. (9) and then into Eq. (8) yields the final formula

$$T_{ev}(Z+1) \approx \frac{2 \times 10^{-5} E_H(J)}{A(cm^2)\,\lambda_H(cm)\lfloor \log_{10} L} , \qquad (17)$$

where we recall the definitions

$$L = \frac{2x}{\lambda_H} ,$$

$$Z_{glass} \approx 0.8\, T_{ev}^{1/2} ,$$

and

$$\lambda_H = 0.4\left(\frac{T_H}{Z_N}\right)^2 \sqrt{Z_N}\, 10^{-4}\ (cm)$$

Thus, given T_H and E_H we can find T_{ev}. And, as the pressure within the preheated material is, in the ideal gas approximation,

$$P = (0.1)T_{ev}(Z+1)\ MB , \qquad (18)$$

the pressure can be found as well.

Several refinements are required for this theory:

- Suprathermals may be affected by electric fields set up by resistive cold-electron return currents and hence would not transport "classically" as is assumed here.
- The temperature may be increased if suprathermals exiting the cold end of the slab are turned around by sheath potentials and redeposited. On the other hand, the temperature may be decreased since once the material is heated it expands, so that internal energy is converted into hydrodynamic energy, lowering T.
- Theoretical predictions for T_H and E_H must take into account the losses of suprathermals as they reflect off the large corona in the underdense plasma. This effect reduces the original source T_H and E_H to that distribution E_H,T_H that actually deposits in the slab. The experimental measurement, on the other hand, is the actual T_H and E_H depositing in the slab and emitting bremsstrahlung, so that is exactly the relevant E_H and T_H for this calculation.

While the treatment presented here is based on the expression hypothesized in Eq. (10), a more careful treatment has been carried out by Caporaso and Wilson,[10] where the full diffusion equation is solved. The final result there is within 20% of Eq. (17) for $1 \leqslant L \leqslant 100$.

Thus far we have calculated how the inside of a pusher is preheated. As far as preheating the fuel, the reader is referred to Ref. 11, which relates specific internal energy deposited in the pusher to the shock it sends into the fuel as it explodes. Also calculated is the useful fraction f of the absorbed energy [in our case $(f)E_H$] that contributes to the shock heating of the fuel, since as mentioned above the hydromotion (explosion) begins as soon as the material begins to heat up.

Shock Propagation. The other contributor affecting the fuel adiabat is the main shock from the laser-driven ablation process. There are many papers in the literature that relate the ablation pressure, P_A, to the laser and target parameters; the reader may choose his favorite. Given a pressure wave of strength P_A propagating through the pusher, how will the fuel be shocked? Standard hydrodynamic theory[12] predicts that the shock speed effectively doubles as it leaves the heavy pusher and propagates into the cold gas fuel. Strong shock theory relates P to $\rho_0 v_s^2$ so that

$$P_f = 4\rho_f \frac{P_A}{\rho_p} , \qquad (19)$$

where ρ_f and ρ_p are the initial fuel and pusher densities, respectively. Typically $\rho_f = 0.01$ and $\rho_p \approx 2$; thus, the fuel is shocked with a pressure that is 1/50 the pusher pressure. The timing of the shock can be approximated through the strong shock relations

$$v_s^2 = \frac{(\gamma+1)P_A}{2\rho_p} ,$$

$$\Delta t = \frac{\Delta R}{v_s} , \qquad (20)$$

where ΔR is the pusher thickness. The temperature of the post-shock-heated pusher is roughly

$$T_{ev}(Z + 1) = 2.5\ P_A(MB)\ ; \qquad (21)$$

this is the same ideal equation as Eq. (18) except that the density is assumed to be shocked to 4 times its initial density [strong shock theory states that $\rho_s = (\gamma + 1)/(\gamma - 1)\rho_0 = 4\rho_0$ for $\gamma = 5/3$].

Equations (21) and (17) should be compared in practice to get a feel for what sets the adiabat—does the preheat dominate or does the shock?

We have done experiments[13] to measure both preheat and shock at the backs of samples; T_H and E_H were also measured in the experiments. Equation (17) successfully predicted the observed preheat temperatures; Eqs. (20) and (21), along with a reasonable model for P_A, successfully predicted the strength and time of arrival of the shock signals. Comparisons with the LASNEX code were also quite favorable. These successes give us confidence in the validity of our simple theories.

Our ability to calculate the fuel adiabat from given laser and target parameters gives us the first ingredient of a simple implosion model; work on completing the model is under way.

Author: M. D. Rosen

References

4. K. G. Estabrook and W. L. Kruer, "Properties of Resonantly Heated Electron Distributions," *Phys. Rev. Lett.* **40**, 42 (1978).
5. W. L. Kruer, *"Breaking Amplitude in Warm, Inhomogeneous Plasma,"* Lawrence Livermore Laboratory, Livermore, Calif., UCRL-76604 (1977).
6. K. R. Manes, V. C. Rupert, J. M. Auerbach, P. H. Lee, and J. E. Swain, "Polarization and Angular Dependence of 1.06 μm Laser Light Absorption by Planer Plasmas," *Phys. Rev. Lett.* **39**, 281 (1977).
7. J. J. Thomson, W. L. Kruer, A. B. Langdon, C. E. Max, and W. C. Mead, *Theoretical Interpretation of Angle- and Polarization-Dependent Laser Light Absorption Measurements*, Lawrence Livermore Laboratory, Livermore, Calif., UCRL-79628 (1977).
8. M. D. Rosen, D. W. Phillion, V. C. Rupert, W. C. Mead, W. L. Kruer, J. J. Thomson, H. N. Kornblum, V. W. Slivinsky, G. J. Caporaso, M. J. Boyle, and K. G. Tirsell, "The Interaction of 1.06 μm Laser Radiation with High Z Disk Targets," *Phys. Fluids* **22**, 2020 (1979).
9. L. Katz and A. S. Penfold, "Range-Energy Relations for Electrons and the Determination of Beta-Ray End-Point Energies by Absorption," *Rev. Mod. Phys.* **24**, 28 (1952).
10. G. J. Caporaso and S. S. Wilson, *A Simple Model for Suprathermal Electron Deposition in High-Z Plasmas*, Lawrence Livermore Laboratory, Livermore, Calif., UCRL-83308 (1978).
11. M. D. Rosen and J. H. Nuckolls, "Exploding Pusher Performance—A Theoretical Model," *Phys. Fluids* **22**, 1393 (1977).
12. R. Lelevier, *Lectures on Hydrodynamics and Shock Waves*, Lawrence Livermore Laboratory, Livermore, Calif., UCRL-4333 (1965).
13. M. D. Rosen, *Analysis of Long Pulse Physics Experiments at LLL: Late 1977–Early 1979*, Lawrence Livermore Laboratory, Livermore, Calif., UCRL-83022 (1979).

Nuclear Preheat Calculations for Heavy-Ion Fusion

Some of the energetic heavy ions incident on a fusion target will produce nuclear reactions. Typically the velocities of the reaction products are comparable to the velocity of the beam. Thus the energy of a reaction product is roughly proportional to its mass; its charge, Z, is also roughly proportional to its mass and to its energy.

At a given velocity, ion energy loss per unit length is proportional to Z^2. The energy of the beam and reaction-product ions, though, is proportional to Z. Thus the reaction fragments can penetrate more deeply into the target than the beam ions. In some cases these fragments may penetrate into and preheat the fuel; it is therefore important to determine if this preheat is large enough to have a deleterious effect on target performance.

A high-gain, ion-driven target of the type shown in Fig. 3-7 can tolerate a fuel preheat of about 10^4 J/g (Ref. 14). The beam energy required to drive such a target is about 1 MJ per mg of fuel. Thus the fuel can tolerate preheat corresponding to about 1 part in 10^5 of the beam energy. Fortunately, only 1 to 10% of the beam energy arrives early enough to contribute to preheat, so that 1 part in 10^3 to 10^4 of the beam energy can be deposited in the fuel without serious consequences. For more complicated multishell target designs one must also consider preheat in materials other than fuel. For the designs we have considered, the allowable levels are also on order of 10^4 J/g, but in some cases this figure represents the total energy input and not just that arriving in the first 1 to 10% of the pulse.

In order to investigate the nuclear preheat level quantitatively we have written a computer code which calculates the energy deposition of beam ions and nuclear reaction products as a function of

Fig. 3-7. Section of a spherical ion-beam fusion target. Additional details about this type of target are given in the 1976 Annual Report.[14]

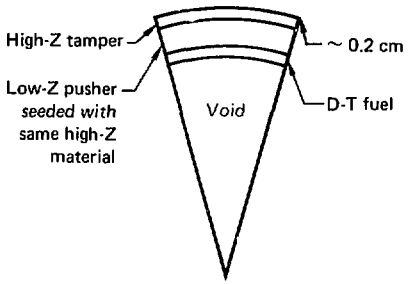

Fig. 3-8. Energy deposition as a function of penetration. The contribution of nuclear debris to energy deposition in the fuel has been multiplied by 10^3 to make it visible. The fuel region extends to 0.2 g/cm^2 in this calculation although it would be much thinner in an actual target.

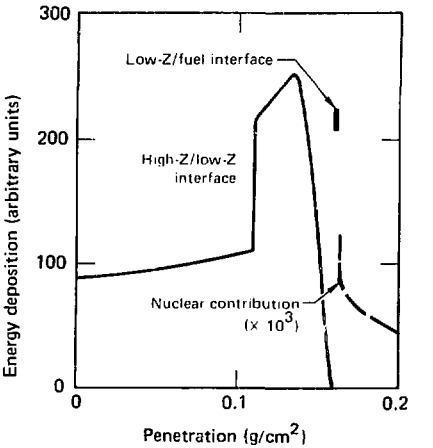

penetration into a planar slab, consisting of layers of different materials to simulate a target. The angular distribution of the incident ions with respect to the normal is chosen to approximate the distribution expected with respect to the sphere radii under plausible assumptions about target radii and beam focusability. Since detailed differential nuclear-reaction cross sections for the multitude of possible fragments are not available at energies of interest for heavy-ion fusion (~1 to 20 GeV), we assume that

- The total cross section is geometric.
- About 20% of the nucleons are emitted as neutrons or isotopes of light elements (H, He, or Li).
- The multiplicity of other nuclear fragments increases slowly with increasing atomic number, with the multiplicity values constrained by baryon conservation.

Thus according to our simple model about 20 light nuclei are emitted per interaction, and the probability of emission of any particular heavier nucleus is on the order of 1%. All fragments are assumed to have the same velocity as the projectile. The use of geometric cross sections is adequate for our purposes,[15] as long as we use an incident ion beam that does not have a large cross section for electromagnetically induced fission.

Figure 3-8 shows the results of a typical calculation for 10-GeV heavy ions incident on a typical high-gain, ion-driven target. Note the jump in deposition at the interface between the high-Z layer and the low-Z layer behind it; the interface between the low-Z layer and the D-T fuel occurs at a penetration of 0.16 g/cm^2. We have ignored statistical range straggling in this calculation because it is not important for calculating nuclear preheat. (We do include straggling in our target design codes.) Because straggling has been ignored, all incident ion beam deposition stops at 0.158 g/cm^2; thus the energy deposition in the fuel represents only the nuclear preheat from the reaction products. The product of density and thickness of the fuel is about 10^{-3} g/cm^2, so we can easily estimate from Fig. 3-8 that the energy deposited in the fuel by nuclear debris is less than 1 part in 10^5 of the total beam energy and is thus too small (by 1 or 2 orders of magnitude) to be significant. It is not possible to construct a multiplicity model that increases the calculated preheat by an order of magnitude without violating baryon conservation.

We conclude that the preheat produced by nuclear reactions of 10-GeV heavy ions is not significant for the target design considered. Preliminary calculations show that this conclusion is also true for multishell targets, and seems likely to be true for nearly all types of targets. To verify this, we plan to extend detailed calculations to a wider

range of ion kinetic energies and targets. The accuracy of our energy-deposition code will be improved by more realistic modeling and by comparison with experimental nuclear data as they become available. Note, however, that while such data are useful for precise target design work, they are not needed to establish the feasibility of heavy-ion fusion.

Author: R. O. Bangerter

References

1. *Laser Program Annual Report—1976*, Lawrence Livermore Laboratory, Livermore, Calif., UCRL-50021-76 (1977), p. 4-44.
2. K. M. DeVries and J. C. Peng, "Nucleus-Nucleus Total Reaction Cross Sections," LASL Preprint, LA-UR-79-3067 (submitted to *Phys. Rev. C*).

Overview: Laser-Plasma Theory and Simulation

In 1979 we continued to address critical laser-plasma coupling issues which impact target design. Particular attention was given to processes which are operative in the large underdense plasmas that characterize reactor targets: hot-electron generation via the Raman and 2-plasmon-decay instabilities, stimulated Brillouin scattering, and self-focusing and filamentation of the laser beam. Based on an examination of options for improving the coupling we chose to undertake experiments with shorter-wavelength laser light, and measurements to date confirm our predictions of improved absorption and reduced hot-electron temperature.

Progress in advancing our understanding of laser-plasma coupling was made in many different areas. The theory of inverse bremsstrahlung was extended to include the self-consistent modification of the velocity distribution of the heated electrons. The classical absorption rate was found to be reduced by a factor of approximately two, by self-consistent modification of the velocity distribution, for many cases of practical interest in high-Z plasmas. Our calculations of electron heating by Raman and 2-plasmon-decay instabilities were extended to include large regions of underdense plasma; we subsequently found a sizable absorption into electrons with a temperature of ~ 50 to 100 keV, provided there is a large region of plasma with a density of about one-fourth the critical density (0.25 n_c). An experimental search for the Raman instability was initiated, and this instability was indeed observed. Further investigations of electron heating via resonance absorption were conducted with simulations of a capacitor model; these simulations allowed us to better assess the effect of the background electron temperature on the temperature of the resonantly-heated electrons, especially in the regime of a severe steepening of the density profile.

Calculations of stimulated Brillouin scattering were given a high priority:

- We developed an improved model for the effect of self-consistent ion heating on the scattering. This model, which focuses on ion-tail formation, compares well with our computer simulations.
- We discovered a possible enhancement of Brillouin scattering by light classically reflected from the critical density surface.
- Our LASNEX model of Brillouin scattering was extended to take into account both ion tail formation and stabilization of the scattering by gradients in the plasma density and expansion velocity. Calculations using this model of the scattering have been very promising, and are currently in at least semi-quantitative agreement with the experiment.
- In addition to calculating intensity profiles for filamented light, we developed a simple model for the effect of filamentation on stimulated Brillouin scattering.

Uncertainties in the plasma conditions and in electron transport continued to receive attention. Hydrodynamic calculations of steady-flow spherical profiles in the presence of electron transport inhibition were found to be in good agreement with a theory we had developed. We examined coronal energy losses into fast ions, and developed an improved description of these losses. The effect of ion turbulence on enhancing the resistivity and reducing the heat transport by electrons was further examined both theoretically and in microwave experiments. Finally, all these developments strongly recommend precise measurements of the plasma conditions in laser-irradiated targets.

Author: W. L. Kruer

Nonlinear Inverse Bremsstrahlung and Heated-Electron Distributions

We have found that when $Zv_0^2/v_e^2 \gtrsim 1$ (where v_0 is the peak velocity of oscillation of the electrons in the high-frequency electric field of the laser, $v_e \equiv (T_e/m_e)^{1/2}$ is the electron thermal velocity, and Z is the ionization state) laser-light absorption in a plasma via inverse bremsstrahlung results in a non-Maxwellian velocity distribution for which the absorption is reduced by up to a factor of two compared to the absorption in a Maxwellian plasma as usually assumed. Transport and atomic processes are also altered. Especially in materials with $Z \gg 1$, but also for $Z = 1$, this is significant at intensities lower than those for which another absorption linearity (analyzed many times before[16-19]) is important, for which the measure is v_0^2/v_e^2. This ratio may be expressed as $v_0^2/v_e^2 = 4 \times 10^{-16}\, I\lambda^2/T_e$, where I is the intensity in W/cm^2, λ is the vacuum wavelength in μm, and T_e is the electron temperature in keV.

Nonlinear inverse bremsstrahlung arises when $Zv_0^2/v_e^2 \gtrsim 1$, as electron-electron (e-e) collisions are not rapid enough to evolve a Maxwellian distribution from the flat-topped velocity distribution produced by inverse bremsstrahlung. Consider the ratio of the e-folding time for electron heating to the e-e equilibration time τ_{ee} required to reestablish a Maxwellian distribution; the ratio is (thermal energy)/$\dot{J}\cdot E = 3\tau_e v_e^2/v_0^2$. We have expressed the absorption[17,20] in terms of v_0 and $\tau_e^{-1} = [4(2\pi)^{1/2}/3]n_e Ze^4 \ln\Lambda\, m_e^2 v_e^3$, the same as the standard Maxwell-weighted e-i scattering rate[21,22] (except for a small modification[20] to $\ln\Lambda$). The heating time is shorter than τ_{ee} ($\cong \tau_e/Z$) when $Zv_0^2/v_e^2 \gtrsim 3$, in which case non-Maxwellian distributions are possible.

In computer modeling of experiments in which inverse bremsstrahlung is thought to be the dominant absorption mechanism, agreement with experimental data often requires that we invoke mechanisms which reduce absorption. Perhaps the effect described here has such a role in experiments on high-Z-doped glass disks.[23] In these experiments, with intensities of $\sim 10^{14}$ W/cm^2 at wavelength 1.06 μm, electron temperatures of ~400 eV and $Z \sim 10$ ("a conservative choice tending not to overestimate absorption"[23]), we find $v_0^2/v_e^2 \cong 0.1$, so the conventional nonlinearity[16-19] makes only a 1.5% reduction in opacity. Since $Zv_0^2/v_e^2 \cong 1$, however, the nonlinearity described here results in a 40% reduction, comparable to other refinements[23] invoked to improve agreement with experiment. The reduction in opacity found here has also been helpful in recent modeling of high-Z disks (see "High-Z Disk Modeling" earlier in this section).

We derive the equation of evolution of the electron distribution function, f, due to e-i scattering in the presence of an oscillating electric field. For $h\nu \ll T_e$, there is good agreement between quantum and classical descriptions[17,19] except for modifications to $\ln\Lambda$, so for clarity we use a simple classical model.[18,22] Assuming uniform density and field, the kinetic equation is

$$\frac{\partial f}{\partial t} - \frac{e}{m_e}\,\underset{\sim}{E}\cdot\frac{\partial f}{\partial \underset{\sim}{v}} = A\frac{\partial}{\partial \underset{\sim}{v}}\cdot\left[\frac{v^2\,\underset{\sim}{1} - \underset{\sim}{vv}}{v^3}\cdot\frac{\partial f}{\partial \underset{\sim}{v}}\right] + C_{ee}(f) \quad , \qquad (22)$$

where $A = (2\, n_e Z e^4\, m_e^2)\ln\Lambda$ in the usual notation; C_{ee} is the e-e collision operator. Expansion in Legendre functions, $f(\underset{\sim}{v},t) = \Sigma f_l(v,t)P_l(\mu)$, simplifies the e-i collision operator. The first two equations in the expansion of Eq. (22) are

$$\frac{\partial f_0}{\partial t} - \frac{eE}{m_e}\frac{1}{3v^2}\frac{\partial}{\partial v}\left(v^2 f_1\right) = C_0 \qquad (23)$$

and

$$\frac{\partial f_1}{\partial t} - \frac{eE}{m_e}\left[\frac{\partial f_0}{\partial v} + \frac{2}{5v^3}\frac{\partial}{\partial v}\left(v^3 f_2\right)\right] = -\frac{2A}{v^3}f_1 + C_1 \quad , \qquad (24)$$

where $eE(t)/m\omega = v_0 \cos\omega t$. We have truncated the expansion by neglecting f_2; this implies $v_0^2/v_e^2 \ll 1$. But the effects of $v_0^2 > v_e^2$ for a Maxwellian distribution have been discussed extensively, and since our purpose is to demonstrate modifications that are possible even when $v_0^2 \ll v_e^2$, we are justified in making this simplification.

At intensities of $\sim 10^{14}$ the time-dependence of f_1 is predominantly at the high frequency ω; it is the slow variation of f_0 which is relevant. C_0 is evaluated using only f_0 (Ref. 22, Eq. 7-71b). As e-e collisions do not much affect the oscillating flux f_1, except indirectly through the slow variation of f_0, we drop C_1. We thus obtain

$$\underline{E}\cdot\underline{J} = \frac{4}{3} A\, n_e m_e v_0^2 \int_0^\infty dv\, g \frac{\partial f_0}{\partial v} \qquad (25)$$

$$\frac{4\pi}{3} A\, n_e m_e v_0^2 \int_0^\infty dv \frac{\partial g}{\partial v} f_0$$

and

$$\frac{\partial f_0}{\partial t} = \frac{A v_0^2}{3} \frac{1}{v^2} \frac{\partial}{\partial v}\left(g \frac{\partial f_0}{\partial v}\right) + C(f_0) \qquad (26)$$

with

$$g(v) = \left[1 + \omega^2 \tau_{ei}^2(v)\right]^{-1} \left(1 + \frac{v^6}{v_\omega^6}\right)^{-1} \qquad (27)$$

where $\tau_{ei}^{-1}(v) \equiv 2A/v^3$ is the electron scattering rate and v_ω is defined by $\omega\tau_{ei}(v_\omega) = 1$. The rate of change of kinetic energy calculated from Eq. (26) is consistent with the absorption in Eq. (25).

The function g accounts for the changeover from the primarily reactive response of the faster electrons to the resistive response of the slow, strongly scattered electrons. Usually, collisions are treated as a perturbation on the oscillation of the entire distribution,[16-20] i.e., $\omega\tau_{ei} \gg 1$ for all electrons; so $g \equiv 1$ and, from Eq. (26), absorption is $\alpha f_0(v = 0)$ for $v_0 \, v_e \to 0$. For Maxwellian f_0, this leads to the standard linear absorption result.[16,17,20,22] Here, we see that absorption is αf_0, evaluated where g increases rapidly from $\cong 0$ to $\cong 1$, i.e., at the velocity v_ω for which scattering and light frequencies are matched, $\omega\tau_{ei}(v_\omega) \cong 1$. Since $v_\omega \ll v_e$ in cases of interest, the absorption is little changed by this correction.[24]

Numerical solutions illustrate the evolution of f_0 and its effect on absorption and other macroscopic properties. We use a numerical scheme similar to one in Ref. 25, in which the Fokker–Planck coefficients are calculated from f_0 without linearization, except that the energy consistency between the finite difference forms of Eqs. (25) and (26) is preserved, and the rapidly decreasing "tail" of the distribution is correctly represented (at least in thermal equilibrium); both properties are independent of the spacing of the velocity zones, which are larger at higher velocities.

We consider first the effect of inverse bremsstrahlung alone, corresponding to the limit $Z v_0^2 / v_e^2 \gg 1$. An initially monoenergetic distribution diffuses and slows in balance so that no net gain in kinetic energy results [curve (a) in Fig. 3-9]. When electrons reach low velocities [such that $\omega\tau_{ei}(v) \gtrsim 1$] their loss of energy is slowed while upward diffusion of faster particles continues, so net absorption begins. This is the meaning of the result that the absorption rate depends on f_0 at $v \cong v_\omega$. By the time the electons have gained only 10% in energy [curve (b) in Fig. 3-9], f_0 is close to its late-time form, described by a similarity solution of the form $u^{-3} \exp(-v^5/5u^5)$, with $u^5 = 5Av_0^2 t/6$, which is derived from Eq. (26) with $g \equiv 1$. For this distribution, the

Fig. 3-9. Evolution of an initially monoenergetic distribution f_0 due to e-i collisions in the presence of an oscillating field; e-e collisions are neglected corresponding to large Zv_0^2/v_e^2. The initial velocity, indicated by the dashed line, is 5.8 v_ω. At first, electrons diffuse both up and down in balance so that f_0 evolves greatly before it gains only 1% in energy (a). Thereafter, the slowest electrons cannot lose more energy, while others continue to diffuse upward, resulting in net absorption. When the energy has increased by 10% (b), f_0 is close to the self-similar solution (c), which is normalized to the same energy as (b). Both axes are linear. A change in initial velocity or in the constant A scales the times corresponding to curves (a)-(c), but does not alter their shape.

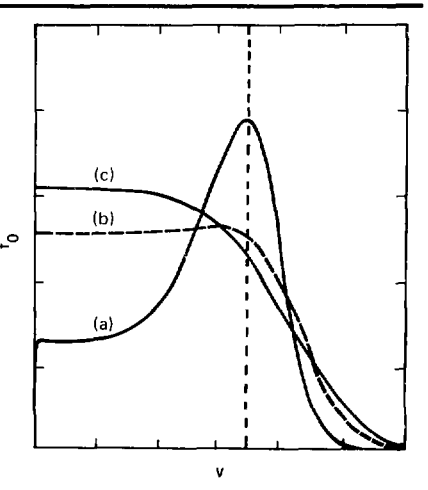

absorption is only 45% of what it would be if electron–electron collisions enforced a Maxwellian distribution.

For $\alpha = Z v_0^2 v_e^2 \gtrsim 1$, e–e collisions alter the results only slightly. For example, with $\alpha = 6$ the absorption is still only 49% of its Maxwellian value, and inverse bremsstrahlung contributes equally with e–e collisions to diffusion of suprathermals into the "tail" of the distribution. With $\alpha = 0.5$, the distribution is still depressed and flattened near $v = 0$ (Fig. 3-10), and absorption is reduced to 67% of normal. When α is only 0.05 the reduction is 12%. For any α, the reduction factor is $1 - 0.553\,[1 + (0.27\ \alpha)^{0.75}]$ within ±0.005; see also Fig. 3-11.

Full quantitative evaluation of this effect requires incorporation of spatial gradients and transport. In turn, the transport itself, and the degree of ionization, Z, are themselves affected by these distributions. Heat conductivity and collisional ionization are determined mainly by the tail of the distribution, which is truncated here. On the other hand, atomic recombination is affected by the slow electrons where our distributions are also deficient compared to a Maxwellian. Enhanced ion fluctuations (above thermal level) act similarly to the high-Z condition in increasing the absorption rate relative to the e–e collision rate[26]; therefore, non-Maxwellian distributions again result, although with a different dependence than discussed here. Finally, we note that the nonlinear results in Refs. 16 to 19 appear to be inapplicable to *any* intensity or ionization state, because for $v_0^2 v_e^2 \gtrsim 1$ we find a much larger effect than they do, while for $v_0^2 v_e^2 \gtrsim 1$ the oscillating electron distribution is not even isotropic, much less Maxwellian as they assume. A correct treatment of the latter situation remains to be done.

Fig. 3-10. Distributions corresponding to various values of Zv_0^2/v_e^2, where $v_e^2 \equiv \langle v^2 \rangle/3$. These are of course not steady-state, but are distributions plotted as Zv_0^2/v_e^2 decreases through specified values while the plasma heats up from a much lower temperature. $Zv_0^2/v_e^2 \gg 1$ corresponds to the self-similar solution, and $Zv_0^2/v_e^2 \ll 1$ is Maxwellian.

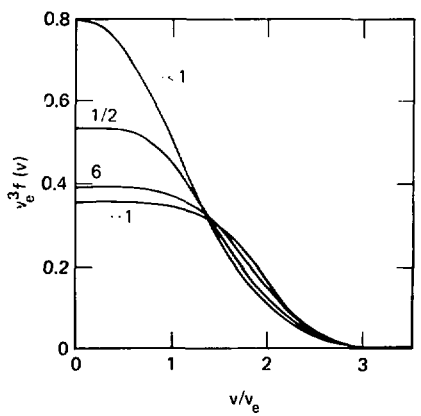

Fig. 3-11. Comparison of reduction in opacity by the nonlinear mechanisms of (a) this article, and (b) of Refs. 16-19. The abscissa of (b) is normalized to correspond to (a) for Z = 1 and equal light intensity in circular polarization. If Z > 1, (b) would remain closer to 1. Thus, for any Z and $v_0^2/v_e^2 \leq 1$, the mechanism of this article dominates.

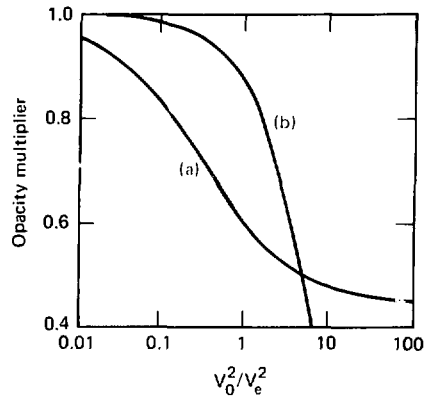

Author: A. B. Langdon

References

16. V. P. Silin, *Zh. Eksp. Teor. Fiz.* **47**, 2254 (1964); *Sov. Phys.–JETP* **20**, 1510 (1965).
17. R. J. Kidder, in *Physics of High Energy Density* (New York: Academic Press, 1971), p. 306.
18. P. J. Catto and T. Speziale, *Phys. Fluids* **20**, 167 (1977).
19. For recent results and listings of earlier work see Y. Shima and H. Yatom, *Phys. Rev. A* **12**, 2106 (1975); H. Brysk, *J. Phys. A* **8**, 1260 (1975); I. Schlessinger and J. Wright, *Phys. Rev. A* **20**, 1934 (1979).
20. J. Dawson and C. Oberman, *Phys. Fluids* **5**, 517 (1962); T. W. Johnston and J. M. Dawson, *Phys. Fluids* **16**, 722 (1973).

21. S. I. Braginskii, in *Reviews of Plasma Physics*, M. A. Leontovich, Ed. (New York: Consultants Bureau, 1965), vol. 1, p. 205.
22. I. P. Shkarofsky, T. W. Johnston, and M. P. Bachynski, *The Particle Kinetics of Plasmas* (Reading, Mass: Addison-Wesley, 1966).
23. H. D. Shay et al., *Phys. Fluids* **21**, 1634 (1978).
24. B. A. Trubnikov, in *Reviews of Plasma Physics*, p. 174.
25. J. Killeen, A. A. Mirin, and M. E. Rensink, in *Methods in Computational Physics*, J. Killeen, Ed. (Academic Press, New York), vol. 16 (1976). B. Alder, S. Fernbach, and M. Rotenberg, Eds., p. 389.
26. J. Dawson and C. Oberman, *Phys. Fluids* **6**, 394 (1963).

Resonant Absorption

Because the dominant laser-plasma coupling mechanisms are enhanced in the relatively thin critical-density layer, it is essential to develop a self-consistent description of the dynamics there. Here we show that even weak resonant absorption[27] acts strongly upon the hydrodynamic evolution of this region, so as to enhance resonant absorption and suppress other mechanisms. The coronal rarefaction exhibits a step in density including critical and hot plasma below the subcritical density at which the flow emerges from the step.

Driven resonant electron oscillations transfer absorbed energy to the plasma via wavebreaking, ejecting particles toward low density.[27] These hot collisionless electrons are confined by the electrostatic potential, and subsequently pose two challenges to laser (inertial confinement) fusion:

- To prevent them from preheating the target.
- To use their associated energy to drive the implosion.

Recent theoretical work[28,29] describes the scaling of hot-electron temperature in the high-intensity regime: briefly, the laser beam or driven wave steepens the density profile from estimates based on the usual coronal rarefaction and thereby slows the increase of the hot-electron temperature with increasing laser intensity. Here we present new and improved scaling laws for the temperature of hot electrons produced by resonant absorption in the modest-intensity regime; we define the modest-intensity regime as that in which the driven wave pressure dominates the laser radiation pressure. We can thus justifiably neglect electromagnetism, as the laser's primary contribution to the system is energy, while in the high-intensity regime it contributes both energy and momentum.

We have derived our results from a study performed with the one-dimensional electrostatic particle simulation code ES1,[30] with which we investigated the scaling of energy, momentum, and charge balance of resonant electron oscillations in driven expanding plasmas. Our simulation code evolves the dynamics of an initially uniform slab of electrons and ions which expand into the vacuum under the influence of a high-frequency pump: the pump strength is independent of position in the critical region. This is the familiar infinite-wavelength or capacitor model.[27] The pump frequency is chosen to be well below the plasma frequency of the initial slab. By mapping the hot-electron heating rate onto absorbed laser intensity we can cast our results into a form useful for laboratory application and comparison to electromagnetic simulations.

Analysis. The critical-density region and driven resonant wave are illustrated in Fig. 3-12. Momentum balance on the underdense side of critical is established by the wave pressure and the reaction pressure of electrons ejected toward the vacuum. In other words, the saturated energy density of the wave is just that which balances the momentum flux of the ejected hot electrons, such that $E^2/8\pi \sim (\pi/2)^{1/2} f I/v_H$. Here f is the absorption fraction of laser intensity I into hot electrons of velocity $v_H \sim (T_H/m)^{1/2}$, and the factor $(\pi/2)^{1/2}$ results from employing a half-Maxwellian distribution in computing the hot-electron momentum flux in terms of its energy flux. The momentum flux of the hot electrons exceeds that of the laser radiation whenever $(\pi/2)^{1/2} f I/v_H > (2-f) I/C$, or

$$(T_H)_{\text{modest}} < \left(511\frac{\pi}{2}\right)\frac{f^2}{(2-f)^2}\ (\text{keV}) . \qquad (28)$$

Experience indicates that 0.3 is a useful estimate for f; Eq. (28) then becomes $T_H < 25$ keV. Evidently the modest-intensity regime in the laboratory[31] is $I(W/cm^2)\lambda^2(\mu)|_{\text{modest}} < 10^{16}$.

Momentum balance on the overdense side of critical is established by the background cold-electron pressure and the wave pressure. Thus $-\nabla(nT_C) \sim -\nabla(E^2/8\pi) \sim -\nabla[(\pi/2)^{1/2} f I/v_H]$, so that by crude integration we can estimate the upper density associated with resonant absorption, n_u^*, to be

$$\frac{n_u^*}{n_c} \sim 1 + \left(\frac{\pi}{2}\right)^{1/2} \frac{fI}{n_c T_C v_H} \qquad (29)$$

For the experimental parameters of Ref. 32 this steepening is more than three times that associated with the radiation pressure.

In general the radiation pressure contribution should be included in estimating the upper density. An upper density greater than that given in Eq. (29), however, should not be expected to change the dynamics of the driven resonant wave qualitatively from what is described here. The longer scale length ($\sim c\ \omega_p$) over which the radiation pressure acts suggests a doubly stepped profile in which the resonant wave dominates locally but for which the maximum density is given by radiation pressure. In this situation our results may be extended to the high-intensity regime.

Driven systems are characterized by the single dimensionless parameter, $v_0\ v_C$. This is the ratio of the jitter velocity of an electron oscillating freely in the pump field, $v_0 = eE_0\ m\omega_0$, and the initial (cold) electron thermal velocity, $v_C = (T_C\ m)^{1/2}$. The space and time scales of the rarefaction and driven resonant wave are determined self-consistently.

Our principal results are the variation with $v_0\ v_C$ of the hot-electron temperature, the heating rate, and the densities delimiting the step. In general the stepped density profile dominates our results, and while a description of the system in terms of a single scale length is not a failure for certain purposes, it is not appropriate. Even for $v_0\ v_C$ less than $(m\ M)^{1/2} \sim 1/30$ we find that wavebreaking governs the system: convection, soliton formation, etc. have never been seen.

In Fig. 3-13, the normalized hot-electron temperature, $T_H\ T_C$, and the normalized hot-electron heating rate, $Q_H\ n_c T_C v_C$, are plotted against $v_0\ v_C$. Note the break in the data at $v_0\ v_C \sim 1$. Cold-plasma modeling is appropriate for $v_0\ v_C > 1$, while $v_0\ v_C < 1$ is the warm-plasma regime.

To identify the hot-electron heating rate with absorbed laser intensity, we begin with $Q_H\ n_c T_C v_C$ and $T_H\ T_C$ as functions of $v_0\ v_C$; we identify $Q_H = fI$, and eliminate $v_0\ v_C$ to obtain the data displayed in Fig. 3-14. Note the role played by the background temperature as $T_H\ T_C$ varies against $fI(W\ cm^{-2})\lambda^2(\mu)\ T_C^{-3/2}(eV)$. The break in the scaling is clearly evident. In the warm-plasma limit, $fI\lambda^2\ T_C^{-3/2} \gtrsim 10^{11}$, curves 1 and 2 have slopes of 2/5

Fig. 3-12. In the critical-density region the driven resonant wave supports itself against the background plasma pressure on the overdense side by the reaction pressure associated with the momentum flux of hot electrons ejected toward the underdense side. The curves are simulation data for $v_0/v_e = 1$ at $t \simeq 1200/\omega_0$; $\omega_0 = \omega p_{max}/\sqrt{5}$.

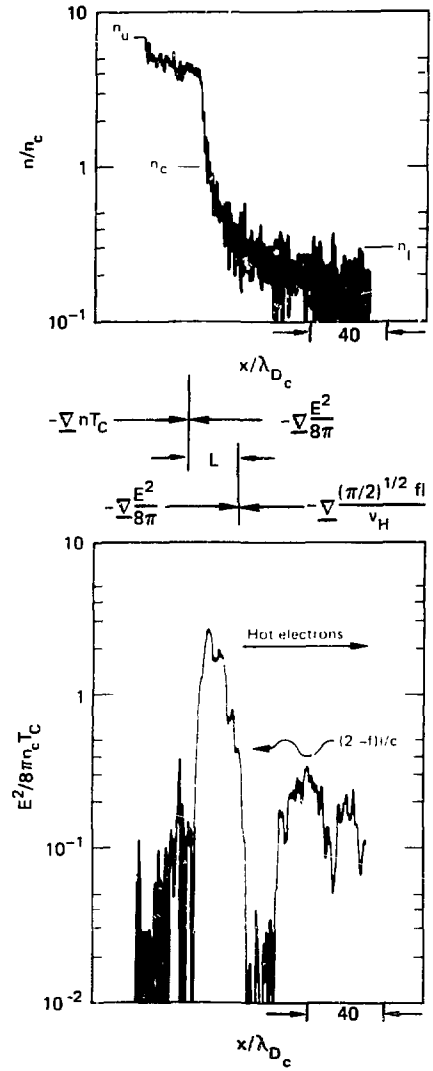

Fig. 3-13. The hot-electron temperature, T_H, and the hot-electron heating rate, Q_H, increase with increasing pump strength, v_0. Note the break in the scaling at $v_0/v_c \simeq 1$ which separates the regimes of warm-plasma dynamics, $v_0/v_c < 1$, and cold-plasma dynamics, $v_0/v_c > 1$. The points plotted at $v_0/v_c = 1$ are runs of the same physical system with different pump frequencies. The difference in results there represents the uncertainty of our results throughout.

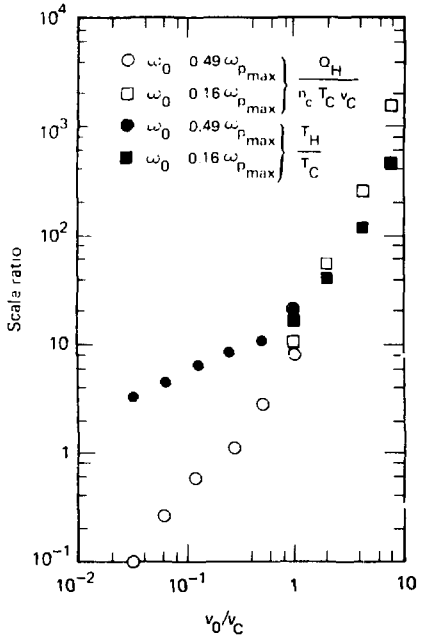

and 1/3, respectively. Curve 1 yields the preferred scaling, $T_H(eV) \sim 9 \times 10^{-4} (I\lambda^2 T_C)^{2/5}$, which compares favorably with that given in Ref. 29; still within confidence limits, curve 2 yields $T_H \sim 4 \times 10^{-3} (I\lambda^2)^{1/3} T_C^{1/2}$, which compares favorably with the scaling given in Ref. 28. Note that the scaling with cold background temperature is as strong as that with intensity. The cold-plasma limit given in Ref. 33 is recovered for $I\lambda^2 T_C^{3/2} \gtrsim 10^{11}$, where $T_H \sim 9 \times 10^{-7} (I\lambda^2)^{2/3}$, independent of T_C.

Comparison of our results with the data of Giovanelli[31] suggests that the interaction in the laboratory is governed by cold-plasma dynamics for $I\lambda^2 < 10^{15}$ where the 2/3 power obtains, and by warm-plasma dynamics for $I\lambda^2 > 10^{15}$ where the 2/5 or 1/3 power obtains.

The 2/3-power scaling of hot-electron temperature was suggested previously by flux-limit and stochastic-heating estimates.[34] We have confirmed the 2/3-power scaling here via cold-plasma estimates for resonant absorption:

- Wavebreaking occurs when electrons oscillate in the wave with a velocity, $v_e \sim eE/m\omega$, which scales with the effective phase velocity of the wave $v_e \propto v_p \sim I$. (2π ω). The hot-electron temperature scales with the energy an electron can gain in riding the wave across the resonant region, $T_H \propto eEL$.
- Combining these we find $E^2/8\pi \sim n_c T_H$ 4π; recall that momentum balance on the underdense side of the wave requires $E^2/8\pi \sim (\pi/2)^{1/2}$ I/v_H.
- Combining again yields $T_H \propto (I\lambda^2)^{2/3}$, exactly the desired result.

Finally, Fig. 3-15 shows the relative upper and lower densities bounding the step at critical density, n_u/n_c and n_l/n_c respectively, as functions of $I\lambda^2 T_C^{3/2}$; the estimated upper density, n_u^*/n_c from Eq. (29), is also plotted. The width of the step region decreases from some 25 local (cold) Debye lengths at $I\lambda^2 T_C^{3/2} \sim 10^9$ to about 1 as $I\lambda^2 T_C^{3/2}$ exceeds 10^{11}. Typical values of the lower density are seen to be less than half critical. The agreement of the estimated upper density is quite good, except for the strongest pumps; neglect of the flow contribution to momentum balance in the step region[27] may be the major source of error.

Summary. We have shown that the dependence of hot-electron temperature upon background cold-electron temperature is as strong as the dependence upon laser intensity. We have also shown that the self-consistent coronal rarefaction, including resonant absorption, exhibits a stepped density profile. We have demonstrated an equilibrium in which the driven resonant wave supports itself against the background plasma pressure by the momentum flux of ejected hot electrons. This demonstration provides a first-principles model of profile modification in the modest-intensity regime, as the local reaction of the flow to the momentum deposited at the critical density surface by hot-electron production. The upper density of the stepped density profile may be much greater than critical density,

Fig. 3-14. Identi… …a heating by hot electron production, Q_H, with absorbed laser intensity, fI. The two curves in Fig. 3-13 are combined to obta… …ing of hot-electron temperature with the laboratory observables f, I (W/cm^2), λ^2 (μ), and T_C (eV). Curve 1 with slope 2/5, c… with slope 1/3, and curve 3 with slope 2/3 are discussed in the text.

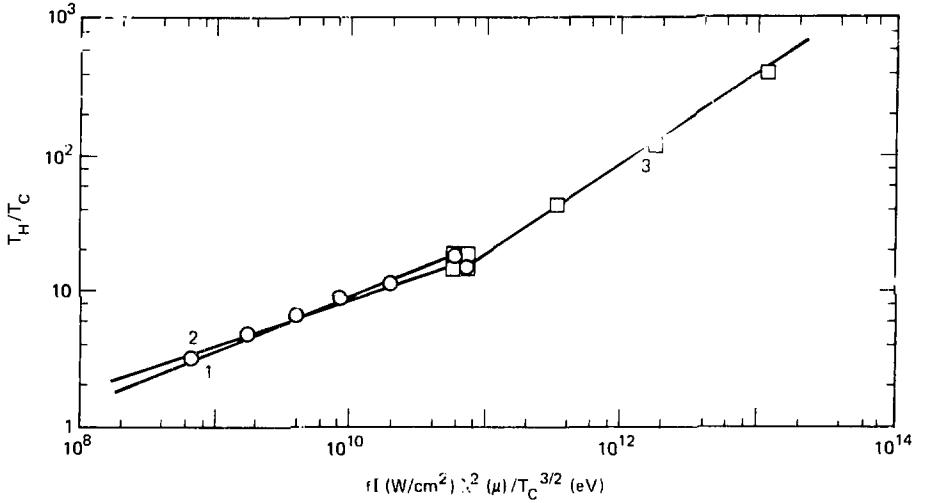

Fig. 3-15. The upper, n_u, and lower, n_l, densities delimiting the step at critical density, n_c, increase and decrease respectively with increasing pump strength. The estimated upper density, n_u^* of Eq. (29), is in agreement with observations except in the most strongly driven systems.

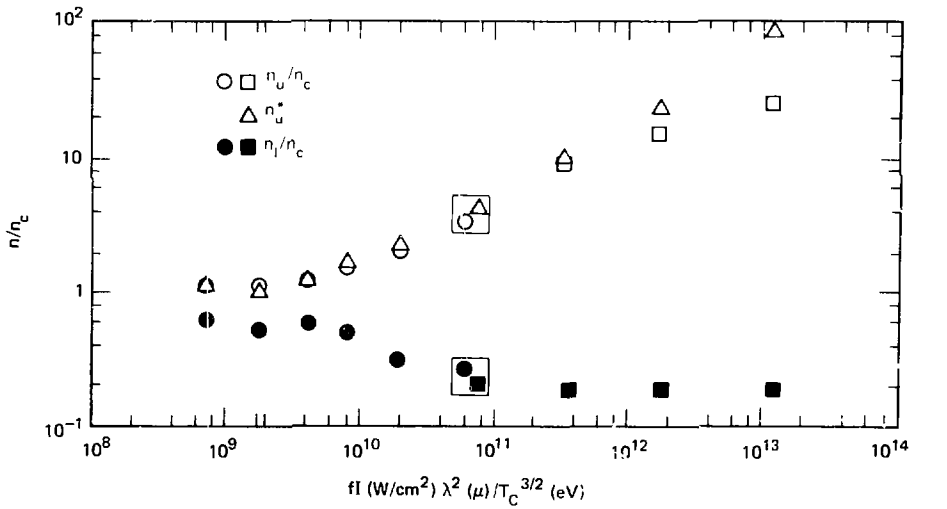

and much greater than that associated with radiation pressure steepening; experimental observations of such structures have been reported recently.[32] The associated lower density and the absence of a turning region with $L/\lambda_0 > 1$ act to reduce the effects of parametric instabilities, classical collisions, and enhanced turbulence. The jump in electrostatic potential associated with the density jump contributes to the formation of a hot corona.

Authors: J. R. Albritton and A. B. Langdon

References

- J. P. Friedberg, R. W. Mitchell, R. L. Morse, and L. I. Rudsinski, *Phys. Rev. Lett.* **28**, 795 (1972); P. Koch and J. R. Albritton, *Phys. Rev. Lett.* **32**, 1420 (1974) and *Phys. Fluids* **18**, 1136 (1975); K. Estabrook, E. J. Valeo, and W. L. Kruer, *Phys. Lett. A* **49**, 109 (1974) and *Phys. Fluids* **18**, 1151 (1975).
- D. W. Forslund, J. M. Kindel, and K. Lee, *Phys. Rev. Lett.* **39**, 284 (1977).
- K. Estabrook and W. L. Kruer, *Phys. Rev. Lett.* **40**, 42 (1978).
- C. K. Birdsall and A. B. Langdon, *Plasma Physics via Computer Simulation* (University of California Press, Berkeley and Los Angeles, 1975).
- R. Fedosejevs, M. D. J. Burgess, G. D. Enright, and M. C. Richardson, *Phys. Rev. Lett.* **43**, 1664, (1979).
- D. V. Giovanelli, LA-UR 76-2242 (1976); K. R. Manes et al., *J. Opt. Soc. Am.*, **67**, 717 (1977).
- J. R. Albritton, E. I. Thorsos, and E. A. Williams, Laboratory for Laser Energetics, Rochester, N.Y., LLE Rept. No. 85 (1978).
- R. L. Morse and C. W. Nielson, *Phys. Fluids* **16**, 909 (1973).
- D. W. Forslund, J. M. Kindel, K. Lee, and E. L. Lindman, *Phys. Rev. Lett.* **36**, 35 (1976).

Heating by the Raman Instability

Stimulated Raman scattering is the parametric decay of an incident photon into a scattered photon plus a longtitudinal electron-plasma wave (epw). The net gain scales with $I(\lambda_0/1.06\,\mu m)^2 \ell/\lambda_0$, where I is the laser intensity (W/cm^2), ℓ is the length of the underdense plasma in the decay region, and λ_0 is the laser wavelength; thus the process can be quite significant for the long scale lengths expected in reactor targets. The frequency matching conditions are $\omega_0 \rightarrow \omega_r + \omega_e$, where ω_0 and ω_r are the angular frequencies of the incident and reflected light waves, respectively, and ω_e is the frequency of the electron-plasma wave. As can be seen from the frequency matching condition, this process can occur for densities $\leq 0.25\, n_c$, where n_c is critical density.

Raman scattering is a resonant, absolute instability for $n \approx 0.25\, n_c$, and occurs most efficiently at that density (with reflection and absorption up to 50%). As the density decreases, the epw wavelength λ_e becomes shorter with respect to the laser wavelength and in particular with respect to the Debye length $\lambda_D = [T_e/(4\pi n_e^2)]^{1/2}$. The electron Landau damping becomes considerable for $\lambda_e \gtrsim 10\lambda_D$, which occurs for high electron temperatures and low densities [$n_c/n\ T_e(keV) \gtrsim 30$, where T_e is the electron temperature]. Here the instability is a variation of Raman scattering called stimulated Compton scattering. There is also an intermediate regime for densities between about 0.1 and 0.25 (depending on T_i) for which the instability is convective, moderately damped, and can still absorb and scatter a significant amount of light.

Since ω_e is much greater than the frequency of an ion sound wave, the Raman instability absorbs much more than Brillouin scattering, but that absorption is typically into fast electrons which can preheat a pellet core.

Theoretical Estimates of Raman Scattering. Kinetic simulations show a rapid evolution of the electron distribution function into the nonlinear state in which the electron distribution is composed of a cold thermal Maxwellian plus a self-consistent tail of heated electrons[36–38], which in turn damps the plasma wave. The characteristic temperature T_{Hot} of this tail is found from the simulations to be about $(m_e/2)v_p^2$, where v_p is the phase velocity of the epw. The electron density of the tail is determined by balancing the energy absorbed by electrons via the damped plasma wave with the heat flux carried off by the electron tail. The epw damping is then estimated from the rate of Landau damping by the heated electrons. This simple model is completed by computing the reflection from the damped plasma wave. The analysis is just like that for the reflection due to a damped ion wave,[39] and results in an analogous expression for the reflectivity:

$$\Lambda(1-\Lambda) = B\left\{\exp\left[\chi(1-\Lambda)\right] - \Lambda\right\}, \qquad (30)$$

where

$$\Lambda = \frac{\omega_0}{\omega_r} r$$

Fig. 3-16. Reflection due to Raman instability as a function (a) of the density and (b) background temperature. The solid lines are the theoretical estimate for noise level $B = 3 \times 10^{-4}$ and the circles are the simulation results for $I(\lambda_0/1.06\ \mu m)^2 = 2.5 \times 10^{15}$, $M_i/m_e = 100$, $\bar{Z}T_e/T_i = 5$, $\ell/\lambda_0 = 127$.

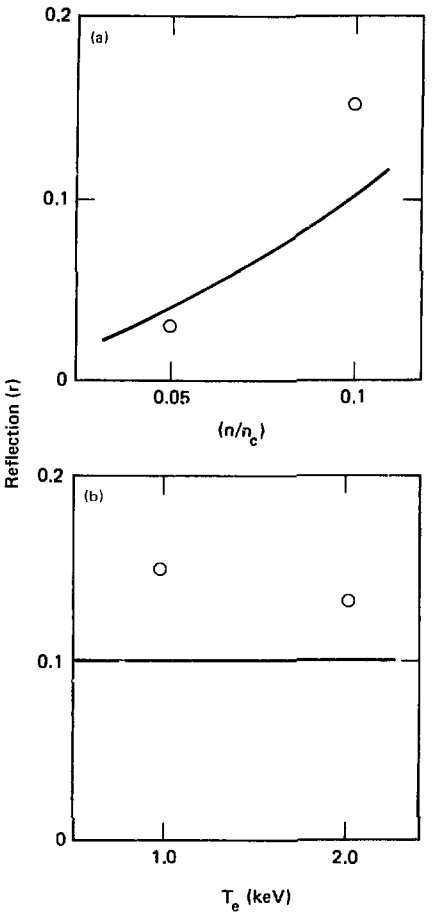

and

$$x = \frac{k_p^2 \ell}{8k_r}\left(\frac{v_{osc}}{c}\right)^2\left(\frac{\omega_{pe}}{\gamma}\right).$$

Here r is the fraction of light reflected, k_p and k_r are the wave numbers of the plasma wave and reflected light wave, respectively, γ is the Landau damping rate, c is the velocity of light, v_{osc} is the oscillation velocity of an electron in the electric field of the incident light wave $\alpha\lambda_0\sqrt{I}$, and B is the initial noise level of the reflected transverse wave.

Our theoretical estimates of the Raman reflectivity are compared with sample simulation results in Fig. 3-16. In these simulations a particle code was used to propagate the laser light through a uniform region of low-density plasma. Note that the variation with background density and temperature of the computed Raman reflectivity of order 10% is in reasonable agreement with the simple model. Note also that rather large regions of plasma are needed to give a significant reflectivity, even neglecting the effect of gradients which are especially significant for Raman scattering. Hence it is not surprising the Raman scattering has only recently been observed in our experiments.

Hot Electrons. Figure 3-17 shows the hot-electron distribution observed in a sample computer simulation. Note the high-energy electron tail which is generated by the electron-plasma wave as it damps. This tail is roughly Maxwellian in shape and has a characteristic temperature of 1.5 keV. As a first approximation, this temperature is independent of intensity, and depends mainly on the density and background temperature which determine the phase velocity of the Raman-generated plasma wave. This hot temperature is approximately

Fig. 3-17. Particle number vs energy, showing the Maxwellian nature of the Raman-heated electrons.

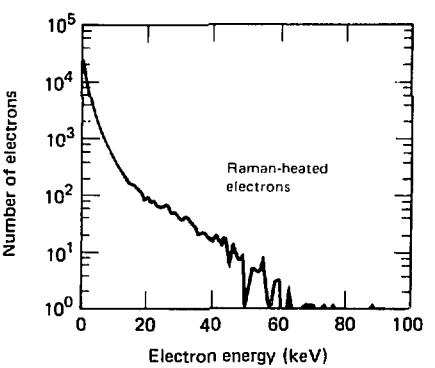

Fig. 3-18. Raman-heated electron temperature, and scattered light frequency vs plasma density. The boxes are simulation results and the fraction of the light absorbed is next to the box.

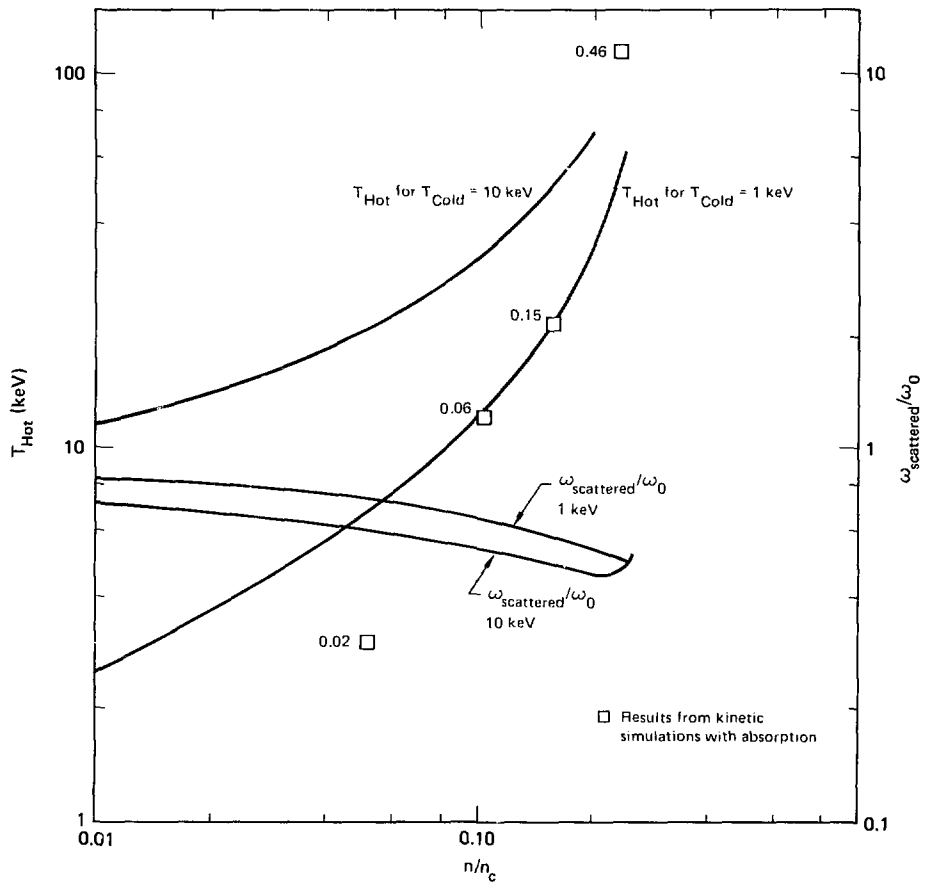

$(m_e/2)v_p^2$. Figure 3-18 plots the hot-electron temperature vs background density for two background temperatures; the theory is described in Ref. 37.

The density gradient threshold of Raman scattering is determined by balancing the growth rate and the convective loss of the electron-plasma wave with the scattered electromagnetic wave across a mismatch length.[40] The threshold is given at 0.25 n_c by $l(\lambda_0/1.06\ \mu m)^2/10^{16} \gtrsim 35\ (\lambda_0/L)^{4/3}\ \alpha\lambda_0^{0.7}$, where $L = (1/n\ dn/dx)^{-1}$. Raman is in natural competition with inverse bremsstrahlung and it is interesting to calculate the inverse bremsstrahlung absorption before the light reaches 0.25 n_c. In a linear density gradient, the e-folding absorption length from $n/n_c = 0$ to 1/4 is $\sim 1.5 \times 10^4 \lambda_{0\mu}^2 T_e^{3/2}(keV)/Z$, where $\lambda_{0\mu}$ is the vacuum wavelength in micrometers. In the free-streaming flux limit, $T_e(keV) = (l\lambda_{0\mu}^2/5 \times 10^{13})^{2/3}$; *this is faster than the* $\lambda_{0\mu}^{0.7-0.7}$ *scaling* from LASNEX (see "High-Z Disk Modeling" earlier in this section). We can now put the absorption length into the density gradient threshold with

the temperature scaling to estimate the intensity for which Raman marginally occurs: $I > 7 \times 10^{12} \bar{Z}^{4/7}/\lambda_{0\mu}^{18/7}$; *for* $\bar{Z} = 40$ *and* $\lambda_{0\mu} = 1$, *the intensity is* 5×10^{13}.

Raman absorption decreases with a large bandwidth, as shown in Fig. 3-19. The bandwidth was chosen to be the same as is projected for an experiment on Cyclops: seven lines of equal intensity separated by 6%, for a total width of 36%. When the growth rate is less than the line separation, we expect each line to behave independently. The linear growth rate at 0.25 n_c was 0.06 ω_0, which is about equal to the line width for the higher intensity shown. At early times the bandwidth does not help, but later, when the heating provides some damping, there is a decrease in Raman absorption. For lower intensity, where the line width is greater than the growth rate, the bandwidth mostly drops the Raman below threshold. Raman and Brillouin act to reduce each other somewhat, since Raman heating partially reduces Brillouin and Brillouin reflection partially reduces Raman.

Some processes self-consistently decrease the instability. Raman scattering occurs most strongly and with the hottest electrons at quarter-critical density, where the $2\omega_{pe}$ instability[41] and Raman sidescattering also occur. All three instabilities act to steepen the density profile and hence drive it below threshold. The hot electrons generated by all these processes as well as by the other absorption processes also help to damp Raman.

Fig. 3-19. Percentage of the light absorbed by Raman vs bandwidth of the laser for several total laser intensities. The simulation plasma had 130 λ_0 from densities 0.14 to 0.37 n_c.

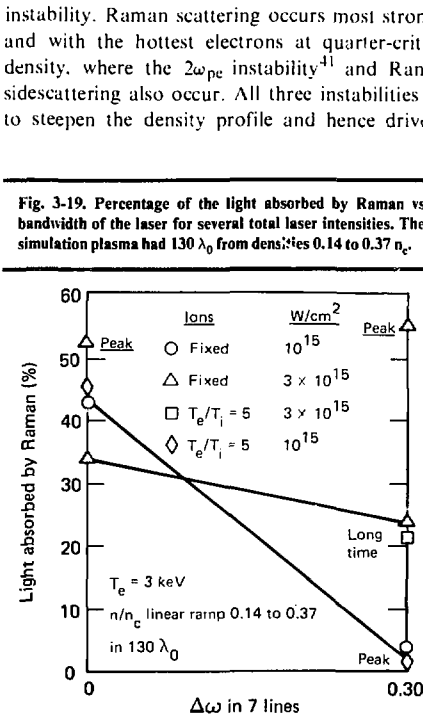

Conclusion. The heated-electron temperature depends primarily on the phase velocity of the electron-plasma wave and is roughly independent of the light intensity. The heated-electron number does depend on the $I(\lambda_0/1.06\ \mu m)^2$, however. For every joule of energy absorbed, 1 to 2 or more joules are scattered (see "Stimulated Raman Scattering Experiments" in Section 6).

The characteristic dimensions of reactor targets are in millimeters, which means that Raman has thousands of light wavelengths in which to grow. Furthermore, a laser hot spot, focus, or filament could raise the light intensity sufficiently to drive Raman scattering vigorously. One problem with a filament is that if it pushes the density below quarter-critical there will inherently be a region where the density will always be at 0.25 n_c; this issue is discussed in "Spatial Structure of Filamented Light" later in this section.

Authors: K. G. Estabrook and W. L. Kruer

References

36. K. G. Estabrook, D. W. Phillion, and V. C. Rupert, *LLL Laser Fusion Monthly*, Lawrence Livermore Laboratory, Livermore, Calif., MM 79-6 (June 1979).
37. W. L. Kruer, K. G. Estabrook, and K. H. Sinz, "Instability-Generated Laser Reflection in Plasmas," *Nucl. Fusion* **13**, 952 (1973).
38. W. L. Kruer, K. G. Estabrook, A. B. Langdon, and B. F. Lasinski, "Raman Backscatter in High Temperature, Inhomogeneous Plasmas," to be published in *Phys. Fluids*.
39. D. W. Phillion, W. L. Kruer, and V. C. Rupert, "Brillouin Scatter in Laser Produced Plasmas," *Phys. Rev. Lett.* **39**, 1529 (1977).
40. M. N. Rosenbluth, "Parametric Instabilities in Inhomogeneous Media," *Phys. Rev. Lett.* **29**, 565 (1972).
41. A. B. Langdon, B. F. Lasinski, and W. L. Kruer, "Nonlinear Saturation and Recurrence of the Two-Plasmon Decay Instability," *Phys. Rev. Lett.* **43**, 133 (1979).

Two-Dimensional Simulations of Quarter-Critical-Density Heating in Large Plasmas

With a view toward planning and interpreting long-pulse-length experiments, we have begun a new ZOHAR[42] simulation study of the high-frequency parametric instabilities which occur in

the neighborhood of quarter-critical density. These instabilities, which have been discussed previously[43,44] in the context of the steep density gradients associated with short-pulse-length experiments, are

- The $2\omega_{pe}$ instability in which the laser light at frequency ω_0 decays into two electron-plasma waves.
- The Raman instability in which the decay waves are an electron-plasma wave and an electromagnetic wave at $\sim\omega_0/2$.

In large regions of relatively flat underdense plasma, these instabilities may absorb a significant amount of the laser light into an unwelcome high-energy electron component. The Raman instability may also scatter the light at frequency $\sim\omega_0/2$ before it can be absorbed at higher densities.

To find upper bounds in this parameter regime, we begin with a simulation in which the ion motion is frozen. The saturation mechanism which we identified in our previous two-dimensional simulations,[43,44] however, cannot then occur; that is, we omit the process by which ion fluctuations driven up by the heating of the instability decay waves couple these decay waves into shorter-wavelength plasma waves which are then damped. The results we present here, then, confirm our understanding of the linear theory and provide upper limits or a worst-case scenario on the absorption, the electron distribution, and half-harmonic emission.

We model in two dimensions (x,y) a plasma slab 21 λ_0 long in the x (laser) direction, at density 0.23 n_c; n_c is the critical density, at which the plasma frequency equals the laser frequency. The oscillatory velocity is 0.03c and the thermal velocity is 0.077c (where c is the speed of light), corresponding to 10^{15} W/cm^2 for an Nd:glass laser and a 3-keV background. At this high electron temperature, $k_0\lambda_D \sim 0.13$ at 0.25 n_c (λ_D is the electron Debye length) and the decay plasma waves are long-wavelength. Much of our work[42,44] on the linear theory of the $2\omega_{pe}$ instability in hot plasmas, when $k_0 \gtrsim k_{plasma}$, is then applicable. The expected modes grow with $k_y/k_0 \sim 0.8$, the most vigorous. The analytically calculated growth rate[44] for that mode,

$$\frac{\gamma}{\omega_0} = \frac{k_0 v_0}{4}\left(1 - 3\sqrt{3}\,\frac{k_y v_e^2}{v_0 \omega_0}\right) = 0.002 \ , \qquad (31)$$

is in remarkably good agreement with the growth rate in the model as determined from the electrostatic energy.

The absorption fraction is 50 to 60% into a hot-electron distribution which cuts off at 500 keV. This generated distribution is not a simple Maxwellian with a well-defined temperature. It is tempting to characterize it as a sum of Maxwellians with the temperature of each one corresponding to the phase velocity of a plasma decay wave. Such a description, with temperatures ranging from 40 to 130 keV and more, is not unique. An alternative parametrization is as a ~50-keV Maxwellian with a very high-energy tail.

About 3% of the incident light is re-emitted at frequency $\omega_0/2$. If we assume that half of the $\sim\omega_0/2$ light produced is reabsorbed at its critical surface, then the Raman instability accounts for ~10% of the absorption at most. Therefore, under the conditions of this simulation, the $2\omega_{pe}$ instability is the dominant absorption mechanism.

We stress again that the ion fluctuations and their associated saturation mechanism are not included in these results. Note also that the angular spectrum of decay waves is too limited in one-dimensional simulations of the Raman instability to drive up ion fluctuations. In applying our results to experimental conditions, we then expect less absorption in a given length into a softer electron distribution than is reported here. More definitive answers await the two-dimensional mobile-ion simulations which are next on our agenda.

In applying our simulation results to experiments in which high Z-disks are irradiated by moderate-intensity laser light, collisional damping of Raman and $2\omega_{pe}$ instability must be taken into account. We find that

$$\gamma_{max}\,\tau_{ei} \cong \frac{14\sqrt{I_{14}}\,\lambda_\mu^2\,T_e^{3/2}}{Z} \qquad (32)$$

at 0.25 n_c. Here, $\gamma_{max} = k_0 v_0/4$, I_{14} is the intensity in units of 10^{14} W/cm^2, λ_μ is the laser wavelength in micrometers, and T_e is the background electron temperature in keV. The growth rate found in the simulation described above for 10^{15} W/cm^2 and 3 keV was one-third the maximum, and if we assume that Z = 50, then

$$\gamma\tau_{ei} \sim 1.7 \ . \qquad (33)$$

In this parameter regime, collisional damping would therefore play a central role.

Inverse bremsstrahlung is the dominant absorption mechanism in this parameter regime, and we need to check whether the laser intensity left at quarter-critical satisfies the $2\omega_{pe}$ threshold condition. To make a preliminary estimate, assume a linear density gradient and note that the threshold condition in Ref. 44 may be expressed as

$$I_{1/4} > \frac{Te}{\lambda_\mu \cdot L_\mu} 1.77 \times 10^{16}\ W/cm^2 , \qquad (34)$$

where $I_{1/4}$ is the intensity at 0.25 n_c. For short scale lengths, as in exploding-pusher experiments, there is little absorption but the intensity must be high enough to satisfy the gradient threshold. On the other hand, for long density gradients, there may be too much absorption below quarter-critical density for this inequality to hold. Thus, there is some minimum intensity as a function of scale length below which $2\omega_{pe}$ will not occur. For fixed background temperature, this minimum incident intensity occurs when the gradient scale length is approximately equal to an absorption length and is $\sim 5 \times 10^{13} W/cm^2/\lambda_\mu^3$. Therefore, prior absorption by inverse bremsstrahlung may reduce the potency of the high-frequency instabilities at quarter-critical density.

Authors: B. F. Lasinski and A. B. Langdon

References

42. A. B. Langdon and B. F. Lasinski, "Electromagnetic and Relativistic Plasma Simulation Models," in *Methods in Computational Physics*, J. Killeen, Ed. (Academic Press, New York) vol. 16 (1976), B. Alder, S. Fernbach, and M. Rotenberg, Eds., p. 327
43. A. B. Langdon, B. F. Lasinski, and W. L. Kruer, "Nonlinear Saturation and Recurrence of the Two-Plasmon Decay Instability," *Phys. Rev. Lett.* **43**, 133 (1979).
44. *Laser Program Annual Report—1977*, Lawrence Livermore Laboratory, Livermore, Calif., UCRL-50021-77 (1978), p. 4-49.

The Effect of Reheating on Hot-Electron Temperature

Theory and simulations of resonant absorption have been described in the past few annual reports and in the literature.[45–47] Briefly, resonant absorption is the direct conversion of the transverse laser light to longitudinal electron-plasma waves (epw) at the critical density [10^{21} $(1.06\ \mu m/\lambda_0)^2$ cm^{-3}]. The oscillating longitudinal electric field of the epw heats the electrons by accelerating them down the density gradient to a temperature of approximately 21 $T_e^{0.25}$ $\{[I(W/cm^2)/10^{16}](\lambda_0/1.06\ \mu m)^2\}$ (Ref. 48). This article extends the previous work by studying the effects of magnetic fields and collisions (albedo) which return the heated electrons for further heating. We find that a magnetic field increases their temperature and collisions do not (see also "Resonant Absorption" earlier in this section).

We studied the nonlinear processes of resonant absorption with ZOHAR, our two-dimensional relativistic, electromagnetic, kinetic simulation code.[45,46,48] We examined processes for forming macroscopic magnetic fields,[49] modeling macroscopic, slowly (time) varying magnetic fields by assuming the field to be an initial condition uniform in space over the simulation region. The time scale of the simulation is less than a picosecond of real time but is about 90 laser cycles, which is adequate if the magnetic field is large enough for the gyroradius of the suprathermal electrons not to run into the boundary condition and for there to be enough time for several gyro cycles [$2\pi/(eB/m_ec)$]. Consequently, we chose a magnetic field of 10 MG for laser intensity 10^{16}. The magnetic field is a factor of 3 to 10 times larger than that determined by two-dimensional LASNEX calculations but this is necessary to fit the problem into the computer in a reasonable amount of computer time. We checked the scaling by also running smaller simulated fields.

Figure 3-20 graphs the heated-electron temperature vs time and shows about a 20% increase in temperature per electron gyro period. The 20% figure is uncertain by a factor of two, because the plasma is diamagnetic, reducing the external magnetic field (Fig. 3-21), and because the ambipolar electric field expands with the hydro motion. Note that the heating nears saturation at late time; this is caused by the reduced magnetic field, and by an effect described by Morales and Lee[50] in which very fast electrons pass though the short region of the epw too quickly to be affected by the electric field.

Short-pulse experiments[51] showed that T_{Hot} deduced from x-ray diagnostics increased with the

Fig. 3-20. Resonant absorption T_{Hot} vs time in laser cycles for the case of a 10-MG magnetic field imposed upon the simulation region as an initial condition ($\omega_c/\omega_0 = 0.1$; laser intensity = 9×10^{15} W/cm^2; T_{Cold} = 4 keV; saturation at (a) may be due to diagmagnetic effect that reduced ω_c/ω_0 to 0.05; heat rate ~20% per pass—or about 7 keV per pass; n_{Hot} does not increase, and the "hots" become hotter).

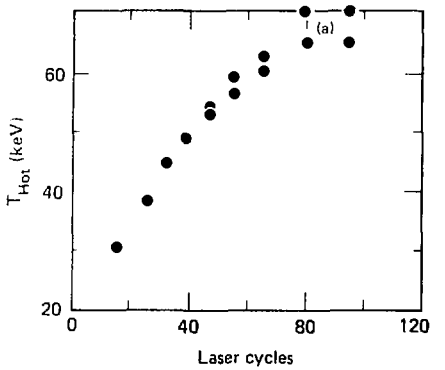

Fig. 3-21. The density profile and modified magnetic field as a function of x/λ_0.

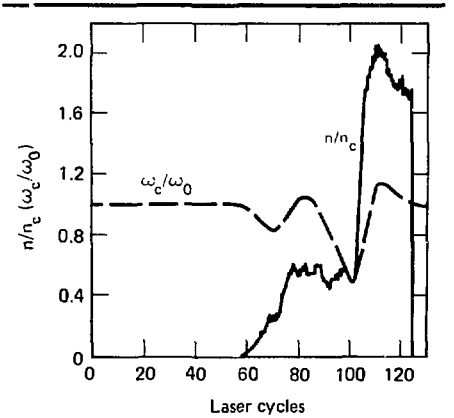

target $\bar{Z}^{0.25}$: it was suggested that perhaps the $\bar{Z}$-dependence might be due to collisions in the high-density region which returned some of the hot electrons to be heated again.[52] The collision frequency is dominantly ν_{ei}, which is proportional to $\bar{Z}$. This "albedo" effect has an extensive literature in secondary emission of electrons from vacuum tube anodes. Typically, a beam of electrons lose about half their number and 0.3 of their energy in the high-collisional medium. We mocked this up in ZOHAR with a boundary condition that analyzed the dynamic electron distribution and returned half the heated electrons with 0.7 of their energy. The hot density increased but the hot temperature remained about the same, since the electrons lost about as much energy in the mock high-density region as they gained from the heating. Rosen[53] analyzed the asymptotic limit of n_{Hot} and T_{Hot} given the scattering material's number albedo β and energy albedo κ, and assuming the electrons receive α of the original energy per reheating pass through the resonance absorption region:

$$T_{Hot} = T_{Hot0}[1 - (1 - \alpha)\beta]/(1 - \beta\kappa) \qquad (35)$$

and

$$n_{Hot} = n_{Hot0}/(1 - \beta) , \qquad (36)$$

where T_{Hot0} and n_{Hot0} are the zero-albedo hot-electron temperature and density. In the ZOHAR simulation just described, $\beta = 0.5$, $\kappa = 0.7$, and $\alpha \approx 0.3$, which explains why T_{Hot} remained the same and n_{Hot} increased. Since the number of electrons returned vs energy is not a simple multiplier, perhaps a more careful treatment of the albedo model might yield results closer to the experiment.

The $\bar{Z}$ effect may be due to the fact that the drift velocity threshold for electron-ion instabilities decreases with increasing Z, and the resulting transport inhibition increases both the density and temperature gradient which can drive macroscopic magnetic fields. Transport inhibition increases T_{Cold} which in turn increases T_{Hot}, but not enough to explain the experiments. Valeo and Bernstein[54] proposed that overdense collisions among the cold electrons provide an increase in T_{Cold} at critical density, since there would not be as much cooling from the cold electrons from the overdense region. Mason[55] suggested that the density dip from a supersonic expanding plasma[56] with spherical geometry could inhibit cold-electron transport by its electrostatic field.

Long-pulse-length experiments show much more scattering in T_{Hot} vs Z and no clear Z-dependance, indicating there may also be a

geometric effect. For example, a low-$\bar{Z}$ target will expand more into the laser, causing somewhat less irradiance than a high-$\bar{Z}$ target. This effect has also been investigated, but preliminary results show that the effect is not strong enough.

In conclusion, we have found that T_{Hot} clearly increases with macroscopic magnetic fields, since the heated electrons are recycled by the magnetic field to be reheated again. The experimentally observed $T_{Hot} \sim \bar{Z}^{0.25}$ for short pulse lengths has not been clearly explained by the albedo effect because the hot electrons cool as much by overdense collisions as they heat by resonance absorption. The $\bar{Z}$-dependence may be due to transport inhibition increasing T_{Cold}, or by increasing magnetic fields from $\nabla n X \nabla T$, or from geometric effects.

Authors: K. G. Estabrook and M. D. Rosen
Major Contributors: W. L. Kruer and J. H. Nuckolls

References

45. K. G. Estabrook, E. J. Valeo, and W. L. Kruer, "Plasma Heating and Gradient Modifications by Resonant Absorption," *Phys. Lett. A* **49**, 109 (1974).
46. K. G. Estabrook, E. J. Valeo, and W. L. Kruer, "Two Dimensional Relativistic Simulations of Resonance Absorption," *Phys. Fluids* **18**, 1151 (1975).
47. D. W. Forslund, J. M. Kindel, and K. Lee, "Theory of Hot-Electron Spectra at High Laser Intensity," *Phys. Rev. Lett.* **39**, 284 (1977).
48. A. B. Langdon and B. F. Lasinski, "Electromagnetic and Relativistic Plasma Simulation Models," in *Methods in Computational Physics*, J. Killeen, Ed. (Academic Press, New York, 1976), vol. 16, B. Alder, S. Fernbach, and M. Rotenberg, Eds.
49. C. E. Max, W. M. Manheimer, and J. J. Thomson, "Enhanced Transport Across Laser Generated Magnetic Fields," *Phys. Fluids* **21**, 128 (1978).
50. G. J. Morales and Y. C. Lee, "Effect of Localized Electric Fields on the Evolution of the Velocity Distribution Function," *Phys. Rev. Lett.* **33**, 1534 (1974).
51. K. R. Manes, H. G. Ahlstrom, R. A. Haas, and J. F. Holtzrichter, "Light-Plasma Interaction Studies with High Power Glass Laser," *J. Opt. Soc. Am.* **67**, 717 (1977).
52. J. H. Nuckols, Lawrence Livermore Laboratory, Livermore, Calif., private communication (1979).
53. M. D. Rosen and K. G. Estabrook, "Analysis of the Z Dependence of Laser Generated Suprathermal Electron Temperature," Lawerence Livermore Laboratory, Livermore, Calif., UCRL-82280, 1979.
54. E. J. Valeo and E. B. Bernstein, "Fast-ion Generation in Laser-Plasma Interactions," *Phys. Fluids* **19**, 1348 (1976).
55. R. J. Mason, "Monte Carlo (Hybrid) Suprathermal Electron Transport," *Phys. Rev. Lett.* **43**, 1795 (1979).
56. C. E. Max and C. F. McKee, "Effects of Flow on Density Profiles in Laser-Irradiated Plasmas," *Phys. Rev. Lett.* **39**, 1336 (1977).

Effects of Driver Bandwidth Upon Resonantly Heated Electrons

It is predicted that broadband or multiple-line drivers can significantly lower the hot-electron temperature due to resonant absorption in a plasma.[57,58] To test the bandwidth-dependence of the hot-electron temperature due to resonant absorption, we constructed an experiment which we then performed at microwave frequencies using bandwidths of $\Delta\omega/\omega \leq 0.01$. We were able to determine, for the range of bandwidths available to us, a scaling law for the hot-electron temperature as a function of bandwidth.

The work was done on the PROMETHEUS I low-density, pulsed-discharge plasma device at UC Davis. Microwaves ($f_0 = 1.2$ GHz) traveled down a cylindrical waveguide in the TM_{01} mode and were incident upon an inhomogeneous, unmagnetized pulsed-discharge plasma ($n_e < 3 \times 10^{10}$ cm^{-3}). The plasma was essentially collisionless so collisional absorption was negligible. The electromagnetic field extended to critical density ($n_c = 1.8 \times 10^{10}$ cm^{-3}) where the electric field ($E_/$ parallel to ∇n_e) resonantly drove electrostatic waves, resulting in resonant absorption of the microwaves. The broadband signal was generated by mixing a Gaussian noise source with the 1.2-GHz center frequency.

The heated-electron data were collected using planar-disk Langmuir probes placed in the overdense region to avoid rf interference. Over one hundred samples of the probe signal were averaged by a computerized data acquisition system.

The result of driver bandwidth upon electron heating is given in Fig. 3-22 (all data are taken at a peak power of 200 W, where $v_0/v_e \approx 0.13$). We see that increasing the microwave bandwidth decreases the hot-electron temperature. We find that $T_H \propto (\Delta\omega/\omega)^{-0.25}$ for the range of bandwidths studied. The temperature of the heated electrons changes temporally as the density profile is modified by the ponderomotive force. Heated electrons appear on the same time scale as the rise time of the rf signal ($\sim$50 ns). The temperatures shown in Fig. 3-22 are the asymptotic values obtained after the density profile has reached a steady state ($\omega_{pi}t \geq 100$). We

Fig. 3-22. Hot-electron temperature and density as a function of bandwidth.

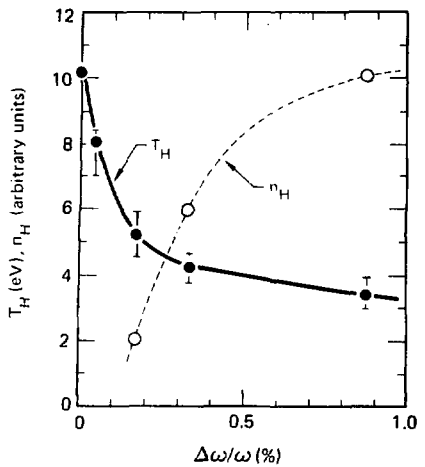

see that the increasing microwave bandwidth lowers T_H while increasing the hot-electron density n_H.

By defining a heat flux proportional to the classical free-streaming value, $Q^H \propto n_H T_H^{3/2}$, we find that the heat flux observed is nearly constant over the range of bandwidths used, as is the absorption (as expected). Our results suggest that a broadband laser driver can reduce the hot-electron temperature produced by resonant absorption while not sacrificing absorption.

Authors: R. B. Spielman, W. M. Bollen, K. Mizuno, and J. S. DeGroot (All University of California at Davis)

References

57. J. A. Williams and J. R. Albritton, Paper C-2, 9th Annual Conference on Anomalous Absorption of Electromagnetic Waves, University of Rochester, Rochester, N.Y., May 15 to 18, 1979.

58. L. Speziale, Paper C-3, 9th Annual Conference on Anomalous Absorption of Electromagnetic Waves, University of Rochester, Rochester, N.Y., May 15 to 18, 1979.

Nonlinear Behavior Of Stimulated Scattering In Large Underdense Plasmas

As lasers increase in energy and targets become larger, longer-pulse-length laser light is used to irradiate them. Much larger underdense plasmas are then created, and the size, L, of this plasma as seen by the light with wavelength λ_0 becomes an important parameter. This size parameter can be crudely estimated as

$$\frac{L}{\lambda_0} \simeq \min \frac{(v_{exp}\tau, R)}{\lambda_0} , \qquad (37)$$

where v_{exp} is a typical plasma expansion speed, τ is the pulse length of the light, and R is either the radius of the target or the focal spot radius. Note that the characteristic size parameter scales as τ/λ_0 and that it is sometimes set by geometrical considerations.

The mix of laser-plasma coupling processes is expected to be sensitive to the size of the underdense plasma. When $L/\lambda_0 \gtrsim 10$, the coupling is primarily determined by processes which occur at or near the steepened, rippled critical-density surface. When $L/\lambda_0 \gtrsim 10^2$, processes such as inverse bremsstrahlung, stimulated Brillouin and Raman scattering, and filamentation can begin to play a sizable role; for example, a significant fraction of the incident light may be scattered by the Brillouin instability before it reaches the critical-density surface.

We consider here several nonlinear effects which limit Brillouin backscattering of intense light in large underdense plasmas. After briefly considering ion trapping and harmonic generation, we focus on the self-consistent ion heating which occurs as an integral part of the Brillouin scattering process. In the long-term nonlinear state, the ion wave amplitude is determined by damping on the self-consistently formed heated ion tail. A simple model of the scattering is presented and compared with particle simulations.

Brillouin Scattering. Brillouin scattering[59,60] can be most simply described as the resonant decay of an incident photon into a scattered photon plus an ion sound wave. Hence

$$\omega_0 = \omega_t + \omega_{ia} , \qquad (38)$$

where ω_0 and ω_t are the frequencies of the incident and reflected light waves and ω_{ia} is the frequency of the ion sound wave. As is apparent from this frequency matching condition, this process occurs throughout the underdense plasma. In addition, since $\omega_0 \gg \omega_{ia}$, nearly all of the energy of the incident light wave is transferred to the scattered wave.

ω_i. Hence Brillouin scattering is a particularly dangerous energy-loss mechanism.

It is easy to show that Brillouin scattering is potentially an important effect in terms of decreasing laser absorption as well. Consider a light wave with electric vector E_i incident on a uniform underdense plasma with density n_p, and let there be an ion sound wave of amplitude δn, with frequency and wave number appropriate to scatter the incident wave into a backscattered light wave with electric vector E_r. Using Maxwell's equations and separating out the fast time- and space-scale dependences, we readily obtain coupled equations for the slowly-varying amplitudes:

$$\frac{\partial E_r}{\partial x} = -\alpha \frac{\delta n}{n_p} E_i$$

and

$$\frac{\partial E_i}{\partial x} = \alpha \frac{\delta n}{n_p} E_r \quad . \tag{39}$$

Here

$$\alpha = \frac{\pi}{2}\left(\frac{1}{\lambda_0}\right)\frac{n_p}{n_c}\Big/\left(1 - \frac{n_p}{n_c}\right)^{1/2} \quad , \tag{40}$$

where λ_0 is the wavelength of the incident light and n_c is the critical density. These equations are readily integrated to determine the reflectivity, r. If we consider a plasma with size L, and neglect $E_r(L)$ compared to $E_i(L)$, we obtain

$$r = \tan H^2\left(\alpha \frac{\delta n}{n_p} L\right) \quad . \tag{41}$$

A simple example is very instructive. Consider an underdense plasma with $n_p = 0.1\ n_c$, $L = 10^3 \lambda_0$, and an ion wave amplitude of only 1% of the plasma density. Equation (41) then predicts that $r \simeq 80\%$, showing that even a small density fluctuation can lead to sizable scattering in a large underdense plasma.

Given that Brillouin scattering can be a significant effect, it is very important to understand what nonlinear effects serve to limit the amplitude of the ion sound wave. We will first estimate the effects of ion trapping and harmonic generation and then concentrate on the important effect of self-consistent ion heating, which produces a tail which damps the ion wave. We will emphasize the nonlinear regime in which the light pressure is less than or comparable to the pressure of the underdense plasma. In the opposite regime, which obtains at very high intensity, enhanced profile steepening will clearly act to significantly reduce the scattering.[61] In order to focus on the nonlinear behavior, we will neglect the effect of gradients and simply treat the underdense plasma as an equivalent region of plasma with uniform density.

Ion Trapping. Ion trapping is one effect commonly invoked to limit the ion wave amplitude. As the ion wave amplitude increases, its potential becomes large enough to nonlinearly bring ions into resonance with the wave. Since such ions are efficiently accelerated by the wave, a strong damping results, which serves to restrict the ion wave amplitude from further increase. If the ions are cold, the trapping condition is simply $Ze\phi = Mv_p^2/2$, where ϕ is the potential, M and Z are the ion mass and charge, and v_p is the phase velocity of the wave. Neglecting Debye length corrections, the trapping condition corresponds to $\delta n/n_p \simeq e\phi/\theta_e \simeq 1/2$, which is a large amplitude.

It is important to realize that even a small ion temperature significantly reduces the trapping amplitude.[62] This temperature effect is readily estimated if one assumes a so-called "waterbag" velocity distribution for the ions. In one dimension such a distribution is constant with a velocity between $\pm\sqrt{3}v_i$ (v_i is the ion thermal velocity) and zero for other velocities. Since the majority of the ions in a Maxwellian distribution have velocities $\gtrsim 2v_i$, the waterbag distribution gives a reasonable first approximation for the onset of strong trapping, which now occurs when the fastest ion is nonlinearly brought into resonance with the wave; that is,

$$\begin{aligned} Ze\phi &= \frac{M}{2}\left(v_p - \sqrt{3}\,v_i\right)^2 \quad , \\ \frac{\delta n}{n_p} &\sim 1/2\left(\sqrt{1 + \frac{3\theta_i}{Z\theta_e}} - \sqrt{\frac{3\theta_i}{Z\theta_e}}\right)^2 \quad , \end{aligned} \tag{42}$$

where θ_i is the ion temperature, Z is the ion charge and θ_e is the electron temperature. For $\theta_i/Z\theta_e = 0.1$, Eq. (42) predicts a fluctuation amplitude of $\delta n/n_p \simeq 0.13$. Clearly the ion temperature serves to significantly reduce the amplitude, but note that the trapping amplitude is still of order 10%, unless the

ions are quite hot [$\theta_i/Z\theta_e \sim O(1)$]. Strong trapping does not in general limit the fluctuation amplitude to a small value.

Harmonic Generation. Harmonic generation is another effect which acts to limit the ion wave amplitude, provided the wave number times the electron Debye length ($k\lambda_{De}$) is small. If we neglect $k\lambda_{De}$ effects, the frequency of an ion sound wave is simply proportional to its wave number. Such a wave will then steepen, since harmonics are resonantly driven. If we consider an ion sound wave of amplitude δn, wave number k, and frequency ω_{ik}, and compute the growth of its second harmonic by linearizing the two-fluid equations, we obtain

$$\frac{\delta n(2k)}{n_p} = \frac{1}{2}\left[\frac{\delta n(k)}{n_p}\right]^2 \omega_{ik} t \quad . \tag{43}$$

We estimate a characteristic steepening time (t_s) by the condition $\delta n(2k) \sim \delta n(k)$, yielding

$$\omega_{ik} t_s = 2 \Big/ \frac{\delta n(k)}{n_p} \quad . \tag{44}$$

When $k\lambda_{De}$ corrections are included, the resonant coupling is spoiled. In particular, we then have

$$\omega_{ik} = \frac{kv_s}{\sqrt{1 + k^2\lambda_{De}^2}} = kv_s + \Delta\omega \quad . \tag{45}$$

where v_s is the ion sound velocity and $\Delta\omega \simeq \omega_{ik} k^2 \lambda_{De}^2/2$ for $k\lambda_{De} \ll 1$. Significant harmonic generation then at least requires that $t_s \gtrsim 1/\Delta\omega$, where $\Delta\omega$ is to be evaluated for the second harmonic. This corresponds to the condition

$$\frac{\delta n(k)}{n_p} \gtrsim 4k^2\lambda_{De}^2 \quad . \tag{46}$$

The estimate in Eq. (46) suffices to show that harmonic generation is not very effective in the hot underdense plasmas which are typical of recent laser-irradiated targets. For example, let us consider the ion wave produced by Brillouin backscattering in an underdense plasma with $n_p/n_c = 0.33$ and an electron temperature of 3 keV. Then $k^2\lambda_{De}^2 \simeq 0.07$; in this case, significant harmonic generation would require that the ion wave reach a very sizable amplitude [$\delta n(k)/n_p \gtrsim 0.3$ for this example].

Ion Tail Formation. Let us now take a somewhat different approach and focus on the important changes in the ion velocity distribution which are a natural consequence of the Brillouin reflection. As shown by computer simulations, the long-term nonlinear state[63] is one in which the Brillouin-generated ion wave is damped by a heated ion tail, which indeed is necessary to carry off the energy deposition into the ion wave. The greater the reflectivity, the larger the ion tail, and so the larger is the ion wave damping. Hence the reflectivity is at least partially self-correcting.

A very simple model can be used to estimate the reflectivity in the nonlinear state. Since the ion tail is produced by an ion wave with phase velocity v_φ, its characteristic temperature is approximately $\theta_H = Mv_\varphi^2$, an estimate within a factor of about two of agreement with our simulation. The magnitude of the ion heating (the tail density, n_H) is then readily determined by balancing the energy flux deposited in the damped ion wave with the flux carried off the tail:

$$rI\frac{\omega_{ik}}{\omega_0} \simeq 0.8 n_H \theta_H \sqrt{\frac{\theta_H}{M}} \quad . \tag{47}$$

where r is the reflectivity, I and ω_0 are the intensity and frequency of the incident light wave, and the heat flux carried off by the ion tail has been estimated in the free-streaming limit. Having determined n_H, we can now describe the ion wave damping simply as Landau damping on the heated ion tail, i.e., $\nu_i \omega_i \simeq 0.8\, n_H/n_p$; more sophisticated estimates, including for example resonance broadening, just enhance the damping.

We complete our simple model by computing the reflection from the damped ion wave. The amplitude to which the wave is driven is essentially the ponderomotive force due to the beat between the incident and reflected waves divided by the damping rate:

$$\frac{\delta n}{n_p} = \frac{Zk^2 e^2 E_i E_r}{2mM\omega_0^2 \nu_i \omega_i} \quad , \tag{48}$$

where Z is the charge of the ions, ω_i and ν_i are the ion wave frequency and energy damping rate, M

and m are the ion and electron mass, and E_i and E_r are the electric vectors of the incident and reflected light waves. Substituting Eq. (48) into Eq. (39) and integrating then gives the well-known result[64] for the reflectivity, r

$$r(1) = r(0)\exp[Q(1 - r(0)^2)],$$

$$Q = \frac{1}{4}\frac{n_p}{n_c}k_0 l\left(\frac{v_{osc}}{v_e}\right)^2 \Big/ \left[\frac{\nu_i}{\omega_i}\left(1 + \frac{3\theta_i}{Z\theta_e}\right)\left(1 - \frac{n_p}{n_c}\right)\right] \qquad (49)$$

Here l is again the size of the plasma, n_p is the plasma density, v_{osc} is the oscillation velocity of an electron in the incident light wave, v_e is the electron thermal velocity, and B is the noise level of the reflected wave at x = l, normalized to the intensity of the incident light wave at x = 0.

The reflection is now determined as a function of plasma conditions. As an example, consider $(v_{osc}/v_e)^2 = 0.4$ (which corresponds to $I\lambda_0^2 = 3 \times 10^{15}$ W-μ^2 cm^2 and $\theta_e = 3$ keV), and $n_p/n_c = 0.33$ (which is a typical density, taking into account modest profile steepening near the critical density), assume also a noise level B = 10^{-4} and an initial ion-electron temperature ratio of 0.2. Our model predictions for the reflectivities and tail density as a function of plasma size for this case are shown by the solid lines in Fig. 3-23. These predictions are in reasonable agreement with simulation results. For comparison, the open circles denote the long-term Brillouin reflectivity calculated in a one-dimensional simulation code which used particle ions and fluid electrons. Note that the reflectivity is rather small (~10%) when $l/\lambda_0 \sim 10$, and gradually increases to a value of ~50% when $l/\lambda_0 \sim 100$. Note also the substantial ion tail which self-consistently forms. The mean ion temperature quickly becomes of order unity. Self-consistent ion heating is a very potent effect.

Figure 3-24 compares the model predictions (solid line) with simulation results for the reflectivity as a function of plasma density, when the scale length and intensity are fixed: $l/\lambda_0 = 20$ and $(v_{osc}/v_e)^2 = 1.3$. The circles denote simulation results using a code which treats both the electrons and the ions as particles. For these runs, the initial ion-electron temperature ratio was 0.2, and the ion-electron mass ratio was 100. The result at $n_p/n_c = 0.33$ provides a point of a comparison with the numerical results using the hybrid code discussed in the previous figure, and the agreement is quite reasonable. Note that the reflectivity is rather sensitive to the density of the plasma, as expected from the ion heating model. The fewer the ions, the larger is the heating consistent with a given reflectivity; hence profile steepening near the critical density can play an important role in reducing the scattering, by limiting it to lower densities.

Fig. 3-23. The reflection due to the Brillouin instability and the ion tail density as a function of the size of the underdense plasma. The parameters are $(v_{osc}/v_e)^2 = 0.4$, $n_p/n_c = 0.33$, and $\theta_i/Z\theta_e = 0.2$ initially. The solid lines denote the model predictions ($B = 10^{-4}$). The circles denote simulation results using a hybrid code (m/M = 1/400).

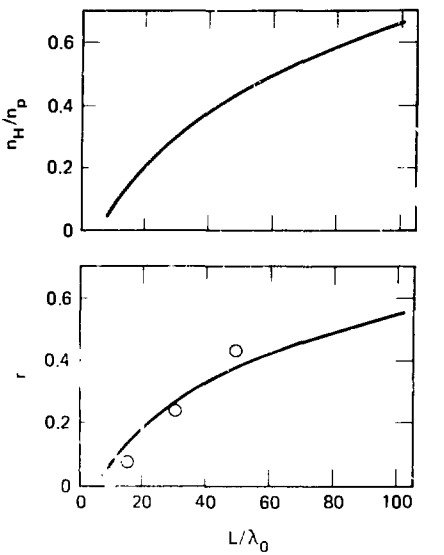

It is particularly instructive also to examine the reflectivity as a function of intensity, keeping the plasma density and size constant ($n_p/n_c = 0.33$, $l/\lambda_0 = 50$). Figure 3-25 shows the simple model prediction for the reflectivity as a function of $(v_{osc}/v_e)^2$. Note that the reflectivity increases with $v_{osc}^2 \propto I\lambda_0^2$ for low intensity, but then tends to saturate as the ion tail becomes sizable. As $I\lambda_0^2$ increases, the self-consistent ion heating increases, which acts to compensate for further increases in reflectivity.

Fig. 3-24. The reflection due to the Brillouin instability as a function of the background plasma density. Here $(v_{osc}/v_e)^2 = 0.4$, $L/\lambda_0 = 20$, and $\theta_i/Z\theta_e = 0.2$ initially. The solid line is the simple model prediction ($B = 10^{-4}$). The open circles denote simulation results using a particle code ($m/M = 1/100$).

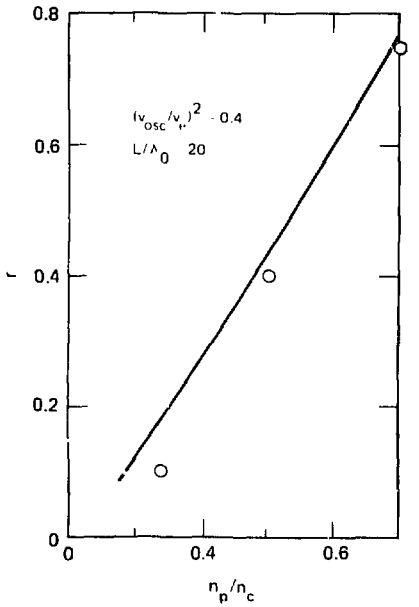

Fig. 3-25. The simple model prediction for the reflection due to the Brillouin instability as a function of $(v_{osc}/v_e)^2$. Here $n_p/n_c = 1/3$, $L/\lambda_0 = 50$, $B = 10^{-4}$ and $\theta_i/Z\theta_e = 0.2$ initially.

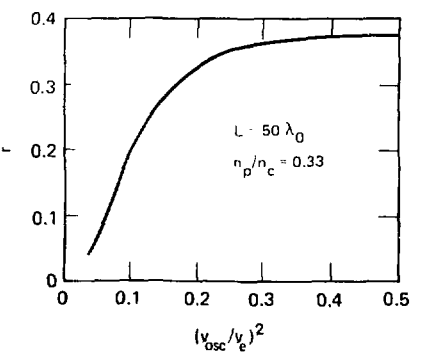

A crude analytic estimate of the reflectivity on the saturated state is

$$R \approx 1 \Big/ \left[\left(1 + \omega_0 B^{-1}\right) \Big/ \frac{\pi}{2} \frac{L}{\lambda_0} \left(\frac{n_p}{n_c}\right)^2 \right] . \qquad (50)$$

Note the dependence of the reflection on the size parameter (L/λ_0) and the plasma density (n_p/n_c); this result indicates that, for a given n_p/n_c and L, long-wavelength lasers are less sensitive to Brillouin scattering at high intensity, simply because there are fewer wavelengths of underdense plasma available to reflect the light. Of course, for a given n_p and L, short-wavelength light undergoes less scattering because the plasma is more underdense to the light.

We note that simpler ion heating models[63,65] give similar results as long as the reflectivity and ion heating are sizable. For example, since the fraction of the ions in the heated tail is sizable, it is convenient to approximate the ion heating as a main body heating. In this case, we simply balance the energy flux deposited into ion waves with the energy flux carried off by a heated Maxwellian distribution with density n_p. The effective temperature of this distribution is then

$$\frac{\theta_i}{Z\theta_e} \sim \left[R \frac{n_c}{n_p} \left(\frac{v_{osc}}{v_e}\right)^2 \right]^{2/3} , \qquad (51)$$

and similar reflectivities are obtained.

The fact that the numbers are not greatly sensitive to the details of the ion heating is another manifestation of the partially self-correcting feature of the scattering in this simple model. It should be noted, however, that details of the ion heating may be significant for understanding the frequency spectrum of the reflected light. The normal modes of a multitemperature distribution differ in detail from the normal modes of a single-temperature distribution. Simulations show that when a heated tail develops, that tail becomes heavily populated and another higher-energy tail is formed. We also note that ion tails are less sensitive to expansion cooling,[66] an effect which can compete with the ion heating in an expanding plasma.

Finally we can crudely estimate the time required for the plasma to approach this nonlinear state. The time, t_{II}, to produce the heated tail is

$$t_{II} \sim \frac{1}{2r}\frac{n_H}{n_c}\frac{v_e^2}{v_{osc}^2}\frac{L}{c_s} \quad . \tag{52}$$

Assuming $n_H \sim 0.2\ n_p$, $(n_p - n_c)v_e^2 v_{osc}^2 = 1$, $r = 1/2$, $\theta_e = 4$ keV, and $L = 50\ \lambda_0$, Eq. (52) gives $t_{II} \sim 20$ ps. Of course, in practice, it may be difficult to observe a transient state in which the ions are initially heated, since this heating can gradually accumulate as the laser pulse increases from low to high intensity. In addition, other effects such as shock heating can independently contribute to the ion heating.

The Effects of Gradients. It should be noted that gradients are not necessarily as effective in reducing Brillouin scattering in the nonlinear regime as they are in the linear regime. It is well known that gradients can greatly increase the threshold intensity for the instability.[59] Gradients limit the region over which any given three waves can resonantly interact. Noting that the wave numbers of the three waves (k_i with $i = 1,2,3$) are now a function of position, let us define

$$K = k_1(x) - k_2(x) - k_3(x) \quad . \tag{53}$$

At some point, $K = 0$ (the waves are resonantly coupled), but away from this point a mismatch develops which spoils the resonant coupling. Hence the three waves can resonantly interact only over some interaction region which can be estimated by

$$\int_0^{x_{int}} \kappa dx \sim 1,2 \quad . \tag{54}$$

Taylor expanding about the point of resonance [$\kappa = \kappa(0) + \kappa^1 x$, where $\kappa(0) = 0$] then gives

$$x_{int} \sim \frac{1}{\sqrt{\kappa^1}} << L \quad . \tag{55}$$

Propagation of wave energy out of this interaction region introduces an enhanced damping rate of approximately v_{gi}/x_{int}, where v_{gi} is the group velocity of the ith wave. Hence the threshold intensity is increased.

Well above the threshold set by gradients, however, the reflectivity from a given interaction region is determined nonlinearly, and one must further add up the contributions of the different interaction regions. Hence the bulk of the plasma still contributes to the net reflection. Note that nonlinearly the reflectivity is not an exponential function of L (see Fig. 3-23), so the net contribution[67] from a number of smaller regions need not be much less than the contribution from one larger region (this assumes a distributed and/or broadband noise source). Gradients will no doubt play a quantitatively significant role, but probably not the crucial role which they often play in the linear theory. Perhaps the most important aspect of allowing for plasma expansion and inhomogeneity will be in properly determining the various density regions available for scattering, since the reflectivity depends sensitively on n_p, n_c.

Experimental Evidence; Options. Recent experiments[63,68-76] with longer-scale-length plasmas do indicate that significant Brillouin scattering is possible. In these experiments, sizable underdense plasmas ($L \gtrsim \lambda_0 \gtrsim 30$) were formed in various ways: by using a prepulse plasma, a long-pulse-length plasma in the sense of $\tau > \lambda_0$, or a preformed plasma. Table 3-1 shows a brief summary of some of the experimental results for the back-reflection of 1.06-μm and 10.6-μm laser light. Note that a peak reflectivity of about 50% has been observed with either wavelength. Note also that the pulse lengths (or prepulse delays) used in the experiments with 10.6-μm light are much longer than those used with 1.06-μm light, reflecting the expected $L > \lambda_0$ dependence.

Finally, if Brillouin scattering does prove to be a serious problem, there are some options for reducing the scattering (although many more experiments are needed to determine the intensity and wavelength windows appropriate for laser fusion applications):

- One option, of course, is to operate at lower intensity ($I\lambda_0^2$), so that the plasma is more collisional and the Brillouin instability is more weakly driven. Indeed, recent experiments[77,78] with several-ns pulses of 1.06-μm light have shown a high absorption (~70 to 80%) at intensities of $\sim 10^{13}$ to 10^{14} W cm^{-2}.
- Increasing the bandwidth and/or reducing the wavelength of the light are other effects[79] in the same direction: the plasma absorbs more by inverse bremsstrahlung and the instability is more weakly driven.
- The complementary approach is to operate at high intensity and try to minimize the scattering by using its dependence on n_c/n_p and L/λ_0.

Table 3-1. A brief summary of recent experimental results for the peak reflectivity (r_B) of laser light (for more details see Refs. 63, 68-76).

Institution	$\lambda_0(\mu m)$	Target	Pulse length	$I\frac{W\text{-}\mu^2}{cm^2}$	Peak r_B
NRL	1.06	disk	pp + 50 ps (~2 ns)	10^{15}-10^{16}	50%, f/2
LLL	1.06	disk, spheres	200 ps – 1 ns	3×10^{14} 3×10^{16}	50%, f/1 15%, f/2.6
U of R	1.06	spheres	pp + 50 ps (~2 ns)	10^{15}-10^{16}	25%, f/2
KMS	1.06	gas jet	100 ps	10^{14}-10^{15}	40%, f/3.5
LASL	10.6	sphere	pp + 1 ns (10-35 ns)	$\sim 10^{17}$	10-50%, f/2.5
U of Alberta	10.6	gas jet ($0.1\ N_c$)	35 ns	$\sim 10^{15}$	60%, f/2
UCLA	10.6	arc ($0.015\ N_c$)	50 ns	$\sim 2 \times 10^{13}$	5%, f/7.5
U of Wash.	10.6	solenoid	~400 ns	$\sim 5 \times 10^{11}$	5%, f/6.6

Summary. The size of the underdense plasma in units of the laser-light wavelength is an important parameter affecting the mix of coupling processes. Stimulated scattering of the light in large underdense plasmas is a very real concern. We have considered several nonlinear effects which limit the Brillouin scattering. Our calculations emphasize the importance of the self-consistent changes in the velocity distribution which are produced when the electrostatic waves damp into the particles. Simple theoretical models, formulated and compared with computer simulations, have shown that the reflectivity is at least partially self-correcting. As the reflectivity increases, the velocity distribution becomes more distorted, enhancing the damping of the electrostatic wave and acting to reduce the reflectivity.

We emphasize that there are significant uncertainties in our attempts to quantitatively understand the level of stimulated scattering; more quantitative predictions will require a realistic treatment of the effects of gradients in the underdense plasma. The incorporation[66,80] of a model for stimulated scattering into a hydrodynamic code is being actively pursued. In general, even the zero-order plasma conditions are rather poorly known, because of uncertainties in the electron transport. More experiments to diagnose the underdense plasma conditions are needed, and the angular distribution[81] of the stimulated scattering also requires further investigation. Two-dimensional simulations suggest that the scattering occurs over a sizable range of angles; thus the back-reflection through a high-f-number lens can be a gross underestimate of the level of stimulated scattering. Finally, the competition of this scattering with other processes such as filamentation is not well understood either theoretically or experimentally.

Authors: W. L. Kruer and K. G. Estabrook

References

59. C. S. Liu, M. N. Rosenbluth, and R. B. White, *Phys. Fluids* **17**, 1211 (1974).
60. D. W. Forslund, J. M. Kindel, and E. Lindman, *Phys. Fluids* **18**, 1002, 1017 (1975).
61. W. L. Kruer, E. J. Valeo, and K. G. Estabrook, *Phys. Rev. Lett.* **35**, 1076 (1975).
62. J. M. Dawson, W. L. Kruer, and B. Rosen, in *Dynamics of Ionized Gases*, M. Lighthill, I. Inai, and H. Sato, Eds. (University of Tokyo Press, Tokyo, 1973), pp. 47 to 61.
63. D. W. Phillion, W. L. Kruer, and V. C. Rupert, *Phys. Rev. Lett.* **39**, 1529 (1977); *Laser Program Annual Report—1976*, Lawrence Livermore Laboratory, Livermore, Calif., UCRL-50021-76 (1977), p. 4-63.
64. C. L. Tang, *J. Appl. Phys.* **37**, 2945 (1966).
65. J. J. Thomson and K. Mima, NA607A, Japan, to be published.
66. K. G. Estabrook and J. A. Harte, Lawrence Livermore Laboratory, Livermore, Calif., UCRL-82620 (1979); R. G. Evans, Rutherford Laboratory RL-79-061 (1979).

67. C. J. Randall, Lawrence Livermore Laboratory, Livermore, Calif., private communication (1979).
68. B. H. Ripin et al., *Phys. Rev. Lett.*, **39**, 611 (1977).
69. M. D. Rosen et al., *Phys. Fluids* **22**, 2020 (1979).
70. R. E. Turner and L. M. Goldman, *Phys. Rev. Lett.* **44**, 400 (1980).
71. F. J. Mayer et al., KMSF preprint U-904 (1979).
72. G. H. McCall, LASL preprint LA-UR-79-1298 (1979).
73. A. Ng et al., *Phys. Rev. Lett.* **42**, 307 (1979).
74. M. J. Herbst, C. E. Clayton, and F. F. Chen, *Phys. Rev. Lett.* **43**, 1591 (1979).
75. R. Massey, K. Berggren, and Z. Pietrzyk, *Phys. Rev. Lett.* **36**, 963 (1976).
76. There are numerous other references to experiments, including L. M. Gorbunov et al., *JETP Lett.* **27**, 226 (1978); A. Maaswinkel, K. Eidmann, and R. Sigel, *Phys. Rev. Lett* **42**, 1625 (1979); S. Nakai et al., *Phys. Rev. A* **17**, 1133 (1978).
77. B. H. Ripin et al., *Phys. Rev. Lett.* **43**, 350 (1979).
78. K. Manes et al., *Bull. Am. Phys. Soc.* **24**, 1011 (1979).
79. C. E. Max and K. G. Estabrook, "Wavelength Scaling in Laser Fusion from a Plasma Physics Point of View," to be published in *Comments Plasma Phys. Cont. Fusion*; D. W. Forslund, Ninth Anomalous Absorption Conference, Paper A-2 (1979); I. Amiranoff et al., *Bull. Am. Phys. Soc* **24**, 1054 (1979).
80. C. J. Randall, J. J. Thomson, and K. G. Estabrook, *Phys. Rev. Lett.* **43**, 924 (1979). D. G. Colombant and W. M. Manheimer, NRL preprint (1979).
81. R. Lehmberg, *Phys. Rev. Lett.* **41**, 863 (1978).

Physical Processes Affecting Stimulated Brillouin Scattering at Different Laser Wavelengths

The relatively large targets appropriate for an eventual laser fusion reactor are expected to produce substantial regions of underdense plasma. Hence they are in a part of parameter space where stimulated Brillouin scattering (SBS) is of concern, due to its ability to cause premature reflection of the incident laser light. We have investigated physical processes which determine the level of SBS for lasers having a variety of wavelengths, in an effort to extend our understanding of wavelength scaling.[82] In particular, it is expected that inverse bremsstrahlung absorption will limit SBS[83] for short-wavelength lasers, whereas ion heating[84] or ion trapping[85] will be more important for longer-wavelength lasers.

To investigate these effects quantitatively we have used a model describing SBS in the presence of inverse bremsstrahlung absorption and SBS-induced ion heating. The incident, scattered, and reflected light waves are treated in the WKB limit, and the ion-wave amplitude is determined either by the ponderomotive force or by an ion-trapping limit, whichever is smaller. The ion waves are assumed to be at the strong damping limit, and ion energy equations determine the ion temperatures parallel and perpendicular to the direction of plasma expansion, $T_\parallel$ and $T_\perp$. The background plasma is taken to be spherical, with given steady-state profiles of velocity and electron temperature $v(r)$ and $T_e(r)$. The background electron number density $n(r)$ is then determined from mass conservation. To account for profile-steepening at the critical-density surface, the electron density profile is assumed to rise steeply to critical as shown in Fig. 3-26, starting from an (adjustable) density $n_\ell < n_c$.

Within this model the equations describing the light waves may be written as follows. We define incident and Brillouin-scattered dimensionless normalized electric field amplitudes A_0 and A_s respectively, by,

$$E_{\pm} = E_0 A_{0,s} \exp\left(\pm i \int \sqrt{\epsilon}\,\frac{\omega_0}{c}\,dr\right), \qquad (56)$$

where $\epsilon = (1 - n/n_c)^{1/2}$, E_0 is the field amplitude incident at large r (in vacuum), and E_+ (E_-) is the electric field of the incident (reflected) light. We also define an inverse bremsstrahlung absorption factor by

$$f_\pm = \exp\left[-\frac{\nu(n_c)}{c}\int\left(\frac{n}{n_c}\right)^2\left(\frac{T_{ec}}{T_e}\right)^{3/2}\frac{dr}{\sqrt{\epsilon}}\right]. \qquad (57)$$

Fig. 3-26. Schematic of electron density profile, n(r), and of the three light waves: A_0 (incident), A_s (Brillouin-scattered), and A_R (reflected from the critical surface). Above a density $n_\ell < n_c$, the density profile is assumed to rise steeply to critical.

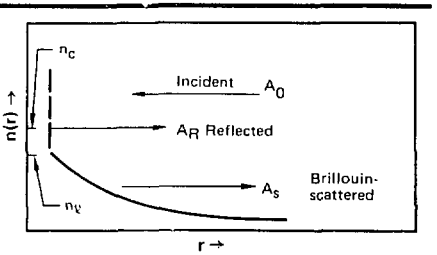

Then the incident, Brillouin-scattered, and reflected light waves (see Fig. 3-26) obey

$$\frac{1}{r^2}\frac{\partial}{\partial r}\left(r^2\sqrt{\epsilon}\,A_0^2 f_-\right) = \frac{k_0}{2}\left(\frac{n}{n_c}\right)A_0 A_s f_-$$

$$\times \min\left[\left(\frac{E_0^2}{8\pi n_c k T_e}\right)\frac{A_0 A_s}{\left(\frac{\nu_i}{\omega_s}\right)\left(1+\frac{3T_i}{ZT_e}\right)}\left(\frac{\delta n_i}{n}\right)_{max}\right], \quad (58)$$

$$\frac{1}{r^2}\frac{\partial}{\partial r}\, r^2\sqrt{\epsilon}\,A_s^2 f_+ =$$

$$\frac{k_0}{2}\left(\frac{n}{n_c}\right)A_0 A_s f_+ \min\left[\left(\frac{E_0^2}{8\pi n_c k T_e}\right)\frac{A_0 A_s}{\left(\frac{\nu_i}{\omega_s}\right)\left(1+\frac{3T_i}{ZT_e}\right)}\left(\frac{\delta n_i}{n}\right)_{max}\right], \quad (59)$$

and

$$\frac{1}{r^2}\frac{\partial}{\partial r}\left(r^2\sqrt{\epsilon}\,A_R^2 f_+\right) = 0 \; ; \quad (60)$$

where $\nu(n_c)$ is the classical electron-ion collision frequency at the critical density, ν_i and ω_s are the damping and frequency of the ion waves, Z is the ionic charge, $k_0 = \omega_0/c$ is the vacuum wave number of the incident light wave, and $(\delta n_i/n)_{max}$ is the maximum ion wave amplitude allowed by ion trapping or wavebreaking.

Ion temperature is found from two ion-energy equations:

$$1/2\, n_i v\frac{\partial T_\parallel}{\partial r} = -(n_i T_\parallel)\frac{1}{r^2}\frac{\partial}{\partial r}(r^2 v) - \frac{\nu_{ii}}{2}(T_\parallel - T_\perp) + \nu_{ei}^E n_i(T_e - T_\parallel) + \frac{\omega_s}{\omega_0}\left[\frac{1}{r^2}\frac{\partial}{\partial r}(r^2 I)\right]_{SBS} \quad (61)$$

and

$$n_i v\frac{\partial T_\perp}{\partial r} = \frac{\nu_{ii}}{2}(T_\parallel - T_\perp) + \nu_{ei}^E n_i(T_e - T_\perp) \; . \quad (62)$$

The terms on the right side of Eq. (61) represent, in turn, expansion cooling, coupling between the parallel and perpendicular ion temperatures at a rate ν_{ii}, coupling of energy from electrons at a rate ν_{ei}^E, and parallel ion heating due to Brillouin scattering itself where I is the scattered light intensity. In the direction perpendicular to the flow velocity v [Eq. (62)], only coupling to ions and electrons contributes to $T_\perp$ directly.

Fig. 3-27. Profiles of background velocity and density to be used in parameter study of Brillouin scattering at various laser wavelengths. Other parameters: $r_c = 0.24$ cm, $I_L = 2 \times 10^{14}$ W/cm^2, $T_e = 1.5$ keV, $T_i(r_c) = 1$ keV, $Z = 2$, and $A = 4$.

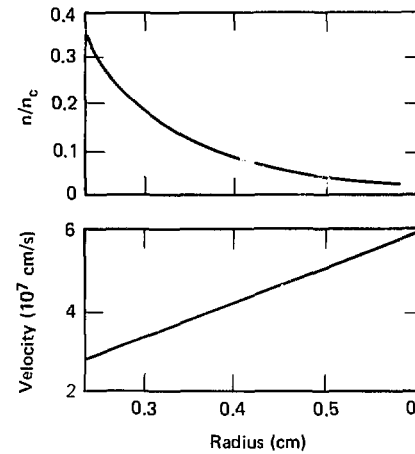

We have written a small computer code called SBS + IB, to numerically solve Eqs. (58) through (62) for fixed background profiles $n_e(r)$, $v(r)$ $T_e(r)$, and $T_i(r_c)$. We shall present below results of a preliminary parameter study using SBS + IB, which kept the background profiles constant and studied mechanisms determining the level of Brillouin for different laser wavelengths. For this parameter study we used profiles which might be typical of a large spherical reactor-sized target: $r_c = 0.24$ cm, $I_L = 2 \times 10^{14}$ W/cm^2, $T_e(r) = 1.5$ keV, $T_i(r_c) = 1$ keV, $Z = 2$, and $A = 4$. The velocity and density profiles are shown in Fig. 3-27. Electron density rose abruptly to critical above the density $n_f = 0.33\, n_c$.

We can use Eq. (61) to estimate when ion heating is expected to dominate over expansion cooling. A dimensionless parameter, H, gives the ratio of the Brillouin heating to the expansion-cooling terms in Eq. (61):

Fig. 3-28. Profiles from code SBS + IB of ion temperature and ion-wave amplitude $\delta n_i/n$, for two different laser wavelengths: (a) long wavelength, (b) short wavelength. Laser is incident from right; the noise level of the scattered wave at critical is 10^{-4}. For $\lambda_L = 2\ \mu m$, ion heating is strong in the low-density plasma and is responsible for the decrease in $\delta n_i/n$ seen at large radii. For $\lambda_L = 1/3\ \mu m$, expansion cooling dominates over ion heating.

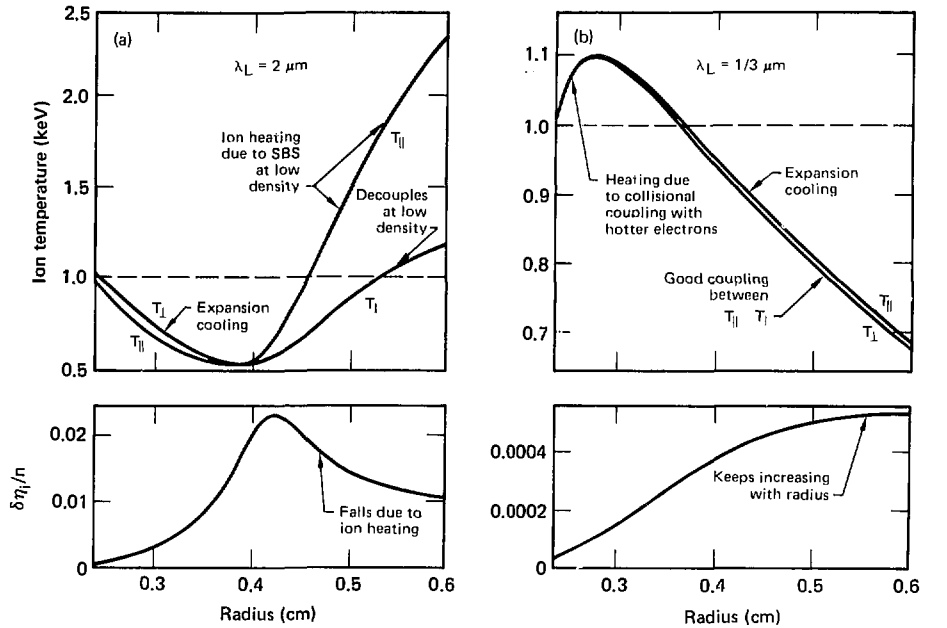

$$H \equiv \frac{\dfrac{\omega_s}{\omega_0}\left[\dfrac{1}{r^2}\dfrac{\partial}{\partial r}(r^2 I)\right]_{SBS}}{(1/2)n_i \nu(\partial T_\parallel/\partial r)} \cong Q\left(\frac{E_0^2}{4\pi n_c T_e}\right)\left(\frac{n_c}{n}\right)\left(\frac{ZT_e}{MT_i}\right), \quad (63)$$

where Q is the number of Brillouin gain lengths in a distance r characterizing the hydrodynamic flow, n_c is the critical electron density, and $M = v/c_s$ is the Mach number. A rough measure of the importance of ion heating in limiting the growth of Brillouin scattering is the ratio H/Q, because the heating rate is only relevant when Brillouin is substantial. This ratio of heating rate to SBS growth is, according to Eq. (63),

$$\frac{H}{Q} \cong 4\left(\frac{I_L}{10^{16}\ W/cm^2}\right)\left(\frac{\lambda_L}{1\ \mu m}\right)^2\left(\frac{1\ keV}{T_e}\right)\left(\frac{n_c}{n}\right)\left(\frac{ZT_e}{MT_i}\right). \quad (64)$$

Ion heating is thus seen to be an important Brillouin limitation process for higher laser intensities I_L, longer laser wavelengths λ_L, lower electron densities n/n_c, cooler ions ($T_i \ll ZT_e$), and smaller Mach numers, M.

Figure 3-28 illustrates this predicted scaling of ion heating with laser wavelength, showing strong ion heating for $\lambda_L = 2\ \mu m$, but only expansion cooling for $\lambda_L = 1/3\ \mu m$. It is interesting that collisions are frequent enough in the $\lambda_L = 1/3\ \mu m$ case to maintain good coupling between the parallel and perpendicular components of ion temperature, and even to provide a bit of collisional heating from the hotter electrons near the critical surface. In contrast the two components of the ion temperature are decoupled when $\lambda_L = 2\ \mu m$. In the $\lambda_L = 2\ \mu m$ case, ion heating at low density causes the size of the ion density perturbation $\delta n_i/n$ to decrease at large radii, whereas when $\lambda_L = 1/3\ \mu m$ the ion density perturbation amplitude is largest at large radii. Despite this ion heating, however, the actual magnitude of the ion perturbation is larger by about a factor of 50

at $\lambda_L = 2\ \mu m$ than at $\lambda_L = 1/3\ \mu m$. Thus according to our model the total amount of Brillouin reflectivity at $\lambda_L = 2\ \mu m$ exceeds that at $1/3\ \mu m$, despite the presence of ion heating.

In contrast to ion heating, which is most important at long laser wavelengths and high intensities, inverse bremsstrahlung absorption can limit SBS at short wavelengths or low intensities. Under the latter conditions one can estimate the Brillouin quality factor,[84] Q, by calculating the number of SBS gain lengths in one absorption length for inverse bremsstrahlung:

$$Q_{ib} \approx \frac{\pi}{2}\left(\frac{I_0^2}{8\pi n_c T_e}\right)\left(\frac{\omega_s}{\nu_i}\right)\int_{\infty}^{L_{abs}} \frac{n(r)}{n_c}\,\frac{(dr/\lambda_L)}{\left(1-\frac{n(r)}{n_c}\right)} , \qquad (65)$$

where L_{abs} is the distance over which the incident intensity is decreased by a factor $1/e$ due to inverse bremsstrahlung absorption (to be more exact one might want to use $2\ L_{abs}$ or $3\ L_{abs}$ as the upper limit for the integral). Reference 83 discusses this expression for a flat density profile n(r) = constant. For a more general profile

$$n(r) = n_c\left(\frac{r_c}{r}\right)^{\beta}, \; r > r_c \text{ and } \beta > 1 , \qquad (66)$$

one obtains, in the strong-absorption limit,

$$Q_{ib} \propto \left(\frac{E_0^2}{8\pi n_c T_e}\right)\left(\frac{r_c}{\lambda_L}\right)\left[\frac{\nu(n_c)}{c}\, r_c^{2\beta}\right]^{(1-\beta/2\beta-1)} , \qquad (67)$$

so that the wavelength scaling of the SBS quality factor is

$$Q_{ib} \propto \lambda_L^{(4\beta-3/2\beta-1)}, \; 1 \leq \left(\frac{4\beta-3}{2\beta-1}\right) \leq 2 . \qquad (68)$$

Thus when inverse bremsstrahlung is strong, Brillouin scattering is predicted to decrease strongly at short laser wavelengths. Figure 3-29 illustrates this decrease, showing the wavelength-dependence of electric field profiles for the incident and Brillouin-scattered waves; the results were obtained with the code SBS + IB, for the parameters described in Fig. 3-27. The incident electric field

Fig. 3-29. Wavelength dependence of electric field profiles for the incident and Brillouin-scattered waves, for (a) λ_L = 0.3 μm, (b) λ_L = 0.5 μm, (c) λ_L = 1.0 μm. Conditions of the laser and background plasma are described in Fig. 3-27; results are from code SBS + IB. Brillouin is predicted to be much stronger at λ_L = 1 μm than at λ_L = 0.3 μm, according to this model.

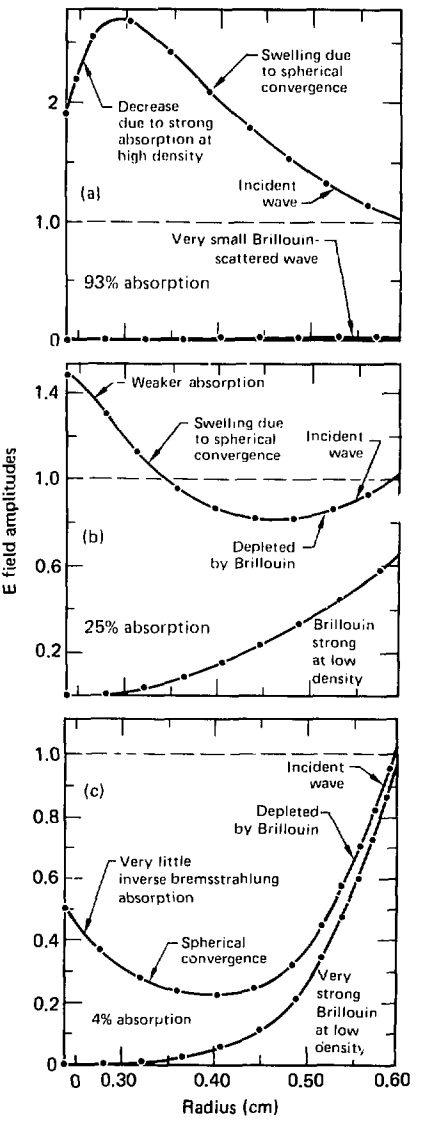

amplitude at r = 6 mm is normalized to unity. When $\lambda_L = 0.3\ \mu m$, there is virtual no SBS: the E-field amplitude first swells due to spherical convergence and then decreases a bit near r_c due to inverse bremsstrahlung absorption. When the wavelength is increased to $\lambda_L = 0.5\ \mu m$, Brillouin becomes stronger as predicted by Eq. (68), and absorption falls to 25%. Near critical density inverse bremsstrahlung is present, but at a weaker level than for $\lambda_L = 0.3\ \mu m$. When the laser wavelength is increased again to 1 μm, Brillouin becomes stronger still, and allows only 4% absorption to occur. Figure 3-29(c) shows the incident wave so strongly depleted by SBS that little amplification of E due to spherical convergence can occur. Our calculations indicate that for these laser and target parameters, ion heating does not begin to limit SBS until the laser wavelength has exceeded $\lambda_L = 1\ \mu m$.

There are several important ways in which the crude SBS model described here could be improved. The Brillouin model developed recently[86] for use in LASNEX simulations incorporates the self-consistent reaction of background conditions into the presence of SBS, a feature crucial for quantitatively accurate modeling. A second important improvement to SBS + IB would be the inclusion of density and velocity-gradient effects[87] on SBS, and a treatment which allowed some of the light reflected from critical to be a source for Brillouin backscattering.[88] Finally, a parameter study incorporating wavelength variation (as in Fig. 3-29) should include the fact that the background profiles of density and temperature are different at each laser wavelength. We have examined the latter effect by using some LASNEX-generated profiles for the laser parameters of Fig. 3-29. More accurate plasma profiles produced even more severe Brillouin scattering at long laser wavelengths, because the plasma profiles tended to be much more extended for long-wavelength lasers, thus providing more underdense plasma wavelengths for SBS to grow in.

Authors: C. E. Max, C. J. Randall, and K. G. Estabrook

References

82. C. E. Max and K. G. Estabrook, "Wavelength Scaling in Laser Fusion from a Plasma Physics Point of View," to be published in *Comments Plasma Phys. Cont. Fusion.*
83. *Laser Program Annual Report—1977*, Lawrence Livermore Laboratory, Livermore, Calif., UCRL-50021-77 (1978), p. 4-63.
84. D. W. Phillion, W. L. Kruer, and V. C. Rupert, *Phys. Rev. Lett.* **39**, 1529 (1977).
85. W. L. Kruer, "Nonlinear Estimates of Brillouin Scatter in Plasmas," *Phys. Fluids* **23**, 1273, 1980; D. W. Forslund, J. M. Kindel, K. Lee, and B. B. Godfrey, *Phys. Fluids* **22**, 462 (1979).
86. K. G. Estabrook and J. A. Harte, "On Reducing Brillouin Scatter," Lawrence Livermore Laboratory, Livermore, Calif., UCRL-82620, Rev. 2, (1979), submitted to *Phys. Rev. Lett.*
87. K. Nishikawa and C. S. Liu, in *Advances in Plasma Physics*, vol. 6, A. Simon and W. Thompson, Eds. (Wiley & Sons, New York, 1976), p. 3.
88. C. J. Randall, J. J. Thomson, and K. G. Estabrook, *Phys. Rev. Lett.* **43**, 924 (1979).

Enhancement of Stimulated Brillouin Scattering in the Presence of a Critical Surface

Previous analyses of stimulated Brillouin scattering (SBS) have not considered the effects of a partially reflecting boundary, such as the critical-density surface in a realistic plasma expansion. Generally, these analyses have found that the instability exponentiates from some small noise level, α, usually taken to be in the range of 10^{-4} to 10^{-2} (relative to the incident power). Thus for SBS to be appreciable, the effective interaction length, which is set by the finite length of the plasma or by density or velocity gradients, must be much greater than the growth length. We discuss here a mechanism by which a reflecting surface can greatly increase the effective noise level so that only a few growth lengths are required for significant scattering.[89]

Consider a homogeneous slug of plasma of length L (Fig. 3-30), moving with respect to a

Fig. 3-30. Schematic representation of simple model for SBS: a homogeneous slug of plasma moving with respect to a partially reflecting surface.

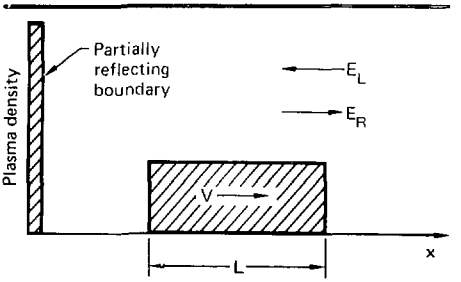

reflecting surface at a speed $v = Mc_s$ toward the laser. Here, M is the Mach number and c_s is the sound speed. In the rest frame of the plasma, the left-going laser light, E_L, is Doppler-shifted up to $\omega_L = \omega_0 + k_0 Mc_s$, where k_0 is the free-space wave number and ω_0 is the laser frequency, while the right-going (reflected) light, E_R, is Doppler-shifted down to $\omega_R = \omega_0 - k_0 c_s (M - 2M_c)$, where M_c is the Mach number of the reflecting surface. The beating of these light waves drives an ion wave, $\tilde{n}$, with frequency $\omega_i = \omega_L - \omega_R = 2 k_0 c_s (M - M_c)$. The equations for the slowly varying amplitudes of these waves are

$$c\sqrt{\epsilon}\frac{\partial E_L}{\partial x} = \frac{i\omega_0}{4}\frac{\tilde{n}}{n_c}E_R , \tag{69}$$

$$c\sqrt{\epsilon}\frac{\partial E_R}{\partial x} = \frac{-i\omega_0}{4}\frac{\tilde{n}^*}{n_c}E_L \tag{70}$$

and

$$\tilde{n}\left[\left(\frac{M - M_c}{\sqrt{\epsilon}}\right)^2 + i\frac{\nu}{2k_0c_s\sqrt{\epsilon}}\left(\frac{M - M_c}{\sqrt{\epsilon}}\right) - 1\right] = \frac{e^2 n_0 E_L E_R^*}{2mMc_s^2\omega_0^2} . \tag{71}$$

Here n_0 and n_c are the background density and critical density, ϵ is the plasma dielectric constant, ν is the ion wave damping rate, and m and M are the electron and ion mass. We assume that the ion waves are heavily damped and so have neglected $c_s\partial\tilde{n}/\partial x$ compared to $\nu\tilde{n}$ in Eq. (71). Substituting for $\tilde{n}$, we find equations for $|E_L|^2$ and $|E_R|^2$:

$$\frac{\partial|E_L|^2}{\partial x} = \frac{\partial|E_L|^2}{\partial x} = \frac{n_0 e^2 k_0}{4n_c\omega_0^2 mMc_s^2\sqrt{\epsilon}}|E_L|^2|E_R|^2 \times \frac{\frac{\nu}{\omega_s}\eta}{(1 - \eta^2)^2 + \left(\frac{\nu}{\omega_s}\eta\right)^2} \tag{72}$$

where $\eta = (M - M_c)/\sqrt{\epsilon}$ and $\omega_s = 2 k_0 c_s\sqrt{\epsilon}$. The boundary conditions are $|E_L|^2 = E_0^2/\sqrt{\epsilon}$ at the right end of the slab, where E_0 is the incident vacuum field, and $|E_R|^2 = f|E_L|^2$ at the left end of the slab, where f is the reflectivity of the boundary. Solving Eq. (72), we find that the fractional transmissivity, T, of the slab is given by

$$1 - T(1 - f) = f\exp[T(1 - f)Q(\eta)] \tag{73}$$

where

$$Q(\eta) = \frac{1}{4}\frac{n_0}{\epsilon n_c}\frac{v_0^2}{v_e^2}\frac{k_0 L}{1 + \frac{3T_i}{ZT_e}}\frac{\frac{\nu}{\omega_s}\eta}{(1 - \eta^2)^2 + \left(\frac{\nu}{\omega_s}\eta\right)^2} \tag{74}$$

and $v_0^2 = (eE_0/m\omega_0)^2$.

In deriving Eq. (73) we have neglected the light scattered by plasma fluctuations (noise) relative to the light reflected by the boundary, $\alpha \ll fT$. If there is no reflecting surface ($f = 0$) then this noise level determines the transmissivity as shown previously,[90]

$$T(1 - T) = \alpha\exp[TQ(\eta = 1)] . \tag{75}$$

There are two important new features in Eqs. (73) and (74). First, the quality factor, $Q(\eta)$, has a resonance function behavior, reaching a maximum at the resonant Mach number $M = M_c + \sqrt{\epsilon}$, and falling off with characteristic width ν/ω_s for other Mach numbers. This behavior is demonstrated in Fig. 3-31, which shows the calculated transmissivity for AURUS[91] simulations of the moving-slug problem. Secondly, the transmissivity in the presence of a reflecting surface [Eq. (73)] is almost always much less than that obtained without the

Fig. 3-31. AURUS results for transmissivity, T, vs relative Mach number $M - M_c$, for the case $Q(\eta = 1) = 3.6$, $f = 0.7$. Curve (a), $\nu/\omega_s = 0.25$; curve (b), $\nu/\omega_s = 1$. The transmissivities are slightly lower than predicted by Eq. (73), because of transient effects.

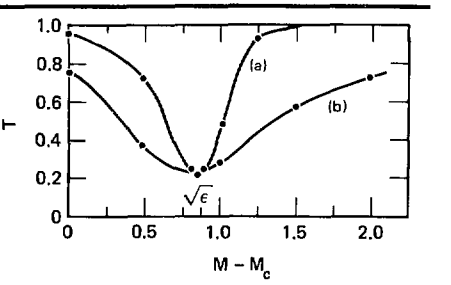

Fig. 3-32. Transmissivity, T, vs Q for exact resonance, $M - M_c = \sqrt{\epsilon}$. Curve (a) is Eq. (75) with $\alpha = 10^{-4}$. Curves (b) and (c) are Eq. (73) with f = 1, 0.27, respectively. The solid circles represent AURUS simulations; squares represents particle simulations. Also shown are AURUS simulations of partially overdense isothermal expansions (triangles).

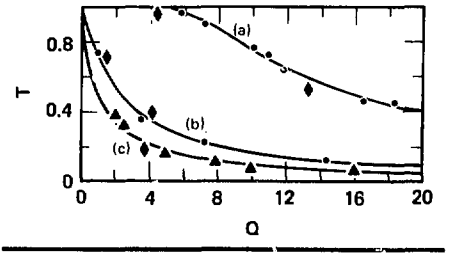

surface [Eq. (75)]. Only if $\alpha T \approx 1$ or $Q(\eta) \ll Q$ (η = 1) are these transmissivities comparable. In fact, for the case of a perfectly reflecting boundary (f = 1) Eq. (73) becomes particularly simple: $T = [1 + Q(\eta)]^{-1}$ (Ref. 89). Figure 3-32 demonstrates this strong enhancement of SBS for various boundary reflectivities.

Our simple moving-slug model (Fig. 3-30) is a good approximation of the case where the critical surface is steepened, either due to the ponderomotive force or to localized heating in a strongly flux-limited plasma.[92] We now consider simulations of SBS in an isothermal expansion, which is appropriate for plasma heating with classical heat transport. Part of the plasma is overdense, so that total reflection takes place at the critical surface (f = 1). We allow various damping rates and scale lengths. Even though the resonance condition, $M - M_c = \sqrt{\epsilon}$, is satisfied only at a single point, the width of the resonance is rather large, as can be seen from Fig. 3-31; essentially, a scale length of plasma participates in the scattering. Figure 3-32 shows the transmissivity points from the AURUS simulations. It can be seen that they fit the theoretical curve $T = (1 + Q)^{-1}$ very well.

Finally, we consider a simulation that includes ablation from solid density. The target was a glass disk, irradiated with 1-μm light at an intensity 10^{15} W/cm^2. Of the light reaching the critical surface, 30% was absorbed (f = 0.7); this corresponds to absorption due to collective plasma effects (parametric decay, resonance absorption, etc.), and agrees with experimental measurements.[93] We allowed classical heat transport, but self-consistent ion heating was

Fig. 3-33. Plot of electron density for a fluid simulation including ablation from solid density. Density fluctuations maximize near the resonance point $M - M_c = \sqrt{\epsilon}$.

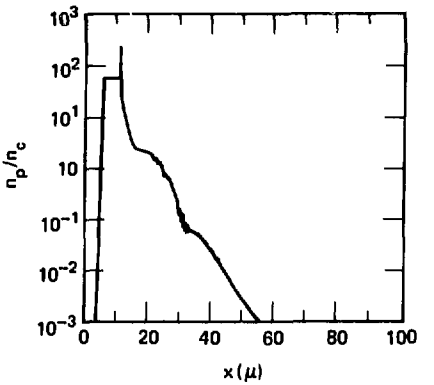

not allowed. Rather, we set $\nu = \omega_s$. Figure 3-33 shows the density profile n_p/n_c at a time 100 ps into the calculation. The SBS-active region is $0.1 \leq n_p/n_c \leq 1$. The position of maximum scattering is at the point predicted by the resonance condition. Evaluating Q at this time we find Q = 1.25. From Eq. (75), for f = 0.7 the predicted transmissivity is T = 0.51, whereas the simulation gives T = 0.48—certainly adequate agreement.

Authors: C. J. Randall, J. J. Thomson, and K. G. Estabrook

References

89. C. J. Randall, J. J. Thomson, and K. G. Estabrook, *Phys. Rev. Lett.* **43**, 924 (1979).
90. D. W. Phillion, W. L. Kruer, and V. C. Rupert, *Phys. Rev. Lett.* **39**, 1529 (1977).
91. *Laser Program Annual Report—1978*, Lawrence Livermore Laboratory, Livermore, Calif., UCRL-50021-78 (1979), pp. 3-53.
92. M. D. Rosen et al., *Phys. Fluids* **22**, 2020 (1979).
93. K. Manes, V. C. Rupert, J. M. Auerbach, P. H. Y. Lee, and J. E. Swain, *Phys. Rev. Lett.* **39**, 281 (1977).

Calculations of Stimulated Brillouin Scattering with LASNEX

Last year's annual report outlined the fundamentals of our Brillouin model in LASNEX, and results of the laser wavelength scaling of an

Fig. 3-34. Absorption and Brillouin reflection vs laser wavelength for several intensities. The number above the line is the intensity in W/cm^2. (Because light that has been reflected by Brillouin may be subsequently absorbed, the fractions of Brillouin scatter and absorption may total more than 1.) The experimental triangles correspond to the absorption of the LASNEX result nearest to it at the same laser wavelength. Note that the density and velocity gradients have essentially pushed Brillouin below threshold for the 3×10^{14} green-light runs.

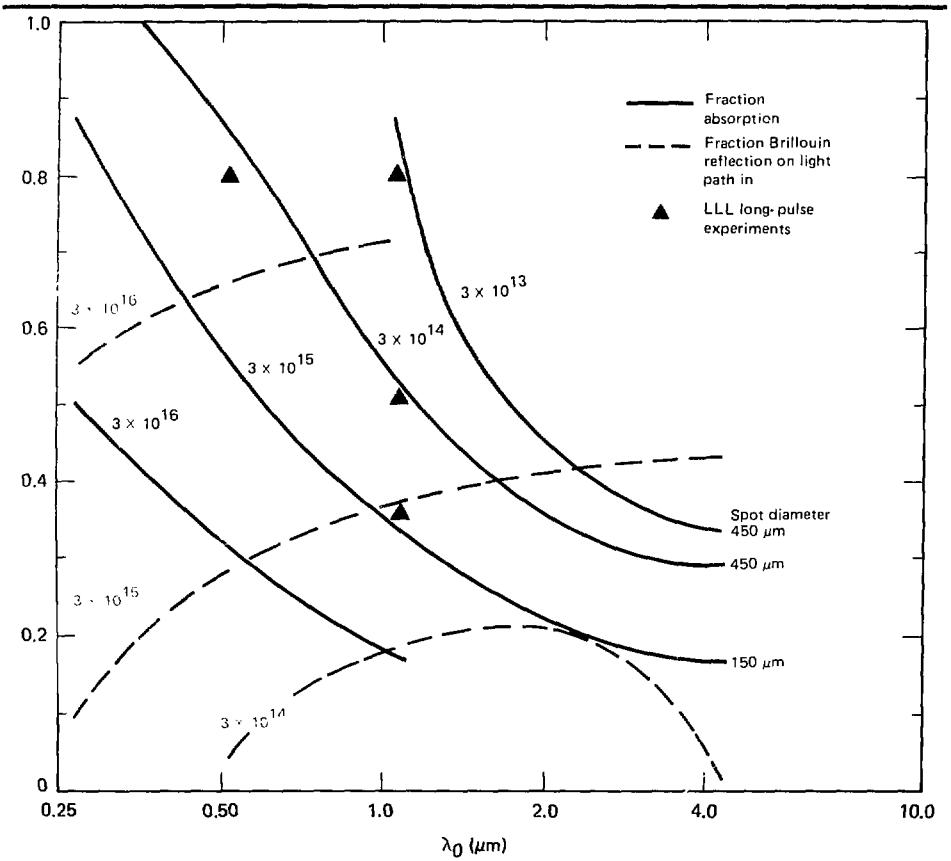

exploding-pusher model.[94] In the last year, we have incorporated and done test runs of a number of improvements (described in detail in "Brillouin Backscattering Model in LASNEX" later in this section).

All simulations were run on a gold disk, with laser pulse length of 1 ns FWHM and spot diameters corresponding to experiments where available (shown in triangles). LASNEX has multipliers on the νn, νv, the heated ion density, and the saturated ion density amplitude; all these were set at 1 in these runs. For consistency, transport inhibition was used in all runs, such that heat was transported no faster than the ion sound speed for $ZT_e/T_i \gg 1$, which is the case of interest. For $I\lambda_2 < 3 \times 10^{14}$, however, there is experimental evidence that perhaps this is not necessary, as less transport inhibition would mean more absorption.

The generators for these runs were modifications of the one discussed above (in "High-Z Disk Modeling") and were adapted to a treadmill rezoner

between 0.1 and 1 critical density, giving 10 zones in all. The absorption and Brillouin scattering changed less than 2% from the coarse-zoned examples.

Figure 3-34 shows the absorption due to inverse bremsstrahlung and resonant absorption (solid lines), and reflection due to Brillouin scattering for light on the way to the target. After the light is reflected by Brillouin, it may

- Be absorbed by inverse bremsstrahlung.
- Be lost due to Brillouin again.
- Escape the target without being affected by

either Brillouin or any absorption mechanism.

Conclusion. We have developed a model which predicts the fraction of light absorbed (±10%) by gold disks over a wide range of intensities and a factor of two in laser wavelength. We point out, however, that though the model is close to the short-pulse, green-light, French experiments, it underestimates (by 10 to 15%) the absorption on CH disks as found by the long-pulse Shiva experiments. We have self-consistently included a new inverse bremsstrahlung multiplier[95] in LASNEX and found that the absorption is then too low. Absorption by ion acoustic turbulence is now being incorporated into LASNEX to find out if we can more clearly resolve the reason why CH and gold absorb about the same fraction and recover some of the absorption lost to inverse bremsstrahlung.[9]

Authors: K. G. Estabrook and J. A. Harte

References

94. *Laser Program Annual Report—1978*, Lawrence Livermore Laboratory, Livermore, Calif., UCRL-50021-78 (1979), p. 3-63 and p. 3-56.
95. A. B. Langdon, *Phys. Rev. Lett.* **44**, 575 (1980).
96. R. J. Faehl and W. L. Kruer, *Phys. Fluids* **20**, 55 (1977).

Steepening of Ion Acoustic Waves

The nonlinear evolution of ion acoustic waves is a subject of both theoretical and practical importance. An interesting characteristic of a long-wavelength ion acoustic wave is its tendency to steepen, i.e., to generate harmonics. Simple arguments[97,98] indicate that this harmonic generation is efficient when the amplitude of the density fluctuation, δn, associated with an ion wave with wave number, k, satisfies the condition $\delta n/n_p \gtrsim 4k^2\lambda_{De}^2$, where n_p is the background plasma density and λ_{De} is the electron Debye length. This condition is easily satisfied, for example, by the ion waves generated via Brillouin scattering in microwave simulation experiments,[99,100] or by the ion waves associated with the electron-ion decay instability in laser-produced plasmas.

We have examined harmonic generation by an ion acoustic wave in a one-dimensional approximation via numerical solutions of the two-fluid description of a plasma. The ion fluid is described by the continuity and force equations

$$\frac{\partial n_i}{\partial t} + \frac{\partial}{\partial x}(n_i u_i) = 0$$

and

$$\frac{\partial u_i}{\partial t} + u_i \frac{\partial u_i}{\partial x} = \frac{ZeE}{M} - \nu_i u_i \ , \qquad (76)$$

where n_i and u_i are the density and velocity of the ion fluid, E is the electric field, Z and M are the ion charge and mass, and ν_i is a collision frequency which models Landau damping of the ion waves. If we neglect electron inertia and include a small ponderomotive force on the electrons, the analogous equations for the electron fluid reduce to

$$n_e = n_p \exp\left(\frac{e\phi}{\theta e} + \alpha\right) \ , \qquad (77)$$

where n_e and θe are the electron density and temperature, n_p is the unperturbed electron density, ϕ is the electrical potential ($E = -\partial\phi/\partial x$), and α is the ponderomotive potential (normalized to $\theta e/e$) that drives the ion acoustic waves. We complete the model with Poisson's equation:

$$\frac{\partial^2\phi}{\partial x^2} = 4\pi e(n_e - n_i) \ . \qquad (78)$$

To investigate the harmonic generation, we expand these equations to second order in the potential ϕ, and then Fourier-transform: this results in a set of nonlinear coupled-mode equations. By appropriately choosing α, we can excite an ion acoustic wave and compute the steady-state spectrum which results.

In the present example, an ion acoustic wave with wave number $k\lambda_{De} = 0.06$ is driven by a ponderomotive force. As the amplitude of this wave increases, energy is nonlinearly coupled with its harmonics. Finally, the wave reaches the steady-state

spectrum shown in Fig. 3-35, in which the energy flowing into the driven wave is balanced by the energy damped from the entire spectrum of waves. Note that a rich spectrum of harmonics is produced. Indeed, the root-mean-square fluctuation amplitude has become nearly twice as large as the amplitude of the directly driven ion wave.

Since the harmonics are supported by the directly driven ion wave, their generation represents an enhanced damping of this wave. This is shown by the results in Fig. 3-36, where the steady-state amplitude of the driven wave is plotted as a function of the amplitude of the ponderomotive force (α) that excites the wave. The open circles are results from the numerical calculations, and the solid line denotes a simple theoretical estimate that includes the effects of enhanced damping (a calculation without the enhanced damping predicts larger steady-state amplitudes). To obtain this estimate, we first define an effective energy damping rate ν_s as $2/t_s$, where t_s is a steepening time. As shown in Ref. 98, $t_s^{-1} \simeq (\omega_i/2)(\delta n/n_p)$, where ω_i is the ion acoustic frequency. The steady-state amplitude is then predicted to be

$$\frac{\delta n}{n_p} = \frac{\alpha}{\nu_i + \nu_s} \,, \qquad (79)$$

This gives fairly [illegible] agreement with the numerical [illegible]. As [illegible] harmonic generation can be more important than the damping of the driven wave when $\delta n/n_p > \nu_i/\omega_i$.

In summary, we have investigated harmonic generation by an ion acoustic wave. Our preliminary results show that this harmonic generation can act like enhanced damping and significantly reduce the amplitude to which a long-wavelength ion wave can be driven. We need to extend our calculations to further explore the efficiency of the harmonic generation as a function of the wavelength of the driven wave, and to allow for other ion waves with wave numbers which are not an integral multiple of the wave number of the driven wave. An important question to be addressed is the role of nonlinear frequency shifts on the harmonic generation. We also plan to describe the ions as particles, in order to explore the effect of harmonic generation on ion trapping.

Fig. 3-35. The steady-state spectrum of ion acoustic waves found in numerical calculations in which one wave is driven by a ponderomotive force. In this example, the driven wave had a wave number $k_0\lambda_{De} = 0.06$, $\nu_i/\omega_i = 0.05$ and $\alpha = 5 \times 10^{-3}$.

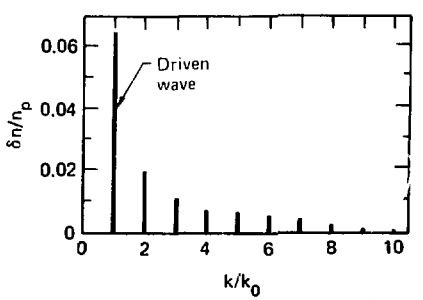

Fig. 3-36. The steady-state amplitude of a driven ion acoustic wave as a function of the ponderomotive potential that drives it. In these calculations, $\nu_i/\omega_i = 0.05$ and the wave number of the driven wave is $k_0\lambda_{De} = 0.06$.

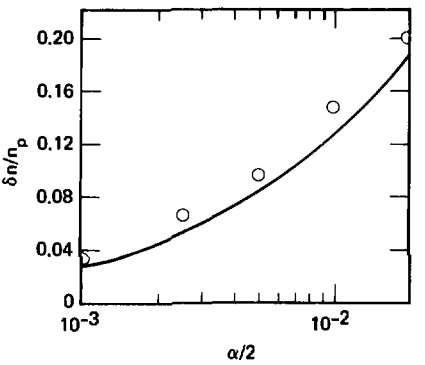

Author: W. L. Kruer

References

97. J. M. Dawson, W. L. Kruer, and B. Rosen, *Dynamics of Ionized Gases*, M. Lighthill, I. Imai, and H. Sato, Eds. (University of Tokyo Press, Tokyo, 1973), pp. 47 to 61.

98. W. L. Kruer and K. G. Estabrook, "Nonlinear Behavior of Stimulated Scatter in Large Underdense Plasmas," prepared for the Fifth Workshop on Laser Interaction with Matter, University of Rochester, Rochester, New York, November 5 to 9, 1979; also available as Lawrence Livermore Laboratory, Livermore, Calif., UCRL-83743 (1979).

99. N. Luhmann, University of California at Los Angeles, Los Angeles, Calif., private communication, (1980).
100. J. S. DeGroot, University of California at Davis, Davis, Calif., private communication (1980).

Simultaneous Self-Focusing and Brillouin Backscattering of Gaussian Laser Beams

Ion heating is probably the major saturation mechanism for stimulated Brillouin scattering (SBS) for long, moderate-intensity laser pulses.[101] If the ions are heated to $T_i \sim ZT_e$, the spatial growth length for self-focusing becomes comparable to that of SBS (Ref. 102), so these two processes should be considered simultaneously. Here we carry out an analysis of their interaction for azimuthally symmetric laser beams in steady state. We assume that the beams are approximately Gaussian. (A discussion of the validity of the Gaussian beam approximation for pure self-focusing may be found in the next article.) We find that a small amount of SBS can cause a self-trapped laser beam to diverge after undergoing a single focusing event.

We begin with the equations for the slowly varying (in r and z) envelopes of the left-going and right-going light waves, E_- and E_+, the time-independent plasma density, n, and the SBS ion wave, $\tilde{n}$:

$$\pm 2ik\frac{\partial I_\pm}{\partial z} + \frac{1}{r}\frac{\partial}{\partial r}\left(r\frac{\partial I_\pm}{\partial r}\right) + \frac{\omega_0^2}{c^2}\left(1 - \frac{n}{n_c}\right)I_\pm - \frac{\omega_0^2}{2c^2} \times \frac{\tilde{N}^{(*)}}{n_c} I_\mp = 0 , \qquad (80)$$

$$n = n_0 \exp\frac{-e^2\left(|E_+|^2 + |E_-|^2\right)}{4m\omega_0^2(T_e + 3T_i/Z)} , \qquad (81)$$

and

$$2ik\frac{\partial \tilde{N}}{\partial z} + i\frac{\nu\omega_s}{c_s^2}\tilde{N} + \frac{\bar{n}}{r}\frac{\partial}{\partial r}\left(\frac{r}{n}\frac{\partial \tilde{N}}{\partial r}\right) = -\frac{2Ze^2nk^2}{mM\omega_0^2c_s^2} E_+^* I_- . \qquad (82)$$

In these equations n_0 and n_c are the background and critical plasma density, ν and ω_s are the ion-wave damping rate and frequency, ω_0 and k are the laser frequency and local wave number, and c and c_s are the speeds of light and sound, respectively; in Eq. (80), (*) means "conjugate" for the + equation only. Appropriate to $T_i \sim ZT_e$ we take the heavy damping limit of Eq. (82), neglecting the convection and diffraction terms:

$$\tilde{N} = \min\left(\frac{2Ze^2k^2 E_+ E_-^*}{mM\omega_0^2\nu\omega_s}, \delta_{WB}\right)\frac{I_+ I_-}{|E_+|^2 |E_-|^2} , \qquad (83)$$

where we have included an upper limit on the SBS ion wave amplitude, δ_{WB}, to model ion trapping. Combining Eqs. (80), (81), and (83), we obtain

$$\pm 2ik\frac{\partial I_\pm}{\partial z} + \frac{1}{r}\frac{\partial}{\partial r}\left(r\frac{\partial I_\pm}{\partial r}\right) + \frac{\omega_{p0}^2}{c^2} I_\pm (1 - \varepsilon) + i\frac{\omega_{p0}^2}{2c^2}\varepsilon \min\left(C_i |E_+ E_-^*|, \delta_{WB}\right)\frac{I_\mp}{I_\pm} I_\pm = 0 , \qquad (84)$$

where $\varepsilon = \exp - \alpha(|E_+|^2 + |E_-|^2)$, $\omega_{p0}^2 = \omega_0^2 n_0/n_c$, $\alpha = \nu_0^2/4\nu_e^2(1+\tau)$, and $C_i = 2\alpha(1+\tau)[(1+3\alpha)(\nu/\omega_s)]$. We have normalized $E_\pm$ to the incident field E_0 with quiver velocity ν_0. The electron thermal velocity is ν_e and $\tau = T_i/ZT_e$ is the normalized ion temperature. This equation can describe the simultaneous SBS and self-focusing of laser beams with arbitrary radial intensity distributions.

We discuss next a set of moment equations describing some averaged properties of the incident and scattered beams. In deriving these equations we make the approximation of replacing the SBS scattering coefficient with its intensity-averaged value,

$$\pm 2ik\frac{\partial I_\pm}{\partial z} + \frac{1}{r}\frac{\partial}{\partial r}\left(r\frac{\partial I_\pm}{\partial r}\right) + \frac{\omega_{p0}^2}{c^2} I_\pm (1 - \varepsilon) + i\frac{\omega_{p0}^2}{2c^2}\beta_\pm I_\pm = 0 , \qquad (85)$$

where

$$\beta_\pm = \frac{\int_0^\infty r\, I_\mp\, \varepsilon \min\left(C_i |E_+ E_-^*|, \delta_{WB}\right)\frac{I_\mp}{|E_\mp|^2}\, dr}{\int_0^\infty r I_\pm\, dr} . \qquad (86)$$

Taking the first two radial moments of Eq. (85) yields equations for power and mean square radius

of the beams. We close this set of moment equations by making the Gaussian beam approximation,

$$I_{\pm 0} = A_{\pm}^2(z) \exp\left[r^2/a^2(z) \right] . \qquad (87)$$

The rest is straightforward (although tedious) to obtain the following equations for $A_\pm$ and a:

$$\left(A_{\pm}^2 \right) + \frac{\omega_{p0}^2}{2c^2k^2} \left(\quad \right) A_{\pm}^2 = 0 , \qquad (88)$$

$$\frac{d^2a}{dz^2} = \frac{\partial V}{\partial a} , \qquad (89)$$

$$V = \frac{1}{a^2} + \frac{\omega_{p0}^2}{c^2k^2} \left\{ 1 - \frac{E_{in}(P)}{P} \right\} , \qquad (90)$$

$$\frac{\partial V}{\partial z} = \frac{1 - (1 + PX_{WB}) \exp(-PX_{WB})}{P^2} \left(\quad \right) \exp(-PX_{WB}) - \exp(-P)}{P} \qquad (91)$$

and

$$E_{in}(x) = \int_0^x \frac{1 - \exp(-t)}{t} dt . \qquad (92)$$

with $P = (A_+^2 + A_-^2)$, and $X_{WB} = \min(1, A_+^2/A_-^2, A_-^2/A_+^2)$.

Equation (88) describes the decay (growth) of the incident (scattered) beam as it propagates through the plasma. Equation (89) is an equation of motion for the root mean square beam radius; this equation has been derived previously,[103] neglecting SBS. The inclusion of SBS has added an explicit z-dependence to the potential function V(a,z), and it is this new feature which allows previously trapped beams to become untrapped in the presence of SBS.

This phenomenon is apparent in the first integral of Eq. (91):

$$\frac{d}{dz}\left[\frac{1}{2}\left(\frac{da}{dz} \right)^2 + V \right] = \frac{\partial V}{\partial z} = \frac{\omega_{p0}^2}{2c^2k^2} \frac{d}{dP}\left[\frac{E_{in}(P)}{P} \right] \frac{1}{a^2} \frac{d(a^2P)}{dz} . \qquad (93)$$

Fig. 3-37. Numerical solution of Eq. (103) (neglecting SBS). Plotted is rms beam radius, a, vs axial distance, z. Parameters are $V_0^2/V_e^2 = 0.1$, $n_0/n_c = 0.2$, $\tau = 1$, $ka(z = 0) = 50$, $da/dz(z = 0) = 0$.

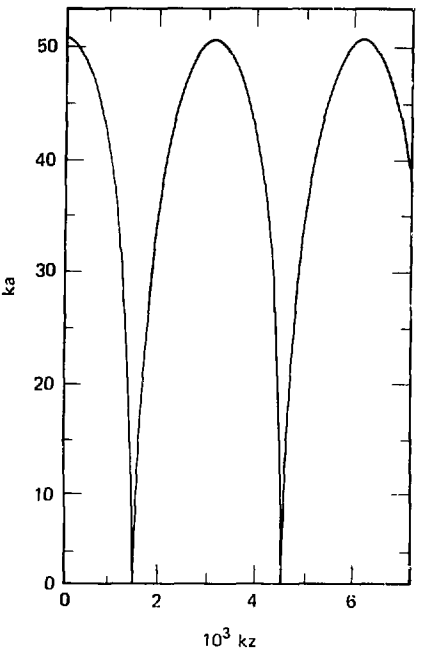

In the absence of SBS, a^2P is a constant. Thus the total "energy" of the beam $E = 1/2(da/dz)^2 + V$ is conserved. If a beam enters the plasma with $E < 0$ then E will always be negative and the beam will be trapped, with its rms radius oscillating nonlinearly as shown in Fig. 3-37. In the presence of SBS, however, $\partial V/\partial z = dE/dz > 0$, so that the beam must eventually escape, i.e., diverge indefinitely as E becomes positive.

An example of this behavior is shown in Fig. 3-38. Physically, the scattered light beam helps to deplete the plasma density so that the incident beam acquires more inward radial momentum per unit intensity then it would in the absence of SBS. Then, as the incident light approaches the focus, scattering rises rapidly due to the increase in intensity. After passing through the focus the incident light intensity is decreased due to SBS. The incident beam does not deplete the plasma density enough for refraction to overcome the large radial momentum it acquired

Fig. 3-38. Same parameters as Fig. 3-37, except that SBS is allowed; $\delta_{WB} = 0.1$, $\nu/\omega_s = 1$, $A_-^2(kz = 6000) = 10^{-4} A_+(kz = 6000)$.

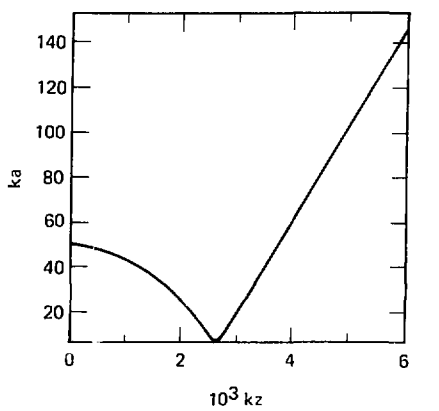

during its flight towards the focus. As a result the beam diverges indefinitely after a single focus.

The simple moment equations derived above suggest a qualitatively new feature of self-focusing when SBS is included. These equations, however, give only very approximate descriptions of the system's true behavior: more quantitative results require full numerical solution of Eq. (84).

Author: C. J. Randall

References

101. *Laser Program Annual Report—1977*, Lawrence Livermore Laboratory, Livermore, Calif., UCRL-50021-77 (1978), pp. 6-12 to 6-17.
102. *Laser Program Annual Report—1978*, Lawrence Livermore Laboratory, Livermore, Calif., UCRL-50021-78 (1979), pp. 3-36 to 3-42.
103. L. F. Lam and B. Lippmann, *Phys. Fluids* **20**, 1176 (1977).

Spatial Structure of Filamented Light

Self-focusing, or filamentation, may become an increasingly dominant effect in present-day and future experiments. In contrast to modeling of earlier short-pulse experiments, we now envision beams traversing 10^3 to 10^4 free-space wavelengths of underdense plasma, and reactor targets as large as a centimeter in diameter.

To investigate the spatial structure of self-focused light, we solve numerically a Schrödinger equation in cylindrical (r,z) geometry with an exponential nonlinearity, which describes the filamentation of laser light in underdense plasmas due to the ponderomotive force. This work complements and extends previous analytic descriptions[104-106] of self-focusing in underdense plasmas.

To derive the equation we want to solve, we start with the wave equation

$$\nabla(\nabla\cdot\mathbf{E}) - \nabla^2\mathbf{E} = \frac{\omega_p^2}{c^2}\mathbf{E} + \frac{1}{c^2}\frac{\partial^2\mathbf{E}}{\partial t^2} \qquad (94)$$

for the laser-light electric field vector $\mathbf{E}$ propagating in a plasma of frequency ω_p. Let

$$\mathbf{E} = \hat{\mathbf{r}}\,\psi(r,z)\exp[i(k_0 z - \omega_0 t)] , \qquad (95)$$

where ω_0 is the free-space laser frequency and k_0 is the wave vector corresponding to propagation in a plasma of unperturbed density n_p. If n_p (assumed here for simplicity to be a constant) is small enough, then space charge effects may be neglected; that is, we may ignore $\nabla\cdot\mathbf{E}$. Also, we assume that $\partial^2\psi/\partial z^2$ is small with respect to $k_0(\partial\psi/\partial z)$. Equation (94) then becomes

$$2ik_0\frac{\partial\psi}{\partial z} + \frac{1}{r}\frac{\partial}{\partial r}\left(r\frac{\partial\psi}{\partial r}\right) + \left(\frac{\omega_0^2}{c^2} - k_0^2 - \frac{\omega_p^2}{c^2}\right)\psi = 0 . \qquad (96)$$

The plasma density is determined by balancing the isothermal pressure against the ponderomotive force; then

$$\omega_p^2 = \frac{4\pi e^2}{m} n_p \exp\left(\frac{1}{4}\frac{v_0^2}{v_{th}^2}\right) , \qquad (97)$$

where e and m are the charge and mass of the electron, respectively, v_0 is the oscillatory velocity of the electron in the laser electric field, with $|v_0| = eE/m\omega_0$; and v_{th} is the electron thermal velocity, with (in the units used here) $v_{th}^2 = c^2(T_e/511)$ where T_e is the electron plasma temperature expressed in keV.

The differencing scheme we use to solve Eqs. (96) and (97) is chosen to preserve the conservation properties of the Schrödinger equation. Variable

zoning in both r and z leads to economy in code size and running time. The Crank–Nicholson scheme is used to advance $\epsilon(r,z)$ in z, and the nonlinearity is obtained by iteration. The flux is monitored as a check of the numerical scheme. The validity of the paraxial approximation as the beam focuses is checked by comparing the magnitude of the second derivative, $\partial^2\epsilon/\partial z^2$, to the first derivative, $|k_0| \cdot |\partial\epsilon/\partial z|$.

To compare to earlier work,[104-106] we first discuss the self-focusing of an initial Gaussian pulse. In order to solve Eqs. (96) and (97) analytically, the assumption is made that the beam remains a Gaussian as it focuses. An advantage of the numerical solution is that no such assumption is necessary.

Although different methods of solution are used in Refs. 104 to 106, the qualitative description is the same. Above a rather low threshold power, P_c, there are self-trapped solutions; for stationary self-trapped solutions the filament radius may be as small as several free-space wavelengths. Numerically, we find that for a given P_c our work verifies the expression for the radius of the stationary self-trapped filament given in Ref. 106. For powers above this critical power, however, the numerical solution predicts very different behavior than that obtained in the analytic solution. The beam does not retain its Gaussian shape, and focuses in a shorter distance than predicted analytically.

As an example, we describe a numerical simulation for $P/P_c \sim 11$. Here, $v_0/v_{th} = 0.1$ and, if v_{th} describes a 10-keV plasma, then the corresponding laser intensity is 2.4×10^{14} W/cm^2 for 1.06-μm laser light. The initial shape is $\epsilon(r,z=0) = \epsilon(r=0,z=0)\exp(-r^2/\sigma^2)$ and $k_0\sigma = 700$. Also, $n = 0.1\ n_c$, where n_c is the critical density (the density at which the plasma frequency equals the laser frequency).

Our results are illustrated by the flux contours of Fig. 3-39. These contours are chosen to give equal spacing for a Gaussian beam. This shape is lost as the inner portion of the beam focuses down to a very narrow filament. The power contained in this central inner portion is approximately the critical power—an intuitively pleasing result.

After this first focus, rings begin to appear beyond the central inner portion. The second maxima at $100 \leq k_0 r \leq 200$ is evident in these flux contours. [The appearance of rings beyond the first focus was first found in numerical work by Marburger and Dawes[107] for a nonlinearity of the form $|E|^2/(1 + |E/E_s|^2)$.]

Fig. 3-39. Flux contours for an initial Gaussian profile with $|v_0/v_{th}| = 0.1$ and $k_0\sigma = 700$. If the beam had retained its Gaussian shape, these contours would have remained equally spaced.

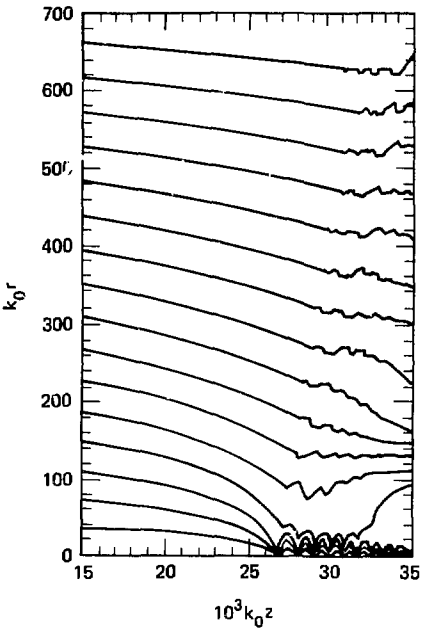

A snapshot of $|v_0/v_{th}|^2$ vs k_0r beyond the first focus is shown in Fig. 3-40. Note the evident non-Gaussian nature: the maximum intensity is not on the beam axis at this point in z. Similar snapshots at any point in z always show this well-defined central portion and a long tail; the Gaussian initial shape is not maintained during the beam evolution. Figure 3-41 shows $|v_0/v_{th}|^2$ at r = 0, vs z. Notice that after first focus at $k_0z = 26\,700$, the intensity oscillates about a large value, never returning to its initial low value.

We compared our results with those of the analytical theory with the Gaussian shape ansatz by numerically integrating Eq. (26) of Ref. 106. The results for $|v_0/v_{th}|^2$ as a function of z are indicated

Fig. 3-40. Plot of $|v_0/v_{th}|^2$ vs k_0r at k_0z = 29 000 for the initial Gaussian of Fig. 3-39. This snapshot is taken beyond the first intensity maximum.

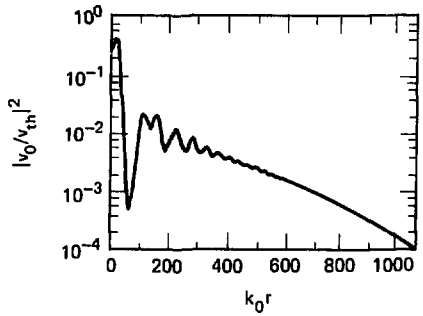

Fig. 3-41. Plot of $|v_0/v_{th}|^2$ at r = 0 as a function of k_0z for the initial Gaussian of Fig. 3-39. The solid curve is the code result with first focus at k_0z = 26 700. The dotted line is the analytic result with the Gaussian shape assumption.

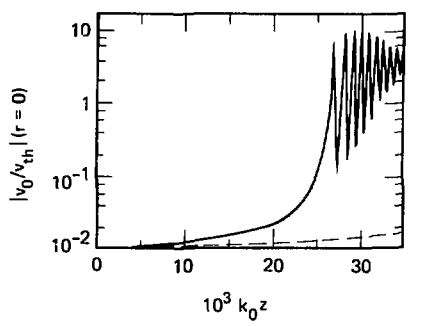

by the dotted line in Fig. 3-41. These analytic results are much too low and the resulting distance to first focus is more than twice that found without the Gaussian shape assumption. At first focus, however, the analytic model has even sharper behavior than the numerical solution. The peak value of $|v_0/v_{th}|^2$ is 1.5×10^2 and the resulting beam radius is less than the beam wavelength. According to the analytic model, the beam then oscillates by continually relaxing to its original state and refocusing. Thus the analytic model as developed in Ref. 106, with its Gaussian-shape ansatz, does not reproduce even the qualitative behavior found in the numerical solution, whether

Fig. 3-42. Plot of initial $|v_0/v_{th}|^2$ vs k_0r for the ring beam (solid curve) and a Gaussian of the same flux (dotted curve).

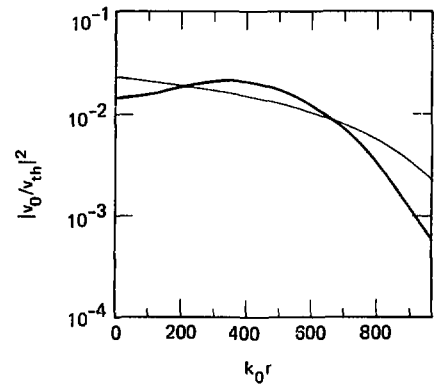

well before first focus, at first focus, or beyond the focus.

We should add a note of caution about the sharp behavior at first focus in our numerical results. There are several simplifications and assumptions in the derivation of Eqs. (96) and (97): steady state, cylindrical symmetry, slow variation with respect to z, scalar rather than vector optics, and no back-reflected light.

An obvious advantage of the numerical solution is the ease with which we can study the propagation of initial pulse shapes other than Gaussian. To date we have tried "super-Gaussians" [$\propto e^{-(r/\sigma)^4}$] and "ring" beams; we find rather similar behavior for both. For the initial profile of Fig. 3-42,

$$\epsilon(r,z=0) = \epsilon(r=0)\left[1 + 2\left(\frac{r}{\sigma}\right)^2\right]\exp\left[-\left(\frac{r}{\sigma}\right)^2\right], \qquad (98)$$

with $k_0\sigma$ = 500 and the central intensity corresponding to v_0/v_{th} = 0.12, or 3.4×10^{14} W/cm^2 at 10 keV for Nd:glass. The flux contours are shown in Fig. 3-43. Again, these flux contours were chosen to give equal spacing for a Gaussian beam, but there is little evidence of Gaussian-like propagation.

The ring beam reaches first intensity maximum at $k_0z \sim 16\,000$. A Gaussian beam with the same

Fig. 3-43. Flux contours for the ring beam described in Fig. 3-42.

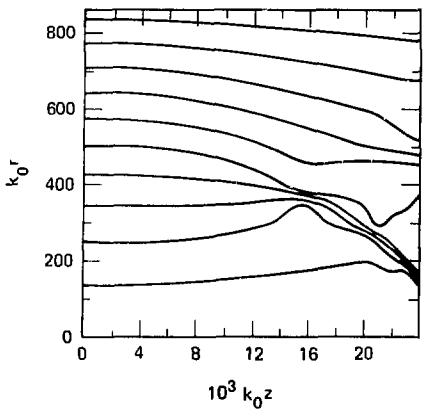

power (v_0/v_{th} = 0.146, $k_0\sigma$ = 922) reaches first focus further downstream, at $k_0z \sim 21\,000$. Also, the maximum intensity at first focus is a factor of five larger for the Gaussian beam.

After the "first focus" of the ring beam other rings appear, and these maxima slam into the center. This singularity at r = 0 is a consequence of the cylindrical-symmetry assumption used in deriving Eq. (96). If azimuthally-dependent behavior were included, we would expect these rings to break off into small-scale filaments.

A central issue in the study of filamentation in relation to laser fusion applications is its competition with other processes in the underdense plasma. As a start toward understanding this competition, we have included the effects of inverse bremsstrahlung absorption with its density-dependence in our code. The absorption length is assumed to be larger than the distance to first focus without absorption.

Not surprisingly, this finite absorption length results in longer distances to first focus and lower maximum intensities. But note also that as the beam focuses, the density is lowered and the absorption rate decreases. Therefore, the behavior of the most intense part of the beam is qualitatively unaffected by the inclusion of an absorption length greater than the distance to first focus.

To apply these results to laser-plasma experiments, we point out the scaling properties of Eq. (95). If the density changes by a factor of α, then adjusting the radial size by α^{-2} and changing the propagation distance, z, by $k_0(n)/\alpha k_0(\alpha n) \sim 1/\alpha$ regains the original equation. Thus one numerical example encompasses a family of results.

Authors: B. F. Lasinski and A. B. Langdon

References

104. C. E. Max, "Strong Self-focusing Due to the Ponderomotive Force in Plasmas," *Phys. Fluids* **19**, 74 (1976).
105. J. F. Lam, B. Lippman, and F. Tappert, "Self-trapped Laser Beams in Plasma," *Phys. Fluids* **20**, 1176 (1977).
106. D. Anderson and M. Bonnedal, "Variational Approach to Nonlinear Self-Focusing of Gaussian Laser Beams," *Phys. Fluids* **22**, 105 (1979).
107. J. H. Marburger and E. Dawes, "Dynamical Formation of a Small-scale Filament," *Phys. Rev. Lett.* **21**, 556 (1968).

Update of Model for Ablative Laser Fusion Implosions

A few years ago[108] we described our preliminary work on a model for ablative laser fusion implosions. Here we present an updated and expanded version of that model, which includes a more detailed description of the density jump at the critical surface.

There is now a rather complete literature describing scaling laws for laser fusion targets of the exploding-pusher variety,[109] in which heat is carried dominantly by hot suprathermal electrons. In the present section we derive scaling laws for a different type of laser fusion target, called an "ablative" target. In ablative implosions hot electrons are not important to the overall energy flow. Rather, the inward flow of energy is via thermal conduction, and is roughly balanced by the outward flux of plasma energy and PdV work from the ablation surface. To conserve momentum the remaining cold material must be accelerated inward, or implode.

We shall present simple expressions describing the ablation pressure, critical radius, and ablation rate for spherical ablative targets. These quantities are functions of the laser intensity, laser wavelength, and target size. Effects of inhibited heat transport of a magnitude inferred from a large body of experimental data[110] are explicitly included. Previous work on spherical laser-driven ablation was largely computational rather than analytic,[111] exploring the regime where heat transport inhibition is not important.[112,113]

Although the present model has been developed for spherical geometry, Ref. 114 shows that it may be applied with some success to planar targets, by setting the effective ablation radius roughly equal to the spot diameter in a planar irradiation.

The Ablative Flow. Classical expressions[115] for conductivity, κ, and heat flux, q, are valid when the scale length for temperature variations, L_T, is much longer than the electron-ion mean free path. When gradients are so steep that L_T becomes less than a mean free path, the classical expression for q implies that the characteristic speed for heat flow is much faster than the electron thermal speed. This seems physically unreasonable, at least for electron distribution functions close to Maxwellian. A common remedy has been to postulate an upper limit on the heat flux in this regime. Frequently one expresses this "saturated" magnitude of the heat flux, q_{sat}, in terms of the electron thermal speed $v_{te} \equiv (kT_e/m_e)^{1/2}$:

$$q_{sat} = f(n_e kT_e) v_{te} = 5\phi\rho c^3 \quad . \tag{99}$$

Here n_e is the number density of electrons, f is the flux limit as usually defined, ϕ is the flux limit scaled to hydrodynamic variables, and $c = (p/\rho)^{1/2}$ is the isothermal sound speed, where p and ρ are the pressure and density.

At present the appropriate value for the flux limit, f, is uncertain. Interpretation of a variety of laser-plasma interaction experiments[110] has been possible only when f is assumed to be approximately 0.03. Work is in progress to understand the size of the flux limit f and the mechanisms responsible for inhibited energy transport.

In the work below, we will take the electron-heat flux to be the minimum of the classical and saturated values. We leave f as a parameter in our solutions; our only restrictions are that f be constant in space, and, for the analytic work, that $f \gtrsim 0.4$ for a D-T plasma.

A typical temperature profile, T(r), for a laser fusion target has a high temperature at the critical radius, and a low temperature at the ablation surface. As a result, one can show that conduction is typically classical near the cold pellet surface, R_a, whereas it may be saturated near the critical surface.

The overall flow is obtained by solving separately in the classical and saturated regimes, and then matching the solutions at the point where the classical and saturated heat flows are equal (details of the derivation not presented here are discussed in Refs. 111 and 116). The equations to be solved are mass conservation,

$$\dot{m} \equiv 4\pi r^2 \rho v = \text{constant} \quad , \tag{100}$$

the equation of motion for the gas,

$$\rho v(dv/dr) = -dp/dr, \; p = \rho c^2 \quad , \tag{101}$$

and the energy equation,

$$r^2(d/dr)r^2\left[\rho v(v^2/2 + 5c^2/2) + \underset{\sim}{q}\cdot\hat{r}\right] = Ib(r - r_c) \quad . \tag{102}$$

In these equations v is the radial flow velocity and I is the absorbed laser intensity at the critical surface. For this work we assume the electron and ion temperatures to be equal; extension to separate values of T_e and T_i is straightforward.[116] The pressure is given by $p = n_e kT_e + n_i kT_i \equiv nkT/\mu$. The mean mass per particle is $\mu \equiv Am_p/(Z + 1)$, where the ion mass and charge are Am_p and Ze. The critical surface for a laser of frequency ω lies at the radius r_c where the electron density is $n_e \equiv m_e\omega^2/(4\pi e^2)$. It is assumed that the laser deposits its energy at r_c. We are thus neglecting absorption in the underdense plasma ($r > r_c$). We also assume that the laser light pressure is negligible. Finally, we assume a quasi-steady state. We discuss the validity of these assumptions below and in the following article.

Inside the pellet surface Eq. (102) may be integrated to obtain

$$(5/2)\dot{m}c^2(1 + M^2/5) + 4\pi r^2 \underset{\sim}{q}\cdot\hat{r} = A = \text{constant} \quad , \tag{103}$$

where $\dot{m} = 4\pi r^2\rho v$ is the mass loss rate and $M = v/c$ is the isothermal Mach number. The constant of integration A is the difference between the outward enthalpy flux and the inward conductive heat flux. For subsonic ablation of an unpreheated pellet, both terms are very small at the pellet surface, so that $A = 0$. Reference 111 shows that this approximation is an excellent one in the regime in question.

In the classical region close to the pellet surface, Eq. (103) can be solved analytically in the limit $M^2/5 \ll 1$:

$$T/T_c = (\dot{m}/\dot{m}_c)^{2/5}(1 - R_a/r)^{2/5} \quad , \tag{104}$$

Fig. 3-44. Dependence on flux limit, ϕ, of M_s, the Mach number in the saturated region; and r_s, the radius where the saturated region begins. The ablation radius is R_a.

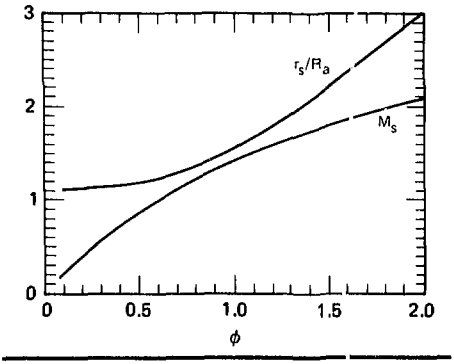

where $\dot{m}_c \equiv 16\,\pi\mu\kappa(r_c)R_a/25k$ is the ablation rate that would obtain if the classical region extended out to the critical surface. In fact, the heat flux reaches the saturated value in Eq. (99) at some radius $r_s < r_c$.

In the saturated region ($r_s < r < r_c$), the energy equation is simply $M_s(1 + M_s^2/5) = 2\phi$ where ϕ is the renormalized flux limit defined by $q_{sat} \equiv 5\phi\rho c^3$. We conclude that the Mach number in the saturated zone, M_s, is constant and depends only on the flux limit ϕ (see Fig. 3-44). The flow is supersonic in the saturated zone for $\phi \gtrsim 0.6$. The momentum and continuity equations yield

$$T = T_c\left(\frac{r}{r_c}\right)^{4/1+M_s^2}, \rho = \rho_1\left(\frac{r}{r_c}\right)^{2\left[2+M_s^2/1+M_s^2\right]} \quad (105)$$

in the saturated region, where $\rho_1 \equiv \rho(r_c - \delta r)$.

The dynamics in the classical zone are discussed in Ref. 115. Briefly, the Mach number increases monotonically, reaching M_s at the point r_s; hence the assumption that $M^2 \ll 5$ made in deriving Eq. (104) is approximately valid for $\phi \gtrsim 1$ ($M^2 \gtrsim 2$). For larger values of ϕ the energy and momentum equations do not decouple, and they must be solved simultaneously[112]; there is a family of subsonic solutions ($M_s < 1$, $\phi \gtrsim 0.6$) and a unique transonic solution.

The ablation rate $\dot{m}$ can be obtained if the above equations are supplemented by the jump conditions at the critical surface. Mass, momentum, and energy conservation imply $[\rho v] = 0$, $[\rho v^2 + \rho c^2] = 0$, and

$$\left(\dot{m}/4\pi r_c^2\right)[v^2/2 + 5c^2/2] + [q] = I\,, \quad (106)$$

where $[y] \equiv y(r_c + \delta r) - y(r_c - \delta r)$ for any variable y. Since the temperature is a maximum at r_c where the laser energy is deposited, the jump in the heat flux at r_c is $[q] \quad 5\phi(\rho_1 + \rho_2)c_c^3$, provided the heat flux is saturated on both sides of critical (the case of classical heat flow for $r > r_c$ is analyzed in Ref. 111). Here $\rho_{1,2} \equiv \rho(r_c \pm \delta r)$, $c_c \equiv c(r_c)$, and T is assumed continuous. Equation (106) then gives

$$kT(r_c) = \mu(I/10\phi\rho_c)^{2/3}\,H^{2/3}(\phi)\,, \quad (107)$$

where the function H is derived in Ref. 111 and is plotted in Fig. 3-45, and I is the laser intensity at the critical surface.

Scaling Laws. We have now described solutions in the classical zone near the ablation surface, and in the flux-limited region inside the critical surface. Next the global structure of the flow and its macroscopic properties are found by matching these separate regions together.

The classical and saturated solutions within r_c must match onto each other at the point r_s where the classical and saturated heat flows are first equal.[111,116] For subsonic flow ($M_s < 1$, $\phi \gtrsim 0.6$) one finds $r_s = R_a(11 + M_s^2)/10$. For $\phi > 0.6$, r_s that radius where the trans-sonic solution for M(r) passes through M_s: $M(r_s) = M_s$. The resulting function $r_s(\phi)/R_a$ is plotted in Fig. 3-44.

Fig. 3-45. Dependence on flux limit, ϕ, of (a) the function $H(\phi)$ defined in Eq. (107), and of (b) the ratio ρ_1/ρ_c, which represents the size of the density jump at critical. Here $\rho_1 = (r_c - \delta r)$, and ρ_c is the critical density.

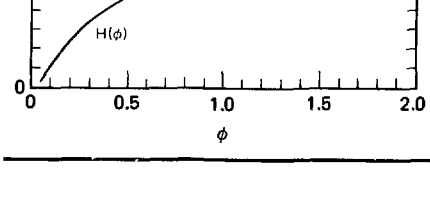

The ablation rate and pressure may be expressed[111] in terms of a numerical parameter, $\hat{\sigma}$, that corresponds roughly to the ratio of the mean free path at r_c to the ablation radius R_a:

$$\hat{\sigma} = 0.11\left[\frac{P_{TW}^{4/3}\, H^{4/3}\, \lambda_{\mu m}^{14/3}\, Z^{4/3}\, A^{7/6}\, \epsilon\delta_T}{(R_a/0.1\ cm)^{11/3}\, \phi^{7/3}\, (Z+1)^{7/2}}\right] \times \left(\frac{10}{\varrho n \Lambda}\right) . \quad (108)$$

Here $\epsilon\delta_T$ is a function of Z (defined in Ref. 115), P_{TW} is the laser power in units of 10^{12} W, $\lambda_{\mu m}$ is the laser wavelength in micrometers, and $\ln\Lambda$ is the Coulomb logarithm.[115]

The ablation rate $\dot{m}$ is then given by

$$\dot{m} = 8.2 \times 10^4\, G(\phi) \times \left[\left(\frac{R_a}{\lambda_{\mu m}}\right)^{4/3} \left(\frac{A}{Z}\right)^{2/3} P_{TW}^{1/3}\right] \times \hat{\sigma}^{Z\left[\left(1+M_s^2\right)\middle/\left(22+7M_s^2\right)\right]}\ g/s , \quad (109)$$

where $M_s(\phi)$ and $G(\phi)$ are shown in Figs. 3-44 and 3-46, and Am_p and Z are the mass and charge of the ions.

The ablation pressure p_a (in cgs units) is

$$p_a = \beta(\phi)\rho_c^{1/3}\, I_0^{2/3}\, \hat{\sigma}^{-\left[\left(2-M_s^2\right)\middle/\left(22+7M_s^2\right)\right]} , \quad (110)$$

where $\beta(\phi)$ is shown in Fig. 3-45 and I_0 is the laser intensity (in cgs units) at the ablation surface R_a. Similarly, the temperature at the critical surface is

$$kT_c = \mu\left(\frac{I_0 H}{10\, \phi\alpha^2 \rho_c}\right)^{2/3} \hat{\sigma}^{-2\left[\left(1+M_s^2\right)\middle/\left(22+7M_s^2\right)\right]}\ ergs . \quad (111)$$

For simplicity we now specialize to the flux limit value $\phi = 0.3$, $f \simeq 0.03$, which to date seems most closely supported by 1.06-μm experiments. We also assume $A \simeq 2Z \gg 1$. Then the ablation rate $\dot{m}$ and pressure p_a are given by[112]

$$\dot{m} \cong 2.3 \times 10^4 \left[\frac{I_{14}^{0.5}}{\lambda_{\mu m}^{8.0}} \left(\frac{R_a}{0.1\ cm}\right)^{1.9}\right] g/s \quad (112)$$

and

$$p_a \cong 7.2 \left[\frac{I_{14}^{0.6}}{\lambda_{\mu m}} \left(\frac{ZR_a}{0.1\ cm}\right)^{0.07}\right] Mbar , \quad (113)$$

Fig. 3-46. The functions $\alpha(\phi)$, $\beta(\phi)$, and $G(\phi)$ appearing in Eqs. (109)-(111).

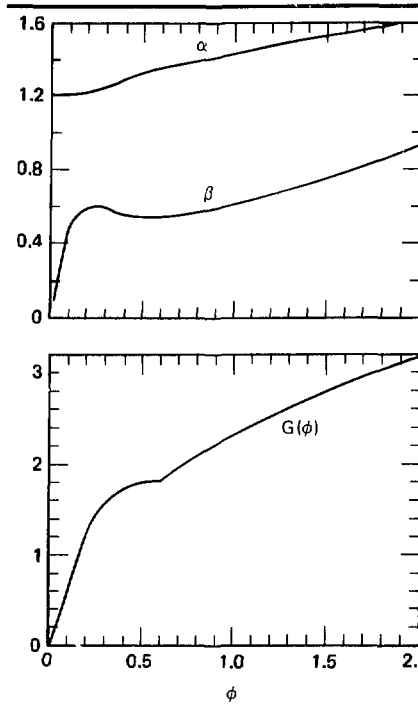

where R_a is the ablation radius of the pellet, I_{14} is the absorbed laser intensity at R_a in units of 10^{14} W/cm^2, $\lambda_{\mu m}$ is the laser wavelength in micrometers, and Z is the ionic charge. Similarly, the radius and temperature of the critical-density surface are

$$r_c \cong 1.6\, R_a \left(I_{14}^{0.1}\, \lambda_{\mu m}^{0.4}\right) (0.1\ cm/ZR_a)^{0.08} \quad (114)$$

and

$$T_c = 1.7 \left(I_{14}^{0.5}\, \lambda_{\mu m}^{0.8}\right) (ZR_a/0.1\ cm)^{0.1}\ keV . \quad (115)$$

Figure 3-47 illustrates these scaling relations, and compares them with LASNEX simulation results (described in Ref. 111 and the next article). Figure 3-48 illustrates typical density and temperature

Fig. 3-47. Parameter study showing (a) temperature at critical T_c, (b) critical radius r_c, and (c) ablation pressure p_a as a function of absorbed laser power P_L in terawatts (1 TW = 10^{12} W). Other parameters are λ_L = 2.65 μm, R_a = 0.1 cm, ϕ = 0.3, Z = 6, A = 12. The solid line is theoretical prediction; points are results of computer hydrodynamics calculations described in the following articles.

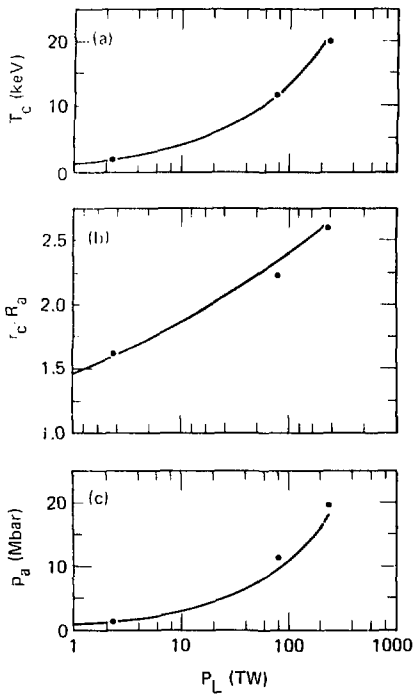

Fig. 3-48. Spatial profiles of density and temperature, for laser power P_L = 78.5 TW and other parameters as in Fig. 3-47. Solid lines show theoretical predictions; dashed lines are numerical results described in the following article from the hydrodynamics code LASNEX. The two agree quite well.

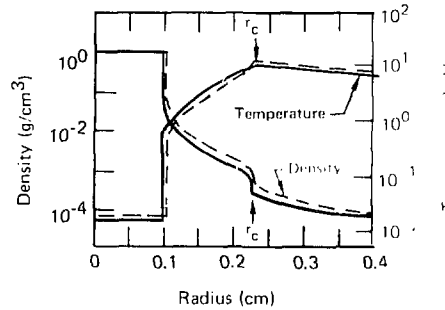

profiles from the present theory, for laser power P_L = 78.5 TW. These compare quite well with the LASNEX calculations.

These results of our model show that shorter-wavelength lasers should produce higher ablation rates and pressures for the same laser intensity and target parameters. Alternatively, to produce a given ablation pressure, i.e., a given target implosion, a higher intensity laser is required at longer wavelengths. From Eq. (113) with p_a, Z, and R_a fixed, the scaling is $I \propto \lambda_L^{1.7}$. A 1-μm laser would thus have to be 3.3 times as intense as a 1/2-μm laser to drive the same implosion. Collective effects of hot-electron production and stimulated scattering not included in our model would tend to exacerbate this already strong wavelength scaling.

We conclude with a brief discussion of limitations on the validity of our theory, due to various assumptions we have made. These limits are considered in detail in the next article and Ref. 111

- Neglect of inverse bremsstrahlung absorption in the underdense plasma places a lower bound on the laser power or a lower bound on the laser wavelength.
- An upper limit on the allowable laser power arises from our assumption that an electron heated at the critical surface will not be able to penetrate to the classical zone without suffering a collision.
- Our neglect of hot electrons is valid when the fraction of suprathermals is $\gtrsim 10\%$ at the critical surface, as is seen in long-pulse or short-wavelength experiments.
- The steady-flow hypothesis means that our theory is valid only when the laser parameters vary slowly, compared to the time it takes a fluid element to travel from the ablation surface to the critical surface. For laser powers near a few hundred TW, wavelengths near 1 μm, and target sizes near 1 mm, this means quantitatively[111] that our theory should apply to portions of a laser pulse where the power is roughly constant over time scales of 1 to 2 ns.

Within these limitations, extensive comparisons with computational hydrodynamics

calculations have shown the present theory to be accurate to better than 10%.

Authors: C. E. Max, C. F. McKee, and W. C. Mead

References

108. *Laser Program Annual Report—1976*, Lawrence Livermore Laboratory, Livermore, Calif., UCRL-50021-76 (1977), p. 4-92.

109. M. D. Rosen and J. H. Nuckolls, *Phys. Fluids* **22**, 1393 (1979); I. K. Storm, J. L. Larsen, J. H. Nuckolls, H. G. Ahlstrom, and K. R. Manes, Lawrence Livermore Laboratory, Livermore, Calif., UCRL-79788 (1977); D. V. Giovanelli and C. W. Cranfill, LC Report LA-7218-MS (1978); B. Ahlborn and M. Key, "Scaling Laws for Exploding Pusher Targets," Rutherford Laboratory Report RL-79033 (1979).

110. R. C. Malone, R. L. McCrory, and R. L. Morse, *Phys. Rev. Lett.* **34**, 721 (1975); R. A. Haas, W. C. Mead, W. L. Kruer, D. W. Phillion, H. N. Kornblum, J. D. Lindl, D. MacQuigg, V. C. Rupert, and K. G. Tirsell, *Phys. Fluids* **20**, 322 (1977); B. Yaakobi and T. Bristow, *Phys. Rev. Lett.* **38**, 350 (1977); M. D. Rosen, D. W. Phillion, V. C. Rupert, W. C. Mead, W. L. Kruer, J. J. Thomson, H. N. Kornblum, V. W. Slivinsky, G. J. Caporaso, M. J. Boyle, and K. G. Tirsell, *Phys. Fluids* **22**, 2020 (1979).

111. C. E. Max, C. F. McKee, and W. C. Mead, *A Model for Laser Driven Ablative Implosions*, Lawrence Livermore Laboratory, Livermore, Calif., UCRL-83542 (to be published in *Phys. Fluids*).

112. S. J. Gitomer, R. L. Morse, and B. S. Newberger, *Phys. Fluids* **20**, 234 (1977); J. Montierth and R. L. Morse, "Stationary Flow Model of Ablatively Imploded Spherical Shells," University of Arizona preprint, 1979.

113. Yu. V. Afanas'ev, E. G. Gamaliĭ, O. N. Krokhin, and V. B. Rozanov, *Zh. Eksp. Teor. Fiz.* **71**, 594 (1976) [*Sov. Phys.-JETP* **44**, 311 (1977)].

114. R. McCrory, R. Morse, and C. Verdon, *Bull. Am. Phys. Soc.* **23**, 787 (1978).

115. L. Spitzer Jr., *Physics of Fully Ionized Gases*, (Wiley-Interscience, New York, 1967), Chapter 5.

116. I. I. Cowie and C. F. McKee, *Astrophys. J.* **211**, 135 (1977).

Hydrodynamic Calculations of Steady-Flow Spherical Profiles

During the gestation of the theory discussed in the preceding article, we performed extensive numerical simulations using the fluid-dynamics computer code LASNEX.[117] We sought consistency and accuracy checks to evaluate important aspects of both the theory and the code. In the process we discovered and corrected several inconsistencies and inaccuracies in both. The theory benefitted from tests of many of the simplifying assumptions involved in obtaining the analytic solutions. The code benefitted from the use of theoretical profiles as a "test case," to evaluate the numerical art of solving simple fluid-dynamics and heat-flow problems.

In this section, we

- Present a description of the numerical modeling.
- Discuss issues involving the algorithm used to calculate heat flow.
- Compare the results of parameter studies with theory.
- Show dynamical calculations performed to test the validity of two of the theoretical hypotheses.

Notation used throughout corresponds to that used in the preceding article.

The Computational Model. The fluid-dynamics code LASNEX has been used for the work presented here, but with simplified physics in order to be consistent with the assumptions of the theory.

Hydrodynamics were modeled in one-dimensional spherical coordinates using a standard Lagrangian explicit differencing scheme.[117,118] Zonal coordinates and velocities are interface-centered. Density and temperature are zone-centered. The artificial viscosity used had the form developed by White.[119] The equation of state of a fully ionized, ideal gas ($\alpha = 5/3$) was used, with pressure and specific energy (in cgs units) given by

$$P_{cgs} = 9.61 \times 10^{14}\left(\frac{Z+1}{A}\right)\rho\, T_{keV} ,$$

$$E_{cgs} = \frac{3}{2}\frac{P_{cgs}}{\rho} . \qquad (116)$$

The computer-code thermodynamics were simplified to agree with the assumptions of the theory:

- All radiation physics and ion conduction were turned off.
- The electrons and ions were described as single-temperature Maxwellians with electron-ion collisional coupling increased by a factor of 10^6 above the Spitzer[120] value, to ensure $T_e \equiv T_i$.

We present here our LASNEX algorithms used to numerically solve the one-dimensional flux-limited diffusion of thermal electrons, followed by a brief description of an older version of the code with which we encountered some numerical difficulties. The notation used to represent plasma parameters in the code is illustrated in Fig. 3-49. For the discussion to follow, temperatures are in keV, and the

Fig. 3-49. Terminology for discussion of numerical heat-flux algorithm. Successive zones are indicated by index K. Density, temperature in keV, pressure, and volume V are zone-centered, whereas radius and velocity are interface-centered.

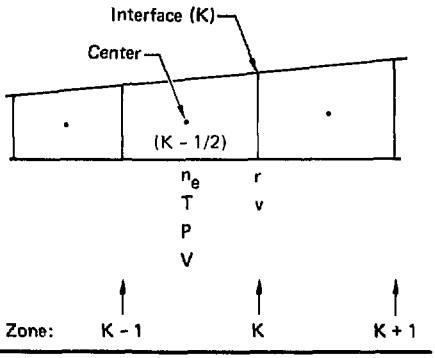

physical quantities will be tagged, as required for clarity, with

- The zonal index K.
- The time step index n, which indicates a quantity evaluated at the end of cycle n. In certain expressions mixtures of cycle-n and cycle-(n - 1) quantities are involved; quantities composed of variables from such mixed time-steps will be indicated by the cycle number "M."
- A superscript C or I as a reminder of cell- or interface-centering.

The heat-flux crossing boundary K during cycle n is obtained by solving

$$\Delta Q^{I}(K,n) = -\kappa^{I}_{eff}(K,M)\,\nabla^{I}_{K,n}T \qquad (117)$$

implicitly, with κ_{eff} (evaluated as described below) held fixed. The temperature gradient is defined as

$$\nabla^{I}_{K,n}T = \frac{T(K+1/2,n) - T(K-1/2,n)}{0.5 \times [r(K+1,n) - r(K-1,n)]} . \qquad (118)$$

Since the conductivity depends strongly on temperature, the solution for ΔQ is actually explicit and the time-step is controlled by limiting the relative change in temperature, $\Delta T/T$, to a maximum value $\ll 1$ for every zone.

The effective conductivity is determined as

$$\kappa^{I}_{eff} = MAX\left[\kappa^{I}_{MIN}, MIN\left(\kappa^{I}_{CLAS}, \kappa^{I}_{F.L.}\right)\right] . \qquad (119)$$

The minimum conductivity is normally set to $\kappa^{I}_{MIN} = 10^{14}$ erg/s-cm-keV, and has no impact on this work.

The classical conductivity at a cell center is well-determined in terms of cell-centered quantities at the end of the previous time-step:

$$\kappa^{C}_{Clas}(K-1/2,n-1) = 3.066 \times 10^{19}\left(\frac{\gamma_0}{\delta_0}\right)\left(\frac{[T(K-1/2,n-1)]^{5/2}}{Z\,\ell n\Lambda}\right)\left(\frac{erg}{s\,cm\,keV}\right) , \qquad (120)$$

as in Braginskii.[121] Here

$$\gamma_0 = \frac{0.9067}{Z^3} + \frac{4.408}{Z^2} + \frac{5.4053}{Z} + 1.20 , \qquad (121)$$

$$\delta_0 = \frac{1.3008}{Z^3} + \frac{1.5956}{Z^2} + \frac{0.7778}{Z} + 0.0961 , \qquad (122)$$

and we take $\ell n\Lambda = 10$ to agree with the theoretical model. In our parameter studies we have assumed a fully ionized plasma, $Z = 6$, for which $\gamma_0/\delta_0 = 8.068$. The averaging to obtain an interface-centered classical conductivity is performed using

$$\kappa^{I}_{Clas}(K,M) = \left\{MAX\left[\kappa^{C}_{Clas}(K-1/2,n-1), \kappa^{C}_{Clas}(K+1/2,n-1)\right]\right\}^2 \times \frac{(\Delta r_{K-1/2,n} + \Delta r_{K+1/2,n})}{\left[\Delta r_{K-1/2,n}\,\kappa^{C}_{Clas}(K-1/2,n-1)\right] + \left[\Delta r_{K+1/2,n}\,\kappa^{C}_{Clas}(K+1/2,n-1)\right]} , \qquad (123)$$

where

$$\Delta r_{K-1/2,n} = r(K,n) - r(K-1,n) . \qquad (124)$$

This averaging scheme was chosen historically to apply to κ_{eff} in order to satisfy the requirement that diagonal flux-limited transport in two-dimensional calculations not exceed transport along the mesh directions. In the code used for this work, however, averaging of this form was used for κ_{Clas} only. This thermal-conduction averaging scheme reported adequately for the calculations reported here.

The flux-limited "conductivity" is computed using

$$\kappa_{FL} \equiv f n_e m_e \nu_e^3 \frac{1}{\nabla T}$$

$$= 2.120\, f\, n_e\, T^{3/2} \frac{1}{\nabla T} \frac{\text{erg}}{\text{s cm keV}} \quad (125)$$

In order to calculate an interface-centered quantity, the three terms in Eq. (125) are "averaged" sepa.ately:

$$\kappa_{FL}^{I}(K,M) = 2.120\, f \times$$

$$\left[\frac{V(K-1/2,n)n_e(K-1/2,n) + V(K+1/2,n)n_e(K+1/2,n)}{V(K-1/2,n) + V(K+1/2,n)}\right]$$

$$\times \text{MAX}\left[T(K-1/2,n-1), T(K+1/2,n-1)\right]^{3/2}\left(\nabla^{I}_{K,M}T\right)^{-1}. \quad (126)$$

Here, the mixed gradient is defined as in Eq. (118), but with coordinates from cycle n and temperatures from cycle (n – 1).

We next briefly discuss a previous numerical scheme which presented some difficulties (discussed later in this article). The "old" heat-flow algorithm differed primarily in the evaluation of κ_{FL} and the sequence in which the averaging to obtain interface-centered quantities occurred. First, the value of κ_{FL}^{C} at zone center K-1/2 was computed from Eq. (125) by taking $n(T^{3/2})_{K-1/2}$ and MAX (1/T) between the interfaces K and K – 1. Next, a cell-centered effective conductivity was obtained using Eq. (119) for cell-centered quantities. Finally, a weighted average of cell-centered κ_{eff}'s of the form of Eq. (123) was used to obtain interface-centered conductivities. As mentioned above, this algorithm had been chosen to prevent faster flux-limited heat-flow diagonal to the mesh in two dimensions. The effect in one dimension, however, was, in cases of strong gradients, to have ∇T in Eq. (117) and $(1/\nabla T)$ in Eq. (125) computed on opposite sides of a cell, yielding a systematic error of significant magnitude.

Calculational Methods. As shown in the previous article, the profiles obtained theoretically have two regions where velocity, density, and temperature gradients are steep: the ablation surface, and the critical surface where the laser energy deposition is localized. The latter, particularly at low flux limits, is the most demanding for the code numerics.

In order to resolve the profiles around the critical surface, a treadmill rezoner was used. Relatively coarse zones were used above a density 10 to 50 times the laser critical density. As the matter ablated and flowed to lower density, it crossed a threshold density where the treadmill rezoner split the zones in half, as required to maintain a transition in zone mass down to a fine-zoned region in the outer part of the profile. Typically a ratio of coarse to fine zone mass of between 3 and 10 was found to be the best overall compromise in resolving the ablation and critical surfaces.

The initial conditions for the calculations were set up by numerically solving for the theoretical profiles, and then transferring them to the Lagrangian mesh. The zones were chosen to have constant mass in the coarse- and fine-zoned regions, with a transition of a few zones, varying mass by a factor of about two, between the two regions. The initial velocity at each vertex was set to the theoretical value at that spatial location. The zone temperature was chosen to conserve internal energy. Typically, the transfer from theoretical profiles to a roughly 200-zone mesh conserved momentum to about 1% and energy to about 0.1%.

The calculations were run for 0.5 to 5 times the flow time (the time for a fluid element to flow from the ablation surface to the critical surface). The shorter runs could be zoned more finely than the longer, since less mass was ablated. The detailed comparisons presented in this and the preceding article were made after $\lesssim 2$ flow times. A dual-treadmill scheme could perhaps be employed to give improved resolution at both the ablation and critical surfaces for longer runs, within the constraints imposed by a reasonable number of zones.

Issues in the Choice of Algorithms for Heat Flow. One of the "artistic" features of numerical problem-solving is the development of suitable differencing algorithms. In the use of a fluid-code, it is frequently necessary to perform repeated calculations, applying both quantitative criteria and "common sense" tests to assess the adequacy of a given algorithm. In the following discussion, we present as an example a numerical algorithm which turned out to be inadequate for calculating strongly inhibited heat transport, yet which produced such sufficiently "reasonable" results that its quantitative failures took a long time to isolate. In fact, its shortcomings would have taken considerably longer to identify had we not been comparing our

numerical results with the theoretical profiles presented in the preceding section. Our motivation in describing our experience with this algorithm is to illustrate the kind of subtle warning signs that may appear when a numerical algorithm begins to fail.

Figure 3-50 shows fluid-code calculations of density and temperature profiles for flux limit ϕ = 0.6 computed using two different flux-limit algorithms, as described above (for the relation between ϕ and f, see Eq. (99) in the previous article). The old algorithm, which uses a local maximum gradient, produced interesting density and temperature structures near the critical surface. These seemed physically reasonable, but calculations performed using different zoning patterns and time-step controllers showed that these structures were very sensitive to simple changes in the details of the calculations. This suggested numerical trouble, but the origin of the problem was very unclear.

Figure 3-51 shows similar profiles calculated for the case ϕ = 0.3. Here the "old" flux-limit algorithm, when zoned sufficiently finely near critical, exhibited a large temperature jump (a factor of two or three between adjacent zones). At this point, direct calculation of the code-generated heat flux inward from critical clearly showed a reduction by a factor of two to three from the expected value. This was traced to the old flux-limit algorithm which used the maximum value of ∇T from adjacent zones, and which could thus systematically un-

Fig. 3-50. Fluid-code-calculated density and temperature profiles using "old" (solid lines) and "new" (dashed lines) flux-limit algorithms for the ϕ = 0.6 case. Several calculations were required to show that the density and temperature structures seen using the "old" flux limit algorithm (see "The Computational Model," and "Issues in the Choice of Algorithms for Heat Flow") changed qualitatively with different time steps and zonings, suggesting numerical problems.

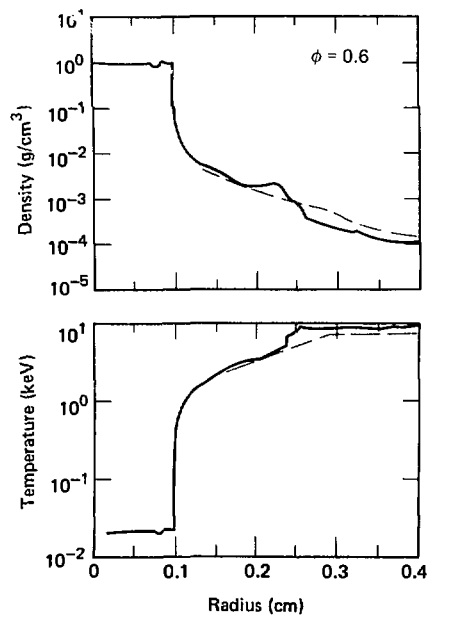

Fig. 3-51. Fluid-code calculations of density and temperature profiles for old and new flux-limit algorithms, for the ϕ = 0.3 case. Here the old algorithm produced a temperature jump at critical which behaved quite physically and systematically modified the calculated plasma parameters. The size of the temperature jump was considerably reduced when an improved heat-flow algorithm was employed.

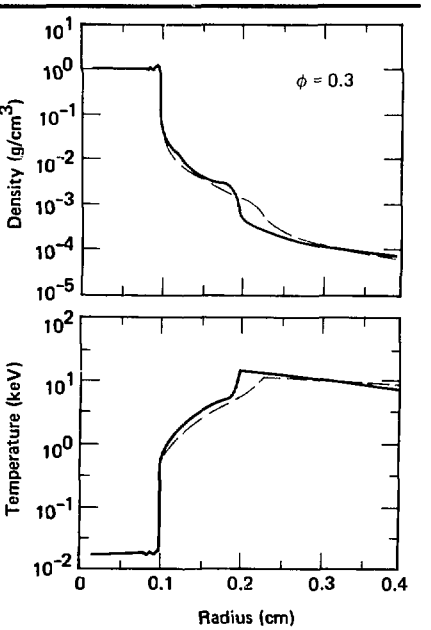

derestimate the heat flow through a given zone in certain steep-gradient situations.

This flux-limit algorithm was replaced by a simpler one which never displaced the temperature gradient used to compute the flux limit by one zone's width. The result was instantly gratifying: numerical behavior was vastly improved, sensitivity to zoning declined, and agreement between the fluid-code results and the theory was greatly enhanced.

Using the new algorithm, the temperature jump at the critical-density surface, which had previously been significant, became quite small. This fact has led us to wonder about the physical reality of the large temperature jumps frequently seen in computer hydro-calculations of strongly inhibited heat flow. Our experience emphasizes that such temperature jumps can sometimes be artifacts of the heat flow algorithm.

In reality, the existence and size of any temperature jump at critical density would be determined by microscopic physical processes occurring within the discontinuity. Neither our present theoretical model nor our hydrodynamics code includes such detailed physics. What our present hydro calculations do show is that it is at least dynamically self-consistent to have no temperature jump across the critical-density surface, for $\phi > 0.3$.

In summary, strong transport inhibition places considerable stress on numerical algorithms used to calculate flux-limited heat flow. Our experience suggests that extensive screening by numerical, analytical, or experimental cross-checks is necessary to establish the trustworthiness of a given heat-flow algorithm. The theoretical profiles developed in the present work may be useful for future investigators as a test-case for the adequacy of various heat-flow algorithms.

Results of Fluid-Code Calculations. Two parameter studies were performed using the improved algorithm: one varying the flux limit ϕ and the other varying the laser power P_L.

In the first parameter study, the flux limit ϕ was varied from 0.3 to 1.4. Laser and target conditions were: $\lambda_L = 2.65\ \mu m$, absorbed laser power $P_L = 78.5 \times 10^{12}$ W, A = 12, Z = 6 (fully ionized carbon), and a solid pellet of initial radius $R_a(t = 0) = 0.1$ cm. The results are depicted as circles or triangles in Figs. 3-52 to 3-55, for comparison with the solid lines which represent predictions of our theory. The code values of $\dot{m}$ shown in Fig. 3-55 represent spatial averages over all $r > R_a$. In general the hydro calculations showed the Mach number in the saturated zone to be constant to a few percent

Fig. 3-52. Variation of the critical radius, r_c, and the radius where heat flow becomes saturated, r_s, with flux limit, ϕ. Solid lines are predictions of theory with absorbed laser power $P_L = 7.85 \times 10^{13}$ W, $\lambda_L = 2.65\ \mu m$, $R_a = 0.1$ cm, A = 12, Z = 6. Points are results of computer hydrodynamics calculations described in the text. The saturated region becomes smaller and r_c larger as ϕ increases.

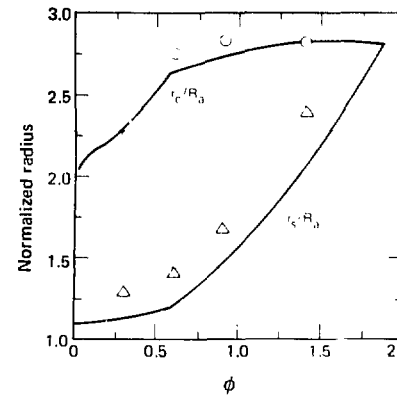

Fig. 3-53. Temperature at the critical surface as a function of flux limit, ϕ, for absorbed power $P_L = 7.85 \times 10^{13}$ W, $\lambda_L = 2.65\ \mu m$, $R_a = 0.1$ cm, A = 12, Z = 6. The solid line is theoretical prediction; points are result of hydrodynamics calculations. To the right of the maximum in $T_c(\phi)$, laser energy deposited at the critical radius is dominantly carried away by inward heat flow; to the left, by outward kinetic-energy flow.

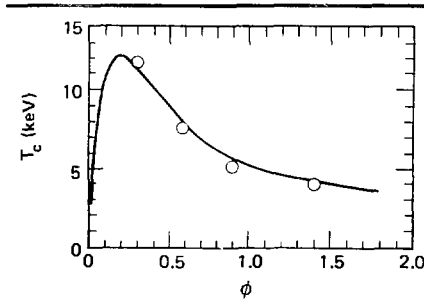

Fig. 3-54. Ablation pressure, p_a, as a function of the flux limit, ϕ. Solid line is prediction of theory with absorbed power $P_L = 7.85 \times 10^{13}$ W, $\lambda_L = 2.65\ \mu$m, $R_a = 0.1$ cm, A = 12, Z = 6. Points are results of computer hydrodynamics calculations described in the text. For fixed laser and target parameters, the ablation pressure falls strongly as transport becomes more inhibited.

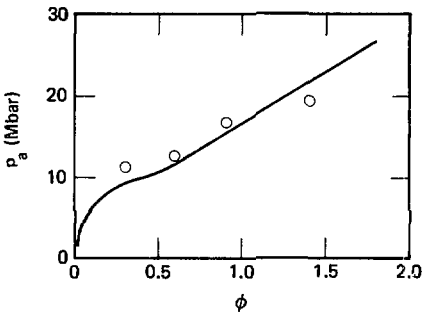

Fig. 3-55. Mass loss rate $\dot{m}$ as a function of flux limit, ϕ, for the same conditions as Fig. 3-54. Solid line is theoretical prediction. Points are results of hydrodynamics calculations; error bars represent $\pm 2\ \sigma$ at a given time in the computer run, and give a feel for the degree of spatial variation in $\dot{m}$. (In a strict steady state, $\dot{m}$ would be constant in space.)

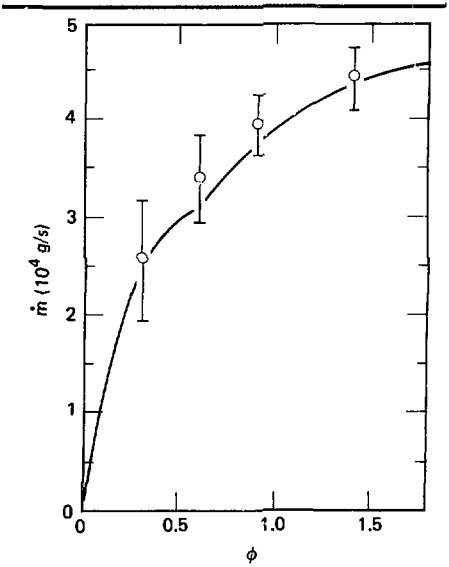

across the region. In contrast, $\dot{m}$ showed more spatial variation at each given time. The error bars in Fig. 3-55, which represent $\pm 2\ \sigma$, are an attempt to illustrate the magnitude of this spatial variation of $\dot{m}$ due to the lack of exact steady flow. The parameters $\dot{m}$, r_c, T_c, and p_a show excellent agreement between theoretical and hydrodynamics results.

The second parameter study varied the absorbed laser power over a factor of 100, from 2.35×10^{12} W to 2.35×10^{14} W. Other conditions were $\phi = 0.3$, $R_a(t = 0) = 0.1$ cm, Z = 6, A = 12, $\lambda_L = 2.65\ \mu$m. Above the upper limit of $P_L = 2.35 \times 10^{14}$ W, $\hat{\sigma}$ was too large to satisfy the validity conditions for the theoretical model. As in the previous study, theoretical profiles were used as initial conditions and the calculations were compared with theory after at least one or two flow times. Figure 3-47 (in the previous article) shows the very good agreement between theory and dynamical calculations for T_c, r_c, and p_a versus absorbed laser power P_L.

We conclude that when the laser and target parameters are within the range where our theory should apply, the steady-state model developed in this work agrees very well with numerical fluid code calculations.

Examples of Validity Checks. In this section we illustrate calculations which delineate the regions of parameter space where our theory should be applied. Predictions of the analytic model are compared with the numerical results, to explore what happens as the model is pushed to the edge of its region of validity. We consider here two examples: the steady-state hypothesis, and the neglect of radiation pressure. More complete results are presented in Ref. 122.

A fundamental assumption of our steady-state ablation model is that characteristics such as the laser intensity and the density and velocity profiles do not change by large amounts in the time it takes a fluid element to flow from the ablation surface to the critical surface. In reality of course, laser pulses often have rise times shorter than the hydrodynamic flow times. For reactor-scale targets, several classes of target designs use laser pulses which start at low, fairly constant power, then rise quickly compared to a flow time, and finally stay at relatively constant power for several flow times. We would like to be able to apply our quasi-steady state theory to such laser pulses during the constant-power intervals.

Fig. 3-56. To test sensitivity to severe transients, the laser power in a fluid code calculation was given the temporal profile shown in (a). Target parameters are R_o = 0.1 cm, A = 12, Z = 6, ϕ = 0.6, λ_L = 2.65 μm. Density profiles (b) are shown at four times during the evolution. At t = 0.16 ns, the profile has not yet begun to respond to the higher incident laser power. The profiles at t = 2.4 and 4.0 ns show a density bulge around $\rho \cong 10^{-4}$ gm/cm^3, which is due to the increased ablation of material in response to higher laser power. By t = 6.7 ns, the density bulge has propagated outward to the critical surface and the code's profile agrees quite well with the steady-state theory.

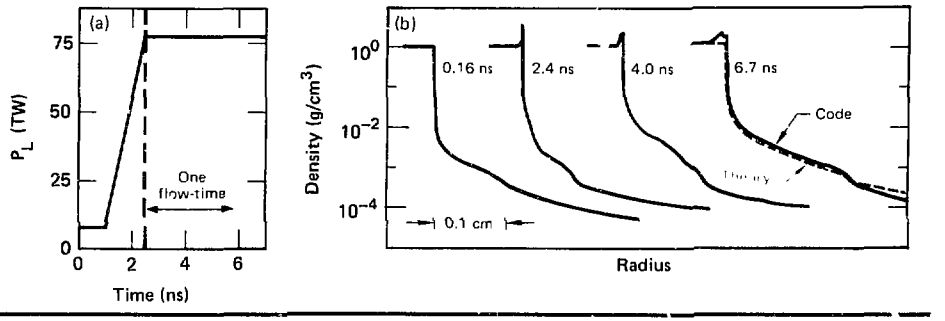

To test whether such a use of our model is likely to be valid, we performed a computer calculation using the laser power temporal profile shown in Fig. 3-56(a). The power was increased by a factor of 10 in less than 1 flow time, and was held constant thereafter. We found that after 1.5 flow times had elapsed after the power transient, the dynamical code results converged to the steady-state theory within better than 10% agreement.

Figure 3-56(b) illustrates in more detail how this convergence occurred. When the laser power was first increased, the critical radius was driven inward because the inner part of the target had not yet ablated enough material to maintain a larger critical surface. As the ablation pressure and ablation rate increased and the newly ablated material began to reach the critical surface, however, r_c increased quite quickly. The evolving density profiles shown in Fig. 3-56(b) show this "bump" of newly ablated material moving outward. In the last profile shown, the computed density has relaxed to excellent agreement with the theory.

We conclude that the quasi-steady model can probably be reliably applied to situations where the laser power remains roughly steady for more than one or two flow times, independent of increases or decreases in transient power which may have preceded such a steady-power regime.

To test the validity of our assumption that $\beta = 8\pi n_e T_e$ is not large in the theoretical model, we performed a hydrodynamics calculation in which the ponderomotive force was included in the hydro code in the WKB limit.[117] We chose a value of ϕ large enough that M_s would be greater than unity (ϕ = 0.9, M_s = 1.33), in the hopes of seeing a steady-state "shock plus D-Front" of the type predicted in Refs. 123 and 124. This structure arises when supersonic plasma approaching the critical density surface encounters a flow restriction produced by the laser radiation pressure: the resulting shock raises the sound speed to permit a subsonic rarefaction wave (D-front) at the critical surface.

Our results are shown by the solid line in Fig. 3-57, illustrating the density profile. As expected, for these parameters the ponderomotive force makes only a small and localized perturbation to the overall plasma density profile. With the exception of the immediate vicinity of the critical surface, the profile from the hydro code is in excellent agreement with the theory developed neglecting the ponderomotive force.

A second issue addressed in Fig. 3-57 is the existence of a steady shock plus D-front for $M_s > 1$. The figure shows that a steady compressional structure did indeed form in the critical surface region, as predicted. An enlargement of this critical region appears in the inset (b), and numerical study of this structure showed it to be a shock plus D-front. This structure persisted in the same form for the entire duration of the computer run. We believe this is the

Fig. 3-57. Fluid-code-generated density profiles included effects of 1 (solid line) and 10 (dotted line) times the WKB ponderomotive force. Laser and target parameters are absorbed power P_L = 78.5 TW, λ_L = 2.65 μm, ϕ = 0.9, R_a = 0.1 cm, Z = 6, A = 12. This figure supports the result that (within the context of our model) the ponderomotive force does not cause any significant modification of the global density profile (a). The inset (b) is a magnification of the critical-surface region, and shows the supercritical density compression, or shock plus D-front, expected in this case, since $M_s > 1$.

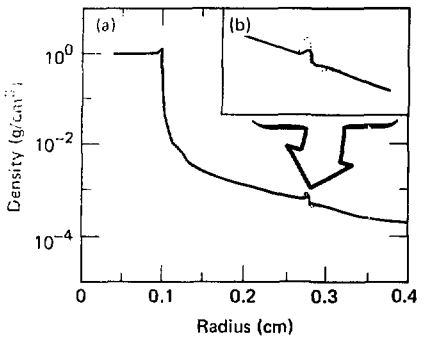

first computational confirmation that steady density structures above the critical density can persist for significant times, for laser pulses whose power is roughly constant in time.

Conclusion. We have presented salient methods and results from numerical simulation of steady-state spherical hydrodynamic flows. We find quantitative agreement to better than ~10% between theory and simulation, over a wide parameter range for which the theoretical model assumptions hold. We have also explored some examples showing the nature and extent of our model's applicability to situations near its limits of validity.

Authors: W. C. Mead, C. E. Max, and C. F. McKee
Major Contributor: G. B. Zimmerman

References

117. G. B. Zimmerman and W. L. Kruer, "Numerical Simulation of Laser Initiated Fusion," *Comments Plasma Phys. Cont. Fusion* **2**, 85 (1975). G. B. Zimmerman, *Numerical Simulation of the High Density Approach to Laser Fusion*, Lawrence Livermore Laboratory, Livermore, Calif., UCRL-74811 (1973); J. A. Harte, and G. B. Zimmerman, Lawrence Livermore Laboratory, Livermore, Calif., UCID-17517 (1977).

118. W. D. Schulz, in *Methods in Computational Physics*, J. Killeen, Ed. (Academic Press, New York, 1964), vol. 3, B. Alder, S. Fernbach, and M. Rotenberg, Eds., pp. 1 to 45.

119. J. White, "A New Form of Artificial Viscosity," *J. Comp. Phys.* **11**, 573 (1973); and J. White, "A New Form of Artificial Viscosity: Postscript," *J. Comp. Phys.* **12**, 553 (1973).

120. L. Spitzer, Jr., *Physics of Fully Ionized Gases*, (Wiley – Interscience, New York, 1967), Chapter 5

121. S. I. Braginskii, "Transport Processes in a Plasma," in *Reviews of Plasma Physics, Vol. 1*, M. A. Leontovich, Ed. (Consultants Bureau, New York, 1965), p. 205.

122. C. E. Max, C. F. McKee, and W. C. Mead, *A Model for Laser Driven Ablative Implosions*, Lawrence Livermore Laboratory, Livermore, Calif., UCRL-83542, submitted to *Phys. Fluids*.

123. F. Mayer, R. Berger, and C. E. Max, KMS Fusion Report No. U878 (1979).

124. C. E. Max and C. F. McKee, *Phys. Rev. Lett.* **39**, 1336 (1977).

Electron Heating Due to Resonant Absorption

Hot-electron production and electron-heat transport inhibition are studied experimentally with the PROMETHEUS I device at the University of California at Davis. This device models laser absorption due to resonant absorption and parametric instabilities, and electron-heat transport inhibition due to ion acoustic turbulence and a dc magnetic field. Intense, p-polarized microwaves are incident onto an inhomogeneous, essentially collisionless plasma. The microwave field is mainly parallel to the density gradient so that electrostatic waves are driven near the critical surface, resulting in electron heating and resonant absorption of the microwaves.

The time history of the electron energy distribution at high power (v_{osc}/v_{eo} = 0.7) is illustrated in Fig. 3-58. The current vs voltage (I-V) characteristic of a one-sided Langmuir probe is shown in Fig. 3-59. This probe is in the overdense region near the critical surface, and pointed so that electrons moving up the density gradient are measured

- Just before the microwave pulse begins (t = 0 μs), the electrons have a Maxwellian distribution (shown by the exponential shape of the current-voltage curve) with a relatively cold temperature ($T_{eo} \approx$ 1.3 eV).
- After a short time (0.1 μs, longer than the estimated wave-breaking time), high-energy electrons are observed ($E_e \geq 30\ T_{eo}$). These must be electrons accelerated by the resonantly driven electrostatic waves, because the ions have not moved significantly. Also, the thermal electrons (those elec-

Fig. 3-58. Time evolution of the electron current-voltage curve.

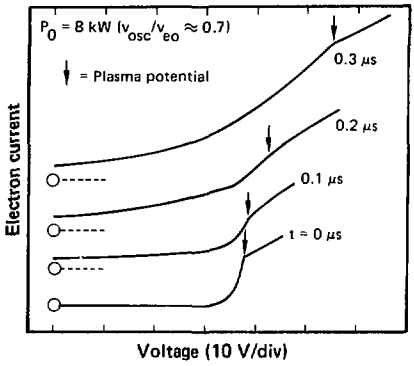

Fig. 3-59. Logarithm plot of typical I-V curves.

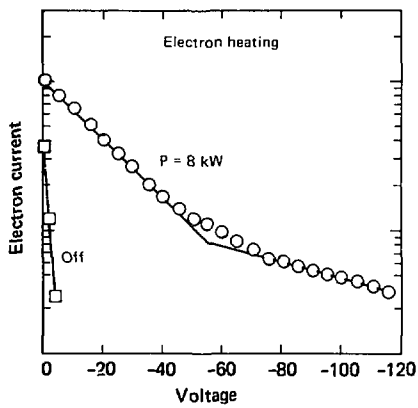

trons with energies near the plasma potential) still have a relatively low temperature.

- A little later (0.2 μs), however, significant thermal-electron heating (and a higher current of high-energy electrons) is observed. In addition, the plasma potential becomes more positive.
- Still later (0.3 μs), the thermal electrons have been significantly heated. The electron energy distribution is bi-Maxwellian[125] as shown in Fig. 3-59.

Notice that the thermal electrons are strongly heated. The hot electrons in a previous experiment,[126] where s-polarized microwaves decayed to electron-plasma waves and ion acoustic waves, were hotter [T_H(s-polarization) $\approx 4T_H$(p-polarization)]. The suprathermal electron temperature, T_H, agrees well (within 40%) with a scaling law[125] which was derived from particle simulation calculations for laser parameters. This agreement is remarkable, because no normalization is used in the comparison; that is, the values of v_{osc}/v_{eo}, T_e, angle of incidence, and absorption from the microwave experiments are directly substituted into the scaling law. In fact, the agreement would be within 10% in absolute value if the initial electron temperature were used.

The key difference between the simulation results and the results from microwave experiments is that the thermal electrons are strongly heated at high power in the microwave experiments. As shown in Fig. 3-60, the thermal electrons in the overdense region are heated as they approach the critical surface (at 10 cm). The estimated thermal-electron drift velocity at high power is much larger than the threshold value for the ion acoustic drift instability, V_c ($T_{eo}/T_{io} \approx 10$, so that $V_c/v_{eo} \approx 0.05$).

Strong ion acoustic turbulence ($\delta n/n \leq 20\%$) and a dc electric field are observed in the overdense region where the thermal electrons are heated. The

Fig. 3-60. Temperature of thermal electrons traveling toward the critical surface in the overdense region. The critical surface is at 10 cm.

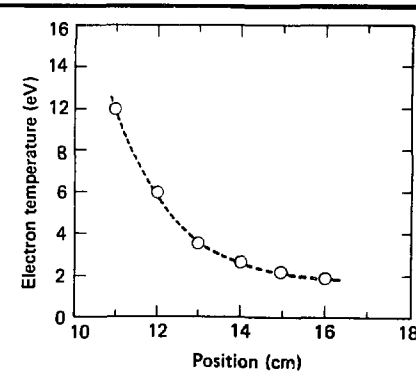

waves travel down the density gradient and have a broad spectrum in angle and frequency. Our measurements imply that effective electron collision frequencies due to the ion turbulence are as high as $\nu_{eff}/\omega_{pe} \approx 0.04$ ($\approx$ 300 times the electron collision frequency). This value agrees with theory [$\nu_{eff}/\omega_{pe} \approx (\delta n/n)^2$, with the measured value $\delta n/n \approx 0.2$]. We also observed large-amplitude ion waves ($\delta n/n \leq 20\%$) in the underdense region which propagate up and down the density gradient. These waves are probably excited by parametric instabilities.

With such large levels of ion turbulence near the critical surface, thermal and even some suprathermal electrons should be scattered and confined near the critical surface. We have verified that thermal electrons are confined near the critical surface, by measuring the decay of the thermal-electron temperature after the end of the microwave pulse. As predicted by diffusion theory, the thermal-electron temperature decays exponentially; the decay time gives $\nu_{eff}/\omega_{pe} \approx 0.03$, in agreement with the above estimates. We also find that the dc electric field is increased by a localized, weak magnetic field ($\omega_{ce}/\omega_0 \leq 1\%$). The magnetic field is transverse to the electron flow and localized so that thermal (but not suprathermal) electrons are confined. The dc electric field must then be increased so that the return current is maintained.

Authors: K. Mizuno, R. B. Spielman, J. S. DeGroot, and W. M. Bollen (All University of California at Davis)

References

125. K. G. Estabrook and W. L. Kruer, *Phys. Rev. Lett.* **40**, 42 (1978).
126. K. Mizuno and J. S. DeGroot, *Phys. Rev. Lett* **35**, 219 (1975).
127. K. Mizuno, R. B. Spielman, J. S. DeGroot, and W. M. Bollen, *Bull. Am. Phys. Soc* **24**, 980 (1979).

Electron-Heat Flux Inhibition Due to Ion Acoustic Turbulence

Electron-heat conductivity in a plasma must be high enough so that the absorbed laser energy is transported to the ablation surface. There are strong indications that the electron-heat flux is severely inhibited in some laser experiments; mechanisms which could inhibit the electron-heat flux are thus under intense investigation.

One commonly invoked mechanism is drift-driven ion acoustic turbulence. Thermal electrons must drift towards the absorption surface to compensate for the flux of suprathermal electrons which carry the absorbed laser energy to the ablation surface. These drifting thermal electrons drive ion acoustic turbulence, if the electron drift velocity, V_d, is large enough (for example, $V_d \gtrsim C_s$ if $ZT_e/T_i \gg 1$). The ion turbulence (in clumps, rather than individual ions) then scatters the electrons. Thus, the electron mean free path can be shorter than the collisional value, and the heat flux is inhibited.

The key unsolved problem is the level of inhibition directly connected to the level of ion acoustic turbulence (the electron mean free path due to the turbulence is $\lambda_{eff} \approx \lambda_{De}/(\delta n/n)^2$, where λ_{De} is the electron Debye length). We are performing modeling experiments[128] and calculations[129] with the objective of finding the level of electron-heat flux inhibition for laser-driven pellet parameters. Our previous results, reported in last year's annual report,[130] showed large dc electric fields, thermal-electron heating ($T_e \approx 10T_{eo}$), and large-amplitude ion acoustic turbulence ($\delta n/n \leq 0.2$, or $\lambda_{eff} \geq 25\ \lambda_{De}$) in the overdense region just above critical density. Even at the highest power ($v_{osc}/v_{eo} \approx 0.7$, where $v_{osc} = eE_0/m\omega_0$ and E_0 is the electric field of the incident microwaves), however, the dc electric field did not significantly inhibit the hot-electron heat flux; flux inhibition was $f_H \geq 0.5$, where f_H is the factor of heat-flux reduction from free streaming. Nevertheless, our calculations indicate that thermal-electron heat flux is strongly inhibited ($f_t \gtrsim 0.06$, $\lambda_{eff} \gtrsim 50\ \lambda_{De}$),[129] and for some conditions the thermal-heat flux is reversed ($q_t \sim \nabla T_e$ instead of $q_t \sim -\nabla T_e$). This strong inhibition is in apparent agreement with the inhibition factors which are required in the hydrodynamic calculations of some laser experiments.

The reason that the thermal electrons can be so strongly inhibited by ion acoustic turbulence is that the heat flux of the thermal electrons is made up of two terms (i.e., $q_t \sim \alpha V_d - \beta \nabla T_e$) which tend to cancel in laser-driven pellets. Thus, under conditions where V_d is large enough to compensate for the hot-electron heat flux, $q_t \approx 0$ or even $-\nabla T_e$. The ion acoustic waves are driven by an effective drift ($v_{eff} \simeq \gamma V_d + \nabla T_e$) however, so that v_{eff} can be large; the

ion acoustic turbulence is strongly driven, but the heat flux is strongly inhibited.

We have made detailed measurements[131] of the ion turbulence, and improved our computational model.[129] Our measurements show that the spectra of ion acoustic turbulence peaks at a lower frequency than the frequency of the fastest-growing mode. This indicates that mode-coupling is shifting the turbulence to lower frequencies. We have therefore incorporated a model of mode-coupling due to induced scattering from the ions[132] and electrons[133] in our calculations. We find good agreement between the calculated and measured ion acoustic spectra. Thus we can understand why the mean free path implied by the measurements is in fairly close agreement with the Sagdeev formula, $\nu_{eff} = 10^{-2}(ZT_e/T_i)(V_d/v_e)\omega_{pe}(\lambda_{eff} \approx v_e/\nu_{eff})$, which was derived[132] assuming that induced scattering is the dominant mode-coupling mechanism.

We have also constructed[134] a computational model of the effect of the dc electric field driven by the ion acoustic turbulence on the plasma density profile near the critical density. We have included hot ions in this model, since ion acoustic turbulence levels seen in the microwave experiments should result in strongly heated ions. Preliminary results indicate that the dc electric field in the overdense region can be large enough to reflect the ions before they get to the critical surface. The importance of this discovery is that the density in the critical region must decrease so that the density profile is not in steady state. When the density has decreased to the point that the critical density is near the point of ion reflection, then a new cycle starts, with the ion reflection point moving farther in the plasma. This suggests that the density profile near the critical density would not have a steady state, but rather that a relaxation oscillation would be set up.

Authors: C. L. Yee, J. S. DeGroot, and W. Woo (All University of California at Davis)

References

128. K. Mizuno, R. B. Spielman, J. S. DeGroot, and W. M. Bollen, "Effects of the Return Current on Electron Heating and Thermal Transport," abstract in *Bull. Am. Phys. Soc.* **24**, 980 (1979), and submitted to *Phys. Rev. Lett.*

129. C. L. Yee, W. Woo, and J. S. DeGroot, "Thermal Heat Flux and Anomalous DC Resistivity," abstract in *Bull. Am. Phys. Soc.* **24**, 934 (1979), and submitted to *Phys. Rev. Lett.*

130. *Laser Program Annual Report—1978*, Lawrence Livermore Laboratory, Livermore, Calif., UCRL-50021-78 (1979), pp. 3-50 to 3-52.

131. W. M. Bollen, J. S. DeGroot, K. Mizuno, R. B. Spielman, and R. L. Walraven, "Experimental Investigation of Current Driven Ion Acoustic Turbulence and Anomalous DC Resistivity," abstract in *Bull. Am. Phys. Soc.* **24**, 935 (1979), and submitted to *Phys. Fluids*.

132. R. Z. Sagdeev and A. A. Galeev, *Non-linear Plasma Theory*, (Benjamin, New York, 1979) pp. 68 to 73.

133. Duk-In Choi and W. Horton, "Modified Kadomtsev Spectrum from Renormalized Plasma Turbulence Theory," *Phys. Fluids* **17**, 2048 (1974).

134. W. Woo and J. S. DeGroot, "Effects of Counter Streaming and Vortex Return Currents on Plasma Temperature and Density Profiles," abstract in *Bull. Am. Phys. Soc.* **24**, 980 (1979), and submitted to *Phys. Rev. Lett.*

Plasma Code Development

Much of the code development effort this year was spent converting codes to run on the Cray-1 computer, and tuning them to run efficiently. The vectorized Cray version of the ES1 code[135] was used for the studies described in "Resonant Absorption" earlier in this section. The ZOHAR code,[136] used in many plasma studies, now runs about four times faster on the Cray than on the CDC 7600; much of this speed is due to the reprogramming for the Cray of the 7600 machine-language particle integrators. In order to achieve similar economies, new physics codes will be written only for the Cray-1, bypassing the CDC 7600. For example, two extensions of the one-dimensional hydrodynamics code AURUS (Ref. 137) are being implemented on the Cray. In one, a PIC model for the ions provides a fully kinetic description of their dynamics. In the second, a WKB treatment of the light allows efficient simulation of stimulated Brillouin scattering over very large plasma regions.

Authors: A. B. Langdon, B. F. Lasinski, and C. J. Randall

Major Contributor: C. Barnes (Stanford University)

References

135. C. K. Birdsall and A. B. Langdon, *Plasma Physics via Computer Simulation* (University of California Press, Berkeley and Los Angeles, 1975)

136. A. B. Langdon and B. F. Lasinski, "Electromagnetic and Relativistic Plasma Simulation Models," in *Methods in Computational Physics*, J. Killeen, Ed. (Academic Press, New York, 1976), vol. 16, B. Alder, S. Fernbach, and M. Rotenberg, Eds., p. 327

137. *Laser Program Annual Report—1978*, Lawrence Livermore Laboratory, Livermore, Calif., UCRL-50021-78 (1979), pp. 3-53 to 3-56.

LASNEX and Atomic Theory Overview

During 1979 we completely restructured and rewrote the LASNEX code for the Cray-1 computer. Several physics improvements were made in the code as a natural consequence of this translation process, and other improvements were made in areas where experiments had pointed out obvious deficiencies in our models or where new capabilities were needed to carry out current design work.

The atomic physics package, XSN, was modified to include electron degeneracy and a formal theory of shell-pressure ionization, and screening coefficients were adjusted to reduce the average error in ionization potentials. These improvements made only small changes in the calculated frequency-dependent opacities; however, pressures and energies, which are needed for non-LTE calculations, have improved significantly, and they are now thermodynamically consistent. We have begun to use XSN as well as a Thomas-Fermi-Dirac model to calculate ion-beam deposition in dense plasmas.

The Brillouin backscattering model that limits the amount of laser light available for absorption has been modified to self-consistently calculate saturation by density gradients and ion damping. Accordingly, calculated laser-light absorption on gold disks is now more in agreement with experiments.

Additional terms have been included in the multigroup diffusion equations used to transport charged particles from thermonuclear reactions. Compared with standard diffusion models, the new methods are less sensitive to zone size and time step and provide better agreement with Monte Carlo calculations.

In transferring LASNEX to the Cray-1 computer, we have made many improvements to the structure, reliability, and speed of the code. By automating the management of memory, we have eliminated many kinds of programming errors and made it possible for as many as eight people to work on the code simultaneously without interfering with one another. Also, we have found that it is now much easier to add new physics packages and user conveniences.

Most of LASNEX has been rewritten to take advantage of the fast vector instructions on the Cray-1. For some procedures, such as matrix inversion, this capability required us to develop totally new methods.

Currently, LASNEX is running about twice as fast on the Cray-1 as it does on the 7600. Compiler enhancements expected in the next few months should allow us to realize vector speeds for most of the coding. We anticipate further improvement in speed by a factor of two.

Author: G. B. Zimmerman

Improvements in the LASNEX Atomic-Physics Package

The LASNEX in-line atomic physics package XSNQ has been revised to improve its treatment of heavy atoms in dense plasmas. The changes give a significant improvement in the physical description of atomic ionization, equation of state, and opacity. The revised code provides a unified atomic model useful for the entire range from low densities (including non-LTE conditions) to very dense, degenerate matter.

XSNQ Subroutine. The LASNEX code uses XSNQ, originally developed by W. Lokke, for calculations of hot plasmas at low densities.[138] The package is a convenient source of atomic data—including ionization state, energy levels, populations, equation of state, and optical-absorption coefficients (opacity)—and it calculates both equilibrium and nonequilibrium problems. We are making a continuing effort to improve this package with respect to computational speed and physical accuracy.[139-141]

Inertial confinement fusion research is uniquely interested in plasmas of high density ($\rho > 0.1$ g/cm^3); however, normal atomic-ionization calculations encounter difficulties when applied to atoms in such a dense plasma. These difficulties, which occur for dense plasmas and are associated with continuum-lowering and pressure ionization, include

- Large regions where the ionization state Z is constant and independent of density and temperature.

- Pressure ionization occurring as discontinuous jumps of ionization state.
- Slow computational convergence near these jumps.
- Disagreement with the statistical-atom (Thomas–Fermi, Thomas–Fermi–Dirac) calculations by as much as a factor of two.

Similar problems arise in other atomic-ionization calculations for dense plasmas, including those based on the Saha equation. An additional difficulty specific to the XSNQ screened-hydrogenic model is produced by inaccurate ionization potentials for heavy elements; this problem is most evident at relatively low plasma temperatures (i.e., <100 eV). Table 3-2 gives a comparison that illustrates this problem for gold ($Z = 79$).

Finally, there has been a continuing difficulty with thermodynamic consistency of LTE and non-LTE equations of state.

We have developed practical solutions to these difficulties. Our changes retain the XSNQ energy-level scheme and preserve compatibility with the opacity calculation and non-LTE equations. The modified code is faster than the original because it achieves self-consistency in fewer iterations.

Screening Coefficients. The ionization potentials are obtained from a screening model originally developed by H. Mayer.[142] For electrons of any shell, n (n = principal quantum number = 1,2,3,...), a screened nuclear charge, Z_n, is computed as

$$Z_n = Z - \sum_{i \le n} S(n,i)\, P_i - T_n P_n \,, \qquad (127)$$

where Z is the nuclear charge, $S(n,i)$ is the matrix of screening constants, $T_n = 1.2[1 - (1 - 2n^{-2})]\, S(n,n)$ is the screening within the nth shell, and P_n is the number of electrons in the nth shell for the ion in question. (In thermodynamic equilibrium, P_n is the average shell population.)

From the screened nuclear charges, a total ion energy, E_{ion}, is constructed by use of relativistic hydrogenic energy levels, and this ion energy is differenced to produce the ionization potentials. The procedure predicts the ionization potentials of all the elements in terms of a single 10-by-10 matrix of screening constants. Mayer calculated the screening constants $S(n,i)$ by applying first-order perturbation theory to hydrogenic wave functions.

To test Mayer's screening constants, we compared the predicted ionization potentials with a large data base[143] calculated with the Hartree-Fock-Slater theory. The data base contains such ionization potentials for 30 elements.

The root mean square fractional deviation of the Mayer-XSNQ ionization potentials from the Scofield data base exceeds 100%—an average error of a factor of two in ionization potential (see Fig. 3-61). The large disagreements occur for the low ionization states of heavy atoms, however, and therefore are important only for cold plasma (T_e < 100 eV).

Because the screening constants enter the theory as fixed parameters, we are able to optimize the results by adjusting the screening constants. This has been done by a least squares procedure. The rms deviation of the new ionization potentials from the Scofield data base is reduced to 25%—this appears to be the best that can be achieved without adopting a more detailed description of subshell splittings. It has been verified that the new screening matrix does not predict negative ionization potentials for any element. Characteristics of the new screening constants are summarized as follows:

- They yield a factor-of-four reduction in the average error of ionization potentials.
- The new matrix retains the important symmetry property $I^2 S(i,j) = J^2 S(j,i)$.
- The matrix-elements are smooth monotone functions of shell indices i,j (see Fig. 3-62).
- The largest alteration in any screening constant is less than 10%.

Figure 3-63 compares ionization potentials calculated from the new screening constants with the Scofield data-base for aluminum, iron, barium,

Table 3-2. A comparison of calculational models, for the first few ionization potentials of gold.

Ionization stage	Original XSNQ [Mayer S(n, i)] (eV)	New XSNQ [New S(n, i)] (eV)	Scofield Hartree-Fock-Slater (eV)
1	69.8	13.4	9.2
2	82.6	23.0	20.5
3	95.7	33.1	32.2
4	109.3	43.6	46.2
5	123.4	54.6	61.1

Fig. 3-61. Ionization potentials of four elements are plotted as functions of the number of bound electrons. The solid line interpolates between the Hartree-Fock-Slater[142] values; the points are produced by the XSNQ package with the original (Mayer) screening. Note the substantial disagreement for nearly neutral heavy atoms.

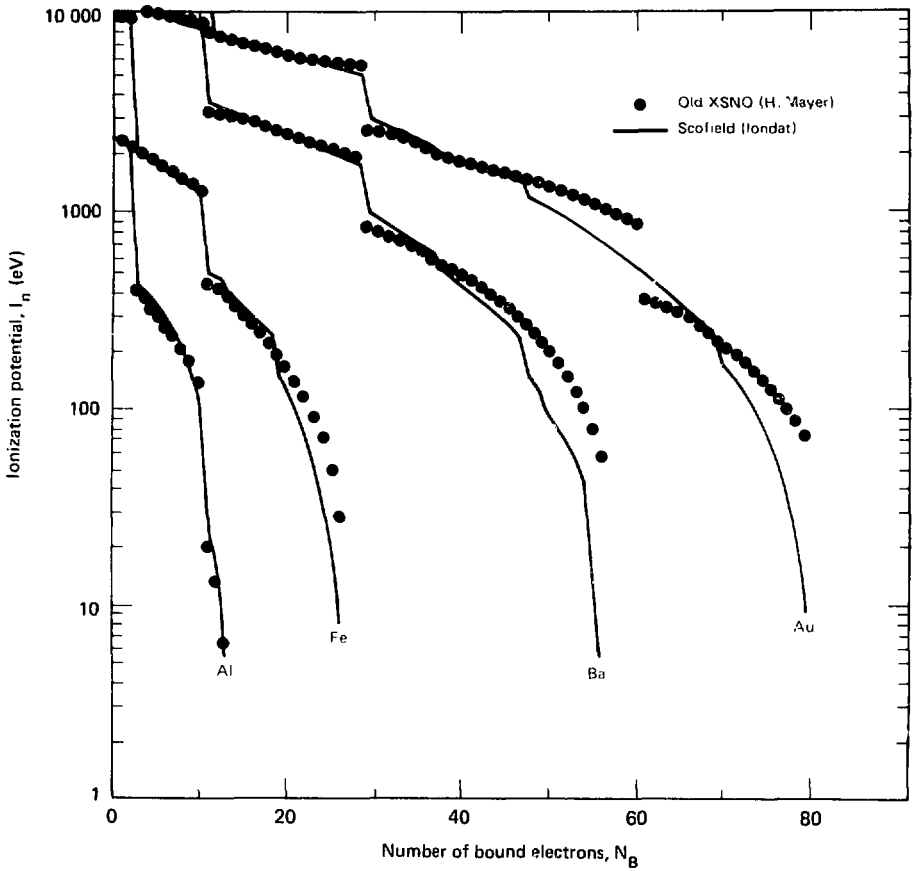

and gold. The first few ionization potentials are significantly improved. Clearly, these new screening constants will improve the ability of LASNEX to describe low-temperature material properties.

Pressure Ionization Model. When atoms press together at high density, bound electrons are released into the free-electron continuum, a process called pressure ionization. In our approach, the pressure ionization is phenomenologically described by introducing a shell degeneracy $D_n(\rho)$ that enforces the removal of the nth shell as the atom is compressed. The electrons of the nth shell are assigned an approximate orbit radius

$$r_n = (0.529 \times 10^{-8}\ \text{cm})\left(\frac{n^2}{Z_n}\right), \qquad (128)$$

where n is the principal quantum number and Z_n is the screened nuclear charge in nth shell: the shell merges smoothly into the continuum when the

Fig. 3-62. The new screening constants $S(i,j)$.

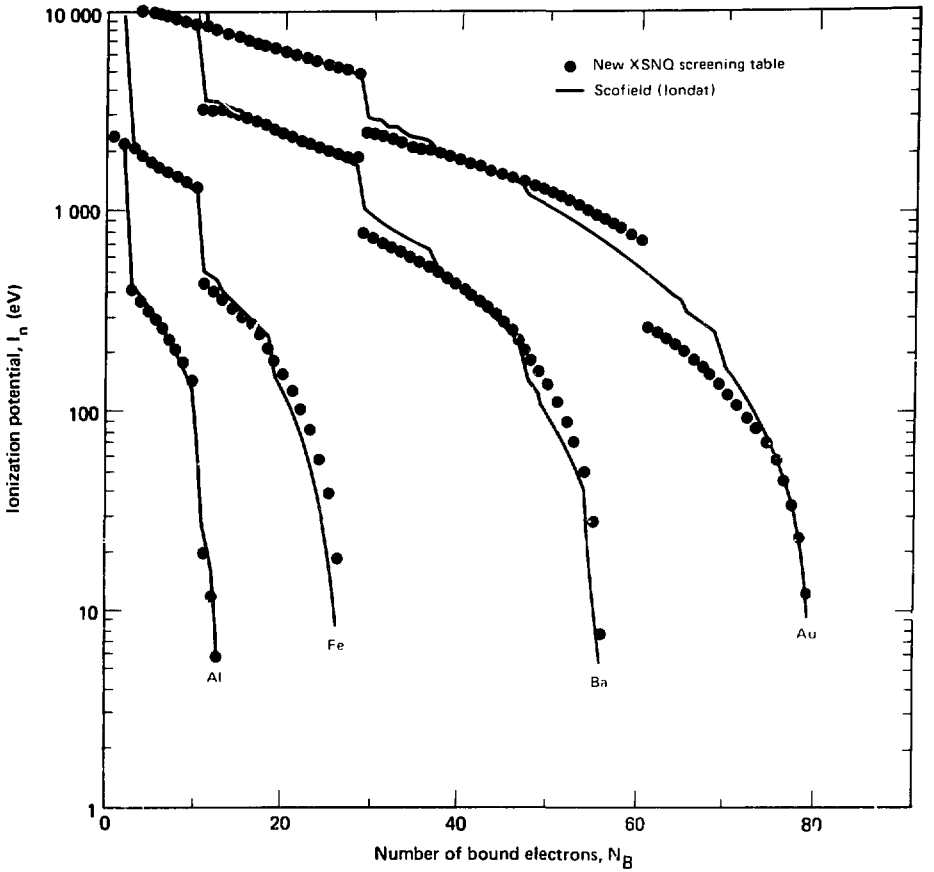

average atomic spacing drops below $2r_n$. In this model, the shell degeneracy is taken to be

$$D_n = \frac{2n^2}{1 + \left(a\rho r_n^3\right)^b} \quad (129)$$

where ρ is the material density. The coefficients a,b are adjusted to produce approximate agreement with the Thomas-Fermi-Dirac theory.

Thermodynamic Formulation. The Helmholtz free energy of the ion is constructed as

- Free Energy: $F_{ion} = E_{ion} - TS_{ion}$.
- Energy: $E_{ion} = \sum_n \epsilon_n P_n$.
- Entropy $S_{ion} = -k \sum [P_n \log (f_n) + (D_n - P_n) \log (1 - f_n)]$, where ϵ_n = one-electron energy ($13.6\ eV / \tilde{n}^2$), $f_n = P_n / D_n$ = occupation = number of electrons per quantum state, and k = Boltzmann constant.

The total free energy F is E_{ion} plus contributions from free electrons and from continuum lowering. The free electrons are allowed arbitrary degeneracy. All thermodynamic averages (f_n, Z, pressure, energy) are derived from this free energy.

Fig. 3-63. Ionization potentials as calculated with the new screening model agree more closely with the Hartree-Fock-Slater values.

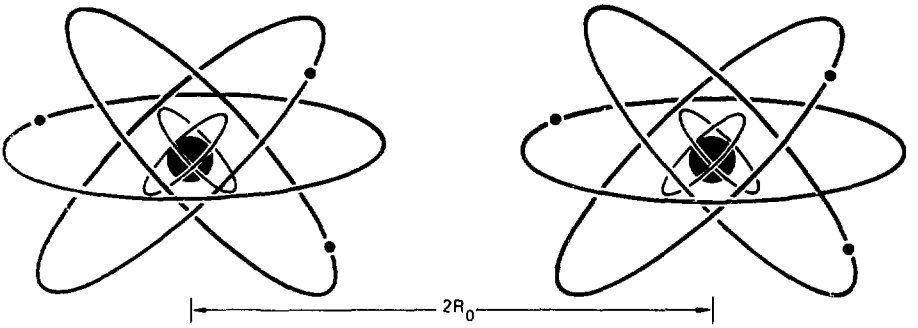

Fig. 3-64. Numerical test of thermodynamic consistency for the modified XSNQ. The quantity shown is $A = [T(\partial p/\partial T) - P]/[\partial e/\partial V]$, which should be unity. The slight deviations from unity are caused by numerical differentiation on a finite (50 × 50) grid.

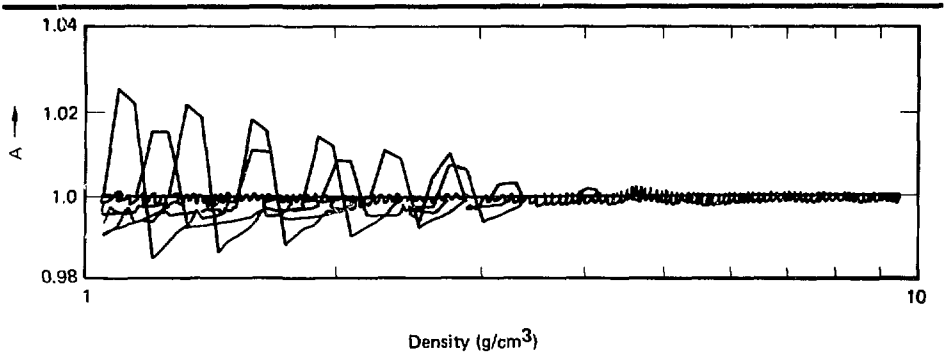

1 The procedure guarantees thermodynamic consistency, which is important for hydrodynamic applications; the numerical results show excellent thermodynamic consistency (see Fig. 3-64).

The pressure obtained from this free-energy model contains three terms: free-electron pressure, including degeneracy effects; an electrostatic contribution obtained from the continuum lowering; and a shell-compression pressure not considered by previous workers. The latter term is given by

$$P_{shell} = kT \sum_n \frac{\partial D_n}{\partial V} \log(1 - f_n) \qquad (130)$$

This term contributes when an occupied shell is squeezed into the continuum. The pressure and energy are plotted in Fig. 3-65 for aluminum. (This is the electronic pressure; solid-state bonding and ion kinetic contributions are omitted.) The ionization state, Z, is plotted in Fig. 3-66.

Addition of pressure ionization (in the form described here) and free-electron degeneracy has required several changes in the opacity and non-LTE portions of the XSNQ code. With these changes installed, the computed results appear to give a more realistic description of very dense plasmas.

The theory described here gives an immediate practical description of pressure ionization in dense plasmas. Efforts are underway to employ more

Fig. 3-65. Modified ionization model results for aluminum: (a) electronic pressure, and (b) electronic energy.

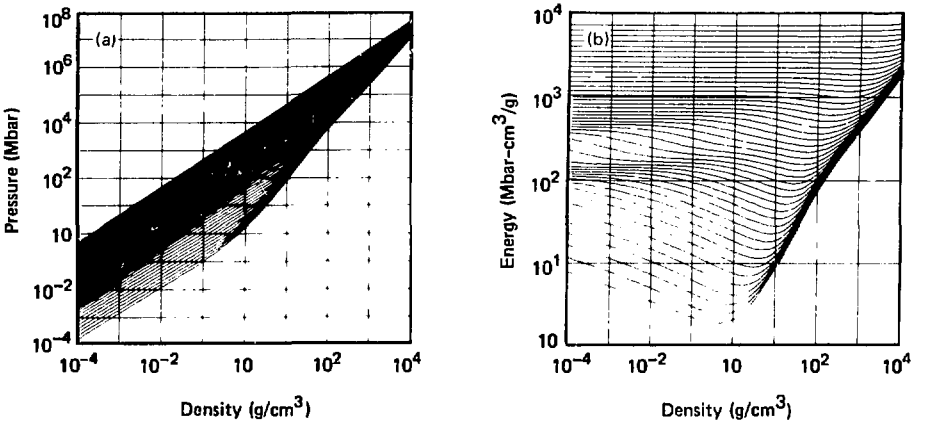

Fig. 3-66. The ionization state Z(n,T) of aluminum: (a) as calculated by the original average atom model and (b) as calculated from the new model. In (a) the density range from 10^{-4} to 10^4 g/cm^3; the temperature from 1 to 10 keV. Note the following unsatisfactory features: flat shelves where Z = constant; very abrupt jumps between shelves; wrinkled extensions of the jumps that continue up to high temperatures. All these features are associated with the pressure-ionization model. The calculation in (b) has been adjusted to give approximate agreement with the Thomas-Fermi-Dirac theory in the range of pressure ionization. The Z(n,T) surface is considerably smoother.

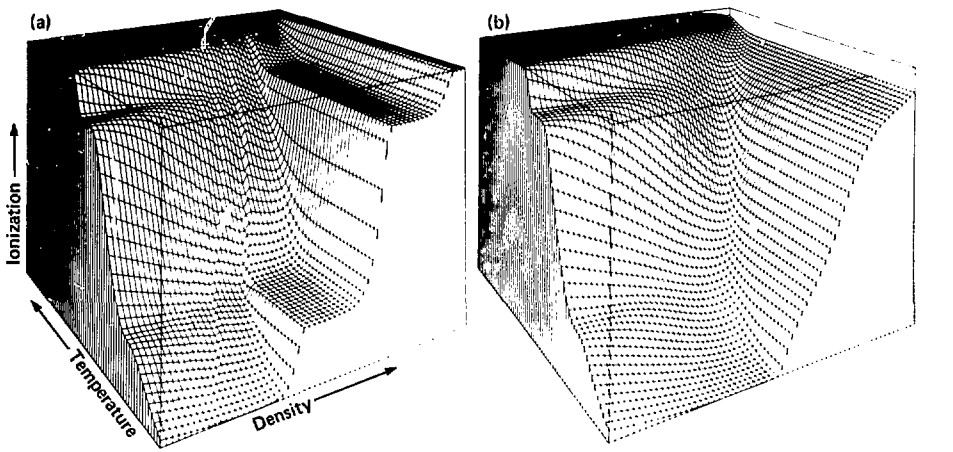

rigorous quantum-statistical calculations to supply more detailed information about spectroscopic phenomena encountered in pressure ionization.

Authors: R. M. More and G. B. Zimmerman

References

138. W. A. Lokke and W. H. Grasberger, *XSNQ-U(A) Non-LTE Emission and Absorption Coefficient Subroutine*, Lawrence Livermore Laboratory, Livermore, Calif., UCRL-52276 (1977).

139. G. B. Zimmerman and R. M. More, *Pressure Ionization in Laser-Fusion Target Simulation*, Lawrence Livermore Laboratory, Livermore, Calif., UCRL-81336 (1978), to be published in *J. Quant. Spectroscopy and Radiat. Transfer*.

140. R. M. More, *Numerical Studies of Dense Plasmas Using Statistical and Ionization Theories*, Lawrence Livermore Laboratory, Livermore, Calif., UCRL-82150 (1979).

141. R. M. More and G. B. Zimmerman, *H-Division Quarterly Report July through September 1978*, Lawrence Livermore Laboratory, Livermore, Calif., UCRL-50028-78-3, p. 1, and More and Zimmerman, *H-Division Quarterly April through June 1979*, UCRL-50028-79-2, p. 1.

142. H. Mayer, "Methods of Opacity Calculation," Los Alamos Scientific Laboratory, Los Alamos, N. Mex., LA-647 (1947).

143. J. H. Scofield, Lawrence Livermore Laboratory, private communication (1979).

Energy Deposition by Fast Ions

Widespread interest in heavy-ion fusion has prompted us to re-examine the LASNEX model for ion energy-deposition in hot dense plasmas. The existing LASNEX deposition package follows textbook theory,[144] separately calculating energy loss to bound and free electrons. The average ionization potential required for energy loss to bound electrons is calculated by a plausible scaling formula that is correct in the two limits of cold matter and fully ionized plasma. However, we believe that ab initio energy-deposition calculations give a more convincing basis for heavy-ion target design. During 1979, we began development of two theoretical models that will be used to calculate heavy-ion energy loss. In the future, we hope to incorporate the results of our development effort into the LASNEX code.

The practical problem concerning heavy-ion energy loss is that all existing experimental information refers to cold matter, but ICF target plasmas reach high temperatures and pressures. The actual rate of energy loss is expected to change dramatically with the thermodynamic state of the target.[145,146]

To briefly describe our calculations, it is useful to write the energy loss per unit of path length in the general form

$$-\frac{dE}{dx} = \frac{4\pi Z^2 e^4}{m v_0^2} N L \qquad (131)$$

where Z is the current charge of the fast ion, v_0 is its velocity, m is the electron mass, and N is the ion number density in the target plasma. L is the stopping number per target atom, often calculated as a logarithm of a ratio of lengths (e.g., maximum and minimum impact parameters). The important unknown quantities are Z and L.

For fast ions, the charge state Z depends mainly on the ion velocity v_0 and is believed to depend weakly on the plasma thermodynamic state. For this case, we currently use the empirical formula given by Betz.[147] For slow ions, Z cannot fall below the thermal ionization state of an impurity ion in the plasma; this is calculated by Thomas-Fermi theory. The XSNQ code contains a useful set of rate equations and cross sections that can be modified to calculate the charge state of moving ions; this calculation is under way and will provide a better estimate of $Z(v_0)$.

The stopping number, L, can be calculated by two methods. In one approach, the ions of the target plasma are described by Thomas-Fermi-Dirac theory.[148] This theory includes many effects of high pressure and temperature, including thermal ionization, electron degeneracy, and strong ion-pair correlation. The theory is not completely quantum mechanical and omits effects of bound-electron energy quantization. To be certain that the omitted effects do not significantly alter the stopping power, we intend to verify our results by using the screened hydrogenic ionization model (XSNQ).

To calculate the stopping number per atom, L_{Atom}, from the statistical model, we have adopted the local-density approximation of Lindhard and Winther[149]:

$$L_{Atom} = \int n(r)\, L_0[n(r), T, v_0] \left[1 - \frac{Ze\, v_1(r)}{E}\right] d^3r \,. \qquad (132)$$

In this equation, $L_0[n(r), T, v_0]$ is the stopping number per electron in a uniform electron gas having

density n and temperature T (for fast ions of velocity v_0). A similar theory is widely used to calculate energy loss in cold matter.[150] We have modified the Lindhard-Winther approximation in the following ways:

- The electron density n(r) is calculated from a finite-temperature theory (i.e., TFD theory).
- The stopping number L_0 is obtained from the finite-temperature dielectric function.
- The factor in heavy brackets in Eq. (132) is a correction for curved orbits followed by heavy ions traversing the volume of a target atom. The term $v_1(r)$ is the ion-pair potential,[151] and E is the energy of relative motion of projectile and target ions.
- The classical Bohr minimum-impact parameter is used where appropriate (heavy-ion projectiles).

We have applied this formalism to calculate stopping of helium ions (alpha particles) in gold at several densities; the results are shown in Fig. 3-67. The normal density results are (generally) within about 20% of experimental data.

A second approach uses the XSNQ ionization-equilibrium model to provide detailed populations and energy levels for the target plasma. The average ionization potential of bound electrons is then formed directly by using hydrogenic oscillator strengths. The usual stopping theory[144] is used to obtain the free-electron contribution. The advantage of this second approach is that it will provide an independent check on the validity of results obtained from the statistical model.

Fig. 3-67. Energy loss per atom for helium ions in gold at three densities calculated from the TFD model. The units of S(E) are eV-cm^2 per 10^{15} atoms; dE/dx is S(E) times the target ion number density.

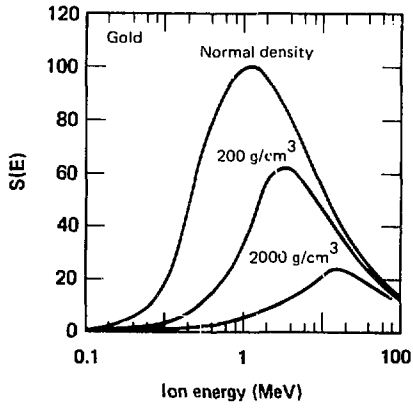

Authors: R. M. More and D. S. Bailey

References

144. J. D. Jackson, *Classical Electrodynamics* (John Wiley & Sons, New York, 1975), 2nd ed.
145. S. Skupsky, *Phys. Rev. A* 16, [illegible] 1977).
146. E. Nardi, E. Peleg, and Z. Zinamon, *Phys. Fluids* **21**, 574 (1978).
147. H. D. Betz, *Rev. Mod. Phys.* 44, 465 (1972).
148. R. D. Cowan and J. A. Ashkin, *Phys. Rev.* **105**, 144 (1957).
149. J. Lindhard and A. Winther, *Danske Videnskabernes Selskab* **34**, 4 (1964).
150. W. K. Chu and D. Powers, *Phys. Rev.* **187**, 478, (1969); *Phys. Rev. B* **4**, 10 (1971).
151. J. Lindhard, V. Nielsen, and M. Scharff, *Danske Videnskabernes Selskab* 36, 10 (1968).

Brillouin Backscattering Model in LASNEX

In the 1978 annual report[152] we described our stimulated Brillouin scattering (SBS) model for LASNEX. In the past year we have made many improvements and additions, to more accurately model the Brillouin backscattering in underdense plasmas. We have changed the density-dependence of our model; included the effects of inhomogeneous media; added a self-consistent calculation of the hot-ion contribution to ion damping; improved the saturation calculation; improved the calculation of backscattering when a very small fraction is reflected; and considerably expanded the treatment of backscattered light. Below, we describe these changes to our SBS model.

The fraction of light reflected in each zone by Brillouin backscattering is obtained by the following equation [compare with Eq. (54) on page 3-63 of Ref. 152]:

$$\text{Reflection} = 1 - \exp\left\{\frac{-A\left(\frac{v_{osc}}{v_e}\right)^2\left(\frac{n}{n_c}\right)\frac{\varrho}{\lambda_0}}{\left(\frac{\omega_i}{\omega_r}\right)_{Tot}\left(1+3\frac{T_i}{ZT_e}\right)\left(1-\frac{n}{n_c}\right)\left[1+\frac{K'_n+K'_{\nabla v}}{64\left(\frac{\omega_i}{\omega_r}\right)^2_{Tot}\left(1-\frac{n}{n_c}\right)}\right]}\right\} = 1 - e^{-Q} \qquad (133)$$

where

$$K'_{\nabla n} = \frac{\lambda_0}{\Delta x}\left(\frac{n}{n_c}\right)\left[\left(\frac{C_s + v}{C_s}\right)^2 \Big/ \left(1 - \frac{n}{n_c}\right)^{1/2}\right] \qquad (134)$$

and

$$K'_{\nabla v} = 2\frac{\lambda_0 \Delta v}{\Delta x}\left[\left(1 - \frac{n}{n_c}\right)^{1/2}\left(\frac{C_s + v}{C_s^2}\right)^2\right] . \qquad (135)$$

The gradients are taken along the direction of the incident light and will be explained below. A is a constant except in the case of very small backscattering, as discussed below; v_{osc}/v_e is the ratio of the oscillation velocity of an electron in the laser electric field to the electron thermal velocity; n/n_c is the ratio of the electron number density to the electron number density at the critical surface (where $\omega_0 = \omega_{pe}$); ℓ/λ_0 is the ratio of the path length to the vacuum laser wavelength; ω_i/ω_r is the ratio of the ion damping to the ion acoustic frequency; T_e, T_i, and Z are the electron and ion temperatures and the ionization state, respectively; C_s is the ion sound speed; $k_0 = 2\pi/\lambda_0$; v is the material expansion velocity, and Δx is zone length.

New Features of the SBS Model. We have thoroughly investigated the density-dependence of the Q factor, and we have now settled on the dependence shown in Eq. (133); this dependence gives the best fit to the simulation data, and is theoretically justified.[153]

Both density and velocity gradients affect the stimulated Brillouin scattering instability. In the presence of inhomogeneities of the plasma properties, the resonance conditions are satisfied only in a finite region of space. Thus the instability is effectively damped if the waves propagate out of the resonant interaction region before significant growth occurs. In Eqs. (133) to (135), we show how the gradient terms are included in Q, the exponentiation length of SBS. The effects of inhomogeneous media on three-wave parametric instabilities were first derived by Rosenbluth.[154] The form we have employed is derived by replacing Nishikawa's[155] integration length in his Eq. III-57 by the mismatch length,[154] as suggested by Kruer.[156] As a diagnostic check, the code calculates the threshold conditions for density-gradient saturation,

$$\left(\frac{v_{osc}}{v_e}\right)^2 < \frac{4}{\pi}\frac{\left(\nabla\frac{n}{n_c}\right)\lambda_0}{\left(\frac{n}{n_c}\right)}\left(\frac{C_s + v}{C_s}\right) \qquad (136)$$

and velocity-gradient saturation,

$$\left(\frac{v_{osc}}{v_e}\right)^2 < 2.55\frac{(\nabla v)\,\lambda_0\left(1 - \frac{n}{n_c}\right)}{C_s\left(\frac{n}{n_c}\right)} \qquad (137)$$

and monitors the number of times that these conditions are satisifed.

In last year's annual report[152] we mentioned that the ions heated by SBS are optimally located in position and velocity space to do the most damping, and that the ion–ion equilibration time is usually large enough to make this nonequilibrium effect visible. Initially, we simply mocked up this phenomenon by a multiplier on the ion temperature in the (ω_i/ω_r) calculation. Now the contribution of the hot ions to the damping is calculated self-consistently. This improvement is indicated in Eq. (133) by the subscript "Tot" on (ω_i/ω_r).

We now use the following equation to calculate ion damping:

$$\left.\frac{\omega_i}{\omega_r}\right|_{Tot} = \left.\frac{\omega_i}{\omega_r}\right|_{Hot}\frac{n_{iHot}}{n_{iTot}} + \left.\frac{\omega_i}{\omega_r}\right|_{Cold}\frac{n_{iCold}}{n_{iTot}} \qquad (138)$$

where n_{iHot} and n_{iCold} are the number densities of the hot and cold ions, and n_{iTot} is the total ion density. The damping frequency of the cold ion is calculated as described in Ref. 152. The ω_i/ω_{rHot} calculation is simplified by assuming $ZT_e/T_{iHot} = 2$; i.e., the hot ions are accelerated by SBS to a temperature $1/2\, M_i C_s^2$.

In our new self-consistent calculation, the density of the hot ions must be found to evaluate ω_i/ω_{rTot}. Ions are heated by the SBS; they remain hot for the ion–ion equilibration time, τ_{ii}, which may be long compared to the other time scales of interest. Thus time histories of the fraction of hot ions as a function of electron density, n_e, are required to calculate n_{iHot}. We have divided the underdense

plasma into the following five sections so that the ratio of electron density to critical density, n/n_c, ranges from 0 to 0.0625, from 0.0625 to 0.125, from 0.125 to 0.25, from 0.25 to 0.5, and from 0.5 to 1.0. The total run time is divided equally into 20 time blocks. For each of these 100 points in (t,n_e) space, the fraction of hot ions is stored and, of course, updated at each time step. Finally, we obtain the current $n_{iHot}(t,n_e)$ where

$$n_{iHot}(t,n_e) = \int_{t-\tau_{ij}}^{t} n_{iHot}(t',n_e)\,dt' \qquad (139)$$

by the appropriate summation.

We found that our nonlinear saturation statement was not suitable for a problem with zones that were greater in width than a few vacuum wavelengths. This is, of course, the usual situation in hydrodynamic calculations. In the old model, the maximum saturated backscattering occurred throughout the entire zone in which the saturation limit was reached, irrespective of the zone size, resulting in nonphysically large amounts of backscattering. In the real world, the maximum backscattering would not occur over many wavelengths; instead, SBS would be self-limiting through the intensity dependence, $(v_{osc}/v_e)^2$, of the Q factor. The backscattering reduces the light intensity reaching λ_0 further into the plasma.

To include this natural self-limitation in our SBS package, we wrote a saturation loop that is short and fast. Each zone in which saturation occurs is treated in pieces of length λ_0. The proper light intensity, with the backscattered part deleted, is used for each plasma slab of thickness λ_0. We have found that this technique works very well to correct the overestimate of scattering that occurred in the simpler model.

For quite small reflection, the total backscattering is smaller than the pump-depletion regime described by Eq. (133). The code monitors the space-integrated Q from the previous time step and sets A so that the total reflection agrees with the more complete description of Ref. 157 for a noise level of 10^{-4}.

Finally, we have expanded the options available for monitoring backscattered light. Last year, we reported that all of the backscattered light was assumed to be scattered out of the target and was lost from the problem. Now, the user may select any of the following four options:

- All of the backscattered light is lost, as before.
- None of the backscattered light is lost except that scattered into vacuum. Instead, the light backscattered on the way up the density gradient into the material is added back into the light ray at the scattering location, as the ray propagates back down the density gradient. Likewise, on the way back out of the material, the backscattered light will augment the ingoing ray on the next time step. This model is one-dimensional and allows only one laser.
- Some of the backscattered light is lost, but the rest is traced. This is a combination of the first two options: the user defines a certain fraction of the backscattered light to be tracked, as in the second option; the rest of the light is then lost, as in the first option. This model may be thought of as allowing a fraction of the scattered light to be sidescattered and lost; the rest of the light is backscattered and tracked.
- The user may track the light that is backscattered as the laser goes up the density ramp, but not the light that is backscattered as the light propagates down the density ramp. Again, this is a combination of the first two options, using the second option on the way into the target and the first option on the way out.

In conclusion, the Brillouin backscatter model has been extensively expanded and improved, and this model now predicts to within 10% the absorptions seen in gold-disk experiments. The results of these predictions are discussed in "Calculations of Stimulated Brillouin Scattering with LASNEX," earlier in this section.

Authors: J. A. Harte and K. G. Estabrook

References

152. *Laser Program Annual Report—1978*, Lawrence Livermore Laboratory, Livermore, Calif., UCRL-50021-78 (1979), pp. 3-63 to 3-69.
153. W. L. Kruer, Lawrence Livermore Laboratory, Livermore, Calif., private communication (1979).
154. M. N. Rosenbluth, *Phys. Rev. Lett.* **29**, 565 (1972).
155. K. Nishikawa, in *Advances in Plasma Physics*, vol 6, A. Simon and W. Thompson, Eds. (Wiley & Sons, New York, 1976), p. 45.
156. W. L. Kruer, Lawrence Livermore Laboratory, Livermore, Calif., private communication (1979).
157. D. W. Phillion, W. L. Kruer, and V. C. Rupert, *Phys. Rev. Lett.* **39**, 1529 (1977).

Charged-Particle Multigroup Diffusion

During the past year we completely rewrote the thermonuclear-burn-product transport routines in LASNEX. We undertook this project in order to take advantage of fast vector operations on the Cray-1 computer, but many physics improvements were incorporated at the same time. These improvements include:

- Consistent isotope production and depletion for all reactions.
- The ability to transport any reaction product or knock-on from elastic scattering.
- Inclusion of all important in-flight reactions and nuclear elastic scattering involving isotopes of hydrogen and helium.
- The ability to use completely arbitrary energy-group structures for all charged particles.
- Inclusion of inertial terms in the flux equation for all charged particles.

The most important improvements have been the last two items of this list. In this article we discuss the importance of including the inertial terms.

Starting from the Fokker–Planck equation, Ref. 158 takes the zero and first moments to obtain

$$\frac{\partial n_E}{\partial t} + \hat{v}\cdot\vec{J}_1 = \frac{1}{\tau_e}\frac{\partial}{\partial E}\left\{\left[1+(E_0/E)^{3/2}\right]E n_E\right\} \quad (140)$$

and

$$\frac{1}{v}\frac{\partial \vec{J}_E}{\partial t} + v\vec{\nabla}\cdot\underline{\pi}_E = \frac{1}{\tau_e}\frac{\partial}{\partial E}\left\{\left[1+(E_0/E)^{3/2}\right]E\frac{\vec{J}_E}{v}\right\} - \sigma_E\vec{J}_E \quad . \quad (141)$$

In these equations n_E is the density of particles at energy E, v is their velocity, $\vec{J}_E$ is their flux, τ_e is the slowing-down time considering only electron collisions, E_0 is the energy at which energy losses to electrons and ions are equal, $\underline{\pi}_E$ is the stress tensor, and σ_E is the scattering cross section. The bracketed term in each equation represents the effects of energy loss. In Eq. (141) we can identify it as an inertial term, since it accounts for the fact that charged particles remember their direction as they lose energy. Previously, we had followed Ref. 158 and simplified Eq. (141) by assuming

$$\frac{\partial \vec{J}_E}{\partial t} = 0 \text{ (steady-state)} \ ,$$

$$\underline{\pi}_E = \frac{1}{3} n_E \text{ (isotropic)} \ ,$$

$$\frac{\partial}{\partial E}\{\ \} = 0 \text{ (noninertial)} \ .$$

For comparison, the current LASNEX charged-particle diffusion model can be characterized by

$$\frac{\partial \vec{J}_1}{\partial t} = 0 \text{ (steady state)} \ ,$$

$$\underline{\pi}_E = D(\omega)\, n_1 \text{ (asymptotic angular distribution)} \ ,$$

and

$$\frac{\partial}{\partial E}\{\ \} \text{ retained (inertial)} \ .$$

To test these modifications, we ran a problem in which 3.5-MeV α particles were emitted from the center of a uniform D-T sphere held at a temperature of 50 keV. Under these conditions the α particles deliver energy to thermal ions only near the end of their range, and thus the deposition to ions as a function of distance from the α source is a critical measure of the α-particle transport. In Fig. 3-68 we compare LASNEX calculations with and without the inertial term to a Monte Carlo calculation of the same problem. We see that the improve-

Fig. 3-68. Charged-particle inertial term produces a peaked deposition profile, in agreement with Monte Carlo calculations.

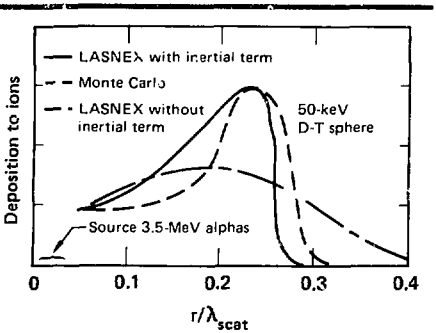

ments made to LASNEX's charged-particle diffusion method have greatly increased its ability to track the accurate Monte Carlo simulation.

Author: G. B. Zimmerman

Reference

158. E. G. Corman, W. E. Loewe, G. E. Cooper, and A. M. Winslow, "Multi-Group Diffusion of Energetic Charged Particles," *Nucl. Fusion* **15**, 377 (1975).

Solving Tridiagonal Linear Systems on the Cray-1 Computer at Vector Speeds

When we examine the numerical algorithms used to solve the physics equations in LASNEX, we find that a large number of subroutines require the solution of tridiagonal linear systems of equations. Radiation transport, thermal- and suprathermal-electron transport, ion thermal conduction, charged-particle and neutron transport, all require the solution of tridiagonal systems of equations. The standard algorithm that has been used in the past on CDC 7600's will not vectorize and so cannot take advantage of the large speed increases possible on the Cray-1 through vectorization. There is, however, an alternate algorithm for solving tridiagonal systems, called cyclic reduction, which allows for vectorization, and which is optimal for the Cray-1. Software based on this algorithm is now being used in LASNEX to solve tridiagonal linear systems in the subroutines mentioned above. The new algorithm runs as much as five times faster than the standard algorithm on the Cray-1.

The Basic Algorithm. Consider a tridiagonal linear system of equations

$$b_{i-1}X_{i-1} + a_iX_i + c_iX_{i+1} = Y_i, \quad i = 1,2,\ldots,n \ , \qquad (142)$$

with $b_0 = c_n = 0$. The standard algorithm for solving these equations is:

$$d_i = (a_i - c_{i-1}c_{i-1})^{-1} \quad \text{for } i = 1,2,\ldots,n \qquad (143)$$

and

$$c_i = b_id_i \quad \text{for } i = 1,2,\ldots,n-1 \ , \qquad (144)$$

followed by

$$W_i = Y_i - c_{i-1}W_{i-1} \quad i = 1,2,\ldots,n \qquad (145)$$

and

$$X_i = d_i(W_i - c_iX_{i+1}), \quad i = n,(n-1),\ldots,3,2,1 \ . \qquad (146)$$

This algorithm is recursive and cannot be vectorized, and therefore will only run about twice as fast on the Cray-1 as it did on the CDC 7600.

But note that the standard scalar algorithm is just LU decomposition.[159] If our original equation is written in matrix notation as MX = Y, with

$$M = \begin{pmatrix} a_1 & c_1 & 0 & 0 \\ b_1 & a_2 & c_2 & 0 \\ 0 & b_2 & a_3 & c_3 \\ 0 & 0 & b_3 & a_4 \end{pmatrix} , \qquad (147)$$

then we may decompose M as a lower-triangular-matrix L with unit diagonal elements and an upper-triangular-matrix U, i.e., M = LU. Here

$$L = \begin{pmatrix} 1 & 0 & 0 & 0 \\ c_1 & 1 & 0 & 0 \\ 0 & c_2 & 1 & 0 \\ 0 & 0 & c_3 & 1 \end{pmatrix} \qquad (148)$$

and

$$U = \begin{pmatrix} d_1^{-1} & c_1 & 0 & 0 \\ 0 & d_2^{-1} & c_2 & 0 \\ 0 & 0 & d_3^{-1} & c_3 \\ 0 & 0 & 0 & d_4^{-1} \end{pmatrix} . \qquad (149)$$

Then we solve LW = Y and UX = W to find X.

To obtain an algorithm which allows some vectorization we reorder the rows and columns of our matrix so that first we take all the odd multiples of 1, then all the odd multiples of 2, then all the odd multiples of 2^2, etc. Thus we apply a permutation P which takes the original ordering, 1,2,3,....,n, into the new ordering

$$1,3,5,7,\ldots,2,6,10,14,\ldots,4,12,20,28,\ldots,8,24,40,56,\ldots,$$
$$2^q,3\cdot2^q,5\cdot2^q,7\cdot2^q,\ldots,2^p \ . \qquad (150)$$

Here p is the highest power of 2 with $2^p \leq n$.

Our original matrix equation now becomes

$$(PMP^{T})(PX) = (PY) \quad . \tag{151}$$

If we perform LU decomposition on this reordered matrix we obtain a new algorithm called cyclic reduction. This algorithm is vectorizable because we are eliminating all the odd variables first (which are not coupled to each other), then all the odd-multiple-of-2 variables (which are not coupled to each other), and so on. Furthermore, the fact that the algorithm is just LU decomposition on a permuted matrix tells us that it is just as stable as the standard scalar algorithm, a virtue not shared by other methods for vectorizing tridiagonal systems such as recursive doubling.

Applying the standard formulas for LU decomposition, and eliminating those terms which are zero because of the particular sparsity pattern of our reordered matrix, we obtain

$$\ell_i^{(0)} = b_i,\ u_i^{(0)} = c_i \text{ and } d_i^{(0)} = a_i,\ i = 1,\ldots,(n-1),n \quad . \tag{152}$$

Then for each $q = 0,1,2,3,\ldots,p$ we take

$$\begin{aligned}
d^q_{(2i-1)} &= 1/\tilde{d}^q_{(2i-1)}, && 1 \le 2i-1 \le r(q,n) \quad , \\
\ell^q_{(2i-1)} &= \tilde{\ell}^q_{(2i-1)} d^q_{(2i-1)}, && 1 \le 2i-1 \le r(q,n) \quad , \\
\ell^q_{(2i)} &= \tilde{\ell}^q_{(2i)}, && 2 \le 2i \le r(q,n) \quad , \\
u^q_{(2i-1)} &= \tilde{u}^q_{(2i-1)}, && 1 \le 2i-1 \le r(q,n) \quad .
\end{aligned}$$

where $r(q,n)$ is the largest integer, r, such that $r \cdot 2^q \le n$.

For the solve, we let

$$\begin{aligned}
u^q_{(2i)} &= \tilde{u}^q_{(2i)} d^q_{(2i-1)}, && 2 \le 2i < r(q,n) \quad , \\
\tilde{d}^{q+1}_i &= \tilde{d}^q_{2i}\ \ell^q_{(2i-1)} u^q_{(2i-1)} - \ell^q_{(2i)} u^q_{(2i)}, \\
& && 1 \le i \le r(q+1,n) \quad , \\
\tilde{\ell}^{(q+1)}_i &= -k^q_{2i} \ell^q_{(2i-1)}, && 1 \le i < r(q+1,n) \quad , \\
\tilde{u}^{(q+1)}_j &= -u^q_{2i} u^q_{(2i+1)}, && 1 \le i < r(q+1,n) \\
& && r \cdot 2^q \le n \quad . \\
W^0_i &= Y_i, && i = 1,2,\ldots,n \quad .
\end{aligned} \tag{153}$$

Then for each $q = 0,1,2,\ldots,(p-1)$ we take

$$W^{(q+1)}_i = W^q_{(2i)} - \ell^q_{(2i-1)} W^q_{(2i-1)} - u^q_{(2i)} W^q_{(2i+1)}$$

$$\text{for } i = 1,2,\ldots,r(q+1,n) \quad . \tag{154}$$

We set $X^p_1 = d^p_1 w^p_1$, and then for each $q = (p-1), (p-2),\ldots,4,3,2,1,0$ we take

$$X^q_{(2i)} = X^{(q+1)}_i, \quad 2 \le 2i \le r(q,n) \tag{155}$$

and

$$X^q_{(2i-1)} = d^q_{(2i-1)} \left[W^q_{(2i-1)} - \ell^q_{(2i-2)} X^q_{(2i-2)} - u^q_{(2i-1)} X^q_{(2i)} \right], \quad 1 \le 2i-1 \le r(q,n) \quad . \tag{156}$$

Finally, $X_i = X^0_i$, for $i = 1,\ldots,n$.

Clearly all the above operations at the q level of reduction are vectorizable with vector length $r(q+1, n)$. Thus we now have a vectorizable algorithm with vectorization on lengths $n/2$, $n/4$, $n/8,\ldots,1$.

Implementation on the Cray-1. The numbers $r(q,n)$ are easily calculated from $r(0,n) = n$ and

$$r(q+1,n) = SHIFTR(r(q,n),1) \quad . \tag{157}$$

where $SHIFTR(n_1,n_2)$ is n_1 (in binary notation) shifted right n_2 positions with the rightmost n_2 bits of n_1 lost off the end.

It is important to give consideration to storage layout and possible memory bank conflicts. Consider for example the forward sweep of the solve. The "natural" storage layout is to store $W^{(q+1)}_i$ in the $[i \cdot 2^{(q+1)}]$ element of the Y array and just keep overwriting $W^q_{(2i)}$ with $W^{(q+1)}_i$. The problem with this is that vector reads from and writes to memory in increments of 2^q on the Cray-1 cause bank conflicts and loss of speed if $q > 2$. For $q = 0,1,2$ we can read or write one word per clock period. For $q = 3$ this degrades to one word every two clock periods and for $q \ge 4$ the performance degrades to one word every four clock periods. To eliminate this problem we use the following storage scheme.

$W^0_i = Y_i$ is stored in the first $n = r(0,n)$ elements of the Y array. W^1_i is stored in the next $r(1,n)$ elements of the Y array, and so on. Thus

$$W^q_i = Y_{[s(q,n)+i]} \quad , \tag{158}$$

where $s(0,n) = 0$ and $s(q+1, n) = s(q,n) + r(q,n)$. X^q_i is stored in the same locations as W^q_i. The matrix elements ℓ^q_i and $\tilde{\ell}^q_i$ are stored in $b_{[s(q,n)+i]}$, u^q_i and $\tilde{u}^q_i$ are stored in $c_{[s(q,n)+i]}$, d^q_i and $\tilde{d}^q_i$ are stored in

Fig. 3-69. Ratio of scalar to vector execution times for the solution of a tridiagonal matrix of length N. For both symmetric (a) and asymmetric (b) matrices, the asymptotic rate of the vector cyclic reduction algorithm is more than six times the scalar rate, but this speedup can be achieved only with relatively long vectors.

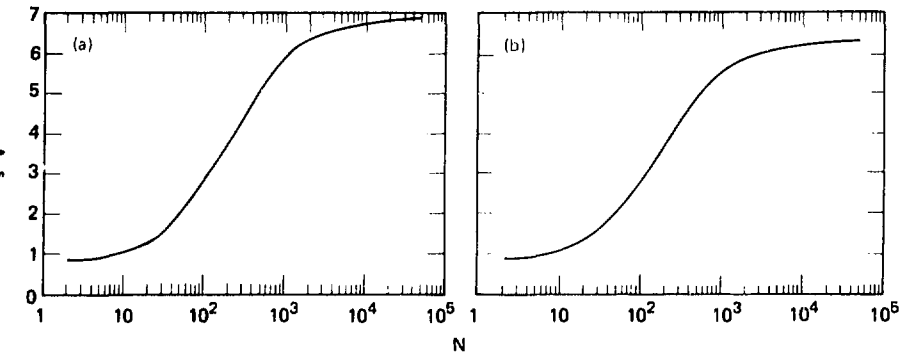

$a[s(q,n) + 1]$. With this storage scheme all memory reads and writes are done in increments of 1 and 2, and all bank conflicts are eliminated. Since

$$\sum_{q=0}^{p} r(q,n) < \sum_{q=0}^{p} (n/2^q) < 2n \ , \qquad (159)$$

the arrays a,b,c, and y must now be 2n elements long instead of n elements long, and so we need twice as much storage as is required for the standard scalar algorithm.

Performance. This algorithm was hand-coded for the Cray-1 by R. E. von Holdt for both the symmetric and nonsymmetric matrix cases. In Fig. 3-69 the hand-coded vector cyclic reduction algorithm is compared with the Cray-1 FORTRAN CFT-compiled standard scalar algorithm. N is the problem dimension and (t_s/t_v) is the relative execution time of the scalar and vector algorithms. The cyclic reduction algorithm was also coded with CFT and it was asymptotically about 4.5 times faster than the CFT scalar algorithm; thus the hand coding made only a 50% improvement over CFT.

Author: D. S. Kershaw

Reference

159. For a good discussion of LU decomposition see J. H. Wilkinson, *The Algebraic Eigenvalue Problem* (Oxford University Press, Oxford, 1965) chap. 4, sec. 36.

A Vectorizable Incomplete Cholesky-Conjugate Gradient (ICCG) Algorithm for the Cray-1 Computer

In LASNEX, the two-dimensional radiation transport, electron thermal conduction, ion thermal conduction and neutron transport all use ICCG to solve the transport equations. We have been using the ICCG method[160] to solve the diffusion equation with a nine-point coupling[161] scheme on the CDC 7600. In going from the CDC 7600 to the Cray-1, a large part of the algorithm consists of solving tridiagonal linear systems on each L line of the Lagrangian mesh in a manner which is not vectorizable. Therefore a direct translation from the 7600 to the Cray would not give much increase in running speed because the vectorization potential of the Cray cannot be used. We have developed an alternate ICCG algorithm for the Cray-1 which utilizes the vector tridiagonal solver described in the previous article. This new algorithm allows full vectorization and runs as much as seven times faster than the old algorithm on the Cray-1. It is now being used in Cray LASNEX to solve the two-dimensional diffusion equation in all the physics subroutines mentioned above.

Thus we have an equation, MX = Y, where M is positive definite and symmetric, and the sparsity

pattern is such that M_{kk}, $M_{k(i\pm1)}$, $M_{k(i\pm KMAX)}$, $M_{k(i\pm KMAX\pm1)}$ are the only nonzero elements.

The ICCG method consists in finding an approximate Cholesky decomposition for $M \approx LDL^T$, and then using the conjugate gradient algorithm. Let $r_0 = Y - MX_0$ and $p_0 = (LDL^T)^{-1}r_0$, then

$$a_i = \left[r_i(LDL^T)^{-1}r_i\right]/(p_i,Mp_i) ,$$

$$X_{(i+1)} = X_i + a_ip_i ,$$

$$r_{(i+1)} = r_i - a_iMp_i ,$$

$$b_i = \left[r_{(i+1)}(LDL^T)^{-1}r_{(i+1)}\right]/\left[r_i(LDL^T)^{-1}r_i\right] ,$$

$$p_{(i+1)} = (LDL^T)^{-1}r_{(i+1)} + b_ip_i ,$$

for i = 0,1,2,...

This algorithm is all trivially vectorizable except for the evaluation of the approximate inverse on the residual, $(LDL^T)^{-1}r_i$. With the choice for the approximate Cholesky decomposition given in Ref. 160 this is a recursive operation which can only go at scalar speeds on the Cray-1. To vectorize it we must use a different approximate decomposition which allows for vectorization.

To see how this is done we first write the exact Cholesky decomposition in block form, in which our matrix M can be written

$$M = \begin{pmatrix} A_1 & B_1 & 0 & 0 & \\ B_1^T & A_2 & B_2 & 0 & \\ 0 & B_2^T & A_3 & B_3 & \ddots \\ 0 & 0 & B_3^T & A_4 & \ddots \\ & & & \ddots & \ddots \end{pmatrix} ,$$

where the A_i and B_i are tridiagonal matrices of dimension KMAX, and i = 1,2,3,....LMAX. The Cholesky decomposition may now be written in block form, $M = LDL^T$, where

$$L = \begin{pmatrix} L_1 & 0 & 0 & 0 & \\ C_1^T & L_2 & 0 & 0 & \\ 0 & C_2^T & L_3 & 0 & \\ 0 & 0 & C_3^T & L_4 & \ddots \\ & & & \ddots & \ddots \end{pmatrix}$$

and

$$D = \begin{pmatrix} D_1 & 0 & 0 & 0 & \\ 0 & D_2 & 0 & 0 & \\ 0 & 0 & D_3 & 0 & \\ 0 & 0 & 0 & D_4 & \ddots \\ & & & \ddots & \ddots \end{pmatrix} .$$

Here the L_i are lower triangular matrices whose diagonal elements are all 1, the D_i are diagonal matrices, and L_i, C_i, D_i are given recursively by

$$C_i = D_{i-1}^{-1}L_{i-1}^{-1}B_i \qquad (160)$$

and

$$L_iD_iL_i^T = A_i - C_{(i-1)}^T D_{(i-1)} C_{(i-1)} = \tilde{A}_i \qquad (161)$$

for i = 1,2,3,....LMAX.

If we write the unknown and right-hand-side vectors in block form,

$$X = \begin{pmatrix} X_1 \\ X_2 \\ X_3 \\ . \\ . \\ . \end{pmatrix} , \quad Y = \begin{pmatrix} Y_1 \\ Y_2 \\ Y_3 \\ . \\ . \\ . \end{pmatrix} ,$$

where X_i,Y_i are vectors of length KMAX, then $LDL^TX = Y$ may be solved by a forward sweep,

$$W_i = L_i^{-1}\left[Y_i - B_{(i-1)}^T L_{(i-1)}^{-T} D_{(i-1)}^{-1} W_{(i-1)}\right] , \qquad (162)$$

for i = 1,2,3,....LMAX, and a backward sweep,

$$X_i = L_i^{-T} D_i^{-1}\left[W_i - L_i^{-1}B_iX_{(i+1)}\right] , \qquad (163)$$

for i = LMAX,(LMAX-1),....,3,2,1.

Now let us examine the sparsity pattern of the L_i and C_i for the case of exact Cholesky decomposition. A_1 is tridiagonal so L_1 will be lower tridiagonal. Since B_1 is tridiagonal, Eq. (160) implies that $C_{(i,j)}$ will be nonzero for $j \leq i + 1$ and zero for $j > i + 1$. Equation (161) thus implies that A_2 is a dense matrix (all elements nonzero) and so

L_2 is dense lower triangular. Thus in general we find

$$L_{i(j,k)} = \begin{cases} 0, & k > j \\ \text{nonzero}, & k \leq j \end{cases},$$

and

$$C_{i(j,k)} = \begin{cases} 0, & k > j+1 \\ \text{nonzero}, & k \leq j+1 \end{cases}.$$

Thus we have extensive fill-in; that is, many elements which were zero in A_i and B_i become nonzero in L_i and C_i. This greatly increases both storage requirements and the amount of computation.

We seek an approximate LDL^T decomposition which has no fill-in. To accomplish this, in Eq. (160) we throw away (i.e., neither compute nor store) all but the tridiagonal part of C_i. Then in Eq. (161) we throw away all but the tridiagonal part of $C_{(i-1)}^T D_{(i-1)} C_{(i-1)}$, thus making $\tilde{A}_i$ and L_i tridiagonal. We thus obtain an incomplete block decomposition, $M \approx LDL^T$, where L_i and C_i have the *same sparsity* pattern as A_i and B_i. Note that the solve [Eqs. (162) and (163)] does not use C_i explicitly, and so the C_i need not be saved once the $\tilde{A}_{(i+1)}$ have been calculated. Only the L_i and D_i need be stored. Now we have reduced our incomplete decomposition and solve to a series of tridiagonal decompositions and solves.

In the previous article we have shown how to vectorize tridiagonal decompositions and solves on the Cray-1 using cyclic reduction. Here we simply apply this algorithm to the incomplete version of Eqs. (160) through (163) and we have a fully vectorizable ICCG algorithm.

In detail the algorithm is as follows:

- If KMAX < LMAX we transpose our grid (interchange KMAX and LMAX) so that LMAX becomes the inner loop and KMAX the outer loop. Thus our block matrices will have the largest possible dimension and our vector tridiagonal solves will vectorize as well as possible.
- The incompleteness of the decomposition is accomplished in Eq. (160) by performing only the first two levels of cyclic reduction in evaluating $E_i = D_i C_i = L_i^{-1} B_i$, and ignoring elements outside the tridiagonal band. All higher levels of reduction couple only elements inside the tridiagonal band with (zero) elements outside the band and so have no effect. If we use the notation of the previous article for the L_i and D_i matrices and suppress the block subscript "i" for clarity, we then have explicitly:

$$\left.\begin{aligned} E_{j,(j-1)} &= B_{j,(j-1)} \\ E_{j,j} &= B_{j,j} \\ E_{j,(j+1)} &= B_{j,(j+1)} \end{aligned}\right\}$$

for all odd j, $1 \leq j \leq KMAX$,

$$L_{j,j} = B_{j,j} - L_{(j-1)}^{(0)} B_{(j-1),j} - L_j^{(0)} B_{(j+1),j},$$

for all even j, $2 \leq j \leq KMAX$,

$$\begin{aligned} L_{j,(j-1)} &= B_{j,(j-1)} - L_{(j-1)}^{(0)} B_{(j-1),(j-1)}, \\ L_{j,(j+1)} &= B_{j,(j+1)} - L_j^{(0)} B_{(j+1),(j+1)}, \end{aligned}$$

for all $j = 2k$ with k odd, $2 \leq j \leq KMAX$, and

$$\begin{aligned} L_{j,(j-1)} &= B_{j,(j-1)} - L_{(j-1)}^{(0)} B_{(j-1),(j-1)} \\ &\quad - L_{(j/2-1)}^{(1)} L_{(j-2),(j-1)}, \\ L_{j,(j+1)} &= B_{j,(j+1)} - L_j^{(0)} B_{(j+1),(j+1)} \\ &\quad - L_{(j/2)}^{(1)} L_{(j+2),(j+1)}, \end{aligned}$$

for all $j = 2k$ with k even, $2 \leq j \leq KMAX$.

To specify Eq. (160) in detail we let $\delta_j = d_k^{(l)}$, where $j = k \cdot 2^l$ with k odd. Then

$$\begin{aligned} \tilde{A}_{jj} &= A_{jj} - \delta_j (L_{j,(j-1)})^2 - \delta_{(j-1)} (L_{(j-1),j})^2 \\ &\quad - \delta_{(j+1)} (L_{j,(j+1)})^2, \\ \tilde{A}_{j,(j-1)} &= A_{j,(j-1)} - \delta_j L_{j,(j-1)} \\ &\quad - \delta_{(j-1)} L_{(j-1),(j-1)} L_{(j-1),j}. \end{aligned}$$

for $j = 1,\ldots,KMAX$, and since A is symmetric, $\tilde{A}_{(j-1),j} = \tilde{A}_{j,(j-1)}$. Once we have determined $\tilde{A}_i$, we simply use cyclic reduction decomposition to solve $L_i D_i L_i^T = \tilde{A}_i$ for L_i and D_i.

We must make one modification of the decomposition algorithm given in the previous article. A negative pivot would destroy the positive definiteness of our approximate identity, $(LDL^T)^{-1} M \approx I$, so we must modify any negative pivot to a positive

value. We do this by changing $d^q_{(2i-1)} = 1/\bar{d}^q_{(2i-1)}$ for $1 \leq (2i-1) \leq r(q,n)$, from the previous article, to $d^q_{(2i-1)} = 1/|\bar{d}^q_{(2i-1)}|$.

- We now solve for X using Eqs. (160) and (161). If Z is any vector (of length KMAX), then $B_i Z$ and $B_i^T Z$ are trivially vectorizable and $L_i^{-1} Z$ and $L_i^{-T} D_i^{-1} Z$ are the forward sweep and the backward sweep of the cyclic reduction solve as described in the previous article.

We now have a completely vectorizable algorithm for finding an approximate Cholesky decomposition, $LDL^T \approx M$, of our matrix and for calculating, $(LDL^T)^{-1} r$, the approximate inverse applied to the residual. Thus we have completely vectorized the ICCG algorithm.

The new vector algorithm has been implemented on the Cray-1 using Cray-1 FORTRAN and is about 10 to 15 times faster than the standard ICCG algorithm coded in FORTRAN on the CDC 7600.

Author: D. S. Kershaw

References

160. D. S. Kershaw, "The ICCG Method for the Iterative Solution of Systems of Linear Equations," *J. Comp. Phys.* **26**, 43 (1978).

161. D. S. Kershaw, *Differencing of the Diffusion Equation in Lagrangian Hydrodynamics Codes*, Lawrence Livermore Laboratory, Livermore, Calif., UCRL-82747 (1980), to appear in *J. Comp. Phys.*

Hot-Electron Momentum Deposition in LASNEX

Theory and simulations of resonant absorption have been described in past annual reports and in the literature.[162-164] Briefly, resonant absorption is the direct conversion of the transverse laser light to longitudinal electron-plasma waves (epw) at the critical density [10^{21} (1.06 $\mu m/\lambda_0)^2$ cm^{-3}]. The oscillating longitudinal electric field of the epw heats the electrons by accelerating them down the density gradient to a temperature of approximately 21 $T_e(keV)^{0.25}$ [$I(W/cm^2)/10^{16}(\lambda_0/1.06\ \mu m^2)]^{0.4}$. The momentum of the accelerated electrons acts with the ponderomotive pressure of the transverse and longitudinal electric field to steepen up the density gradient at critical. The consequences of this steepening are:

- Resonant absorption becomes accessible to a wide range of angles[162,163] (LASNEX users can use an absorption-vs-angle mode).
- The ($T_{Hot} n_{Hot}$) helps to push back critical density, n_c, which helps to explain why gold disk experiments have a red shift in the backscattered light.[165]
- The ∇ steepening affects inverse bremsstrahlung absorption.
- Brillouin scattering.

LASNEX models resonant absorption in a very simple way. A user-defined fraction, 1 - XLRFLFR, of the laser energy reaching or exceeding a given density, XLTHRESO*n_c, is deposited at the ray turning point. The energy dumped is deposited in the electron bins (if they are present) at a temperature specified (XLALPHA) or determined by a semi-empirical formula (LTHOT). LASNEX has no knowledge of the resonant field nor of the directed motion of the heated electrons.

The momentum imparted by the resonant electrons may be calculated by energy flux conservation. Therefore the force exerted by the hot electrons at n_c can be included in the "dump-all" (resonance absorption) model in LASNEX. A calculation of the time rate of change of momentum due to the hot electrons created by resonance absorption is given below with an equation appropriate for inclusion in LASNEX.

This model assumes that all of the laser energy deposited by resonance absorption is transferred to the hot electrons which are ejected from n_c and stream down the density gradient. Thus, the conservation of energy density flux gives

$$f\left(\frac{\underline{E}\times\underline{B}}{8\pi}\right)_c = \frac{m_e n_{Hot}}{\sqrt{\pi} v_{Hot}} \int_0^\infty dv \left(\frac{1}{2}\right) v^3 \exp\left(-\frac{v^2}{v_{Hot}^2}\right), \quad (164)$$

which may be solved for n_{Hot}, the number density of hot electrons. In this equation, $\underline{E}$ and $\underline{B}$ are the laser field quantities, f is the fraction absorbed by resonance absorption, m_e is the election mass and $v_{Hot} = (2T_{Hot}/m_e)^{1/2}$ is the thermal velocity of the hot electrons. Equation (164) gives

$$\frac{n_{Hot}}{n_c} = \left(\frac{\pi}{2}\right)^{1/2} f \left(\frac{v_0}{c}\right)^2 \left(\frac{m_e c^2}{T_{Hot}}\right)^{3/2}, \qquad (165)$$

where c is the speed of light and v_0 is the peak oscillation velocity of electrons in the laser electric field. The total flux of hot-electron momentum flowing down the density gradient is then

$$G = \frac{n_{Hot}}{\sqrt{\pi} v_{Hot}} \int_0^\infty dv\, m_e v^2 \exp\left(-\frac{v^2}{v_{Hot}^2}\right). \qquad (166)$$

Combining Eqs. (165) and (166), one finds

$$G = \frac{\sqrt{\pi} f I}{v_{Hot}}. \qquad (167)$$

Thus the force due to the hot electrons is the rate of change of momentum as the hot electrons are created at n_c and flow away down the density gradient. So, for a zone of cross section A,

$$F_{Hot} = \frac{\sqrt{\pi} f I A}{v_{Hot}}, \qquad (168)$$

or, in LASNEX units,

$$F_{Hot} = 0.095 \frac{f I A}{\sqrt{T_{Hot}(keV)}}, \qquad (169)$$

where F_{Hot} is directed up the density gradient. In deriving Eq. (167) we have used

$$\left(\frac{v_0}{c}\right)^2 = \left(\frac{2I}{c}\right)\left(\frac{1}{m_e c^2 n_c}\right) = 0.082\left[I(\text{jerks/sh/cm}^2)(\lambda_0/1.06\ \mu\text{m})^2\right], \qquad (170)$$

where I is the light intensity with vacuum wavelength λ_0.

Including Eq. (169) in LASNEX will improve the resonance absorption model. LASNEX does not know, however, that the hot electrons are all moving down the density gradient, so that the total problem momentum will not be conserved. But the local affect near critical density should be correct.

The importance of the hot-electron force may be estimated by comparing it with the ponderomotive force. The ratio of the two forces is

$$\frac{F_{Hot}}{F_{Pon}} = 28.4 \frac{f}{2 - f} \frac{1}{\sqrt{T_{Hot}(keV)}}, \qquad (171)$$

so for a plasma with f = 0.3 and T_{Hot} = 25 keV, the two forces are equal; whereas for a lower T_{Hot} = 3 keV, F_{Hot} is almost three times F_{Pon} (T_{Hot} is also discussed in "Resonant Absorption" earlier in this section).

Authors: K. G. Estabrook and J. A. Harte

References

162. K. G. Estabrook, E. J. Valeo, and W. L. Kruer "Plasma Heating and Gradient Modifications by Resonant Absorption," *Phys. Lett. A* **49**, 109 (1974).

163. K. G. Estabrook, E. J. Valeo, and W. L. Kruer, "Two Dimensional Relativistic Simulations of Resonance Absorption," *Phys. Fluids* **18**, 1151 (1975).

164. D. W. Forslund, J. M. Kindel, and K. Lee, "Theory of Hot-Electron Spectra at High Laser Intensity," *Phys. Rev. Lett.* **39**, 284 (1977).

165. M. D. Rosen, D. W. Phillion, V. C. Rupert, W. C. Mead, W. L. Kruer, J. J. Thomson, H. N. Kornblum, V. W. Slivinsky, G. J. Caporaso, M. J. Boyle, and K. G. Tirsell, "The Interaction of 1.06 μm Laser Radiation With High Z Disk Targets," *Phys. Fluids* **22**, 2020 (1979).

Target Fabrication

Target Fabrication

4

Contents

Target Fabrication

4

Introduction

Our primary task in target fabrication continues to be the development and application of techniques for producing and characterizing targets used in current experiments. In addition, we must carry out the research and development that will make it possible to produce the advanced targets required for future ICF studies.

The complexity of the targets, the diversity of materials used, and the variety of characterization methods required in our work all require expertise in a large number of technical fields. Materials science, plasma physics, optics, electron microscopy, analytical chemistry, and cryogenics are only a few of the scientific fields in which the staff must be proficient in order to solve the problems of target fabrication.

The past year has seen several particularly noteworthy achievements in the area of target fabrication:

- The yield of target-quality glass shells from the high-temperature furnaces has increased to 99% in some batches.
- Special diagnostic gases have been put into the glass shells during their formation.
- High-Z glass shells have been developed; these include lead glass (~50% lead oxide) and tantalum glass (~50% tantalum oxide).
- Target-quality coatings of hydrocarbon (CH) polymers more than 100 μm thick have been deposited on glass shells.
- Layers of beryllium, platinum, and other metals have been applied to glass shells.
- By using modern highly sophisticated micromachining techniques, we have produced hemishells of CH polymers with microinch surface finishes (on the order of 250 Å).
- A powder or "sand" of frozen hydrogen spheres (80 μm diameter) has been produced as a potential method of filling cryogenic fusion targets to high densities.
- We have assembled multiple shell targets that have exceptionally good geometrical tolerances. (In Fig. 4-1, the components of a double-shell target oriented for assembly are shown suspended from a human hair.)

Detailed descriptions of these and many other advances in target fabrication are included in subsequent articles.

As target designs change and become more complex, both materials research and the development of characteriza-

tion and assembly techniques must provide the means for producing these advanced targets. Creative, highly competent, and hardworking scientists, engineers, and technical support personnel will continue to be needed to achieve our goals.

The continued support of "outside" contractors will also be a necessary and highly valued part of our program. The contributions of such organizations as the Rockwell International Rocky Flats Plant, the University of Illinois Charged Particle Research Laboratory, and the National Bureau of Standards Laboratory at Boulder have been invaluable to the success of the target fabrication effort.

Author: C. D. Hendricks

Glass Sphere Development and Production

During the past year we continued both to meet the needs of the Laser Fusion Program for quality glass microspheres and to improve and extend the scope of our techniques. Our fabrication processes are now refined to the point where we can tune our droplet system to produce microspheres with the desired diameters and wall thicknesses. Our dried-gel capabilities are enhanced by density- and diameter-sieve-cutting the resultant microspheres to narrow the mass distribution. We showed that filling the microspheres during fabrication with such highly reactive gases as bromine is feasible. We used our droplet systems to make lead oxide microspheres; we also began developing tantalum glass spheres using the dried-gel technique. In addition, we initiated a study of sol-gel and pelletizing techniques as possible improvements to our dried-gel processes. Finally, based on studies of the working strengths and permeability of the glass microspheres, we developed improved techniques for filling the spheres with D-T. These advances are discussed in more detail in the articles that follow.

Sphere Fabrication Processes

We have continued to refine our understanding of the liquid-droplet process.[1] In this process, we use acoustic disintegration of a liquid jet to produce uniform drops of an aqueous solution of glass-forming compounds. The size of the liquid drop is affected by the solids content in the glass-forming solution, the feed pressure of the solution, the orifice size, and the acoustic driving frequency. The uniformity of the drops is evidence that the resultant microspheres all have the same mass. In the past, we obtained batches of spheres with uniform wall thickness by sieve-cutting over a narrow diameter range.

We now obtain directly from the furnace narrow-diameter distributions tunable to the desired sphere sizes. This advance is directly attributable to our understanding of the interplay among the size of the droplet, the temperature profile of the drying region, and the flow rate of the furnace air. A key aid to this understanding is our use of a fast and accurate device for measuring sphere diameters that enabled us to develop an exhaustive statistical model of the liquid droplet process. A diameter distribution of a batch from a furnace tuned to produce 140-μm-diam spheres appears in Fig. 4-2(a). The spheres continue to have narrow thickness distributions as well as excellent concentricity [see Fig. 4-2(b)]. The capability of tuning the diameter of the sphere has greatly enhanced our yield, so that only a couple of hours of running time are needed to produce a batch large enough to be processed through the fill and coating stages of target fabrication.

We also produce microspheres by using a dried-gel process.[1] Although more flexible in terms of available sizes, the dried-gel process has the disadvantage that the microspheres produced have a broad range of wall thicknesses, which means that simple diameter-sieving will not result in a batch with a narrow wall-thickness distribution.

To narrow the wall-thickness distribution, we developed a density-sieve-cutting procedure to use in conjunction with diameter-sieve cuts. For spheres with densities between 0.6 and 1.5 g/cm^3 we successively sink and float the spheres in liquids such as pentane and chloroform to separate the desired wall

Fig. 4-2. Droplet production: (a) diameter distribution of droplet batch and (b) interference picture of spheres showing excellent concentricity and narrow-thickness distribution.

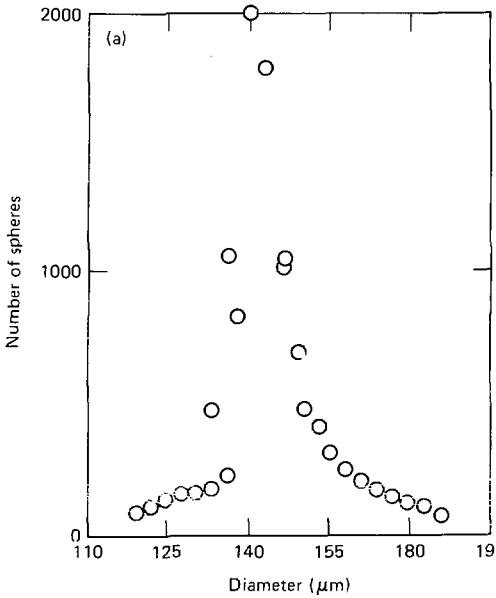

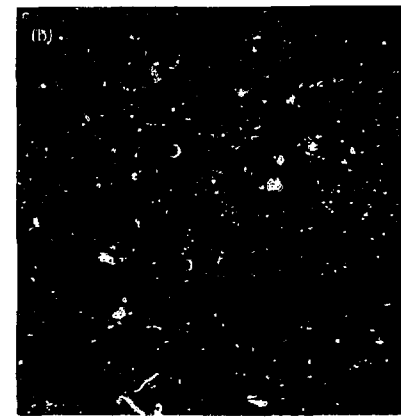

90% of the spheres have the same diameter within ±10%

thicknesses for given diameter ranges. An example of a resulting dried-gel batch is shown in Fig. 4-3.

Such batches obtained from the dried-gel process can be useful for coating. By combining spheres produced by the liquid-droplet and dried-gel techniques, we can tailor the thickness distribution of spheres in a coating batch such as shown in Fig. 4-4. This gives us the flexibility to match target fabrication resources to the target requirements. Consider the request for a 100 μm i.d. × 10 μm glass sphere coated with 100 μm of CH. Although calculations indicate that 10 μm is the optimum glass thickness, there is a reasonable likelihood that spheres between 5 and 20 μm thick will also be desired. Rather than coating batches with a variety of narrow thickness distributions (which would take months if done sequentially), it is more efficient to coat microspheres having the tailored distribution shown in Fig. 4-4. The spike guarantees a reasonable probability of obtaining 10-μm spheres and the broad background covers the range of other potentially useful sizes.

Although a few more days of sorting time is required to separate the spheres after coating, it is well

Fig. 4-3. Broad-thickness-distribution batch for coating spheres approximately 100 μm in diameter with thicknesses ranging from 6 to 17 μm. This batch was obtained by both density- and diameter-sieve cutting a batch that was produced by the dried-gel method and that initially had a much broader distribution. Note the excellent concentricity.

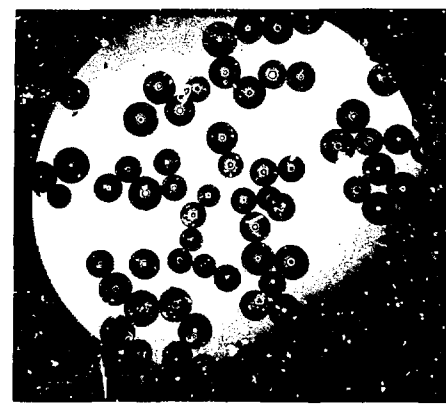

Fig. 4-4. Tailored thickness distribution of spheres for efficient coating with hydrocarbon polymer.

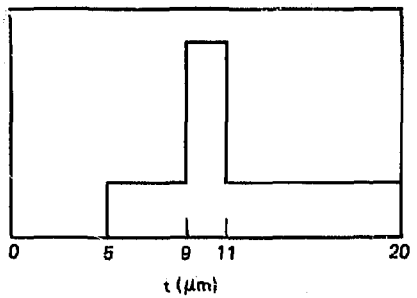

worth the effort in view of the time that would otherwise be spent making and coating separate batches of spheres. When target requirements are more well-defined, as in the past with 140-μm × 5-μm spheres, we can use just the narrow distribution batch produced by the liquid-droplet process.

Authors: R. L. Woerner and V. F. Draper
Major Contributors: J. E. Andrews, M. H. Corzette, W. E. Elsholz, G. A. Gleeson, C. L. McCaffrey, R. J. Moore, and S. L. Weinland

Reference

1. *Laser Program Annual Report—1978*, Lawrence Livermore Laboratory, Livermore, Calif., UCRL-50021-78 (1979), pp. 4-2 to 4-7.

Diagnostic Gas Fills

Adding special gases to the D-T fuel in fusion targets provides the capability of making measurements to determine the D-T fuel density attained during implosions.[2] At present, imaging and broadening of the x-ray lines emitted by argon seed gas is used. However, this technique is limited to relatively thin-walled targets because of the attenuation of the x-ray lines.

For the thicker-wall targets (i.e., ablative targets), we would like to extend the neutron-activation techniques[3] used on the glass pusher to find the ρR of a diagnostic seed gas; ^{79}Br has been proposed as the best choice for a gas from the standpoint of diagnostics.

Although we routinely use simple permeation to fill glass spheres with D-T, this method is not practical for the desirable diagnostic gases. By introducing argon into the furnace atmosphere, we have been able to trap up to 0.2 atmospheres (at room temperature) of argon in the microspheres during the fabrication process.[4] Bromine is highly reactive and therefore much more difficult to handle. During the latter part of 1979, we began a series of experiments to determine the feasibility of adding bromine to the internal atmosphere of the microspheres.

Using a dried-gel system, we produced glass microspheres with up to 0.31 atmospheres of bromine trapped inside. The bromine is probably present as HBr and Br_2. The small experimental furnace used for this experiment is capable of producing target-quality spheres 70 to 300 μm in diameter with wells 1.5 to 3 μm thick on a selection basis (i.e., by sorting through batches to find acceptable spheres). A major effort is still required to adapt this process to a liquid-droplet system for producing batches of acceptable spheres.

In our experiment, we used two furnaces, one located above the other. The upper furnace was operated at 1440°C and produced the spheres in a static air atmosphere. Below the upper furnace, separated by a cooled 12-in. zone, is a second furnace containing a bromine atmosphere. This furnace is operated at 1200°C. The 12-in. cooled zone prevents the bromine from rising to the upper furnace. If too much bromine is present in the upper furnace the glass material and bromine react violently, preventing glass spheres from forming. However, if the spheres are first produced and then immediately passed through a bromine atmosphere, the bromine does not react with the glass but appears simply to permeate through it.

Authors: R. L. Morrison and R. L. Woerner

References

2. J. T. Larsen, V. W. Slivinsky, S. M. Lane, and N. M. Ceglio, *Diagnosis of Laser Produced Implosions Using Argon X-Ray Lines*, Lawrence Livermore Laboratory, Livermore, Calif., UCRL-83313 (1979).
3. E. M. Campbell, S. M. Lane, Y. L. Pan, J. T. Larsen, R. J. Wahl, and R. H. Price, *Determination of Fuel ρR of ICF Targets by Neutron Activation*, Lawrence Livermore Laboratory, Livermore, Calif., UCRL-83073 (1979).
4. J. C. Koo, J. L. Dressler, and C. D. Hendricks, *Low Pressure Gas Filling of Laser Fusion Microspheres*, Lawrence Livermore Laboratory, Livermore, Calif., UCRL-81417-1 (1979).

High-Z Glass Spheres

We have continued development of lead-glass spheres, which we began last year using the dried-gel process.[5] By extending the process to the liquid-droplet system, we produced several batches of thin-walled, lead-glass microspheres that contain about 30 mole % of lead oxide. Since these microspheres were produced at an oven temperature below the critical evaporation temperature of lead oxide in the glass, the percentage of lead oxide in these microspheres is uniform and approximately equal to the oxide percentage in the aqueous solution. This was verified by secondary x-ray emission data together with index-of-refraction measurements. At 300°C the characteristic D-T fill time for these spheres was several hundred hours.

In an attempt to decrease the fill time constant and aid permeation studies, we reduced the lead content. Spheres with diameters of ~150 μm and walls 0.5 μm thick and containing 25 mole % lead were filled at 400°C. The measured permeability indicates that similar composition spheres 100 μm in diameter and 10 μm thick would take approximately 100 hours to fill. The concentricity of the thin, 25 mole % spheres needs to be improved.

We also produced lead-oxide glass spheres with reasonably thick walls (5 to 13 μm). Some spheres were concentric, but problems remain in controlling the geometry and composition of the spheres.

The wash used for the alkali-silicate glasses[6] is unsuitable for our high-Pb content glasses because of excessive surface deterioration. All the Pb-glass spheres washed with this technique showed some degree of cracking with subsequent uniform stripping of the surface.

We found that hydrogen peroxide was the best wash solution of those we examined. At all ranges of temperature and concentration, the surface appearance was enhanced, and we obtained the quality shown in Fig. 4-5. (An ethanol rinse follows the H_2O_2 wash in all cases.)

Additionally, we have developed a very promising new tantalum glass that may well provide all the characteristics required of high-Z glasses. We have blown a glass containing 50 wt% tantalum into good quality microspheres by the dried-gel production method.

The dried gel is produced by using organometallic compounds in an ethanol solution. The gel forms very rapidly and can dry overnight because of the high volatility of the alcohol. The spheres produced from this gel show good surface characteristics and can be filled with D-T by presently used methods. We have also demonstrated good concentricity in these spheres.

Fig. 4-5. Typical Pb-glass microsphere surface after H_2O_2 wash.

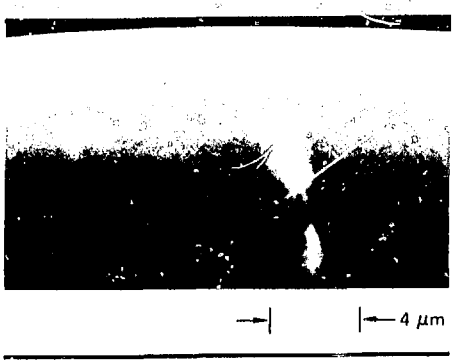

Further experiments with this glass will be devoted to controlling the diameter and wall thickness. If we can achieve this control, tantalum glass will very likely replace lead glass in satisfying our high-Z glass requirements. In future experiments, we will develop production of tantalum glass by the liquid-droplet technique. This method of production is important because it permits us to manufacture batches of very narrow diameter and wall-thickness distribution.

Authors: R. L. Morrison and R. L. Woerner
Major Contributors: J. C. Koo and J. E. Andrews

References

5. *Laser Program Annual Report—1978*, Lawrence Livermore Laboratory, Livermore, Calif., UCRL-50021-78 (1979), p. 4-5.
6. *Laser Program Annual Report—1977*, Lawrence Livermore Laboratory, Livermore, Calif., UCRL-50021-77 (1978), pp. 5-13 to 5-16.

D-T Fill Techniques

During attempts to fill glass microspheres for both the low-density thermonuclear-burn Shiva targets and the argon-diagnosed intermediate-density experiments, a high proportion of the desired thin spheres broke. We reviewed the

available data from past fills and precrush studies to determine whether the breakage could be correlated with the expected mechanical properties of the glass spheres. It appears that the spheres are failing under compression that is due to buckling.

We avoided this problem by combining our present understanding of the mechanical properties of the spheres with the known permeation rates for D-T and He to prescribe the appropriate fill-pressure steps and times for the various aspect-ratio spheres.[7] More experiments are required to confirm and refine our knowledge of the mechanical strength and permeability of the spheres.

When a sphere is subjected to a uniform external pressure, the sphere wall undergoes a compressive-hoop stress. The failure limit for compressive-hoop stress is indicated by Curve I in Fig. 4-6, where we have used a compressive stress limit of 10 kbar (10^9 Pa). This value is probably accurate to within ± 15%; it was chosen on the basis of the measured value for bulk samples of multicomponent glass systems that are reasonably close to the glass sphere composition.

Because of buckling, however, thin spheres will fail at much lower pressures than indicated by Curve I. In Fig. 4-6, Curve II is a plot of the elastic buckling pressure limit of the microspheres; it is also based on the measured values for bulk samples of similar multicomponent glass.

The expression for the elastic buckling limit is valid as long as the stress remains less than the elastic limit or—since there is no well-defined elastic limit for glass—(at most) less than the yield point. As seen from Fig. 4-6, this is the case for microspheres with aspect ratios greater than about 65. For smaller aspect ratios, inelastic buckling is the failure mode, and it occurs at pressure values lower than predicted for elastic buckling. For spheres with aspect ratios less than 65, the compressive-hoop-stress curve serves as an upper limit. The unsafe region above both limits is indicated in Fig. 4-6.

Along with the estimated curves for the strength limits of the microspheres, we have also plotted some rough data from various D-T fills. The points represent the thinnest sphere known to have survived the various fill pressures. The results are quite consistent with elastic buckling as the failure mode, even though the limit curves are approximations for ideal spheres, and concentricity and other structure defects greatly reduce the buckling pressure and provide scatter in the data. To be safe, the external overpressure on the spheres should be kept a factor of 5 to 10 less than the failure limit indicated in Fig. 4-6.

How large a fill pressure the spheres can hold is governed by the tensile strength, σ_t, of the sphere material. Unfortunately, it is difficult to estimate accurately the tensile strength of glass. Unlike compressive strength, the tensile strength is unpredictable and highly dependent on cross section. Measurements of σ_t for some glass compositions have varied from as low as 0.7 kbar for bulk samples to as much as 100 kbar for thin fibers. Additional factors, such as surface imperfections, also produce wide scatter in the data. Because the microspheres are relatively thin in cross section (1 to

Fig. 4-6. Strength limits of glass microspheres. Curve I (hoopstress) indicates the compressive pressure limit that applies to spheres with aspect ratios, d/t < ~65 and, since $\sigma_c \sim \sigma_t$ (~10 kbar), the extensive limit for all spheres. [Here, $P_H = 4\sigma/(d/t)$.] Curve II (elastic buckling) indicates the compressive limit for spheres with d/t ~ 65. The points represent the thinnest spheres known to have survived the various fill pressures. During fill (700 K), 20 mg/cm³ = 233 bar; after fill (300 K), 20 mg/cm³ = 100 bar. ($P_B = [8E/\sqrt{3}(1-\nu^2)][1/(d/t)^2]$.)

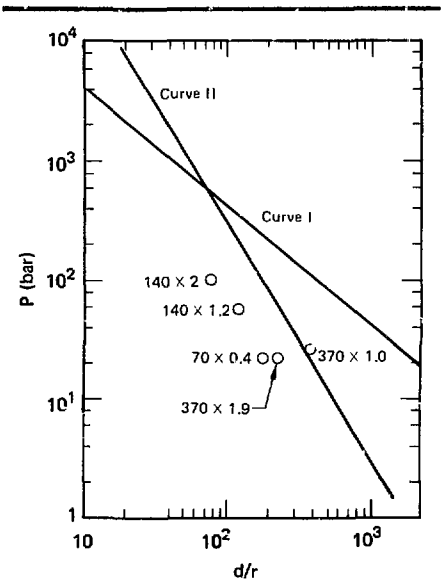

10 μm), 10 kbar is a reasonable estimate for σ_t. Thus Curve I in Fig. 4-6 can also represent the bursting limit of the spheres.

As seen from comparing Curves I and II in Fig. 4-6, the glass microspheres will buckle under compression at a lower pressure than they are capable of containing under extension. If we wish to fill a sphere to a pressure higher than its buckling point, we can simply ramp-fill the sphere. This is done by applying the maximum allowable pressure difference and subsequently increasing the external pressure at the same rate as the pressure increases in the microspheres, thus maximizing the pressure differential and minimizing the fill time.

The time, Δt, needed to ramp-fill a sphere to a final pressure, P_F, is given by $\Delta t = \tau P_F/\Delta P_{max}$, where ΔP_{max} is the maximum overpressure that can be applied. Current fill times are typically 35 to 50 hours. The time constant, τ, depends on the geometry of the sphere and the permeability of the sphere material. Based on preliminary experiments, we use $\tau_{D-T} = 2 \times 10^{-2}$ (ℓr_i $2/r_o$)($h/\mu m^2$) where r_i and r_o are the internal and external radii and ℓ the wall thickness of the sphere. A more accurate value for τ remains to be established, especially for spheres with walls less than 3 μm thick, many of which lose their fill at a faster rate than anticipated.

To supply the ramped pressure, we have developed a vanadium D-T hydride gas generator. Vanadium will form a hydride at room temperature, but will release the hydrogen at high pressure when heated. A pressure of 10,000 psi can be obtained at less than 300°C. The generator consists of a high-pressure chamber filled with vanadium granules that is connected to two transducers (one for control and the other connected to a recorder). These

Fig. 4-7. Schematic for vanadium hydride D-T ramp-filling system.

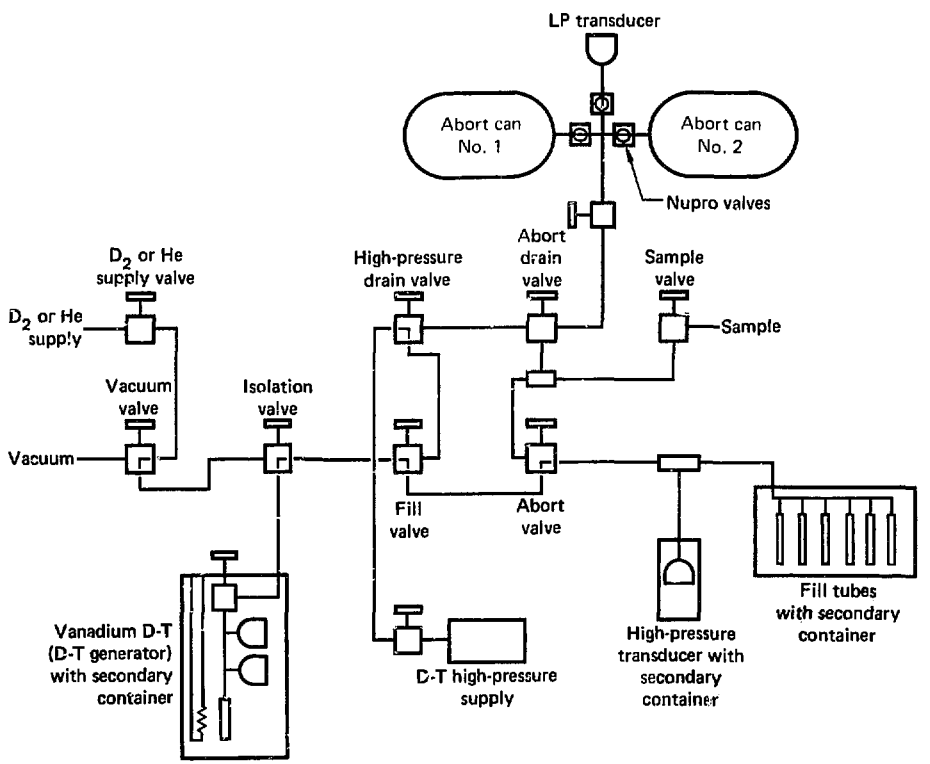

are connected through two high-pressure valves to the sphere-loading system (Fig. 4-7). A heater surrounds the vanadium chamber, and two thermocouples are also connected to the chamber. (One connects to a recorder and the other to an oven-temperature cutoff.) This entire unit is placed in a secondary container to prevent the loss of tritium in the event the chamber, or a transducer, or other equipment should rupture. Because there is no consistent relationship between pressure and temperature, we used the voltage signal from the pressure transducer to control the heater power. This signal is compared to a voltage that represents the desired pressure at a given time. This power-required voltage signal notifies a power controller to supply the power for the heaters. Oven temperature and overpressure safety cutoffs are connected to this unit.

Authors: R. L. Woerner and L. D. Christensen
Major Contributors: I. M. Moen and B. W. Weinstein

Reference

7. R. L. Woerner, B. W. Weinstein, I. M. Moen, and J. G. Rittmann, "Working Strengths and D-T Fill Procedures for Glass Microsphere Laser Fusion Targets," prepared for *J. Appl. Phys.*, February 15, 1979 (also Lawrence Livermore Laboratory UCRL-82728).

Coatings and Layers

The performance of many laser fusion targets can be improved by the addition of one or more layers around the microsphere fuel container. Coating these layers onto targets, whether the simple D-T filled glass shells or the double-shell assemblies described in "Assembled Second Shells," is a difficult, two-step effort. We must first develop the coating processes to deposit materials with the desired properties, and then we must coat the microspheres and assemblies with extremely smooth and uniform layers of these materials.

Low-Z coatings have been formed by plasma-polymerization of hydrocarbons as well as by sputtering beryllium. High-Z coatings have also been formed by sputtering platinum. For both plasma polymerization and the sputtering process, the exacting surface-finish requirements (≤ 0.1 μm) constrain the choice of coating material, the deposition rate, and the energy deposition at the coating surface. The processes must virtually eliminate all defect-causing particles greater than 0.1 μm (these particles originate from a number of sources). With D-T filled microspheres, the processes are further constrained: they must not heat the microspheres above 100°C, a temperature that could cause loss of the fill gas by diffusion.

We must provide continuous, random motion of the microspheres during these processes to ensure a uniform coating. Strong electrostatic forces, however, cause these moving microspheres to adhere to one another, forming clumps. Further, in coating soft metals or coating with high fluxes, the shells additionally tend to clump or cold weld to each other or to the coating apparatus as a consequence of complex, poorly understood processes.

Microsphere adhesion and many of the problems with particulate contamination can be overcome by levitating single glass spheres in a coating process. One successful levitation scheme relies on a molecular beam support for the spheres, a process that we describe in detail under "Molecular Beam Levitation During Coating," below.

An entirely different approach to depositing metallic layers is electroplating. Intrinsically a low temperature process, electroplating provides low mechanical stress for the shells during coating, and it is versatile in the materials it can deposit. Soft metals are the first coating that electroplating can add to our coating capability.

Our first article, "Hydrocarbon Coatings," describes advances in the plasma polymerization of hydrocarbons, which we initiated last year and which we now use in current production. Thereafter, "Beryllium Coatings" describes progress in sputtering beryllium. We discuss platinum sputtering used for a high-Z, high-density tamper layer on microspheres in "Sputtered High-Atomic Number Coatings." Finally, we review our progress toward electroplating metallic layers in the article "Electroplating."

Authors: S. F. Meyer and W. L. Johnson

Hydrocarbon Coatings

During 1979, we continued development of a plasma polymerization process to produce ultrasmooth hydrocarbon coatings in response to the

need of the Laser Fusion Program for an intermediate-density target. The coating for this target must be far thicker than any ultrasmooth coating previously deposited on microshells by plasma polymerization. The specifications require a coating thickness greater than 100 μm with a density of 1.0 g/cm^3 and a finish better than 0.2 μm over the entire surface.

A number of factors enabled us to provide hydrocarbon coatings that satisfy the specifications:

- Improved knowledge of and control over defect growth in the plasma polymerization process.
- Completion of an automated plasma coater.
- Rapid and accurate characterization of the developed coatings provided by the Surface Analysis and Target Characterization Groups.
- Improved glass microshell quality provided by the Glass Shell Group.

As a consequence, we are now able to produce hydrocarbon coatings up to 135 μm thick, while maintaining a surface smoothness of better than 0.1 μm.

Plasma Coating Process. Plasma polymerization of hydrocarbon gases has been studied extensively by others.[8-10] Our own process is very similar to the process we used to form fluorocarbon coatings. We have described that process—as well as associated hardware—in the 1978 Annual Report.[11] Briefly, the plasma-polymerization process activates a hydrocarbon monomer gas as it passes through an electrical discharge formed in a helical resonator. The activated molecules then condense to form a polymer on a substrate. The plasma is formed inside a quartz discharge tube covering a piezoelectrically driven vibrator pan that holds the glass microshells. Vibrating the microshells into continuous random motion allows a uniform coating of polymer to be deposited.

The parameters that must be carefully controlled to give good reproducible coatings with the desired surface finishes include the total gas pressure in the discharge tube, the flow rates of the monomer gas that forms the plasma, hydrogen, and a possible third gas that helps control polymerization. Coating rates are typically 1 μm/h, and it is impractical to hand-control these parameters for the 100 h needed to produce a 100-μm coating. We have overcome this difficulty by constructing an automated coater with prevision for self-protection in case of system failure. Gas-flow rates and total system pressure are independently controlled, and the coater is capable of unattended operation in excess of 100 h.

Coating Defects. Early efforts at coating microshells produced surfaces that were completely covered with dome-shaped defects. (When magnified, a target would resemble a cauliflower.) Such coatings have been traced to the presence of small particles that can nucleate defects any time they settle on the surface being coated. The sources of these particles are atmosphere-borne dirt and particles formed during the polymerization process itself.

We minimize intrusion of atmosphere-borne dirt by shielding the apparatus when it is open for loading. We also clean the quartz discharge tubes for two hours in an argon discharge that further reduces particulates introduced to the system. The Glass Shell Group maintains a high standard of surface cleanliness on the glass spheres themselves by using a series of washes.[12]

Polymer, of course, forms on any surface in contact with the plasma. The coating deposited on the interior walls of the quartz discharge tube becomes a source of particulate contamination because tensile stress in the deposited coating causes the coating to crack and peel. The intrinsic stress leading to the contamination is neutralized by controlling the system gas composition and thus the coating properties. We have found that a combination of trans-2-butene and hydrogen (flowing at 0.3 and 1.9 sccm, respectively) maintained at a total system pressure of 75 mTorr produces a minimum stress coating. In addition, it is necessary to surround the gas-discharge section of the plasma coater with a water jacket. This dielectric layer reduces the electric field at the quartz reaction vessel wall and consequently decreases electron and ion bombardment that in part cause intrinsic stress in the film. Reduced discharge-power levels also reduces this sputtering effect. We have found that 20-W discharge power is optimal.

Finally, thick polymer coatings are typically deposited in two separate steps with a change of discharge tube between the steps. This prevents thick coatings from developing on the wall. Neutralization of intrinsic stress has increased coating thickness from a maximum of 2 μm (the thickness at which the first flake contamination appears) to over

100 μm, which makes it possible to deposit thick coatings on targets in a single batch run. (As an aside, in contrast to tensile stress, a large compressive stress in the polymer coating on the discharge tube wall can cause the tube to explode after several hours of coating. This problem is also solved by the remedies discussed above.)

A second source of particulate contamination arising from the coating process itself is generation of particles in the gas phase.[13] These particles, ranging in size from a few hundred angstroms to several micrometres, are created by gas-phase polymerization. The extent of gas-phase polymerization is limited by turning the discharge off for one second every ten seconds. This allows growing particles, which are levitated in the electrostatic fields of the discharge, to be swept out of the coating region.

Even after eliminating all these sources of particles, we found that defects were still appearing in the microsphere coatings. We suspected the cause of these defects to be irregularities present on the glass microshell itself.

The effect of a surface irregularity on coating quality is shown in Figs. 4-8 and 4-9. The surface quality over most of the microshell surface is better than 0.1 μm. The target quality of the coating, however, was destroyed by a substrate irregularity which, when covered by the growing coating, became a dome-shaped defect. We now have a clear understanding of the growth behavior of these defects and can predict the aspect ratio of defects based on a knowledge of substrate irregularities. We quantitatively studied the effect of coating substrate surface irregularities on coating defects and found that, to achieve target quality coatings, it is necessary to eliminate not only particles in the coater environment but also irregularities larger than 0.1 μm on the glass microshell.

Known surface irregularities (polymer latex beads) were dispersed on a clean glass substrate. We masked the beads in a way that permitted us to produce a gradient of polymer coating. In the foreground of Fig. 4-10, the coating is less than 1 μm thick, while further back the coating grows to 20 μm thick. We found that the size of the defect expands laterally as the film thickness increases. However, the aspect ratio (the ratio of height to width) diminishes as the film thickness increases. Close examination of a thinly coated latex bead reveals that the coating has increased the width of the particle as well as its height. This can happen only with an omnidirectional coating flux.

Fig. 4-8. SEM photomicrograph of a defect in a 41-μm-thick coating that originated at the microshell surface.

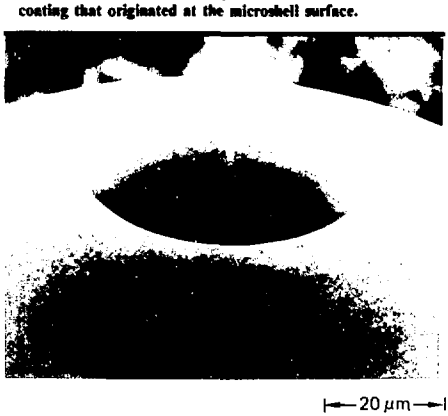

Fig. 4-9. Optical photomicrograph obtained by oil immersion showing the profile of a defect growing from a substrate irregularity in a 135-μm-thick coating.

Fig. 4-10. Known surface irregularities (1.1-μm-diam latex spheres) coated with a gradient of plasma polymer up to 20 μm thick.

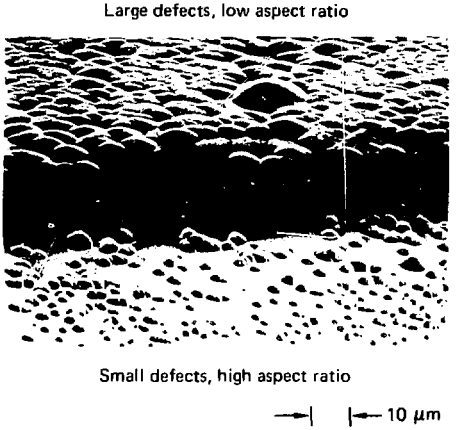

To further measure the spatial distribution of the coating flux, we mounted a single microshell on a stalk in the plasma discharge. Figure 4-11 is a radiograph of the coated ball: the outside diameter of the glass ball is 144 μm, and a portion of the mounting stalk is still visible. The coating is nearly uniform over the entire surface, indicating a uniform spatial distribution of the coating flux.

If an omnidirectional coating flux is assumed, the topology of defect growth becomes a simple geometric problem. For a hemispherical surface irregularity, successive layers of coating will replicate the contour of the original, forming a spherical defect that is concentric with the original (Fig. 4-12). The locus of the intersection of the defect with the smooth, unaffected surface can then be geometrically determined. Thus the defect size grows laterally as the film thickness increases; however, its height remains constant. Similar geometrical arguments for defect growth have also been made for spherical irregularities and defect growth on spherical substrates.

To investigate the growth rate of defects and to check the model, we plasma coated a range of sizes of latex beads. Figure 4-13 shows a normal view of the film defects resulting from coating over 1.1-μm-, 0.3-μm-, and 0.1-μm-diam latex spheres. The smallest sphere produced the smallest defects with the lowest aspect ratio. This shows that small defects produce disproportionately large defects

Fig. 4-11. Microshell mounted on a stalk coated with polymer. The uniformity of the coating indicates an omnidirectional coating process. (Ball diameter = 144 μm; coating thickness = 24.6 μm top, 23.4 μm side.)

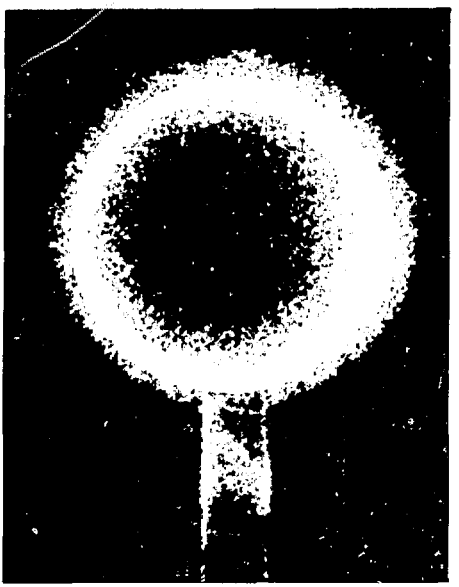

Fig. 4-12. Defects in plasma polymerized coatings grow by replication of the original irregularity. The defect radius is a function of the coating thickness and irregularity radius.

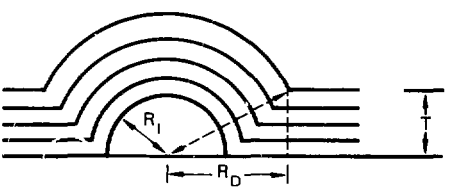

$$R_D = \sqrt{(R_I + T)^2 - T^2}$$

$$R_D = \sqrt{R_I^2 + 2R_I T}$$

$$\left(\frac{R_D}{R_I}\right)^2 = \left(\frac{1}{\text{Aspect ratio}}\right)^2 = 1 + 2\frac{T}{R_I}$$

Fig. 4-13. SEM photomicrographs of defects nucleated by known surface irregularities (coating thickness = 13.8 μm).

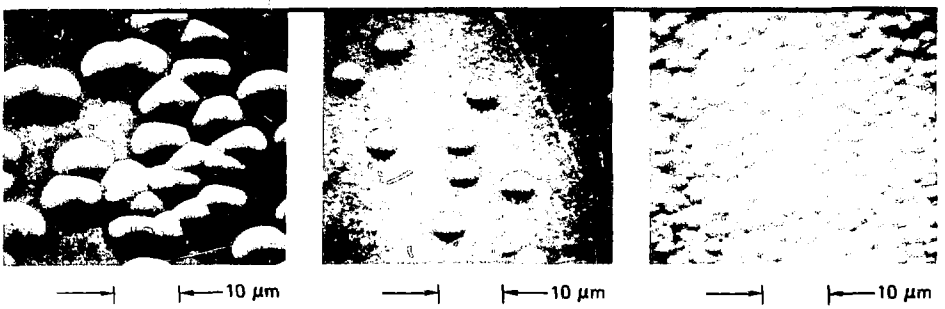

Fig. 4-14. Reduced defect diameter as a function of reduced film thickness. Data points are measured defects. The solid lines show the growth behavior expected for spherical and hemispherical irregularities as predicted by the geometrical growth model.

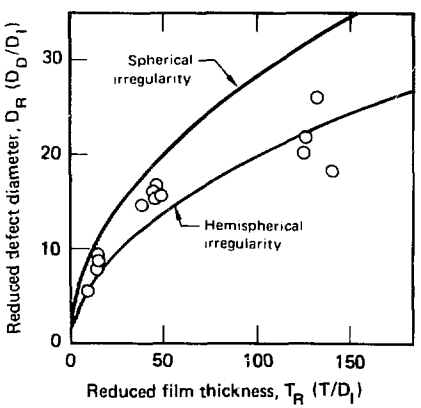

when the defect size is normalized to the size of the starting irregularity.

The data are summarized graphically in Fig. 4-14, where reduced defect diameter (normalized by the latex sphere diameter) is plotted against reduced film thickness. The two solid lines show the behavior expected for the geometric growth models for films growing on hemispherical and spherical

Fig. 4-15. Hydrocarbon coating (110 μm thick) on a 140-by-5-μm glass microshell broken for inspection.

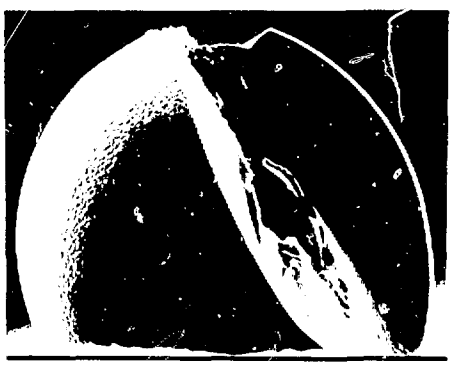

irregularities. Most of the experimental points lie between the expected curves. The close fit shows that the physical behavior is fairly well-modeled as an omnidirectional coating flux.

Production Results. Figure 4-15, a scanning electron microscope (SEM) photomicrograph of a target broken for examination, shows the coating to be concentric, homogeneous, and smooth. The coating thickness (measured from the photomicrograph) is 110 μm, and it took 106 h to deposit. The clean fracture displays the typically homogeneous, void-free coating. Inspection of the interface between the glass and the hydrocarbon coating shows it to be also void-free. The surface finish shown in Fig. 4-15 is better than 1 μm, which is still not adequate for target use. Further improvements in par-

Fig. 4-16. Hydrocarbon coating (135-μm-thick) with a surface finish better than 0.2 μm.

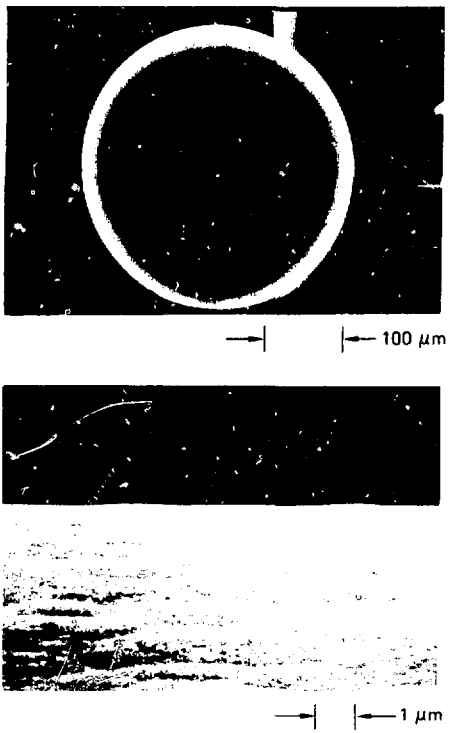

Fig. 4-17. X-ray radiomicrograph of a 110-μm-thick hydrocarbon-coated target.

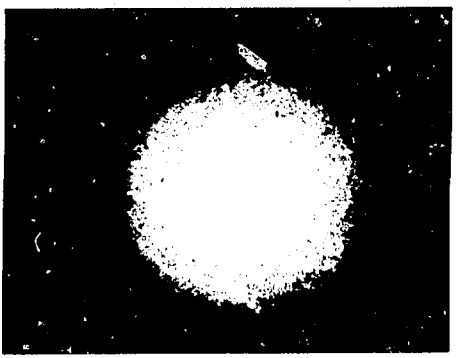

ticulate elimination and glass-shell quality resulted in surface finishes better than 0.1 μm on coatings 135 μm thick (Fig. 4-16).

Thick hydrocarbon coatings require different thickness characterization techniques than are used for the thin fluorocarbon coatings. Coatings thicker than 40 μm are beyond the range of the Zeiss interferometer. The Target Characterization Group instead applied x-ray microradiography to the nondestructive measurement of the thick coated targets. Figure 4-17, an x-ray microradiograph of a hydrocarbon coated microshell, shows that the coating is concentric with the substrate and measures 110 μm thick. Volumes calculated from the measured thickness were combined with coating weights (determined on a quartz fiber balance) to yield coating densities of 1.00 ± 0.05 g cm^{-3}.

Immersing the targets in an oil having nearly the same index of refraction as the coating reduces diffraction effects and allows a penetrating view of the internal structure of the coating. Figure 4-9 shows a glass shell (130-μm outside diameter, 12-μm wall thickness) that is coated with hydrocarbon polymer (hydrogen:carbon ratio averages 1.3:1; shorthand notation: $CH_{1.3}$) to a total thickness of 135 μm. A nondefected coating is shown in Fig. 4-65 (in "Materials Analysis Developments and Surface Studies," this section). The polymer coating is typically deposited in two separate steps to prevent intrinsic stress buildup in the coating that deposits on the discharge tube. The change of discharge tube to prevent highly stressed thick coatings causes a definite color change in the coating. Other rings are also visible within the coating that correspond to slight variations in process conditions.

Oil immersion also allows us to examine the glass microshell surface after coating. Through this technique we have verified the relationship between coating defects and substrate irregularities. The result is that we have set quantitative quality standards on microshell surface contamination.

Author: S. A. Letts

Major Contributors: R. J. Hayes, C. W. Jordan, R. M. Krenick, S. E. Mayo, D. W. Myers, and L. A. Witt

References

8. H. Kobayashi, M. Shen, and A. T. Bell, "Effects of Reaction Conditions on the Plasma Polymerization of Ethylene," *Macromol. Sci.-Chem.* **A8(2)**, 373 (1974).
9. A. T. Lowe and R. J. Fries, "Plasma Polymerized P-xylene as a Laser Fusion Target," *Surface Sci.* **76**, 252 (1978).
10. R. Lipins, M. Cambell, and R. J. Fried, "Plastic Coatings for Laser Fusion Targets," *Prog. in Polymer Sci.* (1979).
11. *Laser Program Annual Report—1978*, Lawrence Livermore Laboratory, Livermore, Calif., UCRL-50021-78 (1979), pp. 4-7 to 4-11.
12. *Laser Program Annual Report—1978*, Lawrence Livermore Laboratory, Livermore, Calif., UCRL-50021-78 (1979), p. 4-5.
13. M. R. Havens, K. G. Mathan, and W. J. James, "Plasma-Deposited Polymer Films. II. Transmission and Scanning Electron Microscopy," *J. Appl. Polymer Sci.* **22**, 2799 (1978).

Beryllium Ablator Coatings

In 1979 we continued development work on coating thick, dense, smooth Be on both microspheres and hemispherical mandrels for second-shell applications. The target shown in Fig. 4-43 (see "Double-Shell Targets," this section) is a typical Be second-shell design. Hemispherical second-shell Be layers may be up to 200 μm thick and should be dense, smooth, and have low impurity content. We use a hemispherically shaped copper mandrel as the Be substrate. The Be coating should also be machinable because the critical concentricity (<2%) and surface finish (<1 μm) requirements of these shells may require precision machining after deposition. The recentering tolerance (1 μm) for remachining the coated mandrel to the required concentricity rules out any high-temperature (≳100°C) deposition process that would thermally strain or deform the mandrel. As one solution, we have developed room-temperature deposition techniques using rf sputtering with a cylindrical magnetron sputtergun to coat thick, adherent, dense Be onto water-cooled, Cu hemispherical mandrels.

The cylindrical magnetron rf sputtering system is capable of depositing Be on a water-cooled mandrel at a rate of 5 μm/h-kW rf using a 0.4-Pa (~3 × 10^{-3} Torr) argon plasma. A schematic of the cylindrical sputtergun and water-cooled mandrel block is shown in Fig. 4-18. We have described our experimental procedures in detail elsewhere.[14,15]

The morphology of beryllium growth on copper mandrels held at 15°C during sputtering depends on the argon gas pressure, sputtering power (rate), and impurity-gas doping. A rough, open, low-density structure grows at high pressure and low power (3.3 Pa and 300 W), as shown in Fig. 4-19(a). This film also has an unusual {101} texture orientation. Low-pressure and higher power (0.49 Pa and 1000 W) sputtering results in thick Be coatings with a fine-grained, polycrystalline surface structure, bulk density, and {100} orientation. An example is the 22-μm-thick film surface shown in Fig. 4-19(h). We can further improve the surface finish on thick Be coatings at 15°C by gas-impurity doping during sputtering. With a 0.5 at.% oxygen and 0.3 at.% nitrogen content in the Be coating, the surface finish is very fine-structured, as shown in Fig. 4-20. Analysis by x-ray diffraction indicates only a very weak Be {100} line, suggesting the Be film is nearly amorphous. These low-temperature, high-rate deposition techniques produce very-fine-grained, dense, smooth Be coatings that we believe are suitable for the precision machining operations necessary in constructing the Be second-shell layer of the proposed double-shell targets.

Thick (>10 μm) Be coatings exhibit large crystal facets and unacceptably rough surfaces when deposited at high power onto uncooled, mechanically floating substrates. This is unfortunately the environment of a thermally isolated, moving-glass microsphere, during any physical vapor deposition (PVD) coating process. We have conducted additional work with rf sputtering of Be onto floating planar glass substrates that are allowed to reach about 200°C during the sputtering process.

We have successfully suppressed the high-temperature grain growth such as the rough-faceted {002} crystallite surface shown in Fig. 4-21 to the much smoother, cone-free surfaces of Figs. 4-22 and 4-23 by gas doping of oxygen or nitrogen. The surface structure in Fig. 4-21 is polycrystalline with a {110} orientation, presumably resulting from the 0.5 at.% of N_2 and O_2 contained in the Be. Heavier doping levels, up to 14 at.% oxygen, produced the amorphous structure shown in Fig. 4-23. From these results, we are optimistic that low-pressure, high-energy rf sputtering with controlled, low levels

Fig. 4-18. Cylindrical rf sputtergun and mandrel substrate holder used for production of Be hemispherical shells.

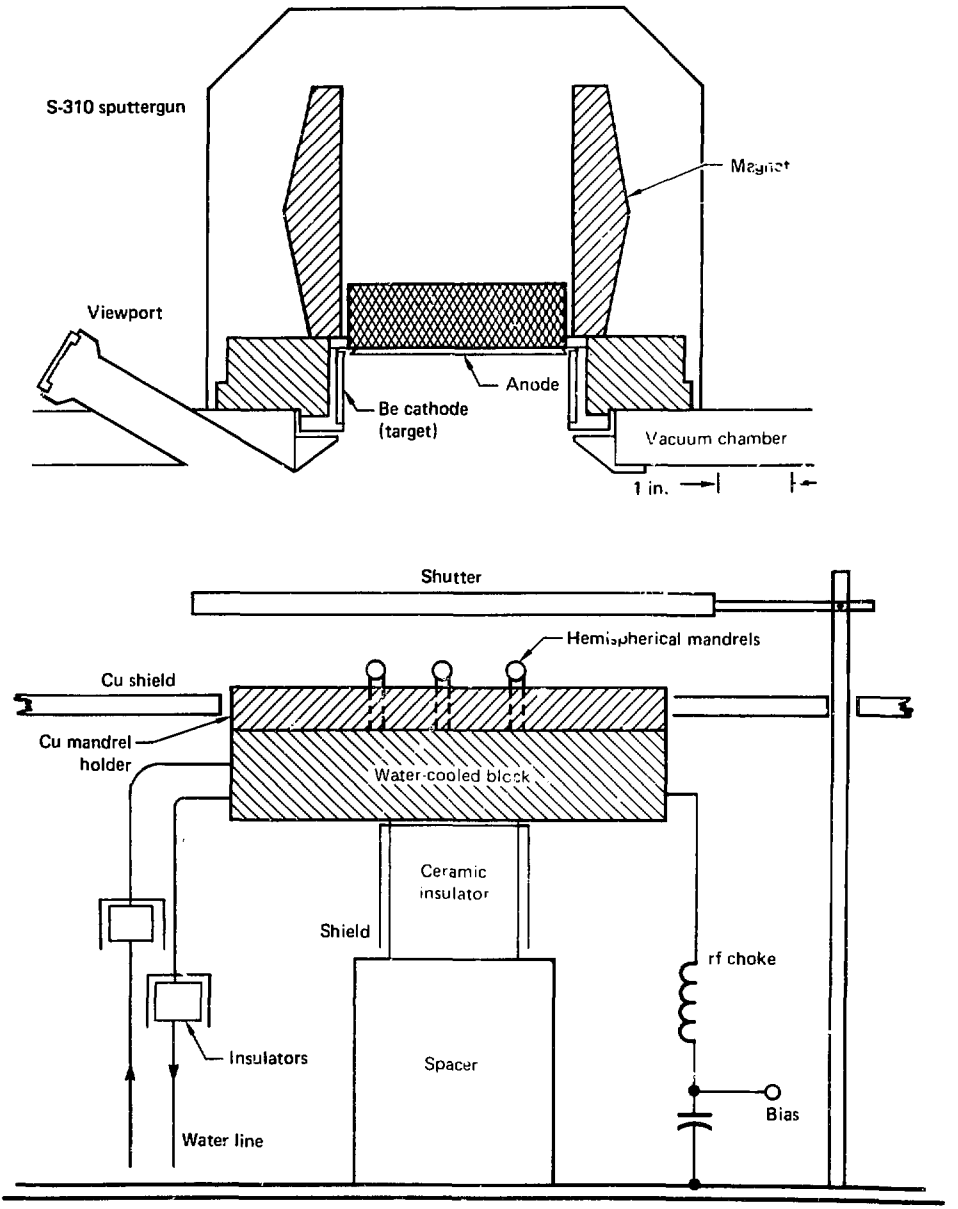

Fig. 4-19. SEM photomicrographs of Be films deposited at 15°C and 0.5 Pa on Cu: (a) showing rough growth from high-pressure sputtering (3.3 Pa, {101} orientation), and (b) the surface of a high-purity, 22-μm-thick film, {100} orientation. Note the replicated Cu mandrel polishing scratches in the center right.

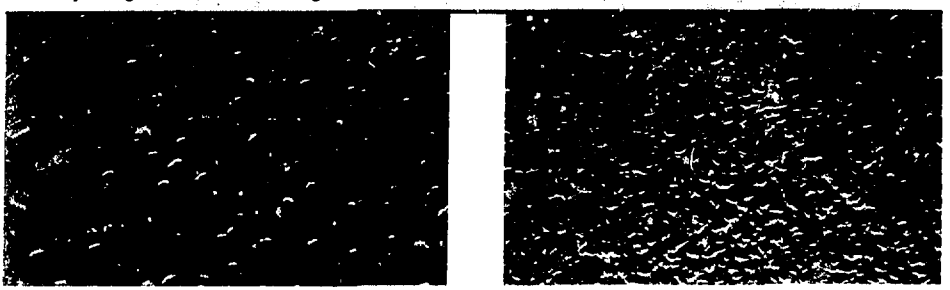

Fig. 4-20. SEM photomicrographs of a Be film deposited at 15°C, showing an improved surface finish with a impurity doping of 1.5 at.%.

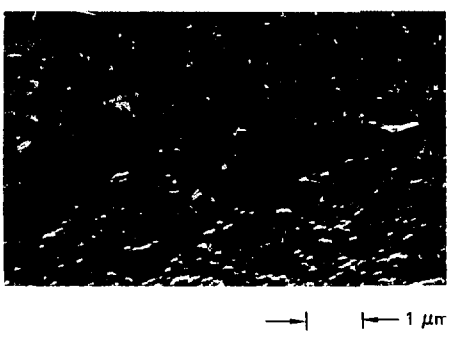

Fig. 4-21. SEM photomicrograph of a high-purity Be film deposited on a hot glass substrate showing faceted {002} crystallites growing from a substrate area.

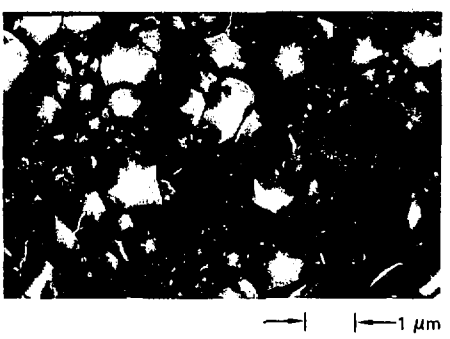

Fig. 4-22. SEM photomicrograph of the surface of a BE film deposited on a hot glass substrate with {110} orientation and 2 at.% total impurity.

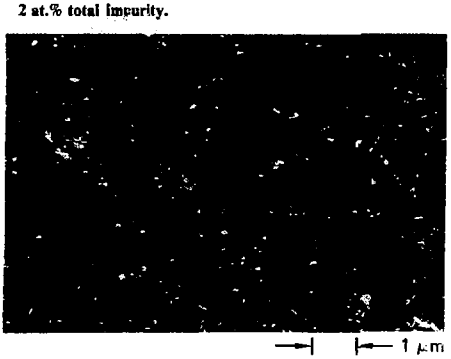

Fig. 4-23. SEM photomicrograph of an impurity-stabilized, amorphous Be film deposited on hot glass substrates containing 14 at.% oxygen.

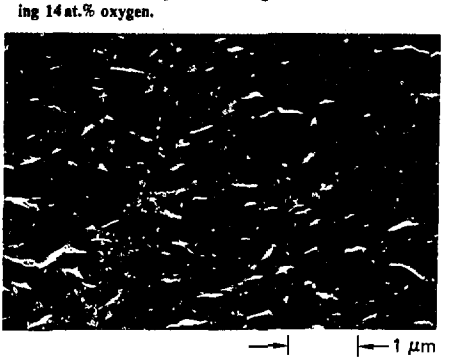

Fig. 4-24. SEM photomicrograph of the surface finish of a Be-coated glass microsphere after Be sputter deposition in a cooled vibrating cage: (a) 2-μm-thick Be coating (b) 7-μm-thick Be coating.

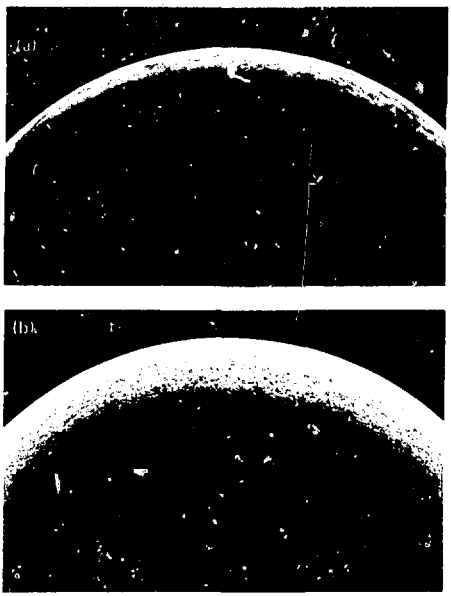

of gaseous impurities is a promising technique to refine the surface finish of thick Be coatings on hollow glass microspheres.

We have sputtered thin Be coatings on glass microspheres using the water-cooled vibrating cage techniques described in detail in the next article, "Sputtered High-Atomic-Number Coatings." These Be coatings required no gas-impurity doping to produce smooth, cone-free surfaces. Two rf-sputtered Be coatings on 140-μm glass microspheres with thicknesses of 2 μm and 7 μm are shown in Figs. 4-24(a) and 4-24(b), respectively.

Authors: R. J. Burt and S. F. Meyer
Major Contributors: F. J. Wittmayer and K. L. Montgomery

References

14. *Laser Program Annual Report—1978*, Lawrence Livermore Laboratory, Livermore, Calif., UCRL-50021-78 (1979), p. 4-17.
15. R. J. Burt, S. F. Meyer and E. J. Hsieh, "RF Magnetron Sputtering of Thick Film Amorphous Beryllium," *J. Vac. Sci. Tech.* 17, 407 (1980).

Sputtered High-Atomic-Number Coatings

High-Z, high-density coatings on glass microspheres are needed as the tamper layer in the proposed double-shell target shown in Fig. 4-43 (see "Double-Shell Targets," this section). The tamper specifications are 30-nm surface smoothness, 100-nm thickness uniformity, and thicknesses in the 5- to 10-μm range. The spherical nature of these substrates—coupled with the small dimensions (~100 μm o.d.)—makes it difficult to achieve the required uniformity and surface finish by using conventional physical vapor deposition processes.

Previous attempts at sputtering onto moving microspheres with a batch process at LLL, at Los Alamos,[16] and at KMS Fusion, Inc.,[17] have suffered from severe sticking problems, thereby preventing the continuous motion needed for coating uniformity. Only the Molecular Beam Levitator moving a single ball (described in "Molecular Beam Levitation During Coating," this section) has been successful in a sputtering environment.[16] Our introduction of the vibrating screened cage reported previously[18] greatly reduced the sticking problems and allowed the first practical batch application of sputtering on microspheres.

We have successfully batch-coated microspheres with up to 6 μm of Pt, with a surface roughness of 100 nm, thickness nonconcentricity of less than 300 nm, and density greater than 98% of bulk Pt. In the remainder of this article we outline the screened-cage batch process technique, the difficulties in microsphere coating, and our various solutions to these difficulties.

Screened Cage and Fixturing. We conduct our microspbere coating experiments in a stainless steel, diffusion-pumped vacuum system equipped with a gas-flow controller and a Sloan S-310 Sputtergun with a custom matching network. Dataloggers and chart recorders monitor the deposition parameters during runs. The sputtergun and screened cage are illustrated schematically in Fig. 4-25.

The screened cage for bouncing and confining the microspheres consists of a piezoelectric crystal compressed between a massive steel base and a low-mass copper block. An axial bolt provides the compression and acts as the spring in the mechanical spring-and-mass system. Three copper rings bolted

Fig. 4-25. Schematic illustration of sputtergun and screened cage showing their relative orientation and major components.

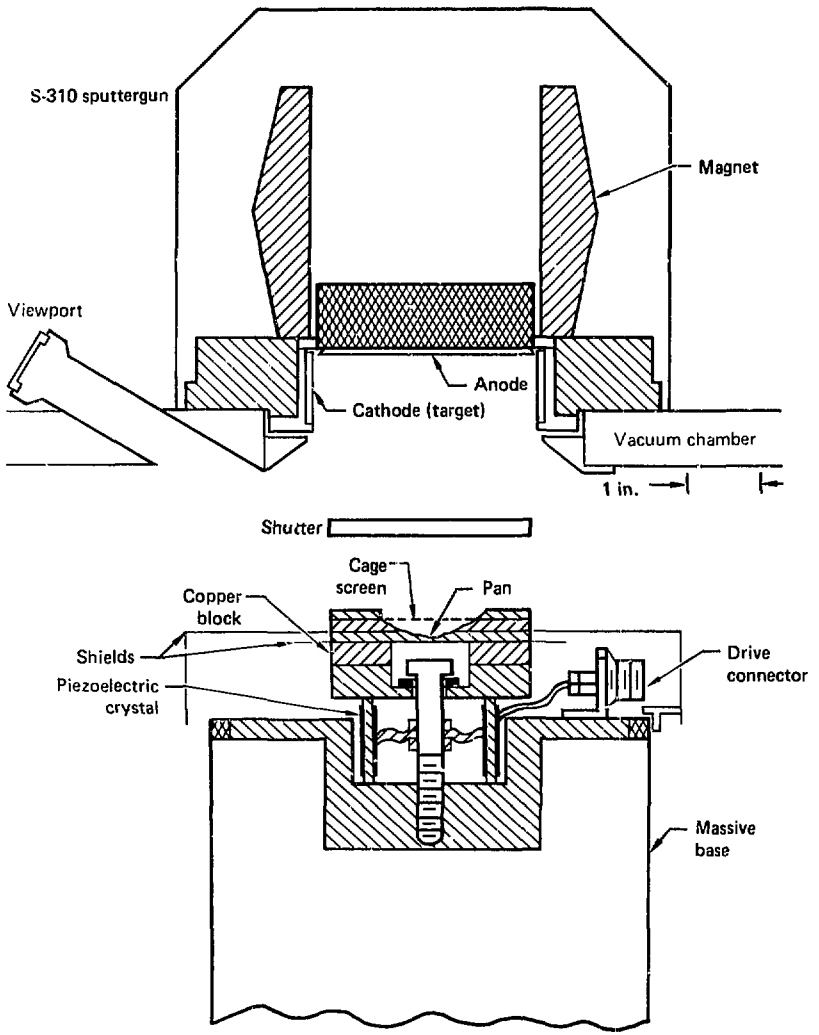

to the copper block clamp the screen and thin copper pan to form the cage. The pan acts like a mechanical amplifier to bounce the balls, since the pan amplitude is much larger than the displacement of the block and crystal. The block is electrically isolated from the crystal electrodes and the grounded base to allow independent biasing of the cage. Of course, the microspheres are not in continuous contact with the cage, so the biasing effect is rather indeterminate. Cooling for the cage is provided by

channels in the copper block for circulating water or liquid nitrogen, and by conduction through the screen and copper pan.

Our initial method for driving the crystal used a frequency-modulated oscillator running at the crystal resonance and swept over a range of pan resonances. Unfortunately, as the cage temperature and mass changed during coating, the drive system required continual tuning to maintain optimum motion, and encountered problems with repeatability. To improve the reproducibility, we switched to a "white noise" drive. Since all frequency components are present, the cage tuning has little effect on the microsphere motion, and the drive can be calibrated with a simple rms voltage measurement.

To confine 70-μm microspheres, we need to use a 300-mesh screen with an initial transmission of only 65%, which is steadily reduced during coating. This small screen mesh restricts both the visibility and coating rate of the microspheres. The microsphere visibility is further restricted by the shallow angle of the side viewport shown in Fig. 4-25, and by the omnidirectional plasma glow. Improved lighting and better optics are highly desirable for reproducible results.

Microsphere Sticking Problem. Two clean metal surfaces, such as those produced in vacuum deposition, can cold-weld together by deforming slightly and bonding under impact.[19] The cold-welding tendency depends directly on hardness and is worst for the soft metals, such as Cu, Au, and Al. The severity of the vacuum welding problem with gold is graphically visible in the SEM micrograph in Fig. 4-26. The thin gold coatings on the two microspheres have stuck together to form a patch which has almost separated from the two spheres. A large number of roughly circular patches where the coating was completely torn away are visible here and on other spheres from the coating run. Such welding either produces unacceptable defects or prevents a uniform coating.

The hard metals, such as Ta, Mo, and W, do not cold-weld easily; however, they present a nearly impossible stress-failure problem. Coatings of these metals flake off the system walls and rip the cage screen as a result of stress buildup, making a thick defect-free coating very difficult to deposit. By contrast, Pt is a nearly ideal metal because of its ductility, high Z and high density, and relative resistance to vacuum welding.

Fig. 4-26. SEM photomicrograph of two gold-coated microspheres showing cold-welding damage spots and torn flap of cold-welded coating.

In addition to the rigid clumping of vacuum welding, a second type of sticking—believed to be electrostatic in origin—produces clumping of the microspheres to each other, to the pan, and to the screen. This sticking action is intermittent and usually reversible when the coating conditions are changed. This sticking usually takes the form of microspheres moving up to the underside of the screen and either adhering motionless to it, or moving intermittently around on it. Sometimes the microspheres clump together and stick to the pan without motion. Increasing the bouncer drive or reducing the sputtering power releases the microspheres, which then return to normal bouncing in the pan. If the operator does not intervene during sticking, the microspheres will either be coated nonuniformly, or will become attached to the screen, pan, or other microspheres. Driving the cage too hard, on the other hand, can cause cracking and breakage in the Pt coating. Keeping the microspheres in constant motion without breakage is a major problem.

We do not yet fully understand the exact mechanism of this sticking process. However, it seems to be caused by microsphere charging from the difference in electron and ion mobility in the sputtering plasma. The evidence for an electrostatic mechanism includes the following:

- The screened cage reduces the sticking relative to an open pan.
- A bias voltage on the cage reduces the sticking.
- Rf sputtering has less sticking than dc sputtering at similar power levels.
- Addition of an electronegative gas such as oxygen to the plasma atmosphere minimizes sticking.
- The degree of sticking is proportional to the plasma power density.
- Closing the shutter relieves the sticking (and stops the coating).

Adding oxygen as a dopant gas in our sputtering process is one of the most effective methods for preventing sticking. We still do not fully understand why oxygen helps, hut its effect is clearly established. Once oxygen is introduced into the plasma during coating, the microspheres immediately become unstuck, and bounce freely. As the oxygen flow is gradually reduced, at a critical level the microspheres clump back together again. The clumping and unclumping actions are reversible and controlled strictly by the oxygen.

Platinum Deposition Process. As with beryllium coating reported in the previous article, we found that coating parameters such as operating pressure, cage bias, temperature, and impurity-gas doping have a substantial influence on the Pt coating that is in good agreement with Thornton's Structure Zone Model[20] shown in Fig. 4-27. The transition region, Zone T, produced by low deposition pressure and low substrate temperature, is the desired region for the very smooth, uniform coatings needed on laser fusion targets.

Our best coatings were achieved with a water-cooled cage using 300-mesh screen. The deposition parameters included total pressure in the vicinity of

Fig. 4-27. Coating-growth structure zone model of Thornton[20] showing how sputtered-coating structures change with temperature and inert gas pressure.

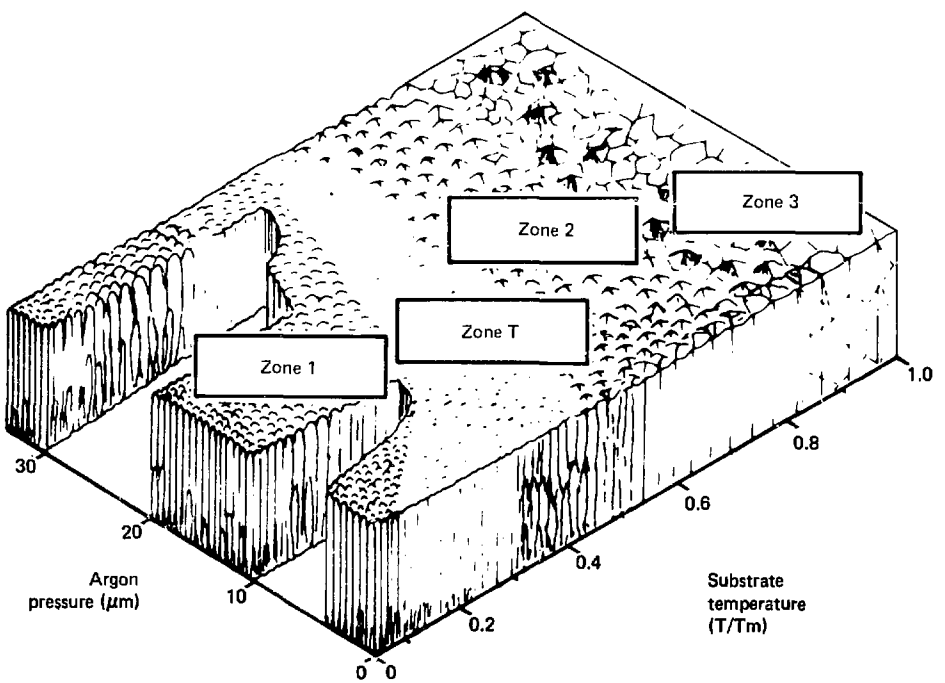

Fig. 4-28. Smooth platinum coating (100-nm surface finish, bulk platinum density) grown on microsphere under best sputtering conditions. Cone defects visible represent 300-nm defects.

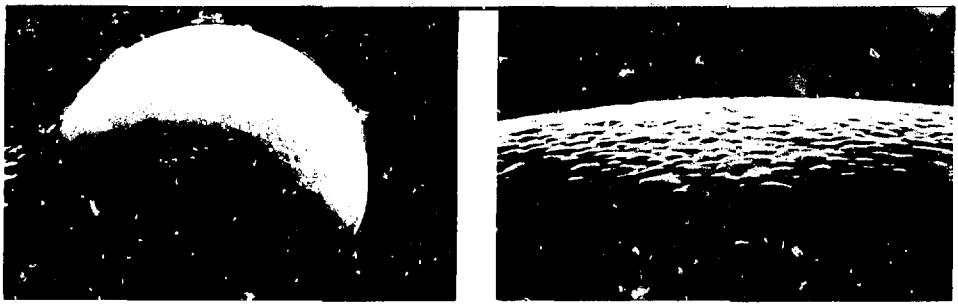

Fig. 4-29. Low-density, porous, Zone 1 structure of Class I platinum coating on microsphere. Sputtering pressure above 1 Pa (7.5 mTorr) promotes this growth.

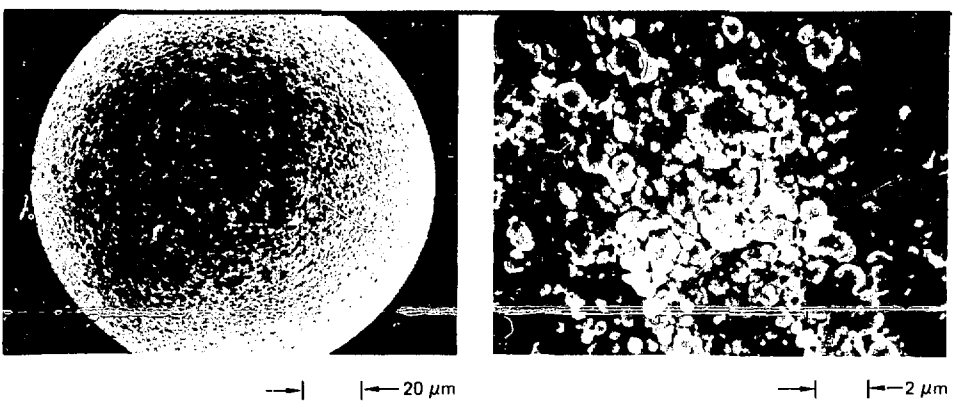

0.8 Pa (6 mTorr), with oxygen flow of 0.5 sccm, argon gas flow of 30 sccm, bias of -100 V, and rf sputtergun power of 300 W. The white-noise-driven bouncing action was set for minimum motion without high-speed impact with the cage walls and screen. A typical Pt-coated microsphere that was coated with these parameters (shown in Fig. 4-28) is ~98% bulk Pt density and has a ~100-nm surface finish. Deposition pressures of 0.8 Pa and lower typically produce dense, smooth coatings which are typical of Zone-T growth. However, the deposition rate of 1 μm/h appears to decrease monotonically with decreasing pressure, so operating at the lowest possible pressure is not necessarily desirable. Different deposition parameters produce coatings with characteristics that fall predominately into three other classes. Below, we discuss in general terms how each coating parameter influences the coating structure.

The quality of the Pt coating decreases with increasing deposition pressure, in agreement with the Structure Zone Model. Pressures above about 1 Pa (7.5 mTorr) produce the Class 1 coating shown in Fig. 4-29, which is indicative of Zone 1 growth.

These Zone I coatings appear grainy, porous, or loosely packed, and they are of low density. The inert gas pressure during sputtering and the degree of oblique incidence appear to be the dominant processes responsible for Zone I structure formation.

The oxygen dopant also affects the Pt-coating characteristics. The addition of about 2% oxygen to the argon sputtering gas (which is the amount provided by the 0.5-sccm oxygen flow rate that produced the coating of Fig. 4-28), refines the grain structure in the growing Pt coating, and hardens the metal against cold welding. With a large amount (~10%) of oxygen, the Pt coating becomes hard and brittle, with evidence of platinum oxide formation. The resulting Class II structure shown in Fig. 4-30 is brittle, extremely fine-grained, and characterized by cracks and broken layers from impact damage. On the other hand, when we use insufficient oxygen (≪1%), the Pt coating is soft and forms the Class III structure shown in Fig. 4-31. Accretion of loose particles within the cage by cold welding probably accounts for the patchy surface. The impact of the bouncing action "hammered" the soft Pt particles into a semismooth surface. The desired oxygen dopant level falls between these two extremes and depends, of course, on both sputtering rate and system throughput.

Fig. 4-30. Class II platinum coating broken by impact with cage. Coating was hardened with excessive amounts of oxygen doping during sputtering.

The bouncing action is the third most important parameter (after total pressure and oxygen dopant) in controlling Pt-coating characteristics. The gross nonuniformity seen in some depositions is obviously the result of inadequate bouncing action. On the other hand, too vigorous a bouncing action causes cracking and breakage of the Pt coating. An effect of vigorous bouncing action that is not so obvious is that the impact of the microspheres onto the cage parts—the Ni screen in particular—can trigger the release of micrometre-sized particles. On impact, the small particles adhere to the Pt coating, producing "cone defect" nuclei. We achieved our cleanest coatings by reducing the bouncing action to to a level where the microspheres barely moved around, with minimum collisions with the screen. We need an improved optical observation system, however, to monitor this bouncing action adequately.

Traditionally, substrate bias voltage is used to increase the argon ion bombardment of the substrate to yield a cleaner and denser coating. With

Fig. 4-31. Platinum coated microsphere showing "soft" Class III coating grown with insufficient oxygen doping.

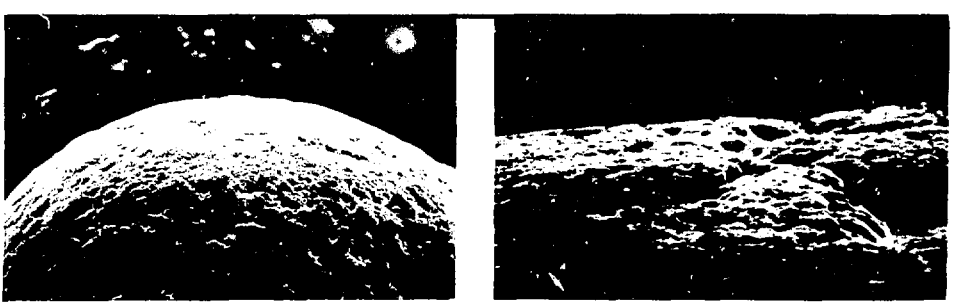

our cage configuration, it is not clear how well the ion flux penetrates the screen. In any case, the microspheres are not at bias potential most of the time because of the bouncing action. We do not observe in the coating a pronounced difference between biased and unbiased runs. However, as noted above, the bias definitely helps prevent sticking.

We have been unable to directly monitor the actual microsphere temperature during coating. We have inferred from measurements on isolated thermocouples that with a water-cooled cage the probable microsphere temperature is on the order of 150°C, considerably lower than the onset temperature for diffusion-dominated grain growth in platinum (Zones 2 and 3 in Fig. 4-27). This coating temperature appears acceptable for all but very thin-walled microspheres, where some evidence indicates that the D-T fill can leak out during the coating process. Preliminary experiments with liquid-nitrogen cage cooling and with magnetic deflection of the plasma electrons have shown some reduction in thermocouple temperature. We will investigate the magnetic deflection coating method further before reaching a conclusion. Efforts are continuing to fine-tune the set of coating parameters to achieve a smoother surface finish and to achieve a higher degree of repeatability.

Authors: S. F. Meyer and E. J. Hsieh
Major Contributors: R. J. Burt, G. T. Jameson, and A. L. Plake

References

16. A. T. Lowe and C. D. Hosford, "Magnetron Sputter Coating of Microspherical Substrates," *J. Vac. Sci. Tech.* **16**, 197, 1979.
17. W. J. Helmlee, KMS Fusion, Inc., private communication (1980).
18. *Laser Program Annual Report—1978*, Lawrence Livermore Laboratory, Livermore, Calif., UCRL-50021-78 (1979), p. 4-14.
19. D. T. Bourgette, D. V. Keller, and R. L. Stephenson, in *Vacuum Metallurgy*, O. Winkler and R. Bakish eds. (Elsevier, New York, 1971), pp. 825-838.
20. J. A. Thornton, "High Rate Thick Film Growth," *Ann Rev. Mater. Sci.* **7**, 239-260 (1977).

Electroplating

High-atomic-number elements required in advanced target designs can be deposited by electroplating under conditions that preserve fragile laser fusion targets. We have therefore begun a project to produce coatings by the use of electroplating, a method that offers unique advantages. It is a well established coating method that can be applied to deposit a wide variety of metals. Figure 4-32 shows the elements that can be electroplated from aqueous solutions. Other elements may be deposited from nonaqueous organic solvents at low temperatures or from fused salts at high temperatures. The solution-plating techniques (electroless, electroplating, and immersion plating) are also complementary to sputtering. It has been found very difficult to sputter smooth coatings of very soft metals such as gold or

Fig. 4-32. The highlighted elements can all be electrodeposited from aqueous solution. (Almost all elements can be electrodeposited with the proper choice of solvent.)

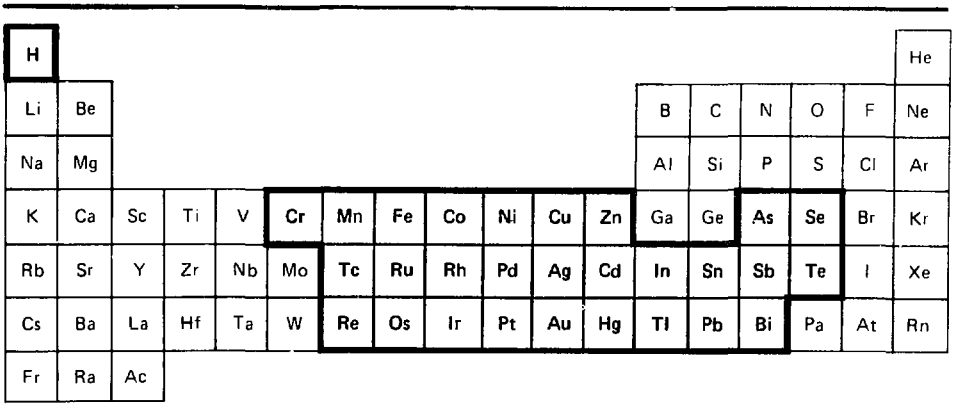

copper.[21] Solution plating is well suited to deposition of these metals in a low-temperature, low-stress environment.

Two major problems arise in the plating of glass microsphere fusion targets: First the ultrasmooth nonconductive glass surface must be treated to achieve a very smooth, adherent and conductive surface (called a strike) for plating. Then, the conductive microspheres must be sustained in random motion while electrical contact with the cathode of the plating cell is retained. (The motion is essential to achieve a uniform coating thickness.)

Fig. 4-33. The typical silver strike surface deposited from an ammoniacal $AgNO_3$ solution.

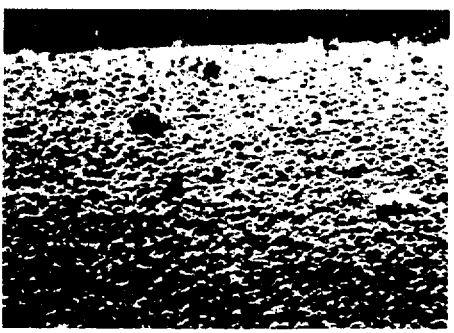

Most industrial processes for plating glass involve a chemical or mechanical etching of the glass to obtain a rough, high-surface-area substrate for plating.[22,23] This is, however, unacceptable for use with fusion targets. Sputtering can produce smooth, relatively hard, thin metallic coatings on glass that accept overcoats of electrodeposited metal, as Fig. 4-33 shows. These sputtered coatings are often strained, however, and this can lead to plating difficulties. We have therefore developed an alternate method for the deposition of a strike layer.

Modifications to ancient mirror silvering techniques (Brashear) allowed us to produce a 0.14-μm-thick silver strike with the surface shown in Fig. 4-34. The silver coating is adhesive and cohesive, and it readily accepts overplates of gold or copper. The nodular silver growths on the surface have formed at the solution-container interface. We can remove most nodules by washing and ultrasonic treatments. Other strikes we investigated—such as colloidal $PdCl_2$ or precipitated metal sulfides—were completely unsatisfactory. Tin deposited by the thermal decomposition of $SnCl_4$ coated unevenly. We expect further changes in the silver process to result in far better surface finishes. We may also find it advantageous to follow the example of target builders at Los Alamos and make a nickel strike by the decomposition of $Ni(CO)_4$ at the surface of glass microspheres.[24]

The second major impediment to uniform electroplated surfaces is the plating tank or cell in which

Fig. 4-34. The surface finish of a thin (~1000 Å) sputtered Pt strike. The utility of this smooth Pt coating is marred by tensile stress in the coating.

the plating occurs. To achieve the random contact of the cathode necessary for electroplating, we found the cells shown in Figs. 4-34 and 4-35 to be acceptable. The cells we have designed and developed also are capable of dispersing gas bubbles on the surface of the target (a problem that disrupts the plating of very small objects).[23]

The cell in Figure 4-35 has a cathode which is vibrated by an electromechanical transducer to impart motion to the microspheres. Solution is also pumped through the screen to further aid microsphere motion and to replace depleted solution. An even more gentle motion can be achieved with the cell shown in Fig. 4-36. Mass flow, viscous forces, buoyant and gravitational forces all can be balanced to produce a rolling motion along the tapering walls of the cell. The result is uniform plating with very small loss of microspheres due to breakage or because they become plated to the cathode.

Fig. 4-35. Vibrating cathode electroplating cell.

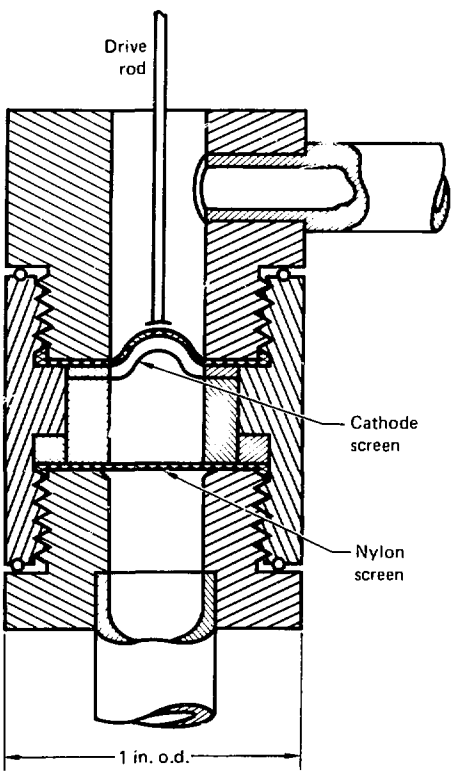

Although electroless and immersion plating would have allowed us to use simple plating cells, each of these processes was unsatisfactory. Immersion plating (also called displacement deposition) is the deposition of a metallic coating by chemical replacement of substrate atoms from a solution of a salt of the coating metal. The thickness of immersion coatings is limited. Once a continuous layer of coating is established, substrate atoms can no longer be replaced by the coating metal. Typically, gold can be immersion-plated only to about 0.025 μm thick.[23]

Electroless plating uses the electrons provided by oxidation of a chemical reagent present in the solution to deposit metal atoms on a catalytic surface. For the electroless process to be useful, it must be autocatalytic. Once the initial catalytic surface is completely covered with coating atoms, the newly produced coating must itself catalyze the deposition of more coating atoms. Ideally, the process should continue until all the coating atoms are removed or the supply of reducing agent is exhausted.

We found that the apparent benefits of the electroless system, simple containers, no external reducing potential, near-perfect throwing power and low

Fig. 4-36. Electroplating flow cell.

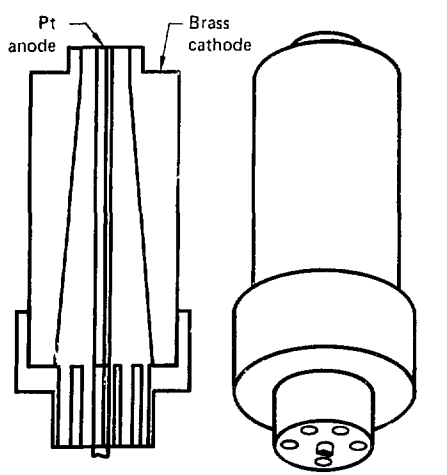

Fig. 4-37. Grain structure in an electroless Au deposit.

porosity were offset by the need for the strike to serve as a catalyst and by the poor surface smoothness caused by the relatively large grain sizes (3 to 5 μm) shown in Fig. 4-37. In addition, in electroless plating—as in electroplating—the solution and microsphere motion must always be maintained to replenish the coating species present in the active plating volume adjacent to the microsphere.

Although electroplating is well developed as an engineering technique, only the gross features of the chemistry of the solutions is understood. These details become very important in the plating of tiny laser fusion targets, whose uniformity and surface finish must be so extremely well controlled. The use of well-developed commercial plating baths has been an aid to producing a consistent plated product. We have found that a commercially available gold-plating solution, BDT-510, offers small grain size (40 to 60 Å), good leveling and high brightness. Figure 4-38 shows a cross section of a gold coating plated on a glass microsphere from BDT-510. We have also plated copper from a commercial pyrophosphate bath.

Author: J. D. Illige
Major Contributors: C. M. Yu, C. W. Jordan, G. R. Korbel, D. J. Lenz, and B. Krenick

References

21. *Laser Program Annual Report—1978*, Lawrence Livermore Laboratory, Livermore, Calif., UCRL-50021-78 (1979), pp. 4-13 to 4-21. (See also "Sputtered High-Atomic-Number Coatings," this section.)

Fig. 4-38. Cross section of electroplated Au 15 μm thick on a 140-μm-diam glass sphere.

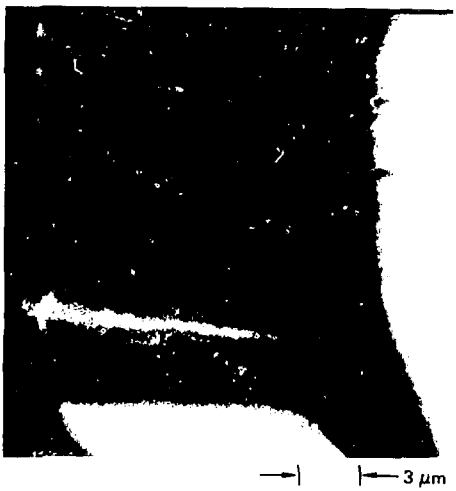

22. J. McDermott, "Plating of Plastics with Metals," Noyes Data Corporation (1974).
23. F. A. Lowenheim, *Electroplating*, (McGraw-Hill, New York, 1978)
24. A. Moyer and D. S. Catlett, "Electrolytic Coating of Microparticles for Laser Fusion Targets," LA6584, Los Alamos Scientific Laboratory publication (1977).

Molecular Beam Levitation During Coating

One attractive possibility for producing the ablative, outer shell of the double-shell targets (Fig. 4-43, next article) is to support them using molecular beam levitation during a coating process. This technique provides a unique means of support for these delicate targets which allows them to rotate freely in a contactless environment while being coated. This method of supporting individual microspheres is also advantageous because it minimizes particulate contamination, which provides nucleation sites for surface defects.[25] Of the various levitation schemes previously proposed (e.g., electrostatic, magnetic, optical, acoustic, etc.), molecular beam levitation appears to be the most easily adaptable to discharge coating techniques.[26,27]

Beams of argon atoms can be formed by flowing argon gas through very small capillary tubes

(10-15 μm diameter) at low pressures.[28] An individual microsphere can be supported on these beams and coated in a plasma.

To understand the physics of this levitation device, we have made careful measurements of flow and pressure of the levitation gas. It is important to identify the gas flow regime in which levitation takes place (viscous or free molecular), because the associated forces are quite different.

The data from one such measurement are shown in the graph in Fig. 4-39, where the rise in chamber pressure, $P_2(t)$, was monitored as a function of different, fixed values of levitator back pressure, P_1, for a 50-μm capillary array. The graph shows that for back pressures less than 1 Torr, the data fall along the same straight line, corresponding to a constant, pressure-independent value for conductance. At a back pressure of 10 Torr, the data deviate significantly, indicating that the conductance of the levitator has changed. Free molecular flow through cylindrical tubes is described by Knudsen's equation,[29] which can be rewritten in the form:

$$P_2(t) = P_1\left[1 - \exp\left(-\frac{C_{mol}}{V}t\right)\right],$$

where V is the volume of the chamber, and C_{mol} is the conductance. Conductance in a cylindrical tube is given by

$$C_{mol} = \frac{8}{3}\frac{r^3}{\ell}\pi\sqrt{\frac{kT}{2M\pi}},$$

and r and ℓ are the tube dimensions. In the case of viscous flow, Poiseuille's equation[30] describes flow through cylindrical tubes, and it can be rewritten in the form:

$$P_2(t) = P_1 \tanh\frac{\phi P_1 t}{2V},$$

where

$$\phi = \frac{\pi r^4}{8\eta\ell}$$

and η is the constant of viscosity for argon. On the basis of these two equations, we infer from the data in Fig. 4-39 that the levitator operates in the free molecular flow regime for back pressures less than 1 Torr with a 50-μm capillary array. A 140- by 5-μm glass microsphere levitates at a back pressure of 100 mTorr using the 50-μm capillary array—well within the free-molecular-flow regime.

Fig. 4-39. Graph showing the rise in chamber pressure, $P_2(t)$, as a function of constant, levitator back pressure, P_1.

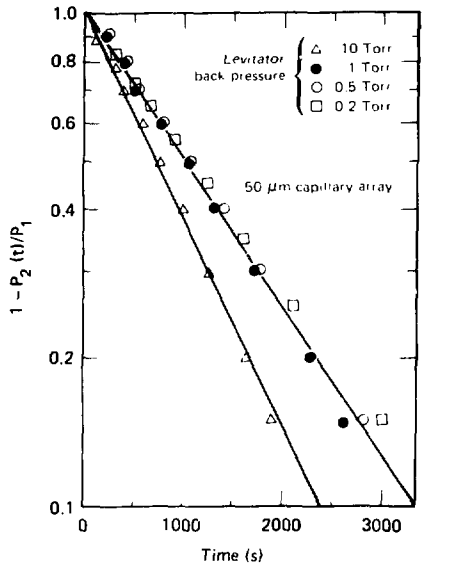

Several problems are associated with molecular beam levitation of a tiny sphere in a coating discharge: stability of the target during coating, electrostatic forces that result from the target charging, and continual adjustment of the levitation flow to compensate for the weight added to the sphere by the coating process.

We have solved the problem of stability by placing a specially beveled, centering ring over the capillary array. The bevel acts as a circular deflector, providing a radially directed force on the microsphere. This force is spring-like in nature, creating a potential minimum at the center of the ring. The levitated microsphere is therefore held very firmly in place at the center of the ring in Fig. 4-40.

A second problem, that of electrostatic force, is especially severe whenever a metallic sphere is levitated above a metallic substrate in a plasma. The

metal sphere charges to the floating potential of the plasma and is consequently attracted to the conducting plane of the levitator by its own image force. This image force attraction can be overcome by producing an opposing field using a d.c.-biased screen placed above the levitated sphere.

In the course of placing thick plastic or other low-Z coatings on spheres, we may have to operate the levitation-coating system for several tens of hours. For this reason, we need a fully automatic levitator-coating system. Schemes for such a system are currently under development. One such scheme consists of imaging the levitated microsphere on a position-sensing detector. Then, as the microsphere lowers because of the increased coating weight, a change in height is detected, and a signal is fed back to the valve that controls the levitator gas flow. This system is shown in Fig. 4-41.

We currently use a manually operated, molecular-beam, levitator-coating system. The function of this system is to evaluate special problems such as coating double-shell targets or multiple-coating targets. Figure 4-42 shows a microsphere that was coated with copper by electroplating, then with C-F plastic coating in the levitator-coating system. Levitation-coating may well be the only alternative for fabricating future generation, multiple shell targets, such as discussed in "Double-Shell Targets" (the next article).

Fig. 4-40. A levitated microsphere is held firmly at the center of the ring by effusive flow from the lip.

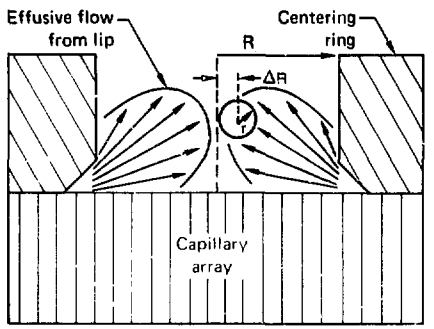

Author: J. K. Crane
Major Contributors: R. D. Smith, G. R. Korbel, and C. W. Jordan

Fig. 4-41. A levitated sphere is imaged on a special detector, producing a signal based on the height of the ball. This signal can then be used to control the flow of levitation gas.

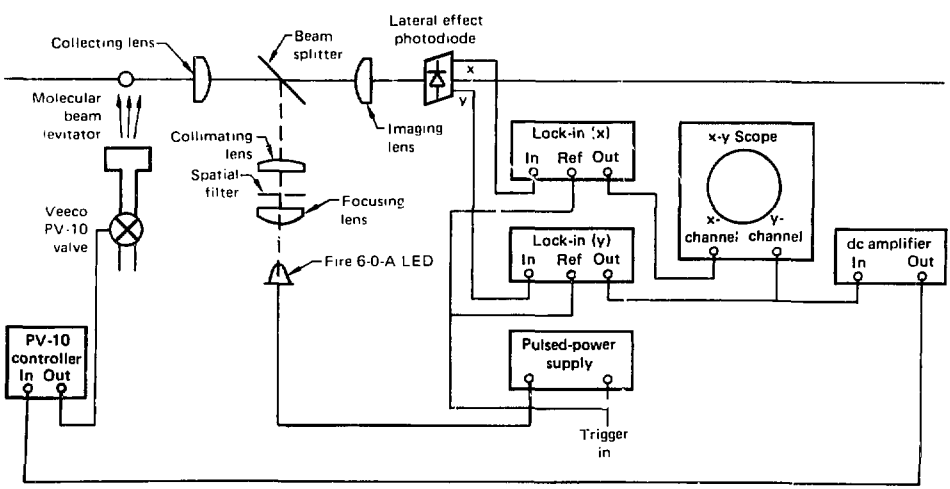

Fig. 4-42. Multiple shell targets produced with the aid of molecular beam levitation: (a) 140-by-5-μm glass sphere coated with 4 μm Cu by electroplating; (b) 140-by-5-μm glass sphere with 1 μm Cu—plus an additional 2 μm CF plastic—coated on levitated sphere.

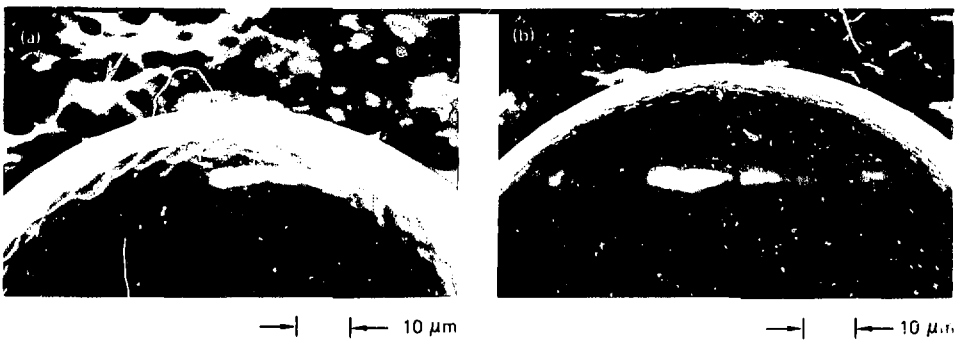

References

25. S. A. Letts and D. W. Myers, "Thick Hydrocarbon Coatings for Laser-Fusion Targets Deposited by Plasma Polymerization," CLEOS ICF 1980. (See also "Hydrocarbon Coatings," in this report.)
26. A. T. Lowe and C. D. Hosford, "Magnetron Sputter Coating of Microspherical Substrates," *J. Vac. Sci. Technol.* **16**, 197 (1979).
27. J. K. Crane, *Molecular Beam Levitation*, Lawrence Livermore Laboratory, Livermore, Calif., UCRL-83379 (1980). (Prepared for submission to the Topical Meeting on Inertial Confinement Fusion, February 26-28, 1980, San Diego, Calif.)
28. C. B. Lucas, "The Production of Intense Atomic Beams," *Vacuum* **23**, 395 (1973).
29. L. I. Maissel and R. Glang, *Handbook of Thin Film Technology* (McGraw-Hill, 1970), p. 1-25.
30. L. I. Maissel and R. Glang, *Handbook of Thin Film Technology* (McGraw-Hill, 1970), p. 1-24.

Double-Shell Targets

One method proposed for obtaining better performance in fusion implosion experiments is the use of a double-shell target design similar to that shown schematically in Fig. 4-43. Double-shell targets make use of the principle of "velocity multiplication": The outer shell is imploded like an ordinary ablatively driven target, accelerating the relatively massive outer shell pusher to a high velocity. When the outer shell pusher strikes the inner tamper, the less massive tamper recoils and implodes with a higher velocity.

In the first versions of these double-shell targets, the outer shell consists of a single layer of CH polymer. In "Machined Hemishells," we describe the micromachining and assembly techniques that have been most successful for producing these targets. In "Alternate Approaches," we describe alternative processes that we hope will improve target quality and reduce fabrication time.

Machined Hemishells

The simplest procedure for fabricating double-shell targets is to assemble two hemispherical shells ("hemishells") around the inner target sphere. So far the most successful method for producing CH hemishells has been machining with an ultraprecision single-point diamond lathe. Two versions of this process have been developed, one at LLL and one at Rockwell International.

The steps in the LLL process are shown in Fig. 4-44: First a copper mandrel is cut with a hemispherical tip whose radius is the desired inner radius of the hemishell. The mandrel is removed from the lathe and a hydrocarbon coating is applied. The mandrel is then replaced in the lathe, and the outer surface of the hemisphere is cut.

In developing this process, we were required to solve a number of difficult machining and materials problems. To ensure that the hemishell wall thickness will be uniform, the mandrel must be repositioned in the lathe with an accuracy better than 0.1 μm. We accomplish this by holding the mandrel in a massive chuck assembly that has been machined to exacting tolerances. This chuck assembly can be replaced in the lathe rapidly with

Fig. 4-43. General double-shell target design with a high-Z, high-density tamper coating on the glass microsphere, and a separate low-Z ablator shell.

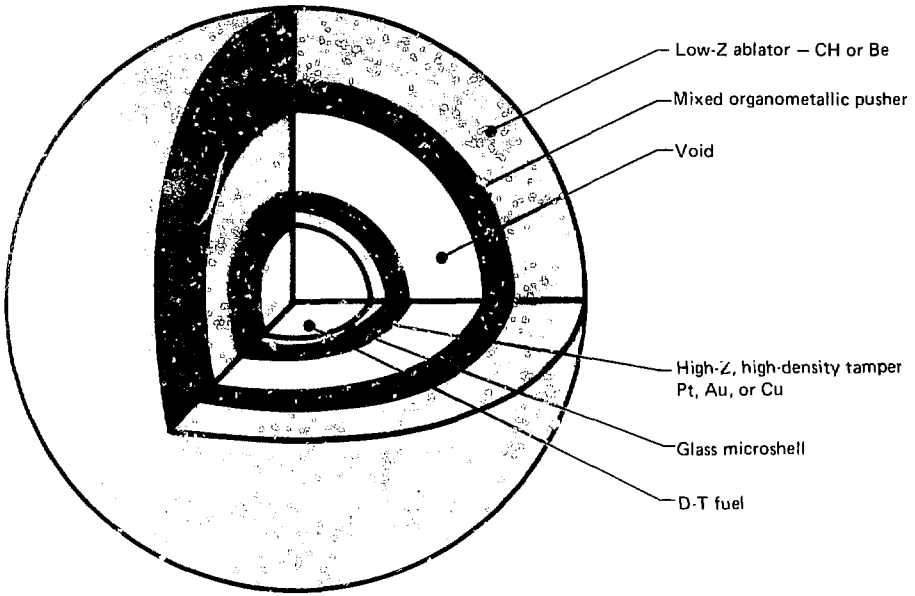

the required accuracy; in addition, it provides a convenient means for holding and transporting the mandrel.

Another problem we encountered was obtaining suitable mandrel material. Ordinary oxygen-free, high-conductivity (OFHC) copper has grain irregularities that cause imperfections in the machined mandrels. To alleviate this problem, we electroplate a layer of high-quality copper onto each mandrel before machining. The machining is done in the fine grained electroplated material, providing a smooth mandrel and, therefore, a smooth inner surface on the hemishells.

One of our most difficult problems was cutting a smooth, flat rim with sharp corners. Conventional diamond-cutting tools have a radius of about 25 μm. These tools tend to push the CH material in front of them, often forming a "lip" of material on the inner edge of the hemishell. This problem was solved by using an extremely sharp diamond tool with a radius of about 0.02 μm.

The hydrocarbon material used for the hemisphere must satisfy several requirements:

- It must not contain any voids or other defects.
- It must be hard enough to be easily machinable but elastic enough that it does not develop cracks.
- The cure cycle must be at less than about 150°C to avoid any distortion of the mandrel and chuck assembly.
- The material must adhere to the mandrel sufficiently that the hemisphere does not come off during machining of the outer surface.

Our best results were obtained with a polybutadiene/vinyl toluene monomer mixture cured with 3% Lupersol 101 peroxide. The polymer cures at 125°C for 16 h. An attractive feature of this material is that by varying the amount of curing agent, we can control the hardness to suit machining demands. We found that a thin coating of polyvinyl alcohol (PVA) over the butadiene improves the curing process. The PVA reduces volatilization of monomer and peroxide and excludes oxygen, which would inhibit polymerization.

Fig. 4-44. Sequence for producing a CH second shell by micromachining: (a) A copper mandrel is machined with a hemispherical tip. (b) The mandrel is coated with CH polymer and remachined to form the outer surface of the hemisphere. The copper mandrel is dissolved away, leaving the hemisphere shown in (c).

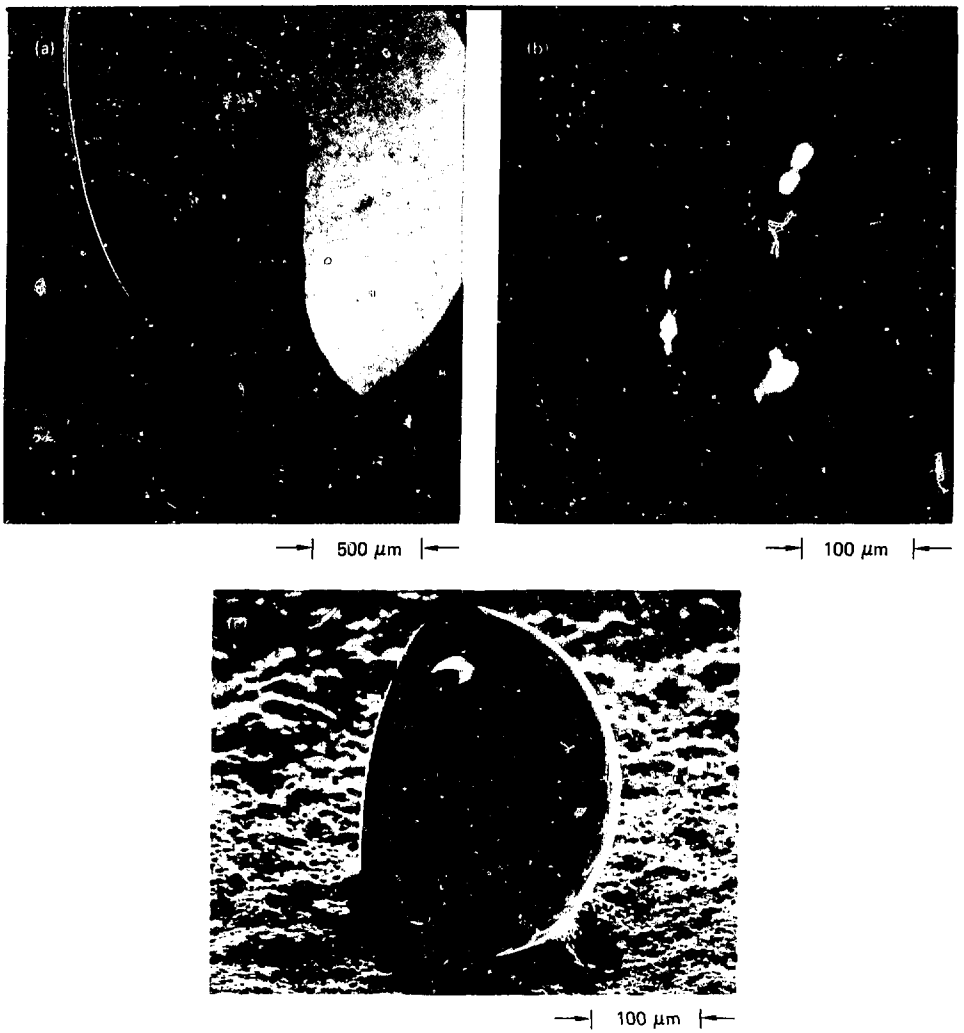

After the CH layer has been applied to the mandrel and the outer surface of the hemisphere has been cut, the machined hemisphere and mandrel are cleaned by ultrasonic agitation in a series of baths. The copper mandrel is dissolved away and the hemishell is cleaned in another sequence of baths. The hemishell is then ready for final inspection and assembly.

Rockwell International has developed an alternate process for making hemishells that provides more rapid processing. The copper mandrel is left in the lathe during the entire machining, coating, and

remachining sequence. Because the mandrel remains in position throughout the process, the problems of repositioning are eliminated. However, the coating processes and materials that can be used are somewhat restricted. The mandrel cannot be placed in a special environment for curing, and the coating must be applied rapidly because the lathe is unavailable while coating is under way. The machining and materials problems encountered in the Rockwell process are similar to those described for the LLL method. The best results have been obtained with a molten polystyrene coating applied to a heated, slowly rotating mandrel. The composition of the polystyrene was carefully chosen to minimize stress caused by thermal shrinkage.

The two methods are complementary. The LLL process allows more flexibility because the mandrel and chuck assembly can be readily moved about for a complicated coating and curing procedure. Also, the lathe is not in use during the coating process. The Rockwell procedure provides more rapid processing and simpler fixturing. Handling is minimized, and there is no need for ultraprecise realignment after coating. Both processes have successfully produced target-quality hemispheres.

Assembly Procedure

A highly skilled operator assembles these double-shell targets under a high-power optical microscope using tiny glass vacuum chucks and precision, hand-operated micromanipulators (see Fig. 4-1).

The inner sphere is placed at the center of a plastic support film stretched over a wire loop. The sphere is covered with a second support film on a smaller wire loop. The two films adhere on contact, trapping the sphere. Severing the first film between the two concentric support rings leaves the sandwiched inner sphere supported by the smaller loop. We apply hydrostatic pressure to force the two films into close contact with the sphere. The CH hemispheres are now bonded around the inner sphere. One hemishell is held in position with a vacuum chuck. Through a fine glass capillary, held in a second manipulator, we extrude a minute bead of fast-curing adhesive on the edge of the hemishell. Then we center the sandwiched inner sphere over the hemisphere and press it onto the adhesive-coated rim. When the adhesive has cured, we repeat the process with the other hemisphere. This procedure requires a great deal of skill. Precise alignment must be maintained, and each sequence must be completed in three to five minutes before the adhesive cures.

The target can be held in position for the laser by using the film sandwich on its wire loop for support. Alternatively, the completed target can be cut out of the support film with a laser machining facility[31] and mounted on a support stalk.

Alternate Approaches

Cleaved Coatings. One alternate approach for making hemishells for multishell targets is to coat a spherical mandrel with hydrocarbon polymer, split the coating into two halves, and then remove the mandrel. The advantages of this method are that many mandrels can be coated simultaneously with the same methods used to deposit CH ablator layers on single-shell targets,[32] and that the two hemispheres will be an exact match for each other, even if the fracture is not smooth or located exactly on the equator. Figure 4-45 shows a coating fractured by this method.

The problem with the method is that it is difficult to propagate a controlled fracture to consistently produce two nearly hemispherical parts with no pieces missing. Also, because neither of the two pieces is ever exactly a hemisphere, problems arise in assembling the target. The two non-hemispherical pieces distort the support films for the inner capsule, causing misalignment. We can overcome this, however, by using a small stalk or several small, hollow plastic spheres for supporting the inner sphere.

Molded Hemishells. Another approach being explored for making hemishells for multishell targets is molding. If successful, such a process would provide reproducible hemishells much faster and more cheaply than precision machining can.

Preparation of a mold cavity for fabrication of these tiny hemispheres is a challenging problem. With the newly developed "zero radius" diamond machining tools, it is possible to cut the male mold section. However there are no tools small enough to allow direct machining of the female half of the mold. We solved this problem by machining a male mandrel from which the female mold section could

Fig. 4-45. An alternate method of producing CH hemispheres for double-shell targets is to coat a glass microsphere with CH and then fracture the coating into two halves. The two halves will match even if the fracture does not lie exactly along the diameter.

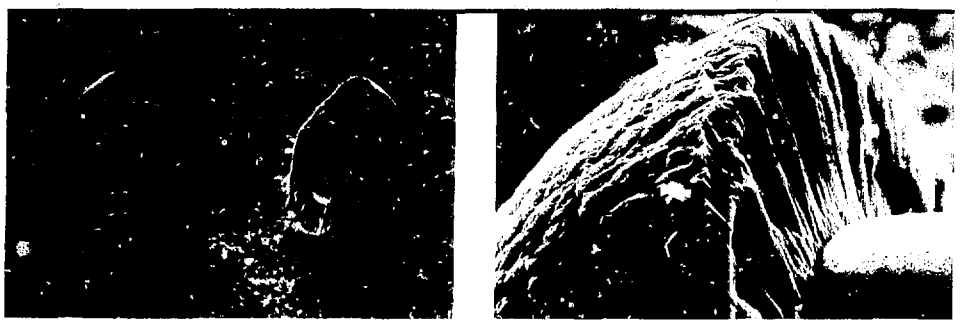

be replicated. By using nickel for the mandrel and electroplating it with copper, we were able to use the differential thermal expansion of the two materials to separate the female mold section from the mandrel. Figure 4-46 shows the mold configuration.

Initial experiments used a room-temperature-cure silicone rubber to avoid damaging the delicate mold. Several hemishells were made with this material, demonstrating the feasibility of the concept. However, when we attempted to polymerize a hydrocarbon monomer (styrene) in the mold, shrinkage and volatilization during cure resulted in voids.

We then tried several epoxies, which are nonvolatile and cure at low temperatures with little shrinkage. Partial cure was achieved, but removing the hemispheres from the mold proved difficult. We found that mold release agents on both the male and female mold sections, along with differential cooling, were required to allow demolding. Scanning-electron microscope photography revealed that great care had to be exercised to prevent surface irregularities that stem from buildup of the mold release agent. Mold cleaning has proved to be quite difficult.

We also tried *thermoforming* in the mold. Preserving the dimensional accuracy of the mold required us to observe an upper temperature limit of 75°C. We formulated a special polystyrene with an unusually low glass-transition temperature, and it appeared to be quite moldable. We obtained improved surfaces by using a preformed, very smooth sheet of polymer, slightly thicker than the ultimate hemishell wall thickness. This sheet was pressed in the mold to form a hemisphere. The first hemispheres made by this process deformed to a partially flattened state in several weeks due to plastic memory effects. Hemispheres made more recently with different thermal treatment appear to be stable. These initial results are promising; however, much additional development is required to establish a viable molding procedure.

Molecular Beam Levitation and Coating. A third possibility for producing the outer shell of the double-shell targets is to assemble a pair of thin hemispheres around the inner capsule, support this preassembly in a levitator (described in "Molecular Beam Levitation During Coating," above), and coat it with CH ablator material. The advantage of this procedure is that the ablator layer contains no seam that would disrupt the symmetry of the implosion. Also, plasma-discharge coating techniques developed for single-shell targets[32] can be used to apply the ablator.

The substrate hemishells are produced by coating a hemispherical mandrel with parylene. In this process, dimer gas is pyrolyzed and gaseous monomer is allowed to condense on the cold mandrel. Polymerization takes place during condensation. This process produces a uniform coating about 5 μm thick. The coated mandrel is placed in an air-bearing spindle lathe and the polymeric coating is cut at its equator using a diamond tool. The mandrel is removed by dissolving in an acid, leaving a

Fig. 4-46. Mold for forming hemispheres: (a) the overall mold configuration (The large shank with "S" curves provides centering of the two mold pieces without binding.); (b) close up of the mold cavity itself; (c) the extremely small inside radius obtained on the male mandrel with "zero radius" diamond machining tools.

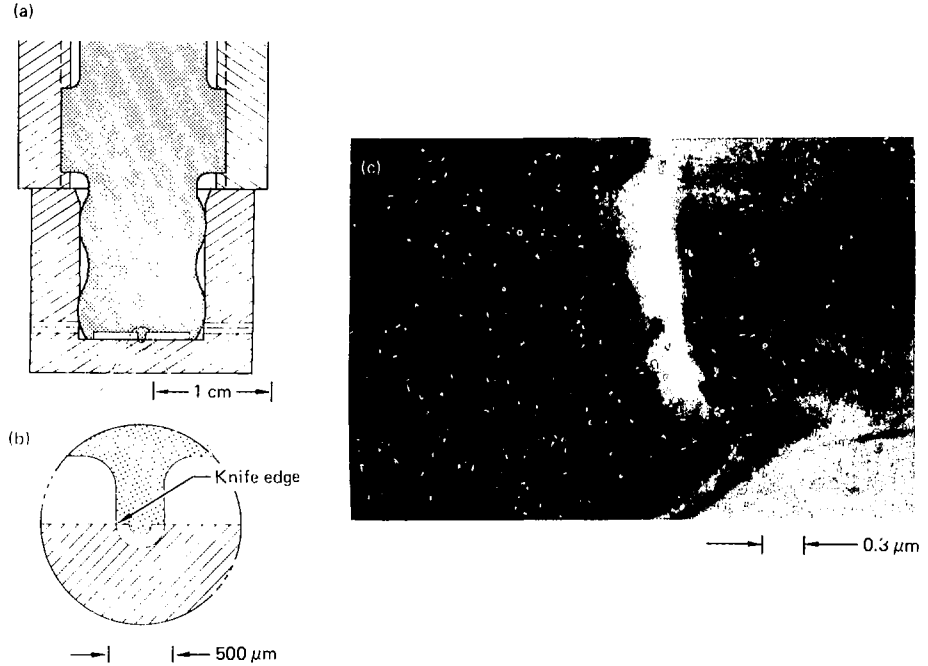

Fig. 4-47. Double-shell target produced by coating CH onto a levitated subassembly of two thin parylene hemispheres. Currently, defects in the subassembly seam produce large defects in the coating. However if these defects can be controlled, this process will provide seamless second shells.

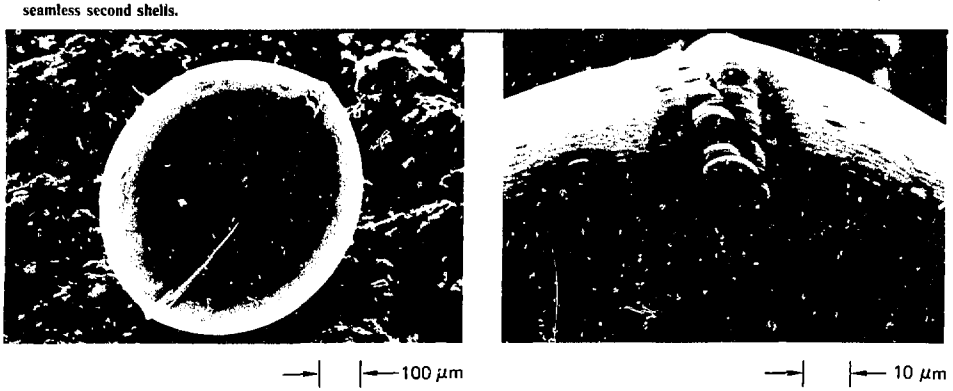

free-standing, thin-wall hemishell. Two of these hemishells are assembled around the inner fuel capsule by the procedure described in the preceding article.

We have successfully levitated and coated several subassemblies using the molecular beam levitator and plasma discharge coating process. Coatings as thick as 50 μm have been achieved. Unfortunately, the seam in the subassembly serves as a nucleation point for defect growth, resulting in a continuous band of thick, rough coating around the target. Figure 4-47 shows an example of a target produced by this technique.

Future work in this area will concentrate on eliminating the defect caused by the seam. With improved assembly procedures, we can reduce the magnitude of the initial defect. By controlling the coating parameters, we can increase the ability of the coating process to "bury" small defects, rather than having these small defects nucleate the growth of larger ones.

Author: B. W. Weinstein
Major Contributors: J. B. Bryan, J. K. Crane, C. W. Hatcher, T. D. Jones, L. L. Lorensen, and W. L. Ramer

References

31. *Laser Program Annual Report—1976*, Lawrence Livermore Laboratory, Livermore, Calif., UCRL-50021-76 (1977), pp. 4-161 to 4-174.
32. W. L. Johnson, S. A. Letts, C. W. Hatcher, L. E. Lorensen, and C. D. Hendricks, "Plasma Polymerization Coating of D-T-Filled Glass Shells for Laser Fusion Targets," in *Plasma Polymerization*, M. Shen and A. T. Bell, Eds., 1979 ACS Symposium Series 108, p. 313-330 (1979). Also "Coatings and Layers," this section.

Analysis and Characterization

Physical, chemical, and structural characterization of targets is necessary both to provide feedback for the continued development of fabrication techniques and for measurement of each target prepared for laser experiments. Development of new target designs requires constant improvement of our measurement capabilities.

In "Production Characterization," we describe the role of characterization in the target production sequence. Most of the measurement techniques used routinely in target production have been described in previous annual reports.[33-35] However the development of new targets, such as those using nontransparent coatings (metals and thick polymer layers) and double-shell designs, has resulted in changes in emphasis and in the development of several new procedures.

In "Development of Automated Characterization Techniques" and "Materials Analysis Developments and Surface Studies," we describe new measurement systems that have been developed to meet the need for increasingly rapid and accurate target characterization, as well as materials analysis.

Fig. 4-48. Fusion target fabrication sequence. Characterization plays a key role: batches of target spheres must be inspected after each fabrication step. The same characterization techniques are also used to select and individually measure each target sphere that is sent to the laser.

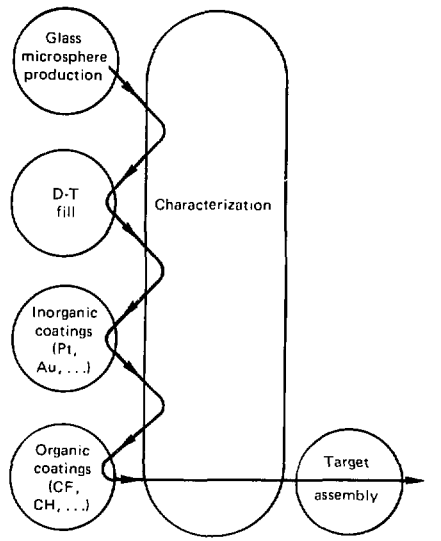

Production Characterization

Figure 4-48 illustrates the typical sequence for target production and characterization. Batches of microspheres must be inspected at each step in the fabrication sequence. We measure the size distribution, thickness and uniformity of each layer, surface finish, and the amount of fuel and tracer gas fill to

Fig. 4-49. Schematic of semiautomated reflection interferometer. The microsphere is rotated under computer control so that the operator systematically scans the entire surface for defects.

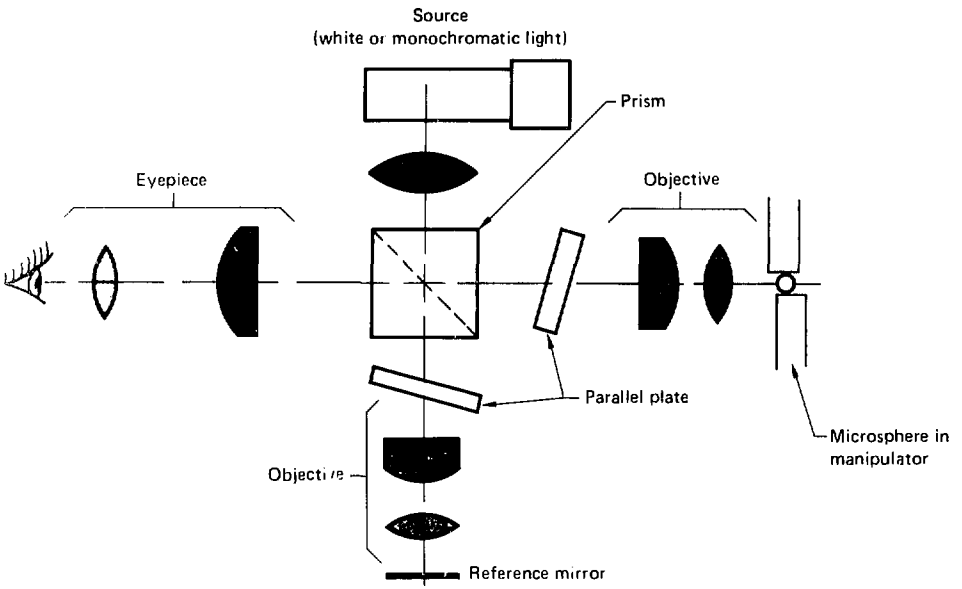

evaluate whether the spheres meet target specifications. We combine these results with measurement of the relevant material parameters such as density, refractive index, chemical composition, crystal structure, and surface contamination to provide feedback about each fabrication process.

Once the batch of spheres has passed through the final fabrication stage, the target-quality spheres must be selected from the batch. This selection is generally a multistep process tailored to each particular batch. Depending on the most prevalent defects and the speed of the various measurement techniques, the order of the sorting steps is chosen to eliminate unacceptable spheres as rapidly as possible. For example, if the batch consists of glass spheres with a narrow wall thickness distribution that received a very uniform, transparent coating, the first sorting process will be interferometric inspection for wall thickness nonuniformities. If, on the other hand, the batch of glass spheres has a broad thickness distribution, the first sorting step will be to look for spheres with the proper wall thickness.

Spheres that have no defects discernible in the batch-sorting processes are removed for individual examination. The thickness of each layer, as well as the amount of D-T fuel and tracer gas fill, is measured. The target sphere is examined in one of our manipulation systems that allow systematic examination of the entire sphere for surface defects and contamination, and measurement of wall thickness variations of transparent targets. As with batch sorting, the order of the measurements is arranged to reject defective spheres as rapidly as possible.

The development of new targets and fabrication processes during the year has resulted in changes in emphasis and the implementation of several new procedures. Microspheres coated with metals or with thick polymer layers (~50 μm) require radiographic measurements to determine wall thickness and uniformity. These radiographic measurements are much slower than optical measure-

Fig. 4-50. The rims of hemispheres for double-shell targets are inspected by interference microscopy and scanning electron microscopy: (a) The interference picture provides accurate measurement of the height of the machine marks (20 to 50 nm) and of a 0.3-μm-high "lip" on the inner rim. (b) the SEM photomicrograph shows detailed defect structure below the limit of optical resolution.

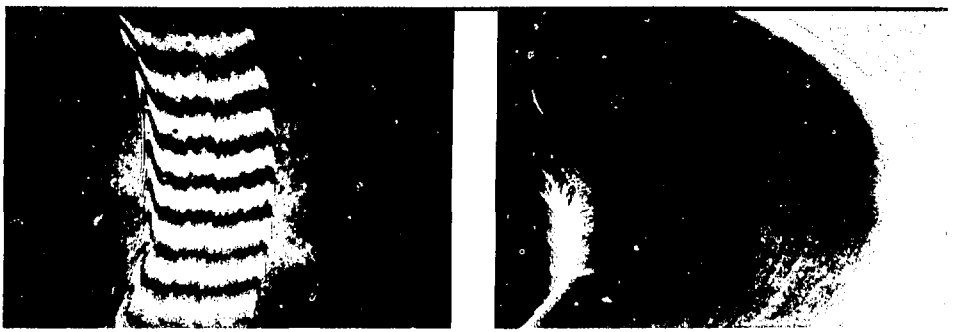

ments, so an optical inspection for surface defects is employed as a screening procedure prior to radiography.

These opaque targets also require an interferometric inspection of the entire surface for small defects that are not measured by radiography. We have modified TOPO I, our semiautomated interferometric inspection system[34,36] to provide these measurements. Figure 4-49 shows a schematic of the modified arrangement. We are able to change from reflection to transmission measurements or back in a few minutes.

Production of hemispheres for multishelled targets has also prompted the development of new measurement procedures. To measure the thickness and refractive index of these hemispheres, we use interferometric techniques similar to those used for measuring glass microspheres.[37,38] However, because of the large wall thickness of these hemispheres, fringe counting under monochromatic light is no longer practical for measuring optical paths. Instead, we use accurate, position-sensitive probes to record the position of the sample relative to the optics of an interference microscope, while a white light interference pattern is used to locate each surface or interface.[35]

A particularly important feature for these hemispheres is the condition of the rim, which must be very flat and smooth to permit accurate assembly. We use reflection interferometry to measure the flatness of the rim within 0.05 μm [Fig. 4-50(a)]. We also use an SEM to obtain high-resolution pictures of the machined surface and to determine the shape of the corners [Fig. 4-50(b)].

Author: B. W. Weinstein
Major Contributors: J. T. Weir, C. M. Mazuch, D. M. Gouveia, T. D. Jones, and V. C. Chen

References

33. *Laser Program Annual Report—1976*, Lawrence Livermore Laboratory, Livermore, Calif., UCRL-50021-76 (1977), pp. 4-161 to 4-174.
34. *Laser Program Annual Report—1977*, Lawrence Livermore Laboratory, Livermore, Calif., UCRL-50021-77 (1978), pp. 5-23 to 5-37.
35. *Laser Program Annual Report—1978*, Lawrence Livermore Laboratory, Livermore, Calif., UCRL 50021-78 (1979), pp. 4-21 to 4-34.
36. B. W. Weinstein, D. T. Willenborg, J. T. Weir, and C. D. Hendricks, "4 Interferometric Measurements of Laser Fusion Targets," presented at the Topical Meeting on Inertial Confinement Fusion, February 7-9, 1978, San Diego, Calif. Also Lawrence Livermore Laboratory, Livermore, Calif., UCRL-80142 (1977).
37. B. W. Weinstein, "White-Light Interferometric Measurement of the Wall Thickness of Hollow Glass Microspheres," *J. Appl. Phys.*, **46**, 5303 (1975).
38. B. W. Weinstein and C. D. Hendricks, "Interferometric Measurement of Laser Fusion Targets," *Appl. Opt.*, **17**, 3641 (1978).

Fig. 4-51. Improvement in resolution from 1977 (a) to 1979 (b). The curve is the approximate upper limit of acceptable defects for a 600-μm-diam, 40-μm-thick target sphere. Our ultimate goal is both surface and integrated-density measurement ($\int \rho dr$) of all unacceptable defects for either transparent or opaque targets.

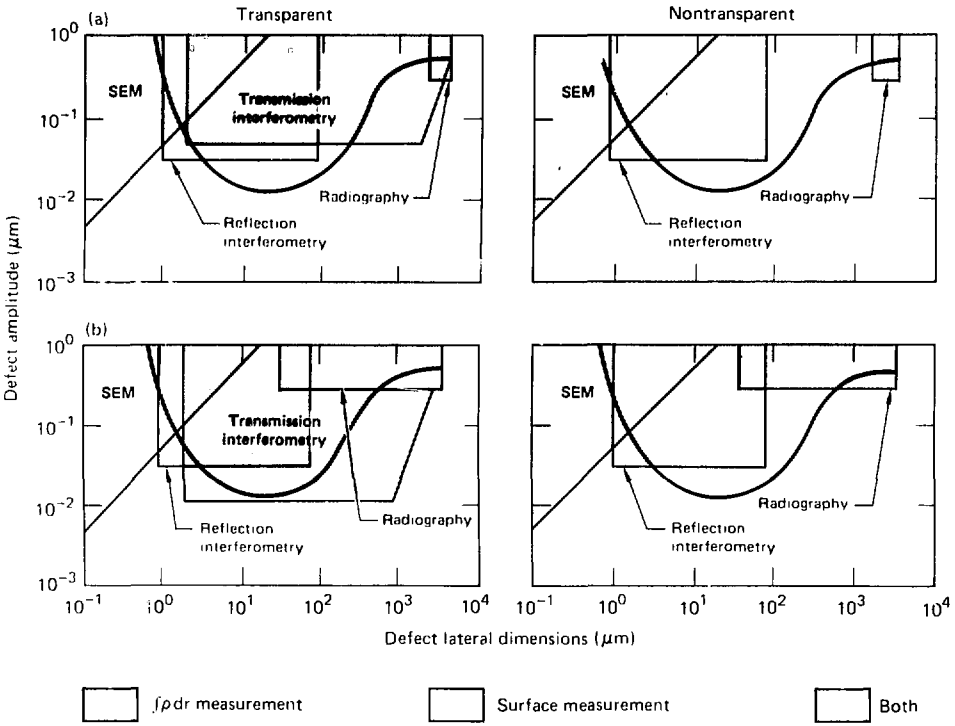

Development of Automated Characterization Techniques

To meet the target characterization needs of laser fusion research, constant improvement is necessary in both the resolution and speed of measurement. Such improvements are, for the most part, gained by automation and on-line data analysis. During the year, we added automated digitization and processing of microradiographic images to our capabilities. This has improved the speed and accuracy of our measurements of nontransparent targets. New x-ray sources improve the quality of the images themselves and reduce the processing time. An automated interferometric measurement and sorting system has been developed that reduces by a factor of five the time required to characterize a batch of transparent microspheres. A fully automated system for mapping the surface of a target with 0.01-μm accuracy is under development. We discuss each of these improvements in detail in this article.

The effect they have made on our target measuring and sorting abilities is shown in Fig. 4-51, which compares the resolution presently available with that of two years ago; and Table 4-1, which shows the improvements in measurement speed that we have achieved in the same time.

Automatic X-ray Image Analysis and Sorting System. We have started the development of a microcomputer-based system to automatically extract measurements of opaque targets from their respective x-ray film images. The microradiographic techniques for recording these x-ray images have

Fig. 4-52. Automatic x-ray image analysis and sorting system (AXIAS). This system provides rapid digitization of microradiograph images and on-line computer analysis. Image processing time is less than one minute (vs turnaround times of a day or more for ordinary digitization and subsequent analysis on a large time-sharing computer).

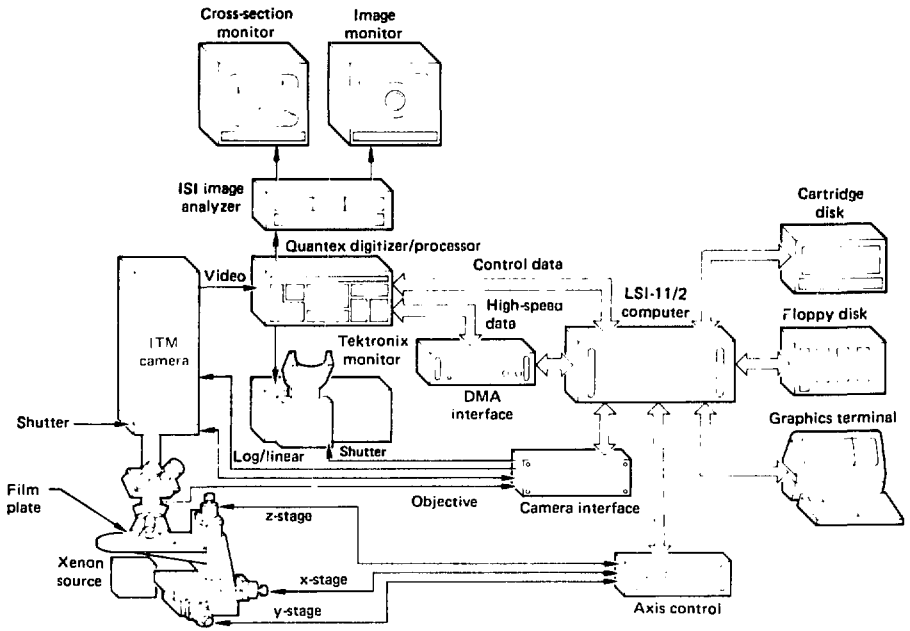

Table 4-1. Improvements in measurement speed from 1977 to 1979. Both the time to measure and sort large numbers of spheres and the time required to completely map a preselected sphere have been reduced by factors of between 5 and 10.

	1977	1979
Transparent targets	5 min	30 s
Opaque targets	15 min	3 min
Thickness map (transparent target)	5 min	1 min
Surface map (transparent or opaque)	–	15 min
Thickness map (opaque target)	–	–

been described in the 1977 and 1978 Laser Annual Reports.[34,35] Previously, the examination of the x-ray images has required manual inspection with an image-splitting microscope for coarse measurements. For precision measurements, microdensitometry and computer analysis on the CDC-7600, a large, timesharing computer system,[39] was required. These techniques are time-consuming and, especially in the latter case, not well suited for large numbers of targets. Thus, we were motivated to develop a rapid and accurate x-ray image measurement system. Specifically, the Automatic X-ray Image Analysis and Sorting (AXIAS) system was designed to accomplish the following:

- Reduce measurement time for 100 spheres to a few hours.
- Provide accuracy comparable to the CDC-7600 analysis.
- Allow several options for speed vs accuracy in order to provide automatic sorting of a large array of images.

This system is shown schematically in Fig. 4-52. A film plate with an x-ray image of an array of targets (see Fig. 4-53) is examined by a television camera through a high-power optical microscope. One individual target image is in view at a time (four ex-

Fig. 4-53. Contact microradiography of an array of fusion targets. In its final form, the AXIAS system will automatically sort through such an array, selecting those of target quality.

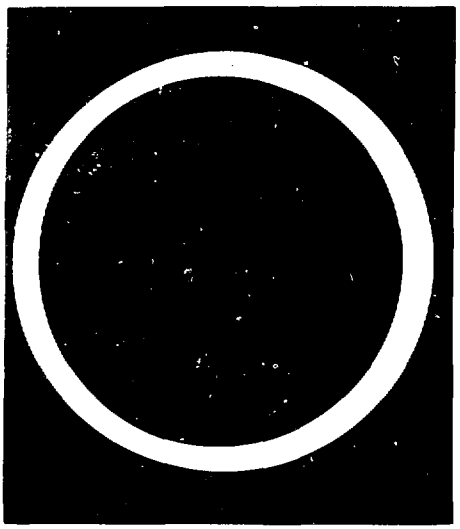

amples are shown in Fig. 4-54). The video image is digitized at high speed into a special-purpose random access memory from which the computer processes the image.

Once the image has been transferred to computer memory, image processing can be used to make precise, rapid measurements. The system currently provides noise-reduced scans and operator-controlled cursors for making measurements. Provisions for high-accuracy, fully-automated measurement and sorting are under development.

The film plate, camera, and microscope system are shown in Fig. 4-55. The camera (manufactured by Image Technology Methods, Inc.) incorporates a logarithmic amplifier to detect optical densities in a linear fashion. By contrast, most commercially available cameras are linear devices, and they detect optical densities in logarithmic fashion. Because of very high signal-to-noise characteristics, the ITM camera can detect an optical density range of 3 (dynamic range of 1000). A very bright xenon source illuminates the image through the microscope, which enables the camera to be set so that shading error and latent image of the vidicon are extremely small. The microscope uses several objectives of different powers to enable examination of different size targets with maximum resolution. The system is capable of viewing target images up to 700 μm in diameter with the lowest magnification. At high magnification, the spatial resolution is less than 0.5 μm.

The video image is digitized by an 8-bit A/D converter in 1 30 s and stored directly into a 512-by-512-by-12-bit random access memory. This digitizer processor (manufactured by Quantex, Inc.) is capable of summing and averaging sequential frames of video images so that the electronic noise is reduced significantly. Shading error from the light source can be subtracted directly from the image, since this error is additive in logarithmic mode.

We have developed a very high speed data channel from the digitizer memory to the DEC LSI-11 2 microcomputer, so that the computer can read or write image data either point by point, line by line (both horizontal and vertical), or block by block. The transfer rate is 5.34 μs pixel (a pixel is a picture element), and an entire image can be transfered in 1.4 s. We have also developed the software to control the video image digitizer processor to control such functions as digitize, frame average, and subtract. This enables the computer to directly and rapidly digitize noise-reduced images in the video processor and then to transfer the images for analysis.

In a measurement, we extract a horizontal cross-sectional scan through the center of the sphere. We determine diameter and wall thickness by locating the edges in the cross-section. Our accuracy in locating these edges is limited by film-grain noise, as shown in Fig. 4-56(a). We can reduce the grain noise by averaging several successive horizontal lines [Fig. 4-56(b)]. However this procedure reduces our resolution because the adjacent lines do not all pass through the center of the sphere and are therefore not identical. We can reduce the grain noise without a loss of resolution by averaging along an arc. This method of averaging, which we refer to as a "wedge scan," is illustrated in Fig. 4-56(c). The resulting cross section,

Fig. 4-54. Microradiograph images of typical fusion targets: (a) glass microsphere, 5 μm thick; (b) thin glass microsphere with a 5-μm-thick platinum coating; (c) 5-μm-thick glass microsphere coated with 50 μm of hydrocarbon polymer; and (d) multilayered target consisting of a 5-μm-thick glass microsphere coated with 15 μm of fluorocarbon polymer and 20 μm of hydrocarbon polymer.

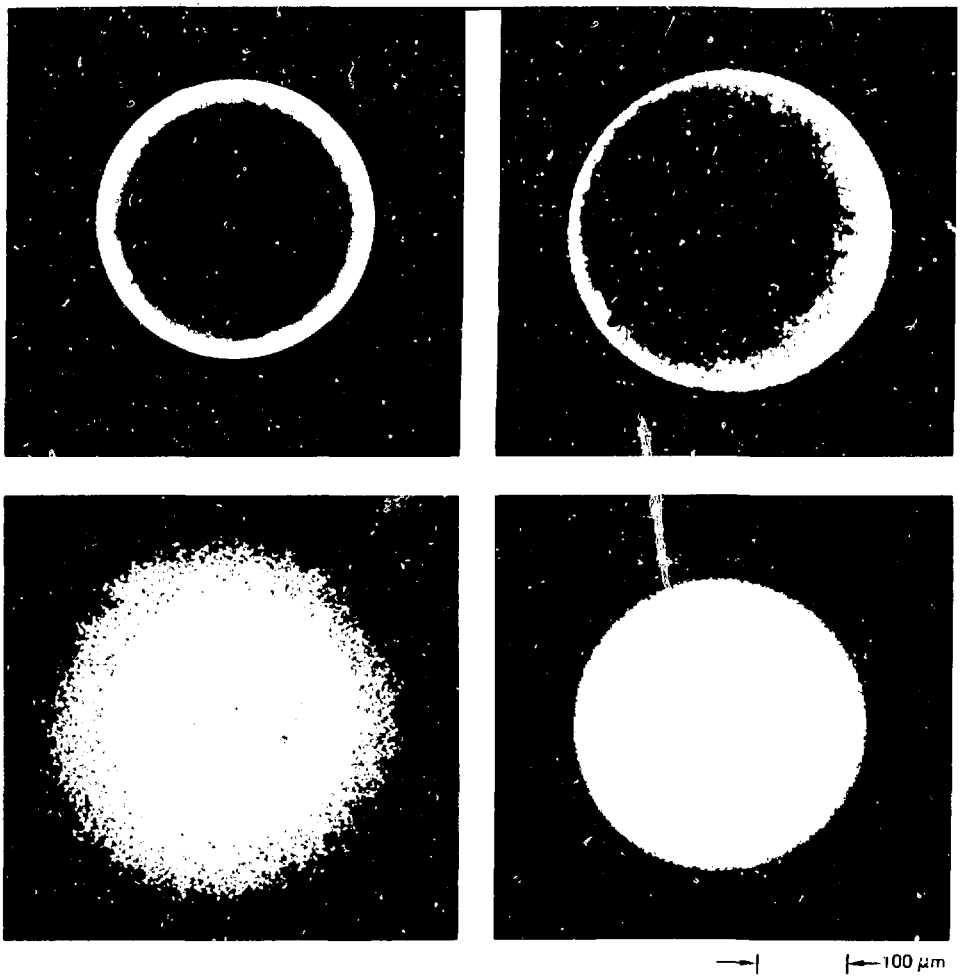

shown in Fig. 4-56(d), is very significantly noise-reduced compared with the unaveraged cross section shown in Fig. 4-56(a). Edge measurements are much more accurate after this averaging.

In the present system, an operator measures thickness by positioning cursors, using fast interactive software. These measurements are usually accurate to 0.5 to 1.0 μm and can be made in a few minutes for each sphere. In the next development stage, the computer will be programmed to recognize these edges and make the measurement automatically, reducing measurement time per sphere to a few seconds. We also plan to implement a least-squares fitting analysis similar to that used

Fig. 4-55. Camera and microscope for the AXIAS system. The film plates in the foreground are placed on the microscope stage for examination and digitization.

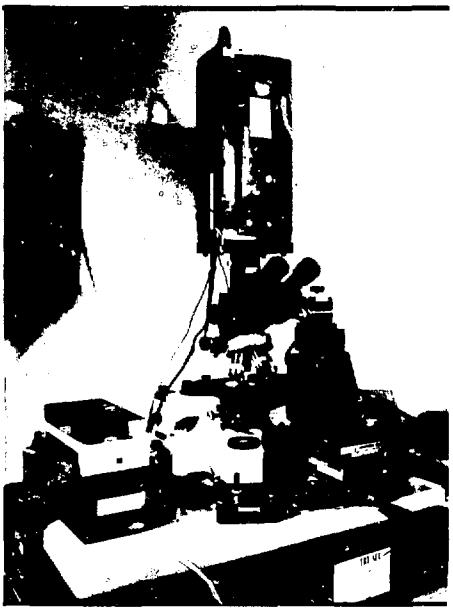

on the CDC-7600.[39] This method has been found accurate to 1.3 μm in diameter measurements, 0.3 μm in wall-thickness measurements, and 0.1 μm in nonconcentricity measurements. In a preliminary test, we have found that this more detailed analysis takes about 70 s on the LSI-11/2 microcomputer. The final development that we have planned at present is to provide totally automated sorting of an array of images. The computer will control the positioning of the film plate and will recognize and measure each target image. Based on a set of criteria provided by the operator, the system will progress from rapid, coarse measurement and selection to more accurate, slower measurement of the better images.

The AXIAS system (Fig. 4-57) is convenient to use, and it provides data that have important implications for microsphere production. One of the main advantages of the AXIAS system is that it is very easily upgraded. Computerized small-scale defect measurement on fusion targets has been demonstrated by Whitman et al.[40] This analysis could be easily implemented on the AXIAS system, using a fast floating-point processor. Another future use of this system would be to directly analyze images as they are recorded by a realtime x-ray system. This type of system would provide even more rapid turnaround in the characterization of opaque targets.

Automated Sphere-Mapping System. During the year, we reached the final design stage of an automated sphere-mapping system (ASM). The ASM system will provide capabilities similar to the TOPO II interferometric mapping system[35,41,42] already in use, but with the significant added ability to map opaque as well as transparent target spheres. In addition, the system optics have been totally redesigned for much simpler operation, and solid-state phase-shift generation has been incorporated to improve measurement speed and accuracy.

The ASM system is diagrammed in Fig. 4-58. A microcomputer will control the sphere-rotator system and will coordinate the rotation with interferometric phase measurement of the surface topography. The topographic data can be stored on a computer disk and displayed in real time on a graphics display. A permanent copy of the graphics display can be made for comparison with other target spheres. The system will be fast enough to map a 150-μm-diam sphere in less than 1 minute with 5-nm amplitude resolution and 1-μm spatial resolution.

The ASM optics consist of an optical phase-shift generator, a phase-shift interferometer, and an optical viewing system. The optical phase-shift generator is diagrammed in Fig. 4-59. A linearly polarized, single-longitudinal-mode HeNe laser is passed through a spatial filter to reduce phase-front distortions. The linearly polarized output beam is passed through a quarter-wave plate and then split by a 50-50 beam splitter. The resulting beams are passed through flint glass acoustooptic modulators that are driven by rf signals with a small, very well defined frequency difference. Typical frequencies are 40 and 39 MHz. Each beam exits the acoustooptic modulator with the frequencies of the first-order diffraction component shifted by the rf driving frequencies. The first-order diffraction components are passed through orthogonal polarizers and then recombined by a beam combiner. In this output

Fig. 4-56. Significant improvements in resolution are achieved by averaging to remove grain noise. Trace (a) is a single line from the digitized image. Identifying the boundaries between different layers is almost impossible. Averaging successive lines [as shown in (b)] reduces noise, but resolution is lost because the scans do not all lie along a diameter of the sphere. A "wedge scan" (c)—in which the data are averaged along arcs—provides the high-resolution, noise-reduced image shown in (d).

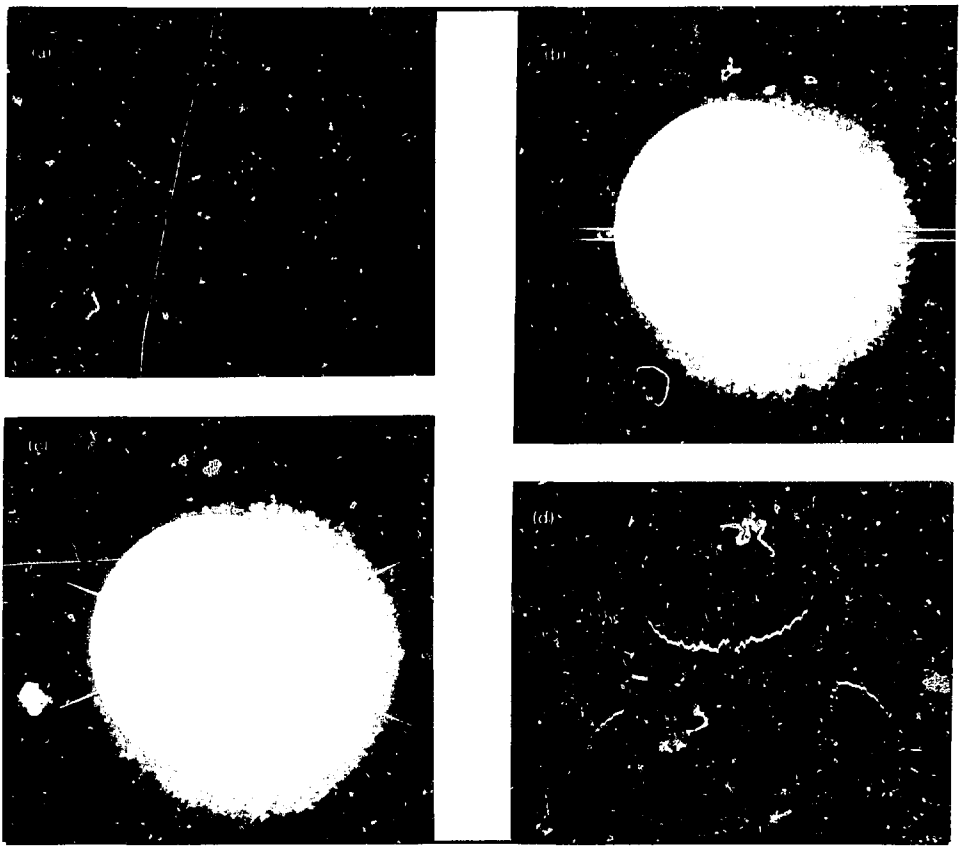

beam, the frequencies of the transverse electromagnetic (te) and transverse magnetic (tm) components differ by 1 MHz. The resulting beam passes through constantly changing states of elliptical polarization at a frequency of 1 MHz. This 1-MHz "rotation" can be detected simply by placing a polarizer at 45° to the te or tm modes, then viewing the resulting 1-MHz intensity variation by using a photodiode detector. Any phase shift between the te and tm polarizations will cause a corresponding shift in the phase of the 1-MHz intensity variation. The ASM interferometer optics [shown in Fig. 4-60(a)] cause the relative phase of the te and tm components to be modulated by path length changes introduced by surface defects on the targets. One polarization component is used as a probe beam, while the other serves as a reference. The probe beam is first focused to a point on the face of the target sphere. The reflected probe beam is then directed around the target onto the reverse side. On the reverse side, the beam is focused towards the center of the target sphere so it strikes the sphere over a fairly broad area and is reflected directly back on itself. After reflection from the

Fig. 4-57. Computer and display hardware for the AXIAS system.

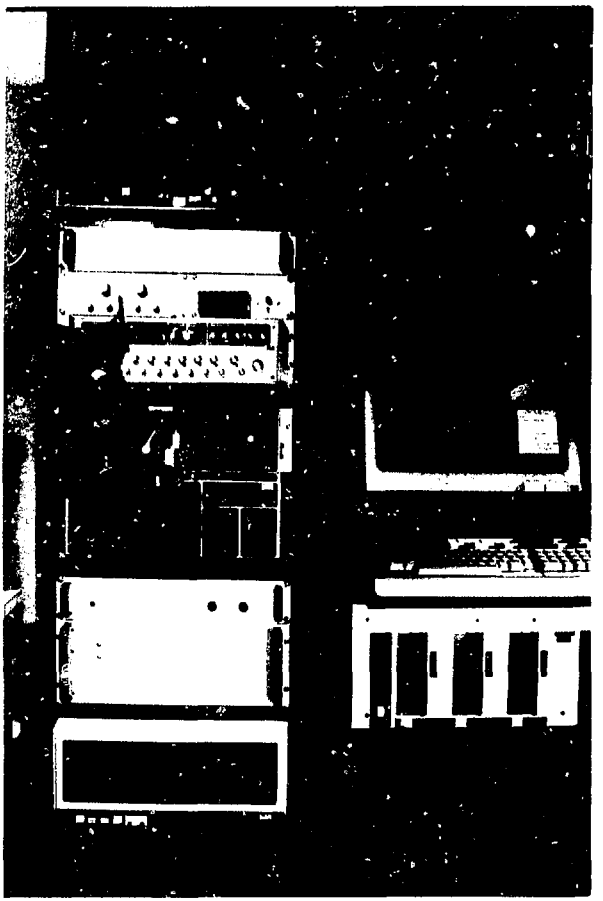

reverse side of the target, the probe beam is recombined with the reference beam.

This output beam is directed through a polarizer at 45° and onto a photodiode detector. As the target sphere is rotated, any changes in diameter, either from nonsphericity or from small surface perturbations on the front surface, will cause a change in optical path of the probe beam and, therefore, a shift in the relative phase of the te and tm components of the output beam. This will, in turn, cause a shift in the phase of the 1-MHz intensity variations seen by the photodiode detector.

An electronic phase detector compares the phase of this output signal with the phase of a reference signal taken directly from the phase-shift generator. This measurement can be very rapid and accurate (easily to 1/100 of a cycle in 1 μs, corresponding to a resolution of better than 5 nm for detecting defects on the target).

The primary advantage of the interferometer arrangement shown in Fig. 4-60(a) is that it is insensitive to changes in position of the target sphere. Small translations of the target along the beam axis cause no change in path for the probe beam. In an ordinary interferometer, where the probe beam is simply focused on one point on the sphere, any motion of the sphere along the beam axis has the same effect as a defect on the surface. Because our interest lies in defect amplitudes of 10 nm, we would need a manipulator able to maintain the sphere position to 10-nm accuracy. (Such a manipulator would be extremely expensive.) With the ASM interferometer, the manipulator is required to maintain the sphere position only within $\sim$1 μm. Another advantage is that we can make minor modifications to the optics of the same system [see Fig. 4-60(b)] to measure wall-thickness variations of transparent spheres.

To measure the surface irregularities of a target in the ASM system, we must place the target between the target rotator tips in accurate coincidence with the optical axis of the measuring branch of the interferometer. To accomplish this, a target-viewing and alignment instrument (shown schematically in Fig. 4-61) has been designed and integrated into the ASM system.

To precisely locate the target in the interferometer, we view the target simultaneously along two orthogonal axes. One viewing arm is coincident

Fig. 4-58. Schematic diagram of the automated surface mapping system. The controlling microcomputer correlates high-speed phase-measurement data from the optics with position data from the target sphere to generate a map of the sphere surface. The apparatus can resolve a defect with an amplitude of 10 nm.

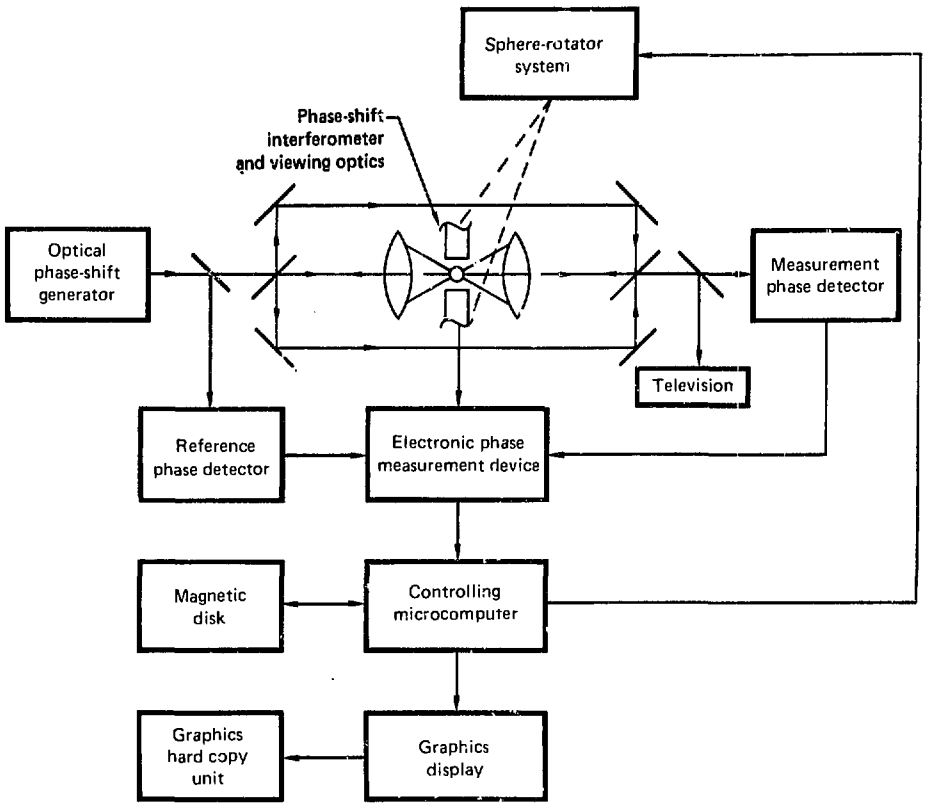

with the interferometer axis and uses the interferometer focusing objective as an imaging objective. The other arm uses an identical objective placed at 90° to the interferometer axis. As Fig. 4-61 shows, the image formed by each of these two objectives is projected onto an alignment reticle. The two targets and reticle images are combined in a central beam splitter so that both images can be seen in the same field of view. The beam-splitter output is directed to both an eyepiece and a TV camera. Once the reticles have been aligned on the interferometer axis, they serve as a reference for positioning the target on the rotator tips. The target is centered on each reference reticle as it is viewed by either the eye piece or TV screen. This system has been tested in an optical bench setup, and the measured resolution limit is 1.5 μm.

Automated Sorting Interferometer. We have automated a white-light Mach-Zehnder interferometer that was originally developed for cryogenic targets[43] to provide quick diameter and thickness measurements of microspheres (Fig. 4-62). This computer-interfaced interference microscope aids the production of glass and transparent coated glass spheres, and it accelerates the presorting of targets.

The Mach–Zehnder interferometer is particularly well suited to this application. The long-working-distance objectives (13 mm, 10-power)

Fig. 4-59. Optical phase-shift generator for the surface-mapping system. This device generates a light beam in which the te and tm components change in relative phase at a frequency of 1 MHz. The resulting beam passes continuously through different states of elliptical polarization.

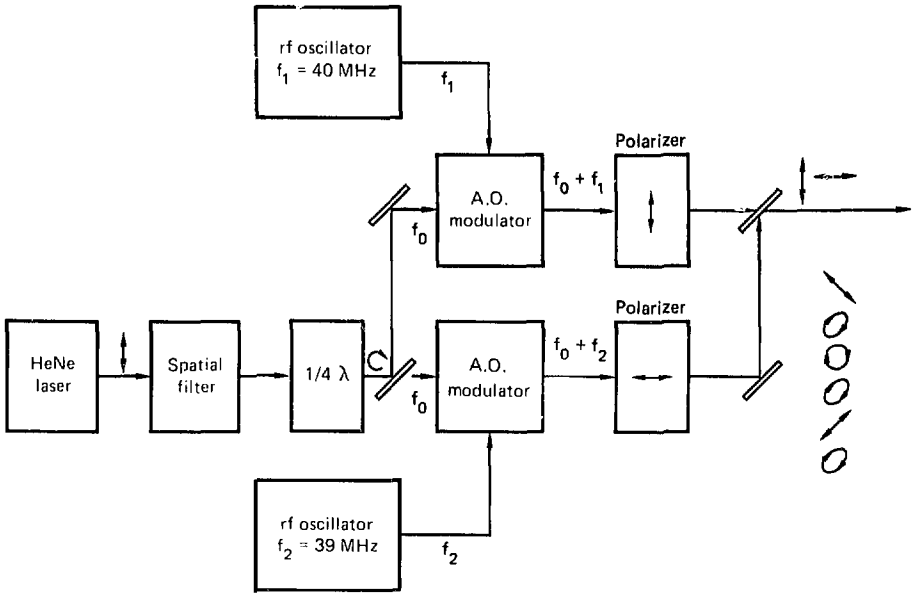

Fig. 4-60. Phase-measurement optics for automated surface mapping. One polarization component is directed onto the sphere, while the other serves as a reference (defects in the sphere cause changes in the optical path of the probe beam, resulting in a relative phase shift between the te and tm components): (a) optics in a reflection mode; (b) changes necessary for a transmission measurement of transparent targets.

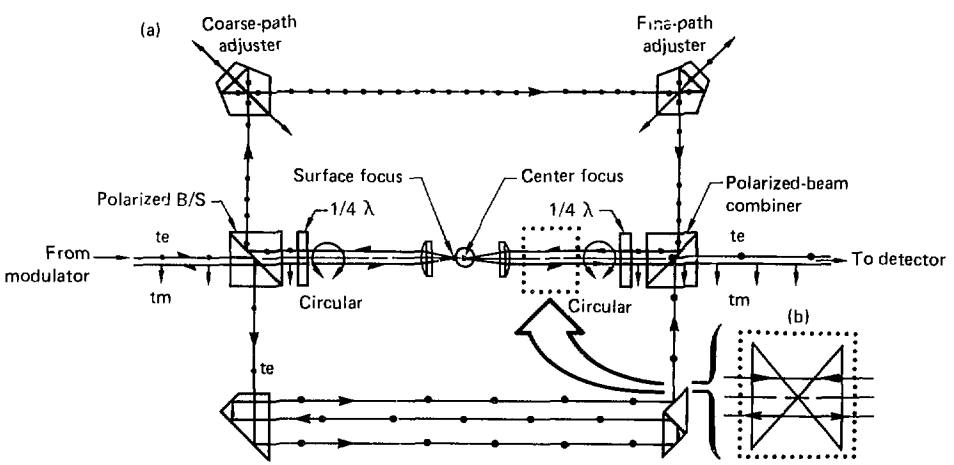

Fig. 4-61. Viewing optics for aligning a target in the automated surface-mapping system. The target is viewed along two orthogonal axes. Each arm includes a reference reticle for target alignment (all dimensions in mm; M = magnification).

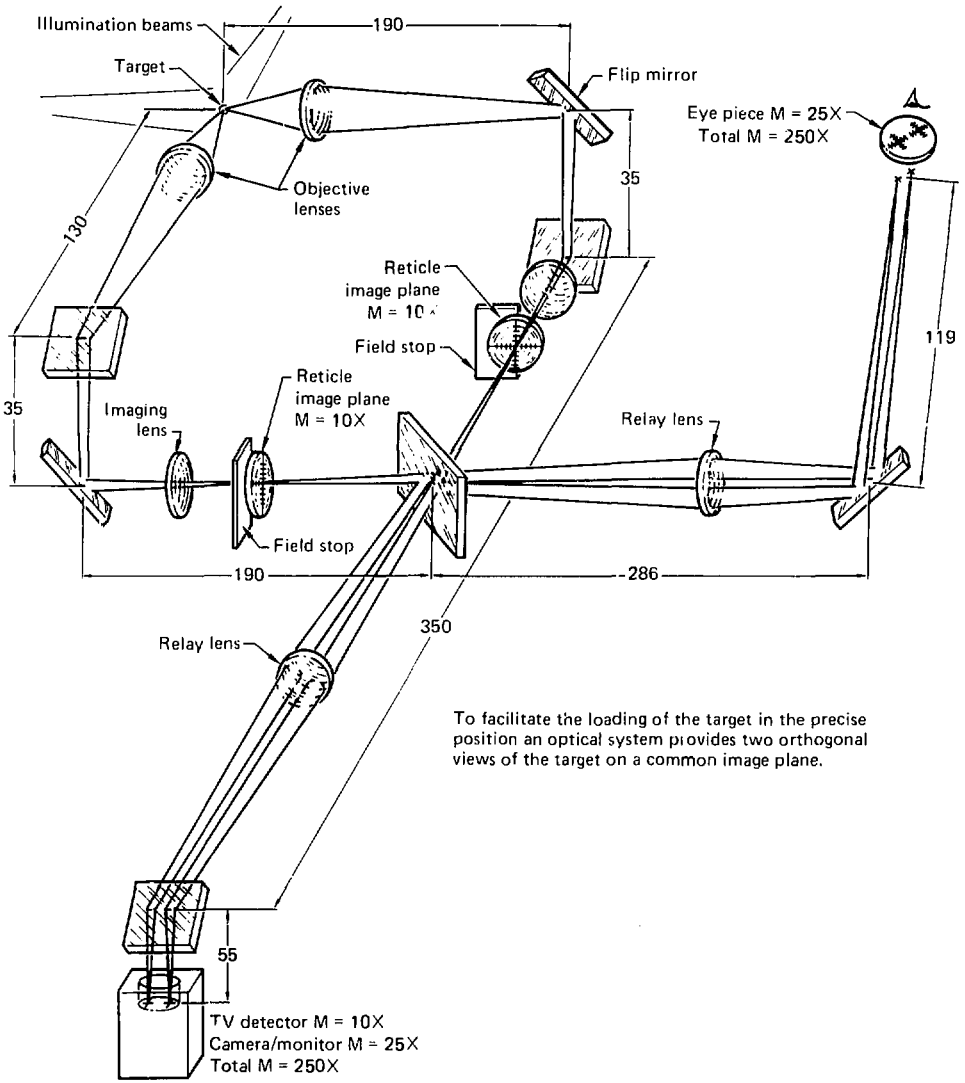

allow ample room for handling the targets and the essentially arbitrary long arm length provides space for phase-measurement hardware.

The spheres to be inspected are placed on a transparent window attached to a motor driven x-y stage. The objective in the stage arm magnifies and focuses the microsphere image, while the compensating objective in the reference arm provides independent control of the interference pattern.

Fig. 4-62. Automated interference microscope diagram. The system automatically measures the thickness of each microsphere selected by the operator. The data are stored in computer memory and can be plotted as histograms of wall thickness and diameter.

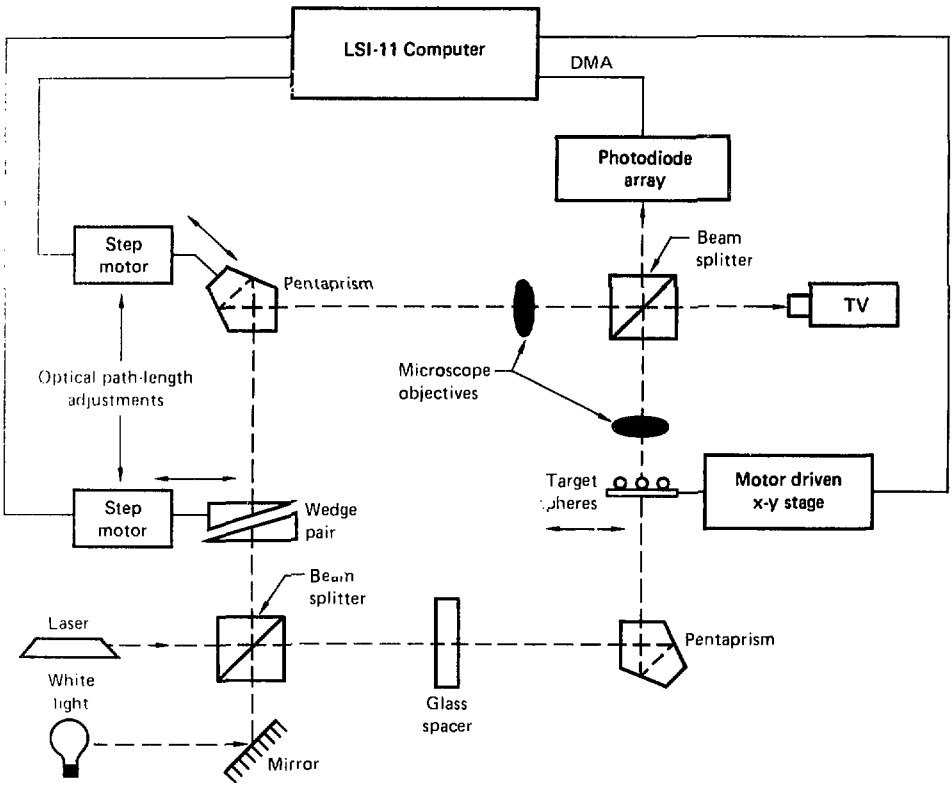

We detect the interference pattern with a photodiode array (a 1024-linear-element Reticon array) interfaced to an LSI-11 computer that also controls path-length adjustments. To measure a sphere, we roughly center the image of the ball over the photo-diode array by viewing a television monitor. The sphere diameter is determined by the number of reticon elements subtended by the sphere image.

Thickness measurements are made by finding the wedge positions for the white-light interference maximum in the background and in the center of the ball.[43] The change in wedge position corresponds to a change in wedge thickness, and from it we can calculate the thickness of the sphere wall. The system is calibrated by counting fringes of laser light vs wedge position. System accuracy is 5 μm for the diameter measurement and 0.1 μm for thickness. Focusing effects in the single-pass Mach–Zehnder interferometer are only half as severe as in our double pass Twyman–Green interferometers. This allows us to measure very thick, high-aspect-ratio targets. We have successfully measured targets with CH coatings of more than 100 μm on a microsphere with an inside diameter of 100 μm.

In addition to measuring target diameter and thickness, the computer also controls the x-y stage

and remembers sphere positions and sizes for later retrieval of the spheres. This, coupled with the short measurement time, enables us to rapidly characterize and sort large batches of spheres.

Authors: J. A. Monjes, R. M. Singleton, B. W. Weinstein, D. L. Willenborg, and R. L. Woerner
Major Contributors: D. E. Perkins, G. T. Reel, and A. L. Richmond

References

39. R. M. Singleton, B. W. Weinstein, and C. D. Hendricks, "X-Ray Measurement of Laser Fusion Targets Using Least-Squares Fitting," *Appl. Opt.* **18**, 4116 (1979).
40. R. L. Whitman, R. H. Day, R. P. Kruger, and D. M. Stupin, "Microradiographs of Laser Fusion Targets 2-D Modeling and Analysis," *Appl. Opt.* **18**, 1266 (1979).
41. D. L. Willenbrog, D. E. Perkins, J. A. Monjes, B. W. Weinstein, G. T. Reel, and A. L. Richmond, "Automatic Transmission Interferometric Mapping of Laser Fusion Targets," presented at the Topical Meeting on Inertial Confinement Fusion, February 26-28, 1980, San Diego, Calif. Also Lawrence Livermore Laboratory, Livermore, Calif., UCRL-83377 (1979).
42. J. A. Monjes, B. W. Weinstein, D. L. Willenborg, and A. L. Richmond, *Microsphere Rotator for Automated Interferometric Target Characterization*, Lawrence Livermore Laboratory, Livermore, Calif., UCRL-83375 (1979).
43. *Laser Program Annual Report—1978*, Lawrence Livermore Laboratory, Livermore, Calif., UCRL-50021-78 (1979), pp. 4-48 to 4-49.

Materials Analysis Developments and Surface Studies

The Surface and Materials Analysis Group concentrated in three new areas this year: optical analysis, surface analysis, and microtopography mapping by SEM.

Optical Microscopy. We have added a Zeiss Axiomat optical microscope to our complement of tools (Fig. 4-63). It is a polarized light instrument capable of magnifications from 10 to 3200× using both transmitted and reflected light, and it is coupled with a temperature-controlled stage for examining objects immersed in index-of-refraction-matching liquids. Figure 4-64 demonstrates the ability of the microscope to see through an immersed, thick plastic-coated ball. The various levels that we have previously observed only by examining a fractured coating on the SEM are now visible, along with defects at the glass-to-plastic interface. Crossed polarizers are used to further enhance detail and locate birefringent particles.

Fig. 4-63. Zeiss Axiomat microscope

Microtopography by SEM. We routinely use an SEM to examine the surface of target material. The simplest way of measuring defect heights is in profile, but this method suffers from two major problems: we can see only a small portion of the surface at one time, and depressions can be obscured by their edges. We are developing a new SEM system that is based on the backscattered-electron technique of Lebiedzik[44] which directly measures height and has a spatial resolution of less than 0.5 μm.

The system is composed of a conventional SEM with solid-state diode detectors for backscattered electrons placed radially about the beam at 0°, 90°, 180°, and 270° to the electron collector. In a plane containing the beam and the sample, these detectors form a 90° cone angle with the sample, as shown in Figs. 4-65 and 4-66. Backscattered electron (BSE) fluxes are strongly dependent on the take-off angle, hence we can use them to determine a local slope by taking differences between the signals seen by two opposing detectors. Because we are using two detector sets, we are able to measure slope in any direction. Since the backscattered signal is also a function of atomic number of the scattering surface, we normalize our data by

$$I_B = \frac{I_0 - I_{180}}{I_0 + I_{180}} ,$$

Fig. 4-64. $CH_{1.3}$ coatings examined in a 1.50 index-of-refraction liquid showing the ability of the optical microscope to see through a thick sample: (a) transmitted light and (b) crossed Polaroids.

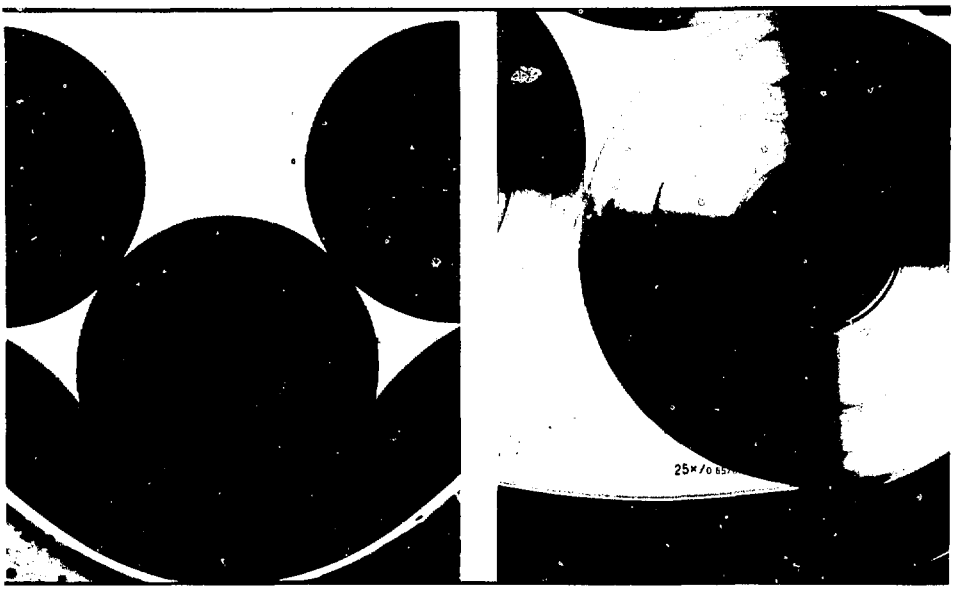

where I_B = the normalized difference of BSE signals,
I_0 = BSE signal from the 0° detector, and
I_{180} = BSE signal from the 180° detector.

The slope, α, of the surface in our geometry is then given by

$$\alpha = \arcsin I_B.$$

This is valid only for slopes up to ±45°.

The computer controlling the SEM receives the slope data and processes them by calculating first a baseline between the detectors and then the height differences, displaying them on a graphics terminal. By scanning a raster pattern over the sample, the computer builds up a topographical image. Figure 4-67 is a topographic plot of aluminum metallization on a silicon wafer; the letters measured 2.5 μm high and are clearly resolved.

Initial tests show good correspondence with both a roughness standard and surface height resolutions on a sphere better than 0.5 μm. Our next steps will be to create microstandards for calibrations at 5000× magnification, establish optimum operating conditions, and evaluate the accuracy of

Fig. 4-65. Orientation of backscattered detectors to the sample for height measurement.

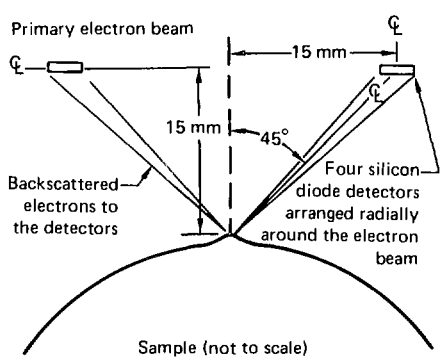

the system on glass- and metal-coated spheres. When complete, the instrument will be used routinely for surface measurements.

Surface Analysis. Analysis of the composition of surfaces is important for solving problems encountered in developing new coating techniques or new high-Z glasses. We have, therefore, installed a Physical Electronics Industries 590, high-resolution scanning Auger spectrometer for surface-composition analysis. (The system is shown in Fig. 4-68.) It has a 0.2-μm spatial resolution and allows studies of the top 5 to 20 $\AA$ of a surface, detecting all elements except hydrogen and helium. Figure 4-69 indicates the mean escape depth of Auger electrons for various elements as a function of the energy of the exciting electron beam. The sensitivity of our instrument is typically 0.5 at.% and a 5-keV argon ion gun is available to make sputter-etch depth profiles. Sample exchange can be made in 15 min through an air-lock system.

The simplest application of Auger spectrometry is for planar surfaces such as metal films and multilayer composites. We have profiled a gold surface cleaned in an oxygen plasma. The result, shown in Fig. 4-70, reveals that the surface contamination layer on regular-production gold discs is less than 30 $\AA$ thick. Most target applications are not this simple and can be severely limited by damage from the exciting electron beam that decomposes SiO_2, evaporates polymers, and causes mobile ions such as Na^+ to move. To minimize the exciting-beam current, we use pulse-counting elec-

Fig. 4-66. Fixture to hold the backscattered electron detector around the electron beam. (The fixture mounts on the final lens of the SEM.)

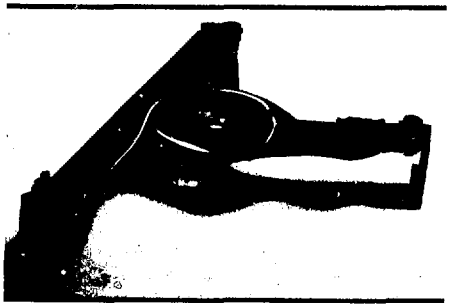

Fig. 4-67. SEM topographical plot of an aluminum metallized silicon wafer. The metallization is 2.5 μm thick. The inset is an SEM picture of the same area.

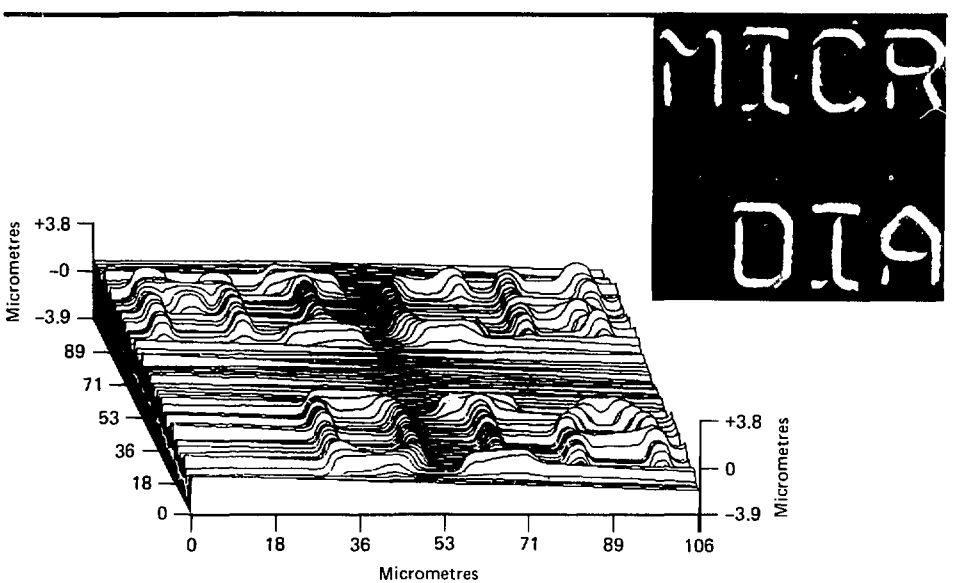

Fig. 4-68. PHI 590 scanning Auger.

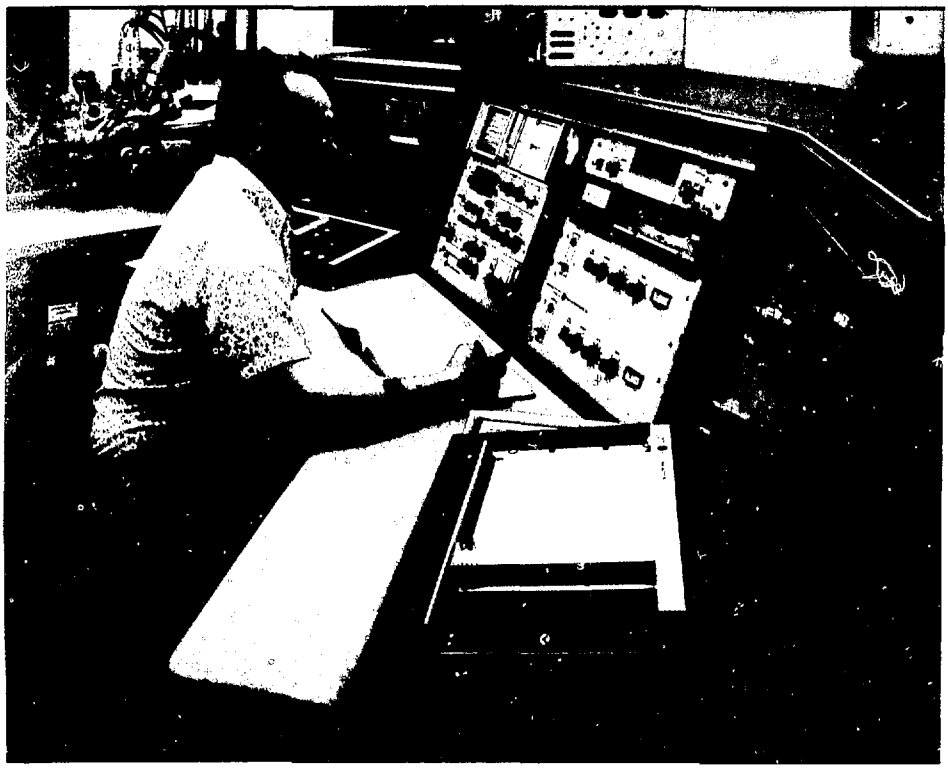

tronics to reduce noise and allow analysis at 1 nA of beam current.

Analysis of metal-coated spheres is more difficult than analysis of planar surfaces. Because the argon-ion etch rate is a function of incidence angle, it varies with location on the sphere. In addition, the etch beam is larger than a single target sphere, hence it sputters substrate material from areas outside the sphere. Some of this material is deposited on the sphere, contaminating the surface and complicating the analysis. To overcome this problem, we use thin silver epoxy as a nonsputtering mounting material. We are also working to calibrate the etch rate as a function of incidence angle so that we can correctly interpret the results of sputtering through the coating on a microsphere. Figure 4-71 shows a 500-Å platinum coating on a glass sphere that is additionally covered by a large number of white particles and holes. Analysis with a 0.2-μm electron beam reveals these particles to be pure platinum and not a contaminant. (Electron-beam-induced x-ray fluorescence cannot make this measurement because the area where x rays are generated is larger than the particles we wish to sample.)

Auger electron energies are affected by the chemical environment of a material. Oxides and carbides appear as peak shifts; they can be used to determine not only the elemental composition of a sample but also to gain information about chemical compounding. Figure 4-72 shows a comparison of beryllium in an oxidized film with pure Be; the shift from BeO to Be is quite evident. Similar effects existing with SiO_2 and PbO are used to analyze glass spheres.

Glass and plastic are the most difficult samples for surface analysis. Not only do they decompose

Fig. 4-69. Mean escape depth of Auger electrons.

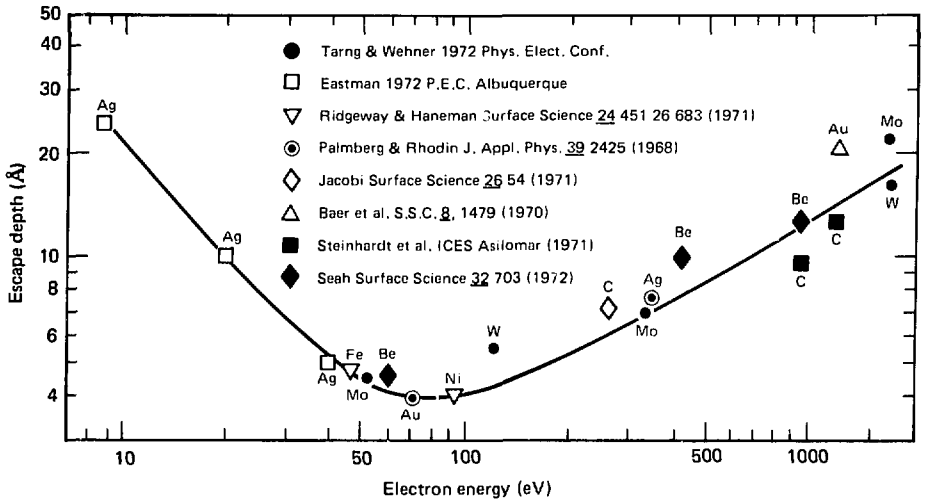

Fig. 4-70. Auger depth profile of an oxygen-plasma-ashed gold surface.

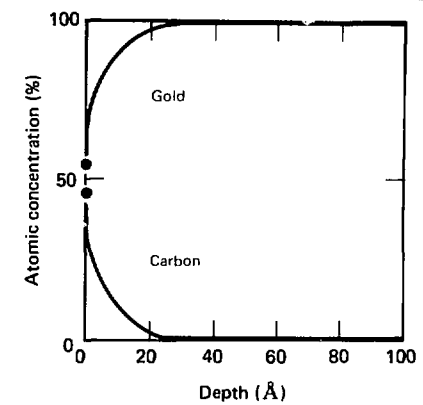

Fig. 4-71. Platinum coating 500 Å thick on a glass sphere. Auger spectroscopy showed the small particles to be composed of pure platinum.

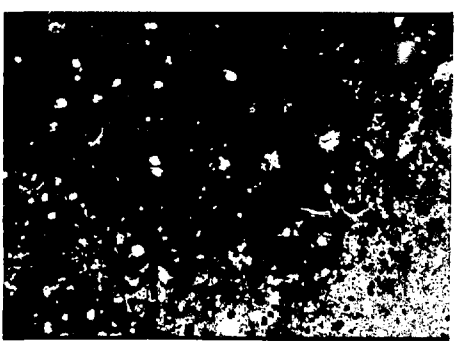

under the electron beam, but they also become charged, causing instabilities in the measured energies. We can, however, reduce charging by lightly gold-coating before analysis, adjusting the electron-beam voltage, and taking data on an edge (see Fig. 4-73). These precautions make analysis of a crystal growing on a glass surface possible. As Fig. 4-74 shows, potassium and sodium form complexes with carbon and nitrogen, which leads to large crystalline defects. Quantitative analysis is not possible on this sample because the intensity of the sodium peak is rapidly reduced by ion migration caused by electron-beam heating and charge implantation. Experiments are underway with lower electron-beam currents and cooler samples that should improve our ability to handle such analyses.

Fig. 4-72. Auger spectra of oxidized and unoxidized beryllium. A pronounced Be shift from BeO to Be is visible.

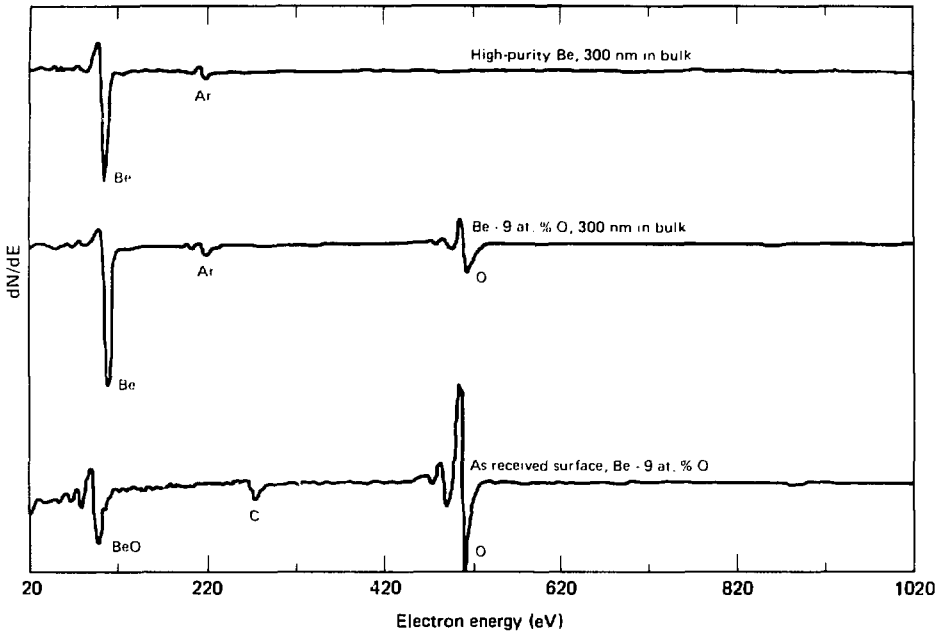

Fig. 4-73. Auger spectrum of a crystal on a glass sphere after sputtering off the surface contamination.

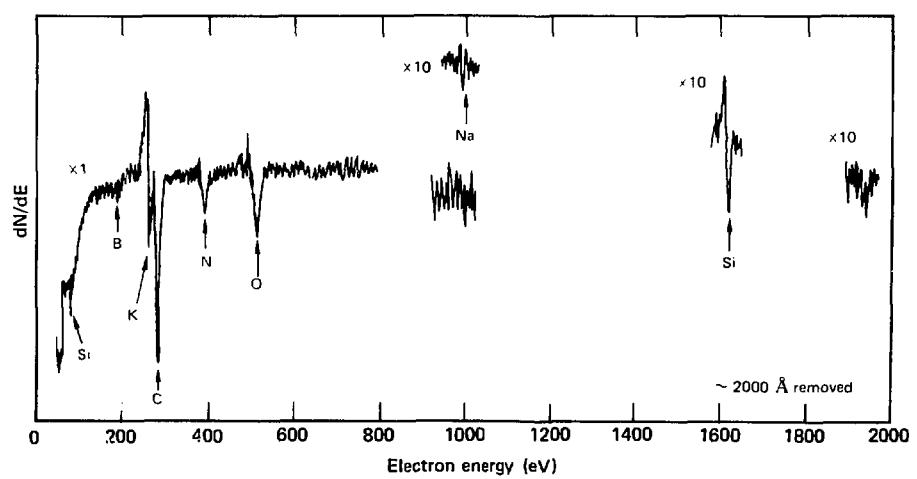

Fig. 4-74. SIMS spectrum of a washed 4-μm-wall glass sphere showing alkali depletion near the surface.

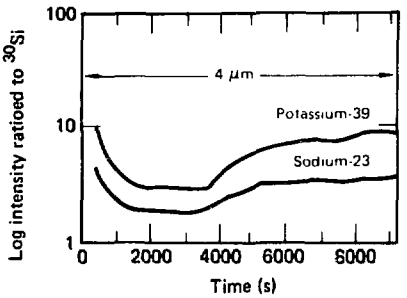

An alternate technique we have used is secondary ion mass spectroscopy (SIMS), which involves similar sputtering of a sample and using a mass spectrometer to detect the ions produced. We are currently adding SIMS to the Auger. Before now we have used an ion-probe mass analyzer at Applied Research Laboratories (Los Angeles) to obtain these data. Figure 4-74 is a SIMS profile that shows surface alkali depletion from washing. The instrument is highly sensitive to alkalis but has only a 200-μm spatial resolution and varies widely in sensitivities to other elements. Combined with Auger spectroscopy, however, SIMS can be used to give accurate materials analysis of a sample.

As with all target fabrication work, surface analysis of spherical samples is more complicated than analysis of planar samples. We are developing new techniques to handle these problems and are further exploring the applications of Auger spectroscopy to glasses and metals.

Author: C. M. Ward
Major Contributors: E. A. Austin, V. K. Chen, D. F. DelGuidice, C. L. McCaffrey, E. A. Pyle, K. L. Montgomery, and D. L. Willenborg

Reference

44. J. Lebiedzick, "An Automatic Topographical Surface Reconstruction in the SEM," *Scanning* **2** (4), 230-237 (1979).

Cryogenic Targets

The Cryogenics Group has responsibility for fabricating targets that contain liquid or solid D-T fuel and for developing the technology for placing these targets for irradiation in the laser target chamber. To these ends, with the participation of NBS, Boulder, we have continued work on a cryogenic pylon (for holding and positioning cryogenic targets) and have built and tested a prototype apparatus for rapidly removing cryogenic shields from around the targets. Additionally, we have initiated investigations of techniques for fabricating more advanced targets with higher fuel fills or more complicated geometries than simple glass fuel microspheres. These techniques involve making, characterizing, and using solid D-T pellets, and using fill tubes in forming thick D-T layers. Finally, we have undertaken an experimental and theoretical analysis of the formation of liquid layers on the interior of glass spheres. Understanding the profiles and stabilities of such layers is important in the continuing development of techniques for producing thin uniform fuel layers in multilayered targets.

Solid Hydrogen Spherical Pellets

Some advanced high-gain target designs are multilayered; one of the layers is a spherical annular space filled with solid D-T fuel, and a central spherical core is also filled with solid D-T[45] (schematically shown in Fig. 4-75). Such targets might be required for power reactors. (See also Fig. 4-83.) Targets with thick annular layers of solid D-T fuel, but with no fuel core, will probably be investigated with the Nova laser facility. Solutions to the problems of forming thick annular fuel layers or voidless cores are difficult. We are investigating two possible approaches: the use of solid spherical fuel pellets, which we discuss here, and the use of fill tubes, which is described in "Condensed D-T Layer Formation," our next article.

Thick annular spaces in multilayered targets might possibly be filled with a "powder" of very small close-packed D-T spheres whose diameters are much less than the thickness of the annulus. Such close packing necessitates uniform sphere size in the powder. We have developed a hydrogen isotope spherical pellet generator to investigate and develop these techniques.

Fig. 4-75. Sector of a spherical inertial confinement fusion target having a central ignitor and an outer solid fuel layer.

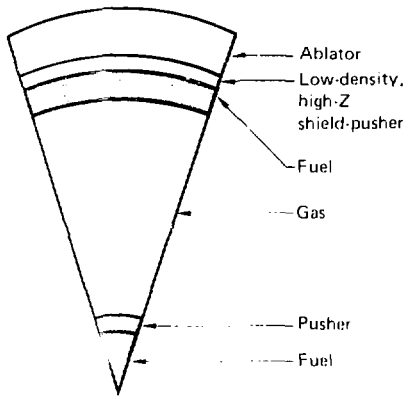

Fig. 4-76. Ten-μm hydrogen powder generator.

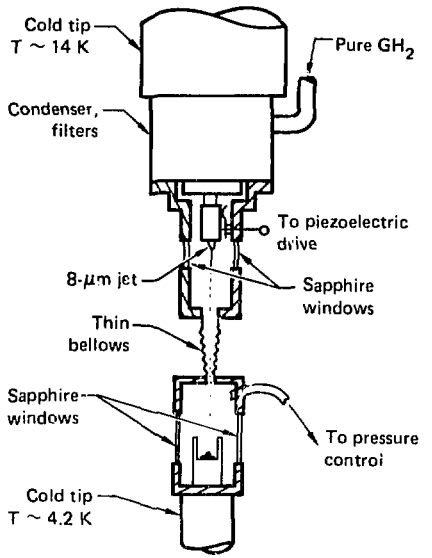

Our pelle generator is similar to that developed by Foste Kim, Turnbull, and Hendricks;[46] it s pictured sc ematically in Fig. 4-76. We liquefy purified hydrogen gas (to avoid the complications of handling D at this stage of our development) in a cryogenic ndenser held on the cold end of a closed-cycle chum refrigerator. The liquefied hydrogen is then forced through an 8-μm-i.d. drawn-glass nozzle to form a jet. We are able to break the je into a stream of uniform liquid spheres, each about 10 μm in diameter, by driving the piezoelectric ceramic that surrounds the nozzle at a frequency of several hundred kHz. By maintaining the to al pressure in the jet chamber just below the tri e point pressure (54 Torr for H_2), we are able to cause the liquid drops to rapidly evaporate, th eby cooling and freezing. The frozen pellets will u mately fall into a cryogenic catcher maintained n r 4 K. For this reason, we use helium gas to maint the jet-chamber pressure, since H_2 would rapidl freeze out on the cold catcher and weld the pellets together.

In order to produce a stable liquid hydrogen jet, we found that the condenser temperature must be maintained between 14 and 18 K. Temperature is controlled by feeding back an electrical signal from a sensor to a heater on the refrigerator. It is also necessary to maintain the jet pressure above 150 Torr absolute and the jet chamber pressure between 51 and 54 Torr. We have designed and constructed a gas control system for purifying control gases and maintaining control pressures.

Maintaining the jet issue from the nozzle requires a good deal of attention to keeping small particles or freezable gas contaminants out of the system. We therefore included liquid nitrogen traps in the gas and vacuum lines of the gas control system. Additionally, the nozzle system was cleaned and assembled in a class 100 clean room. With these precautions, we were able to repeatedly produce a liquid-hydrogen jet, and break up the jet by means of the piezoelectric transducer. Our optics, however, were incapable of resolving individual spheres.

In the future, we plan to upgrade our optics for single-particle characterization. In addition, we will incorporate the cryogenic catcher into the system to begin characterizing the aggregate character of the solid hydrogen powder, and study its close-packing properties. We will also increase the pellet diameters for possible use as central cores.

Author: T. P. Bernat
Major Contributors: B. H. Ives, B. C. Borman, and K. Kim (University of Illinois)

Fig. 4-77. Schematic of apparatus to study cryogenic fill tubes and fuel layers.

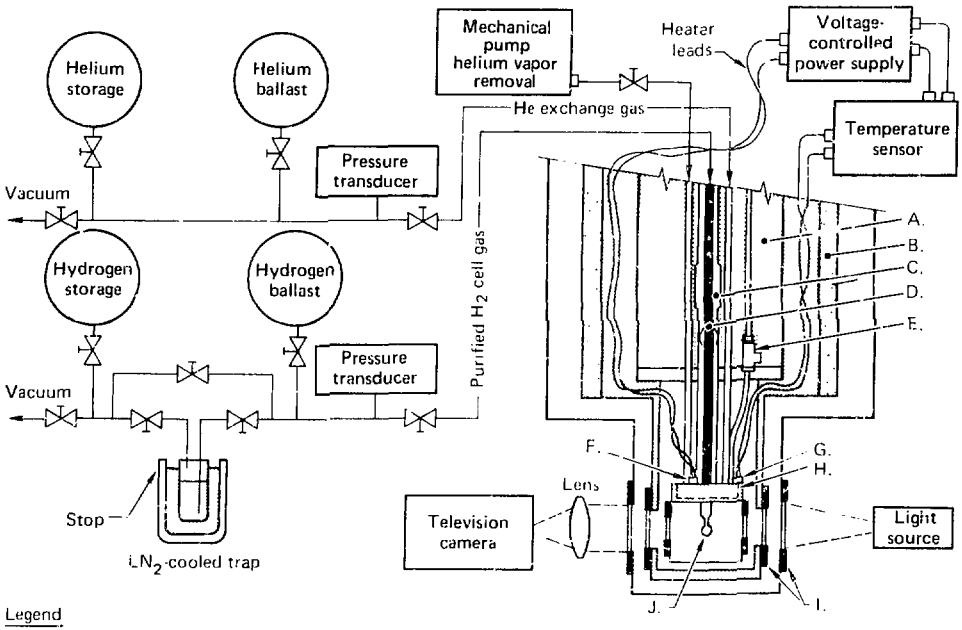

References

45. *Laser Program Annual Report—1977*, Lawrence Livermore Laboratory, Livermore, Calif., UCRL-50021-77 (1978), pp. 4-15 to 4-19.
46. C. A. Foster, K. Kim, R. J. Turnbull, and C. D. Hendricks, *Rev. Sci. Inst.* **48**, 625 (1977).

Condensed D-T Layer Formation

Layers Condensed Through Fill Tubes. A second method for forming thick, uniform annular layers in the multilayer target shown in Fig. 4-75 is to condense the fuel through a small fill tube. Such an approach overcomes the problem of the very high pressure fills necessary if the fuel were diffused into the glass ball prior to assembly and freezing. It also allows the fuel to be introduced at a convenient time in target assembly. It is difficult to imagine how such a target would be assembled without this or a similar method of introducing the fuel. Fill tubes might also be useful in void-free filling of central cores.

Our objectives in this study are fourfold:

- To explore the size limitations imposed on fill tubes by mechanical, materials, and fabrication problems.
- To learn techniques for keeping fill tubes clear during fuel fill.
- To study the formation and structure of thick layers solidified from the gas phase.
- To form void-free central cores.

To achieve these objectives, we have designed and built a variable-temperature cryostat capable of temperature control in the range 2 to 40 K, shown schematically in Fig. 4-77. Temperature is controlled by balancing the liquid-helium flow—from the main reservoir to the cold flange through which it circulates—against electrical heating produced in a resistance wire wound on the cold flange. We

determine liquid helium flow by setting a needle valve that is located in the helium reservoir. Temperature is sensed by a germanium resistance thermometer and the sensing signal is fed back to the heater. The optical windows on the cryogenic shield and chamber are made of sapphire, a material with good thermal conductivity that absorbs well in the infrared. As a result, room-temperature radiation is prevented from reaching the experimental cell in the interior of the chamber. Helium exchange-gas provides thermal contact between the cell and chamber. We can introduce purified hydrogen gas into the cell through a vacuum-jacketed capillary that passes through the liquid-helium reservoir. The gas is cooled by radiation and by "spring fingers" that establish thermal transfer between the lower portion of the capillary and the liquid helium. To prevent frozen hydrogen from clogging the capillary, which would result from the temperature of liquid helium (4.2 K; hydrogen freezes below 14 K), we have installed a coaxial, small-radius heating wire through the capillary. An additional heater below the cold flange prevents clogging in the vicinity of the flange. By controlling the two heaters, we can control the temperature of the hydrogen gas entering the cell.

As in any cryogenic experiment, all gases introduced to the cryostat must be free of dirt or condensible impurities. We have constructed the gas-handling system shown in Fig. 4-77 to provide purified helium and hydrogen. We can accurately measure and control gas pressures and can control the hydrogen-gas flow rate.

At the time of this writing, we are just beginning experiments on layering and voidless filling of a 1-mm-diam blown glass sphere equipped with a 0.05-mm-i.d. fill tube. After gaining experience, we will attempt smaller spheres with approximately 0.01-mm-diam fill tubes. Techniques must be developed for fabricating these spheres for cryogenic survival.

Liquid Layers on the Interior of Glass Spheres. Current laser fusion targets are fabricated by coating diffusion-filled glass microspheres with one or more layers of organic or inorganic materials. The glass microspheres range in size from 70 to 140 μm and contain only a few tens of micrograms of D-T fuel. When such targets are cryogenic, the D-T fuel must form a thin, uniform, and smooth layer on the interior of the glass microsphere. These layers will typically be 1 to 5 μm thick. Two methods for forming the frozen D-T layers on the interior of uncoated glass microspheres developed at LLL and LASL[47] are reviewed in the 1977 Annual Report.[48] Briefly, the irregular frozen fuel in a cooled target is vaporized by a heat pulse and allowed to rapidly refreeze on the interior wall directly from the vapor. This process consistently produces uniform frozen layers in these thin-walled (1 to 3 μm) bare-glass microspheres. The process relies on rapid heat removal from the vaporized D-T fuel, however, and the extrapolation of the technique to layered, multishelled targets may not be simple. It is possible that in thickly coated targets the D-T fuel may condense out as a liquid that then freezes. While liquid, the fuel can flow to the bottom of the sphere. In designing specifically cryogenic ICF targets, it is important to know the time- and temperature-dependence of the *liquid* D-T layer structure, so that the maximum permissible time in the liquid state for a given layer sphericity can be determined. The thermal transfer properties of the target must then be designed to ensure that the liquid freezes before this time. With this consideration in mind, we have begun a theoretical and experimental study of the structure and stability of the liquid fuel layer. Our objective is to develop a quantitative, physical model of such layers that will be useful in the design of cryogenic ICF targets.

An earlier, unpublished liquid layer model by Campbell[49] is available, but it is not consistent with the behavior of D_2 liquid layers observed in recent experiments performed at the University of Illinois.[50] In these experiments (see Fig. 4-78), initial liquefaction produced—far above the triple point—a uniform layer of D_2 that became thicker as the temperature of the sphere was decreased [Fig. 4-78(b)]. Below a certain temperature, the thick layer became unstable and collapsed into a localized droplet that collected at the coldest part of the sphere when a temperature gradient was present [Fig. 4-78(c)], and in the bottom of the sphere when the temperature was uniform. Increasing the temperature reversed the behavior of the liquid layer. Similar behavior has been observed by other groups.[51]

The thick uniform layer of Fig. 4-78(b) is not indicated by Campbell's model, which instead predicts that the layers will always have zero

Fig. 4-78. Mach-Zehnder interferograms of liquid D_2 behavior formed from 186 standard atmospheres in a 200-by-7-μm glass sphere: (a) no D_2 liquefied; (b) a 5-μm uniform liquid layer far above the triple point; and (c) collapse of the layer to a droplet.

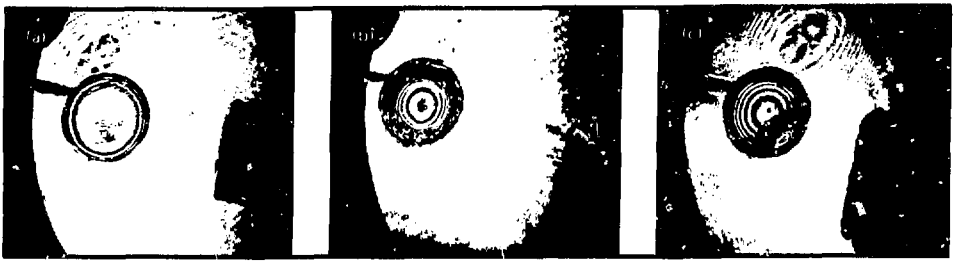

thickness at the top of the sphere. Campbell's model includes the cohesive attraction between the liquid and glass substrate only through the contact angle. The model therefore precludes continuous liquid layers, since, in such layers, contact angle plays no role.

We include the cohesive substrate attraction explicitly in our model, because it is the only possible explanation for the continuous layer of Fig. 4-78(b). We express the attraction through a surface potential of the form $V(r) = -\alpha r^{-3}$, where α is a constant that depends on the substrate material, and r is the distance between the substrate and the liquid surface. This form for the potential is taken from the literature that deals with superfluid helium film profiles on vertical substrates.[52] A simple balance between this surface potential and gravitational energy, with no bulk surface tension effects included (appropriate near the critical point), yields the liquid profile on the interior of a sphere shown in Fig. 4-79. To continue this work, we will include the effects of surface tension, which must lead to the collapse of the layer to a spheroid [Fig. 4-78(c)]. We will also study the dynamics of the instability leading to the collapse in order to predict the collapse time scale.

Fig. 4-79. Thickness profile of liquid D_2 layer on the interior of a sphere for a substrate potential $V(r) = -\alpha r^{-3}$. The layer is thickest at the bottom (180 degrees down from vertical).

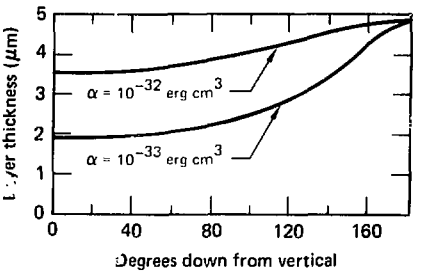

Author: T. P. Bernat
Major Contributors: K. Kim (University of Illinois) and B. H. Ives

References

47. J. R. Miller, "A New Method for Producing Cryogenic Laser Fusion Targets," *Adv. in Cryog. Eng.* **23**. K. D. Timmerhaus, ed. (Plenum Press, New York, 1978), p. 669.
48. *Laser Program Annual Report—1977*, Lawrence Livermore Laboratory, Livermore, Calif., UCRL-50021-77 (1978), pp. 5-38 to 5-42.
49. L. J. Campbell, Los Alamos Scientific Laboratory, unpublished (1974).
50. K. Kim and H. Rieger (both University of Illinois), unpublished; H. Rieger, "Fabrication and Characterization of Cryogenic Targets for Inertial Confinement Fusion," Master's Thesis, University of Illinois at Urbana Champaign (1979, unpublished).
51. T. M. Henderson, R. B. Jacobs, D. L. Musinski, R. J. Simms and G. H. Wattke, in *Adv. in Cryog. Eng.*, 4, New York, Plenum Press, 1976, p. 690; E. R. Grilly, *ibid.*, p. 676.
52. K. R. Atkins, "Helium Films," *Progress in Low Temperature Physics, Vol. IV.*, North Holland, 1957.

Cryogenic Target Systems for Shiva Target Chamber

Cryogenic Pylon. In our last Annual Report,[53] we described a cryogenic pylon that has two capabilities: It can transport a cryogenic target containing a preformed solid D-T layer to the Shiva target chamber. It can also form the layer after the target has been placed in the target chamber at

room temperature. Workers at the NBS, Boulder, have tested several components of this original design.

They tested the electromagnetic repulsion system for the cryogenic target cell at room temperature. The electromagnet inductance was 150 μH; discharging a 160-μF capacitor at 435 V through it gave an average velocity of 259 cm/s to a 5.1-gm aluminum test cell with a 3.6-cm-diam repulsion flange. The flange would thus clear the target in less than 10 ms. This performance should be improved with both the repulsion coil and the cell at cryogenic temperatures.

NBS, Boulder, also tested the thermal performance of the intermediate cryogenic shield surrounding the target cell (the shield is held to the cryogenic tip of the pylon by gold-plated spring fingers). When the point of attachment of the shield to the pylon was at 20 K, the temperature of the shield itself was 40 K at the attachment and 43 K at the free end. No other cryogenic shields were located between the test shield and the room-temperature vacuum chamber, hence the heat load was due only to radiation. We conclude that this intermediate shield arrangement would be more than adequate in actual use.

As we discussed in the last Annual Report,[53] firing any cryogenic target in the target chamber will require the presence of a cold, light, rapidly removable cryogenic cell to maintain the target during final positioning. The cell must be coolable to 10 K or below while exposed to ambient radiation and must contain several hundred millitorr of helium exchange gas to provide thermal contact with the target. The exchange-gas escape rate must be less than 0.5 sccm to prevent the target chamber pressure from rising above 10^{-5} Torr. The cell seal must, however, be completely dry and easily broken to ensure that the target will not be jarred by the cell removal.

We are developing two types of seal, which are shown schematically in Fig. 4-80. The lapped flange seal can be cooled by a cryogenic target mount flange. Thermal transport occurs by means of the exchange gas in the seal gap, whose pressure must be high enough to fall in the gas-conduction regime. For a 10-μm gap, this pressure is above 300 mTorr. In preliminary work, we measured a leakage rate of

Fig. 4-80. Schematic of two types of dry, demountable cryogenic seals: (a) lapped flange and (b) layered mylar.

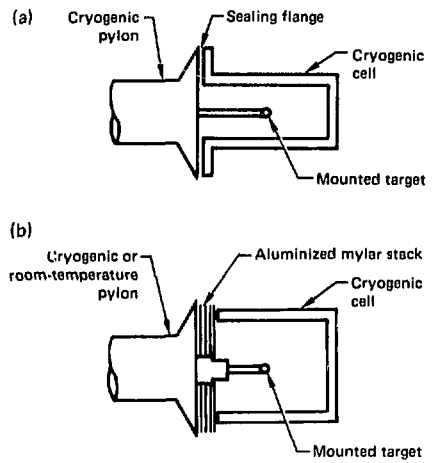

0.3 sccm with a cell-gas pressure of about 500 mTorr. The mounting flange was cooled to about 10 K, and the 12.7-mm-o.d., 6.4-mm-i.d. flange was lapped to a 10-μm finish. These results are encouraging. However, the lowest cell temperature obtained was only about 20 K, and in continuing work we will attempt to lower this by surface treatment of the mating flanges and by varying the geometry of these surfaces.

The layered mylar seal provides thermal insulation, as well as a slow leak rate, and it is very useful when the target is held by the sort of noncryogenic pylons that are currently in use. In this case, all cooling must be provided by the cell retraction mechanism. In our initial tests with the cell around 20 K the seal leak rate was 0.018 sccm with 1 Torr cell pressure. The leak rate for this type of seal is a strong function of sealing force.

We have embarked on the development of a cell retractor capable of providing cryogenic cooling to the target and target cell. Figure 4-81 is a schematic of the cryogenic cell retractor. The cryogenic shield is thermally coupled to the cold finger by helium exchange gas. This shield can act as the freezing cell for a target held on a room temperature mount using the layered mylar seal (as shown in Fig. 4-81). Alternatively, it can completely

Fig. 4-81. Schematic of cryogenic retractor. Cooling is provided by the retractor mechanism, but can also be supplied by the target mount.

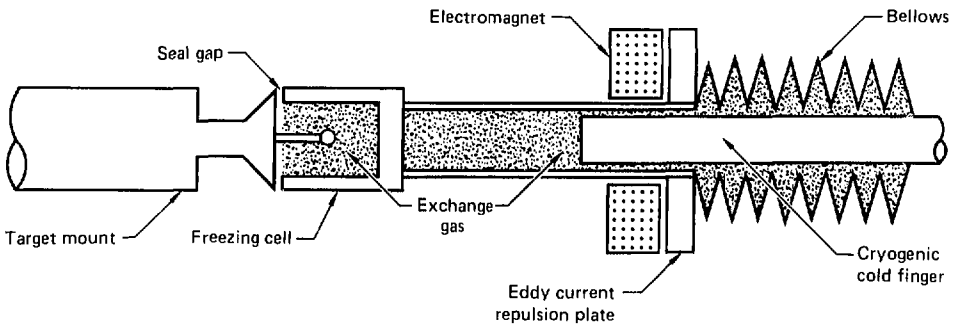

cover a freezing cell held on a cryogenic mount, thereby providing a radiation shield. Again, NBS, Boulder, is participating in this work.

In operation, the cryogenic shield is retracted from the target by an electromagnet repulsion scheme similar to that used in our earlier retractor designs. The retraction compresses the soft bellows, which thus absorbs the impulse from the electromagnet. NBS, Boulder measured the shield position vs time of a prototype retractor at room temperature to obtain the results shown in Fig. 4-82. The time for the tip of the shield to clear a target is about 3 ms. This is at least an order of magnitude faster than the fuel vaporization time in the presence of radiation.

They have also tested the thermal performance of the prototype and found that the cryogenic shield varied between 5 and 14 K, depending on radiant heat load, even though the temperature of the thin sleeve around the cold finger remained at 5 K. This indicates a high thermal resistance between the shield and the sleeve, probably due to an epoxy layer between the two. We will replace this epoxy with a more highly thermal conductive solder.

Author: T. P. Bernat
Major Contributors: R. O. Voth (NBS, Boulder) and D. H. Roberts

Reference

53. *Laser Program Annual Report—1978*, Lawrence Livermore Laboratory, Livermore, Calif., UCRL-50021-78 (1979), pp. 4-45 to 4-49.

Fig. 4-82. Results of tests on cryogenic retractor: shield position vs time measured in air at ambient temperatures.

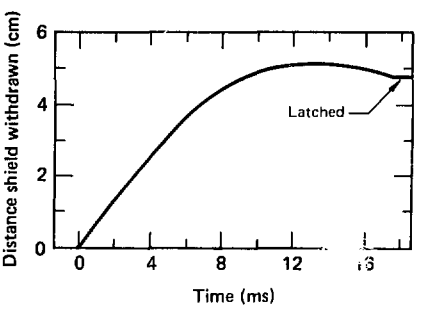

High-Rate Manipulation, Coating, and Transport in Target Production

To continue our efforts of 1977 and 1978, we are studying the problem of producing ICF targets at a high rate and with high yield in a "Target Factory." In this article, we evaluate possible incorporation into a factory scenario of some techniques developed or perfected during 1979; we also attempt to identify areas where further work is needed. In what follows, we consider the double-shelled target shown in Fig. 4-83, which has many of the features

Fig. 4-83. The target designed for use in reactors is a 0.5-cm-diam nested multishell (each shell consists of several layers.)

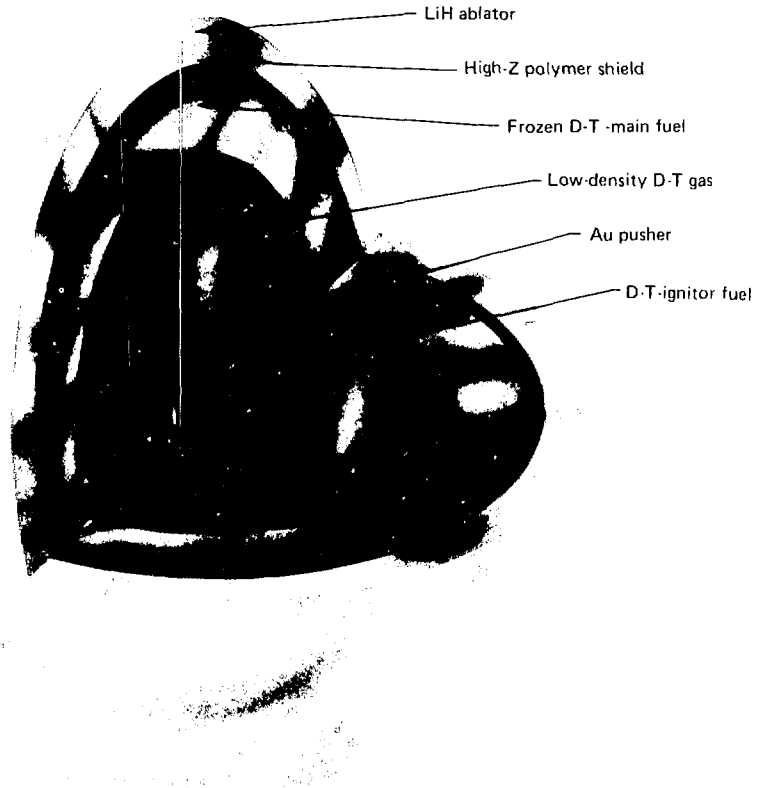

of the complex, reactor-type targets that must be built in an automated processing system. We discuss the production processes for each of the elements of the target in the paragraphs that follow.

Inner Shell Production. The inner high-Z, high-density coated shell can be fabricated with a system that we outlined in the 1977 Annual Report.[54] In this system, the shells are formed, filled, characterized, and coated with several layers.

Second Shell Production. The technique of nesting a multilayer shell inside a larger second shell with centering tolerances of ± 1 μm has been demonstrated (described in "Double-Shell Targets," this section). Considerable development is needed to bring this technique to production rates. The inner shell could be delivered to the thin films at high rates and sandwiched between two films in much the same way that small parts are packaged. The lower film would constitute a conveyer belt upon which the shells are deposited, and the upper film is pressed over it in a compression system that is shown in Fig. 4-84. The success of this approach would depend on the development of noncontact suspension techniques of very thin films (0.1 μm). With this technique of inner-shell suspension, the second shell must be assembled about the inner shell from hemishells. (Several techniques of forming the hemishells are described in "Double-Shell Targets.") Machining complete hemishells is a process that could extend to a production system

but may be very expensive and may preclude our trying to provide these targets for a few cents each. There are other approaches, such as molding, that offer the possibility of reducing the cost of complete hemishells.

Assembling hemishells accurately about a sandwiched shell has a comparable analog in current production technology. Mask alignment in the semiconductor industry is routinely accurate to well within 5 μm. Probably an automated optical feedback manipulator system could align hemishells, though the expense of such a process could again be prohibitive.

Assembling these hemishells in a high-pressure D-T chamber can provide the fuel inside the outer shell that is later frozen to a uniform layer, as discussed in "Condensed D-T Layer Formation," this section. Since the bulk of the fuel in these targets is contained in this layer, filling towards the end of a target process minimizes the tritium inventory in the target factory. The tritium inventory will then be essentially the fuel in those targets stockpiled against an interruption in target factory output.

The last technique for forming the outer shell is an extension of the technique discussed in "Molecular Beam Levitation During Coating," above. An assembly consisting of the inner coated shell and webbing is nested in a mandrel shell formed from thin hemishells. These hemishells are very thin and are only a small fraction of the thickness of the ablator layer. This complete assembly is then coated as a shell to provide a seamless second shell.

Because the mandrel is very thin, it cannot contain the fill at noncryogenic temperatures. The coating process is then constrained to coat with optimum surface finish at cryogenic temperatures. Physical vapor-deposition coating techniques would be required at low coating rates to minimize heating, as well as in the presence of an exchange gas. These constraints make the coating process very difficult. The resultant low coating rates would require that the targets spend a much longer time in processing. The extended processing time can boost the tritium inventory to an unacceptable level. A better option may be to coat targets unfilled except for the fuel in the inner high-Z coated shell and develop drill and plug techniques to fuel the target late in the processing sequence.

Transport Levitator. Projected laser fusion targets for power reactors will require surface finishes on the order of 100 to 1000 Å; further, the targets must be delivered with reliabilities approaching 100%. One concept for providing these targets is to sequentially lead a single target through several well-characterized processes.[54] Contact-free support, manipulation, and transport of these targets ease contamination problems and should improve the controllability of any process. Several levitation schemes seem capable of this task, but none is universal. The suitability of any scheme is specific to the material of the target and the coating process.

Fig. 4-84. The shells are placed on a thin plastic film and then sandwiched by the addition of a second film.

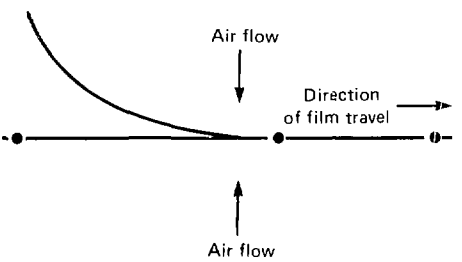

Optical levitation[55] uses photon momentum to support and move shells. The photon flux capable of supporting targets will heat the target to a few hundred degrees Centigrade in the vacuum environment required in many processing steps. This heating may be unacceptable. Acoustic levitators fail to operate in a vacuum, but they may find use for transport between processes because of their simplicity and reliability. This is true even though the target must be brought to near atmospheric pressure before transport and must be returned to a vacuum environment before a subsequent vacuum process could proceed.

Our efforts in developing the molecular beam levitator[56,57] show it is capable of providing support in the range 10^{-4} to 10^{-5} Torr, which is sufficient for many processes. One possible drawback to the molecular beam levitator is that advanced manipulation systems could require elaborate, very low-pressure pneumatic systems.

Magnetic levitators[58] require some process to provide a high-quality ferric coating before the shell

Fig. 4-85. The transport levitator consists of a quadrupole rail, each of whose electrodes is segmented to provide the propelling or lifting force.

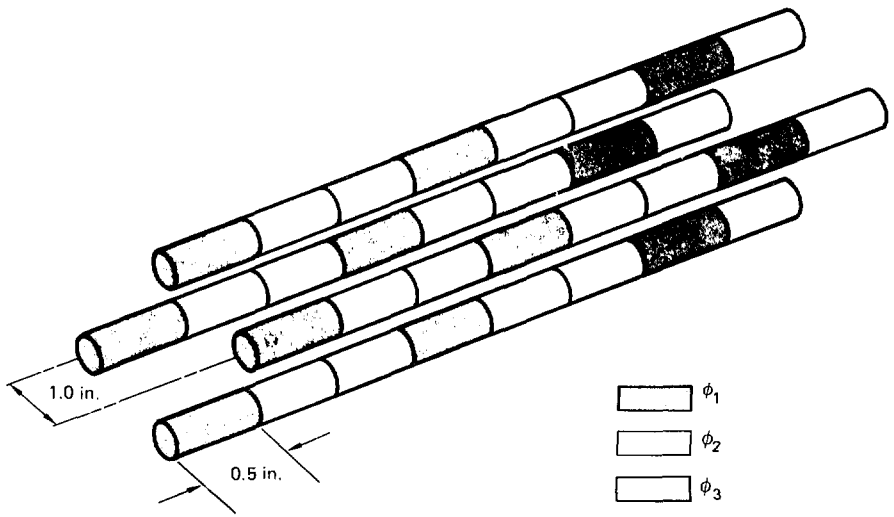

could be injected into the general handling system. The use of ferric material could also be detrimental to the target design.

Electrostatic and electrodynamic levitators (shown in Fig. 4-85) apply a force to the charged shell by controlling the electric fields at its surface.[59] This type of levitator is independent of pressure, material, and temperature, but the shell must remain reliably charged during processing. We earlier demonstrated this type of levitator in a quadrupole ring configuration[60] that was unable to transport charged targets; it could only support them. We have now extended this effort to incorporate transport.

We have again constructed a prototype linear electrostatic levitator around a basic quadrupole rail that is segmented, as shown in Fig. 4-85. As in any quadrupole, the opposite electrodes A + C are driven 180° out of phase from electrodes B + D. In addition, a dc potential is applied between the vertical electrodes A + C to offset gravity. With the currently used charge-to-mass ratio of 10^{-4} C/Kg, this offset potential is 300 to 500 V. Impressed on these electric fields are the fields to transport. The schematic in Fig. 4-86 shows the voltages delivered to the transport rail. Every third segment of each rail is driven in phase from a source of three-phase ac at ±1 kV peak to peak. This voltage (whose frequency is variable from 0.008 to 1000 Hz) provides possible target velocities of 0.03 cm/s to 3.8 × 10^3 cm/s, allowing a wide range of transport velocities to be investigated.

With the levitator operated horizontally in air, we have demonstrated that velocities of 4.87 cm/s can be reached before the air drag exceeds the transport fields. In the vertical or lift position, the system has been capable of velocities of 3.6 cm/s.

Production Rate. We anticipate that any target factory will incorporate a number of sequential processing steps, some of which we can identify already, and some that may lie in the future. Both target production rate and target inventory (including the very important consideration of tritium inventory) will be determined by types of processes and their sequence. We have begun a parametric study of how production rate and inventories are affected by proposed processing systems. A study of this type will lead to an understanding of the factors that have a major influence on the operation and cost of a target factory. By recognizing the production processes that may have difficulty in meeting

Fig. 4-86. The potentials are applied to the transport levitator with a very simple system operating at 60 Hz.

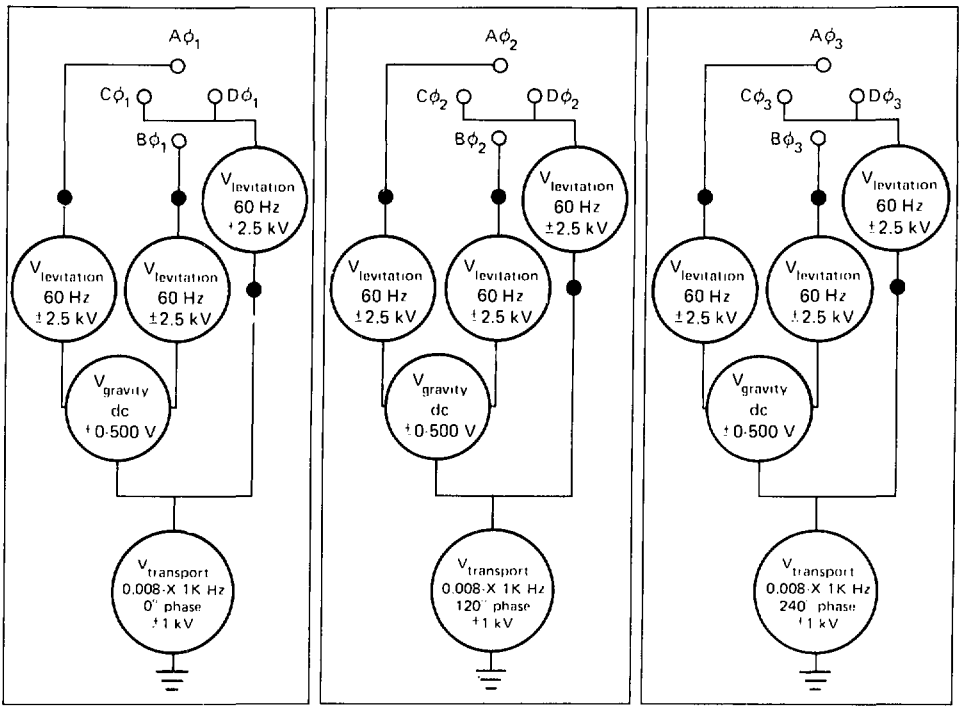

target production criteria, we can focus our research efforts or emphasize more favorable processing systems. This study is now in its infancy, but we anticipate its completion during 1980.

Author: W. L. Johnson
Major Contributor: J. W. Sherohman

References

54. *Laser Program Annual Report—1977*, Lawrence Livermore Laboratory, Livermore, Calif., UCRL-50021-77 (1978), pp. 5-42 to 5-50.
55. C. D. Hendricks and W. L. Johnson, *Power Plant Production of Inertial Confinement Fusion Targets*, Lawrence Livermore Laboratory, Livermore, Calif., UCRL-52539 (1979).
56. A. Ashkin and J. M. Dziedzic, "Optical Levitation in High Vacuum," *Appl. Phys. Lett.* **28**, 333 (1976).
57. J. K. Crane, *Molecular Beam Levitation*, Lawrence Livermore Laboratory, Livermore, Calif., UCRL-83379 (1979).
58. A. T. Lowe and C. D. Hosford, "Magnetron Sputter Coating of Microspherical Substrates," *J. Vac. Sci. Technol.* **16**, 197 (1979).
59. F. Garris and K. O. H. Zinck, "A Dynamically Regulated Levitation Electrometer Used in Search for Fractional Charges," *Nuclear Instruments and Methods*, **117**, pp. 467-475 (1974).
60. *Laser Program Annual Report—1978*, Lawrence Livermore Laboratory, Livermore, Calif., UCRL-50021-78 (1979), pp. 4-49 to 4-52.

Diagnostics Technology

5

Contents

Diagnostics Technology 5

Introduction

The mandate of the Laser Fusion Program's diagnostics effort is to provide appropriate measurement technology at a pace consistent with our rapidly evolving interaction and implosion experiments. At the same time, we must perform diagnostics on target physics and dynamics whose parameters vary on the scale of micrometers and picoseconds. To meet these twin goals of extreme accuracy and rapid evolution, our diagnostics program is necessarily both sophisticated and developmental.

In general we approach diagnostic problems in two ways:

- Using state-of-the-art (perhaps commercially available) detection systems, which provide reliability and modest resolution as on-line diagnostics.
- Pursuing in-house development of high-resolution, high-technology instrumentation and techniques, in some cases in collaboration with university or industrial groups.

Because of the high temperatures involved in fusion experiments, target emissions of primary interest are

- X rays of 100 eV to 100 keV.
- Thermonuclear reaction products such as neutrons, alpha particles, and MeV protons.
- Several neutron-activated species.

During the past year we made significant progress in our ability to diagnose drive, preheat, and final-fuel conditions in high-convergence targets. We can also field diagnostics and retrieve data on the large and complex Shiva laser system in an automated, more reliable fashion.

In high-convergence target designs, we have traded the high temperature of earlier thin-shell targets for higher density and ρR in the compressed fuel and surrounding glass pusher. As a consequence, valuable compression diagnostic techniques such as alpha-particle images and keV-range x-ray images are no longer suitable, because of reduced emissions and increased opacities for both. Several diagnostics which address these problems are discussed in separate sections below, and are then brought together in a discussion of their application to intermediate-density targets.

Several representative articles describe recent advances in spatially, temporally, and spectrally characterizing x-ray emission from laser-irradiated targets. These include

- Improved spectral and temporal characterization of our broad-band sub-kilovolt spectrometer "Dante."
- Similar work with, and absolute calibration of, our sub-kilovolt x-ray streak cameras.
- Continued developments of x-ray mirrors and lenses for future experiments.

Other articles describe

- The mating of an x-ray microscope and streak camera, which will allow us for the first time to study space-time dynamics of selected Shiva targets (Fig. 5-1).
- Work on measuring stimulated scattering and associated target preheat.
- Recent advances in our ability to diagnose neutron yield and relative emission time; this is of particular significance for anticipated experiments next year with velocity-multiplying double-shell targets.

Fast data retrieval and analysis, an aspect of our work which received significant attention during the past year, is important to us in two ways. Expeditious data management

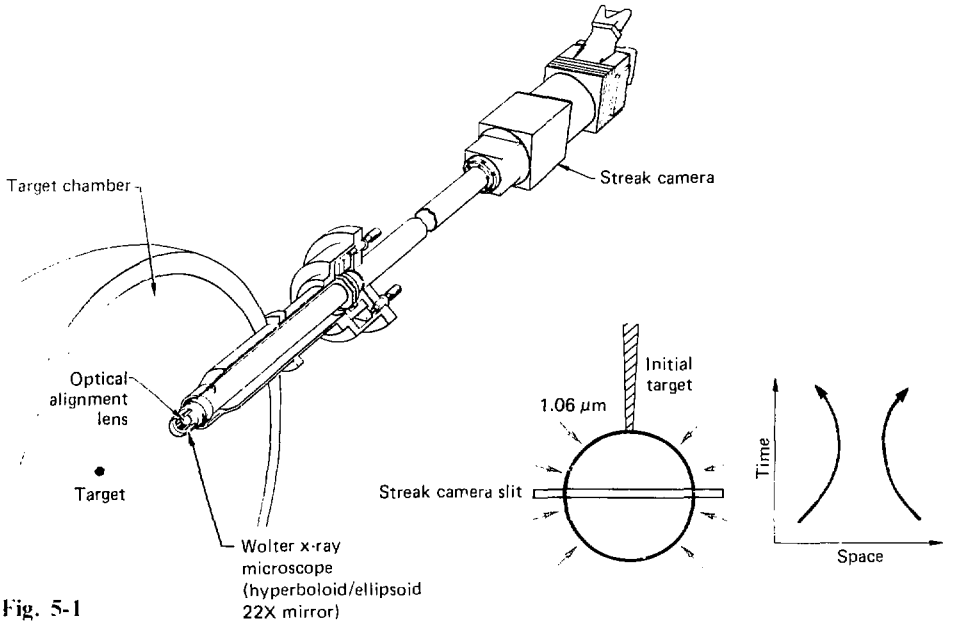

Fig. 5-1

allows us to effectively digest and utilize in a timely fashion the considerable amount of information produced in our rapidly evolving experimental program; this in turn permits more efficient use of valuable manpower. A long-term approach to data handling and storage, a new diagnostic-data computer facility, and a sampling of new data-handling routines are described in this section. A substantial effort has been made, for example, in computer-compatible readout systems employing charge-coupled devices (CCDs); applications of such systems to streak cameras, imaging devices, and transient digitizers are also presented.

We expect a significant payoff from our accrued capability in data retrieval and analysis to manifest itself in a more timely, effective and complete digestion of experimental results, as well as in a substantial reduction of manpower now invested in relatively routine procedures.

Authors: D. T. Attwood and V. W. Slivinsky

Temporal Response of the XRD-31 X-Ray Diode

The LLL laser program uses fast x-ray diodes (vacuum photoelectric diodes) to provide spectral and temporal information about low-energy x rays emitted from Argus and Shiva fusion targets.[1,2] For x-ray energies below 1.5 keV, the typical detector channel consists of a filter, an XRD-31 x-ray diode[2] (made by EG&G to LLL specifications), high-quality signal cable, and a large-bandwidth transient recorder. We recently measured the temporal response of a high-quality XRD-31 detector system at the Monojoule laser facility.[3] Those measurements and results are described in this article.

The XRD-31 system being characterized consists of

- A vanadium filter 4000 Å thick.
- An XRD-31 with 2.1-mm anode-cathode spacing, biased at 5 kV.
- 30 ns of 1/2-in. air-dielectric coaxial cable.

- A 4-GHz TSN 660 (Thomson-CSF) oscilloscope.

The impulse response of a fast x-ray detector system is best determined using a pulsed x-ray source with an emission time much less than the detector-system FWHM. The Monojoule laser facility, equipped with x-ray diodes and an x-ray streak camera, is a well-characterized x-ray source; with an incident 50-ps optical pulse, x-ray bursts of 70 to 110 ps are generated with sufficient intensity to test our detectors. We measure the temporal characteristics of the x-ray source with a 15-ps x-ray streak camera,[4] then unfold them from the recorded diode signal to determine the diode system impulse response.

In our measurements, a 1-J, 50-ps, 1.06-μm laser pulse focused on a planar Ti target generates a nominal 100-ps FWHM x-ray pulse (depending on energy). An XRD-31 detector system and a soft x-ray streak camera (SXRSC) simultaneously detect emitted x rays. For x-ray burst durations significantly longer than the 15-ps resolution, the SXRSC provides a direct temporal measurement of the x-ray source. The SXRSC is also fitted with a 4000-$\AA$-thick V filter; with the V filters, both detectors respond to x rays between 300 and 500 eV.

X-ray signals measured on a typical 1-J laser shot are shown in Fig. 5-2. Raw data for the XRD-31 system show a 197-ps FWHM, and some ringing [Fig. 5-2(a)]. The SXRSC data [Fig. 5-2(b)] show the x-ray pulse on this shot to have a 102-ps FWHM. To determine the impulse response of the XRD-31 detector system, we unfold the x-ray temporal distribution from the recorded XRD-31 signal; the XRD-31 system impulse response thus determined is shown in Fig. 5-2(c). It is about 140 ps FWHM, and shows some ringing.

We also recorded data using a series of x-ray pulses separated by 217 ps, to demonstrate the resolving power of the XRD-31 system. To generate the x-ray pulse train, the incident laser beam was passed through a 217-ps etalon. Figure 5-3(a) shows XRD-31 data recorded on a typical shot. The pulse has a 565-ps FWHM, with 10% modulation near the peak. From the raw XRD-31 data, it is unclear what the input x-ray temporal distribution looks like. The modulation near the peak suggests multiple pulses, and the broadening suggests the x rays are emitted over several hundred ps.

Using the previously determined impulse response function for the XRD-31 system [Fig. 5-3(b)], the XRD-31 data recorded on this shot can be unfolded to determine the x-ray-source temporal characteristics [Fig. 5-3(c)]. Temporal output of the x-ray source as recorded by the SXRSC is shown for comparison in Fig. 5-3(d). The unfolded XRD-31 data shows the same basic detail as the SXRSC measurement, thus demonstrating the 200-ps capability of the diode detection system when properly characterized.

In Fig. 5-4, the running integral of the unfolded XRD-31 data is compared with that of the SXRSC data, showing that relative area under the individual peaks is preserved.

The ability to unfold a set of data, as demonstrated above, is dependent on the data quality. Typically, detailed structure on time scales

Fig. 5-2. XRD-31 system impulse response determined from data recorded on a 1-J laser shot: (a) XRD-31 data; (b) soft x-ray streak camera (SXRSC) data; (c) inferred XRD-31 system impulse response, found by unfolding the x-ray temporal distribution (b) from the measured XRD-31 data (a).

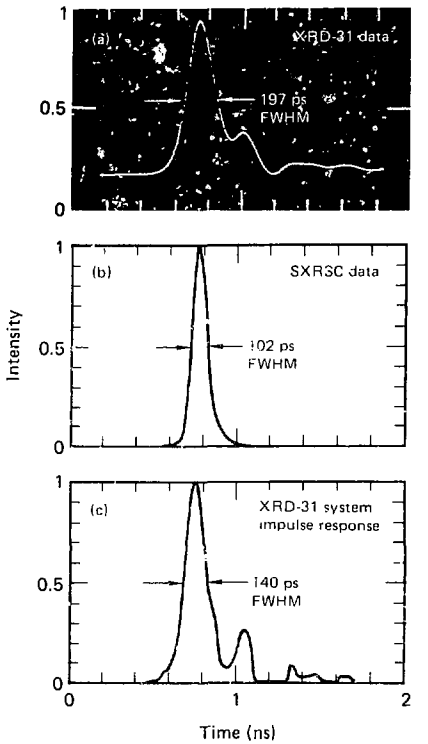

Fig. 5-3. XRD-31 system response on a laser shot producing a series of x-ray pulses separated by 217 ps: (a) XRD-31 data; (b) XRD-31 system impulse response, as determined from single-pulse experiment; (c) x-ray source temporal distribution, found by unfolding the system impulse response from the recorded XRD-31 data; (d) x-ray source temporal distribution measured with the SXRSC, for comparison.

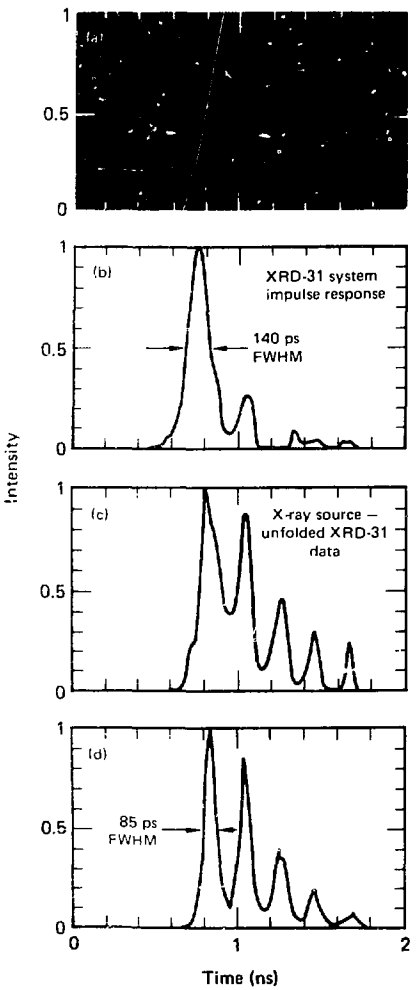

Fig. 5-4. Fraction of x rays emitted vs time. A comparison of the SXRSC data [Fig. 5-3(d)] with the unfolded XRD-31 data [Fig. 5-3(c)] shows that the relative intensities of the five pulses remain the same for both methods of measurement.

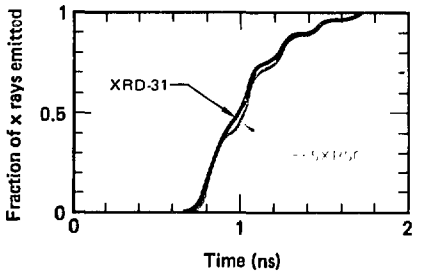

less than 75% of the width of the system impulse response should be seriously questioned. The unfold in Fig. 5-3(c) is correctly interpreted as a series of short x-ray pulses spaced about 215 ps apart. The relative energy in each pulse can be determined from its total integral.

The data presented show what can be done with a well-characterized XRD-31 system in a low-noise environment. The single-pulse data show that an XRD-31 system with a 4-GHz TSN 660 oscilloscope has an impulse response of 140 ps FWHM. The etalon data demonstrate that such a system can just barely resolve x-ray pulses spaced 217 ps apart. We have also demonstrated that under favorable conditions the XRD-31 data can be unfolded to a resolution somewhat better than the system impulse response. With a slower recorder, such as the 1-GHz Tektronics 7912 transient digitizer, we would expect an XRD-31 system to show an overall impulse response of 400 ps.

Authors: R. A. Lerche and D. E. Campbell

References

1. *Laser Program Annual Report—1978*, Lawrence Livermore Laboratory, Livermore, Calif., UCRL-50021-78 (1979), pp. 6-5 to 6-7.
2. *Laser Program Annual Report—1977*, Lawrence Livermore Laboratory, Livermore, Calif., UCRL-50021-77 (1978), pp. 3-57 to 3-60.
3. *Laser Program Annual Report—1974*, Lawrence Livermore Laboratory, Livermore, Calif., UCRL-50021-74 (1975), p. 290.
4. *Laser Program Annual Report—1978*, Lawrence Livermore Laboratory, Livermore, Calif., UCRL-50021-78 (1979), pp. 6-2 to 6-5.

Filtered-Mirror Sub-keV X-Ray Measurement System

A ten-channel filtered windowless x-ray diode system has been used at the Shiva laser since January 1979.[5] This system has a problem, inherent in all filter/detector x-ray measurement schemes: because the filter transmission above the absorption edge of the filter material makes contributions to the recorded signal, the resolution and accuracy of channels at or below the peak of the spectrum to be measured are significantly degraded. We therefore designed and installed a five-channel filtered-mirror system, using critical-angle reflection by vitreous carbon and beryllium mirrors to remove the unwanted high-energy response. The mirrors were aligned to an accuracy of 0.01° and pinned in position with a rigid cassette mounting to ensure proper alignment [the mirrors and their mounting hardware were designed and built by Lockheed Palo Alto Research Laboratory (LPARL) to LLL specifications].

Figure 5-5 shows the mirror reflectivity and the boron filter transmission for the lowest energy

Fig. 5-5. Carbon mirror reflectivity and 1-μm boron filter transmission, for lowest energy channel.

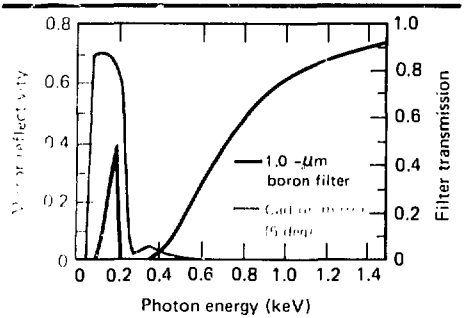

Fig. 5-6. Experimental geometry for Shiva filtered-mirror x-ray diode system.

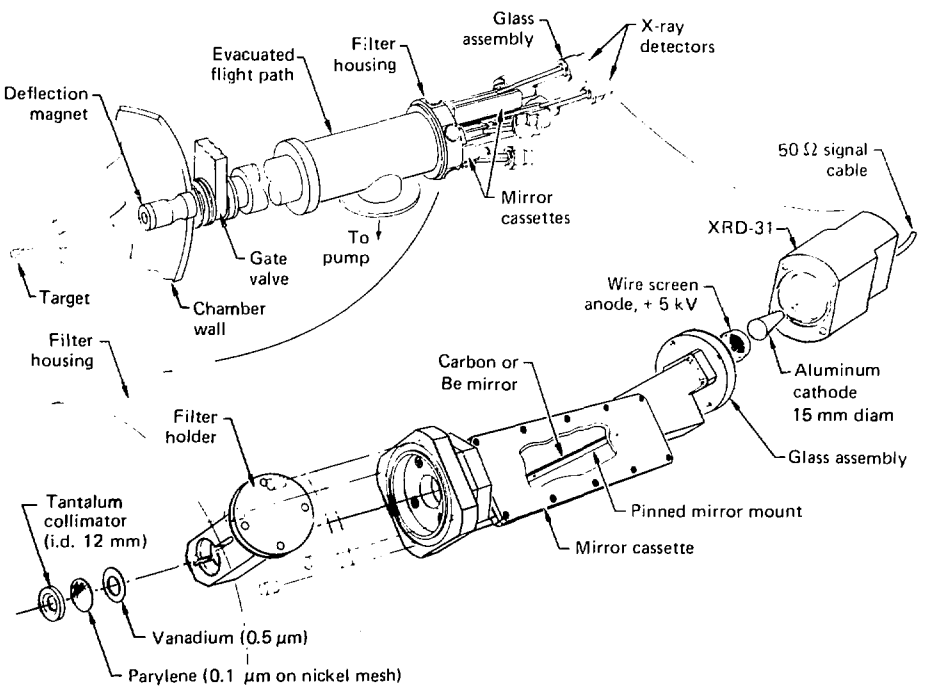

channel. Note how with increasing energy the mirror reflectivity drops to zero as the filter transmission increases. The mirrors suppress the response to energetic photons by at least an order of magnitude.

The physical arrangement of the filtered-mirror system is shown in Fig. 5-6. Table 5-1 outlines the essential parameters of each channel, and Fig. 5-7 gives the response of each channel to a flat spectrum.

Except for the presence of the mirrors, the filtered-mirror system is similar to the ten-channel system mounted directly below it on the Shiva target chamber. The system consists of six low-energy x-ray channels; five are filtered-mirror channels and one is a higher-energy (aluminum K-edge) channel that does not use a mirror. The six-channel system uses 0.1-μm parylene blast shields for UV absorption, and fast, small, x-ray diodes. Data recording is done on Tektronix R7912 digitizing oscilloscopes, for preliminary analysis on the Shiva 11/70 computer and eventual transfer to the Octopus system for final processing.

We have been using the filtered-mirror system routinely since August 1979. The system not only provides us with a valuable new sub-kilovolt x-ray

Table 5-1. Characteristics of the Shiva filtered-mirror sub-keV x-ray measurement system.

Filters			Mirrors	
Absorption edge	Thickness (μm)	Edge energy (keV)	Material	Angle
Boron-K	1.0	0.19	Carbon	5.04°
Carbon-K	1.9	0.28	Beryllium	3.41°
Vanadium-L	0.5	0.52	Carbon	2.43°
Chromium-L	0.6	0.58	Carbon	1.91°
Cobalt-L	1.0	0.79	Carbon	1.98°
Aluminum-K	9.2	1.56	None	

Fig. 5-7. Filtered-mirror system channel responses to a flat spectrum.

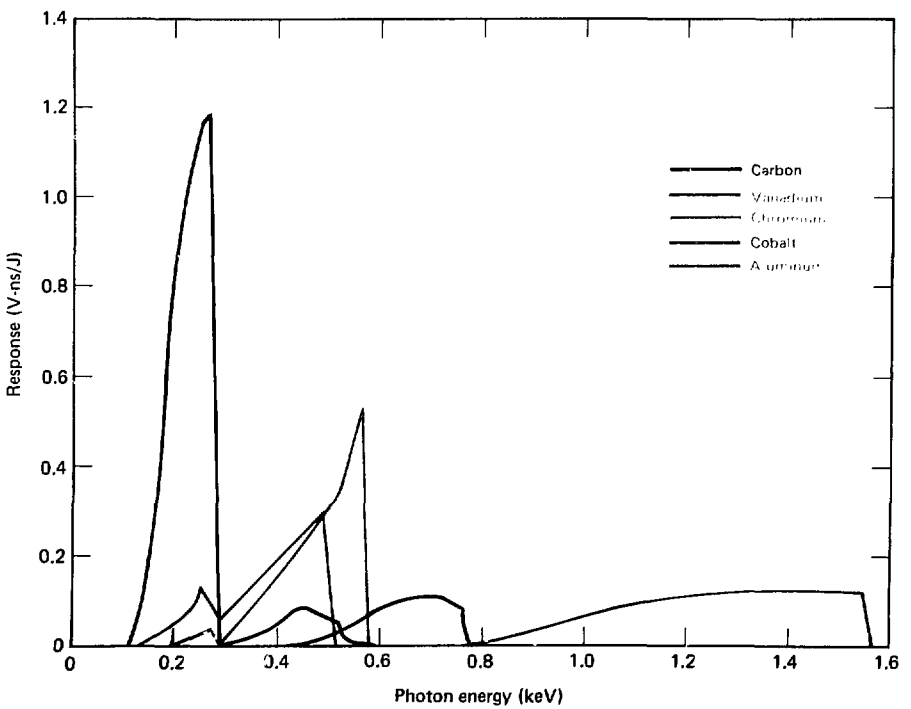

diagnostic instrument, it has provided us with more accurate information about the low-energy photon spectrum. Further, by comparing spectral results from the six-channel filtered-mirror system with those of the ten-channel system, we have obtained additional information about the angular distribution of soft x rays.

Authors: R. A. Heinle and K. G. Tirsell

Reference

5. *Laser Program Annual Report—1978*, Lawrence Livermore Laboratory, Livermore, Calif., UCRL-50021-78 (1979), p. 6-5.

Development of a Time-Resolved, Broad-Band Sub-Kilovolt X-Ray Spectrometer for Absolute Flux Measurements

We have previously described the development of a soft x-ray streak camera (SXRSC) which is sensitive to x rays > 100 eV and has a time resolution of 15 ps[6]. A version of the camera has been used at Argus to measure the time history of the x-ray emission in three broad-band energy channels below 1 keV. The SXRSC has established its value as an important diagnostic tool, recording data on a routine basis for a variety of targets.

We have now designed and implemented a technique to perform intensity calibrations of the SXRSC which will make possible absolute flux measurements of x-ray emission below 1 keV. Preliminary results from the calibrations, and the techniques used, are discussed below; we also describe the SXRSC as it will be fielded on Shiva.

Shiva Spectrometer. The SXRSC is similar to the instrument whose development is described in previous annual reports[6–8]; as it will be fielded on Shiva (Fig. 5-8), the SXRSC is designed to make spectrally resolved absolute flux measurements of the sub-kilovolt x-ray spectrum from laser fusion targets. Using methods similar to those used at Argus, we obtain broad-band spectral resolution using x-ray mirrors and transmission filters. Seven mirror-filter combinations, listed in Table 5-2, have been designed to cover the range from 100 to 930 eV. Calculated relative spectral responses for the seven channels are compared in Fig. 5-9.

The mirror materials and angles were chosen to provide efficient reflection in the x-ray region of interest and discriminate against x rays having energies greater than the filter cutoff. The seven material/angle combinations require only two separate mirrors, one at two degrees and one at four degrees. The mirrors are fabricated by polishing the carbon and germanium surfaces to optically flat finishes and vapor-depositing nickel and aluminum over part of their respective surfaces. Using such composite mirrors greatly simplifies the alignment procedure, by reducing the number of mirrors which must be positioned.

The SXRSC data recording medium will be a CCD active-readout detection system[9] directly linked to the Shiva computer system. Data in the form of a digitized two-dimensional image will be available for analysis immediately after the shot, bypassing the time-consuming processing and

Fig. 5-8. A schematic of the SXRSC as it will be fielded on the Shiva laser system.

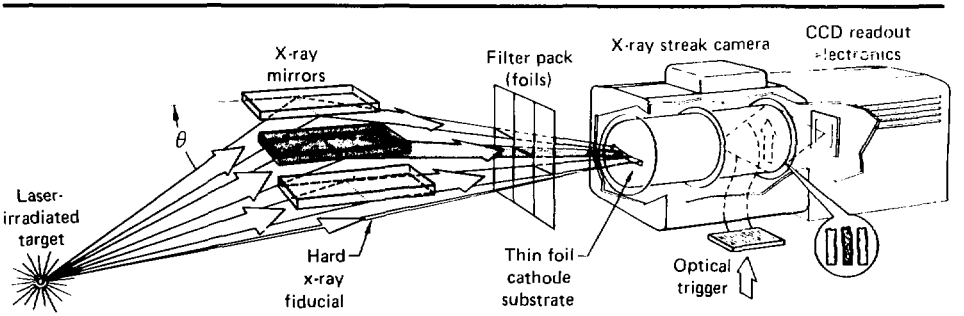

Table 5-2. Mirror/filter combinations for the SXRSC x-ray channels at Shiva.

Mirror	Angle	Filter	Thickness ($\mu g/cm^2$)	E_{abs} (eV)	E (eV)	ΔE_{FWHM} (eV)
Carbon	4°	Carbon	300	280	230	72
Nickel	4°	Vanadium	250	513	476	86
Nickel	4°	Chromium	300	575	525	114
Aluminum	2°	Iron	500	708	633	117
Aluminum	2°	Cobalt	600	778	700	143
Germanium	2°	Nickel	600	855	766	168
Germanium	2°	Copper	600	930	819	224

Fig. 5-9. Calculated relative spectral responses of the seven x-ray channels to be used with the SXRSC at Shiva; included in the response curves is the gold photocathode sensitivity. (See Table 5-2 for further characterization of each channel.)

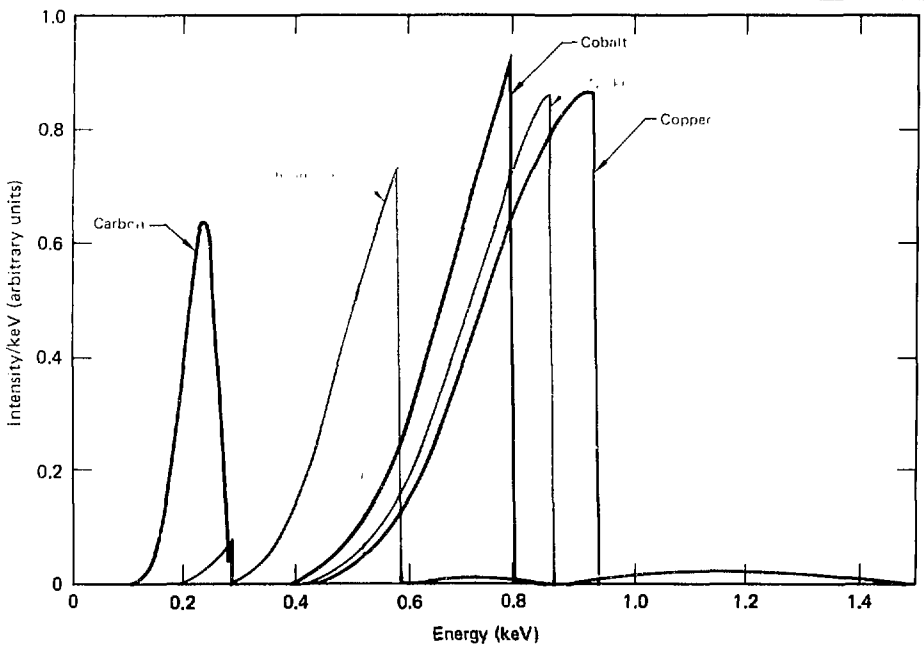

digitizing of film data presently required for quantitative analysis.

Capacity for a hard x-ray fiducial and for coarse pinhole imaging has been incorporated into the SXRSC design on Shiva. The hard x-ray fiducial allows us to determine the time of emission of the sub-keV x rays relative to x-ray energies greater than 1 keV. The fiducial is a direct line of sight from the target to the entrance aperture of the SXRSC; the x-ray mirror is not used, but a K-edge filter can be placed so as to define the higher-energy x-ray channel. Complemented by other streak camera data, the fiducial will allow us to investigate the timing relationships among the total x-ray spectrum.[10] The pinhole imaging system will permit us to spatially localize observed emission areas.

Calibration of the SXRSC. Calibration of the SXRSC is done in a pulsed mode, approximating as nearly as possible the experimental configuration in

Fig. 5-10. A schematic of the calibration set-up at the Monojoule laser, for calibrating the SXRSC using a pulsed source.

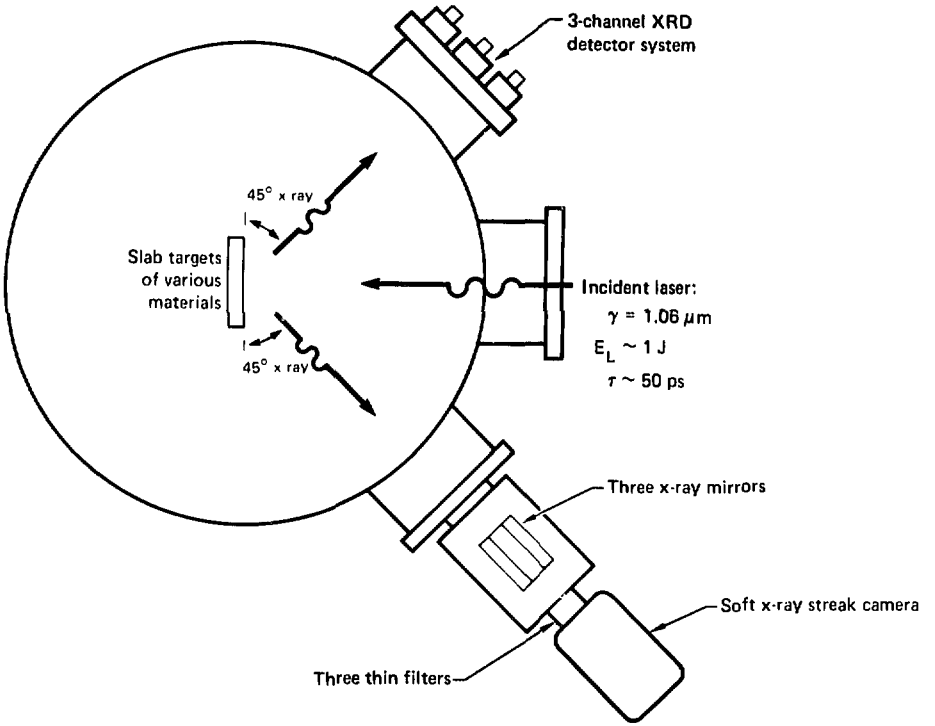

which it is used. Pulsed-mode calibration is inherently as reliable and accurate as the steady state method employed with other detectors used for low-energy x-ray measurements, although source characterization may be more difficult in the pulsed mode. The SXRSC's fast timing characteristics discriminate against unwanted late signals, which presently preclude calibration in a steady-state mode.

We have assembled a calibration facility using the Monojoule laser to create a pulsed x-ray source. A schematic of the arrangement is shown in Fig. 5-10. A 50-ps pulse of 1.06-μm light having energy up to 1 J irradiates slab targets of various materials at normal incidence. Three absolutely calibrated x-ray diode (XRD) detectors on an angle of 45° to the target normal measure the sub-kilovolt x-ray fluence from the target. The SXRSC is also placed at 45° to the target normal, at 90° from the XRDs. To obtain the calibrations, time-resolved signals from the SXRSC are integrated and compared with integrated fluences measured by the XRDs.

The SXRSC is calibrated in three x-ray energy channels defined by thin x-ray transmission filters and grazing-incidence x-ray mirrors. Similar channels are defined for the XRDs, also using sets of x-ray transmission filters. A comparison of the spectral channels for the SXRSC and the XRDs is shown in Fig. 5-11; responses of the SXRSC and XRD channels have been matched as closely as possible in order to reduce errors due to variation in the spectral emission shape.

Fig. 5-11. A comparison of normalized channel responses for the XRD detectors and SXRSC used for the calibrations. The response functions between the different detectors have been matched as nearly as possible to minimize effects due to structure in the x-ray spectrum.

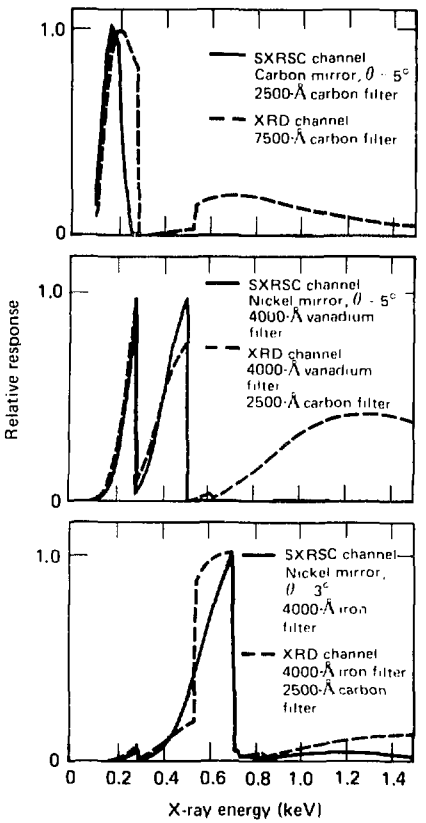

We have measured each of the components of the channels to accurately determine the spectral dependence of the camera response (Figs. 5-12 to 5-14). X-ray transmission by the filter foils is measured using proton-induced line sources in the sub-kilovolt region. Figure 5-14 shows data for a typical set of filters; the data are fit using tabulated absorption coefficients to determine foil thickness.

Fig. 5-12. Representative measured x-ray fluences from the various laser targets used to calibrate the SXRSC. Large fluence variations among the targets at higher energies are evidence for emission in this region.

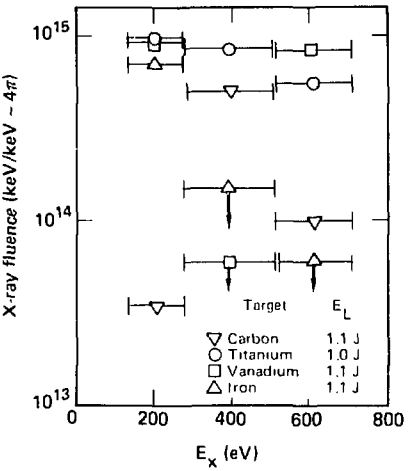

We have also measured the reflection efficiency of the x-ray mirrors (Fig. 5-13). Below 1 keV we use proton-induced line emission; at higher energies we use a continuum x-ray source produced by electron bremsstrahlung. The curves drawn through the data are predictions of the reflection efficiency, using a semiclassical calculation adjusted to fit the data.[1] The three XRD detectors with aluminum cathodes have been calibrated in the normal fashion and agree with stable and reproducible calibrations from similar instruments.

Various target materials are used for the calibrations. For our laser operating parameters, the target spectrum above 250 eV is dominated by line emissions. By using various targets we can change the energy of the line emission and thus test the dependence of the calibrations on the source spectrum. Source spectra from various targets measured by the three-channel XRD system are shown in Fig. 5-12. Near 200 eV the fluences from titanium, vanadium, and iron are similar, while the carbon target fluence is greatly reduced. At higher energies the fluences vary greatly depending on the target because the spectrum is dominated by lines. For example, by changing the target atomic number Z by one, from titanium to vanadium, the fluence in

Fig. 5-13. Measured reflectivity of the three SXRSC x-ray mirrors; curves were generated from a semiclassical reflectivity theory adjusted to fit the data.

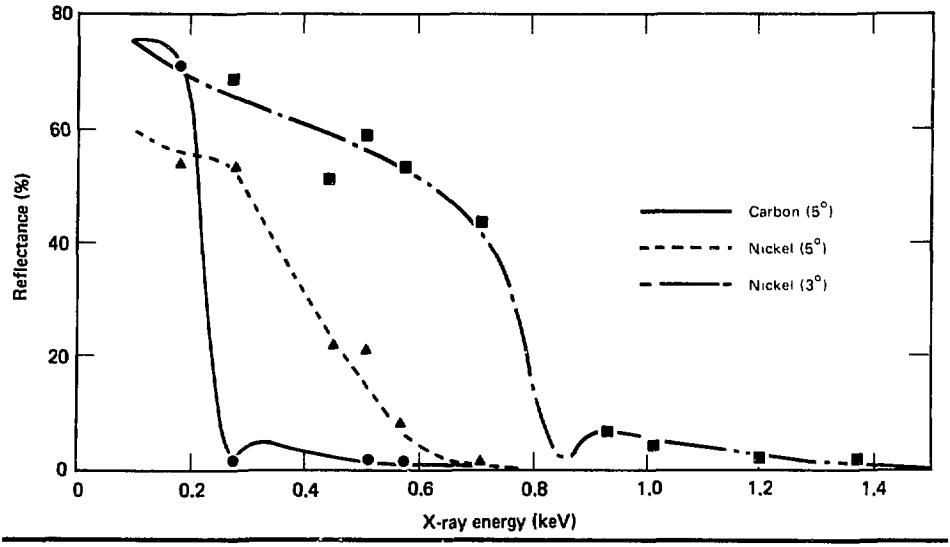

Fig. 5-14. Measured transmission of the filter foils used in the SXRSC calibrations.

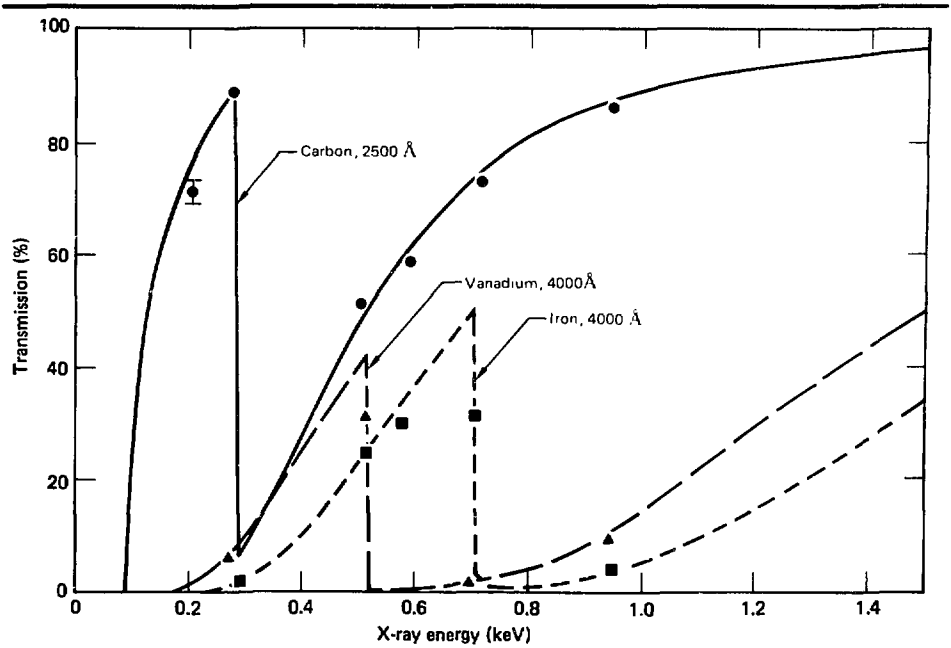

Fig. 5-15. The two-dimensional streak image of typical SXRSC calibration, showing (a) the film image and (b) a contour plot of the two-dimensional digital image. Calibrated streak records of the three x-ray channels are shown in (c).

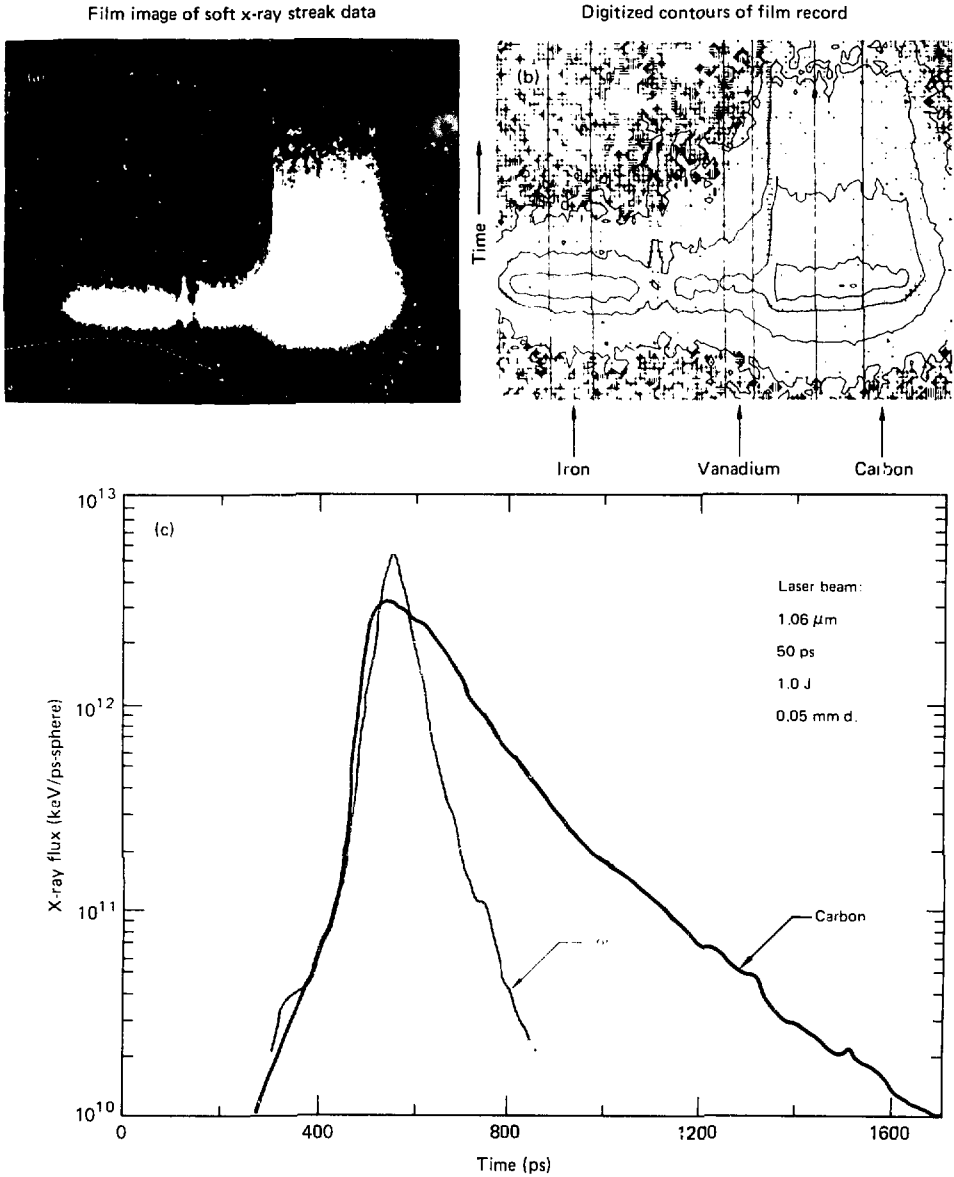

Fig. 5-16. Typical SXRSC calibration data from various targets, for three soft x-ray regions; lines represent fits to the data.

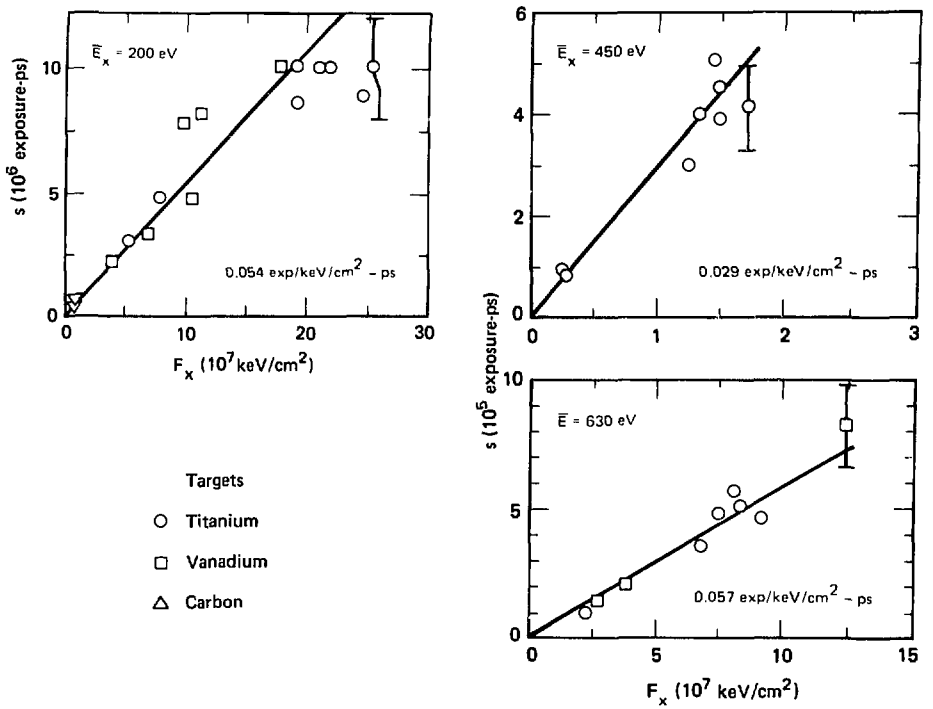

the 500-eV channel decreases by more than an order of magnitude. Line emission from highly ionized vanadium is at a higher x-ray energy than that from cold vanadium; the strongest vanadium lines shift above the L absorption edge of a vanadium filter, while the hot titanium lines lie below the edge. Similarly, an iron target signal observed through an iron filter is also greatly reduced. For the carbon target, peak output is observed in the 280-to-510-ev channel which includes the highly excited carbon lines.

An example of SXRSC calibration is shown in Figs. 5-15 and 5-16. Each data set consists of a number of laser shots taken with various targets. Figure 5-15(a) gives film data from a titanium target (calibrations have also been performed using a CCD active readout system). Film density is converted to light exposure, using a calibration curve produced for each shot on the film. The film data is processed and converted to a digital contour plot [Fig. 5-15(b)] using a microdensitometer; the pairs of vertical lines parallel to the streak direction denote the x-ray channels. The data are further reduced [Fig. 5-15(c)] to time histories of the three x-ray bands, by averaging across each x-ray channel; the curves have been plotted using calibration factors determined for each channel.

The calibration factors are determined by comparing the integrated time history of each SXRSC channel with XRD measurements of total fluence in the corresponding energy bands. The data are then corrected to account for the difference in channel spectral response between the SXRSC and the XRDs. These corrections are usually less than 10%, but can be as large as 50% depending on the target

material. Figure 5-16 shows plots of the integrated response of the SXRSC vs fluence into the instrument for three x-ray energy channels.

Errors in the plots, including errors in film data reduction and integration of the XRD output, are estimated at 20%; this is consistent with the scatter for this set, which is about 25%. Systematic errors in calibrating channel components increase the estimated error of the measurement to 35%. Potential systematic errors in the method of data reduction, such as averaging over the x-ray spectra and channel response, are being investigated. These uncertainties in data analysis are due to using broad-band channels in the calibration, and can be reduced by measuring the x-ray spectra from the targets, or by using much narrower channels which reduce the spread of energies over which the channels must be averaged.

In summary, we have developed a calibration procedure to measure the absolute spectral sensitivity of the SXRSC. A further improvement, involving a more accurate characterization of the lines emitted from the source, is presently underway; when this spectrum is measured, a more thorough data analysis will be possible. We will continue to refine the calibrations and investigate the x-ray response of the camera. Other photocathode materials are also being investigated, as discussed in the following article.

Author: R. L. Kauffman
Major Contributors: H. Medecki, E. L. Pierce, and G. L. Stradling

References

6. *Laser Program Annual Report—1978*, Lawrence Livermore Laboratory, Livermore, Calif., UCRL-50021-78 (1979), pp. 6-2 to 6-5.
7. *Laser Program Annual Report—1974*, Lawrence Livermore Laboratory, Livermore, Calif., UCRL-50021-74 (1975).
8. *Laser Program Annual Report—1975*, Lawrence Livermore Laboratory, Livermore, Calif., UCRL-50021-75 (1976).
9. *Laser Program Annual Report—1978*, Lawrence Livermore Laboratory, Livermore, Calif., UCRL-50021-78 (1979), pp. 6-54 to 6-59.
10. D. T. Attwood, L. W. Coleman, J. T. Larsen, and E. K. Storm, *Phys. Rev. Lett.* **37**, 499-502 (1976).
11. A. H. Compton and S. K. Allison, *X Rays in Theory and Experiment*, 2nd ed. (Van Nostrand Co., Princeton, N.J., 1935), pp. 263-315.

Gold and Cesium Iodide X-Ray Photocathodes

Time-resolved x-ray measurements using x-ray streak cameras are an important means of diagnosing inertial confinement fusion experiments. To measure incident x-ray flux intensity over time, our streak cameras utilize the emission current from a transmission x-ray photocathode. Gold films ~ 100 Å thick are commonly used for this purpose. In some applications, however, such as x-ray backlighting or time-resolved crystal spectroscopy, insufficient x-ray flux can limit the effectiveness of gold photocathodes. Improving the sensitivity of the streak camera photocathode can thus extend the range of application of x-ray streak cameras.

Initial efforts to establish the optimum thickness of gold photocathodes under standard streak camera operating conditions have been previously discussed.[12] Cesium iodide, a photocathode material whose sensitivity and secondary-electron temporal-emission characteristics are reported to compare favorably with those of gold, has also been tested.[13,14] We have utilized the soft x-ray streak camera's convenient interchangeable-photocathode design to make side-by-side sensitivity and temporal-response comparisons of CsI and Au in typical picosecond-scale pulsed operations. For these comparisons we used composite photocathodes, consisting of up to six CsI and/or Au samples of different thicknesses, vapor-deposited on a single carbon-foil substrate.

We used the Monojoule laser as our x-ray calibration facility. X rays were produced by irradiating 8-μm-thick titanium foils in an evacuated chamber with short, intense (10^{13} to 10^{14} W/cm^2) laser pulses. The target emission was filtered using x-ray absorbers and reflectors, to define a moderately narrow energy channel. A 4000-Å vanadium foil and a 3° nickel reflector were used to form a spectral channel between 400 and 500 eV. The x-ray pulse width, which varies significantly with channel energy, was measured at ~70 ps FWHM.

A composite-photocathode profile of relative x-ray intensity over time, obtained with 1080-Å-thick CsI and 150-Å-thick Au, is shown in Fig. 5-17. The curves confirm the greater sensitivity of CsI and show its temporal response to be comparable to that of Au for this pulse width. The response curves of

Fig. 5-17. Plot of relative intensity over time for the 1080-Å CsI and 150-Å Au composite photocathode. X rays are from a target heated with a laser pulse train produced by sending a 50-ps, 1.06-μm laser pulse through a 500-ps, 50%-transmitting etalon. The temporal response of cesium iodide matches that of gold, with nearly identical pulse shapes down to ~1/30 of pulse peak intensity; all pulse widths are FWHM.

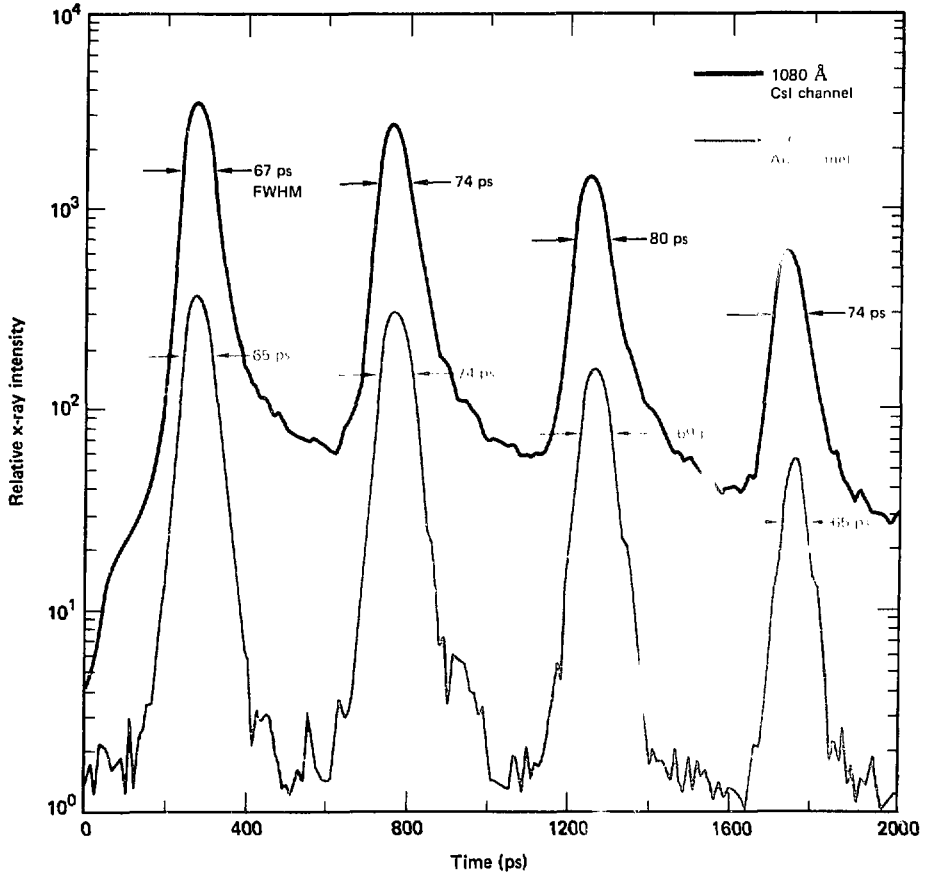

both materials to each incident x-ray pulse are nearly identical down to 1/30 of pulse peak intensity, at which point the CsI curve begins to exhibit a low-intensity tail. This late tail may indicate some electron straggling from cesium iodide which is not present in gold, although other possibilities have not been discounted.

The cesium iodide and gold photocathodes we tested range in thickness from 50 to 4000 Å. The relative sensitivities of all these photocathodes were correlated with component samples common to different composite photocathodes, to scale the Au and CsI photocathode response levels. The correlate relative intensities of both materials, for a nominal x-ray energy of 500 eV as described above, are plotted as a function of thickness in Fig. 5-18.

The data points in Fig. 5-18 represent the relative-response measurements of individual samples for given material-thickness combinations. The vertical bars indicate the shot-to-shot spread in each sample's response. These variations stemmed from

Fig. 5-18. Relative response-vs-thickness of CsI and gold in response to 500-eV x-ray excitation. The data points represent the relative-response measurement of individual samples of a given material-thickness combination. The vertical bars indicate the shot-to-shot spread of each sample response; the horizontal bars show the measurement uncertainty (±30 Å) in sample thickness. Also plotted are intensity-versus-thickness data, taken with dc, monochromatic, 573-eV excitation and scaled for comparison.

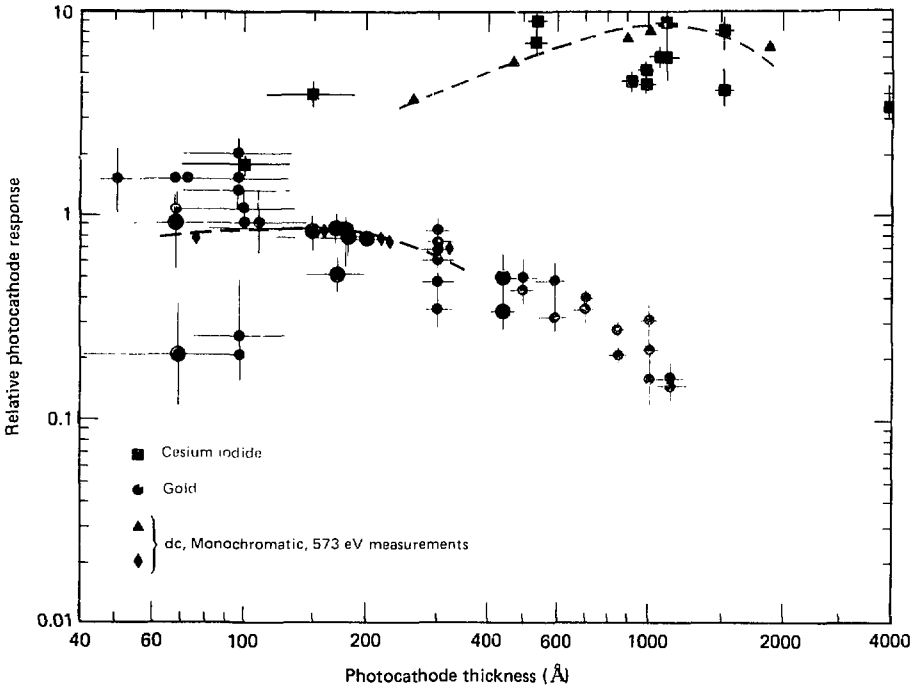

fluctuations in the target emission spectrum and from camera noise. Other variations arose when the range of flux levels required to measure the span of component sensitivities on several composite photocathodes exceeded the camera's dynamic-range limitations.

Horizontal bars in the figure show the measurement uncertainty (±30 Å) in photocathode thicknesses. Very thin (~100 Å) gold samples show a wide sensitivity range; this variation is seen among thin samples from any of the several evaporation facilities used, and even among samples produced in the same evaporation run. The lack of consistency in thin photocathode production may be due to variable surface properties, uncertainties in thickness measurements, or other unknown effects characteristic of very-thin film deposition. Because of the variable reproducibility of very thin samples, we recommend 200 Å as a minimum thickness for gold photocathodes.

Also plotted in Fig. 5-18 are previously measured intensity-versus-thickness data taken with dc, monochromatic, 573-eV excitation,[14] which have been scaled for comparison with our measurements. Our observations of sensitivity-versus-thickness maxima correspond well with these findings. At 500 eV, the optimum CsI thickness of 1100 Å is more sensitive than 200-Å Au by a factor of five; larger factors (~30) are expected at photon energies of 1.5 keV. The difference between the two sets of data, regarding the relative sensitivity of cesium iodide and gold, may be attributable to the mix of x-ray energies in our source. Efforts are in

progress to measure the source spectra, and to confirm the larger sensitivity ratios above 1.5 keV.

Cesium iodide photocathodes are seen to significantly increase x-ray streak camera sensitivity without appreciably affecting the camera's temporal response to ~70-ps structure. We are now implementing these photocathodes in selected applications requiring increased sensitivity.

Authors: G. L. Stradling, R. L. Kauffman, and B. L. Henke (University of Hawaii)

References

12. *Laser Program Annual Report—1978*, Lawrence Livermore Laboratory, Livermore, Calif., UCRL-50021-78 (1979), p. 6-2.
13. B. L. Henke, J. Liesegang, and S. D. Smith, *Phys. Rev. B* **19**, 3004 (1979).
14. B. L. Henke, J. P. Knauer, and K. Premaratne, *Bull. Am. Phys. Soc.* **24**, 1098 (1979).

CCD Applications for Transient Digitizers

Streak Camera Readout System. The ultrafast streak camera is one of the most valuable high-temporal-resolution diagnostic tools available in laser fusion research. The need for a totally computerized data acquisition system with which to take full advantage of the ultrafast camera has been previously addressed.[15] This year we report the development of a high-resolution, large-dynamic-range, all-solid-state data acquisition system designed specifically for the LLL laser fusion program's x-ray and 1.06-μm ultrafast streak cameras.

Our system design philosophy seeks to achieve three primary goals:

- Minimization of computer processing of raw data.
- Immediate viewing of raw and processed data on a standard TV monitor, to determine the validity of the information captured.
- Minimization of the overall external hardware and software support requirements.

Based upon these criteria and our previously reported research,[16] we have chosen a newly developed RCA all-buried-channel charge-coupled-device (CCD) as our sensor. This two-dimensional solid-state silicon CCD has a resolution of 512 lines, each of which contains 320 individual pixels. Because of the all-buried-channel construction of the CCD, its dynamic range is greater than 256:1. We have also previously determined that this type of sensor provides linear response to both photon and electron excitations.

Using the RCA SID53601-XO CCD sensor satisfies our first goal, which is the minimization of computer processing before the acquired information is valid. Since the CCD is a linear device and shows no reciprocity failure even in the picosecond time domain,[17] no computer processing, analogous to D-log(E) corrections of film, is required. These ideal properties of the CCD thus translate directly to a higher level of confidence in the acquired streak data.

Our second design goal for a streak camera readout system is the ability to display streak data on a standard TV monitor immediately after the event. This instant playback is especially important during the initial streak-camera setup and/or calibration period, during which prompt feedback is required for such critical parameters as timing, jitter, and input-beam alignment. In many earlier systems, analog video recording devices (such as video disks) were employed to accomplish this task.[18] Unfortunately, these analog techniques require a compromise between instantaneous playback and the dynamic range of the instrument.

To circumvent this trade-off while preserving the all-important instant playback feature, we have developed a unique all-solid-state, random-access, high-speed image memory capable of recording and subsequent playback of all 320 × 512 pixels of CCD data with an intensity resolution of 256 gray levels (8 bits). Furthermore, the image-memory readout unit is designed to the specific requirements of the streak camera application: timely computer processing of the large volume of CCD data is ably promoted by such features as high-speed direct-memory-access data transfer in the column, row, or diagonal read/write modes.

A number of design features combine to satisfy our third goal, that of minimizing the data acquisition system's external support requirements:

- With a set of special control lines we can program the instrument's operating characteristics totally by means of software control.
- To integrate the readout system into a large, instrument-laden laser facility like Shiva, we

Fig. 5-19. General view of the CCD data acquisition system for an existing LLL ultrafast x-ray streak camera.

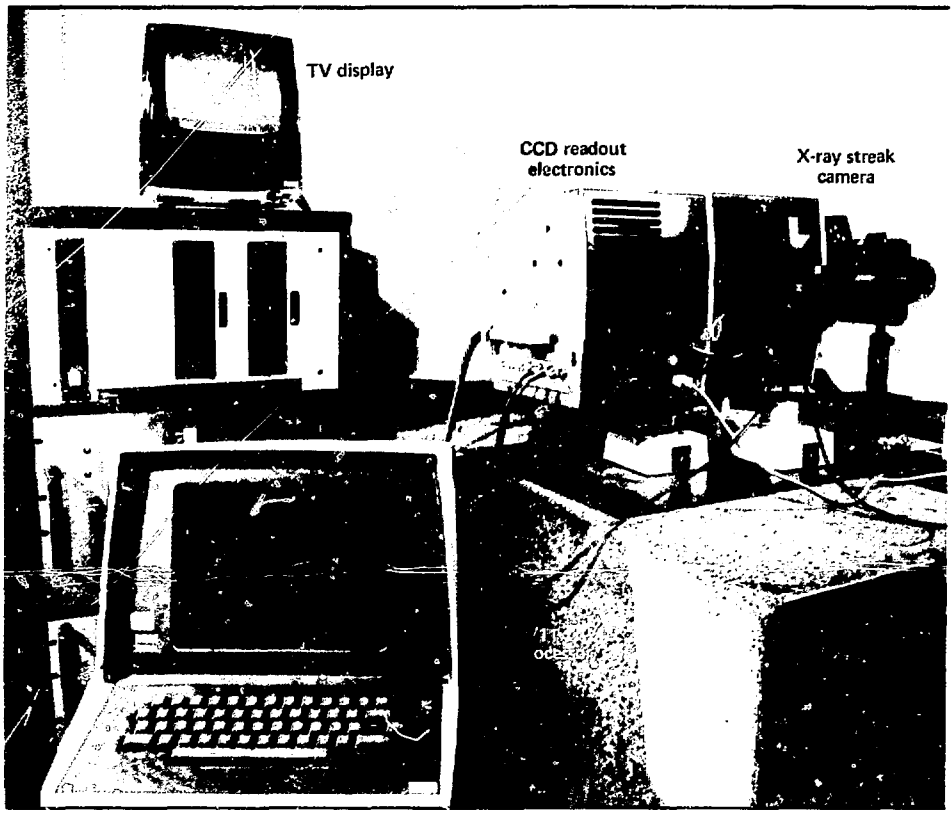

have included options which initialize, enable computer, trigger the system, and provide calibrated background, gain, and sweep speeds.

- To simplify the operation of the readout unit, we have developed a new CCD scanning mode which removes the need for a pre-event trigger. This simplification is of great importance in a large laser diagnostic system where various other instruments may require complex and precise pre-event triggers: an additional load to the master timing network may be inconvenient or difficult to achieve. With the advent of this new CCD continuous scanning mode, the readout instrument need only be triggered at event time (zero time trigger). The source of this zero time trigger can be conveniently derived directly from the streak camera's own sweep circuit.

Figure 5-19 shows a general view of one version of the LLL streak camera diagnostic system. In this version, the CCD camera portion of the readout system is optically coupled to the phosphor end of a standard LLL 10-ps streak camera with a 2.5-to-1 coherent fiber-optics minifier. (This external coupling technique of course offers the advantage of minimal hardware redesign in retrofitting existing streak cameras with a CCD readout system.) A cable connects the camera portion of the instrument to the image memory unit; the two sections can be separated by at least 100 feet, and data transmissions between the two sections are totally digital. Figure 5-19 also shows the instant-playback TV

Fig. 5-20. Schematic of an x-ray streak camera data acquisition system, implemented in a stand-alone configuration.

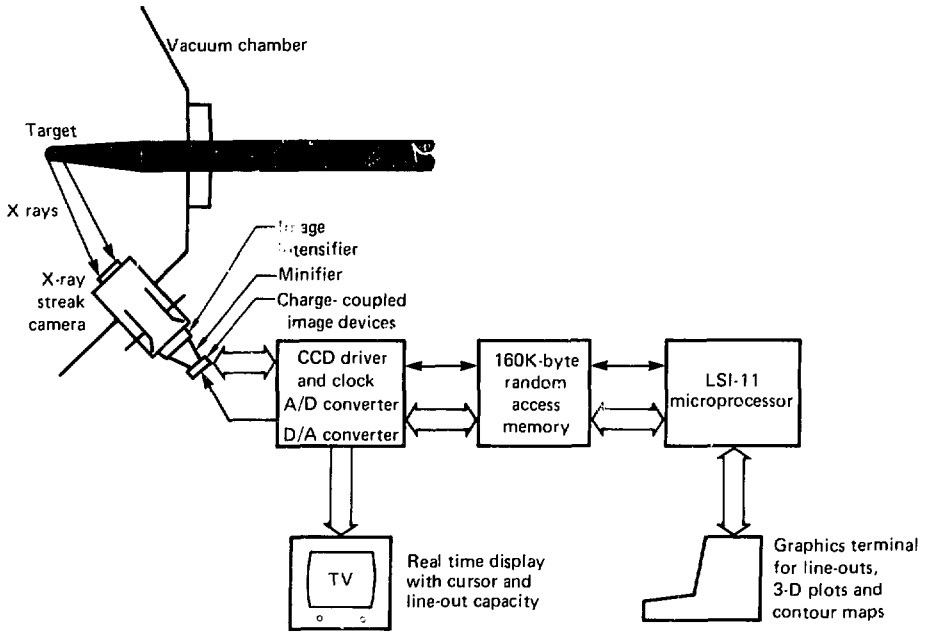

monitor, a local LSI-11 processor, and a Tektronix 4006 graphics terminal. In this case, the system has recorded a series of 1.06-μm etalon pulses, and has displayed the recorded data on the video monitor both as a two-dimensional intensity-modulated picture and as a computer-generated line-out profile (also visible on the graphics terminal).

Figure 5-20 shows a schematic of the main segments of a complete x-ray streak camera data acquisition system and computer interface network:

- X rays generated by the target in an experiment are recorded by an x-ray streak camera.
- The phosphor image is transmitted by a fiber-optics minifier to an all-buried-channel CCD sensor.
- The analog CCD data is digitized to an intensity resolution of 8 bits at standard video rate (6 MHz) and stored in the solid-state image memory unit.
- The digitally recorded data in memory are accessible either by a computer (in digital format) or by the TV monitor (in analog format) as a standard interlaced video NTSC picture.
- The memory unit can be interfaced to a local LSI-11 computer bus, for example, or to a custom bus (such as the CMOS power conditioning bus at Shiva; see Section 2, "Engineering Summary and Update: Power Conditioning") which totally bypasses the need for a local microprocessor.
- Finally, the system is capable of external composite synchronization. Video information displayed either from memory or at real time can be joined with all other video data from diverse sources (streak cameras, TV cameras, etc.), and viewed through a standard studio TV switching network.

CCD Ultrafast Transient Recorder. Multigigahertz oscilloscopes, like streak cameras, are a primary diagnostic tool for many laser fusion experiments. From studies using intensified (i.e., electron-in mode) CCD readout for an EG&G

Fig. 5-21. The LLL/Tek 4-GHZ R7912/CCD transient digitizer system, along with the associated LSI-11 microprocessor, image memory, TV, and graphics terminal.

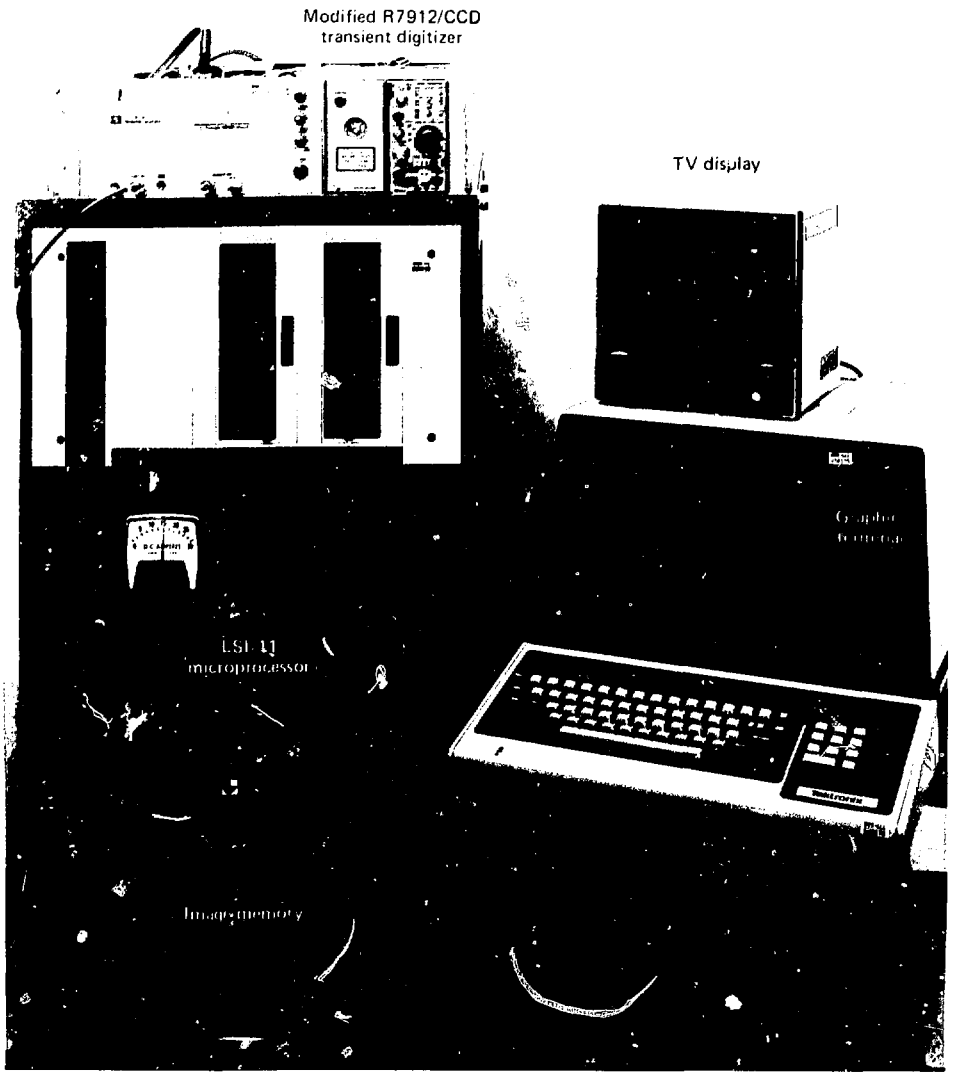

KR23 oscilloscope, it became clear that a CCD sensor has many advantages over conventional phosphor/film readout techniques.[19] During the past year we have made significant progress toward producing a practical CCD transient digitizer for use in a CCD multigigahertz oscilloscope system: advances were made possible by joint efforts of LLL, RCA, and Tektronix research groups.

The 4-GHz CCD ultrafast oscilloscope we developed uses many components already developed for the CCD/streak camera data acquisition

system, as a general view of the LLL Tek CCD transient digitizer system shows (Fig. 5-21). The instrument itself is basically a Tektronix R7912 whose original diode target array and read gun have been replaced with a vacuum-compatible back-thinned 52501 surface-channel CCD sensor. Prior research determined that the CCD sensor exhibited many advantages over the original R7912's diode target array, the two most important being

- A low dead-layer voltage. The dead-layer voltage is the amount of energy an input electron must dissipate before it can begin generating useful electron-hole pairs within the CCD sensor. The writing rate of the electron gun sensor package is directly related to the final number of signal electrons generated per incident electron. Since the CCD requires a smaller dead-layer dissipation energy than the original diode target array, a correspondingly lower electron beam energy can maintain the same writing rate; this lower electron-gun energy translates directly to a higher deflection bandwidth for the modified R7912 CRT. We are able to operate the electron gun at 7 keV, rather than the original 11 keV, which produced a better match between the electron propagation velocity and the deflection voltage's phase velocity within the helix traveling wave deflection structure.
- Superior antiblooming property. The antiblooming property of a CCD is the sensor's ability to prevent both vertical and horizontal charge spillage into adjacent CCD cells when the sensor is overloaded. In the original R7912, a diode target array was used to record the electron beam. In that design, there was a trade-off between the target's antiblooming property and its sensitivity to electron excitations. Now, with the incorporation of a CCD into the R7912, the excellent antiblooming property and the high electron sensitivity can be achieved simultaneously, which will significantly improve the overall performance of the transient recorder.

Figure 5-21 also shows a 160K-byte solid-state image memory and an LSI-11 local microprocessor, designed to be incorporated into the existing R7912 commercial housing unit. The system has here recorded a 100-ps electrical pulse and is redisplaying the captured data from memory onto a TV monitor. A corresponding computer-generated scope trace of the pulse also appears on the Tektronix 4006 graphics terminal.

In summary, the major advances in the CCD CRT area this year are

- The successful incorporation of a CCD sensor into a Tektronix high-speed R7912 electron-gun envelope; this combination has resulted in a wider bandwidth and higher writing rate, due mainly to the R7912 electron gun's smaller spot size (40 μm) and higher beam current (5 μA).
- The development and usage of the 160K byte 8-bit-resolution image memory unit which enables the combined instrument to capture, process, and display the transient digitizer data in an efficient and timely manner.

Author: J. C. Cheng

Major Contributors: G. R. Tripp, J. T. Noonan, R. J. Schnetz, E. Savoye (RCA), and L. Riley (Tektronix)

References

15. *Laser Program Annual Report—1976*, Lawrence Livermore Laboratory, Livermore, Calif., UCRL-50021-76 (1977), pp. 4-63 to 4-67.
16. *Laser Program Annual Report—1978*, Lawrence Livermore Laboratory, Livermore, Calif., UCRL-50021-78 (1979), p. 6-84.
17. J. C. Cheng, G. R. Tripp, and J. W. Coleman, "Intensified CCD Readout System for Ultrafast Streak Cameras," *J. Appl. Phys.* **49**, 5421 (1978).
18. *An Improved TV Scanning Method for Recording Time-Resolved Optical Spectra of Transients*, Argonne National Lab. Report ANL-78-62 (March 1976), p. 27.
19. J. Cheng, *J. Appl. Phys.* (to be published).

Reflector-Diffractor Spectrograph Measurements on Shiva

We are interested in making high-resolution x-ray spectroscopy measurements in the photon energy region from 0.9 to 1.2 keV, because this region contains characteristic lines (in the N and O series) of gold and other heavy elements. There are two types of instruments that can be used in this region, the diffraction crystal spectrograph and the grazing-incidence grating spectrograph, although it is difficult to obtain accurate quantitative data from either instrument in the region of interest.

Despite the practical advantages of the crystal spectrograph, including lower initial cost, easier

Fig. 5-22. Schematic of the Shiva reflector-diffractor spectrograph, with grazing-incidence mirror reflectivity limited to 1.2 keV; actual size of mirror is 4 in. × 4 in.

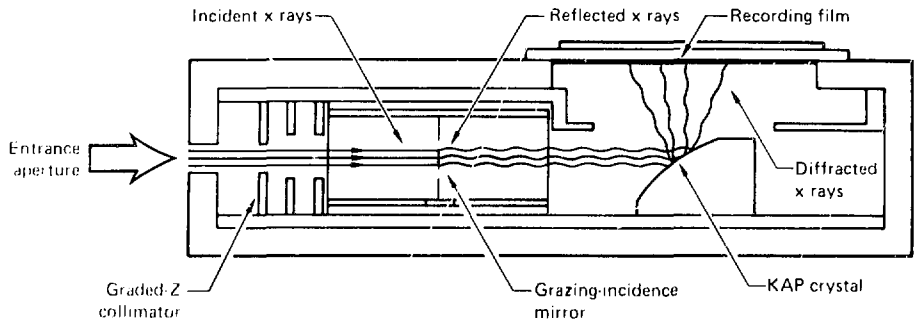

Fig. 5-23. X-ray response of key components of the crystal spectrograph.

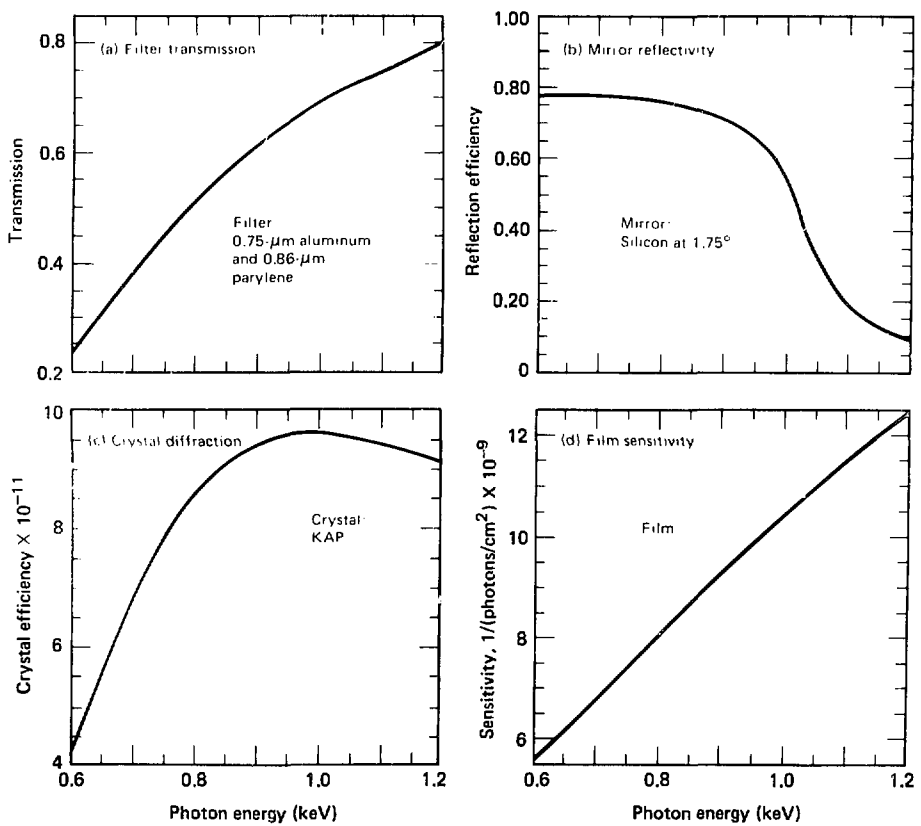

alignment and maintenance, and higher x-ray sensitivity, previous attempts to use crystals to record sub-kilovolt spectra have demonstrated a basic problem with the method: the sensitivity to x rays of greater photon energy than desired (such as the M lines of gold near 2.5 keV). This unwanted response results from the nonnegligible second- and third-order diffraction efficiency of crystals, and from the greater x-ray transmission and sensitivity of filters and photographic film, respectively, at higher photon energies. To suppress unnecessary sensitivity, a reflector-diffractor spectrograph in operation at Shiva (Fig. 5-22) uses a grazing-incidence mirror whose reflectivity falls abruptly above 1.2 keV, effectively filtering the x-ray beam reaching the KAP crystal. Measurements obtained with this instrument for titanium, vanadium, and gold disk shots at Shiva have provided useful qualitative information, indicating whether significant energy in the region from 0.6 to 1.2 keV is contained in characteristic lines.

Low response characteristics also make it difficult to obtain accurate quantitative data with the spectrograph, because small errors in the calibration of the components can produce significant errors in the reduced spectral data. Figure 5-23 shows the x-ray response of the spectrograph's key components. At low photon energies (near 0.6 keV) the light-tight filter does not transmit well, the crystal reflectivity is low, and the photographic film is not sensitive; Fig. 5-24 shows the same general result for the total instrument response. Under these conditions, small calibration error may translate into significant error in reduced data. To date agreement between the spectra (Fig. 5-25) obtained

Fig. 5-24. Complete reflector-diffractor spectrograph sensitivity.

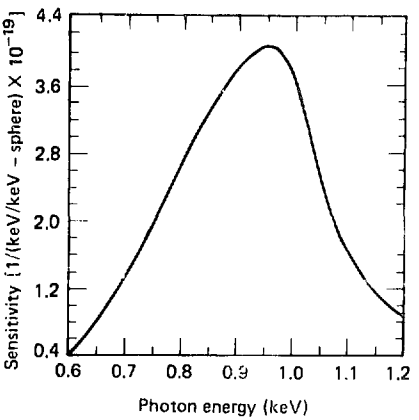

Fig. 5-25. X-ray spectra in the region of 0.6 to 1.2 kev, obtained for (a) titanium and (b) vanadium disk shots at Shiva.

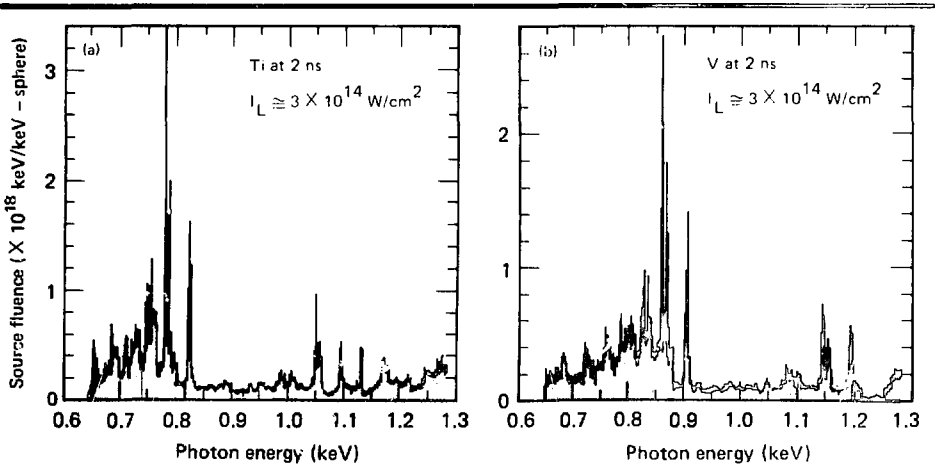

with the crystal spectrograph and with the Dante spectrometer systems has not been good. A careful recalibration of the spectrograph components is proceeding, and the situation should improve.

Spectra obtained with the instrument for several types of disks are shown in Fig. 5-25. The disks were irradiated with 3×10^{14} W/cm^2, in pulses of 2 ns. The data for the titanium and vanadium disks show many sharp lines in the L series, due to the beryllium-like and lithium-like species (4 or 3 electrons remaining bound to the ion). Despite a wide range of irradiation conditions, however, distinct lines for gold in the N and O series have never been observed.

Author: L. N. Koppel

Fig. 5-26. X-ray reflectivity of a tungsten-carbon synthetic multilayer structure (SMS) mirror, in the region from 4 to 12 keV; each profile results from diffraction at a particular θ from 1.4° to 3.5°.

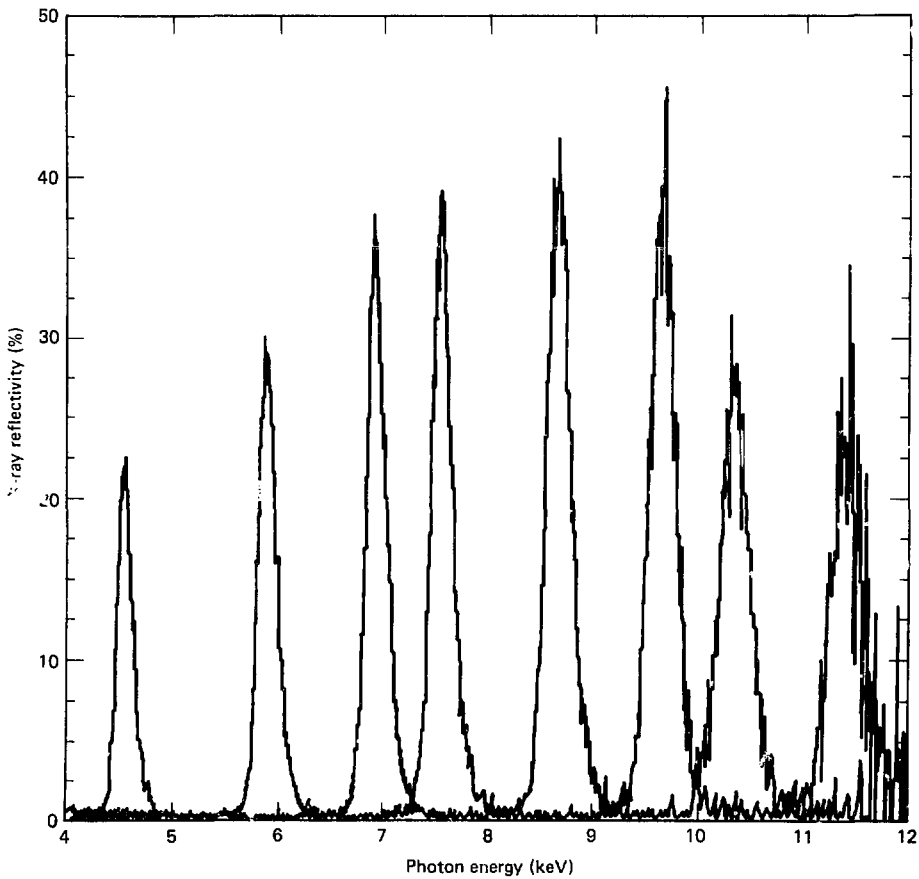

Fig. 5-27. Comparison of tungsten-carbon and lead myristate multilayer x-ray mirrors in the region from 500 to 1000 eV, for various layer pairs. Reflection probability is plotted vs 2θ.

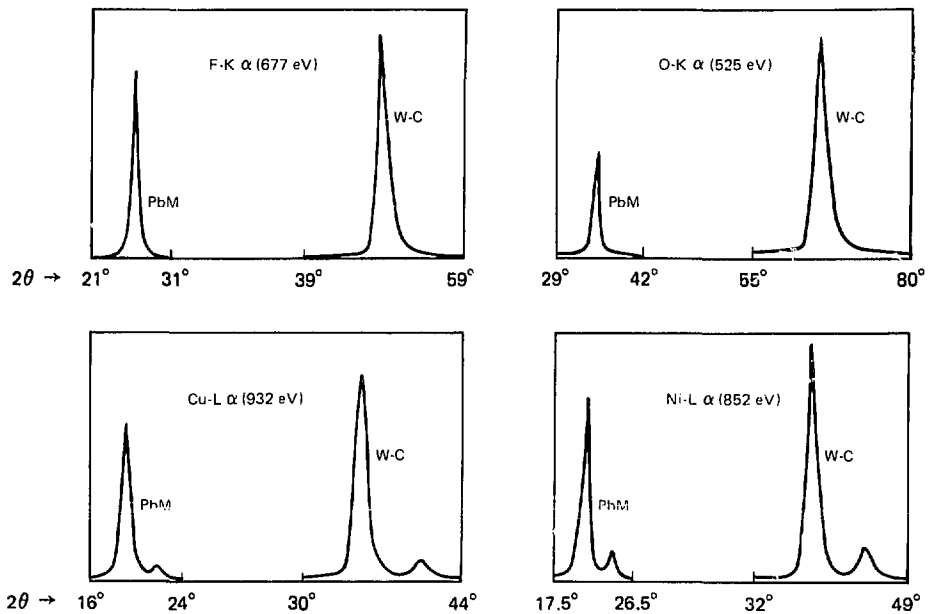

Synthetic Multilayer Structure Characterization

We are participating with the Center for Materials Research (CMR) at Stanford University in a project to develop and refine a new type of x-ray mirror based on x-ray interference within a synthetic multilayer structure (SMS). On a smooth substrate we use vacuum sputtering deposition to build up a stack of films, where each film is 7 to 15 or more Å thick. Each layer of the stack is actually a pair of films (called a layer pair), one each of a high- and low-Z material; a typical layer pair consists of tungsten and carbon. The spatially-periodic variation in coherent scattering power produced by this construction results in efficient medium-bandwidth x-ray diffraction. We have observed, for example, peak x-ray reflectivities of 20 to 40% and resolutions of $E/\Delta E = 30$ to 40 for tungsten/carbon structures.

Dispersion by the SMS is controlled by the Bragg relation: $\lambda = 2d \cdot \sin\theta$, where θ is the grazing incidence angle of an x-ray beam and d is the thickness of a layer pair. Samples with values of d as small as 14.5 Å have been built and tested, making feasible the use of the SMS in the wavelength region from 1 to 100 Å. Figure 5-26 (opposite) illustrates the x-ray response of a tungsten-carbon SMS with a d value of 22.4 Å; each profile results from diffraction at a particular θ in the range from 1.4° to 3.5°.

X-ray testing was performed in a vacuum diffractometer equipped with a Henke tube x-ray source (this facility is maintained by the L-division X-ray Measurements Group at LLL). The x-ray beam was continuous in energy in the region from 4 to 12 keV and was collimated to 1/2 arcmin in the plane of dispersion. Spectra of the beams incident on and reflected by the sample were obtained with a high-resolution Si(Li) detector. At each of several values of incident angle, a raw band-pass curve was obtained by dividing the reflected spectrum by the

incident spectrum; the curves in Fig. 5-26 were obtained in this manner.

Multilayer mirrors have the following advantages when used as spectrometers in the region from 1 to 10 Å:

- The resolution of the SMS bridges the gap between those of natural crystals and spectrometer channels defined by Ross filter techniques.
- The dispersion and resolution of the SMS can be tailored by adjusting the value of d and number of layer pairs.
- An SMS with equal layer thicknesses and graded interfaces suppresses high-order diffraction response.

When used in x-ray imaging instruments, the attractive properties of the SMS are

- Efficient reflection of x-rays whose photon energies exceed the practical limit of total external reflection.
- Adaptability to curved substrates, making feasible x-ray optic elements of complex curvature.

Multilayer mirrors can also be used to good advantage in the region from 10 to 100 Å, where the choice of x-ray dispersion elements has previously been limited to grazing-incidence ruled gratings and stearate-type (soap film) artificial crystals. For measurements requiring high spectral resolution ($\lambda/\lambda\Delta > 100$) there is no alternative to gratings. The SMS, however, appears to be better suited than the stearate-type crystal for medium-resolution applications in this region, because

- The d value for the SMS is not controlled by the carbon chain length of high-melting-point fatty acids, but can be freely selected.
- The particularly pernicious higher-order diffraction response of stearate crystals can be avoided by proper SMS fabrication.
- Proper selection of SMS component elements preserves sensitivity in the region from 25 to 50 Å where the reflectivity of stearate crystals is very low.

Measurements at the University of Hawaii have provided the most thorough characterization of the SMS in the soft x-ray region. As shown in Fig. 5-27, the reflectivity of a tungsten-carbon SMS is about twice as high as that of a lead myristate crystal.

Author: L. N. Koppel
Major Contributors: T. W. Barbee (Center for Materials Research, Stanford University) and B. L. Henke (University of Hawaii)

Shiva Optical Pyrometer

The Shiva optical pyrometer is designed to measure visible light emitted by a target. An achromat telescope focuses light magnified by about ten onto the slit of a streak camera; the beam is split to provide two spectral channels, usually chosen to be in the orange and blue regions of the spectrum (Fig. 5-28). Also, a portion of one of the incident laser beams is doubled to provide a 5320-Å timing fiducial for the streak camera. This 5320-Å fiducial is necessary because the streak tube has an S-20 photocathode. Each streak camera photograph will thus have three concurrent, but spatially separate, streaks.

The fiducial is timed by irradiating foils with rod shots of short pulse length. For these shots both spectral channels are set up to respond to 2ω light from the target. We assume that the peak intensity of the 2ω light is coincident with the peak intensity of the 1.06-μm light.

The KDP doubling crystal is aligned using the collimated beam from the Argus oscillator; the phase-matching direction is indexed by two crosshairs. The entire optical assembly is on a kinematic mount.

The streak camera detects light coming from a part of the target that is typically only several hundred micrometers across; such a source requires that we check the alignment of the optical assembly before every shot if our results are to be believable. For alignment, the target is illuminated at the specular angle, as shown in Fig. 5-28 (plan view). We view the target in reflection, rather than simply shadowing it, because the laser-irradiated side of the target is usually masked off by a large shield many millimeters in size; this shield is necessary for the complementary low-energy Dante diagnostics, which presently have no imaging capability.

We have measured the transmission of the two optical paths as a function of wavelength, using unpolarized light, and have measured the spectral response of the streak camera photocathode. With this information, we can calculate preheat temperature from the ratio of the orange and blue chan-

Fig. 5-28. Plan and side views of the Shiva optical pyrometer; the two achromat lenses in the telescope are not shown.

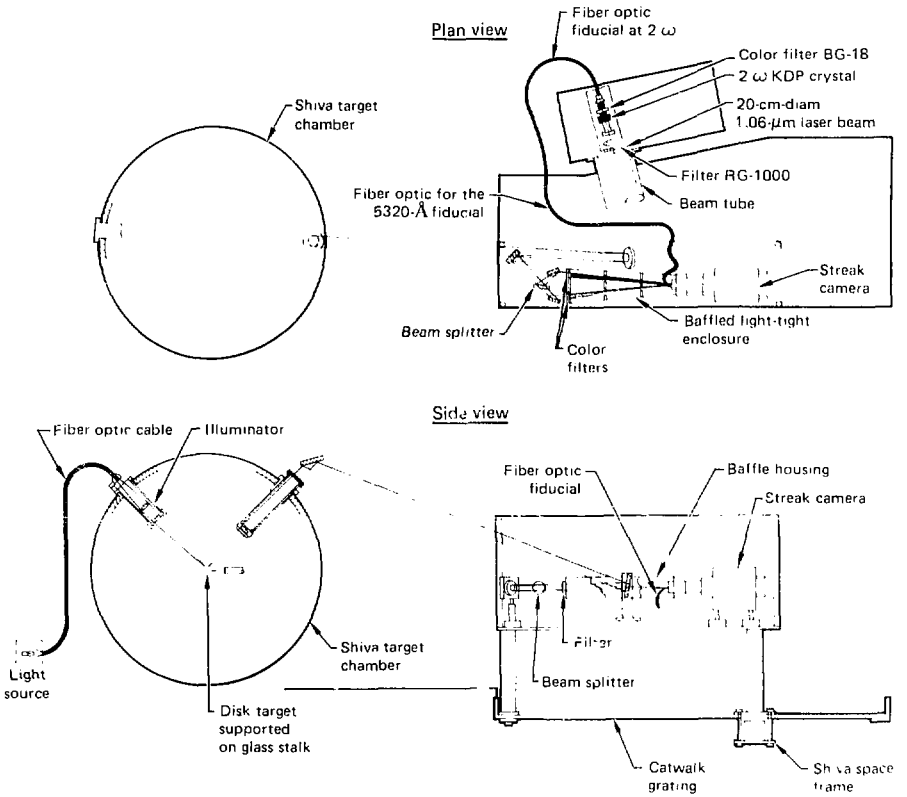

nel fluences, provided $T \gtrsim 1$ eV.

If the temperature is too high, both channels see emission in the Rayleigh-Jeans portion of the blackbody spectrum, where the flux is simply proportional to the temperature; the ratio of the two fluences will then tell us only that the temperature is high. The streak camera has been absolutely calibrated, however, so that we can also deduce a temperature from the film exposure, using the calibrated step-wedge exposed on the film; the spectrum and duration of the light exposing the step-wedge match those of the light radiated by the P-11 phosphor at the output of the streak camera microchannel plate.

Author: D. W. Phillion and M. W. Kobierecki
Major Contributors: D. L. Banner and R. D. Rudd

Shiva Raman Light Spectrograph

We are setting up an optical experiment at Shiva that will give far greater spectral resolution of the Raman-scattered light than was achieved at Argus, where the spectrum had to be obtained from many laser shots by changing interference filters. The heart of this experimental diagnostic is a 25-element indium arsenide array fabricated by Judson Infra-red. The array is mounted in a stainless steel Dewar flask and cooled to the liquid nitrogen temperature of 77 K. The array will be read out by

Fig. 5-29. Experimental setup to spectrally resolve Raman-scattered light at Shiva.

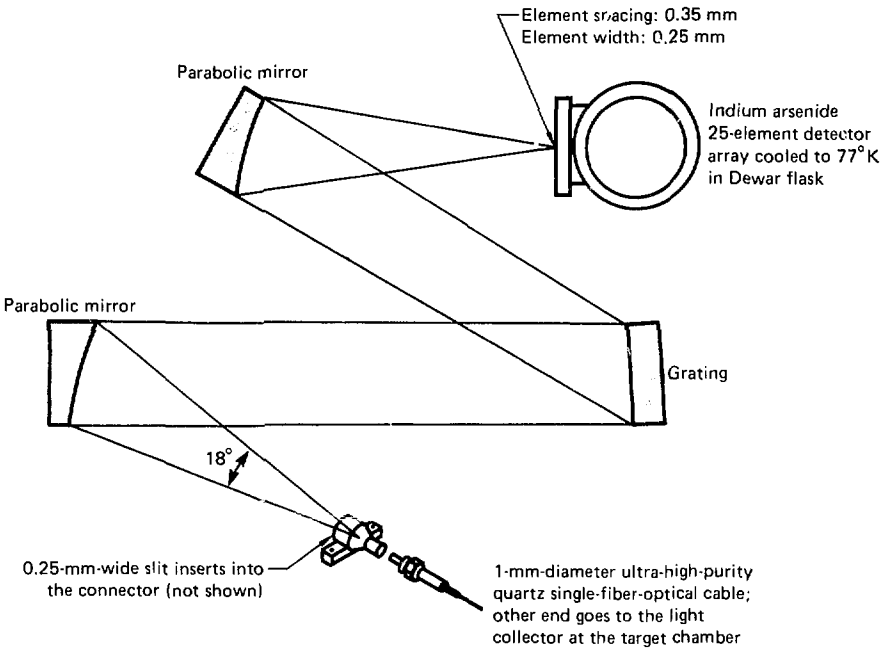

programmable charge-integrator modules interfaced with the Shiva data acquisition system. Each single-width module contains four channels, whose sensitivities are set by computer control.

The spectrograph (Fig. 5-29) is compact: the Dewar flask is 2-1/2 in. in diameter and 5-1/2 in. high, the optics are 2 in. in diameter, and the effective focal length of the two parabolic mirrors is 6 in. (f/3.2). A $2\lambda_0$ wavelength fiducial is provided by the 1.06-μm light in second order; the light is brought by fiber optic from one of the cw alignment lasers.

The light collector (Fig. 5-30) is designed to fit on a dome port of the Shiva target chamber at either $\theta = 20$ or $\theta = 160$; we use the folded design because all dome ports at Shiva are located under lens positioners, allowing only about 2 in. of vertical clearance. The Raman-scattered light is expected to be highly collimated by refraction along the density-gradient direction. For most of the experiments we plan, this demands a location as close to the axis as possible. Mirrors are used instead of lenses so that we can align the light collector using visible light and still be confident it is also aligned for the Raman-scattered infrared light. A diamond-turned ellipsoidal mirror focuses the light from the target onto the fiber optic with a magnification of 0.0825. The ellipsoidal mirror that determines the light-collection solid angle is 40 mm by 40 mm, and is placed 1265 mm from the center of the target chamber; the light-collection solid angle is about 1.0×10^{-3} steradians.

Since the quartz optical fiber is one millimeter in diameter, the field of view is 12 mm across laterally; longitudinally, the field of view is hundreds of millimeters deep. A dielectric coating on the Infrasil window is highly reflective of 1.06-μm light, but transmits in the spectral region of interest from 1.2 to 2.6 μm. Color filters (such as the Corning 7-56 visible-light-absorbing filter and the Corning 4-64 near-infrared-absorbing filter) will also be

Fig. 5-30. Light collector for a Shiva dome port, to be fit at $\theta = 20°$ or $\theta = 160°$.

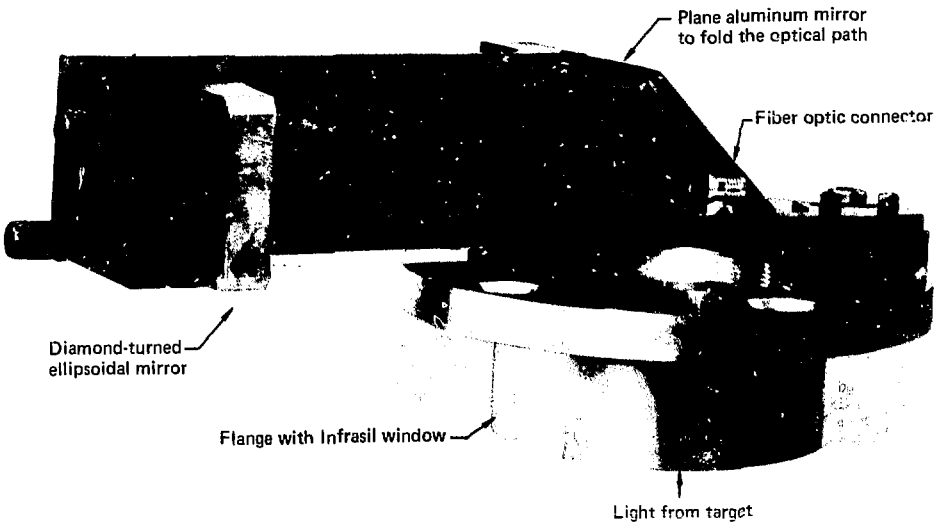

used to ensure that only the Raman-scattered light is collected.

The entire system is calibrated with a blackbody source placed in the field of view of the light collector. Since the blackbody source has an emissivity known to ±1%, an aperture area known to 0.1%, and a temperature (variable up to 1273 K) which is known to ±2 K, the absolute spectral intensity in watts/(μm-steradian) can be accurately calculated. We will make a dc measurement of the current generated by each indium arsenide detector using a nanovoltmeter shunted by a small resistance. The background current can be cancelled with a high-impedance adjustable-current source, so that with the blackbody source blocked, no voltage appears across the small shunt resistance. This measurement technique has worked well in calibrating other indium arsenide detectors and has agreed with the pulsed calibration within error. We can thus calibrate the entire system with the same filters as are used in the experiment.

We make the assumption that the cw calibration will agree with a pulsed calibration in the low-power, low-energy limit. The somewhat nonlinear response to a short high-energy light pulse can be corrected for by measuring the curve giving the output charge as a function of the relative energy of the incident light pulse. The relative energy scale can be made absolute by assuming that the low-energy linear asymptote agrees with the low-power cw calibration. Should questions arise, however, a pulsed calibration will be carried out off-line.

Author: D. W. Phillion
Major Contributors: W. B. Laird, R. K. Reed, D. K. Walton, and T. D. Schwinn

Neutron and X-Ray Emission Time Measurements

Neutron diagnostics have been used since the beginning of the laser fusion program at LLL to measure thermonuclear yield and reaction temperature in "exploding-pusher" ICF targets. With optimum exploding-pusher targets, the laser pulses were 30 to 100 ps FWHM; implosion times were typically less than 200 ps. For these conditions we determined implosion times using our x-ray streak camera.[20] Now, as we change our emphasis to colder targets with thicker shells and higher ρR's, x-ray studies become more difficult and our diagnostics become much more dependent on

Fig. 5-31. (a) Schematic of the experimental setup for neutron emission time measurement. (b) Example of raw data; x-ray, neutron, and 1.06-μm light signals are delayed and combined to give a convenient order and spacing on the oscilloscope trace.

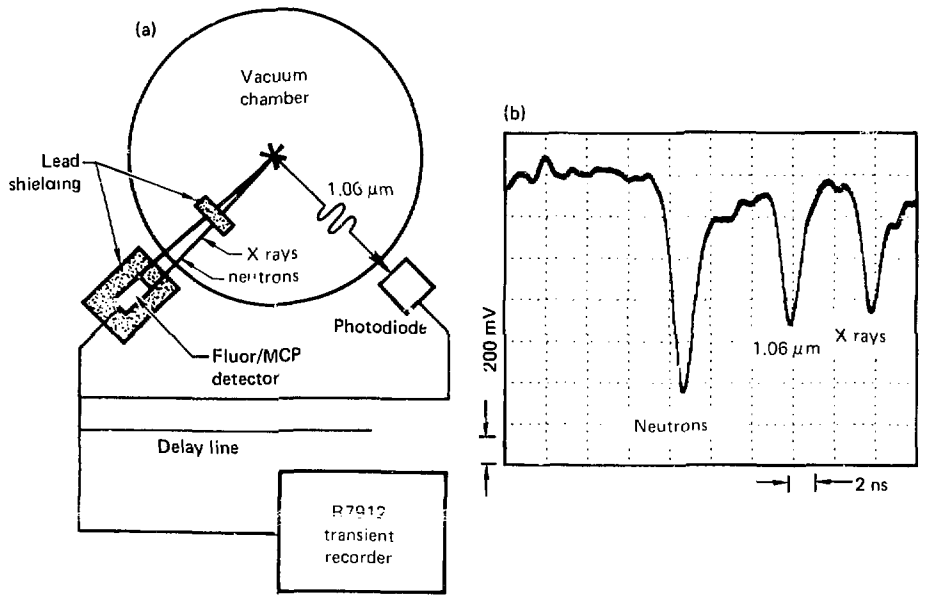

Fig. 5-32. (a) Schematic of the fast neutron/x-ray detector. (b) Detector impulse response.

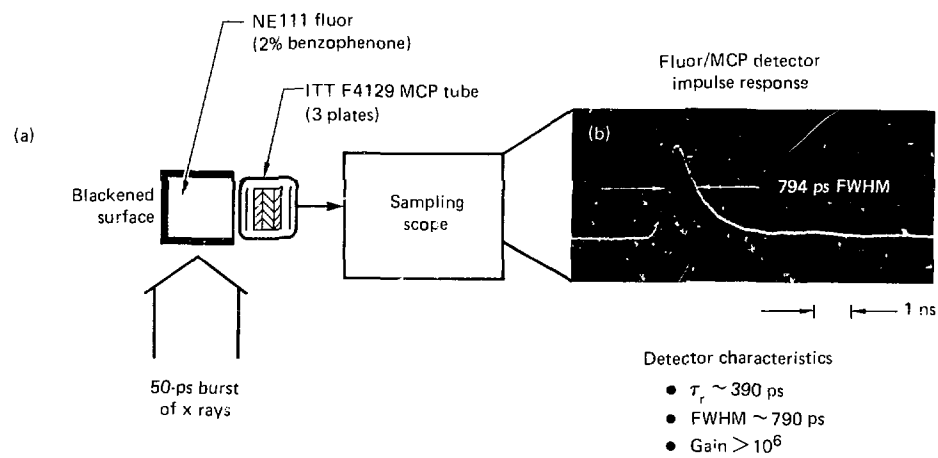

Fig. 5-33. Neutron emission time relative to the laser pulse peak, for 10 shots that had similar laser and target characteristics. For these shots, the average emission time is 295 ps (solid line) ±85 ps (shaded area).

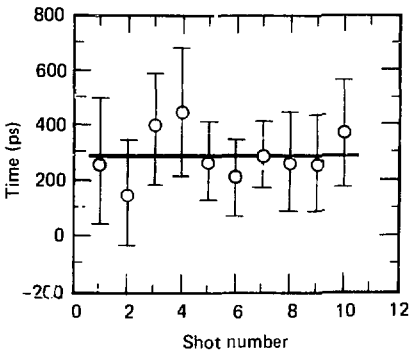

penetrating radiations such as neutrons (see "Compression Diagnostics for High-Density, Low-Temperature Targets" later in this section).

A diagnostic which can be particularly valuable for providing information about the implosion dynamics of double-shelled targets is "neutron interval timing," whereby an implosion time is deduced from the time difference between laser and neutron signals recorded with a single transient recorder. We have built and used such a device, coupling a fast neutron detector and a separate fast photodiode (for laser light) to a single recording instrument. This neutron system[21] is designed to

- Measure neutron and high-energy (>40 keV) x-ray emission times relative to 1.06-μm laser pulses, with a precision of ±100 ps.
- Be useful with neutron yields in the range from 10^6 to 10^{14}.
- Function in the presence of large x-ray bursts.

Figure 5-31 shows (a) a schematic of the system and (b) an example of raw data. The fast neutron detector used in our studies is an NE111 plastic scintillator 46 mm in diameter and 25 mm thick, quenched with 2% benzophenone.[22] The scintillator is coupled to a three-stage ITT F4129 microchannel plate (MCP) photomultiplier tube, as shown in Fig. 5-32(a). The external scintillator surfaces are painted black to reduce dispersion by internal light reflections; lead shielding attenuates the intense x-ray bursts and concomitant fluorescence.

The detector response, shown in Fig. 5-32(b), has a 390-ps rise time, a 790-ps FWHM, an electron gain of 10^6, and recovers to baseline in several ns. A yield of 10^7 neutrons produces approximately 300 interactions in the scintillator, located 0.9 m from the target.

The detector setup to monitor scattered light from the target consists of an ITT F4018 biplanar vacuum photodiode with an S-1 photocathode. Signal levels in the 300-ps rise-time detector are controlled with a 100-Å-wide band-pass filter centered on 1.06 μm, and appropriate neutral-density filters. X-ray and neutron signals from the neutron detector and the scattered light signal from the photodiode are mixed with 50-Ω power-splitters and recorded by 500-MHz Tektronix 7912 transient recorders. We select appropriate cable lengths and use an open-circuit delay stub to display the three signals with optimal sweep speed, in conveniently displaced positions [Fig. 5-31(b)].

Emission time measurements are subject to both systematic and statistical errors:

- Systematic errors are associated with instrument time-delay uncertainties, which affect the absolute position of all timing data in the same manner. Systematic errors are estimated to be less than ±175 ps for neutron data and ±120 ps for x-ray data.
- Statistical errors are associated with uncertainties in neutron interaction with the detector, deconvolution of the system response, and data reduction of the scope traces. These uncertainties are typically ±175 ps, and are primarily associated with making two readings from a single transient recorder trace.

Initial experiments have demonstrated the capabilities of our neutron interval timing technique. Figure 5-33 shows the implosion time deduced for 10 shots that had similar laser and target characteristics; in these tests the interval time was determined to be 295 ps, with a reproducibility of ±100 ps. This clearly indicates that the technique will be one of great value for the longer time intervals expected with larger, double-shelled targets.

X-Ray Measurements. Along with measuring relative x-ray spectra and pulse shapes, we are currently interested in monitoring the x-ray emission times relative to the incident 1.06-μm laser

pulse. We have implemented two similar systems for this purpose, one for x rays from 300 to 800 eV, another for x rays from 40 to 70 keV:

- To detect low-energy x rays from 300 to 800 eV, we use a filtered XRD-31 x-ray diode,[23] and an ITT F4014 vacuum photodiode to monitor a small fraction of the incident laser beam. Signals from the two detectors are fed to signal and marker inputs of a 4-GHz TSN 660 (Thompson-CSF) oscilloscope. Used with a TSN 660 oscilloscope, these detectors have impulse responses of about 200 ps FWHM. Representative outputs, for gold disk targets irradiated at two different intensities, are shown in Fig. 5-34.
- To monitor x rays in the 40 to 70 keV range, we use an ITT F4128 MCP photomultiplier tube with about a 400-ps FWHM time response. X rays pass through a filter pack, then interact in the MCP tube; the resultant signal is recorded on a TSN 660 oscilloscope, along with a photodiode signal applied to the marker input.

The object of data analysis for the x-ray systems is to detect small shot-to-shot shifts in x-ray emission time relative to the incident laser pulse, using the photodiode signal as a precise time fiducial. (No attempts have been made to determine the absolute emission times from these systems.)

Two digitized oscilloscope traces produced by our data analysis technique are compared in Fig. 5-35. The delayed photodiode signals (negative pulses) are normalized to facilitate alignment of the trace time axis. Then we translate the trace of interest so that the leading edge of its fiducial signal coincides with that of the reference shot. Next, the x-ray signals are normalized to permit better comparison of the signal shapes and relative shifts in emission times.

With this method we can detect relative time shifts of about 100 ps. We have arbitrarily chosen the peak of one of the x-ray pulses as the zero reference time; we have not yet attempted to determine the absolute x-ray emission time using the present systems because of the relatively large uncertainties in transit times through the various system components.

Authors: R. A. Lerche, H. N. Kornblum, and K. G. Tirsell

Fig. 5-34. Typical gold disk data recorded by the low-energy x-ray system. On each trace, the pulse to the left is the XRD-31 x-ray signal and the negative pulse on the right is the 1.06-μm photodiode signal. Note that the emitted x-ray pulse shape and intensity change with increasing incident laser intensity: (a) 3×10^{14} W/cm^2; (b) 1.5×10^{16} W/cm^2.

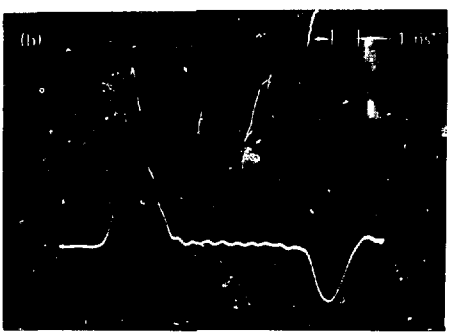

References

20. D. T. Attwood, L. W. Coleman, J. T. Larsen, and E. K. Storm, *Phys. Rev. Lett.* **37**, 499 (1976).
21. R. A. Lerche and J. T. Ozawa, "Neutron and X-ray Emission Time Measurements," Lawrence Livermore Laboratory, Livermore, Calif., UCRL-83092 (1979).
22. J. C. Cheng, K. G. Tirsell, G. R. Tripp, E. M. Lent, and R. A. Lerche, *Rev. Sci. Instrum.* 49(5), 650 (1978); P. B. Lyons, S. E. Caldwell, L. P. Hocker, D. G. Crandall, P. A. Zagarino, J. Cheng, G. Tirsell, and C. R. Hurlbut, *IEEE Trans. Nucl. Sci.* **24**, 1 (1977), p. 177.
23. See Section 5, "Temporal Response of the XRD-31 X-Ray Diode."

D-D Neutron Measurements

In 1979 we shot the first LLL laser-irradiated target with a significant D-D neutron yield. Of the four techniques we use to monitor D-T neutron yields—fast time-resolved scintillator/photo-

Fig. 5-35. Comparison of two TSN 660 oscilloscope traces for gold disk shots. The digitized laser (negative pulses) and x-ray (positive pulses) signals are normalized to facilitate comparison.

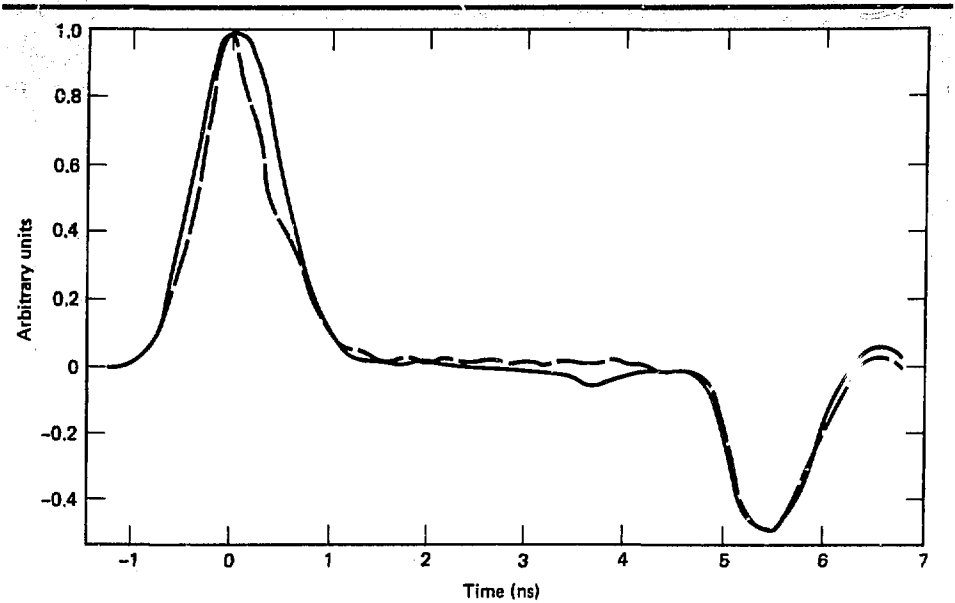

multiplier detectors,[24,25] copper activation,[26,27] lead activation,[28] and silver activation—all but copper activation can also be used to determine D-D neutron yields. The 10.9-MeV neutron activation threshold of copper renders it useless for measuring the 2.45-MeV D-D neutron yields.

The fast scintillator/PM tube system is perhaps the most important diagnostic technique. For a neutron source of subnanosecond duration, distinguishing which neutrons are truly D-D and which neutrons are D-T is easily accomplished by time-of-flight (TOF) separation. Signal strengths are used to determine the relative yield of the two species. We calibrate our scintillator detectors for D-T neutrons by comparing their output with laser-shot results obtained with a copper activation system carefully calibrated previously at the LLL RTNS facility; we then estimate the scintillator's D-D neutron sensitivity using Monte Carlo simulations and light response curves for D-D and D-T neutrons. For our scintillator/PM tube detectors, D-D neutron sensitivity is 12 times less than D-T neutron sensitivity. Figure 5-36 shows a representative scintillator detector output for a D-D neutron signal.

We developed our lead activation system as a sensitive monitor of low D-T neutron yields. The lead detector is calibrated for D-T neutrons by comparison with copper activation results on laser shots. To estimate the D-D neutron sensitivity of lead activation, we multiply the D-T sensitivity by the ratio of the cross section for forming Pb-207m with 2.45-MeV neutrons to the cross section for forming Pb-207m with 14-MeV neutrons. Using this technique, we determine the lead detector to be 62 times sensitive to D-D neutrons than to D-T neutrons.

A silver activation system mounted at Shiva has been monitoring neutrons from D-T targets since late 1978. D-T neutron calibration is determined by comparing the silver activation output with copper and lead activation results on laser shots. Monte Carlo calculations for the silver detector show the D-D sensitivity to be 1.25 times greater

Fig. 5-36. Oscilloscope trace for time-resolved scintillator/photomultiplier detector located 7.47 m from the target, showing 7.1×10^8 D–D neutrons; this trace shows no evidence of D–T neutrons. X rays arrive 119 ns before D–T neutrons and 319 ns before D–D neutrons. Sensitivities are 50 mV/div and 50 ns/div.

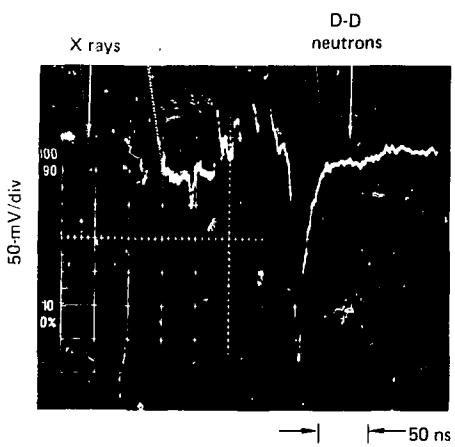

than its D-T sensitivity. D-D calibration of the detector has been done with D-D neutrons from a neutron generator, which provides a D-D calibration independent of the D-T calibration of the other detectors.

The D-D neutron yield values determined by the three systems are in good agreement; any one of the three can be used for diagnosing the yield from a D-D neutron source. If there are D-T neutrons present, however, the analysis is less simple. A D-T yield of only 1.6% of the total neutron yield produces a 50% error in the lead activation system; the silver system shows a similar inability to distinguish between D-D and D-T neutrons.

The most accurate D-D neutron measurement when D-T neutrons are also present is obtained with a combination of the scintillator, silver, and copper detectors. Estimates of D-D and D-T neutron yields can be made from scintillator data, and an accurate D-T yield determined from copper activation data; the silver counter output corrected for D-T yield gives the D-D yield. The lead system can duplicate the silver system, but has significantly poorer D-D sensitivity.

Authors: R. A. Lerche, M. S. Singh, and G. E. Phillips

References

24. *Laser Program Annual Report—1974*, Lawrence Livermore Laboratory, Livermore, Calif., UCRL-50021-74 (1975), pp. 337 to 339.
25. *Laser Program Annual Report—1975*, Lawrence Livermore Laboratory, Livermore, Calif., UCRL-50021-75 (1976), pp. 407 to 409.
26. *Laser Program Annual Report—1976*, Lawrence Livermore Laboratory, Livermore, Calif., UCRL-50021-76 (1977), pp. 3-105 to 3-108.
27. *Laser Program Annual Report—1977*, Lawrence Livermore Laboratory, Livermore, Calif., UCRL-50021-77 (1978), pp. 3-82 to 3-84.
28. *Laser Program Annual Report—1978*, Lawrence Livermore Laboratory, Livermore, Calif., UCRL-50021-78 (1979), pp. 6-53 to 6-54.

Compression Diagnostics for High-Density, Low-Temperature Targets

A significant task of our diagnostic program is developing techniques to determine the final fuel conditions in laser-compressed targets. The measurements of final fuel density and ρR have posed a particular challenge during the past year, as our program evolved from an earlier interest in thin-walled exploding pushers to concentration on thicker-walled targets designed to achieve higher fuel densities. As a consequence, present imploded cores are colder, but more dense, and are surrounded by a significantly less transmissive pusher.

These new conditions adversely affect the usefulness of previous diagnostics in two ways:

- Temperatures are lower, and thus targets emit fewer keV-range x rays and fewer thermonuclear reaction products such as neutron and alpha particles, each of which provided valuable diagnostic information for thin-walled targets.
- Because the surrounding glass pusher is of a higher $(\rho\Delta R)_p$ (our shorthand for ${}_0\int^R \rho dr$), fewer x rays and reaction products can escape and be used for diagnostic purposes.

These problems are summarized in Figs. 5-37 and 5-38. Figure 5-37 shows the transmission of x rays of 2, 3, 4, 6 and 8 keV, as a function of glass $(\rho\Delta R)_p$, for glass temperatures from 100 to 500 eV.

Fig. 5-37. Calculated x-ray transmission coefficient as a function of areal density of a compressed and heated glass pusher. The vertical yellow band labeled "EP" represents typical behavior for exploding pushers; targets which might achieve higher fuel densities are represented by the yellow bands labeled "10×" and "100×," indicating 10 and 100 times the liquid D-T density of 0.2 g/cm^3.

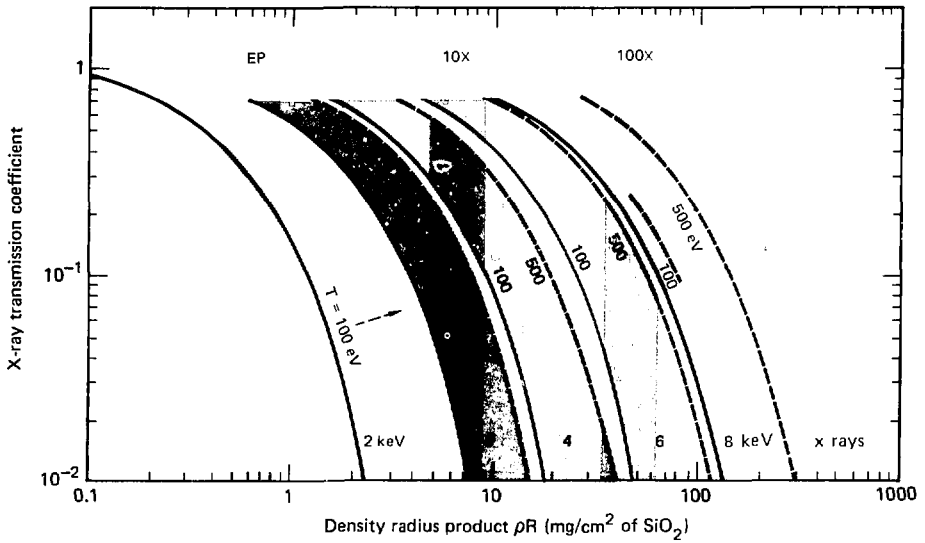

Fig. 5-38. Particle energy loss as a function of glass pusher areal density, for some common thermonuclear reaction products.

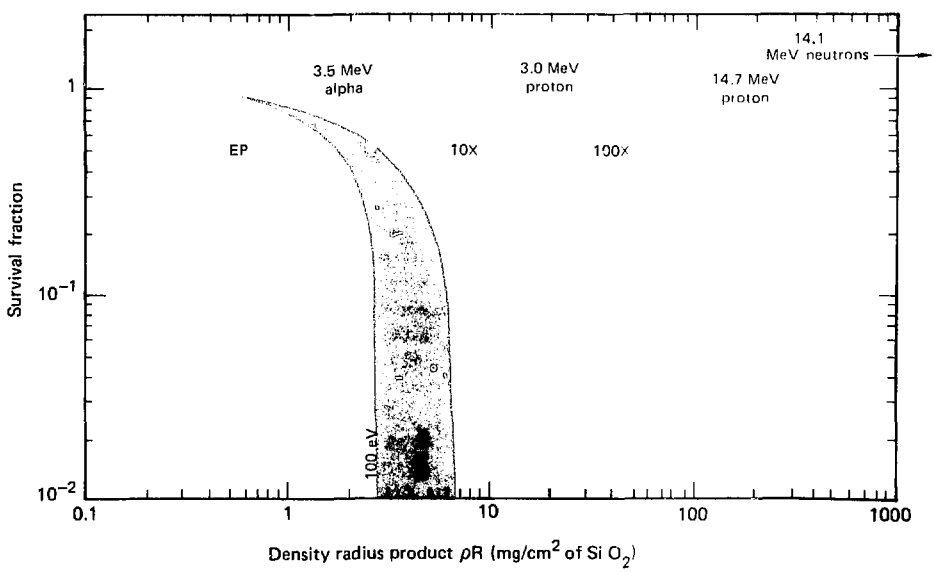

Fig. 5-39. Calculated operating regimes for various density diagnostics for ranges of experimental interest.

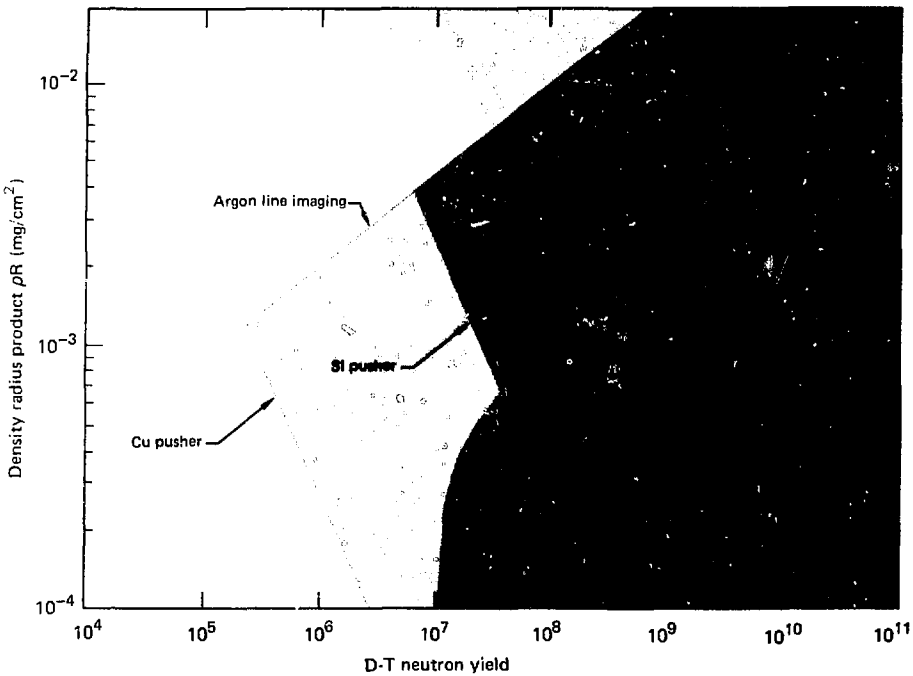

Note for instance that whereas 2-keV x rays are appropriate for diagnosing thin-shelled targets achieving final $(\rho\Delta R)_p$'s of < 1 mg/cm^2, targets that would achieve values as high as 30 mg/cm^2 require a photon energy of 6 to 8 keV to provide information regarding the fuel region or fuel-pusher interface.

The situation is similar for reaction-product alpha particles and protons, which also must pass through the compressed pusher if they are to provide diagnostic information on final fuel conditions. In Fig. 5-38 we see, for example, that 3.5-MeV alpha particles readily pass through the compressed glass of an exploding pusher [$(\rho\Delta R)_p \simeq$ 0.5 mg cm^2], permitting alpha imaging of the thermonuclear burn; with targets achieving $(\rho\Delta R)_p$'s $>$ 10 mg/cm^2, however, the alphas no longer escape. Thus our compression diagnostics must take advantage of higher-energy photons and more penetrating particles, such as multi-MeV protons and neutrons. Several such diagnostics are discussed in other articles in this section.

While Figs. 5-37 and 5-38 address the issue of photon and particle transport through the surrounding glass pusher, they do not address the issue of temperature-sensitive emission rates. Figure 5-39 includes such information in providing a simple guide to diagnostic operating regimes, given the parameters of (temperature-sensitive) neutron yield and target ρR (of either fuel or pusher, as appropriate). Although only a sampling of possible diagnostics is shown, the parameter space is well overlapped. Note that not only is the value of $(\rho\Delta R)_p$ important for alpha imaging, but the final fuel temperature, and thus neutron yield, must be high enough to produce a detectable image.

The role of neutron-activated bromine and argon tracer gases for measurement of fuel region $(\rho R)_f$ is also shown in Fig. 5-39, with an explicit inverse relation between neutron yield and achieved $(\rho R)_f$. We can see that for the assumed seed conditions, a $(\rho R)_f$ of 10 mg/cm^2 would require a neutron yield in excess of 10^7. Threshold for silicon pusher

$(\rho\Delta R)_p$ measurements is ten times lower, but these diagnostics require modeling to relate pusher and fuel conditions. Not shown in the figure are variable-energy x-ray images which can provide two-dimensional compression symmetry as well as stability information, but whose emission levels are quite sensitive to fuel-pusher interface temperatures—a situation difficult to summarize in a single illustration.

Our program is presently pursuing a broad-based approach to compression diagnostics, emphasizing the need for multiple, complementary diagnostics, such as

- Two-dimensional broad-band images.
- Spectral broadening and one-dimensional imaging.
- Neutron activation.
- The use of numerical simulations to consistently explain the various observable phenomena peaking at different times during implosion.

A preliminary example of our work in this area is described in Section 6, "10× Liquid Density Target Experiments."

Authors: D. T. Attwood, N. M. Ceglio, E. M. Campbell, and J. T. Larsen

X-Ray Imaging of Laser Fusion Targets

Zone-plate-coded imaging cameras now routinely provide multispectral x-ray images of intermediate-density laser fusion targets.[29] Figure 5-40 shows representative multispectral data: a series of two-dimensional x-ray images in distinct spectral bands within the range from 2 to 20 keV. The isointensity contour maps are of x-ray emission in four spectral bands centered at 2.7, 4.6, 6.1, and 16 keV. Adjacent to the contour maps are linear plots of x-ray intensity versus position along a slice through the target center. The images are from a D-T-filled 145-μm-i.d. glass microsphere target whose 5-μm glass wall was coated with 16.5 μm of teflon: the target was irradiated at the Shiva facility, with 3.4 kJ in a 200-ps, 17-TW pulse.

Such an array of image data is useful in the diagnosis of intermediate-density targets:

Fig. 5-40. A series of x-ray images in discreet spectral bands, for a laser-irradiated intermediate-density microsphere target. (In these images, the two 10-beam clusters of the Shiva laser facility were incident on the teflon-coated target from the top and bottom.)

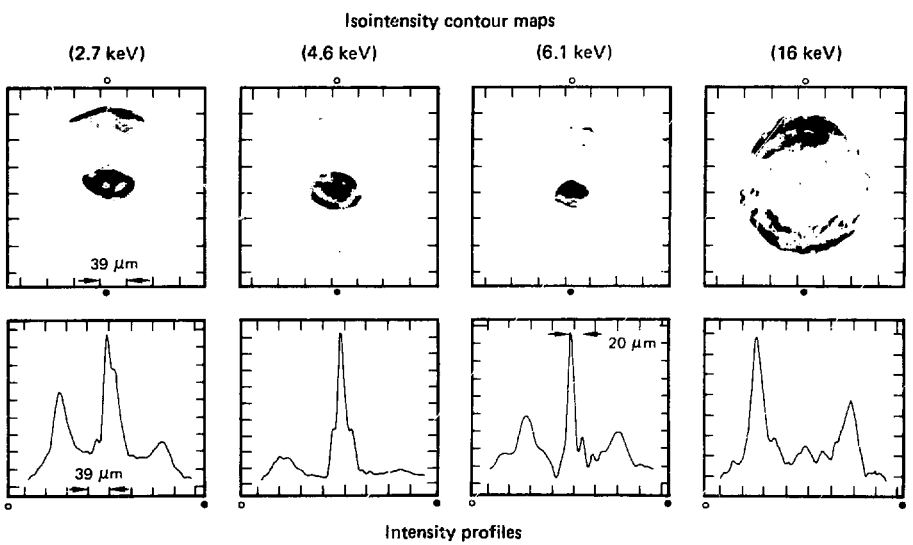

Fig. 5-41. A representative pair of x-ray images from two nominally identical target experiments. The variations in the geometry of the depression in the central core suggest that in some of these experiments, two-dimensional effects perhaps compromise the integrity of the fuel-pusher interface at compression.

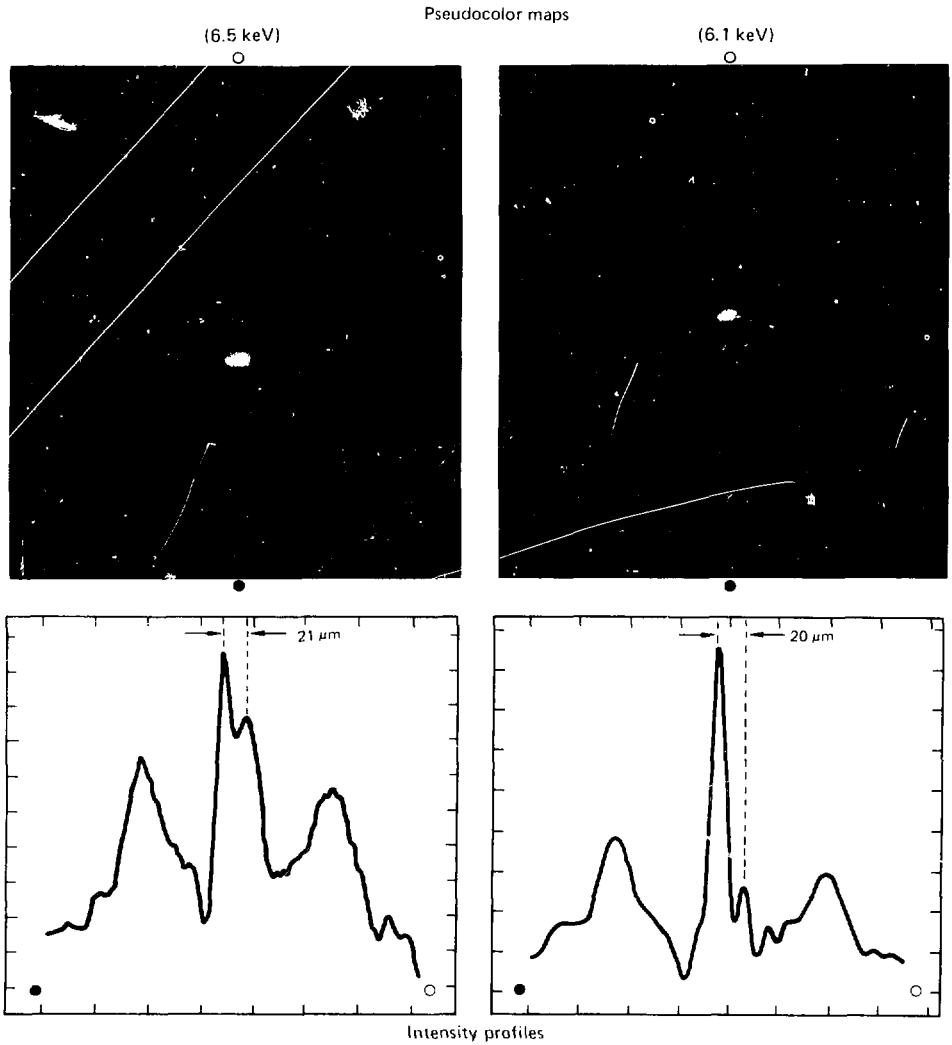

● The low-energy (≈2 keV) image shows thermal emission from the laser-illuminated teflon coating, thereby providing an indication of the illumination symmetry on target; it also shows the compressed core. To unambiguously "see" into the compressed core of intermediate-density targets, which are designed to achieve a fuel density of 3 to 10 gm/cc and a glass $\rho\Delta R \approx 5$ to 10 mg/cm^2, requires higher-energy x-ray images.

● The intermediate-energy (≈4 to 6 keV) images allow us to see further into the compressed

target core, and perhaps evaluate the quality of compression: the symmetry and volume of the core, and the integrity of the fuel-pusher interface (interpretation of time-integrated images of the compressed cores of intermediate-density targets is discussed later in this article).

- The high-energy image (≈16 keV) shows the hollow shell of suprathermal x-ray bremsstrahlung arising from interaction of long-range (approximate target wall thickness) suprathermal electrons with the high-Z pusher material. The suprathermal image provides a snapshot of the pusher shell at around the time of intense laser irradiation, that is, in the early stages of target implosion. Such an image allows us to monitor the initial stages of pusher motion, to diagnose target illumination asymmetries (through local inhomogeneities in STX, and therefore in STE, production), and to detect an early break-up of the pusher shell if it should occur.[30] There is no apparent break-up of the pusher shell during this experiment's 200-ps laser irradiation.

As mentioned above, this class of experiments is particularly concerned with the quality of compression of the laser-imploded target. Because local parameters such as electron and ion density and temperature vary on a scale of micrometers and tens of picoseconds, it is important to combine several independent direct diagnostic methods in order to provide a comprehensive description of the target in its compressed state.

Although a time-integrated x-ray image cannot be expected to tell the whole story, intermediate-energy images (Fig. 5-41) can raise some interesting questions. For example, a one-dimensional calculation of the target implosion leads us to expect a dip in the center of the compressed core, the locus of the D-T fuel; in such a case we can "see" the fuel-pusher interface, and estimate the volume of the enclosed fuel. In this regard, Fig. 5-41 shows ≈6-keV images from two nominally identical target shots. In image (a) the compressed core shows a distinct central dip, as expected, whereas in (b) the evidence for such a depression in the central core emission is less convincing; this indicates that two-dimensional effects may compromise the integrity of the fuel-pusher interface at compression. Note that the target shot in image (a) exhibits a higher degree of symmetry than that in image (b). The illumination pattern on the target—as monitored by the outer ring of suprathermal emission—is more symmetric; this results in a more symmetric (21 by 25 μm) compressed core, with a dip in the x-ray emission at its center. It should be further noted that a closer inspection of Fig. 5-41(a) shows that the dip or depression in the central core emission is not fully enclosed by regions of higher emission; that is, if we are indeed looking at a fuel-pusher interface, it is one that does not appear to fully enclose the compressed fuel.

Although a clear interpretation of the phenomena displayed in Fig. 5-41 is not yet in hand, the data seem to suggest that two-dimensional effects play an important role in this class of target experiments; one-dimensional simulations of target performance may be insufficient. Such conclusions should not be surprising, considering the illumination asymmetry of the Shiva facility. The very interesting matter of repeating these intermediate-density target experiments using symmetric target illumination is being pursued.

Author: N. M. Ceglio
Major Contributors: G. L. Howe, G. Wurden, G. Stone, C. H. Dittmore, W. C. Herrmann, and D. R. Ciarlo

References

29. *Laser Program Annual Report—1978*, Lawrence Livermore Laboratory, Livermore, Calif., UCRL-50021-78 (1979), p. 6-30.
30. N. M. Ceglio and J. T. Larsen, *Phys. Rev. Lett.* **44**, 879 (1980).

Implosion Measurements with Neutron Activation Techniques

In an imploded laser fusion target, consisting of compressed D-T gas encapsulated in a glass microshell, the thermonuclear neutrons activate the ^{28}Si atoms in the glass via the ^{28}Si(n,p)^{28}Al reaction. By measuring the neutron yield and the total number of ^{28}Al atoms created, we can determine the areal density $\rho\Delta R$ of the compressed glass shell at the time of peak neutron production.[31-35] The compressed-glass $\rho\Delta R$ can then be used in simple models or computer simulations to estimate the compressed density of the fuel. This article describes experiments at the Shiva laser facility in which the activity found in the collected target debris was

Fig. 5-42. Laser-fusion target consisting of a teflon-coated glass microshell filled with 50 atmospheres of D-T gas. The initial glass $\rho\Delta R$ was 0.001 g/cm^2.

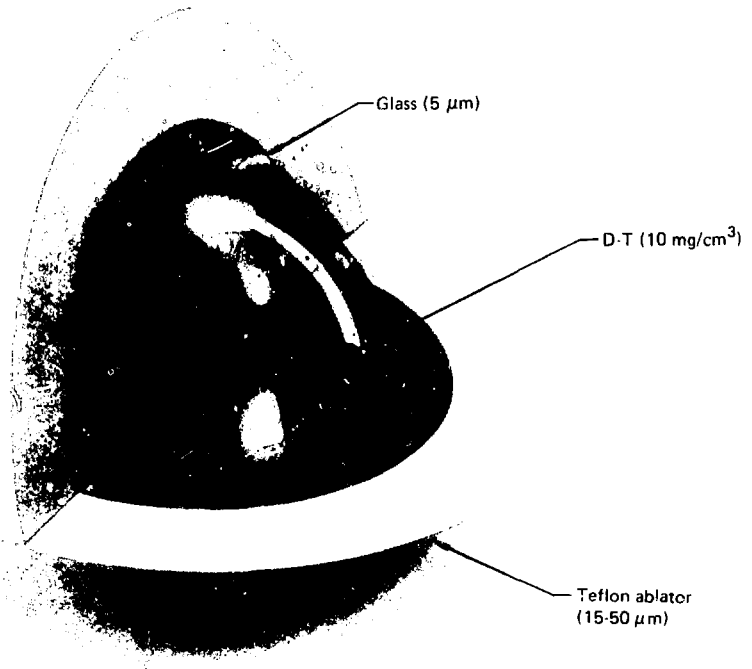

Initial inner diameter ~ 140 μm

identified by its decay rate as ^{28}Al. The amount of activity was then used to derive the compressed-glass $\rho\Delta R$.

The targets we used in these experiments (described in greater detail in Section 6, "10× Liquid Density Target Experiments") were glass microshells with inner diameters of 140 μm and wall thicknesses of 5 μm, filled with a 10-mg/cm^3 equimolar mixture of D-T gas and coated with μm of teflon (Fig. 5-42). The glass constituents by weight, 76% SiO_2, 7.5% B_2O_3, 14% Na_2O, 2.25% K_2O.

kJ of laser energy in a 200-ps Gaussian were directed by 20 individually focused to the teflon ablation layer of the target. The heating and subsequent blowoff of the ablator compressed the glass pusher and the fuel. It was estimated from both optical and plasma calorimetry that 20% of the incident laser energy was absorbed. Typical neutron yields of 3 to 6 × 10^8 were obtained.

To collect a portion of the debris from the exploding target, we used an aluminum collector cylinder placed 10 mm from the target, opposite a dish-shaped tantalum reflector placed 25 mm from the target (Fig. 5-43). The cylinder was lined with 20-μm-thick, 99.9995%-pure titanium foil, and measured 50 mm in diameter by 165 mm long; the reflector was also 50 mm in diameter. The front 30 mm of the cylinder were covered with an additional 50-μm-thick layer of tantalum foil to

Fig. 5-43. Target debris collector. An aluminum tube lined with titanium foil was placed 10 mm from the target and opposite a dish-shaped reflector. With this arrangement 55% of target debris adhered to the foil.

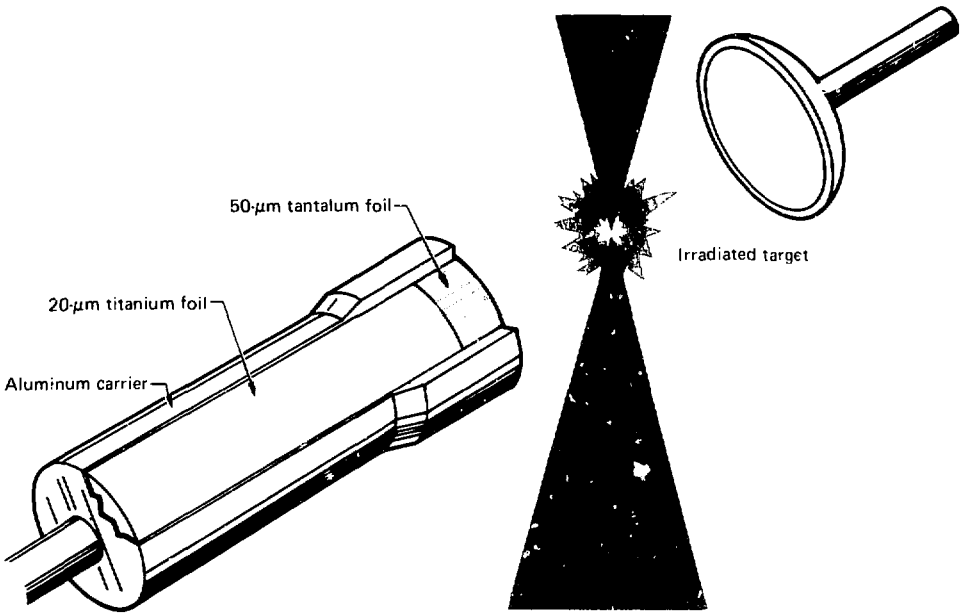

protect against blast damage. It took 17 seconds for an automated system to withdraw the collector from the evacuated target chamber and transfer it to the counting facility.

The amount of collected debris was determined in two auxiliary experiments using targets and laser conditions identical to those described above. In these experiments,[36] however, the microshells were made slightly radioactive by placing them in a light water reactor and allowing thermal neutron capture to create radioactive $^{24}Na(t_{1/2} = 15$ hours) from the ^{23}Na present in the glass. We were then able to measure the fraction of target debris collected by taking the ratio of the ^{24}Na activity found on the collector foils following a laser shot to that known to be present in the target. The average amount of target debris collected in these two experiments was 55.3% ± 0.5%. We also found in other experiments that < 1% of the debris was collected in the absence of the reflector, and that <0.5% of the target debris adhered to the reflector.

We measured both the ^{24}Na and ^{28}Al activities with a NaI(Tl) detector 250 mm in diameter and 250 mm long, having a well 150 mm deep and 50 mm in diameter.[34] We surrounded the detector with a 100-mm-thick lead shield to reduce the background in the 300-keV-wide 1.78-MeV window to 88 counts/minute. Aluminum decays with a 2.24-min half-life by emitting a β^- particle and a 1.78-MeV gamma ray; this gamma ray was detected by the NaI(Tl) crystal with a measured efficiency of 33% ± 4%.

In one of the the $\rho\Delta R$ experiments, we loaded the detector with the collector foils and were able to start counting the 1.78-MeV gamma ray 1.36 min after the laser shot. Figure 5-44 shows that the measured activity decayed with a half-life of 2.16 ± 0.16 min. This, together with the fact that the observed level of activity is consistent with the neutron yield and reaction cross section, gives us confidence that we are indeed measuring the 2.24-min decay activity of ^{28}Al; previous experiments reported in the literature have not had sufficient activity to identify the radioactive nuclide.

Equation (1) relates the detected number of decays (N_c) to the total number of activated atoms

Fig. 5-44. Decay curve obtained from gamma activity (1.63 to 1.93 MeV) detected in the collected target debris. The approximately 2.2-min half-life indicates that we are observing ^{28}Al.

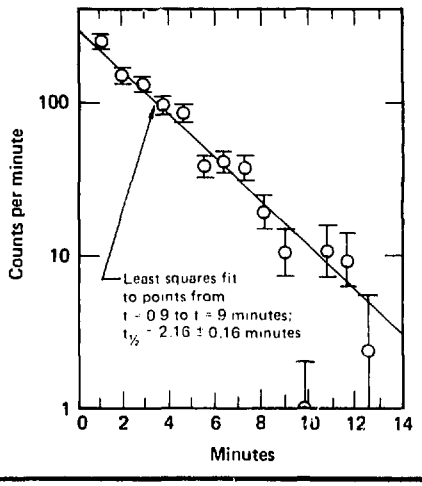

created (N*), by accounting for the collection efficiency η_c, the detection efficiency η_d, the delay time (between laser shot and commencement of counting) t, the counting interval Δt (taken to be 5 min), and the ^{28}Al decay constant λ.

$$N^* = \frac{N_c}{\left[\eta_c \eta_d e^{-\lambda t}\left(1 - e^{-\lambda \Delta t}\right)\right]} \qquad (1)$$

In Fig. 5-44, the 770 net counts detected in the first 5 min of counting indicate that 7960 ^{28}Al atoms were created. Thus, we are able to detect nearly 10% of the *total* activation yield of the target, which clearly demonstrates the extreme sensitivity of neutron activation technique. Using our more sophisticated β-γ coincidence counting technique[34] which reduces the background rates by a factor of 200, we are able to detect total activation yields of only 100 atoms.

We can now relate the number of activated atoms created to an average $\rho\Delta R$, using the equation

$$\rho\Delta R = \frac{N^*}{Y_n \sigma f \frac{A_0}{A_w}}, \qquad (2)$$

where Y_n is the neutron yield (6.7×10^8), σ is the $^{28}Si(n,p)^{28}Al$ cross-section (0.250 b), f is the fraction of ^{28}Si atoms in the pusher (0.25), A_w is the average atomic weight of a pusher atom (20 g), and A_0 is Avogadro's number.

In our experiments, we found the pusher areal density to be 5.9 ($\pm$1.5) $\times 10^{-3}$ g/cm^2. This represents a 4.8-fold increase in $\rho\Delta R$ from its initial value of 1.2×10^{-3} g/cm^2, and indicates a fuel density at burn time of 1 to 2 g/cm^3.

Author: S. M. Lane
Major Contributors: E. M. Campbell, W. M. Ploeger, C. K. Bennett, and C. E. Thompson

References

31. E. J. Mayer and W. B. Rensel, "Plastic Bubbles and Tamper $\rho\Delta R$ Measurements for Laser-driven Fusion Experiments," *J. Appl. Phys.* **47**, 1491 (1976).
32. *Laser Program Annual Report—1976*, Lawrence Livermore Laboratory, Livermore, Calif., UCRL-50021-76 (1977), pp. 3-108 to 3-109.
33. *Laser Program Annual Report—1977*, Lawrence Livermore Laboratory, Livermore, Calif., UCRL-50021-77 (1978), pp. 3-84 to 3-90.
34. *Laser Program Annual Report—1978*, Lawrence Livermore Laboratory, Livermore, Calif. UCRL-50021-78 (1979), pp. 6-45 to 6-52.
35. E. M. Campbell, W. M. Ploeger, P. H. Lee, and S. M. Lane, "Exploding-Pusher Tamper $\rho\Delta R$ Measurement by Neutron Activation," Lawrence Livermore Laboratory, Livermore, Calif., UCRL-83096 (1979), submitted to *J. Appl. Phys.*
36. E. M. Campbell, H. G. Hicks, W. C. Mead, L. W. Coleman, C. W. Hatcher, J. H. Dellis, M. J. Boyle, J. T. Larsen, and S. M. Lane, "Collection-Fraction Determination Utilizing a Radioactive Tracer," Lawrence Livermore Laboratory, Livermore, Calif., UCRL-83072 (1979), submitted to *J. Appl. Phys.*

Plasma Diagnostics Using X-Ray Spectroscopy

During 1979 we utilized x-ray line spectroscopy to measure compressed-fuel density achieved in exploding-pusher and ablatively driven targets. Owing to the small amount of argon mixed with the D-T in these microballoons, we were unable to make density determinations from Stark-broadened Ar x-ray lines. We have instead concentrated on one-dimensional line imaging to measure fuel x-ray emission volume, which can then be related to the fuel density; two separate series of experiments were performed, one at Argus and the other at Shiva. We

Fig. 5-45. Schematic of argon line imaging crystal spectrograph (ALICS), with typical data.

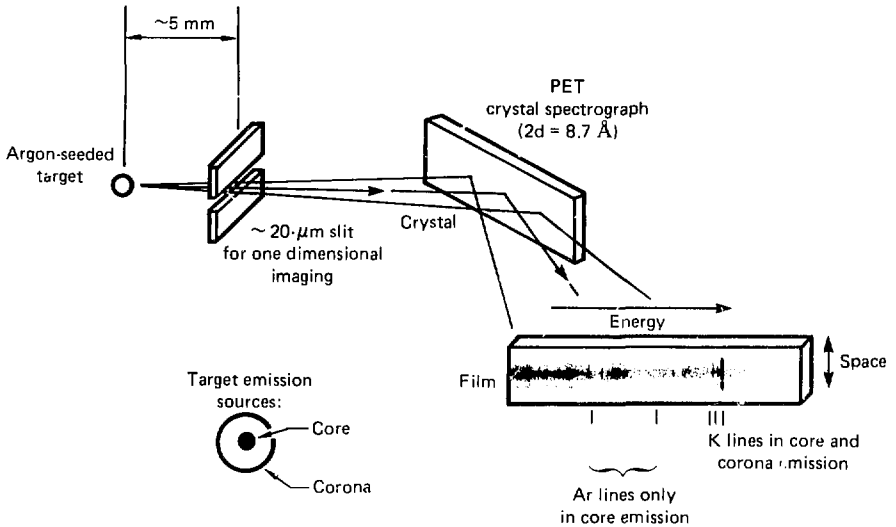

discuss some problems with the present imaging diagnostics as well as some plans for future improvements.

We also studied line emission intensity from various disk materials as a function of laser parameters such as pulse length and intensity. This effort was begun in order to characterize efficient, intense, x-ray line sources for future x-ray backlighting or time-resolved x-ray radiography experiments. We obtained encouraging results concerning the production of suitable x-ray lines by laser-generated plasmas. We discuss these experiments in the second part of this section.

Density Diagnostics. We have developed argon x-ray line imaging as an ICF target diagnostic technique. This technique measures the diameter of the compressed fuel core to provide an independent and direct measurement of fuel compression achieved by the imploded target. A small amount of argon gas is loaded into the target along with the D-T fuel. Near the time of maximum compression the argon radiates its characteristic and penetrating x-ray lines. A spatially-resolving x-ray crystal spectrograph then measures the extent of the line emission region in one dimension, producing an estimate of the size of the compressed core. This technique has been tested

- In Argus exploding-pusher target shots for which zone-plate-camera alpha-particle images were also obtained.[37]
- In experiments at Shiva in which the compression achieved by ablatively driven targets was measured with the pusher neutron activation technique described in the previous article.

It is expected that the argon x-ray technique will be useful only for targets whose final fuel density is no greater than 50 times that of liquid D-T. Targets expected to achieve higher compressions require pusher shells that are too optically thick at stagnation to permit transmission of argon x-ray lines. The value of argon imaging, then, is to corroborate and increase confidence in the neutron activation technique for medium-density targets; results from neutron activation measurements on higher-density targets can then be interpreted more confidently.

The miniature crystal spectrograph shown schematically in Fig. 5-45 was used in the argon line measurement. Because high resolution is required in order to isolate the narrow x-ray lines of argon from the continuous spectrum radiated by the glass of the

target, the spectrograph was designed for deployment very close to the target. The recording film is shielded from direct exposure to target radiation by a thick tantalum block located above and forward of a flat diffraction crystal.

A fine slit placed between the target and the analyzing crystal produces information about the extent of the x-ray source in space, by constraining x rays from any given region of the target to fall on a unique area of the spectrograph film. The axis of the slit, located 5 mm from the target and 65 mm from the film, was aligned parallel to the crystal's plane of dispersion, causing the source spatial distribution to be recorded on the film from side to side with an image magnification of 12 (slits, with widths of 20 or 30 μm, were built by the Laser Fusion Program's target fabrication group).

As x rays emerge from the target, they strike the crystal over a limited range of angles of incidence. For each angle value, the crystal selects a unique x-ray photon energy for reflection to the film. This band of photon energies from 2.6 to 3.7 keV is analyzed along the length of the film, for the instrument geometry shown. The band includes the most intense helium-like and hydrogen-like argon lines (denoted as Ar-Heα and Ar-Hα), whose energies are 3.14 keV and 3.32 keV, respectively.

The argon line imaging technique was tested with exploding-pusher targets at the Argus laser facility. The purposes of the test series were

- To determine if the x-ray lines radiated by helium-like and hydrogen-like argon were strong enough to be visible above the continuum radiation.
- To compare the argon line images with those produced by the proven alpha-particle zone-plate images.

It was important to verify that the electron temperature in the compressed fuel was high enough to produce nearly complete stripping of the argon, because only the lines radiated by the helium-like and hydrogen-like ion species (with two or one electrons remaining bound) could penetrate the glass shell. We hoped to show in the Argus shot series that the targets did perform as typical exploding pushers, while still radiating argon x-ray lines of sufficient intensity to allow the compression measurement. Thus the amount of argon gas seeded into the fuel in all of our targets was very small, so that the implosion dynamics of the fuel and other observables (such as the neutron yield) would be only slightly altered by the presence of the high-Z gas.

One important question about the argon imaging technique could not be answered directly in the Argus series, that question being whether or not the times of argon x-ray line emission and of D-T fuel burn coincided. The boundary of the fuel volume converges very quickly during an implosion, and unless the timing is good, the x-ray images will be larger than the fully compressed fuel core. Computer simulations of the implosion (which showed that the high electron temperatures required to strip the argon would be achieved only late in the implosion) suggested that there would indeed be no significant errors introduced by this timing factor—a conclusion we hoped to verify by correlation of the x-ray and alpha-particle images.

The argon imaging spectrograph and the zone plate camera were positioned diametrically opposite each other in the Argus target chamber. A second imaging spectrograph, modified to image the silicon lines emitted by the target's glass shell, was located in a third quadrant; the mission of this spectrograph was to determine the extent to which the glass mixed with the fuel during the implosion. The plane containing these instruments was normal to the direction of propagation of the two opposed laser beams.

The glass pellets used in the test series were formed by the liquid droplet method, in a "drop tower" suffused with argon. The density of argon in the targets was about 0.15 mg/cm^3, while the density of D-T fuel subsequently loaded into the pellets was 5.0 mg/cm^3. The initial diameter of the pellets was 140 μm; the wall thickness was 2 μm. When exposed to the Argus laser beams, each delivering an energy of 300 joules in 140 ps, it was expected that the pellets would be compressed to a final diameter on the order of 30 μm and heated to a temperature of 16 million degrees Kelvin. Potassium is a significant constituent of the target glass (11% by weight) and the x-ray lines of this element, with photon energies near 3.5 keV, were observed in the argon spectrograph data.

For a typical test series shot, x-ray images of argon and potassium were recorded by the two spectrographs. While the lines of the glass constituent, potassium, were radiated at both the initial target boundary (the region heated by the laser

Fig. 5-46. Direct size measurements of the compressed target core, obtained by (a) ALICS and (b) an alpha-particle zone plate camera (ZPC).

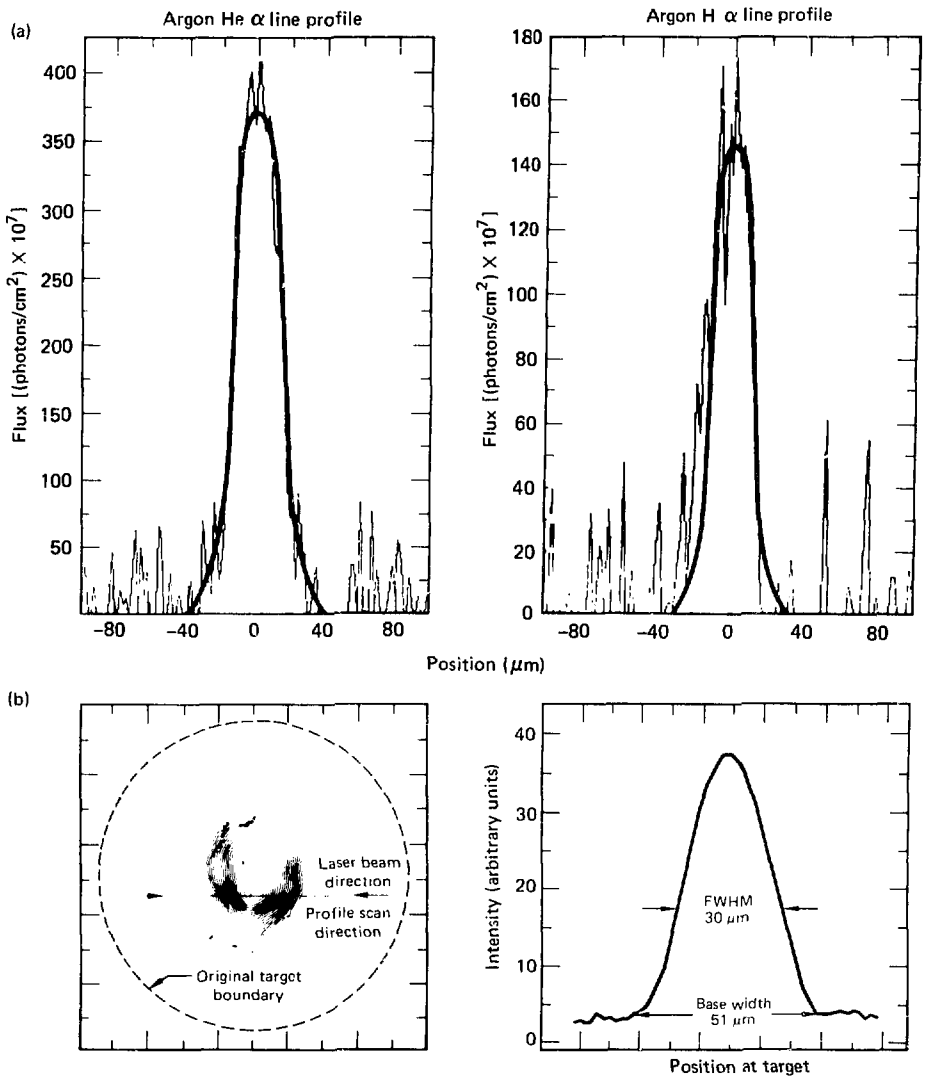

beams) and at the core, the source region for the argon lines is obviously confined to the compressed core. The ratio of intensities of the Ar-Heα and Ar-Hα lines indicates a core electron temperature on the order of 16 million degrees. Stark broadening of the lines was not observed.

The argon line images were analyzed by computer, to correct for the width of the slit and other effects of the imaging technique. The spatial profiles produced by the analysis are shown in Fig. 5-46(a).

The width of the Ar-Hα image is about 35 μm, while that of the Ar-Heα image is somewhat larger. Because the electron temperature in the core increases during implosion, the radiation from the lower-ionization-state He-like ions necessarily precedes, and thus occurs within a larger volume than the H-like species. An alpha-particle emission profile, scanned in the same direction as the argon images, is shown in Fig. 5-46(b). The width of the profile, which is an accurate measure of the burn-region diameter for exploding-pusher targets, is about 30 μm. Thus there is reasonably good agreement between measurements of the size of the compressed-fuel region obtained by Ar-Hα imaging and by alpha-particle imaging. The targets performed as typical exploding pushers in terms of compression and neutron yield achieved, which suggests that the argon seed had no effect on the implosions.

10× Experiment Series at Shiva. The argon line imaging crystal spectrograph (ALICS) was used at Shiva in experiments whose main purpose was to correlate different types of density diagnostics. The so-called "10×" series (Ref. 38; see also Section 6, "10× Liquid Density Target Studies") embodied the study of density achieved for 140-μm-diam microballoons with a glass-pusher wall thickness of 5 μm and an ablator thickness typically of 15 μm $CF_{1.4}$. These targets were filled with ~10 mg/cm^3 of D-T and usually about 0.05 to 0.06 atmospheres of argon. Because of Shiva's asymmetric irradiation geometry we assumed the compression would be nonspherical. Therefore, we oriented ALICS such that its spatial resolution dimension was parallel to the direction of irradiation.

Figure 5-47 shows a typical argon x-ray spectrum obtained from one of the shots. Note that we observe only one line, the He-like Ar resonance transition. Because of the poor signal quality we could make only spatial measurements to determine the diameter of the Ar emission region; because of the width of the slit (~20 μm), the spatial resolution is also certainly not optimum for our imploded target sizes. Figure 5-48 further illustrates the difficulty in data reduction. We assume different sizes for a uniformly emitting spherical source which is convoluted with a slit function, then plotted and compared to the measured spatial distribution; this method was essentially the same one used to analyze

Fig. 5-47. X-ray spectrum in region of He-like argon lines from 10× shot series.

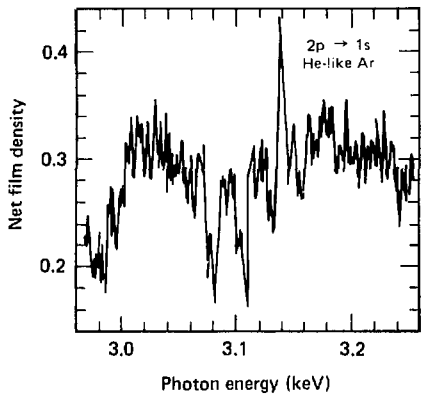

our exploding-pusher target data. Since the data are of poor quality as well as statistically uncertain, it is difficult to assign a source size to represent the data. Best guesses give a value of ~30 μm, since that value corresponds to the orange curve (in the figure) that more or less traverses the mean of all the data points. Table 5-3, however, does outline our best estimates of the source sizes for all the 10×-series shots. Since ALICS gives only a one-dimensional image we had to assume spherical symmetry for the source. If we assume 2-to-1 asymmetry with the narrow axis being the dimension measured, then we obtain final density values which are ~4 times less than in the spherical case; these values are also tabulated in the table. Future imaging measurements will employ two ALICS instruments imaging along orthogonal dimensions so as to circumvent uncertainties introduced by asymmetric sources.

Problems with Present Spectroscopic Density Measurements. Present target-capsule designs have jeopardized the utility of using Ar x-ray spectral and spatial line widths to determine density. The combination of too much glass (thick pushers) and too little argon (an average of 0.05 atm in the 10× series) in the target capsules results in a small line/continuum ratio (continuum is the Si free-bound emission). When this small ratio is coupled with normal spectral noise, it becomes very difficult to separate important line wings (line intensity far from line center) from continuum and film noise. As a result, the (10× series) data obtained thus far are of poor quality.

Fig. 5-48. Spatial emission profile for argon He-like resonance transition. The three colored curves are calculated for indicated source sizes, convoluted with a 20-μm slit and imaged onto the spectrograph film plane.

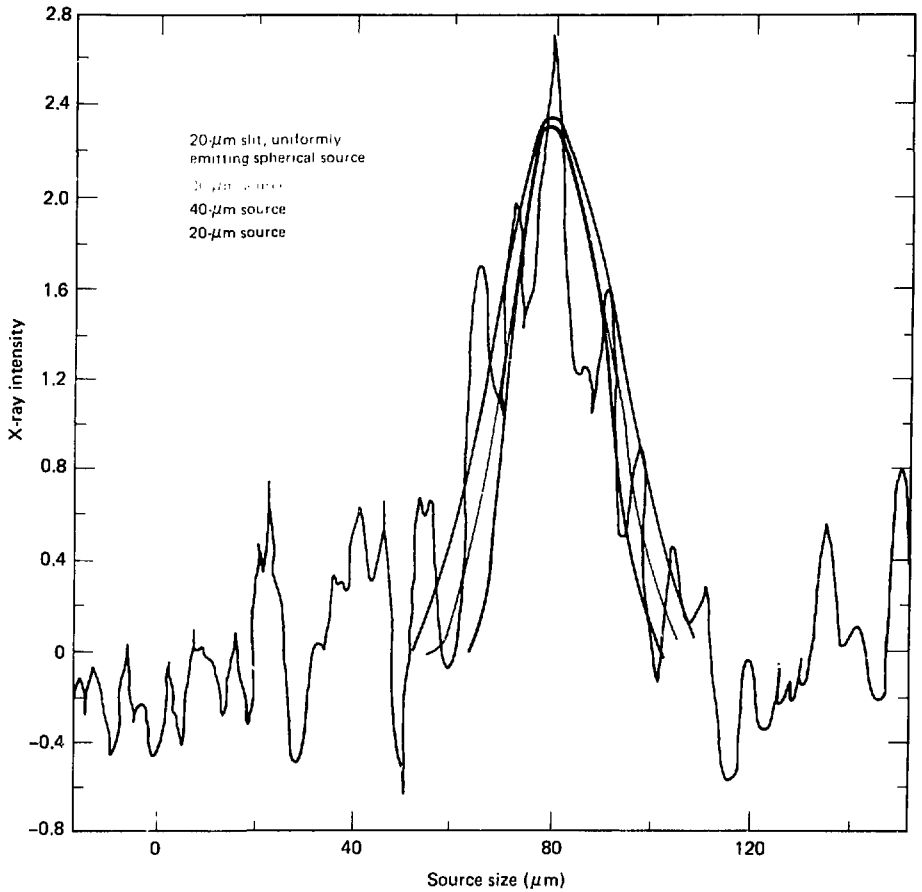

Table 5-3. ALICS results on 10X targets.

D-T fill (mg/cm^3)	Ball size[a]	Dia from ALICS (μm)	ρuniform sphere (units of $\rho_{D\text{-}T}$ liquid)	$\rho_{2:1}$ ellipsoid[b] (units of $\rho_{D\text{-}T}$ liquid)
10	152 X 3.7 X 15	30-40 μm	7-3	1.8-0.8
8.7	136 X 4.6 X 15	15-20 μm	32-14	8.0-3.5
10	141 X 4.6 X 15	30 μm	5	1.3
10	135 X 4.3 X 15.4	30 μm	4.5 (= 5)	1.3

[a]Dimensions represent outer diameter, glass thickness, and CF ablator thickness, all in μm.
[b]ALICS measures diameter of semiminor axis of ellipsoid of revolution.

The most obvious solution to the weak signal problem is to put more argon into present target capsules. LASL has had good success observing Ar lines when using a 0.2-atm loading.[39] Their targets are twice the diameter of ours and they report achieving the same final D_2 (in our case, D-T) densities. Since x-ray yield is proportional to compressed-argon density, they can expect a minimum of 32 times our signal strength (taking into account the difference in initial argon loading). Scaling their results would suggest an initial Ar loading of our targets with 1.5 atm, although we believe that ~1 atm is a reasonable compromise that should yield numerous lines (resonance and higher-series members) from both He-like and H-like Ar charge states. Each line offers an independent check of density by using both its spatial and Stark profile; this provides redundancy in the measurement.

Fig. 5-49. He-like argon $2^1P_1 \rightarrow 1^1S_0$ transition intensity vs electron temperature.

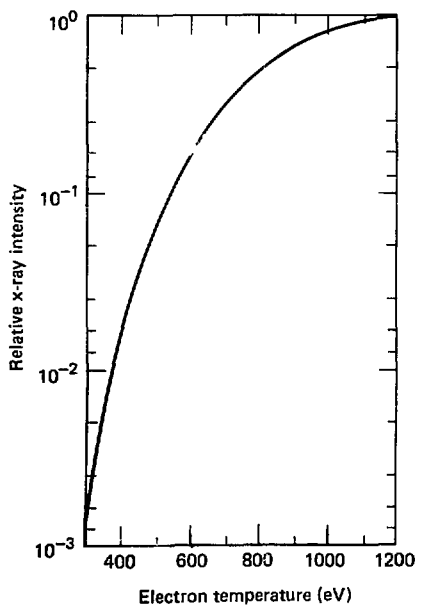

Argon may not always be the most prudent choice as a seed gas. Since some of our present target-capsule designs do not achieve significant final-fuel electron temperature (Te ≃ 500 eV), maximum He-like Ar line emission is down by a factor of about 15 (see Fig. 5-49). Even more important is the fact that He-like argon lines are readily absorbed by the silicon in the glass pusher. Figure 5-50 illustrates the effect of the glass pusher opacity on Ar line transmission.

Our first choice among solutions to the above-mentioned problems would be to replace argon with phosphorus as a seed gas. Ignoring the obvious target fabrication problems with handling it, phosphorus would make an ideal choice since it has one He-like and one H-like x-ray line each below the absorption edge in heated glass (Fig. 5-50). The phosphorus XV line ($2^1P_1 \cdot 1^1S_0$) at 2.152 keV and the phosphorus XVI line ($^2P_{1\,2,3\,2} \cdot 1^2S_{1\,2}$) at 2.303 keV could provide both Stark and spatial-profile analyses for final-density determination.

Bromine is a more practical seed gas candidate, and would improve both the absorption and production problems encountered with argon; bromine can also be utilized by radiochemistry methods to measure fuel ρR. Unfortunately for our purposes, bromine can only provide a measurement of fuel x-ray spatial extent, since at present fuel temperatures we can only excite the bromine Ne-like

Fig. 5-50. Opacity of LLL microballoon glass at a temperature of 500 eV and normal density.

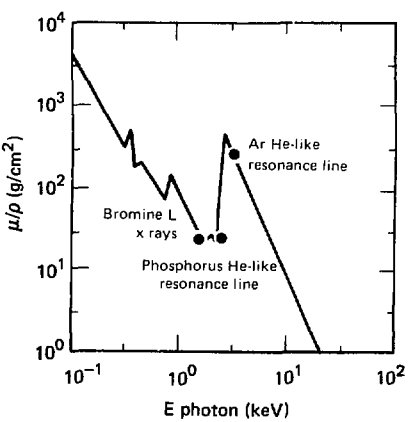

lines to Be-like L x-ray lines at ~1.5 → 1.9 keV, whose Stark profile is presently not modeled. Bromine will, however, produce much better signal strengths than argon.

Measurements of X-Ray Spectra from Laser-Disk Interactions. In last year's report[40] we discussed x-ray probing diagnostics for studying ablative implosions. In order to image the pusher-fuel interface of near-term target designs, it will be necessary to use well-characterized x-ray sources with energies from 6 to 8 keV. X-ray line sources will be utilized, since

- They provide for easier discrimination against target self-emission, and hence better signal-to-noise ratios and sensitivity.
- Narrow x-ray lines eliminate the dependence of target opacity on probing x-ray energy; this leads to simpler and more accurate determination of target component interfaces.

In this section we describe the results of a series of measurements of x-ray line intensity I_x versus K, L and M x-ray emitters, as well as versus Z of the target, versus laser pulse lengths $\Delta\tau$, and versus intensity I_l.

The first series of experiments was performed to obtain I_x versus Z and to study emission-type (K, L, or M) x rays. The experiments were done on Argus with 1-ns FWHM laser pulses and $I_l \simeq 3 \times 10^{14}$ W cm^2. We made these and subsequent measurements with our time-integrated x-ray line spectrograph; Table 5-4 gives the results. The obvious conclusion is that x-ray intensity is constant for K, L or M x-ray emission. The big difference is in the strength of the line continuum ratio; titanium produced very strong and narrow line emission. This is a significant discovery, since it implies that if a narrow-energy-band imaging device is used, the sensitivity and contrast ratio can be greatly increased.

To achieve this sensitivity we therefore chose to study K x-ray emitters versus target Z, τ_l, and I_l. A series of measurements to study some of the above was performed at Shiva, using from one to ten of its beams to achieve $I_l \simeq 3 \times 10^{16}$ W cm^2 in source sizes from 140 to 500 μm in diameter; a summary of the data obtained to date is shown in Table 5-5. Although incomplete with regard to measurements at all pulse lengths and laser intensities, present data does indicate that prolific line emission can be produced at E_x as high as 9.0 keV (Zn lines). Creation of the high-energy Zn and Ni lines does, however, require high laser intensity. In measurements so far, the laser spot diameter was 140 μm and $E_l \simeq 3$ kJ; these shots required 10 Shiva beams. In the coming year we plan to complete this measurement series to determine I_x versus laser

Table 5-4. X-ray line intensity and signal-to continuum ratio for K, L, and M emission types.

	K x rays (titanium)	L x rays (tin and barium)	M x rays (gold uranium-niobium)
I_x (photons per sphere)	Ti = 10^{15}	Sn = 4×10^{14}	Au = 10^{15}
Signal / continuum	~100	~5	~6
E_x	4.8 keV	3.8 keV	2.5 keV

Table 5-5. K x-ray line emitters.[a]

Element	Laser intensity (W/cm^2)	Pulse length (ps)	Strongest line energy (keV)	Strongest line intensity (keV/keV - sp)	$\mathcal{E}_L$ total energy all lines (J/sp)	$\mathcal{E}_x/\mathcal{E}_{laser}$ (%)
Titanium	3×10^{14}-Argus	1000	4.75	film saturated	–	–
	3×10^{14}-Argus	2000	4.75	5.8×10^{16}	0.27	0.05
	3×10^{15}-Shiva	600	4.75	2.6×10^{17}	1.6	0.06
Vanadium	3×10^{14}	2000	5.20	1.5×10^{16}	0.09	0.02
Nickel	4×10^{14}	600	7.80	no lines observed		
	3.3×10^{15}	600	7.80	no lines observed		
	2×10^{16}	600	7.80	no lines observed		
	3×10^{16}	600	7.80	1.2×10^{17}	2.45	0.08
Zinc	1.5×10^{16}	600	8.9	not analyzed		
	3×10^{16}	600	8.9	1.4×10^{16}	0.50	0.02

[a]Spot size at 3×10^{15} W/cm^2 = 500 μm at 3 kJ; spot size at 3×10^{16} W/cm^2 = 140 μm at 3 kJ.

Fig. 5-51. Titanium K x-ray spectrum from Shiva disk shot.

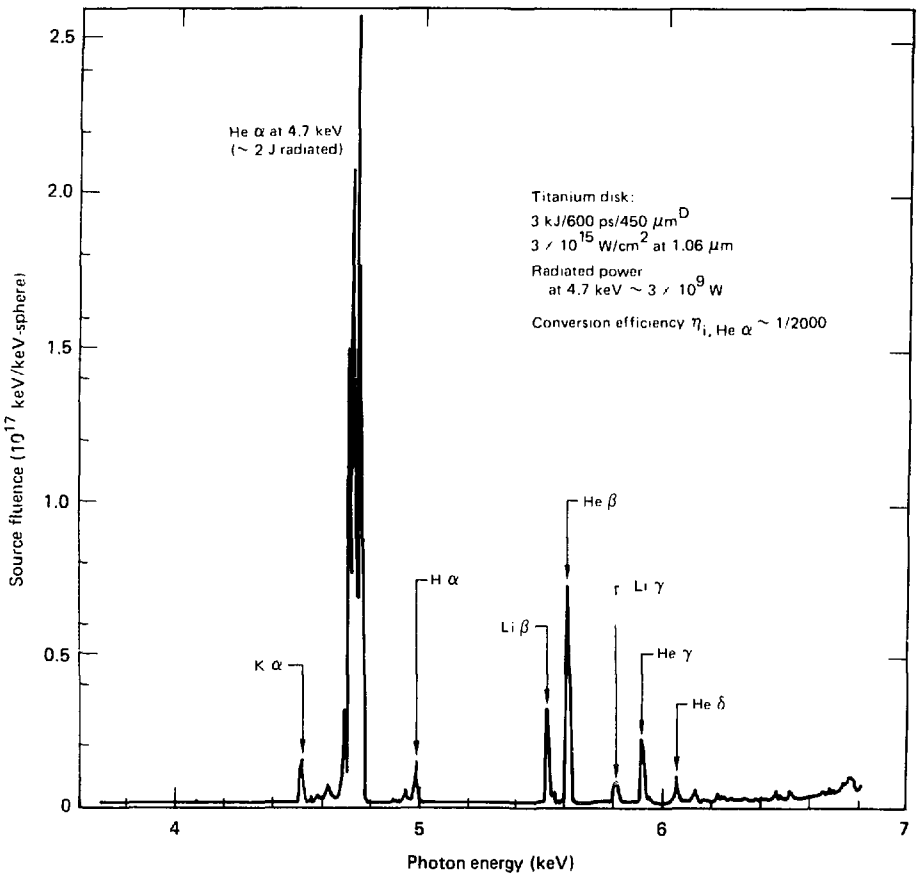

pulse duration τ_L = 100 ps, 600 ps, and 2000 ps, and $I_L \simeq 3 \times 10^{14}$, 3×10^{15}, 3×10^{16}, and 1×10^{17} W/cm^2. Knowledge of the scaling of I_x with these parameters is essential to the design of future backlighting efforts at Shiva and Nova.

We have initiated a modest effort to understand the mechanism(s) by which the higher-energy x-ray lines are produced. Figures 5-51 and 5-52 show the x-ray spectra observed for some laser-produced Ti and Ni plasmas. The experimental results indicate that

- Strong line emission is observed for Ti at $I_L \simeq 3 \times 10^{15}$ W/cm^2 and for Ni with $I_L \simeq 3 \times 10^{16}$ W/cm^2.
- The conversion efficiency (energy in line to energy in the laser) is high.
- For Ti, the He-like to H-like line intensity ratios indicate a time- and volume-averaged electron temperature $T_{e\,t,volume} \simeq 1.5$ keV.
- A strong characteristic Kα (cold matter K x-ray line) was observed for both Ti and Ni; this cold line was produced by high-energy electron and photon-induced ionization of target atoms residing deep in the slab.

Careful examination of the Ti x-ray spectrum near the n = 2 to n = 1 resonance line indicates that the plasma from which it is emitted can only be described by a non-LTE model. For long-pulse

Fig. 5-52. Nickel K x-ray spectrum from Shiva disk shot.

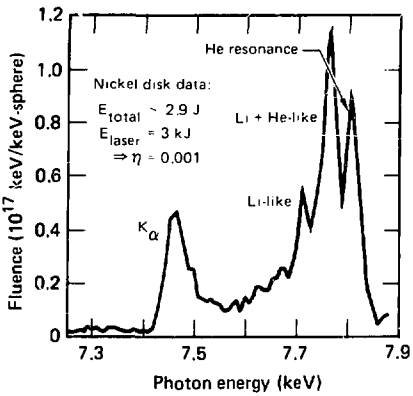

Fig. 5-53. Calculated titanium spectrum, assuming local thermodynamic equilibrium (LTE) in plasma.

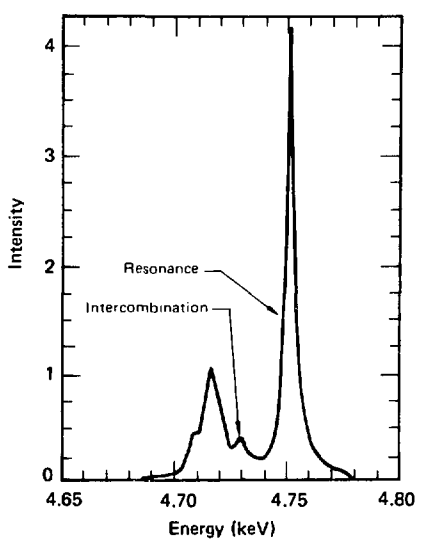

irradiation, however, the line spectra indicate that the plasma approaches LTE. Figure 5-53 illustrates a theoretical Ti x-ray spectrum in the region of the He-like resonance line, derived assuming local thermodynamic equilibrium. The two lines of interest in this spectrum are labeled as the resonance transition

Fig. 5-54. Measured titanium spectrum at two different laser pulse lengths: (a) 600 ps and (b) 2000 ps.

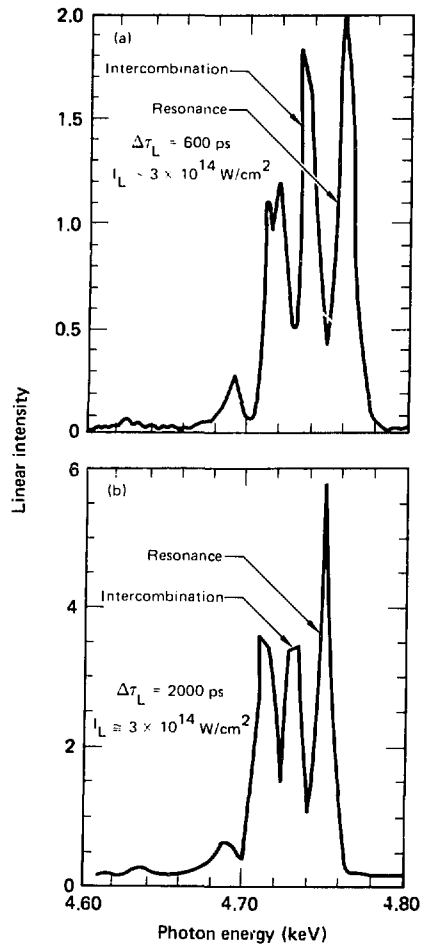

$1s^2\ {}^1S_0 \leftarrow 1s2p\ {}^1P_1$ (Resonance) and the intercombination line $1s^2\ {}^1S_0 \leftarrow 1s2p\ {}^3P_1$ (Intercomb). In LTE, line intensities are proportional to their oscillator strengths; the calculated ratio[41] of the oscillator strength of the intercombination line to the resonance line is 0.04. Therefore, the intercombination line is very weak in this theoretical spectrum. In the measured spectrum of Fig. 5-54(a), however, we

Fig. 5-55. Dependence of the intensity ratio of the resonance R ($1s^2\ ^1S_0 \leftarrow 1s2p\ ^1P_1$) and intercombination I ($1s^2\ ^1S_0 \leftarrow 1s2p\ ^3P_1$) lines of He-like ions.

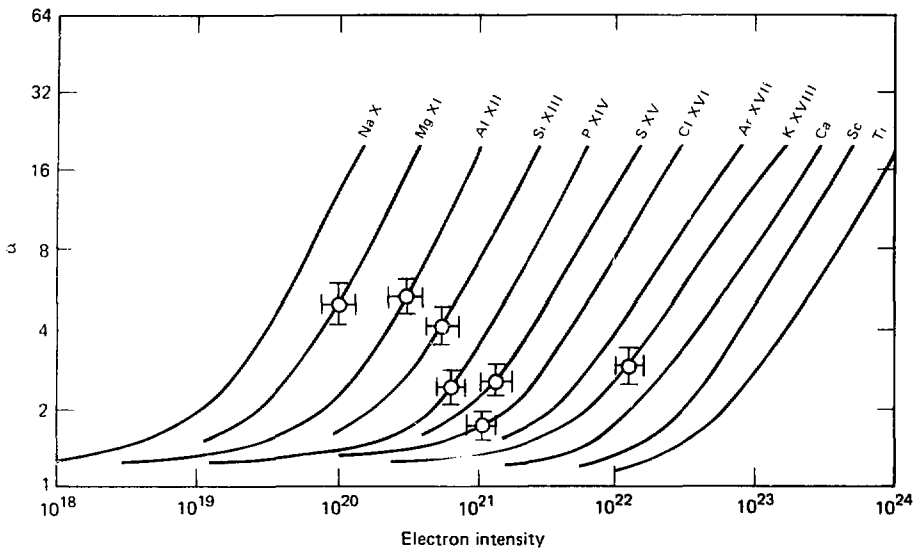

clearly see an intense intercombination line, which indicates that the plasma is not in LTE. Note that in Fig. 5-54(b), with a pulse length of 2000 ps [compared to 600 ps in (a)], the intercombination line strength has diminished relative to the resonance transition. This may indicate that the plasma is in fact equilibrating during the longer laser pulse. It could also mean that the emission is coming from a high average electron density plasma.

Boiko et al.[42] have modeled the ratio α of intercombination-to-resonance line intensity for non-LTE plasmas where the resonance line is optically thin: the ratio of the lines is strongly dependent on electron density over certain density intervals. A sample of their calculations is given in Fig. 5-55. Analysis of our data using their calculations would indicate electron densities $N_e > 10^{22}$ cm^{-3} for Ti at $\Delta\tau_I \simeq 600$ ps and $N_e \gtrsim 6 \times 10^{22}\,cm^{-3}$ for Ti at $\Delta\tau_I \simeq 2000$ ps. We have simulated these plasmas using our conventional (LASNEX) hydrodynamics computer code: of course this crude analysis does not consider line transfer effects or the fact that the plasma may be approaching LTE at 2000 ps.

Figure 5-56 is a "snapshot" of the plasma conditions at the peak of the laser pulse ($\Delta\tau_I$ = 1000 ps, $I_I \simeq 3 \times 10^{14}$ W cm^{-2}), giving the electron density, electron temperature, and He-like resonance-line emission strength as a function of distance normal to the surface of the Ti disk. These calculations indicate that the majority of the x-ray emission comes from the coronal plasma instead of the denser plasma near the disk's surface. This could explain why the line emission indicates a plasma more in coronal rather than local thermodynamic equilibrium.

Note that the plasma emission region or "scale length" in Fig. 5-56 is very large ($\sim 100\ \mu m$ for the FWHM of line intensity). This large emission scale length is beneficial for producing copious line radiation. This benefit is not present for lower-Z elements at the same laser parameters, because lower-Z elements will be ionized past their He-like states

Fig. 5-56. LASNEX calculation of electron density and temperature at peak laser pulse intensity vs distance normal to surface of a disk, and non-LTE calculation of He-like argon resonance line intensity as function of electron density and temperature.

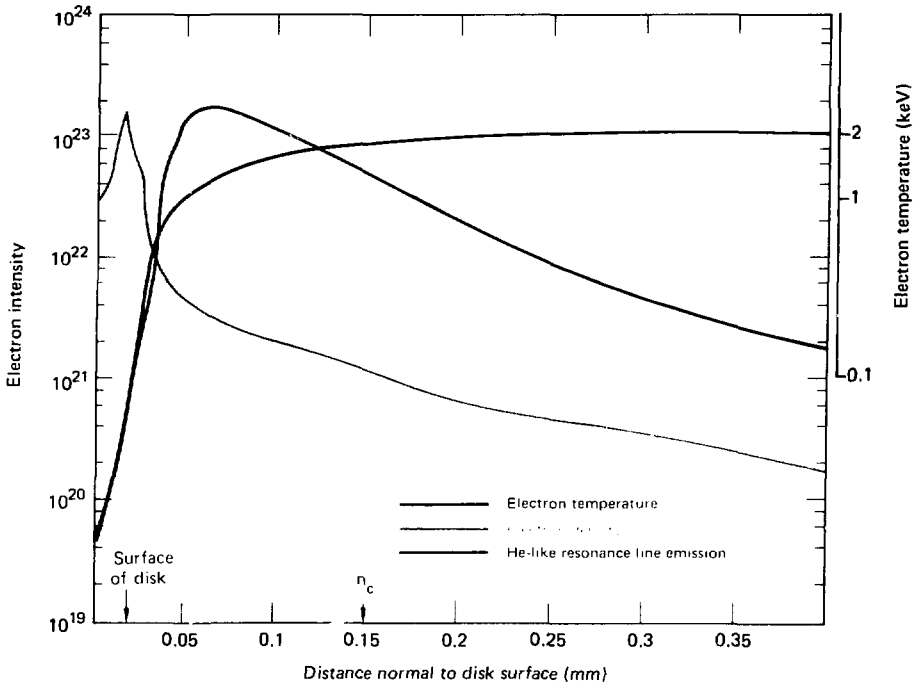

at a lower electron temperature and hence at a smaller distance from the disk's surface. Thus they will emit radiation from a smaller scale length. We should add that lower-Z elements also suffer from an intensity suppression owing to the Z^4 scaling of radiative rate. This scaling certainly favors higher-Z elements provided one has enough laser power to sufficiently ionize the high-Z atoms.

The final point concerning these calculations is that the average electron temperature at the peak of the laser pulse is ~1.5 keV. This is identical to the value derived by the line ratios taken from our experiment, and indicates that the effects of time averaging on experimental line intensities are minimal.

Authors: D. L. Matthews and L. N. Koppel

References

37. N. M. Cegio and L. W. Coleman, *Phys. Rev. Lett.* **39**, 20 (1977).
38. J. M. Auerbach et al., "Compression of Polymer Coated Laser Fusion Targets to 10× Liquid D-T Density," Lawrence Livermore Laboratory, Livermore, Calif., UCRL-83989 (1980).
39. K. Mitchell, Los Alamos Scientific Laboratory, Los Alamos, N.M., private communication (November 1979).
40. *Laser Program Annual Report–1978*, Lawrence Livermore Laboratory, Livermore, Calif., UCRL-50021078 (1979), pp. 6-38 to 6-40.
41. C. D. Lin, W. R. Johnson, and A. Dalgarno, *Phys. Rev. A* **15**, 154 (1977).
42. V. Boiko et al., *J. Phys. B* **12**, 1889 (1979).

X-Ray Backlighting with a Wolter Microscope and X-Ray Streak Camera

The process by which laser light is used to compress D-T fuel and cause thermonuclear burn can be broken down into four parts: absorption, energy transport, target hydrodynamics, and thermonuclear burn. Over the last several years, we have devoted significant effort to improving our theoretical and experimental understanding of absorption,[43] energy transport,[44-49] and the state of the target at burn time[50-52]; to date, we have made few measurements of target hydrodynamic behavior. One recent exception is our use of a pinhole x-ray streak camera diagnostic to measure radius-vs-time behavior of exploding-pusher targets.[53]

NRL has previously used visible-light shadowgraphs to measure ablative acceleration of slab targets.[54] Optical probing, however, is limited by refraction effects and the light can penetrate only to the critical density surface, which is itself moving with respect to the target slab. The use of x rays, which can penetrate dense material, permits determination of the density profile of the moving object through the relation between areal density and the attenuation of x rays. Measurements of this type have been initiated at the Rutherford Laboratory in England[55,56] and at Limeil in France.[57] These experiments have provided proof of principle, and have also previewed some of the problems (such as dynamic range, resolution, and target alignment) which must be addressed before x-ray backlighting can provide high-quality, interpretable data from a variety of targets.

We have developed an x-ray backlighting system (Fig. 5-57) designed to minimize the problems of dynamic range, target alignment, and resolution. The system uses a 22× magnification Wolter (hyperboloid-ellipsoid) axisymmetric grazing-incidence x-ray microscope as its objective element and an x-ray streak camera of LLL design as the detecting device; the development of the Wolter microscope[58,59] and streak camera[60] have been described in previous annual reports. The Wolter microscope currently being used has a resolution of 2 to 3 μm, depending on the mode of operation. In the apertured mode, the depth of field can be greater than ± 100 μm. The solid angle of the full-aperture x-ray microscope is approximately 1.1×10^{-6} sphere, with a high-energy cutoff of 2.1 keV. Other Wolter microscopes being fabricated are designed to have high-energy cutoffs in the range from 3 to 4 keV.

Because the streak camera has a thin photocathode it is sensitive to x rays with energies from 100 eV to more than 10 keV. The overall spatial resolution of the system is limited to about 4.5 μm at the object plane by the 22× magnification of the x-ray microscope and the 100-μm resolution of the x-ray streak camera. The time resolution of the streak camera is 15 ps; its dynamic range is approximately four orders of magnitude. In practice, the overall dynamic range of the system is limited by backlighter source intensity and imaging optics to about three orders of magnitude.

The x-ray backlighting system is aligned using a visible-light target viewer mounted coaxially along the x-ray microscope line of sight (Fig. 5-58). A visible-light lens is mounted in the center of the axisymmetric x-ray microscope mirror such that its principal plane and optical axis coincide with the principal plane and optical axis of the x-ray microscope. The focal lengths of the lens and the x-ray mirror are the same, so that the object and image focal points also coincide. During an initial alignment phase, the x-ray microscope is adjusted in tilt (± 20 arcseconds) to minimize coma. Then the image of a single-mode optical fiber, mounted at the center of the chamber, is projected onto the streak camera slit; the streak camera is then moved so that the image is centered on the slit.

A pellicle splits the beam and projects it also onto a second image plane, mounted rigidly on the streak camera at right angles to its face; this visible-image plane then moves when the streak camera moves. A set of cross hairs in the visible-image plane is moved to coincide with the image of the optical fiber and then locked into position. From this point, aligning targets to the streak camera slit is equivalent to aligning them to the cross hairs in the visible-image plane; the alignment is accurate to 10 μm and reproducible to 5 μm from shot to shot. The visible-image plane is equipped with a Polaroid film pack for documentary photos of target alignment, though the secondary image is bright enough that real-time alignment can be performed with the unaided eye.

The target is illuminated by a band-pass-filtered mercury arc lamp (5461 Å) with an annular

Fig. 5-57. Schematic of the x-ray backlighting system at Shiva. The main components are a 22× magnification Wolter x-ray microscope, an x-ray streak camera, and a mercury arc lamp illuminator.

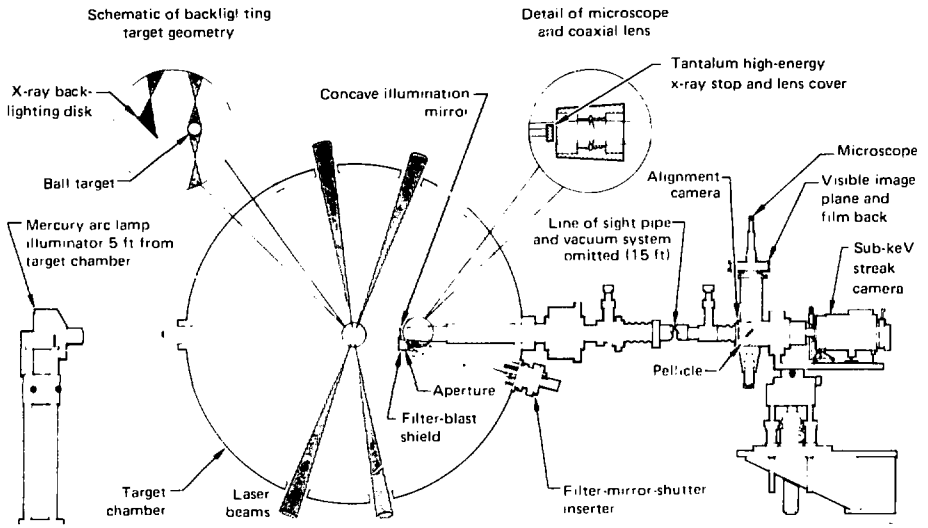

Fig. 5.58. Schematic of the x-ray backlighting optical alignment configuration.

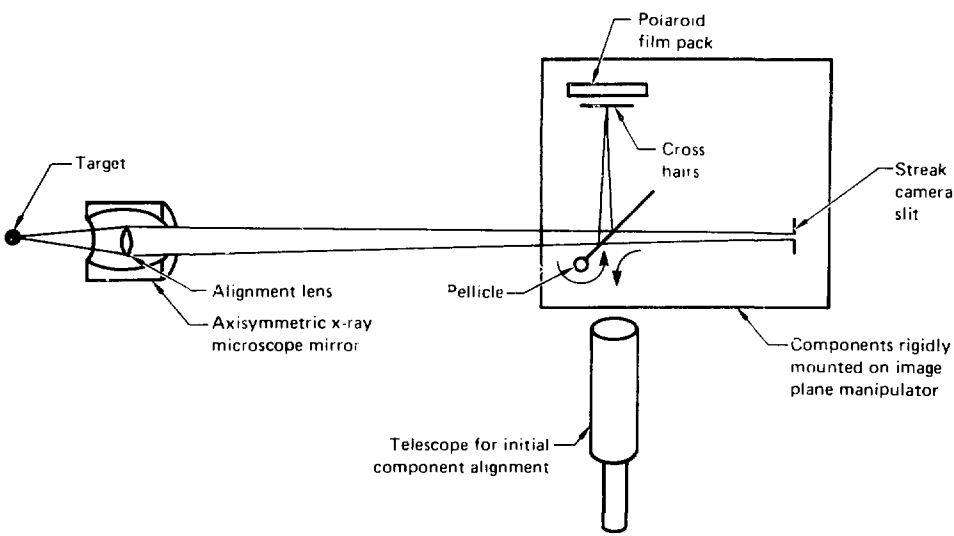

Table 5-6. X-ray backlighter intensities and x-ray optic solid angles required for streaked x-ray backlighting.

Material	Laser intensity (W/cm^2)	Spot diameter (μm)	X-ray line	$h\nu$ (keV)	$\left(\frac{I_\nu \text{ keV}}{cm^2 \text{ sphere}}\right)$	Figure of merit ($\Omega R^2/M^2$) (sphere)
Ta	2×10^{15}	250	M	2.0	4×10^{28}	5×10^{-11}
Au	6×10^{14}	400	M	2.5	4×10^{27}	2×10^{-10}
U-Nb	6×10^{14}	400	M	3.5	1×10^{27}	8×10^{-10}
Sn	6×10^{14}	400	L	3.9	1×10^{27}	8×10^{-10}
Ti	3×10^{15}	440	K	4.7	1×10^{28}	7×10^{-11}
Ni	3×10^{16}	130	K	7.9	2×10^{29}	1×10^{-11}

... of 50 mm o.d. and 25 mm i.d. The lens ...uces a collimated beam of light that is focused ... annular concave mirror onto the side of the ... facing the x-ray microscope and alignment ...stem. The diverging beam passing through the ...ter of the annular lens is focused by a 1-in.-diam ... at the target chamber port so that it illuminates ... target from behind. This combination allows the ...rget to be viewed in its reflected light against a ...ght background.

A mechanism inserted through the port next to ... x-ray microscope allows the concave annular ...rror, as well as filters, blast shields, apertures, and shutters, to be moved in and out of position in front of the x-ray microscope. At shot time, a tantalum shutter is placed in front of the coaxial alignment lens, to protect it from blast damage and to shield the streak camera from high-energy x rays (< 1 MeV) that would pass down the center of the line-of-sight pipe without being focused by the x-ray mirror. Additional x-ray filters can be inserted at shot time with a pneumatic filter inserter, without interfering with the optical alignment system.

The streak camera photocathode support foil is fragile and can withstand only slight pressure differentials. An automated vacuum system controller ...ow being constructed will cycle the system to and from atmosphere at a controlled rate, and will also interlock the valves, filter inserter, shutter mechanism, and pellicle to prevent damage to the ...gnostics, target chamber, and vacuum system.

Use of the streaked x-ray microscope for ...cklit slab acceleration experiments is presently ...der intensive investigation. Measurements can be made which will follow the target sample from a standstill, through its initial acceleration phase, to its asymptotic velocity. During the latter part of the streak record, it may be possible to measure the density profile of the sample as it disassembles.

The x-ray microscope can also be used with self-luminous targets. Initially, it will be capable of viewing targets in radiation from 270 eV to 2 keV. This range will later be extended up to 8 keV and perhaps down to 180 eV. The system will be used to measure the self-luminous interface near the absorption region on ball targets as they implode. With 8-keV backlighter sources, we expect to measure the dynamics of the core during the ablative implosion of high-density ball targets.

To extend backlighting capability to the 8 keV range requires both intense backlighter sources and high-energy x-ray microscopes with large solid angles. We have measured a number of backlighter sources at Argus and Shiva; results are given in Table 5-6. Column 6 lists the source brightness for the most intense line (or band of lines) at the x-ray energy listed in column 5 for the given laser parameters. A combination of target output and the sensitivity of the streak camera used with the microscope sets the parameters of the figure of merit $\Omega R^2 M^2$ required of an imaging device, where R, Ω, and M are reflectivity, solid angle, and magnification, respectively. Column 7 lists the figure of merit required to obtain a dynamic range of three orders of magnitude for the various lines listed in column 5.

We are currently constructing a 22× magnification Kirkpatrick–Baez–type x-ray microscope with multilayer interference x-ray mirrors[61] for use in the range from 3.5 to 8 keV. Multilayer interference x-ray mirrors allow reflection of high-energy x-rays at much larger angles than single-layer grazing-incidence x-ray mirrors; preliminary estimates are that the instrument under construction

can obtain a figure of me[illegible] 0^{-10}, which should be satisfactory for ba[illegible] experiments at 8 keV.

In summary, we are deve[illegible]ing x-ray backlighting at LLL to address questions abo[illegible] the dynamics of laser fusion targets. A system presently being assembled will perform preliminary experiments using 2-keV x-ray backlighting sources; we plan to develop instruments which will allow us to extend our studies to h[illegible] energies and thus to *probe the dense core regions of laser fusion targets.*

Author: R. H. Price

Major Contributors: A. Cappahianca, B. A. Jones, M. W. Kobierecki, W. B. Laird, W. M. Ploeger, J. R. Zickuhr, R. D. Rudd, D. L. Holeman

References

43. W. L. Kruer, "Theory and Simulation of Laser Plasma Coupling," Lawrence Livermore Laboratory, Livermore, Calif., UCRL-83149 (1979).

44. W. L. Kruer, "Electron Energy Transport in Laser Produced Plasmas," *Comments Plas. Phys. Cont. Fus.* **5**, 3 (1979).

45. C. E. Max et al., "Enhanced Transport Across Laser Generated Magnetic Fields," *Phys. Fluids* **21**, 1 (1978).

46. F. Amiranoff, et al., "Experimental Transport Studies in Laser-Produced Plasmas at 1.06 and 0.53 μm," *Phys. Rev. Lett.* **43**, 7 (1979).

47. J. S. Pearlman and J. J. Thomson, "Polarization-Dependent Energy Transport in Laser-Produced Plasmas," *Appl. Phys. Lett.* **32**, 11 (1978).

48. B. Yaakobi and T. C. Bristow, "Measurement of Reduced Thermal Conduction in (Layered) Laser-Target Experiments," *Phys. Rev. Lett.* **38**, 7 (1977).

49. F. C. Young et al., "Laser-Produced-Plasma Energy Transport Through Plastic Films," *Appl. Phys. Lett.* **30**, 1 (1977).

50. E. M. Campbell et al., "Radio Chemistry as a Diagnostic in Laser Fusion Experiments," *Bull. Am. Phys. Soc.* **22**, 9 (1977) (abstract only).

51. E. M. Campbell et al., "Determination of Fuel ρR of ICF Targets by Neutron Activation," submitted to *J. Appl. Phys.*

52. L. N. Koppel et al., "Diagnosis of Laser-Produced Implosions Using Argon X-ray Lines," Lawrence Livermore Laboratory, Livermore, Calif., UCRL-83313 (1979).

53. D. T. Attwood et al., "Space-Time Implosion Characteristics of Laser-Irradiated Fusion Targets," *Phys. Rev. Lett.* **38**, 6 (1977).

54. R. Decoste et al., "Ablative Acceleration of Laser-Irradiated Thin-Foil Targets," *Phys. Rev. Lett.* **42**, 25 (1979).

55. M. H. Key et al., "Pulsed-X-ray Shadowgraphy of Dense, Cool, Laser-Imploded Plasma," *Phys. Rev. Lett.* **41**, 21 (1978).

56. M. H. Key et al., "X-ray Streak-Camera Study of the Dynamics of Laser-Imploded Microballoons," *Appl. Phys. Lett.* **34**, 9 (1979).

57. C. Boyer et al., "Fast Electron Preheating in Exploding Pusher Experiments," presented at Fifth Workshop on Laser Interaction with Matter (1979), pp. 17 to 22.

58. *Laser Program Annual Report—1978*, Lawrence Livermore Laboratory, Livermore, Calif., UCRL-50021-78 (1979), pp. 6-23 to 6-25.

59. *Laser Program Annual Report—1977*, Lawrence Livermore Laboratory, Livermore, Calif., UCRL-50021-77 (1978), pp. 3-68 to 3-69 and 3-71 to 3-73.

60. *Laser Program Annual Report—1978*, Lawrence Livermore Laboratory, Livermore, Calif., UCRL-50021-78 (1979), pp. 6-2 to 6-5.

61. [illegible] Barbee, [illegible] Research, Stanford Univ., private communication (1980).

Micro-Fresnel Zone Plate Developments

Fresnel zone plates can operate [illegible] focusing elements that use diffraction rather than refraction or reflection. Our goal has been to fabricate zone plates suitable for imaging x-ray emission from laser-produced plasmas. A typical application is to image the helium-like Ar_K line emission (0.395 nm) from a laser-compressed D-T target containing an argon seed gas; such a measurement provides information about the size and symmetry of the compressed fuel region.

The theoretical resolution of a zone plate, when used with monochromatic radiation, is of the order of the minimum zone width; since a spatial resolution of ≥ 1 μm is desirable to allow observation of the smallest structures of interest, we chose a minimum zone width of 0.3 μm. The opaque zones are made of gold with a thickness >1 μm to keep transmitted power below 1% at a wavelength of 0.4 μm. The bandwidth of the argon line is of the order of a few electron volts, centered at 3.14 keV, so the zone plate should be limited to a few hundred zones to minimize chromatic aberration.

Fabrication. Minimum zone widths near 1000 Å have been achieved using holographic lithography, electron-projection-lithography, and *diamond-turning techniques* to generate zone plate patterns.[62,63] The zone plates produced by these methods, however, were limited to gold thicknesses on the order of 1000 Å, which has restricted their use to very soft (4.5 nm) x-ray wavelengths.

We have developed a process which allows zone plates with submicrometer line widths to be

fabricated in thick gold. The zone plate pattern is first generated on an x-ray mask, using scanning-electron-beam lithography (SEBL); the pattern on the x-ray mask is then replicated using carbon K-line soft-x-ray lithography. Though the original mask absorber pattern is fabricated in gold less than 1000 Å thick, the x-ray-lithography replication produces very high aspect-ratio resist profiles which serve as a "mold" during a subsequent electroplating step that produces the final thick gold structure.

Although in principle any of the methods mentioned above for fabricating zone plates in thin gold could be used to form the x-ray mask absorber pattern, scanning-electron-beam lithography has several advantages:

- It is possible to extend the SEBL technique to line widths of 1000 Å or less; at the present time, other methods have not demonstrated comparable resolution.
- Changes in zone plate parameters, such as focal length or minimum zone width, are simply entered from a keyboard on the SEBL computer control; holographic zone plate generation requires time-consuming modification of the optical setup.
- Free-standing zone plates require support structures; using SEBL the support structure is written at the same time as the zone plate pattern. Complex support structures are easily generated and modified through software changes.
- SEBL exposure can easily be varied across the zone plate to compensate for cooperative exposure effects due to changes in periodicity; this allows good line width control and a uniform resist profile across the zone plate.
- Spherical aberration can be easily avoided. With holographic lithography, the zone plate is used at a different wavelength than the exposure wavelength, resulting in spherical aberration unless special correcting optics are used during exposure of the zone plates.[62]
- As described below, it is possible to ensure that the electron beam scan raster is free of distortion which would impair the optical performance of the zone plates.

In order to produce accurate zone plate patterns, we require the distortion of the electron beam scan raster to be less than the minimum zone width (3160 Å) over the zone plate diameter (0.632 mm); about 5 parts in 10 000. Using a Moiré technique,[64] we have reduced scan distortion to <2.5 parts in 10 000. The ETEC Corp. model LEBES-D Scanning Electron Beam Lithography system has a distortion correction module which allows small correction terms to be added to the deflection signals, to compensate for predominant irregularities such as pincushion and trapezoidal distortion. By observing on the display CRT a Moiré pattern produced by rastering the electron beam over a distortion-free gold reference grating, any distortion in the scan raster is easily visualized and can be corrected using the distortion correction controls. Our reference gratings were holographically generated, and consisted of 5000-Å-period etched gold lines on a silicon substrate. The grating lines could be oriented parallel to either the X or Y deflection axis, to check distortion in both axes. We also used grids of gold dots, formed by holographic double-exposure of orthogonally oriented grating lines.

Figure 5-59(a) shows a Moiré pattern indicating that there is some pincushion distortion in the scan raster. In Fig. 5-59(b), the pincushion distortion has been corrected and only straight, equally spaced fringes are visible; the fringes appear because the spacing between the raster lines does not match the grating period exactly. In Figs. 5-59(c) and (d), the scan-line spacing has been adjusted to match the grating period exactly; by translating the scan raster one-half period (2500 Å) with respect to the reference grating, the entire pattern can be made dark (c) or bright (d) as the scan raster falls exactly between or on the gold lines, respectively (a similar result is obtained by scanning with an orthogonally oriented raster/grating combination). These scans, of a field 1 mm square, indicate that the SEBL machine has a distortion of less than 2500 Å over 1 mm, or <2.5 parts in 10 000. Raster distortion could also be reduced to approximately 2500 Å over a 1-mm-square field.

The Moiré distortion correction technique brings the X and Y deflection axes into precise registration with the lines of the X- and Y-oriented reference gratings. For our zone plates, we require that the scan axes be orthogonal to within 7 min of arc and that the X and Y axis gains match to 1 part in 1000. The orthogonality of our X and Y reference gratings is within 1°, but is not precisely controlled. Slight adjustments were performed to reference the

Fig. 5-59. Moiré patterns formed by scanning the electron beam in a raster over a 5000-Å period gold reference grating while viewing the secondary electron image. The field of view is 1 mm square. (a) Pincushion distortion is visible. (b) The Moiré fringes are straight and equally spaced, indicating freedom from scan raster distortion, though the scan raster period is not identical to the grating period. By matching the scan raster and grating periods, a completely dark (c) or bright (d) pattern can be obtained, demonstrating less than 2500 Å of distortion over the entire 1-cm^2 field.

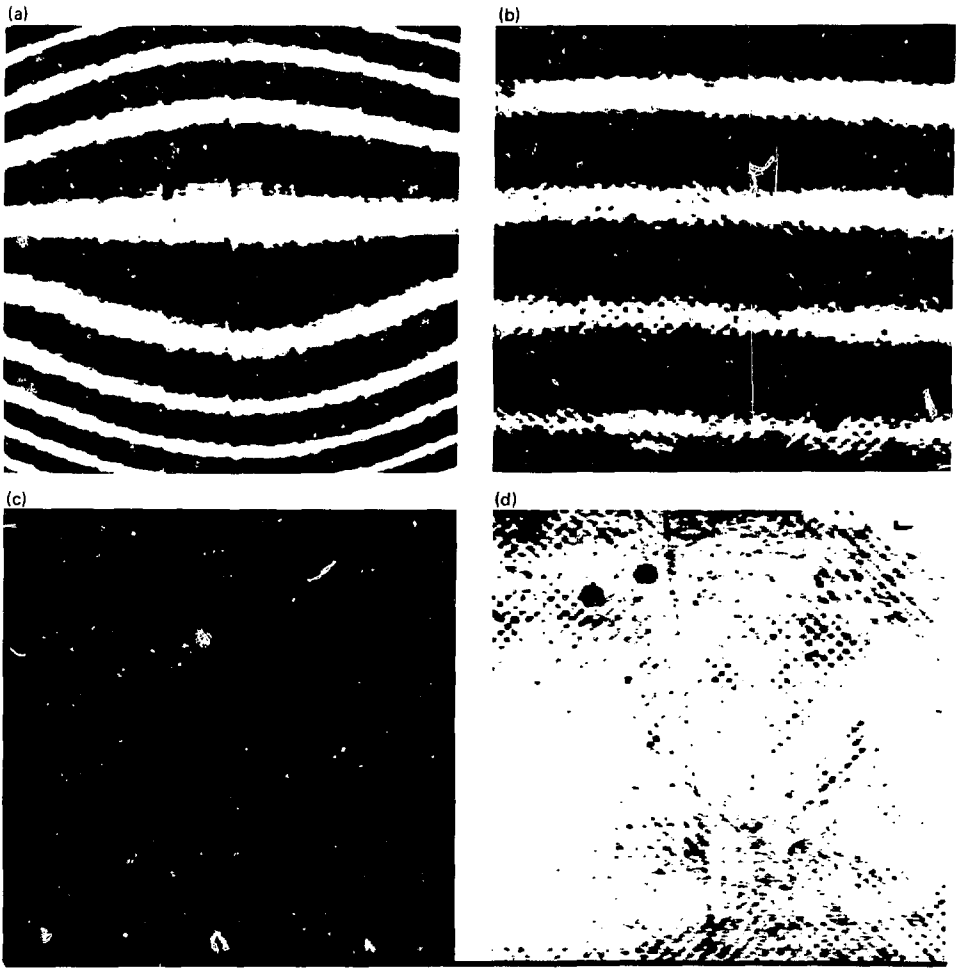

scan axes to the X and Y axes of our laser interferometer which measures X and Y sample stage motion; the interferometer axes are orthogonal to <1 min of arc.

Beam position drift during writing is another potential source of pattern distortion. Large zone plates with minimum zone widths of 3000 Å take about 1 hour to write, and may be affected slightly by drift. Beam drift in our system is typically less than 5000 Å per hour, as measured by observing shifts in Moire fringe patterns.

Our zone plate patterns were written in a layer of Polymethylmethacralate (PMMA) 1500 to

Fig. 5-60. A 4000-Å-period grating exposed in PMMA using scanning-electron-beam lithography (SEBL).

3000 Å thick, over a 9000-Å-thick layer of polyimide on a 76-mm-diam silicon substrate. The polyimide layer serves as the support membrane of the X-ray mask; we use the 76-mm-diam silicon substrate because of its convenience in our SEBL system. We operated the SEBL system with a tungsten filament, and used a beam current of 0.2 nA for all writing to ensure a beam diameter of <1000 Å. Patterns were written in 950 000-molecular-weight PMMA at a dose of 1.8×10^{-4} C/cm^2; development took one minute in a solution of 2 parts methyl isobutyle ketone (MIBK) to 3 parts isopropanol. The resist profile in Fig. 5-60 shows 2000-Å-wide lines with vertical sidewalls, produced by SEBL; lines as narrow as 1000 Å have also been exposed in 3000-Å-thick PMMA with vertical sidewalls suitable for liftoff.

The zone plate pattern is written by drawing concentric circles with the system's minicomputer, functioning as a point-plotting circle generator. Since the circles are generated on-line, the entire zone plate (including the struts) can be represented algorithmically, providing data compaction and allowing exposure to be varied radially to improve line width control. A zone plate 0.63 mm in diameter is composed of about 3×10^7 discrete points, and takes about 1 hour to write.

After the PMMA has been developed, a gold absorber pattern 500 Å thick is formed on the polyimide layer, using standard liftoff techniques. Figure 5-61 shows scanning-electron micrographs of some gold absorber patterns; note [Fig. 5-61(d)] that we have fabricated line widths as small as 1000 Å.

The polyimide layer with the absorber pattern is then transformed into a polyimide-membrane x-ray mask. We used a procedure similar to that used with glass substrates[65]:

- The entire top side and most of the underside of the silicon wafer, except for about a 30-mm-diam region under the zone plate patterns, is protected while the wafer is immersed in a solution of 4% concentrated nitric acid, 96% concentrated HF. This etches a hole through the silicon to form a polyimide membrane supported by the surrounding unetched silicon.

Fig. 5-61. Scanning-electron micrographs (SEMs) of zone plate gold absorber patterns on an x-ray mask. The patterns were written by SEBL, followed by a liftoff of 500 Å of gold. Micrographs (a) and (b) show the inner and outer zones of a zone plate with a minimum zone width of 2000 Å; (c) and (d) show sections of a zone plate with a minimum zone width of 1000 A.

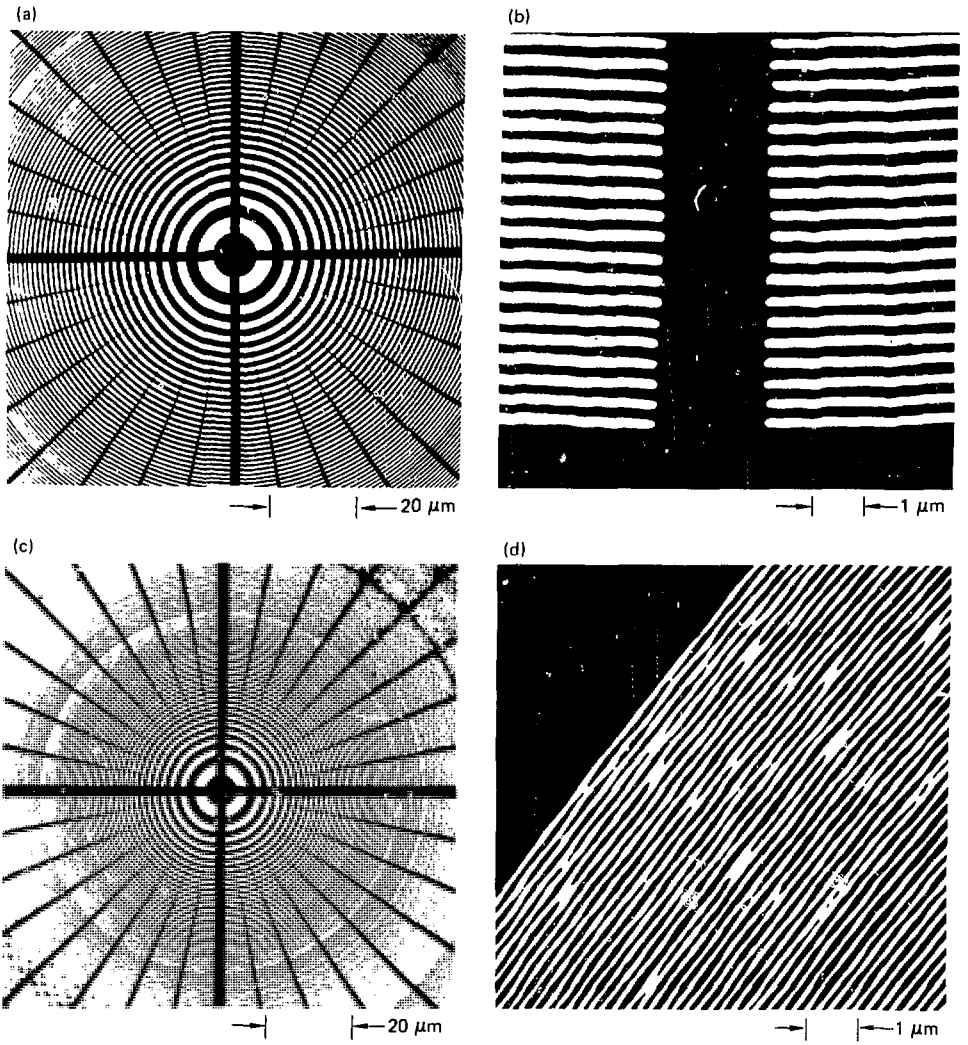

● A flat plastic ring is then epoxy-bonded to the polyimide on the absorber pattern side.

● The polyimide membrane surrounding the plastic ring is cut away, leaving a polyimide-membrane mask on a plastic ring.

● A 400-Å-thick layer of aluminum is then evaporated onto the polyimide on the absorber side. This aluminum layer serves as an electrode, to hold

Fig. 5-62. Gold lines electroplated between very high aspect-ratio PMMA lines exposed by x-ray lithography. The slight bending of the tops of the PMMA lines occurred during SEM observation.

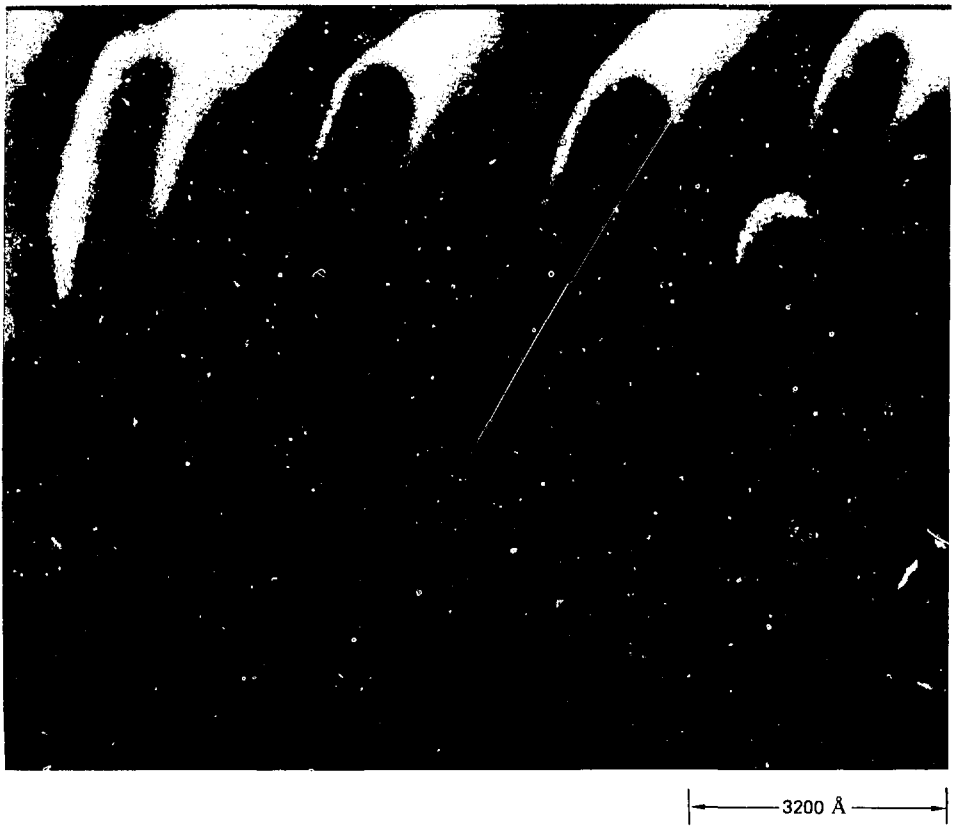

the mask electrostatically in intimate contact with the substrate during x-ray exposure; the polyimide membrane serves as a dielectric.

Using this x-ray mask, the zone plate pattern is exposed onto 225-μm-thick Corning 0211 glass substrates coated with, in order, 50 $\AA$ of chromium, 50 $\AA$ of gold, 2 μm of PMMA, and 100 $\AA$ of chromium. The chromium on top of the PMMA serves as the second electrode for electrostatic hold-down of the x-ray mask; the chromium is etched away before development of the PMMA. The thin gold under the PMMA serves as a plating base. We used the carbon K wavelength (4.5 nm) to expose the resist; a 9-h exposure was required at a 60-mm source-to-substrate distance. The C_K x ray was used in order to obtain high contrast with our thin (500 $\AA$) gold absorber patterns, and to minimize problems with photoelectrons generated by x-ray absorption at the plating base. With harder x rays and a higher bremsstrahlung background, the partial exposure produced by these photoelectrons results (during development) in rapid undercutting of resist profiles at the plating base surface, causing adhesion loss for small structures. All x-ray exposures were developed in 2:3 MIBK:isopropanol, with typical development times of 5 to 10 min.

After development, patterned slots extending down to the plating base are present in the resist.

Fig. 5-63. A completed zone plate in 1.3-μm-thick gold; the minimum zone width is 3000 Å.

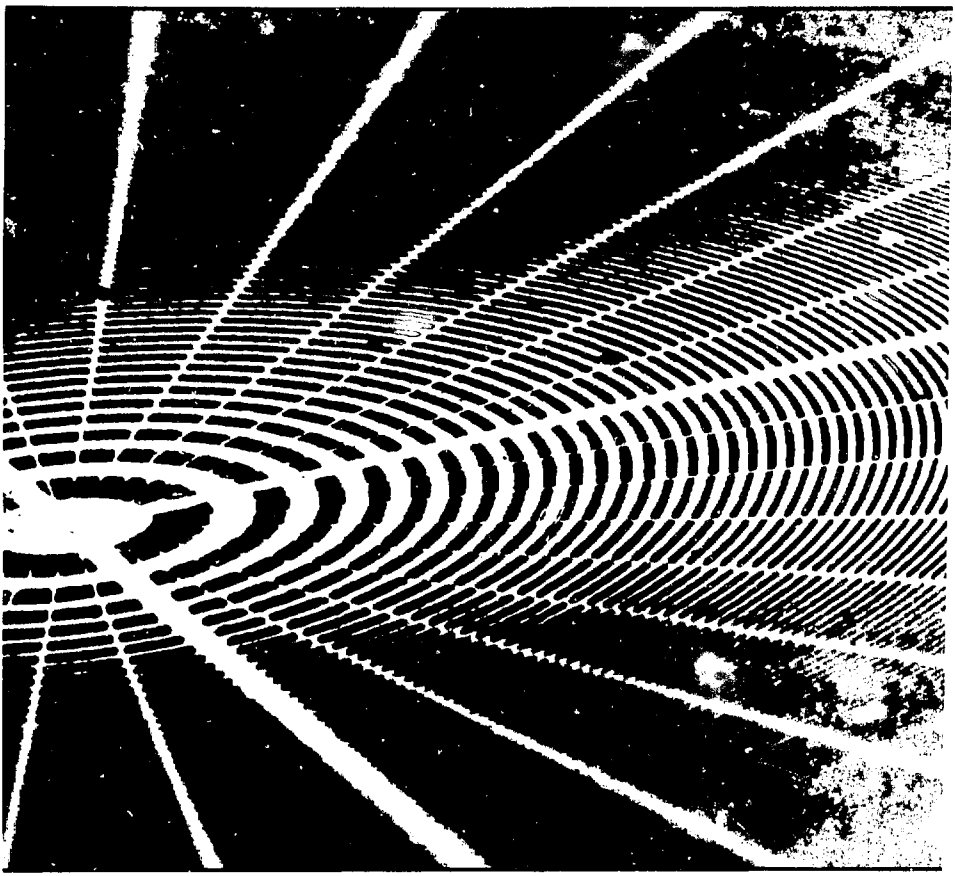

After a 10-s exposure to a 3% oxygen plasma to remove a thin resist scum which covers the plating base, gold is electroplated to a height of 1.3 μm, using BDT-510 plating solution maintained at 40 K with a plating current of 1 mA/cm^2 or less. Using this plating solution, we have been able to produce bright gold films with no graininess observable under the scanning electron microscope. Our plated films are under considerable compressive stress, which can lead to deformation of the completed free-standing zone plates. Figure 5-62 shows 1600-Å-wide gold lines plated to a height of 7200 Å using a 3200-Å-period grating exposed in PMMA as the "mold" for the plating.

After electroplating, the PMMA is dissolved away, and a copper support tube 1.5 mm bore in diameter is epoxy-bonded to the continuous gold film surrounding the zone plate. The glass substrate is then etched away in concentrated HF to produce a free-standing gold zone plate supported on a copper tube (in some cases, the thin chromium and gold of the plating base, which have little effect on the zone plate performance, were also removed by chemical etching). Figure 5-63 shows a free-standing, 1.3-μm-thick gold zone plate with a minimum zone width of 3000 Å.

Testing. Preliminary x-ray testing of these zone plate lensing elements has already begun. Figure

Fig. 5-64. Resolution tests of a Fresnel zone plate x-ray lensing element are conducted on a rigid optical bench. The lensing element being tested has a minimum line width of 3200 Å, a gold thickness of 1.5-μm, and a 0.632-mm diameter. It is used to image a free-standing crude Fresnel zone plate with a 2.5-μm minimum zone width backlit by an aluminum Kα x-ray source. The radial strut patterns on both the zone plate lens and the zone plate test pattern are used to support the free-standing gold microstructures.

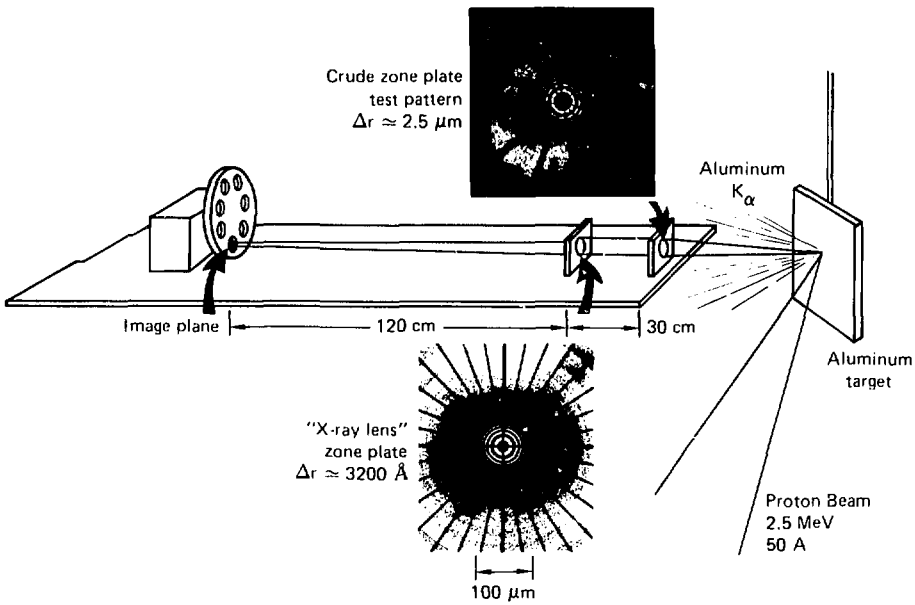

5-64 illustrates the test setup in which the zone plate "lens" is used as the optical component of a 4-power microscope. In this experiment the lens is used to image a 1-mm-diam crude (2.5-μm minimum line width) Fresnel zone plate used as a test mask. The zone plate test mask acts as an ideal resolution pattern since the line widths vary predictably over a wide range. The test pattern is backlit with aluminum K_α radiation at $\lambda = 8.34$ Å, produced by irradiating a water-cooled aluminum target with a 2.5-MeV 50-μamp proton beam from a Van de Graff generator. The x-ray images are recorded on single-sided type M x-ray film. A representative x-ray image of the 2.5-μm-line-width test pattern is shown in Fig. 5-65; note the resolution of the outermost zones of the test pattern. This is more clearly illustrated in the data of Fig. 5-66, in which the x-ray image has been scanned by a PDS microdensitometer and a plot made of the radial density distribution over the outermost 20 dark zones (from "A" to "B" in the image). The individual zones are clearly resolved, while also apparent are modulations in the image density level produced by nonuniformity of the backlighting source and spatial shot noise in the image. Additional simple tests of the zone-plate-lens field of view and depth of focus (in the image plane) were made by translating the test mask off the optical axis (±1 mm) and by varying the image plane position (±20 mm). As expected, these variations had no affect on the ability of the lens to resolve the 2.5-μm lines of the test pattern.

Additional Development. Also included in this x-ray lens development program are the fabrication and testing of off-axis micro-Fresnel zone plates intended for use as imaging spectrometers for

polychromatic x-ray sources. The imaging characteristics of an off-axis Fresnel zone plate are illustrated in Fig. 5-67. The off-axis zone plate is simply a circular, off-axis segment of a circularly symmetric (on-axis) Fresnel zone plate. The off-axis zone plate has the same focal length as its "parent" on-axis zone plate ($f = r_1^2/\lambda$) and similar chromatic aberrations. Due to its off-axis geometry, however, the off-axis zone plate holds the possibility of spatially separating chromatically distinct emissions from the same source, thereby providing two-dimensional, chromatically distinct, multiple images of a polychromatic source (Fig. 5-67).

In order for an imaging spectrometer employing an off-axis zone plate as its optical element to successfully separate spectrally distinct images from a given source, certain design criteria must be met for both the source and the instrument. Using simple ray-tracing calculations, we arrive at the following qualitative criteria:

- Spectral lines (λ_1, λ_2, ...) must be well separated.
- Source size (in the offset direction) must not be too large.
- Zone-plate offset distance must be sufficiently large ($r_0 < \Delta_0$).
- Minimum line width must be as small as possible.

Representative parameters, for an imaging spectrometer currently being fabricated for use with laser fusion targets, are listed in Table 5-7.

A practical consideration for the imaging spectrometer is the apparent need for microscopic recording media to capture the separated images without blocking shorter-wavelength images to be recorded downstream (see Fig. 5-67). This problem can be obviated and macroscopic recording media used if the imaging planes for the long-wavelength images are appropriately tilted back toward the horizontal. The maximum angle of tilt toward the horizontal is limited by the depth of focus (in the

Table 5-7. Qualitative criteria for an off-axis zone plate imaging spectrometer.

Maximum zone width	$\Delta r = 1600$ Å
Off-axis zone plate radius	$r_0 = 0.375$ mm
Offset distance	$\Delta_0 = 0.5$ mm
Spectral lines	$\lambda_1 \simeq 4$ Å
	$\lambda_2 \simeq 6.9$ Å
Maximum source size for separable images	$S \simeq 500$ μm

Fig. 5-65. Initial resolution tests of the zone plate lens were conducted using a test pattern (a) with a minimum line width of 2.5 μm, even though the anticipated resolution of the instrument is roughly 0.5 μm. The enlargement (c) of the "lens" image in (b) shows the 2.5-μm outermost lines of the test pattern are clearly resolved.

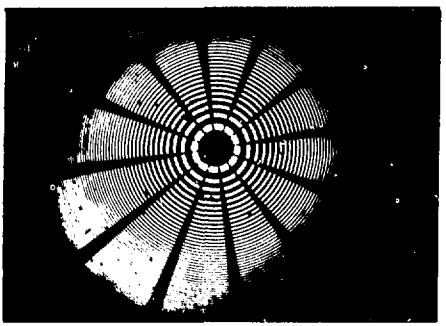

Test pattern (2.5-μm lines)

(b)

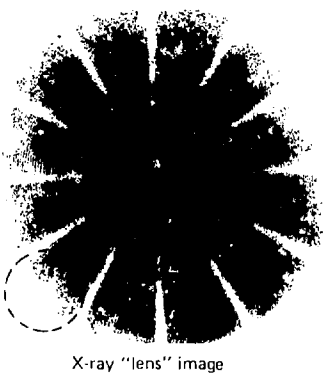

X-ray "lens" image

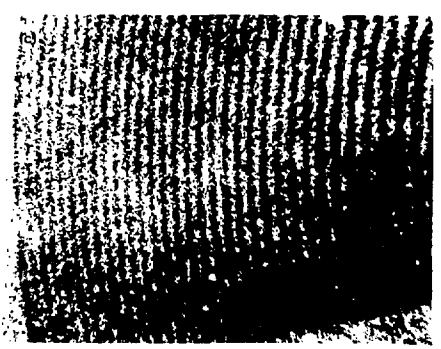

X-ray "lens" image (2.5-μm lines)

Fig. 5-66. The ability of the zone plate lens to clearly resolve the 2.5-μm minimum lines of the test pattern is illustrated by a microdensitometer analysis of the x-ray image. A microdensitometer scan from "A" to "B" across the outermost twenty dark zones of the image shows clear resolution of the individual zones.

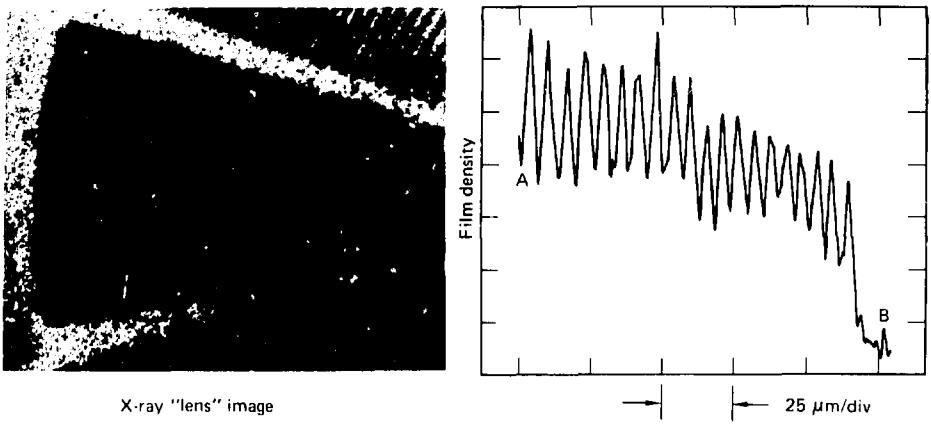

Fig. 5-67. An off-axis segment of a Fresnel zone plate can be used as an imaging spectrometer to spatially separate distinct spectral emissions from a polychromatic source.

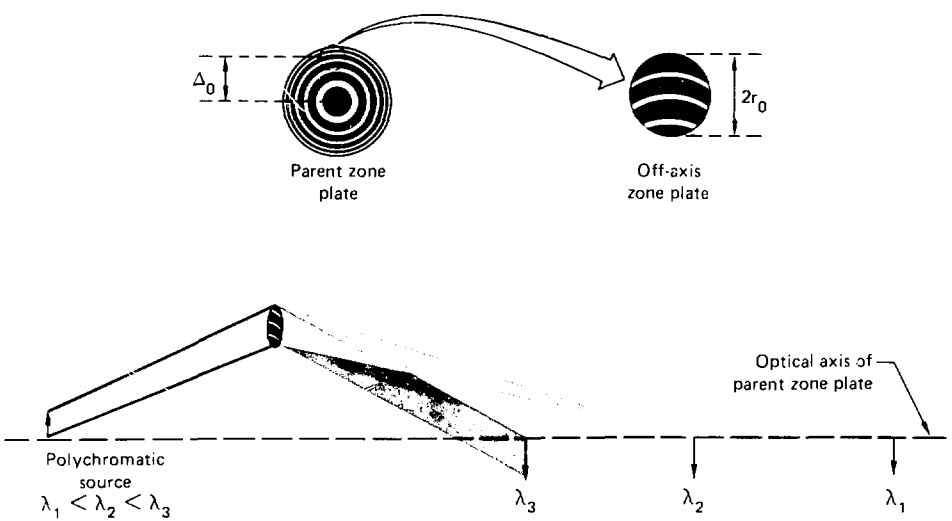

image plane) and can be determined from simple calculations. For the example in Table 5-7, the maximum tilt angle is roughly 81.5°, yielding a recording-medium width ≃2.5 mm for the image at $\lambda_2 = 6.9$ Å.

Off-axis zone plates used as imaging spectrometers will very likely find a wide range of application in the laser fusion program (and other

fields as well). In the particular example cited above, the spectral lines chosen are the argon and silicon K_α emissions from the multiply-ionized laser fusion target. Argon is added as a tracer element in the D-T fuel, and silicon is a natural constituent of the glass microsphere. The imaging spectrometer, therefore, will provide separate and distinct images of the glass pusher and the enclosed fuel during the laser-driven target implosion.

Authors: N. M. Ceglio, D. C. Shaver (MIT), D. C. Flanders (MIT), and H. I. Smith (MIT)

References

62. D. Rudolph and G. Schmahl, "High Power Zone Plates for Soft X-rays," Presented at the *Conference on Ultrasoft X-ray Microscopy: Its Application to Biological and Physical Sciences*, June 13-15, 1979, New York City. To be published in *Annals of the New York Academy of Sciences*. Also, B. Niemann, D. Rudolph, and G. Schmahl, *Opt. Commun.* **12**, 160 (1974).
63. H. Brauninger, P. Predehl, and K. P. Beuermann, *Appl. Opt.* **18**, 368 (1979).
64. H. I. Smith, S. R. Chinn, and P. D. De Graff, *J. Vac. Sci. Technol.* **12**, 1262 (1975).
65. D. C. Flanders and H. I. Smith, *J. Vac. Sci. Technol.* **15**, 995 (1978).

Management and Analysis of Experimental Data

Laser experiments at LLL are designed to study particular aspects of laser-target interactions and fusion target physics. Experiments typically have one or a few primary diagnostics on which the experimenter expects to rely for his main measurements. Often several diagnostics are included in a "desirable but not essential" category; occasionally diagnostics are used on a target experiment purely for diagnostic development purposes not necessarily directly related to the primary measurements being attempted. The flood of data so produced must be intelligently managed so that important data are accurately, completely, and promptly reduced. Less critical data must not consume the experimenter's time to the detriment of programmatic progress.

At the point of taking data, the operations group continuously monitors the diagnostic instrumentation. If they judge that a diagnostic system deemed primary for a given study is inoperative, they delay the shot until the fault has been corrected. Such attention can only be expended on the most critical diagnostics; those judged merely desirable are simply dropped for the shot if they are questionable. These precautions reduce the chances that laser-target irradiations will be wasted.

Given a shot considered successful in any sense, the data produced take several standard forms:

- Raw data from detectors exist as records in computer memory or on film that must be processed and densitometered or digitized.
- The configuration of the diagnostics on the target chamber, including their angular orientations, sensitivity settings, and the like, is preserved as a configuration data base.
- Finally, the experimenter's notes on alignment and orientation of the target are recorded in a shot book provided for each target irradiation.

Within about two weeks of any target shot, results from the shot are distributed in several locations. The best summary is contained in the experimenter's shot book. By this time the responsible investigator will have accumulated and stored in the shot book most of the relevant information gleaned from the shot. These data are reduced using the characteristics of the particular diagnostics (stored in the configuration data base), and whatever additional calibration data are required. Each of several diagnosticians retain copies of the data provided by the measurement systems for which they are responsible. Digitized photographic data exist in memory in the LLL central computer facility; raw electronic data are stored, along with the configuration data base, in the memory of the Shiva computer system. In some cases, all steps beyond the initial collection of the raw data are accomplished using LLL's central computer system.

At this point, data collected in the shot books are compared with preshot expectations, the dominant issues being adequate experimental controls, significant differences between data sets, diagnostic calibration and reliability, and the rest of the concerns which are the experimenter's stock in trade. Meanwhile, the data technicians in the Data Management and Analysis Group archive the shot books in a central vault.

In former years, entire experimental sequences were grossly modified or aborted after the first target shots when results deviated too wildly from

predictions. As knowledge has grown and diagnostic systems have become more sophisticated, however, instances in which laser-plasma interaction experiments produce unintelligible results have become rare. Generally, sequences of several tens of shots are designed and executed more or less as planned, sets of shot books are produced, labeled with the name assigned to the experimental series.

When it is complete, an experimental sequence is reported, often in the archival literature. Contact is made with past work (and work at other laboratories) here and abroad. These experimental reports, together with the shot books, constitute the (readily available) primary record of the experiment, and are stored together in the same area. Generally, few additions or corrections are made to the shot books after the experimental report is written. Completed reports and shot books are used by target designers to correct and or augment simulation codes such as LASNEX.

Summaries of each shot are written and stored in the shot books. During the coming year we will establish and maintain a summary data base on the Data Management and Analysis Group VAX computer system. Such a data base will contain results from all our experiments and will permit statistical trend analysis. Partial data bases have been maintained in past years but these, while helpful, were time-consuming, often incomplete, and never entirely satisfactory. With the advent of better data reduction codes, more of the shot data can be automatically entered into the data base. This development will greatly facilitate the discovery of parametric fits, scaling relations, and weak trends, as well as the reevaluation of old data in the light of new results.

Author: K. R. Manes

Diagnostic Configuration Data Base

There are 220 openings, or ports, in the Shiva target chamber. Twenty of these ports are used as windows for the twenty laser beams, one is used for the target positioner, and the remainder are available for target diagnostic instruments. Because of this large number of ports, each of which usually contains a diagnostic device, we have developed a configuration data base, TDB, to keep track of them.

The configuration data base has three different purposes:

- From the operations point of view, TDB permits easy identification, modification, or retrieval of different experiments or detectors in the target chamber.
- It allows the data analysis programs to determine data paths and the computer location where raw target diagnostic data is stored.
- TDB provides a record of the position and characteristics of the diagnostic instruments during a shot; this then becomes a part of the archived data.

TDB contains all the information necessary to describe the following items:

- Port position, dimensions, and function.
- Experiment use, position, dimensions, detector and electronic specifications and data paths.
- Logical and physical interaction between several experiments placed at several locations.

One of the main characteristics of this data base is its flexibility in terms of adding, changing, or deleting instruments. Because of its special characteristics, we will give a brief description of TDB.

TDB is a commented file structure (like a text) in which every entry (line) starts with an English abbreviation that allows immediate identification of the numbers, keywords or comments that follow. Every line in the TDB file is a logical record. Words, comments or numbers are delimited by blank spaces or tabs, and may be located anywhere in a line. Any blank or tab is assumed to be a word terminator; any string of characters started and terminated by blanks or tabs is assumed to be a word. Any line can have up to a maximum of 120 characters and or 15 words; words can be up to 8 characters long.

The first words on a line are usually reserved for keywords or flags, with the rest reserved for identifiers or numeric values. There can be any number of entries between keywords. Lines started with the exclamation symbol (!) are assumed to contain comments, and are ignored by the retrieval subroutines.

There are two basic types of keywords: descriptives and globals. Descriptives indicate the characteristic, its ID number, and amplifier gain or position in the target chamber. Descriptives usually

refer to information contained in one line, such as DETEC NUMBER LC27 148, which translates as "detector type LC27, unit number 148."

Globals indicate that all entries that follow belong to the same global group. For example, the global keywork "PORT" indicates tht the rest of the line, and all subsequent entries until an "EOP" (end of port) entry is encountered, contain information directly related to that port.

After the "PORT" entry there can be a comment entry to describe the specific use of the port, which might include an "EXP" (experiment entry) An EXP entry indicates that all subsequent entries, until an "EOEXP" (end of experiment) entry, describe the experiment named in the following word. Under the present format, any number of entries can be made to describe the experiment in detail. The PORT entry may contain several experiments; each experiment may contain several detectors.

Table 5-8 shows a small facsimile segment of TDB for one PORT entry, which is interpreted as follows. The port at angles theta = 148° and phi = 126° is in use. The port size or aperture is 2 in. or 5.08 cm, and the outside dimension to the nearest obstruction is 8 in. or 20.32 cm. The experiment or instrument XRADO1 currently in use is mounted on the port and belongs to the XA (x-ray) logical module; Dr. Wang is the individual responsible for the experiment. Delta X = 5.08 cm, delta Y = 5.08 cm, and radial distance = 0.0 are the dimensions of the instrument inside the target chamber. The instrument XRADO1 uses detector type FLPD with serial number 10.0.

Since TDB has a text-like structure, any text editor can be used to make changes. Queries or searches can be done by a specially developed subroutine named PULL, which will search TDB for any given port, experiment, or instrument and return all the relevant information. For example, TDB and PULL are used to produce target chamber diagrams containing port and experiment usage. TDB and PULL can also be used to obtain target chamber statistics, such as the latest configuration at the time of writing of this report:

- Number of used ports = 114.
- Number of free ports = 73.
- Number of blocked ports = 25.
- Number of reserved ports = 8.

Table 5-8. Facsimile of readout from Shiva configuration data base TDB, for sample PORT entry.

PORT	IN USE		
THETA		148.	
PHI		126.	
SIZE		2.	5.08
OUTSIDE DIM		8.	20.32
!			
!	ANGULAR X-RAY EXP		
!			
EXP	XRADO1 XA	2.	IN USE
OWNER	WANG		
DELTA X		5.08	
DELTA Y		5.08	
RADIAL DIST		0.0	
DETEC, NUMBER	FLPD	10.0	
EOEXP	XRADO1 XA	2.0	
!			
EOP			
!			

Author: J. E. Vernazza
***Major Contributor*: J. M. Auerbach**

Data Acquisition and Processing

During the last year, we have made substantial progress towards automation and computerization of data from laser fusion experiments. Our goal is to relieve the experimenter of time-consuming routine data reduction so that more time can be devoted to interpretation. At the beginning of 1979, almost all data processing was done on Octopus through manual data input. Since that time, we have implemented automated processing of several diagnostics on the Shiva PDP 11/70 computer, which requires much less user interaction than Octopus (for a comparison of data processing steps on Octopus and the Shiva PDP 11/70, see Fig. 5-68). We are also acquiring a new VAX computer to provide more efficient fusion experiment data processing and analysis.

Data are currently recorded electronically (by digitization of analog data) and on film. Eventually CCD array cameras may replace nearly all of the film recording. Electronic data are transmitted via a CAMAC serial highway and stored on a floppy disk by the TACAI computer system; TACAI, standing for Target Acquisition, Control, and Instrumentation, has been described in previous annual reports.[66] The TACAI computers at Shiva and

Fig. 5-68. Comparison of functional diagrams of data processing steps for the Octopus and Shiva PDP 11/70 computer systems.

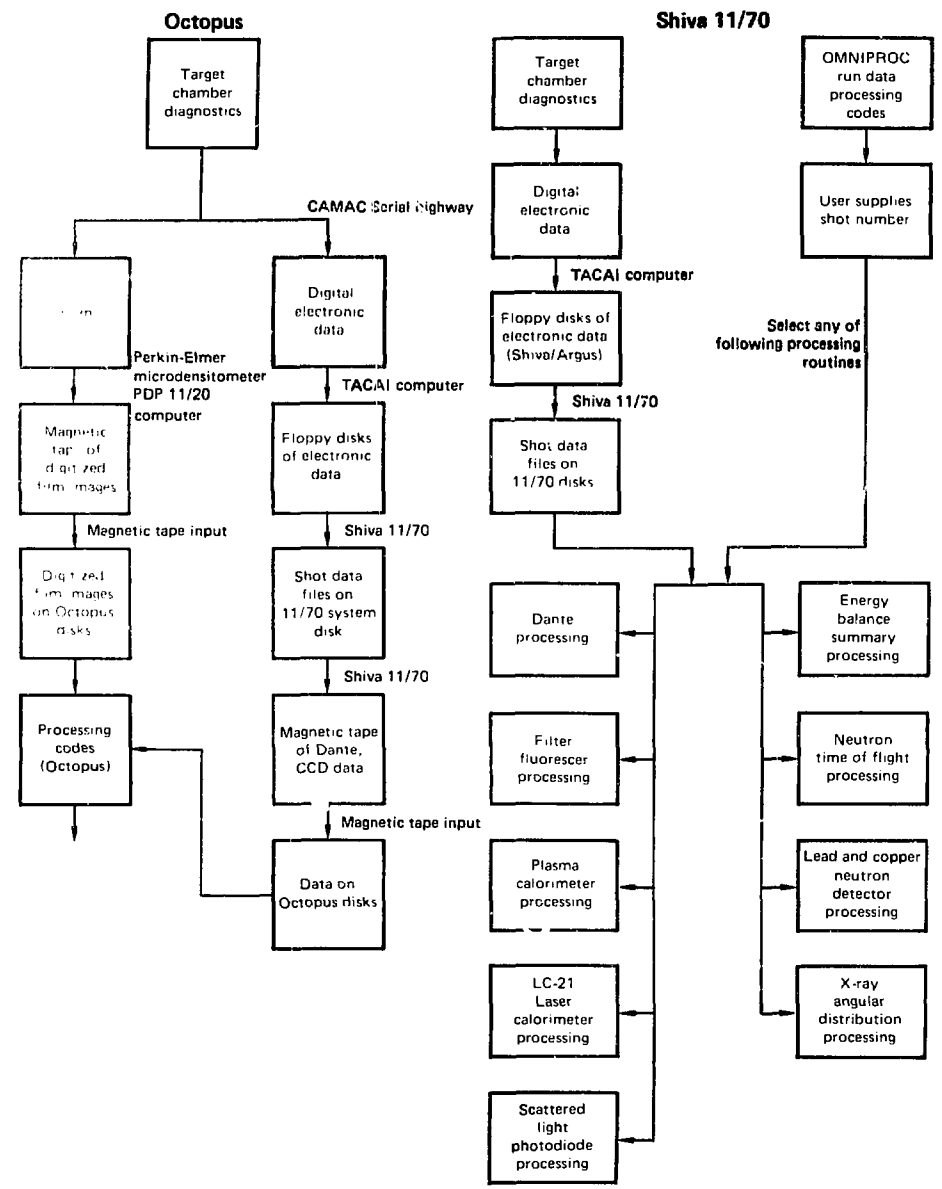

Argus write experimental data on floppy disks, which are then read onto the Shiva PDP 11/70 system disks for further processing. At Shiva we also have the capability for transmitting data directly from the TACAT computer to the 11/70 computer, using Digital Equipment Corp.'s intercomputer communications software, DECNET.

Examples of electronic data for which final processing is done on the Octopus System include data in the shot file for the Dante spectrometer, and data from our soft x-ray streak camera equipped with a CCD array readout. These data are transferred daily from the 11 70 to Octopus on magnetic tape reels hand-carried between computer centers.

Film images are converted into digitized data arrays using a Perkin Elmer Microdensitometer controlled by a Digital Equipment Corp. PDP 11 20 computer. Data are written on magnetic tape, transported to the Octopus tape readers, and stored on the system disks; processing is then accomplished through user terminals. (Details of film data processing are given in "Film Image Processing" later in this section.)

Processing of fusion experiments data on the Shiva PDP 11 70 is a highly automated sequence, due to the nature of the operating system and the lack of need for the manual data transfers required for film processing. Various levels of automated processing have been implemented for the following diagnostics:

- Dante low-energy x-ray spectrometer.
- Filter fluorescer high-energy x-ray spectrometer.
- Plasma calorimeters.
- LC-21 laser calorimeters for scattered light.
- Scattered-light photodiodes.
- Neutron time-of-flight detector.
- Lead and copper activation neutron yield detectors.
- X-ray angular distribution detectors.

In following subsections we will describe the processing software for the first five of these diagnostics. Processing for the last three of these five diagnostics are incorporated with the processing of laser system calorimetry to give an energy balance, also described in a following section.

To allow automated processing, all processing codes utilize files on the PDP 11/70 system disk for setup and calibration parameters. These files are updated daily or as required to reflect the current diagnostic configuration. In the sections that follow, these files are referred to with their standard Digital Equipment Corp. nomenclature. This is the form NAME.XXX, where NAME can be up to a nine-letter name and XXX is a three-letter type; thus SETUP.PAR is a parameter (PAR) file named SETUP.

Automated processing is accomplished by use of command files which contain groups of processing commands. In the sections which follow, these command files have the typical label NAME.CMD, where CMD is the abbreviation for command. The processing for all diagnostics is controlled through one command file called OMNIPROC.CMD. Upon execution, this code lists the various diagnostics that can be processed, asks the user to choose the diagnostic(s) of interest, and asks for an (eight-digit) shot number so the appropriate raw data can be accessed.

Author: J. M. Auerbach
Major Contributor: J. T. Ozawa

Reference

66. *Laser Program Annual Report—1977*, Lawrence Livermore Laboratory, Livermore, Calif., UCRL-50021-77 (1978), pp. 3-90 to 3-93.

GETSD: A General Shot Data Retrieval Routine

Digital data from the Argus and Shiva diagnostic data acquisition systems are organized by CAMAC crate, CAMAC station, and a disk file containing all the shot data. For subsequent higher-level analysis, processing programs must extract certain parts of the data from the disk. To avoid duplication, with each experimenter/programmer writing his own routine for data extraction, we have written a single versatile data extraction routine called GETSD (GET the Shot Data).

Implementation. GETSD is implemented using ISHOT, a 9-word integer array containing the 8-digit shot number (used to access the appropriate shot data file) and one additional word reserved for future expansions. Users then employ ILOC, a 3-

word integer array, to specify the location parameters of the device producing the data of interest.

The overall assignments for ILOC(1) are as follows:

- ILOC(1) = 0-99 indicates target diagnostics.
- ILOC(1) = 100-199 indicates laser diagnostics.
- ILOC(1) = 200-299 indicates alignment.
- ILOC(1) = 300-399 indicates power conditioning.
- ILOC(1) = 400-499 indicates central controls.

The meaning of the elements in the ILOC array is dependent on the diagnostic system containing the particular device. For target diagnostic data produced by the Shiva or Argus TACAI systems, ILOC(1), (2), and (3) are the CAMAC crate, station, and unit numbers, respectively. For data produced by the laser diagnostics system at Shiva, ILOC(1) provides the following parameter assignments:

- 100 = Beam energies.
- 101 = Detector sensitivities.
- 102 = Amplifier gain.
- 103 = Amplifier offset.
- 104 = Autozero setting.

For the laser diagnostics system at Shiva ILOC(2) is the coded number of the laser component (oscillator, preamps, Pockels cells, rotators, calorimeter groups, etc.) from which the ILOC(1) data were recorded; each component also carries a 4-character name for call by other GETSD routines. [ILOC(3) is ignored for laser diagnostic devices.]

The meaning of elements in MODNAM, an 8-word integer array containing the ASCII name of the device producing the data of interest, is also system-dependent. For data produced by target diagnostic systems at Shiva and Argus, device names are CAMAC interface module names. Device names for laser diagnostic data are the 4-character component names used in ILOC(2). Users must also supply the abbreviations for the types of analog-to-digital converters on each diagnostic; examples are "TK7912" for a Tektonix Model 7912 transient digitizer, and "PRCHIN" for a programmable charge integrator.

Data Arrays. The four data arrays in GETSD are called IPARM, SCALE, IDATA, and BUF:

- IPARM is an integer array, receiving parameter data from the specified shot data file for the specified diagnostics device.
- SCALE is a real array, receiving scale data. ILOC(1) = 100 returns beam energy data; ILOC(1) = 101 returns detector sensitivity data. In the future, SCALE will also receive data on amplifier gains, amplifier offsets, and autozero settings.
- IDATA is an integer array, receiving data sets returned by GETSD.
- BUF is an integer array, receiving the common buffer data returned from a common buffer CAMAC device.

The first three arrays need be dimensioned no greater than 128, though this limit is arbitrary and may be changed in the future; BUF must be dimensioned at least 3000 to accommodate most common buffer sets.

Table 5-9. Status calls returned by subroutine ISTAT of the shot data retrieval routine GETSD.

ISTAT = 1	Successful GETSD call.
ISTAT = -1	Error detected while attempting to open the shot data file; most likely cause is locked file or no file.
ISTAT = -2	Data in shot file out of sequence or not found; caused by a bad shot file or bad calling arguments.
ISTAT = -3	Error encountered while reading the shot data file; this is likely an I/O error, but may also arise because end-of-file was found before requested data was found or recognized.
ISTAT = -4	Premature end-of-file found while accessing the shot file; occurs when end-of-file is found before all data are complete.
ISTAT = -5	Bad shot number; nonnumerics not currently allowed in shot number.
ISTAT = -6	Bad ILOC value(s); negative values not allowed for location parameters.
ISTAT = -10	More than one of the four data arrays was too small to hold all the data found for the specified device; check values passed for array sizes.
ISTAT = -11	IPARM array is too small for number of data points found.
ISTAT = -12	SCALE array is too small for number of data points found.
ISTAT = -13	IDATA array is too small.
ISTAT = -14	BUF array is too small.
ISTAT = -15	Common buffer data were found to be flagged as incomplete or in error.

Each data array has an associated integer variable routine which is both an input and output parameter for the GETSD routine; these subroutines are called, respectively, NPARM, NSCALE, NDATA, and NBUF. The value of the integer variable is set to the size of the actual data array on entry; then, using IPARM and NPARM as an example,

- If the number of data points read from the shot data file is less than the number of elements in the IPARM array, GETSD sets the value of NPARM to the number of points read.
- If the number of data points in the shot data file exceeds the number of elements in the IPARM array, the IPARM array will be filled to its limit and an error code will he returned by the status subroutine ISTAT.
- If NPARM is set to zero before the GETSD call, GETSD will not read parameter data and the IPARM argument may be omitted from the call. Similarly, if any integer variable is set at zero before the GETSD call, the argument of its data array may be omitted and no data will be returned to that array.

GETSD's status subroutine, ISTAT, is an integer variable whose values are listed in Table 5-9.

Authors: J. T. Ozawa and J. M. Auerbach
Major Contributors: J. E. Krammen and J. Wilkerson (Bendix)

Automatic Diagnostic Data Processing: Dante

The Dante system[67] uses fast x-ray diodes as detectors. Output currents from these detectors are related to the incident x-ray energy flux through the detector and filter response functions. The x-ray spectrum emitted by the target in the direction of the instrument can be obtained from approximately 200 eV to 2 keV with ten appropriately filtered channels.

At Shiva, the detectors are impedence-matched to 50 Ω and their outputs are recorded by Tektronix R7912 transient digitizers. Each digitizer is associated with a given crate, station, and unit in the CAMAC system through which the digitized data are transferred to the shot file. Preprocessing of the Dante data is then performed on the Shiva 11/70 according to the process described in this article.

A data file named DANCHN.SET contains the crates, stations, and channels connected to active Dante channels; the program TKDANT (adapted from programs written at LLL to handle R7912 transient digitizers data) uses these pointers to extract from the main shot file the data from each of the R7912's. A subroutine of TKDANT, TD7912, then unpacks the data and, using subroutine N7912Z (Ref. 68), determines the centroids of the trace; representative raw and fitted data are given in Fig. 5-69.

The output of TKDANT is a single file, DANRAW.DAT, containing x blocks of data where x equals the number of Dante channels; the output structure of one such block is shown in Table 5-10. An identical file named TK7NORM-.BSL contains similar information, obtained during a rod shot immediately preceding the shot to be analyzed. This file, created by TK7BASE, a general R7912 baseline program which follows the same steps as TK7912, is used to establish baseline levels.

The two files, DANRAW.DAT and TK7-NORM.BSL, are used by program ANDANT2 (ANalyze DANTe) to obtain voltage-vs-time information from the recorded counts; to do so, the baseline is subtracted from the data. Tests are then performed to determine whether the remaining baseline is indeed zero. Should this not be the case,

Table 5-10. TKDANT output structure.

Word number	Content
1	Crate number
2	Station number
3	*Channel number*
4	Not used
5	Total number of data points = 512
6	R7912 vertical sensitivity (mv/cm)[a]
7	R7912 horizontal sensitivity (ns/cm)[a]
8	Number of data points
9	Index of first valid vertical datum
16 - 23	Shot number
257	First vertical value (centroid)
•	
•	
•	
768	512th vertical value (centroid)

[a]For direct-access plug-ins the horizontal sensitivity in ps/cm is in word 6; word 7 is not used.

Fig. 5-69. (a) Typical Dante channel output; (b) the same data normalized to trace centroid.

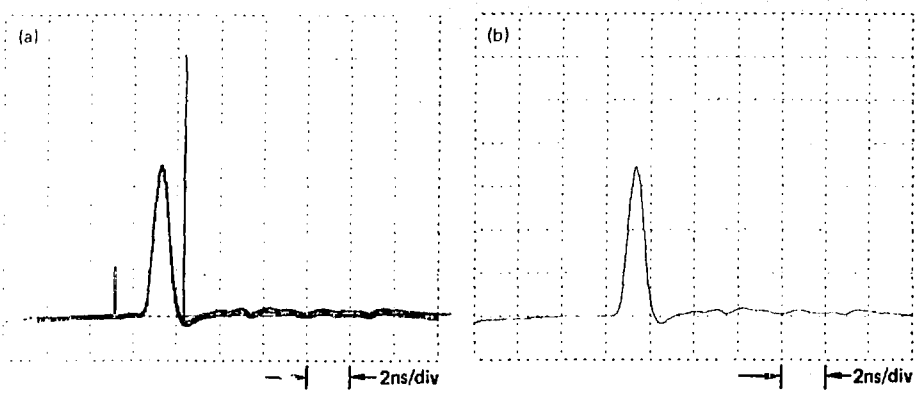

a data-derived baseline is obtained and the process repeated. The following quantities are then calculated:

- The location of the peak of the pulse with respect to a fiducial.
- The voltage at the peak.
- The FWHM about the peak.
- The integral of the signal over the full range excluding the fiducial.
- The integral of the signal for one FWHM on each side of the peak.
- The index location of the fiducial peak.
- A flag indicating the data quality.

Two files are generated to utilize these quantities: DANDAT.INP is used for further processing on the 11/70; (shot #).DAN is transferred via tape to the LLL Octopus system. A third file, DANERR.TMP, provides the experimenter with information on the program's handling of baseline data, as well as characteristics of the fiducial pulse.

The final preprocessing step is performed by UNDANT2 (UNfold DANTe). The basic role of this program is to combine the data accumulated in DANDAT.INP with the characteristics of the associated detectors and provide a summary file (Table 5-11) for inclusion in the shot book. The column labeled "Integral v. ns" provides the necessary input for the UNSPEC (UNfold SPECtrum) routine which is used through Octopus on a CDC 7600 to obtain the final unfolded spectrum; and example of this final output is shown in Fig. 5-70. Given a reference spectrum, this program is also capable of providing, for quick-look purposes, a ratio spectrum based on the current shot data (Fig. 5-71); this option is normally not exercised, however, since appropriate reference spectra are not generally available.

Fig. 5-70. Representative unfold Dante spectrum.

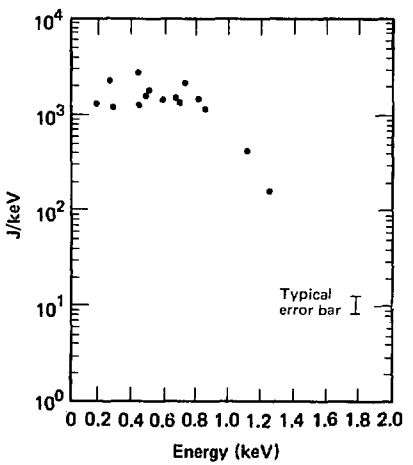

The (shot#).DAN file is read into the Octopus system where is operated on by the frequency

Table 5-11. Representative Dante summary for Shiva target shot.

POSITION: THETA = 90, PHI = 234
BIAS: 5 KV

DET #	CAMAC CR	CAMAC STA	CAMAC UN	EDGE ENERGY KEV	CHARACTERISTICS CATHODE	FILTERS NAME	FILTERS BLAST SHIELD	FILTERS #1	FILTERS #2	SCOPES V/DIV	SCOPES NS/DIV	ATTN	FLAG
1	11	4	1	0.28	AL43	FV2	PY.1	FV.63	FV.63	4.000	2.000	20	20010
2	11	4	2	0.52	AL52	VV1	PY.1		V.55	4.000	2.000	8	20000
3	11	4	3	0.58	AL53	CR1	PY.1		CR. 6	4.000	2.000	8	20000
4	11	4	4	0.71	AL54	FE2	PY.1		FE.45	1.000	2.000	40	20000
5	11	4	5	0.79	AL49	CO1	PY.1		CO1.1	1.000	2.000	8	20000
6	11	4	6	0.86	AL50	NI1	PY.1		NI. 7	1.000	2.000	40	20000
7	11	4	7	0.94	CR19	CU1	PY.1		CU1.	1.000	2.000	40	20000
8	11	4	0	0.94	CR23	CU2	PY.1	CU1.	CU1.	1.000	2.000	4	20010
9	11	2	7	1.56	NI15	AL9	PY.1		AL9.2	4.000	2.000	2	20000
10	11	2	6	1.56	NI16	AL2	PY.1	AL9.2	AL9.2	0.500	2.000	2	20000

FLAG = XXXX1 IF BASELINE WAS SHOT DERIVED
= XXX1X IF FWHM*MAX IS LESS THAN 90% INTEGRAL
= XX1XX IF MAX DEFLECTION < 10 COUNTS
= X1XXX IF FWHM OR INTEGRAL < 0
= 1XXXX IF NO BASELINE AND CANNOT DERIVE IT FROM SHOT

DET	FIDO PEAK COUNTS	PEAK LOC -NS REL TO LASER	FWHM NS	PEAK VALUE VOLTS	INTEGRAL V.NS	SUM/ FWHM*PV	SUMP V.NS
1	418	-0.108E+02	0.254E+01	0.401E+02	0.118E+03	1.16	0.104E+03
2	440	-0.114E+02	0.266E+01	0.113E+02	0.312E+02	1.04	0.308E+02
3	436	-0.104E+02	0.261E+01	0.992E+01	0.266E+02	1.03	0.259E+02
4	444	-0.110E+02	0.267E+01	0.147E+02	0.361E+02	0.92	0.331E+02
5	448	-0.935E+01	0.262E+01	0.468E+01	0.119E+02	0.97	0.109E+02
6	445	-0.105E+02	0.274E+01	0.134E+02	0.351E+02	0.96	0.341E+02
7	503	-0.122E+02	0.282E+01	0.126E+02	0.369E+02	1.04	0.333E+02
8	450	-0.102E+02	0.206E+01	0.174E+01	0.541E+01	1.51	0.339E+01
9	459	-0.119E+02	0.250E+01	0.499E+01	0.120E+02	0.96	0.113E+02
10	442	-0.116E+02	0.251E+01	0.607E+00	0.146E+01	0.96	0.143E+01

Fig. 5-71. Representative ratio spectrum for Dante data.

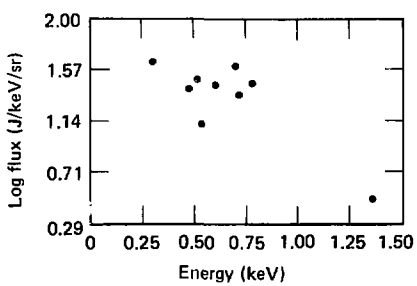

domain deconvolution code DCON, which deconvolves the temporal response of the detectors, cables, and oscilloscopes in the Dante diagnostics system. After removal of the temporal response, spectral unfolds of "snapshots" in time are done with UNSPEC. Using this method, we have produced time-dependent spectral unfolds with a resolution of 120 ps FWHM on direct-access R7912 data and 300 ps on amplified R7912 channels.

Authors: V. C. Rupert and R. A. Heinle
Major Contributor: G. S. Chinen

References

67. *Laser Program Annual Report—1978*, Lawrence Livermore Laboratory, Livermore, Calif., UCRL-50021-78 (1979), pp. 6-5 to 6-7.

68. J. Greenwood and J. Ozawa, *X7912Z—A Normalized Routine for the R7912 Transient Digitizer on the PDP 11*, Lawrence Livermore Laboratory, Livermore, Calif., UCID-17810 (1978).

Automatic Diagnostic Data Processing: Filter Fluorescer

The filter fluorescer high-energy x-ray (FFLEX) spectrometer, described in detail in last year's annual report,[69] is used to produce a spectrum of the high-energy (>1 keV) x rays from laser-plasma interaction experiments. The detector signals (given amounts of charge from photomultiplier tubes) can be processed automatically to yield the desired spectra. Before the spectra are generated, routines are executed that detect very low or saturated detector channels and establish the signal-noise ratios for all channels. This preprocessing requires that we maintain a set of parameter and setup data files, which will be described in conjunction with the processing steps enumerated below.

The PM tube output of each detector is connected via three different attenuators to three channels of a LeCroy Research Systems Charge Integrator/ADC module (LS2249W). Each module is assigned a crate and station in either the Shiva or Argus CAMAC systems. In addition, the high voltage applied to each PM tube is set and monitored through a computer interface, with a LeCroy Research System HV 4032 programmable high-voltage power supply; the voltage-sensing circuits of the supply are interfaced to the TACAI computer through a CAMAC crate and station.

Thus the recording of shot data and detector voltages has been automated. At shot time the outputs of all the active charge integrator modules are transferred via the CAMAC serial highway to the TACAI LSI-11, where the data are written on floppy disks and then transferred to the Argus or Shiva data acquisition computers along with other diagnostic data. The FFLEX data are incorporated into the shot data file on the Shiva PDP 11/70 using the routine PROCESS, which transfers the TACAI raw data from the floppy disk to the main computer disk.

The LS2249W module outputs generally have non-zero baseline values; that is, they show non-zero dc outputs with no signal input. This necessitates "dry-run" data processing before a shot, so that baseline values can be subtracted from the total detector charge signals obtained during a shot.

With the 11/70 shot data file as input, data processing proceeds in the sequence described below (and summarized in Fig. 5-72).

The processing program FFBDP checks a disk file which gives the active detector channels for the shot. The program then opens a data file containing CAMAC crate, station, and ADC channel numbers for each detector channel. Only the CAMAC parameters corresponding to the active channels are extracted.

Using the GETSD routine (described in a previous article) and the CAMAC data, a baseline processing routine is run which extracts from the dry-run file the baseline values for the active detector channels. Still using GETSD and the CAMAC data, the main processing program extracts from the actual shot data file the high-voltage readings and LS2249W ADC outputs for the active channels; there are three ADC readings for each detector, corresponding to the three attenuators. Next the program opens a file which contains the maximum linear current of each PM tube as a function of bias voltage.

A summary of system performance is now calculated, a sample tabulation of which is given in Table 5-12. For each attenuator value, the summary provides the total channel ADC output, baseline, and charge output in picocoulombs. Each ADC count corresponds to 0.25 picocoulombs. If an ADC count is within 10 counts of baseline, it is flagged as NOISE LEVEL; if an ADC count exceeds 1900 it is flagged as SATURATION, which occurs in the LS2249W between 1800 and 2000 counts. The program then selects the value farthest removed from NOISE LEVEL or SATURATION as the BEST SIGNAL. Readings are also printed for the HIGH VOLTAGE, the MAXIMUM LINEAR CHARGE (maximum linear current at the bias voltage times scintillator pulse width), and the ratio of BEST SIGNAL to MAXIMUM LINEAR CHARGE. A ratio greater than or equal to 1 indicates that the PM tube may have been in the nonlinear regime of operation, in which case the calibration factors used in processing would be inaccurate.

Channels 1 and 10 of the filter fluorescer are "background" channels. Channel 1 is used to obtain a background figure for detectors with NE 111

Fig. 5-72. Summary of automatic filter fluorescer diagnostic data processing.

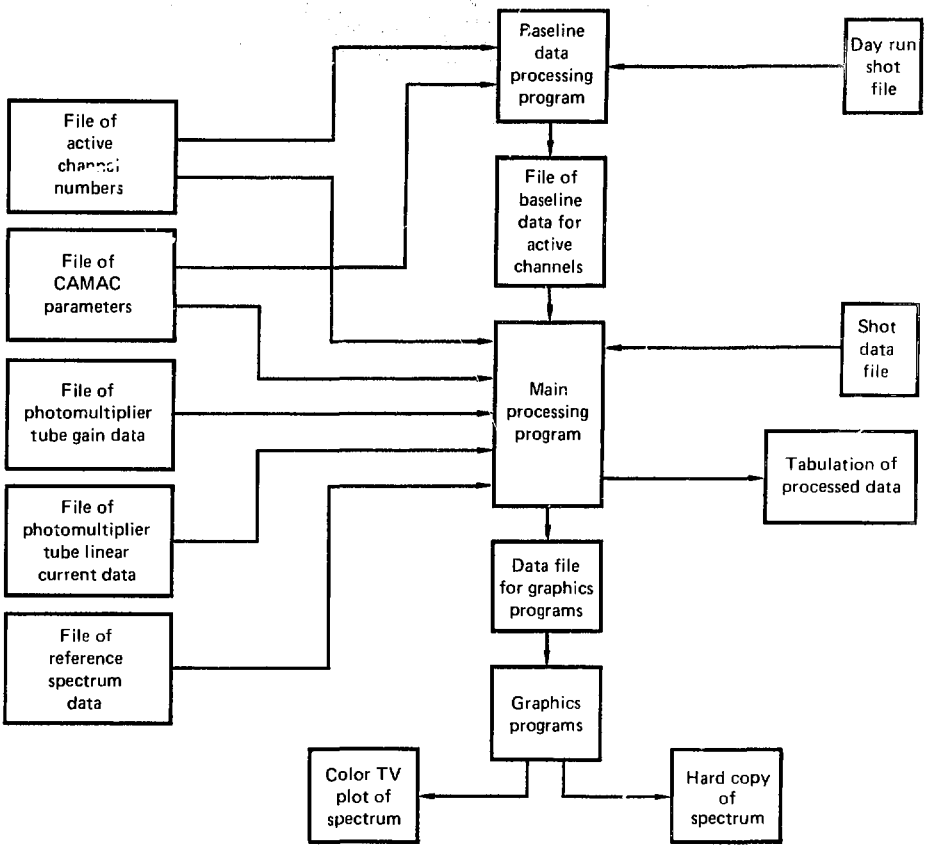

scintillators; channel 10 is used to obtain a background figure for detectors with NaI scintillators. These background channels contain no fluorescer and hence produce a charge signal arising from electromagnetic pickup and high-energy x rays impinging directly on the PM tubes. The ratio of these signals to the signal on each active channel is an indication of noise to signal ratio. Using a file which contains the gain of each PM tube as a function of voltage, the main program normalizes the background signals to the gain of each active channel tube at 2500 volts, and calculates a noise to signal ratio. This summary for all active channels is displayed in the second section of the program output.

The last part of the data processing involves computation of the x-ray spectrum from the "good" channels, that is, from those detectors having outputs that are neither in SATURATION nor near the NOISE LEVEL. If S(E) denotes the x-ray spectrum, Q_n the output from the nth channel, and $R_n(E)$ the response function of the nth channel as a function of energy E, then we must solve for S(E) from the set of integral equations

Table 5-12. Sample FFLEX channel summaries.

CHANNEL NO. 7				
ATTENUATOR	ADC OUTPUT	BASE LINE	PICOCOULOMBS	REMARKS
1.	1995.	35.	0.147E+04	SATURATION
10.	535.	37.	0.374E+04	
100.	30.	23.	0.525E+03	NOISE LEVEL
HIGH VOLTAGE	BEST SIGNAL (PC)			
3000.	0.374E+04			
	MAX. LIN. CHGE. (PC)		BEST SIGNAL/(MAX. LIN. CHGE.)	
	0.115E+06		0.032	

CHANNEL NO. 8				
ATTENUATOR	ADC OUTPUT	BASE LINE	PICOCOULOMBS	REMARKS
1.	1995.	32.	0.147E+04	SATURATION
10.	447.	27.	0.315E+04	
100.	46.	29.	0.128E+04	
HIGH VOLTAGE	BEST SIGNAL (PC)			
3000.	0.315E+04			
	MAX. LIN. CHGE. (PC)		BEST SIGNAL/(MAX. LIN. CHGE.)	
	0.110E+05		0.029	

$$Q_n = \int_0^{\infty} S(E)R_n(E)dE \quad n = 1, 2, \ldots N \qquad (3)$$

Finding a rigorous solution for S(E) requires much interaction between user and computer, accomplished using the unfolding code UNSPEC2. For experiments having similar targets and laser irradiation conditions, however, the rigorous unfold procedure can be supplemented by a ratio calculation using one rigorous unfold as the reference spectrum; this procedure, known as a ratio spectrum calculation, is often used in our automated data processing.

Let $S_0(E_n)$ be the value of the reference spectrum at energy E_n (usually the mid-energy-point of a detector channel). Let Q_{0n} be the calculated or measured charge for channel n due to the reference spectrum (they should be equal) and Q_n be the measured signal in channel n due to the x-ray spectrum to be determined. Then the new spectrum S(E) can be determined for a *similar* class of experiments by

$$S(E_n) = S_0(E_n) \times \frac{Q_n}{Q_{0n}} . \qquad (4)$$

In calculating a spectrum, all signals Q_n are referenced to a PM-tube voltage setting of 2500 volts. The processing program opens a file containing the PM tube gains as a function of voltage, and extracts gain data for the active channels. Then if Q_v is the measured signal at voltage V and G(v) the gain at V, the processing program calculates Q_n in Eq. (4) by

$$Q_n = \frac{G(2500)Q_v}{G(v)Q_0} . \qquad (5)$$

The ratio calculations, tabulated in the third part of the program output, give the values of Q_n, E_n, $S_0(E_n)$ and $S(E_n)$ for each detector channel. The

Fig. 5-73. Sample printout of an x-ray spectrum obtained with the FFLEX spectrometer.

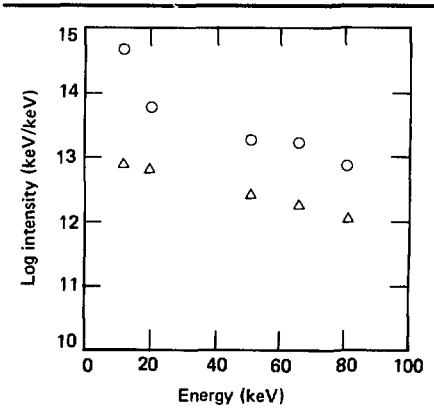

program also plots the experimental and reference spectra on both a color TV monitor and a Versatec printer: a sample plot is shown in Fig. 5-73.

Automation of this simple set of calculations for processing filter fluorescer data has reduced the experimenter's workload by 2 to 3 hours per experiment.

Author: J. M. Auerbach
Major Contributors: G. S. Chinen, H. N. Kornblum, B. L. Pruett

Reference

69. *Laser Program Annual Report—1978*, Lawrence Livermore Laboratory, Livermore, Calif., UCRL-50021-78 (1979), pp. 6-8 to 6-12.

Automatic Diagnostic Data Processing: Calorimeters

Various types of calorimeters have been described in Ref. 70 as well as in previous annual reports.[71,72] For a given heat input, the sensing elements of calorimeters provide a time-varying voltage which is amplified in two stages. The first stage is a fixed-gain (1000) preamplifier[73]; the second stage is a 16-channel programmable-gain amplifier of LLL design.[73] The gain of this latter amplifier is selected through a computer interface so that its value is available in the shot data file and can be accessed directly for automatic data processing. The amplified data are digitized by "calorimeter modules," designed at LLL,[74] which provide multiplexed data from up to sixteen data channels.

Processing of all calorimeters (plasma, light, x-ray, and special-purpose) is conducted simultaneously. The programmable amplifier module and each calorimeter module are assigned a crate and a station in the CAMAC system through which data are recorded in the shot file; each of the amplifier channels is also assigned a unit number in the CAMAC system.

Program CALRED uses CALCHN.SET, which contains the crate, station, and unit numbers, to extract appropriate data from the shot file. For each crate and station, data from the sixteen channels are demultiplexed and the corresponding amplification factors determined. The main output of CALRED is a single file, CALRAW.DAT, containing blocks of data. Each block includes the crate and station number, followed by the amplification factors for the 16 channels, and the 16 sets of demultiplexed data headed by the channel number. CALRED also contains an option (normally not exercised) which plots the data from each channel.

Program CALIN2, a simplified version of a thermopile data analysis program,[75] uses the shot data from CALRAW.DAT and associates each channel with a calibration factor, detector ID, and location provided by data file CALNAM.SET. The basic role of CALIN2 is to calculate an energy flux from the time-dependent raw data. Two output files are generated:

- CALFIT.DAT provides the experimenter with various indicators of the data quality, and information concerning the fits used.
- CALOUT.INP contains, for each channel (in the order recorded), the calorimeter ID, polar and azimuthal angles, the energy flux measured, and an "error" value indicative of the smoothness of the data and its deviation from the fitted curve; CALOUT.INP also provides a flag indicating various possible data conditions, such as noise level and saturation.

Final data for plasma and special calorimeters are provided by program CALOUT; data for light calorimeters are further processed by program ENERGY (described later in this section). CALOUT performs two separate tasks. The first consists in sorting the various types of calorimeters according to three categories: "plasma," "light," and "others." Data from plasma and light calorimeters are further sorted according to azimuthal angles and for each azimuth according to polar angle. The data are then printed out in the shot-book format displayed in Table 5-13.

The second task consists in obtaining an absorbed energy value based on plasma calorimeter data. This procedure is valid for axisymmetric configurations only, such as balls or untilted disks. Since the plasma calorimeter data are strongly affected by any diagnostic extending close enough to the target to seriously distort the plasma distribution, the calculation of absorbed energy is usually suspect if any such diagnostic has been used. For the same reason, energy balances obtained from scattered-light diagnostics are also suspect under these conditions.

Table 5-13. Representative Shiva plasma calorimeter data, as printed out in shot-book format.

THETA DEGREES	PHI DEGREES	ENERGY FLUX J/SR	DE/E %	COMMENTS
160.00	18.00	3.21	6.36	
45.00	36.00	0.00	100.00	LOW SIG
60.00	36.00	8.38	1.95	
75.00	36.00	0.00	100.00	LOW SIG
90.00	36.00	4.32	4.10	
105.00	36.00	3.49	3.36	
120.00	36.00	2.20	8.11	
45.00	90.00	0.00	100.00	LOW SIG
45.00	126.00	36.84	0.43	
60.00	126.00	29.88	3.02	
75.00	126.00	0.00	100.00	LOW SIG
90.00	126.00	0.37	100.00	
105.00	126.00	0.97	100.00	
120.00	126.00	0.16	89.73	
135.00	126.00	3.10	3.97	
45.00	162.00	46.73	0.36	
160.00	162.00	2.55	7.80	
45.00	216.00	107.18	0.81	
60.00	216.00	60.04	1.58	
75.00	216.00	51.84	0.42	
90.00	216.00	42.16	0.33	
105.00	216.00	29.49	0.48	
120.00	216.00	20.69	0.92	
45.00	270.00	54.91	0.92	
45.00	306.00	39.43	1.54	
60.00	306.00	37.15	1.25	
75.00	306.00	35.97	0.68	
90.00	306.00	20.72	1.03	
105.00	306.00	8.20	1.50	
120.00	306.00	5.14	3.68	
135.00	306.00	2.59	10.18	
45.00	342.00	32.84	1.33	

For appropriate configurations, CALOUT fits the azimuthally averaged data for energy flux versus polar angle to a curve of the form $\Sigma a_n \cos n\theta$. Each coefficient of this fit is then tested for statistical significance based on the collected data, and deleted if necessary. The final fit, containing only significant coefficients, is then integrated to yield total absorbed energy; an example of such a fit for a disk shot is given in Fig. 5-74, along with the collected data.

Because the requirements for a meaningful calculation of total absorbed energy are often not met in an experiment, this value is not automatically printed in the output intended for the shot book, but is manually entered (when appropriate) on the plasma calorimeter summary page. This value is also extracted from CALOUT's output data by program ENERGY, which prints it on its own summary page. It must be emphasized that this value is not to be considered useful unless verified by the experimenter.

Author: V. C. Rupert

References

70. S. R. Gunn and V. C. Rupert, "Calorimeters for Measurements of Ions, X rays, and Scattered Radiation in Laser Fusion Experiments," *Rev. Sci. Inst.* **48**(11), (1977).
71. *Laser Program Annual Report—1975*, Lawrence Livermore Laboratory, Livermore, Calif., UCRL-50021-75 (1976), pp. 404 to 407.
72. *Laser Program Annual Report—1976*, Lawrence Livermore Laboratory, Livermore, Calif., UCRL-50021-76 (1977), pp. 3-55, 3-93 to 3-95.
73. D. Campbell and J. Severyn, *The Electronics of the Target Diagnostics System for the Shiva Laser Fusion Facility*, Lawrence Livermore Laboratory, Livermore, Calif., UCRL-52521 (1978).
74. *Laser Program Annual Report—1976*, Lawrence Livermore Laboratory, Livermore, Calif., UCRL-50021-76 (1977), pp. 3-131 to 3-133.
75. S. R. Gunn, *On The Calculation of the Corrected Temperature Rise for Isoperibol Laser Calorimeters*, Lawrence Livermore Laboratory, Livermore, Calif., UCRL-52019 (1976).

Fig. 5-74. An example of collected and fit data for the Shiva plasma calorimeters, used to estimate total absorbed energy. Triangles are the collected data (all azimuth and polar angles); the solid line is a fit of the form $a_n \cos n\theta$ to the azimuthally averaged data. The disk was located normal to the Shiva beam cluster and irradiated by the lower 10-beam cluster only.

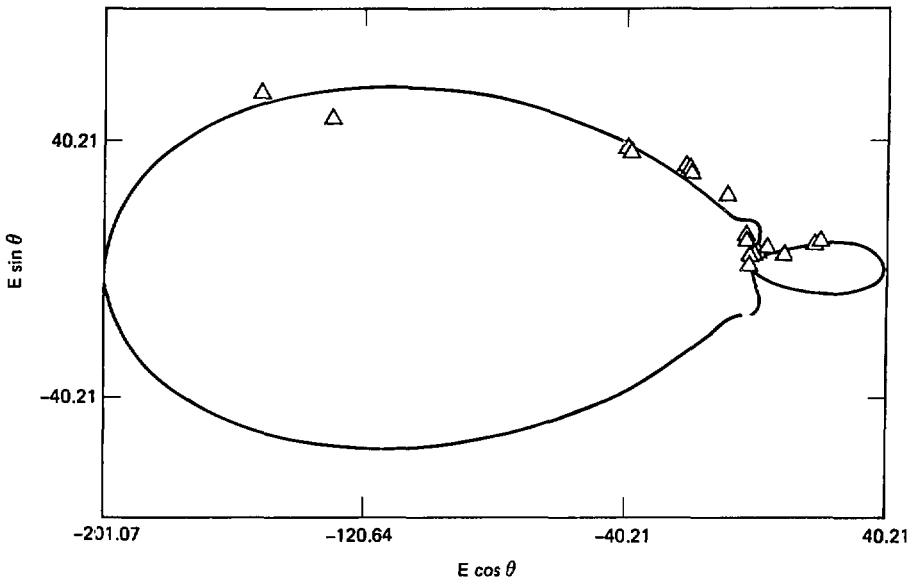

Automatic Diagnostic Data Processing: Photodiodes

Automatic reduction of the photodiode data required for the Shiva energy balance measurement (EBM) is processed by program LIGHT (Fig. 5-75) on the Shiva PDP 11/70. LIGHT is controlled by the processing command file EBF.CMD, which also controls the calorimeter data processing and energy balance routines. LIGHT gets raw shot data from the TACAI system, and employs two input files:

- SETUP.PAR (read into the program at run time), containing parameters necessary for the reduction of the photodiode data.
- CAL.FAC (incorporated into the program at compiling), containing the programmable charge integrators' sensitivity calibrations.

SETUP.PAR contains, for each photodiode detector, its

- Number, CAMAC crate and station, serial number (denoting the programmable charge integrator module), and channel.
- Spherical angular coordinates, distance R from the target, window transmission index, and sensitivity factor R' (in picocoulomb/Joule/cm^2).

SETUP.PAR also contains

- The total number of active diode detectors.
- A conversion factor of 5.0 volts per 4095 full counts; any reading greater than 4092 is considered (and flagged as) saturated.
- A flag to denote a blocked detector and to specify the diode used to measure the x-ray background.

CAL.FAC contains the data statements for two arrays in LIGHT:

- SENS(8), which contains the detectors' sensitivity per volt full scale, in picocoulomb/volt. This value is obtained from the TACAI file and passed to LIGHT via the data acquisition routine GETSD.
- PC(8,4,20). The first dimension of this array corresponds to the sensitivity setting of the amplifier; the values are the elements of the array SENS described above. The second dimension corresponds to four detectors grouped into one module, and is thus the channel assignment read in from SETUP.PAR. The third dimension corresponds to 20 modules of amplifiers, thus corresponding to the serial number read in from

Fig. 5-75. Flowchart of automatic photodiode data processing at Shiva.

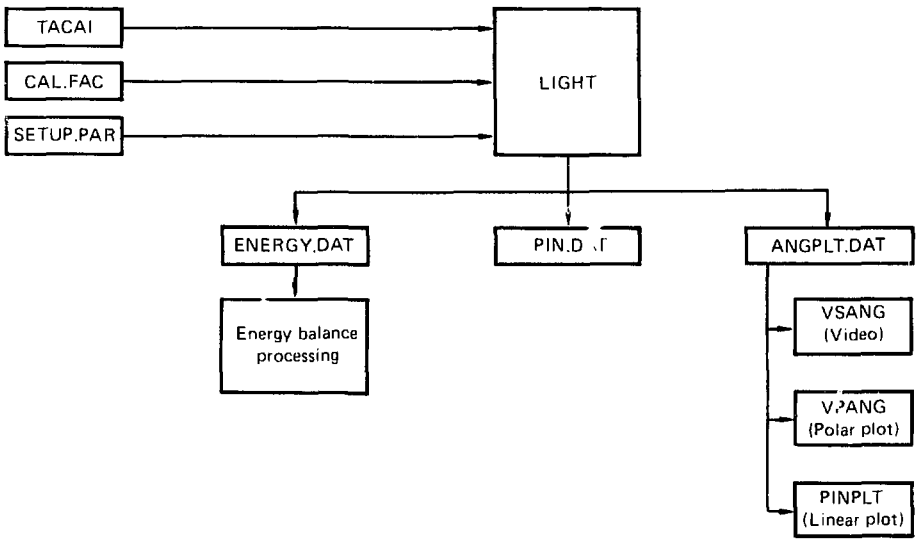

Table 5-14. Sample tabular output of subroutine PINDAT of Shiva scattered-light photodiode data automatic processing program LIGHT.

DETR	RPRIME	TRANS	R (CM)	PHI	THETA	SR	CH	POS	CR	ST	PC/VOLT	PC/CNT	ADC	ENERGY (J/SR)
020	0.10E+07	0.95	92.1	126.0	120.0	1	0	6	5	3	0.30E+05	0.37E+02	240	0.79E+02
010	0.69E+06	0.95	92.1	126.0	105.0	1	1	6	5	3	0.30E+05	0.37E+02	162	0.77E+02
034	0.12E+05	0.95	110.8	54.0	20.0	1	2	5	5	3	0.10E+05	0.12E+02	51	0.69E+02
035	0.12E+06	0.95	110.8	198.0	20.0	1	3	5	5	3	0.10E+05	0.12E+02	68	0.88E+02
033	0.12E+06	0.95	110.8	90.0	160.0	2	0	5	5	5	0.10E+05	0.12E+02	63	0.85E+02
032	0.11E+06	0.95	110.8	306.0	160.0	2	1	5	5	5	0.10E+05	0.12E+02	58	0.84E+02
031	0.12E+06	0.95	110.8	216.0	160.0	2	2	5	5	5	0.94E+04	0.11E+02	58	0.73E+02
037	0.77E+06	0.95	92.1	126.0	45.0	2	3	6	5	5	0.30E+05	0.37E+02	17	0.73E+01
017	0.12E+07	0.95	92.1	126.0	60.0	5	0	6	5	7	0.30E+05	0.37E+02	248	0.69E+02
024	0.88E+06	0.95	92.1	126.0	75.0	5	1	6	5	7	0.30E+05	0.37E+02	241	0.95E+02
030	0.12E+07	0.95	92.1	126.0	90.0	5	2	6	5	7	0.30E+05	0.37E+02	388	0.10E+03
027	0.11E+07	0.95	92.1	126.0	135.0	5	3	6	5	7	0.30E+05	0.37E+02	200	0.58E+02
028	0.11E+07	0.95	92.1	216.0	45.0	15	0	6	5	9	0.30E+05	0.37E+02	-4	-.12E+01
013	0.75E+06	0.95	92.1	216.0	60.0	15	1	6	5	9	0.30E+05	0.37E+02	137	0.60E+02
070	0.11E+07	0.95	92.1	216.0	75.0	15	2	6	5	9	0.30E+05	0.37E+02	265	0.81E+02
011	0.13E+07	0.95	92.1	216.0	90.0	15	3	6	5	9	0.30E+05	0.37E+02	354	0.91E+02
080	0.11E+07	0.95	92.1	216.0	105.0	12	0	6	5	11	0.30E+05	0.37E+02	257	0.74E+02
050	0.74E+06	0.95	92.1	216.0	120.0	12	1	6	5	11	0.30E+05	0.37E+02	124	0.55E+02
038	0.12E+06	0.95	92.1	54.0	45.0	12	2	4	5	11	0.30E+04	0.37E+01	428	0.12E+03
010	0.75E+06	0.95	92.1	54.0	60.0	12	3	6	5	11	0.30E+05	0.37E+02	171	0.75E+02
016	0.78E+06	0.95	92.1	54.0	75.0	17	0	6	5	13	0.30E+05	0.37E+02	261	0.11E+03
019	0.66E+06	0.95	92.1	54.0	90.0	17	1	6	5	13	0.30E+05	0.37E+02	285	0.14E+03
021	0.11E+07	0.95	92.1	54.0	105.0	17	2	6	5	13	0.30E+05	0.37E+02	328	0.10E+03
015	0.84E+06	0.95	92.1	54.0	120.0	17	3	6	5	13	0.30E+05	0.37E+02	229	0.89E+02
060	0.11E+07	0.95	92.1	306.0	45.0	20	0	6	5	15	0.30E+05	0.37E+02	210	0.61E+02
023	0.10E+07	0.95	92.1	306.0	60.0	20	1	6	5	15	0.30E+05	0.37E+02	241	0.78E+02
029	0.11E+07	0.95	92.1	306.0	75.0	20	2	6	5	15	0.30E+05	0.37E+02	243	0.75E+02
014	0.82E+07	0.95	92.1	306.0	90.0	20	3	6	5	15	0.30E+05	0.37E+02	178	0.71E+01
039	012.E+06	0.95	92.1	306.0	105.0	11	0	4	5	17	0.30E+04	0.37E+01	327	0.90E+02
022	0.93E+06	0.95	92.1	306.0	120.0	11	1	6	5	17	0.30E+05	0.36E+02	203	0.71E+02
040	0.11E+06	0.95	92.1	306.0	135.0	11	2	4	5	17	0.30E+04	0.37E+01	227	0.68E+02

Fig. 5-76. Flow chart of Shiva energy balance measurement (EBM) automatic data processing.

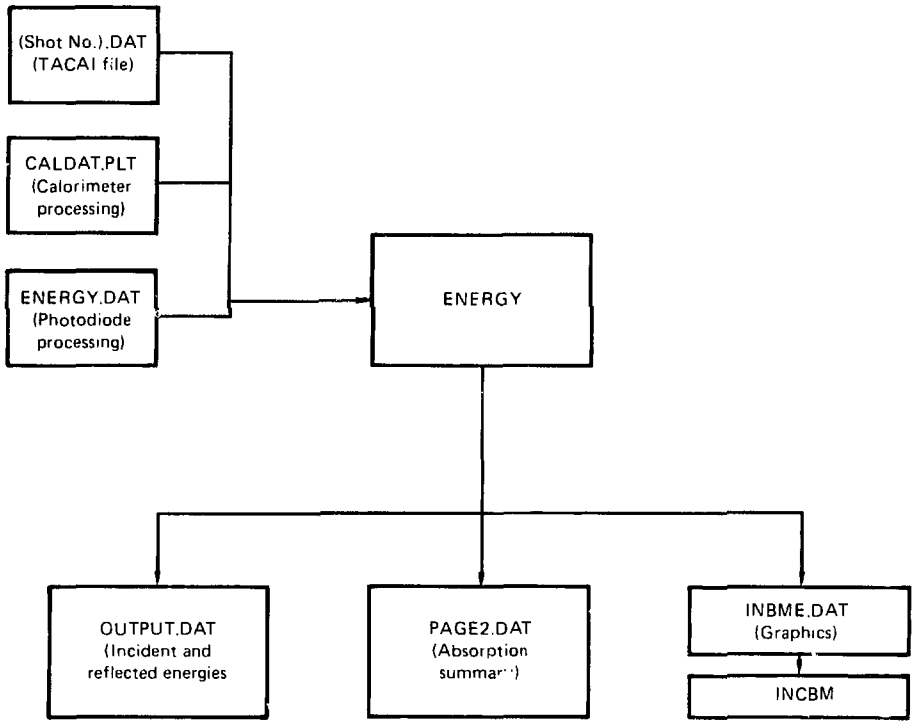

SETUP.PAR; the elements of this dimension are essentially the scaling factors necessary to scale the detector to full voltage.

Having identified the proper detector, conversion coefficients, and scaling factors, LIGHT proceeds to calculate the energy flux per count and to subtract the x-ray background. This is done by the algorithm E(Joules/count) = (R^2 R' × Transmission) times (picocoulombs/count), where R is the distance (in cm) between the target and the diode and R' is the diode sensitivity factor in terms of charge per energy flux (picocoulomb/Joule cm^2). The result of this calculation is in turn multiplied by the counts corresponding to the integrator output for each detector.

LIGHT then creates three output files:

- ENERGY.DAT, an input file to the energy balance routine.
- PIN.DAT, a hard-copy tabular file (see Table 5-14 for a sample PIN.DAT output).
- ANGPLT.DAT, an input file to the graphics routines VSANG, VPANG, and PINPLT. These routines generate, respectively, a color video polar distribution display, a hard-copy polar plot, and a hard-copy linear plot.

Author: G. S. Chinen

Automatic Diagnostic Data Processing: Energy Balance

The primary purpose of the energy summary routine ENERGY (Fig. 5-76) is to integrate the angular distributions of scattered light and plasma energy in order to obtain a relative measurement of

the laser energy absorbed by the target from the top and bottom beam clusters. ENERGY is controlled by the indirect command file EBF.CMD (on the PDP 11/70), which requires three input files:

- (Shot #).DAT, which contains the incident beam energies and the back-reflected light energies measured by Reflected Beam Diagnostics (RBDs). These latter data originate from a laser diagnostics PDP 11/34 and are appended to the end of the LASCAT data at shot time.
- ENERGY.DAT, which contains the photodiode energy fluxes and spherical coordinates (polar and azimuthal angles).
- CALDAT.PLT, which contains the plasma and light calorimeter energy fluxes and spherical coordinates, as well as the integrated total plasma energy.

ENERGY appends the back-reflected beam energies to the photodiode intensity averages and calculates energy intensity at $\theta = 0°$, where θ is the polar angle of the target chamber. The intensity at $\theta = 9.7°$ is assumed to be the same as at $\theta = 0°$, and the intensity at $\theta = 17.7°$ is extrapolated to be a straight-line fit from $\theta = 45°$ to $\theta = 20°$. This calculation is then done for the lower beams.

The output totals are appended to the light (LC-21) calorimeter intensity averages and then both the photodiode intensities (with back-reflected energies) and light calorimeter intensities (with output total energies) are sorted and integrated over the entire sphere by a straight line fit.

ENERGY then calculates

- Total output energy (in kJ).
- Total back-reflected energy (in kJ and as a percentage of the total output).
- Beam balance, i.e., the relative output energies from the upper and lower beam clusters, using the formula

$$\text{Beam}_{\text{bal}} = (E_T - E_B)/(E_T - E_B) \times 100\%,$$

where E_T is total upper output energy and E_B is total lower output energy

- The absorption percentages of the photodiodes and light and plasma calorimeters, as well as their average absorptions.
- The absorption deviations of the photodiodes and calorimeters.

Table 5-15. Representative summary of Shiva automatic energy balance diagnostics.

Incident energy		
Upper beams		**1.849 kJ**
Lower beams		**1.733 kJ**
Total energy		**3.632 kJ**
Beam balance parameter		**1.830 %**
Reflected beam outputs		
Upper	**0.070 kJ**	**3.769 %**
Lower	**0.115 kJ**	**6.462 %**
Total	**0.185 kJ**	**5.091 %**
Diagnostic outputs		
LC-21 calorimeters		**3.1680 kJ**
Photodiodes		**3.0318 kJ**
Plasma calorimeters		**0.9760 kJ**
Absorption summary		
Plasma		**26.8691 %**
LC-21 calorimeters		**12.7853 %**
Photodiodes		**16.5339 %**
Mean absorption		**18.7295 %**
Deviation from the mean		
Plasma calorimeters		**8.1397 %**
LC-21 calorimeters		**-5.9442 %**
Photodiodes		**-2.1955 %**

A sample output summary is given in Table 5-15. The absorption parameters indirectly summarize the amount of energy absorbed by the target, and provide a measurement of energy balance as indicated by the relative contribution of the various energy components.

Author: G. S. Chinen

Film Image Processing

Photographic film has long been recognized as one of the most versatile detectors for recording electromagnetic energy signals. Film produces an archivable record of the signal and is relatively immune to undesirable electromagnetic interference. Film also has a dynamic range of over 5 orders of magnitude of input energy—a range which can be further extended using different kinds of film and/or changing the development parameters—and can therefore be trusted to record signals under conditions of large uncertainty about the intensity of the input energy.

We process film images by first developing the film under highly controlled conditions, and then digitizing the density values very accurately with a

photomicrodensitometer. The resulting record or file is then read into a computer for processing. We have written several MATHSY programs[76] to manipulate our film data files and to plot the results (Figs. 5-77 to 5-82). Some of these programs are discussed below.

Film has a nonlinear response to energy, and must be calibrated so that its nonlinear density value output translates into the input energy fluence used for evaluations. We use film for three regions in the electromagnetic spectrum:

- X rays from 200 eV to >50 keV; images in this region are produced by x-ray microscopes, x-ray spectrographs, pinhole cameras, and Fresnel zone plate cameras.
- Green light (from 2ω laser light and the visible light output of x-ray streak cameras).
- 1-μm laser light (produced by laser system diagnostics).

The calibrations for each of these regions are quite different.

The calibration procedure for x-ray film uses an x-ray machine and requires many hours of exposure time and much interpretation of the data. We presently use Kodak types AA, M, R, and no-screen for x-ray detection. Of these we have a fair calibration on type M; quite a lot of work has been done on types AA and no-screen; very few reliable calibration data have been obtained for type R.[77]

There are several variables relating the exposure of x-ray film to the resulting film density, including the photon energy of the x ray, the fluence of the exposure, and the film development parameters (time, chemical strength, and chemical temperature). By keeping the development parameters constant we can produce experimental curves for converting film data to energy exposure.

To calibrate film used in the x-ray streak camera for imaging green light, we pre- or post-expose the film with a known light source and a step wedge. A plot of the digitized step wedge provides the necessary calibration curve. Since green 2ω laser light is often produced by a pulsed source, however, we derive its calibration using the same technique as that used for 1-μm light.

To derive a calibration curve for 1-μm light we use a multiple-image camera at the laser output that produces two images with known differences in intensity (~50%). These exposures are on the same film, thus eliminating the errors introduced by variations in development parameters. We then produce for each image a histogram, or plot of number of points vs film density. These plots are compared, using the known 50% intensity difference in the exposures, to produce plots of density vs energy (exposure); this is done with a MATHSY command program called CALIB2.

PDSMIES. PDSMIES is a MATHSY command file written to do the necessary unfolding of the densitometer-produced data file from an x-ray microscope film image. The density measurements are affected by

- Source, intensity, and spectral distribution.
- Filter transmission.
- Mirror reflectivity.
- Film sensitivity vs photon energy.
- Film development parameters.

Typical target spectral distributions were not well known at the time this code was written and are therefore not considered in the unfold. Spectral distribution is nonetheless certainly one of the prime parameters for consideration in improving the code.

The source intensity seen by the film is determined by target emission, reflecter-filter combinations, and microscope geometry; PDSMIES is aware of microscope geometry as a geometrical factor. Both the filter transmission and the mirror reflectivity are used by PDSMIES when it unfolds the data; values for these parameters come from the data in the L-Division Library and are stored as a file in the tape library. Parameter files are read into MATHSY program FFF, where we calculate

- The average channel energy.
- The effective energy width of the channel.
- The average channel efficiency.

These values are stored in the data file, MSPY.

Film sensitivity data are contained in PDSMIES in two forms. The original program contained a fit for M-type film; AA-type film was added later. M-type fitting is done from a set of tables generated from three parameter curves that were computer-fit to experimental data. Data for AA-type fitting is stored in a functional form, derived from a best fit to experimental curves. Film development parameters are controlled to match as nearly as is practical those used for the experimental curves.

PDSMIES produces output as shown in Fig. 5-77, in which the row and column scans are taken through the centroid of the data.

POWER. A MATHSY command file called POWER takes the density file from a streak camera

Fig. 5-77. Isodensity contours (a) of a computer-converted density scan from an x-ray microscope image, showing where row (b) and column (c) profiles are taken.

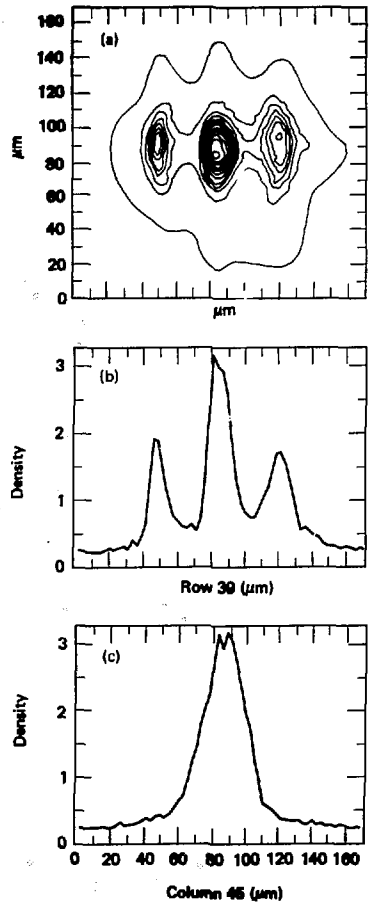

image of a laser beam and produces a plot of intensity vs time. A step wedge is also exposed onto the film; these images are developed together to control for all development parameters. From the step

Fig. 5-78. Spatially integrated streak image of the laser beam, overlaid with a Gaussian curve having equal energy. FWHM of the Gaussian is equal to that of the oscillator pulse width.

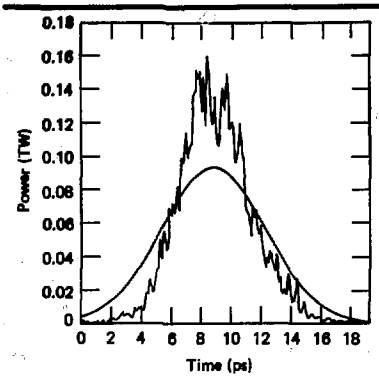

wedge we produce a d-log E curve which is used to unfold the relative exposure value from the density file produced by the densitometer reading of the streak image. This relative exposure is then integrated in the spatial direction and normalized to input energy from a laser system output calorimeter; thus we produce a curve showing power vs time (Fig. 5-78).

Having recorded the FWHM of the Gaussian laser oscillator pulse, we then overlay a Gaussian curve for comparison with the measured temporal pulse. In this way we can easily evaluate the temporal change in a pulse that passes down a chain of amplifiers.

EXTRACT. There is always a compromise in computer reduction of film data; if the densitometer sample size is too small the number of samples in the file becomes large, and data processing efficiency deteriorates. On the other hand, if the sample size is too large, thus keeping the file small, the data statistics suffer. To minimize errors and maximize speed, we have written the program EXTRACT, which allows us to display any part or all of the processed data. With this capability we can choose a section of the file, write it into an output file created by EXTRACT, and then trim and average the output file to the optimum size for both maximum processing efficiency and minimum statistical distortion. The output binary file created

Fig. 5-79. Isointensity contour of the laser beam characterization, converted by FOCUSED from the measured density scan.

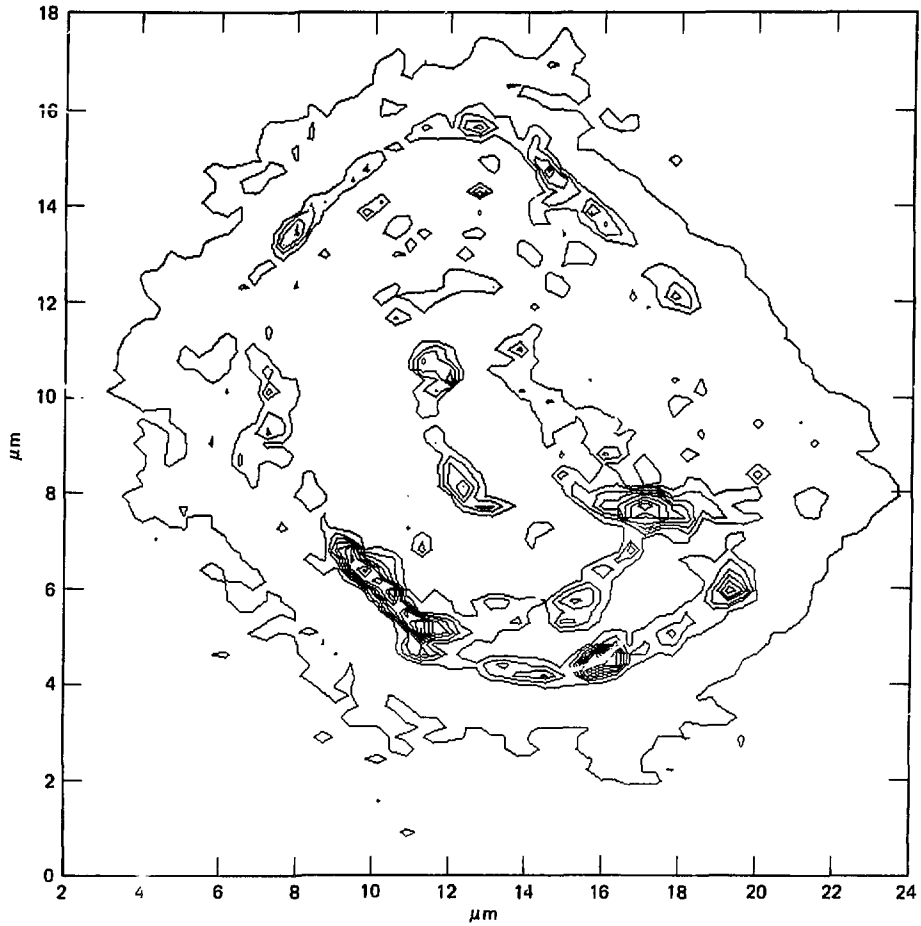

by EXTRACT can also be read by any of our other film image processing routines.

AUTOEX. The data file that characterizes our x-ray microscope consists of an array of point sources projected through the microscope; we use the file to determine the resolution of the microscope as well as the distortion in its field of view.[78] The file is so large, however, that the computer memory cannot contain it and do processing on it at the same time; we must therefore read in and process small sections of the file one at a time. AUTOEX is a MATHSY code that was written to process a very large file in an automatic mode, but which also has a manual mode enabling us to see the data as it is processed.

The first problem to be solved by AUTOEX is locating the point source near the center of the array, to be defined as the starting point for the automatic processing. This is done with a pattern-search algorithm that looks for three points located within a total maximum spacing differential; the points are located using a routine that finds the centroid of the small file, based on the density values

Fig. 5-80. Laser beam radial power profile, showing power radius normalized with energy as read from the calorimeter.

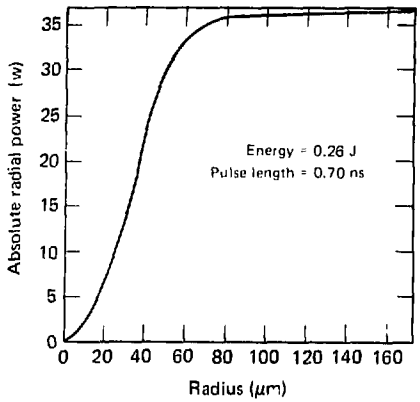

about the 50% of maximum value of that small file.

The output file created by AUTOEX consists of the following listing derived for each point:

- Background, found by averaging the intensity value found in the corners of the small file.
- Peak value of the signal with noise removed.
- X-position in row number and micrometers, as found by the centroid routine.
- Y-position in column number and in micrometers.
- The FWHM value of a row taken through the centroid.
- The FWHM of the column through the centroid.
- The diameter of the radial average of the intensity about the centroid taken at the half maximum value.

Fig. 5-81. Three-dimensional plot of the laser beam profile.

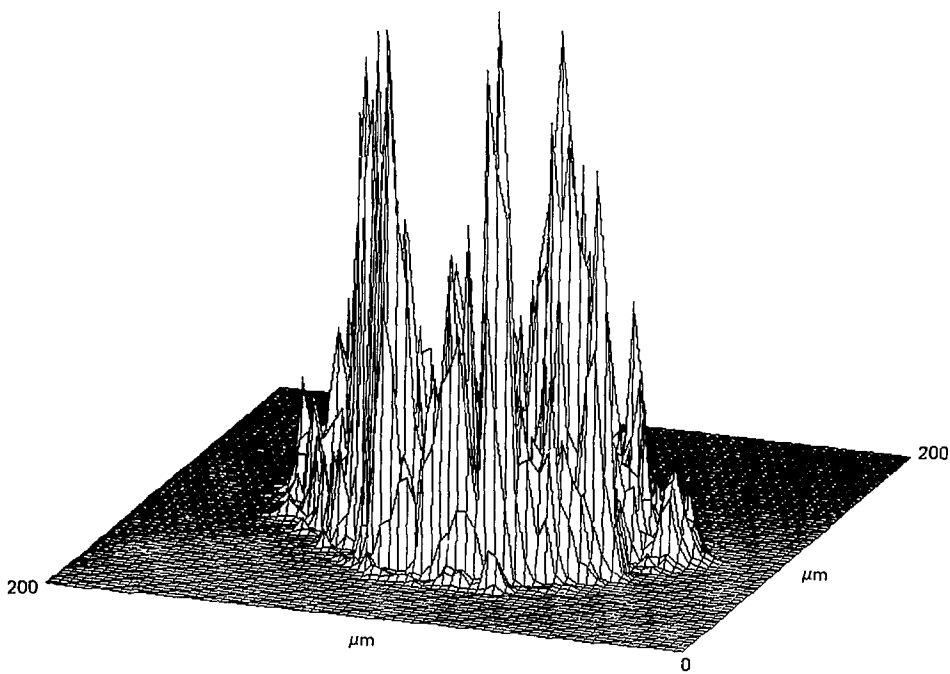

Fig. 5-82. Intensity histogram, showing the number of samples at a given intensity vs the intensity of the samples.

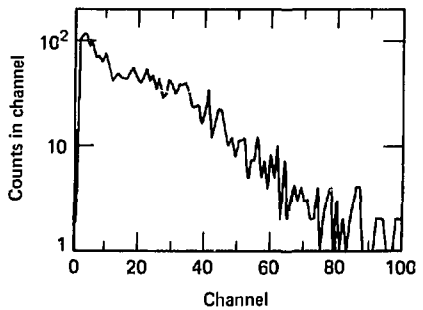

We compare the position of these points at different places in the array to look for field distortions; by comparing widths and diameters we can see the spatial resolution of the x-ray microscope.

FOCUSED. FOCUSED was written to do beam analysis. CALIB2 is used to create a calibration file; FOCUSED then employs the file to convert the density data into intensity values and present a display of the calibrated data with isointensity lines (Fig. 5-79). Superimposed on this display is a series of concentric circles; if the image appears to be more elliptical, the circles can be changed to ellipses. These circles or ellipses are then used to calculate a radial average of the beam intensity. By integrating and normalizing with the known input energy we can calculate and plot the radial power profile of the beam as in Fig. 5-80.

We can delete bad spots in the data with FOCUSED by using the command CEN to center about the point to be operated on. The command AVOUT will then remove the values from the area inside the inner diameter and fill it in with the average value of the data contained between the inner and outer diameters.

FOCUSED also allows us to

- Look at either a single data row or column, or at the average of several rows or columns from any place in the array.
- Do a three-dimensional display (Fig. 5-81).
- Do an intensity histogram (Fig. 5-82) which displays the number of data points contained in each channel of energy vs the energy of that channel.

Author: K. J. Pettipiece

References

76. *Laser Program Annual Report—1976*, Lawrence Livermore Laboratory, Livermore, Calif., UCRL-50021-76 (1977), pp. 2-359 to 2-364, 3-136.
77. T. L. Harper, *Kodak M X-Ray Film Calibration Calculations used for Microscope Data Analysis*, UOPB-76-73, May 1976. J. P. Stoering and A. Toor, *X-Ray Calibration of Kodak No-Screen, Type AA, and Type M in the 1-4.5 keV Region*, UCID-16775, May 8, 1975. A. Toor, *A Physical Model for X-Ray Film Sensitivities*, XRM-79-143, Sept. 20, 1979.
78. *Laser Program Annual Report—1978*, Lawrence Livermore Laboratory, Livermore, Calif., UCRL-50021-78 (1979), pp. 6-27 to 6-29.

CCD Array Processing

In laser fusion experiments, target and laser parameters are measured using various cameras, including oscilloscope cameras, ultrafast streak cameras, and x-ray microscope cameras. Film has been the usual recording medium, but as more instruments are added to diagnose target experiments, the need for automatic digital readout becomes essential. Transient digitizers such as the Tektronix R7912 have replaced some oscilloscopes, aiding our efforts to implement digital readout of both streak camera images and oscilloscope traces. We have successfully obtained a direct readout of streak camera images using a CCD (charge coupled device) array camera, which bypasses film retrieval, development, scanning with a microdensitometer, and data correction for film response. The hardware description for the CCD streak camera is given earlier in this section, and in last year's annual report[79]; this article covers CCD image processing and our plan to handle all image processing in a unified manner.

Because we anticipated that a number of these CCD array cameras would be installed at the Shiva facility, we have undertaken to acquire the images from all the CCD cameras through one system, using Shiva's existing computer architecture.[80] Our solution is to attach the CCD memories to the bus implemented under Shiva's power conditioning system[81]:

- Data are accessed through an LSI and a four-port memory from either the PDP 11/34 or PDP 11/70.

Fig. 5-83. SXRSC data from a Shiva shot. Color contours of intensities are overlayed with temporal distribution from a channel.

- Data are transferred from the CCD memory in either column or row mode; normally, 160 K-bytes of data are transferred in approximately 30 s.
- Data can be manipulated in the PDP 11/70; the data format is given in Table 5-16.

We presently operate CCD camera and memory systems on output-beam-diagnostic optical streak cameras and on a target-diagnostic soft x-ray streak camera (SXRSC)[82]; we discuss processing for the SXRSC in this article.

Initial quick-look processing of SXRSC data is performed on the streak image immediately after the shot, using the Shiva PDP 11/70. The image is displayed on a color monitor, with intensity values converted to color contours. Lineouts in one spatial direction can be obtained to display the temporal profile of the x-ray distribution. These can be superimposed on the color-enhanced distribution or drawn by the Versatec printer/plotter (Fig. 5-83).

The final unfolding of the data is performed through Octopus on the LLL central computer system. The image data are converted into an 8-bit

Table 5-16. CCD memory data format (160 K-bytes of image).

Byte offsets		
Decimal	Octal	Contents
1	1	Last shotnumber (ASC II)
9	11	ASC II time of day (HH:MM:SS)
17	21	Taskname of task generating the file
19	23	(RAD50)
21		Mode: 1 = continous, 0 = TV
23		Number of records written (binary)
25		Error status of return (binary)
27		Memory number (0-99)
29		
*		
*		
*		
1024		

ASCII file and written on magnetic tape as a PDP 11/70 RSX-11/M file. An interface program is then run on the Octopus system to decode the tape into a standard Octopus 6-bit ASCII file. The analysis program, SXRSCX, is written in MATHS[83]. SXRSCX obtains lineouts for each energy channel, and then folds the temporal profiles with responses for each channel to obtain x-ray flux as a function of time. Integration of this distribution gives the total flux.

Streak camera data still recorded on film and digitized are analyzed with a program called ATTWOOD. ATTWOOD is identical to SXRSCX except for the input routines and the fact that the CCD image no longer needs to be corrected for the many nonlinear effects which complicate the analysis of film images.

The ultimate goal is to obtain all target diagnostic data, including images, in computer-compatible digital form. In the meantime, since some film images and oscilloscope traces will need to be digitized after intermediate development steps, the interim goal is to integrate all digitized data in a comprehensive analysis package. Progress was made toward both goals by implementing the CCD camera and its software on the Shiva SXRSC, and by using existing film data processing programs for data analysis.

Author: J. T. Ozawa

References

79. *Laser Program Annual Report—1978*, Lawrence Livermore Laboratory, Livermore, Calif., UCRL-50021-78 (1979), pp. 6-54 to 6-59.
80. *Laser Program Annual Report—1978*, Lawrence Livermore Laboratory, Livermore, Calif., UCRL-50021-78 (1979), pp. 2-45 to 2-54.
81. *Laser Program Annual Report—1977*, Lawrence Livermore Laboratory, Livermore, Calif., UCRL-50021-77 (1978), pp. 2-41 to 2-47.
82. *Laser Program Annual Report—1978*, Lawrence Livermore Laboratory, Livermore, Calif., UCRL-50021-78 (1979), pp. 6-2 to 6-5.
83. *Laser Program Annual Report—1976*, Lawrence Livermore Laboratory, Livermore, Calif., UCRL-50021-76 (1977), pp. 2-359 to 2-364.

Target Alignment Codes

With the advent of the Shiva laser system, we have been challenged with the problem of aligning *many laser beams to achieve specified illumination* patterns on microscopic targets. Solved manually, the problem requires hours of drawing complicated graphs of targets and beam cones, as well as tedious computing of the results using diffraction theory; checking several alignment schemes manually would become prohibitively costly in terms of the manpower required. The need for an efficient alternative provided the motivation for the target alignment codes described in this article. The codes can be divided into two categories:

- Those which produce beam position information.
- Those which produce the intensity distribution on a given target as a result of a preselected beam alignment and power scheme.

All of the codes are based on relationships between the target and focusing-lens coordinate systems diagrammed in Fig. 5-84. Normally the origin of the target coordinate system is at the center of the chamber. Positive X is directed along the target positioner, with Z pointing up. Each focusing lens coordinate system is defined by the axis along which the focus moves towards or away from chamber center; the origin of each lens coordinate system is the chamber center. As shown in the figure, the Z_i axis is defined by two spherical angles, θ_i and ϕ_i.

For the i^{th} lens system, the z coordinate Z_i lies outwards along the beam axis. The lens can be offset in two perpendicular directions from the Z_i axis; these are the X_i and Y_i coordinate axes. Positive Y_i points towards the nearest pole of the

Fig. 5-84. Target and lens coordinate systems used by the Shiva target alignment codes.

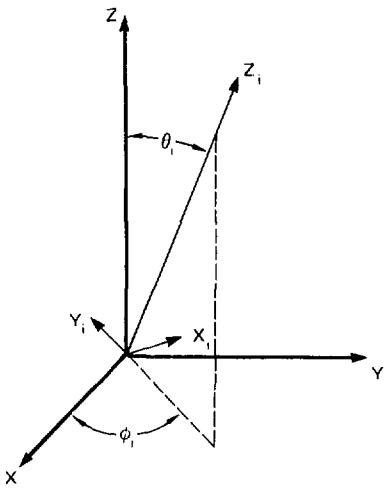

chamber, while positive X_i is such as to form a right-handed system with Y_i and Z_i.

The target and lens coordinates are related by a transformation matrix T_i, the elements of which are given in Table 5-17, along with the 20 values of θ_i and the 20 values of ϕ_i for the Shiva illumination system. All the beam-position and intensity calculations involve the use of this transformation matrix.

ALIGN and GEOBM. Most Shiva alignments are done under conditions of no tangential offset ($X_i = 0$) and the same Y_i and Z_i values for all beams in a cluster. In this case one has to work with only two (an inner beam and an outer beam) of the ten beams in a cluster. For this situation, we have developed a simple computer code named ALIGN. *Given a set of lens offsets* (Y_i, Z_i), *and either a* spherical target or a disk target of specified diameter and tilt angle, ALIGN

- Draws a graph showing the cones of an inner and outer beam positioned on the target.
- Allows one to rapidly change the lens coordinates (presets).
- Can position beams on an arbitrarily tilted disk so that all energy is incident on the target.

Table 5-17. Transformation matrix T_i, and Shiva illumination coordinates.

$$T_i = \begin{vmatrix} -\sin\phi_i & \cos\phi_i & 0 \\ -\cos\theta_i\cos\phi_i & -\cos\theta_i\sin\phi_i & \sin\theta_i \\ \sin\theta_i\cos\phi_i & \sin\theta_i\sin\phi_i & \cos\theta_i \end{vmatrix}$$

Beam, i	Azimuthal angle, ϕ_i	Polar angle, θ_i
1	234	170.303
2	270	162.264
3	306	170.303
4	342	162.264
5	18	170.303
6	54	162.264
7	90	170.303
8	126	162.264
9	162	170.303
10	108	162.264
11	54	9.697
12	90	17.736
13	126	9.697
14	162	17.736
15	198	9.697
16	234	17.736
17	270	9.697
18	306	17.736
19	342	9.697
20	18	17.736

Fig. 5-85. Sample Versatec printer output from ALIGN, showing the parameter for tangential focusing on a sphere.

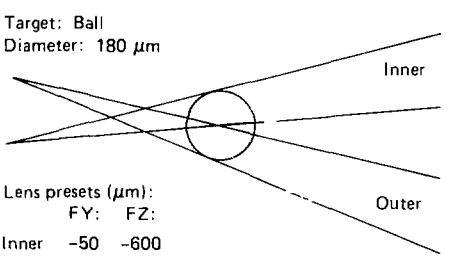

- Draws various diagrams showing, for example, when the beam cones are positioned so that the outer ray of each cone is tangential to the surface of the sphere; Fig. 5-85 is a sample diagram for the case of such "tangential focusing."

● Computes the displacement of the center of each beam axis from target center and the beam diameter at the target central plane, expressed as fractions of the target diameter. These data are useful for alignment verification and are displayed on each alignment diagram, as illustrated in Fig. 5-85.

The second computer code which produces beam positioning information is named GEOBM. GEOBM has two independent routines: GEOSPH, which gives data for alignments on a spherical target, and GEOPLN, which gives data for alignments on a planar target. The computational method for GEOPLN is explained here in detail; GEOSPH uses very similar methods.

The GEOPLN user specifies both the lens presets (x_i, y_i, z_i) for the 10 beams in one of the Shiva clusters and the diameter, tilt angles, and vertical displacement of a planar target in the target coordinate system whose origin lies at the chamber center. Tilts can be specified as an angle of rotation about the stalk and a tilt angle about an axis perpendicular to the stalk. The disk target is then subdivided into a polar grid with a maximum azimuthal resolution of 2° and a maximum radial resolution of 1/45 of the radius. For GEOSPH, spherical coordinate mesh is set up. The maximum azimuthal resolution and the maximum polar angle resolution are both 2°.

On polar grids having radial lines every 20° and circles of equal radii at intervals of 1/10 of the target radius, GEOPLN draws diagrams showing the intersection of the geometric optic cone of each beam with the planar surface. These intersections are calculated according to the following procedure.

Each point on the disc (x_t, y_t, z_t) is transformed into the coordinate system of the i^{th} lens; any point X_t may lie out of the X-Y plane of the target coordinate system (see Fig. 5-84) as a result of specified tilts or displacements.

The corresponding lens coordinates X_i are given by

$$\vec{X}_i = T_i \vec{X}_t \ . \tag{6}$$

If we let $\vec{F}_i$ be the focus of i^{th} lens, then relative to this focus the point $\vec{X}_i$ has the coordinates

$$\vec{X}_i = \vec{X}_i - \vec{F}_i \ . \tag{7}$$

Fig. 5-86. Diagram showing the basis of the GEOPLN calculation for finding the intersection of a beam cone with a planar surface.

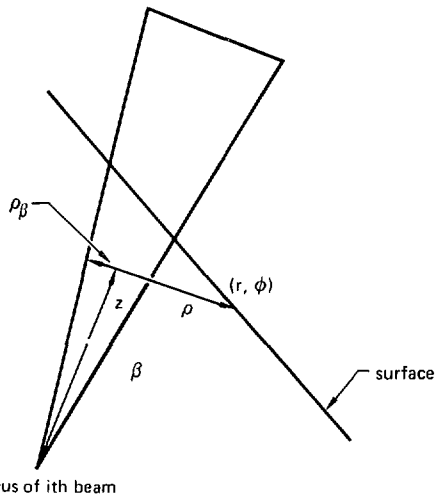

$\vec{X}_i$ is next expressed in terms of polar coordinates (ρ, z), where

$$\rho = \sqrt{X_i^2 + Y_i^2} \tag{8}$$

and $z = z_i$.

At this point, the code determines whether or not the point $\vec{X}_i$ is intercepted by the i^{th} beam cone. The radius of the cone corresponding to the distance z is given by

$$\rho_\beta = |Z| \tan_\beta \ , \tag{9}$$

where β is the lens half-angle for the i^{th} beam. Then the point $\vec{X}_i$ is on the cone if

$$\rho = \rho_\beta \ . \tag{10}$$

A diagram showing the conditions expressed by the above equations is given in Fig. 5-86.

Fig. 5-87. Sample GEOPLN output showing the intersection of 10 Shiva beams with a disk tilted 30°.

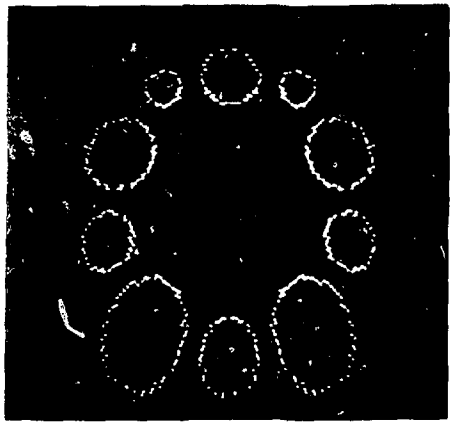

Fig. 5-88. Sample GEOSPH output showing the intersection of 10 tangentially focused Shiva beams with a 180-μm-diameter hemisphere.

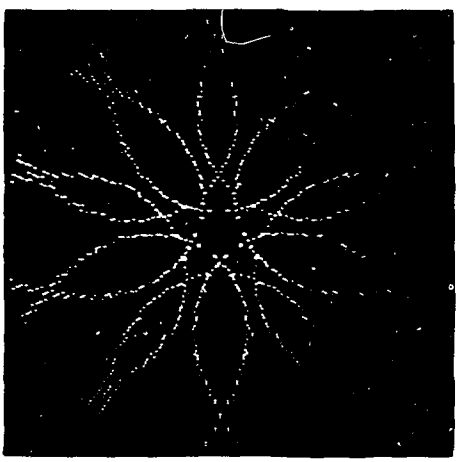

After determining all points of the polar mesh which intercept any of the 10 beam-cones in a cluster, GEOPLN draws beam-position polar diagrams (Figs. 5-87 and 5-88). Figure 5-87 shows a GEOPLN output for beams positioned on a disk tilted 30°. Figure 5-88, a sample GEOSPH output, shows a plot for 10 beams tangentially aligned to a sphere. Recall that this is a polar plot of a hemisphere:

- The radial coordinate corresponds to the spherical angle θ.
- The azimuthal coordinate corresponds to the spherical angle ϕ.
- Circles of constant theta are separated by 10°.
- Radial lines on the grid are separated by 20°.

Using GEOBM, the user can rapidly select several sets of lens presets and view the resulting beam positions on target until the desired alignment is obtained.

LITAR, PLANAR, and NOVAL. The next set of codes to be described produces more than beam position information; these codes calculate and display the incident and absorbed intensity distribution for preselected target type, lens presets, and power in each beam. The three codes and their functions are

- LITAR, which computes the incident and absorbed intensity distributions on a hemisphere irradiated by a Shiva beam cluster.
- PLANAR, which computes the incident and absorbed intensity distributions on a plane irradiated by a Shiva beam cluster.
- NOVAL, which computes the incident and absorbed intensity distribution on a hemisphere irradiated by both proposed beam clusters on the Nova laser system. This code allows the user to specify the lens axis angles θ_i, Φ_i and thus evaluate various proposed beam geometries.

Each code divides a hemisphere or disk of user-specified diameter into a spherical or polar grid, respectively. The grid can have a maximum of 2700 points. For each point the codes calculate its distance from the focus of the i^{th} lens, using Eqs. (6) through (8) above. To calculate the intensity at that grid point, the code provides a model of the beam profile using a series of Gauss-Laguerre polynomials $\Psi_i(\rho, Z)$, where ρ is defined as in Eq. (8) and $z = Z_i$.

Fig. 5-89. (a) Sample PLANAR output showing the incident intensity distribution on a disk tilted 30°; (b) absorbed intensity distribution of (a) based on a resonance absorption model.

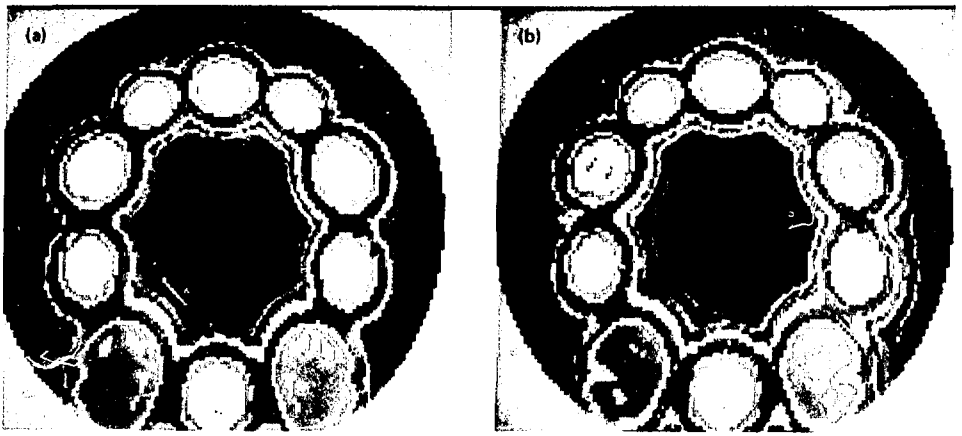

White:	1.5×10^{16} W/cm^2	White:	4.6×10^{15} W/cm^2
Pink:	7.5×10^{15} W/cm^2	Pink:	1.5×10^{14} W/cm^2
Yellow:	3.8×10^{15} W/cm^2	Yellow:	2.5×10^{15} W/cm^2
Orange:	1.9×10^{15} W/cm^2	Orange:	5.75×10^{14} W/cm^2
Red:	9.5×10^{14} W/cm^2	Red:	2.89×10^{14} W/cm^2
Brown:	4.8×10^{14} W/cm^2	Brown:	1.45×10^{14} W/cm^2

The user specifies the power P_i in each beam. The function Ψ is normalized so that at any value of Z,

$$P_j = 2\pi \int_0^\infty |\Psi_i(\rho,Z)|^2 \rho d\rho \ . \qquad (11)$$

The function $\Psi_i(\rho,Z)$ is also parameterized by the beam waist size at focus, W_0; for example the Shiva f/6 lenses focus spatially filtered 1.06-μm beams to an effective waist size of 12 μm.

At each grid point the angle between the surface normal and the local beam direction is computed. The incident intensity at the N^{th} grid point is computed as follows:

$$I_n = \sum_{i=1}^{N} |\Psi_i(\rho,Z)|^2 \cos\phi_i \ , \qquad (12)$$

where ϕ_i is the angle of incidence.

The codes also calculate total incident and absorbed power using the formulas

$$P_{inc} = \sum_{j=1}^{M} I_n \Delta A_n \qquad (13)$$

and

$$P_{abs} = \sum_{j=1}^{M} \alpha_n I_n A_n, \qquad (14)$$

where ΔA_n is the area increment for the N^{th} grid increment and α_n is the absorption fraction based on either a resonance absorption or inverse bremsstrahlung model.

The codes calculate and produce incident and absorbed intensity distributions, in either tabular or graphic form; graphic outputs can be either symbolic contour plots from a Versatec printer or a color-coded intensity plot produced on a color TV monitor. Examples of the latter are shown for PLANAR (Fig. 5-89), LITAR (Fig. 5-90), and NOVAI (Fig. 5-91).

Fig. 5-90. (a) Sample LITAR output showing the incident intensity distribution on a hemisphere on which the Shiva beams are tangentially focused; (b) absorbed intensity distribution of (a) based on a resonance absorption model.

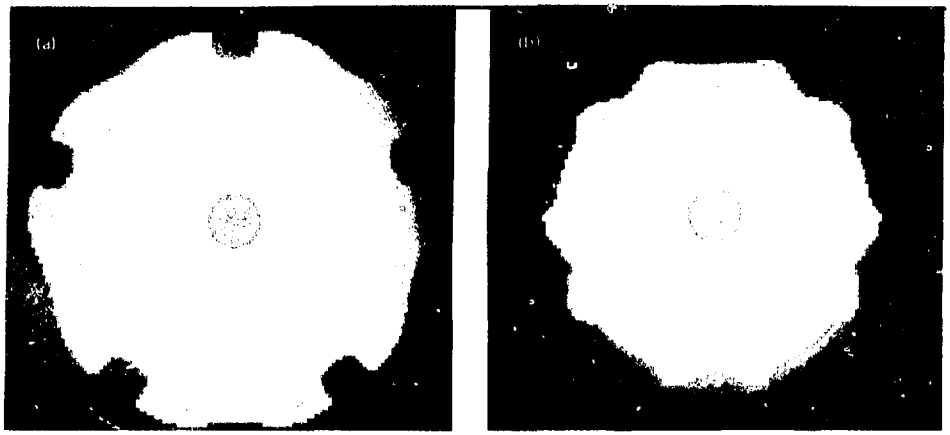

White:	2.1×10^{16} W/cm^2	White:	6.6×10^{15} W/cm^2
Yellow:	1.05×10^{16} W/cm^2	Yellow:	3.3×10^{15} W/cm^2
Orange:	5.2×10^{15} W/cm^2	Orange:	1.6×10^{15} W/cm^2
Red:	2.6×10^{15} W/cm^2	Red:	8.2×10^{14} W/cm^2

The intensity plot generated by PLANAR is in polar coordinate form. For PLANAR outputs, the outer radius of a plot corresponds to the outer radius of the target. For LITAR and NOVAI, the plot is a representation of a hemisphere in polar coordinates. The radial coordinate corresponds to the polar angle ϕ. The center of the circle is the pole ($\theta = 0°$ or $\theta = 180°$) and the outer radius is the equator ($\theta = 90°$); other values of θ are found by linear interpolation between the two. The azimuthal spherical angle ϕ corresponds one to one with the angular coordinate around the circle. The $\theta = 0°$ radial is the line at the three o'clock position on the plots that follow. Correspondence between colors and the intensities they represent appear with the plots.

Figures 5-89(a) and (b) present color-coded intensity plots for a PLANAR calculation; (a) shows the incident intensity distribution, and (b) shows the absorbed intensity distribution based on resonance absorption. The lens presets correspond to the beam positions shown in Fig. 5-87. Each of the 10 beams in the Shiva cluster is given an output power of 0.5 TW. The effect of the disk tilt on the intensity distribution is very evident. Of the total power (5 TW) incident on the disk, 26% was absorbed.

Figures 5-90(a) and (b) are the incident and absorbed intensity distributions for the "tangential focusing" alignment on a 180-μm-diam hemisphere previously described in Figs. 5-85 and 5-88. Note the rapid decrease in intensity from pole to equator. This is a consequence of the high angle of incidence between the beam and the target normal in the equatorial regions. Of the 10 TW incident, 99% intercepted the target. The calculated absorption fraction using a resonance absorption model was 33%.

Figures 5-91(a) and (b) present results from the recently developed alignment code NOVAI. Shown are the calculated incident and absorbed intensity distributions for a Nova Phase I irradiation geometry on a 2000-μm-diam sphere. In the Nova Phase I configuration there are five f/4 lenses with beam axis angles of $\theta_i = 55°$ and Φ_i = a multiple of 72°. The resulting large beam-cone angles allow a more uniform illumination than with Shiva, as a comparison of Figs. 5-90(a) and 5-91(a) shows. Figure 5-91(b) shows an absorbed intensity dis-

Fig. 5-91. (a) Sample NOVA1 output showing the incident intensity distribution upon a 2000-μm-diameter hemisphere irradiated by a cluster of Nova beams. (b) Absorbed intensity distribution of (a) based on an inverse bremsstrahlung model.

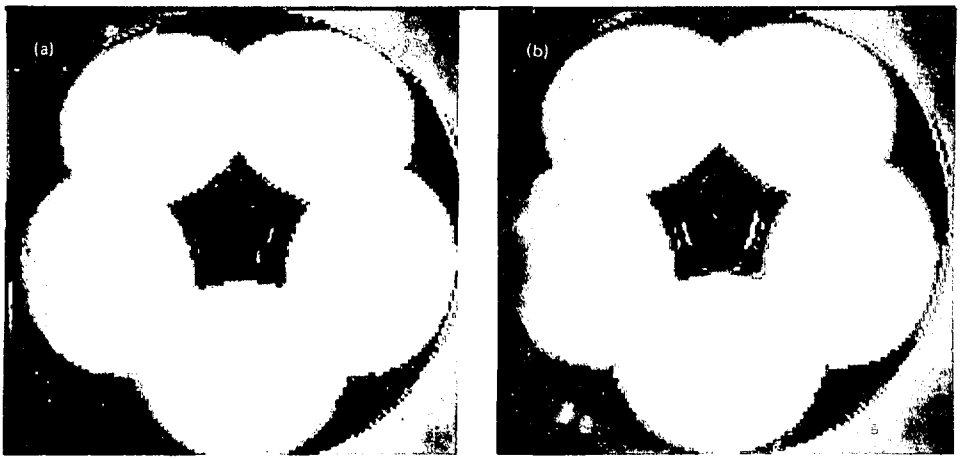

White:	1.15×10^{15} W/cm^2
Yellow:	5.8×10^{14} W/cm^2
Orange:	2.9×10^{14} W/cm^2
Pink:	1.45×10^{14} W/cm^2
Red:	7.2×10^{13} W/cm^2

White:	8.4×10^{14} W/cm^2
Yellow:	4.2×10^{14} W/cm^2
Orange:	5.25×10^{13} W/cm^2
Pink:	1.05×10^{14} W/cm^2
Red:	2.6×10^{13} W/cm^2
Tan:	2.1×10^{14} W/cm^2

tribution; of the 50 TW which irradiated the hemisphere, 78% was absorbed based on an inverse bremsstrahlung calculation.

In the past year the ALIGN, GEOBM, LITAR, and PLANAR codes have become indispensable tools both for determining proper lens positions and for saving many hours of experimenters' time.

Author: J. M. Auerbach
Major Contributors: F. O. Feiock and K. R. Manes

Fusion Experiments Data Analysis Facility

As more diagnostics have been added to the Shiva and Argus laser facilities, the volume and complexity of the data collected have increased rapidly. During the past year we reviewed the procedures and techniques used to analyze the target and laser diagnostic data, identifying areas where improvement was possible. At the same time we were concerned with integrating any planned improvements into future needs arising from the Nova facility now under construction.

We concluded that the most efficient way to handle and analyze our target and laser diagnostic data was to

- Concentrate in one location the analysis resources and facilities currently scattered throughout the laboratory site.
- Ensure that the personnel responsible for data analysis should have easy access to such a centralized facility.

To achieve our goals, we plan to set up a data analysis facility (Fig. 5-92), the center of which will be a DEC VAX 11/780 computer system; this system is compatible with the existing Shiva and Nova DEC computers, thus permitting transfer of existing software without modifications. Delivery and operation are scheduled for the third quarter of fiscal 1980. One of the major tasks this facility will

Fig. 5-92. Schematic of the planned Fusion Experiments analysis facility.

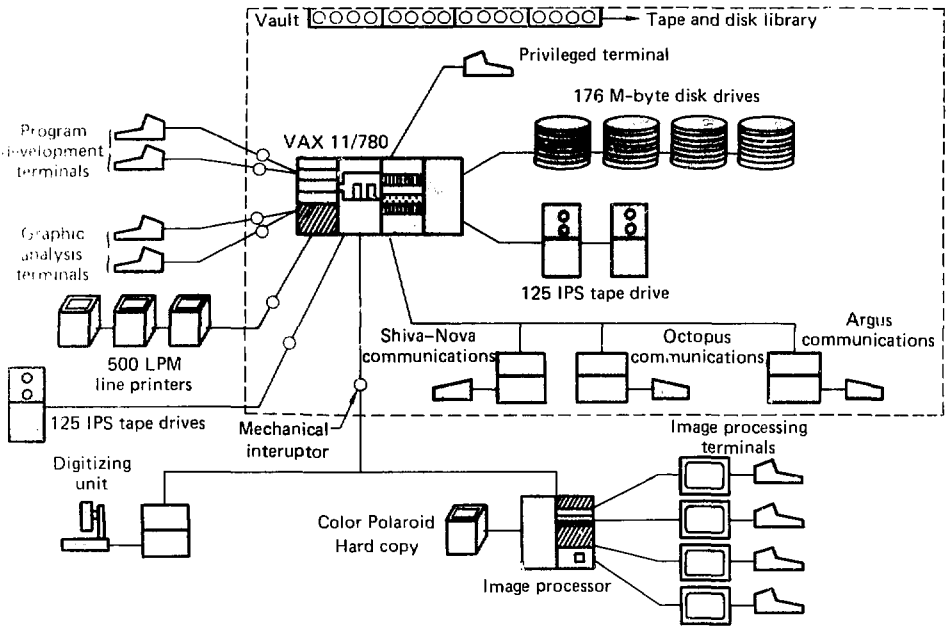

support is digital image processing. The image processing system will be used to analyze all two-dimensional data, in particular x-ray and streak camera data, and will be equipped with a directly linked digitizing unit for rapid digitizing of film data. In addition to standard contour and lineout capabilities, the system will have color display and color hard copy capabilities.

Once this analysis facility is operational, it will vastly improve the efficiency and increase the volume of data processing and analysis, by

- Increasing the capacity and throughput for analyzing most of our data and results from the Shiva and Argus facilities.
- Permitting the operation of Nova as an unclassified facility except during the brief periods when classified targets are shot (this is the current practice at Argus and Shiva); this will reduce operation costs and enable us to maintain an open facility.
- Improving analysis capability and reducing the effort and time required to process x-ray imaging and streak camera data.
- Reducing the load on the overtaxed Shiva PDP 11/70 control and analysis computer. Most of the analysis codes now at Shiva will be moved to the new facility, which will provide the needed additional capacity to handle various operational codes for Shiva.
- Linking the Fusion Experiments data analysis effort with Octopus (the laboratory central computer system) whenever greater computational capacity is required. This link (via Octoport) will make the computer facility part of the Octopus Far Support Network.

During the first six months of operations, raw target and laser diagnostic data will be hand-carried to the analysis facility on magnetic tape. Later a

Fig. 5-93. Schematic of the planned communication network for laser fusion data transfer.

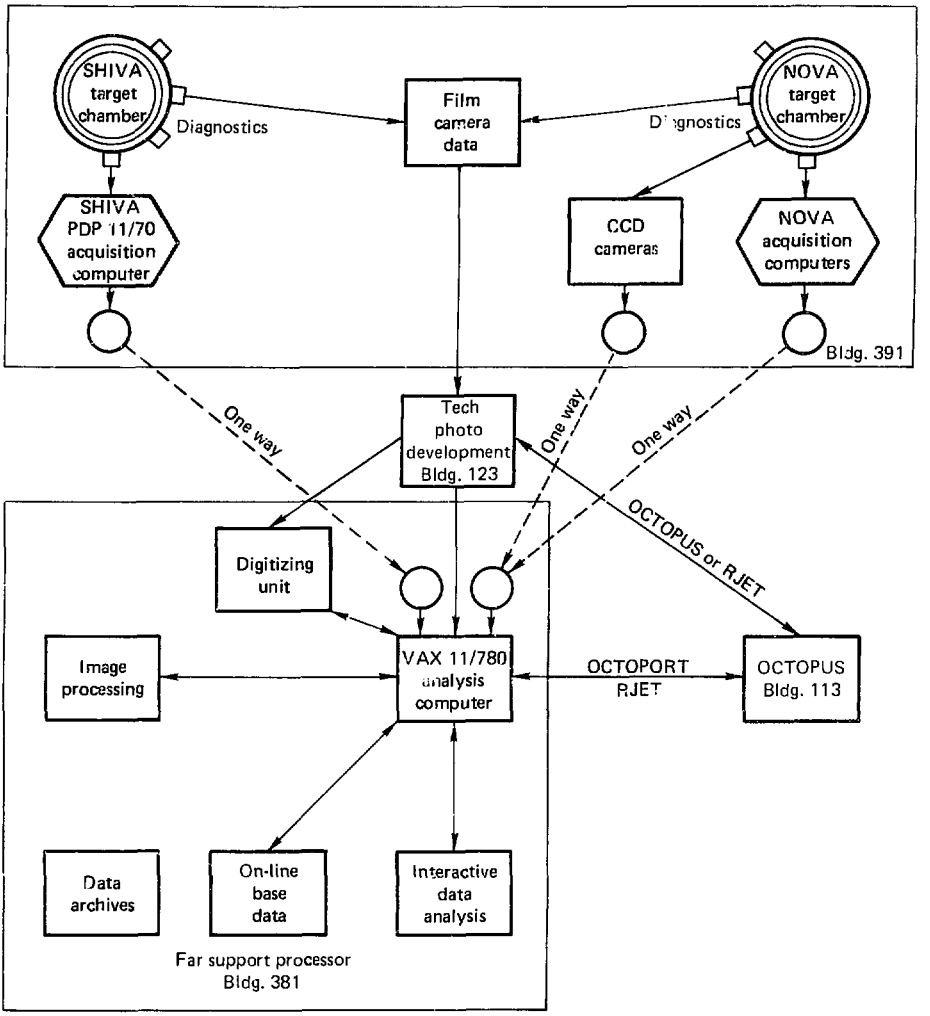

one-way fiber optics communications link will be established to carry data from Shiva directly to the analysis computer. Figure 5-93 shows a diagram of the planned communication network.

It is envisioned that in its initial stage this system will support approximately 25 interactive users performing data reduction and analysis in the fusion experiments area.

Author: J. E. Vernazza

Laser Fusion Experiments and Analysis 6

Contents

Laser Fusion Experiments and Analysis 6

Introduction

The primary goal of our laser fusion program is to demonstrate the feasibility of inertial confinement fusion. In conception, planning, and execution we have found it useful to group our calculations, experiments, and analyses into six catagories:

- Absorption and scattering experiments, designed and conducted primarily to measure and characterize the amount of incident laser energy absorbed by the target, and the fraction, angular distribution, and other characteristics of laser radiation reflected and scattered by the target plasma.
- Plasma conditions experiments, performed to determine the density and temperature distributions of the plasma in laser interaction and ablation regions.
- Shell dynamics experiments on accelerated slabs and cylindrical and spherical shells, to measure the dynamics, symmetry, and stability of their motion.
- High-density implosion experiments, conducted for the express purpose of achieving and diagnosing high-density fuel conditions.
- Drive and preheat analysis, to explore the preheat of shells and fuel and the transport of energy in the capsule that produces the pressure driving the implosion.
- Diagnostics development, to develop and implement instruments and data-acquisition systems appropriate to the experimental efforts outlined above.

Our experimental program for the first five areas is discussed in this section; the sixth category is discussed in Section 5 of this report.

Generally, one of the above categories represents the primary goal of planned experimental sequences, although in almost all cases data are obtained in one or more of the other categories as well. This structuring of objectives helps us balance and prioritize our program.

Disk experiments have extended our data base and understanding of absorption to include the effects of pulse lengths of 2 ns at 1.06 μm, and we have begun to obtain data at 600 ps and 0.53 μm. Long pulse lengths (0.5 to 10 ns) appropriate to the achievement of high-density fuel conditions produce long gain regions for stimulated Brillouin and Raman scattering; we continue to study these phenomena so that our target designs minimize their deleterious effects.

Implosion experiments performed on several target types have achieved fuel densities ranging from 10× liquid-density D-T to nearly 100×. Figure 6-1 shows high-energy x-ray images from a target which achieved 10× liquid D-T density. Density was measured using pusher activation, by diagnosing x rays emitted by seed argon in the fuel, and by the 6.5-keV-continuum x-ray image. The suprathermal (16.5 keV) image shows nonuniform heating of the pusher by the suprathermal electrons. Advances in our understanding of suprathermal electrons, including particularly the confirmation of the conjecture that they may be temporally delayed with respect to the laser pulse, have made possible significant improvements in our ability to model high-density experiments.

Energy transport has been studied in disk targets with Z varying from Be to U, and with CH- and Al-layered targets. LASNEX calculations require both inhibited-transport and non-LTE physics to reproduce the experimental observation on these absorption and transport disk experiments.

The categories of plasma conditions and shell dynamics will receive more emphasis in the future, as diagnostics technology enables us to gather more and better target data. Until

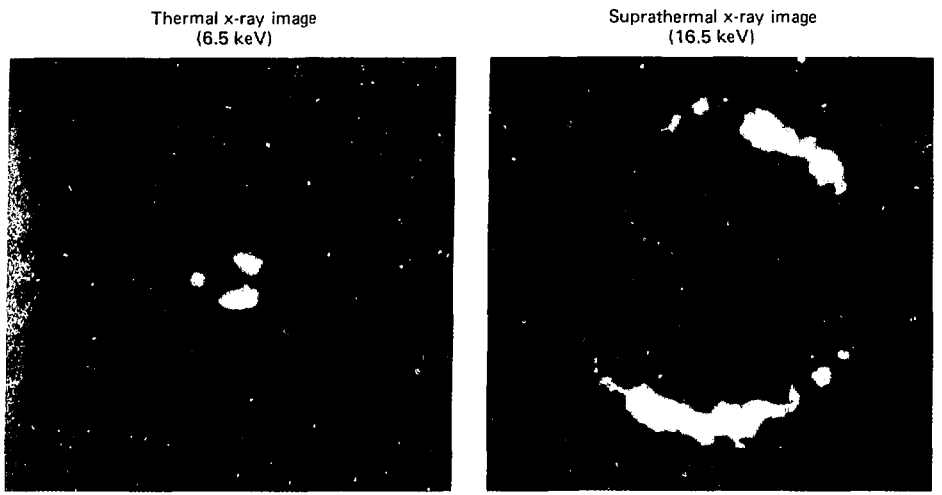

Fig. 6-1

plasma conditions are better known we will not be able to fully quantify our understanding of absorption and scattering processes. Diagnostic techniques are now becoming available which will allow sophisticated shell dynamics experiments in the coming year.

Authors: H.G. Ahlstrom and J.H. Nuckolls

Shiva 2-ns Disk Experiments

Laser-heated ICF targets capable of achieving breakeven energy output will most probably be driven by carefully shaped pulses many nanoseconds in duration. During the last year we conducted disk experiments with 2-ns (FWHM) laser pulses to investigate several of the conditions that arise when very large regions of plasma are irradiated with such long laser pulses; these conditions include such dangerous instabilities as Brillouin scattering, filamentation, and Raman scattering. Efficient Brillouin scattering would mean low light absorption, while filamentation and Raman scattering would produce high-energy electrons which can contribute to target preheat. At longer pulse lengths, however, inverse bremsstrahlung absorption is also expected to increase. There is thus a competition between inverse bremstrahlung absorption and the instabilities; inverse bremsstrahlung absorption dominates if the light is absorbed before Brillouin scattering or filamentation can occur.

Earlier 1-ns experiments[1] were performed with a single Gaussian optical pulse, while the 2-ns experiments we report here were carried out with a stacked pulse obtained by using a Mach–Zehnder interferometer to coherently add two 1-ns Gaussian optical pulses separated in time by 1.2 ns. Since the coherent addition of two pulses requires the difference in optical path lengths to be stable to better than $\lambda/10$, the optics for combining the two pulses were mounted on an NRC super-Invar table. The optical phase of one of the two pulses was adjusted by tilting an etalon in one arm of the Mach–Zehnder interferometer; the etalon's surfaces were plane-parallel and antireflection-coated.

The correct optical phase for coherent superposition was located by first finding two successive etalon angular positions for which a null occurred in the center of the pulse (as recorded by a streak camera with an automated readout). The etalon was then adjusted to approximately the midpoint. If the two optical pulses are not nearly colinear, their

Fig. 6-2. Absorption measurements for 2-ns gold and parylene disk experiments. The "smaller spot" data are from experiments in which the spot diameter was reduced from 900 to 450 μm, the same spot size used for the 1-ns, 3×10^{14} W/cm^2 experiments.

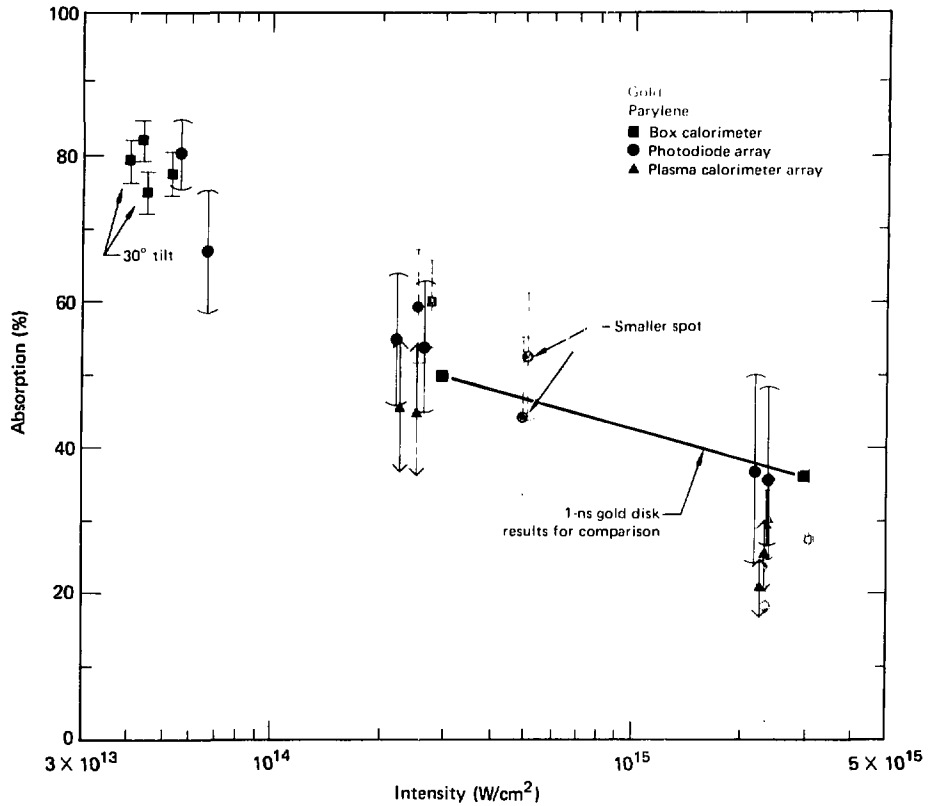

relative phase will vary significantly across the wave front. Given the beam diameter d and a maximum phase error $\Delta\phi$ across the wavefront, we can find the maximum angular alignment error ϵ_{max} from $\Delta\phi = k_0 \epsilon_{max} d$. For $\Delta\phi = k_0 \lambda/10$ and $d = 5000\,\lambda_0$ (the beam diameter at the pulse stacker), we have $\epsilon_{max} = 20$ μrad. A computer-controlled pointing and centering sensor enabled us to attain this alignment accuracy. On most of the shots the output pulse shape of one or two beams was measured by the output streak camera and a fast photodiode located in the target room.

Parylene and gold disks were irradiated at three intensities: 5×10^{13}, 3×10^{14}, and 3×10^{15} W/cm^2. The spot diameter was 900 μm for the two lower intensities and 250 μm for the highest intensity. The principal measurements made were of the fraction of light absorbed, of the radiative losses into soft x rays ($\leq$1 keV), and of the high-energy x-ray spectrum. We found little difference between the 2-ns results and our earlier 1-ns results for the two intensities we could compare. The spot diameters for the 1-ns experiments were 450 μm for 3×10^{14} W/cm^2 and 150 μm for 3×10^{15} W/cm^2. Absorption (Fig. 6-2) was measured either by a box calorimeter or an array of photodiodes, calibrated to better than 5% relative accuracy and 5 to 10% absolute accuracy.

An understanding of the measurement limitations is important for Fig. 6-2. The photodiode measurement of the scattered light is nominally 15%

Table 6-1. Scattered-light measurements showing the existence of a back-reflected peak for a 2-ns gold disk experiment in which beams 16 and 18 irradiated the disk at 5×10^{13} W/cm^2 and were incident at 30° to the target normal. The light was p-polarized, the major-axis spot diameter was 900 μm, and the total energy on target was 585 J. Measurements were made with photodiodes (PD) and a reflected-beam diagnostic (RBD) calorimeter.

Detector	Intensity in (J/sr)	Target chamber coordinates		Rotated coordinates	
		ϕ	θ	ϕ'	θ'
PD-38	113	270°	20°	0°	2.3°
Beam 16 RBD	100.3	234°	17.74°	−72.9°	10.8°
Beam 18 RBD	No data	306°	17.74°	+72.9°	10.8°
Beam 17 RBD	59.6	270°	9.70°	0°	8.04°
Beam 15 RBD	54.5	198°	9.70°	−32.5°	17.4°
Beam 19 RBD	30.2	342°	9.70°	+32.5°	17.4°
PD-35	35.2	198°	20°	−60.3°	22.0°
PD-40	27.5	342°	20°	+69.9°	20.3°
PD-37	4.7	126°	20°	−20.1°	35.8°
PD-34	3.6	36°	20°	+30.1°	33.5°

accurate for an axially symmetric light distribution, while the incident energy is known to 5%. Thus the error in the measured absorption fraction f can be as high as 20% of (1 − f). The more accurate box calorimeter measurement is expected to be in error by less than 10% of (1 − f). We have also included plasma calorimeter results when available. When the absorption fraction is small, the plasma calorimeter will provide the more accurate measurement.

Absorption at normal incidence is slightly higher at 2 ns than at 1 ns for 3×10^{14} W cm^{-2}, but is lower at 3×10^{15} W cm^{-2}. At high intensity it thus seems likely that stimulated Brillouin scattering dominates. Perhaps the most surprising result of these experiments is the failure of the absorption to vary significantly with Z. The inverse bremsstrahlung intensity absorption coefficient is given by

$$\kappa_{CL} = \frac{4\sqrt{2\pi}}{3}\left(\bar{Z}\, r_0^2\right)\frac{n_e^2/n_c}{\beta_{te}^2\sqrt{1 - n_e/n_c}}\, F(\alpha)\ \text{cm}^{-1}, \qquad (1)$$

where r_0 is the classical electron radius 2.818×10^{-13} cm, n_e is the electron density, n_c is the critical electron density, β_{te} is the thermal velocity expressed as a fraction of light speed ($\beta_{te} = \sqrt{KT_e/mc^2}$), and $F(\alpha)$ is a function which depends upon v_{osc}/v_{te}; for $v_{osc} \ll v_{te}$, $F(\alpha) = 1$. The mean ionization $\bar{Z}$ for gold exceeds that for parylene by an order of magnitude.

There are several possible partial explanations of why we do not observe an order-of-magnitude difference in the integrated inverse bremsstrahlung absorption coefficient:

- The integrated absorption coefficent is proportional to the density scale length L, and we would expect L for parylene plasmas to be much longer than for gold plasmas. The sound speed

$$C_s = \sqrt{\frac{\bar{Z}\, k\, T_e}{A m_N}} \qquad (2)$$

will be higher for a parylene plasma than for a gold plasma of the same temperature. In Eq. (2) m_N is the mean nucleon mass, Z is the mean ionization state, A is the nucleon number, k is Boltzmann's constant, and T_e is the electron temperature.

- Heat-flux inhibition is expected to be more severe for higher Z. Strong inhibition will steepen the density profile and raise the electron temperature.

- Slow electrons, which are principally responsible for inverse bremsstrahlung absorption, collide with ions Z times more often than they collide with other electrons. But electron-electron collisions are necessary to repopulate this group of slow electrons. When $\bar{Z}\, v_{osc}/v_{te}^2 \gtrsim 1$, we find the electron distribution is no longer Maxwellian but more flat-topped. This parameter is much smaller for parylene than for gold.

As these partial explanations show, a full explanation for the small difference in measured ab-

Fig. 6-3. Angular distribution of the x-ray energy for the 2-ns gold disk experiments at 3×10^{14} W/cm^2. The major-axis spot diameter was kept constant at 900 μm.

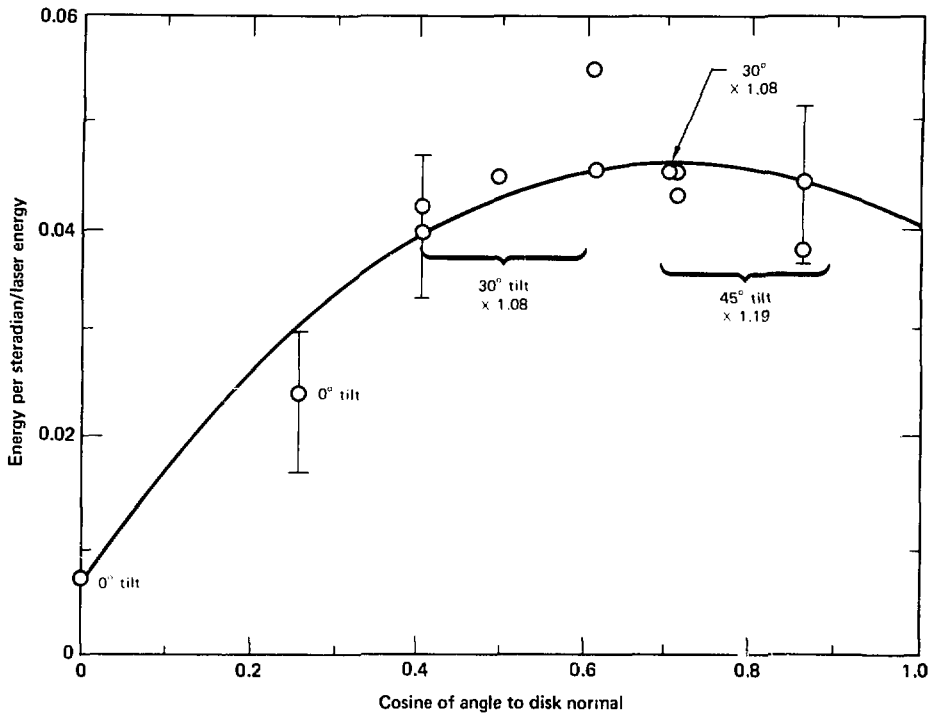

sorptions between parylene and gold will probably be a complicated one, arrived at only after considerable computer simulation.

Even at 5×10^{13} W cm^2 some Brillouin scattering must occur. We see a highly collimated peak in the backward direction (see Table 6-1), in addition to the much broader specular peak when the target is tilted 30° from the laser beams. To obtain the data in Table 6-1, the target was irradiated only by two adjacent outer beams of the upper 10-beam cluster, nos. 16 and 18, which have azimuths ϕ = 234° and ϕ = 306°, respectively; their common polar angle is ϕ = 17.74°, and the lenses are f/6 with a marginal ray half-angle of 5.05° (the beam is somewhat smaller). We have also tabulated the rotated coordinates ϕ', θ' which are based upon an axis at ϕ = 270°, θ = 17.74°. The azimuth ϕ' is zero on the plane of incidence. We find that about 5 to 6% of the incident light is scattered into the backwards peak by fitting the light distribution to the equation $I = I_0 \cos^n\theta$. We find n is quite high, about 15 to 18. For a gold disk tilted 30° and irradiated by the upper ten beams at 3×10^{14} W/cm^2, about 9 to 10% of the incident light appeared in the back-reflected peak.

Table 6-2. Summary of the fraction of the absorbed energy radiated as soft x rays from a gold-disk target, determined from the date in Figs. 6-3 and 6-4.

Time (ns)	Intensity level (W/cm^2)		
	5×10^{13}	3×10^{14}	3×10^{15}
1	–	35% ± 7%	35% ± 7%
2	62%	38% ± 7%	–
	(64%)[a]	(43%)[a]	–

[a]Based upon multiplying the Dante measurement at 60° to the target normal by a 2π solid angle.

Fig. 6-4. Angular distribution of the x-ray energy for the 2-ns gold disk experiments at 5×10^{13} W/cm^2. All targets were irradiated by two adjacent beams incident at 30° to the target normal (p-polarization). The major-axis spot diameter was 900 μm.

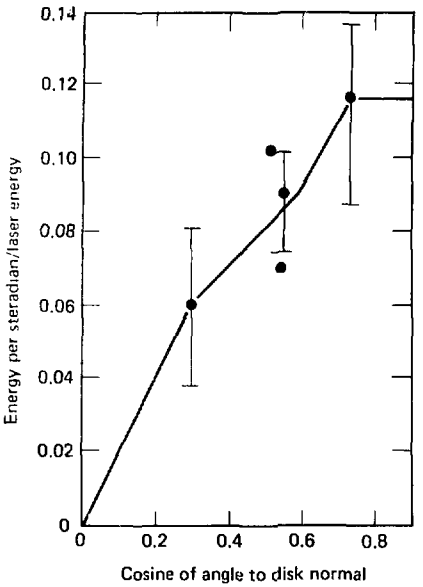

Table 6-3. Summary of the LASNEX predictions for x-ray conversion efficiency, expressed as a percentage of the absorbed energy, for both the 1- and 2-ns gold disk experiments. Both the inhibited (IL) and noninhibited (NIL) LASNEX model results are included.

Time (ns)	Intensity level (W/cm^2)		
	5×10^{13}	3×10^{14}	3×10^{15}
2 (IL)	50%	45%	36%
2 (NIL)	67%	58%	44%
1 (IL)	–	33%	36%
1 (NIL)	–	62%	58%

For gold a large fraction of the absorbed light energy is radiated away in soft x rays. Table 6-2 summarizes these results and compares them to the 1-ns results.

Figure 6-3 shows the angular distribution for the 2-ns, 3×10^{14} W/cm^2 gold disk experiments; a third-power polynomial in cos θ has been fitted to these data. To obtain this angular distribution, targets were tilted to different angles in different shots. Unfortunately, we have no 2-ns absorption data at angles other than normal. We do have a measurement for the 45° angle at 1 ns, however, for which the absorption is 42%, compared to 50% at normal incidence. We assume the absorption at 2 ns to be reduced proportionally at a 45° incidence angle; the 45° results shown in Fig. 6-3 therefore equal the actual measurements multiplied by 1.19, while the 30° measurements have been multiplied by the in-between value of 1.08. Upon doing the angular integration, we find the x-ray energy is 23% of the incident laser energy; if we do not correct for target tilt, the figure is ≈21%. This percentage is then divided by the 0.60 absorption fraction to find the fraction of the absorbed energy appearing in soft x rays at 3×10^{14} W/cm^2 (Table 6-2).

In assigning the error brackets (in parentheses in Table 6-2) we have assumed the Dante measurement of the integral at a particular angle to be 20% accurate. This error is added in quadrature both with our estimate for the probable error in integrating over the angular distribution and with the probable error in the absorption measurement. For 3×10^{14} W/cm^2, the absorption is known to be 60% (±5%) at 0°. The angular integration is probably 10% accurate.

At 5×10^{13} W/cm^2, we have the necessary absorption data, but fewer measurements (Fig. 6-4). Thus the 62% radiated efficiency measurement is probably uncertain to ±10% just from inadequate knowledge of the angular distribution. The absorption measurement for the 5×10^{13} W/cm^2 30°-tilt gold disk experiment is 77% (±4%). We feel the angular integration is about 20% accurate; thus we find it unlikely that the radiated percent for gold at 2 ns and 5×10^{13} W/cm^2 is outside the range of 48 to 80%.

Table 6-3 gives LASNEX predictions for both strong heat-flux inhibition (IL) or none at all (NIL). Again, these x-ray conversion efficiencies are expressed as a percent of absorbed energy. Strong heat-flux inhibition is conclusively required in the mid-10^{14} W/cm^2 intensity region and above. Some inhibition may be required for 5×10^{13} W/cm^2, but the strongly inhibited model gives a conversion percent which is at the extreme lower bound of the experimental error bracket.

The suprathermal x-ray spectra for several representative shots on gold disks at several intensities are plotted in Fig. 6-5. For 3×10^{14} W/cm^2 we estimate the fraction of the laser energy appearing

Fig. 6-5. Filter fluorescer measurements of the high-energy x-ray spectrum for several representative gold disk shots.

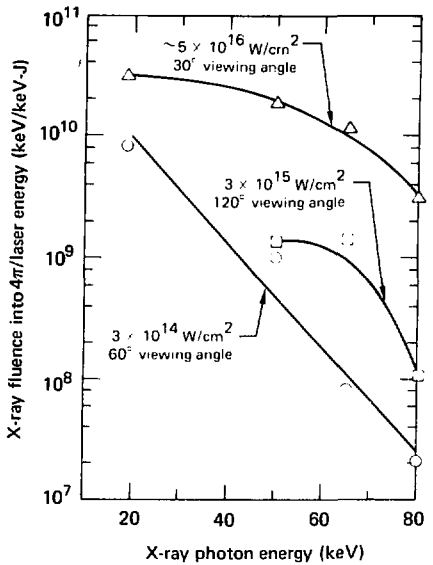

in suprathermal electrons to be approximately 5% (±3%); the "hot" temperature is about 17 keV. For 3×10^{15} W cm^{-2}, the high-energy x-ray spectrometer looked through the 18.5-μm thick gold disk at an angle of 30° to the disk face, and thus all that could be measured was the level of the high-energy tail at 50 to 80 keV.

We find that where there are data to compare, lengthening the laser pulse from 1 to 2 ns changes the experimental picture little. It therefore seems unlikely that absorption or stimulated scatter will change dramatically at somewhat longer pulse lengths. The weak Z-dependence of the absorption, even at long pulse length, has also been observed by AWRE[2] in their experiments at 1 and 3 ns.

Authors: D. W. Phillion, V. C. Rupert, and M. D. Rosen

References

1. M. D. Rosen, D. W. Phillion, V. C. Rupert, W. C. Mead, W. L. Kruer, J. J. Thomson, H. N. Kornblum, V. W. Slivinsky, G. J. Caperaso, M. J. Boyle, and K. G. Tirsell, "The Interaction of 1.06 μm Laser Radiation with High Z Disk Targets," *Phys. Fluids* **22**, 2020 (1979).
2. B. R. Thomas, private communication.

Sidescatter in Laser-Irradiated High-Z Targets

Since stimulated scattering is a potential loss mechanism in the coupling of laser light to an ICF target, it has been studied extensively. Most experiments[3] have concentrated on the characteristics (spectral, temporal, etc.) of backscattered light, generally defined as the light collected by the focusing optics. Data have also been obtained on the angular distribution of scattered light, showing that more light is scattered out of the plane of polarization of the incident light than in the plane. As discussed by Phillion,[4] the observed large asymmetries can be ascribed to Brillouin sidescattering, but little data have been gathered on how sidescatter varies with the characteristic parameters of the laser-plasma interaction.

Recent experiments with high-Z disks at long pulse lengths (conditions which enhance stimulated scattering) have added some information regarding the variation of sidescatter with target orientation relative to the laser beam. Indeed we determined that, for 1.06-μm irradiations of a target tilted at 30°, sidescatter out of the plane of polarization becomes large enough to be comparable to the sum of the specular and backscattered radiation. Since sidescattering is a strong function of incident intensity,[5] the data discussed below are limited to results of experiments conducted at 3×10^{14} W cm^{-2}.

Diagnostic Configuration

During absorption measurements on gold and titanium disks at 1.06 μm, we obtained an indication of the magnitude of sidescatter out of the plane of polarization. When a finite number of discrete instruments, such as PIN diodes,[6] are used, the spatial extent of the specular peak cannot be accurately determined; thus the required spatial interpolation of the measured flux can mask or distort the effect which we seek to observe. This problem does not arise when experiments are conducted in a box calorimeter.[7] Since each of the six panels of the Argus box calorimeter are read independently, a value of the total light scattered into a given sector can be obtained.

Fig. 6-6. Diagram of experimental box calorimeter configuration at Argus. The laser beam was incident through the North panel (1); the target is inserted through a hole in the top panel (3). The E vector lies 104.8° east from the vertical. The West panel (6) has a diagnostic hole, whereas the East (5) and bottom (4) panels are integral.

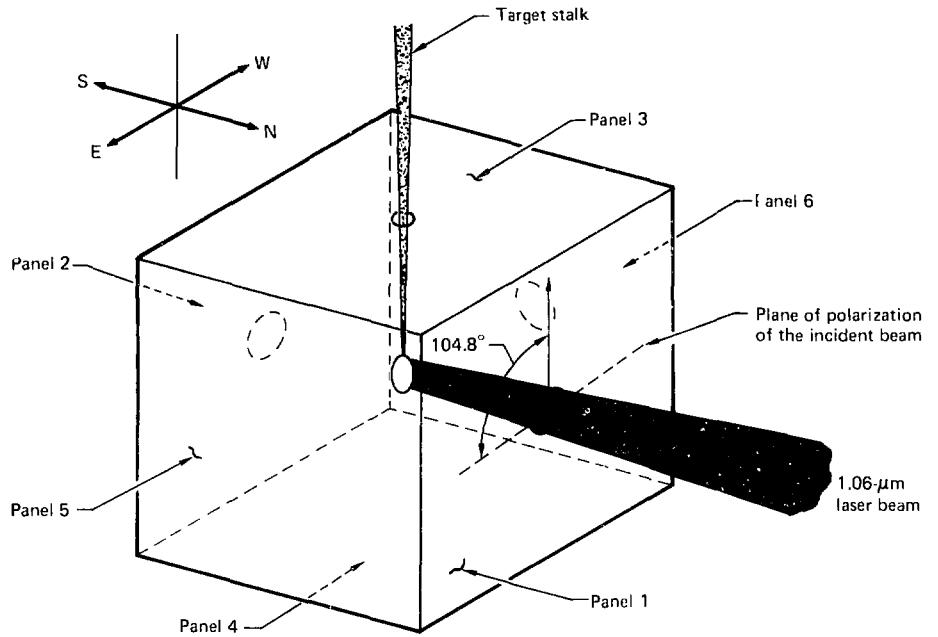

We performed our box calorimeter experiments at Argus, where the plane of polarization of the incident light (measured from the vertical target positioner) is 104.8° (Fig. 6-6). Panels 3 and 4 of the calorimeter are almost parallel to the plane of polarization of the incident beam, and therefore collect the light scattered "out of the plane of polarization" of the incident light. Conversely, panels 5 and 6 collect the light scattered "in the plane of polarization." These four panels receive all the light scattered between 55° and 125° from the incident beam in their respective directions, and receive part of the light scattered between 45° and 55° or 125° and 135°; this contribution to the total scattered light will be called "large-angle scattering."

Panel 1 receives the light scattered between the edge of the f/2.2 focusing lens and 45°, as well as light scattered between 45° and 55° that is not absorbed by panels 3, 4, 5, and 6; this contribution will be referred to as "small-angle backscattering" to distinguish it from the contributions of panels 3 through 6 and the backscatter collected by the focusing optics. By analogy, panel 2 receives "small angle forward-scattering," while the "transmitted" or "forward-scattered" light is collected by the lens set behind the panel. With the thick (13 μm) targets used in these experiments, however, the amount of "forward-scattered" light collected by either panel 2 or this lens is small and will not be considered in the following discussion. Note that we will continue to refer to "large-angle scattering" and "small-angle backscattering" in the special sense defined above.

Experimental Results

For the box calorimeter experiments we irradiated high-Z (mainly gold) disks at 3×10^{14} W/cm^2 with a ~900-ps pulse of 1.06-μm light. Three target orientations were used:

- The first experiment was conducted with the disk normal to the incident beam. In this case the small-angle backscattering and backscatter ac-

Table 6-4. Percent of incident light scattered in various directions, for plasma targets tilted at 30° and irradiated at 3×10^{14} W/cm^2 with 1.06-μm light for a 900-ps pulse.

Scatter characteristics	Gold target	Titanium target
Large-angle, out-of-plane	23	30
Large-angle, in-plane; and specular peak	9	16
Small-angle and backscatter	20	13

counted for 36% of the incident light. Panels 3 and 4 recovered 3% (out-of-plane large-angle scattering) of the incident light; panels 4 and 5 recovered 2% (in-plane large-angle scattering).

- The next set of experiments had the disk tilted 45° towards panel 4. Here the specular reflection adds to the expected larger out-of-plane scattering, so that little information on the magnitude of the scattered (as opposed to specular) light could be obtained. For this configuration small-angle backscattering and backscatter accounted for 24% of incident light, in-plane large-angle scattering accounted for 5%, out-of-plane large-angle scattering with specular reflection accounted for 18%, and 4% was recovered on the panel which looked mostly at the back of the target in the out-of-plane large-angle scattering direction.
- The most interesting experiments however, were conducted with disks (both gold and titanium) tilted 30° towards panel 5. The specular peak[8] now adds to the in-plane large-angle scattering, so that we would have expected a much larger increase in the light absorbed by panel 5 than by either panels 3 or 4. In fact, the amount of light scattered towards panels 3 and 4 was comparable both to the sum of light scattered towards panels 1, 5, and 6, and to the direct backscatter (Table 6-4). In other words, the large-angle scattering out of the plane of polarization was comparable to the sum of scattering in all other directions.

Other Experiments

Data were also collected with large numbers of discrete detectors (PIN diodes) located at various polar angles both in and out of the plane of polarization of the incident light. When comparing these data with the box calorimeter results we must remember that

- Each panel of the box calorimeter represents a spatial integration over a large azimuthal range ($\pi/2$), whereas the PIN diodes are centered on the azimuth corresponding to maximum or minimum flux and have an acceptance angle of 1°. Hence, differences in the scattered light with respect to the plane of polarization are emphasized by PIN diode measurements.
- For tilted targets, PIN diodes will measure specularly reflected light that could lie in a relatively narrow region. Although the effect of the specularly reflected light might mask all other for diodes, its total contribution to a calorimeter panel may be small.
- A difference between the measurements will arise due to the respective bandwidths of the instruments: PIN diodes are fitted with 100-Å bandpass filters about the main laser frequency, whereas the box calorimeter panels absorb light from 270 nm to several micrometers.

Figure 6-7 shows an extreme case (for PIN diode measurements) of differences between in-plane and out-of-plane scattering for a disk irradiated at normal incidence by an f/2.2 lens under the same conditions as the box calorimeter experiments (3×10^{14} W/cm^2 and a 900-ps pulse). Note the logarithmic flux scale. These data show that for large-angle scattering the maximum ratio between out-of-plane and in-plane flux is of the order of 2.5 (compared to 1.5 measured by the box calorimeter), and that the integrated flux is of the order of 10% of the incident light. As for the box calorimeter data a large fraction (approximately 45%) of the incident light is recovered in "small-angle backscattering" and backscatter.

Figure 6-8 shows another example, but for a shorter (200 ps) pulse length. Here we used one beam of the Shiva laser, obtaining an effective angle of incidence of 9.7° since the target normal was along the Shiva beam cluster axis as shown on the figure. In this configuration, specular reflection is combined with small-angle scattering. The ratio of out-of-plane to in-plane large-angle scattering is on the order of 3, while the integrated flux is approximately 13% of the incident flux. No PIN diode data are available for a larger angle of incidence in p-polarized irradiance at 10^{14} W/cm^2.

Summary and Interpretation

More experiments, both with the box calorimeter and PIN diodes, are necessary to study

Fig. 6-7. Polar plot of 1.06-μm fluxes scattered both in and out of the plane of polarization, as measured by PIN diodes; note the logarithmic scale. The target was a gold disk irradiated at 3×10^{14} W/cm^2 for a 900-ps pulse.

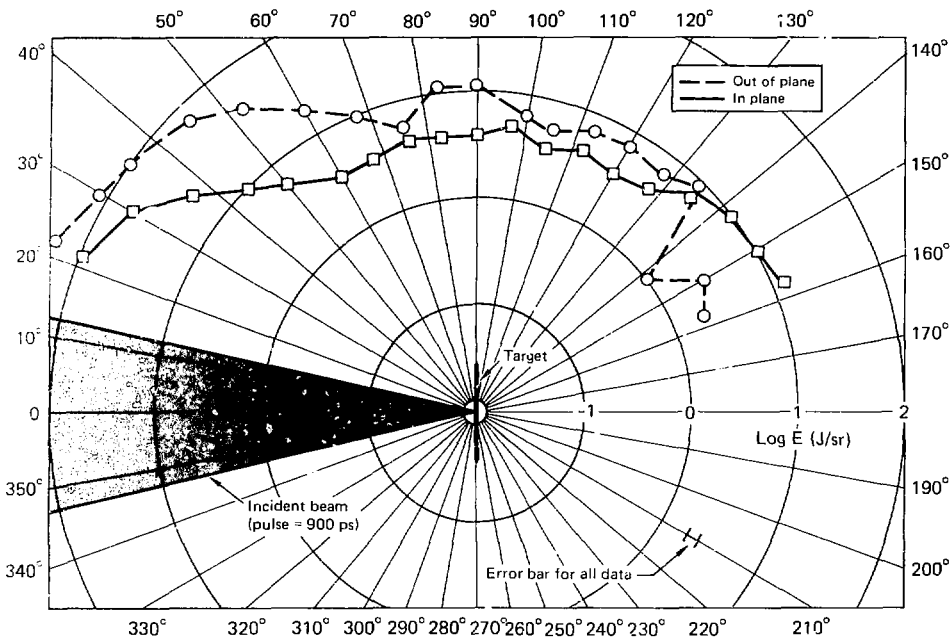

the intensity dependence of sidescatter, as well as how it varies with angle of incidence at a fixed intensity.

The data available at this time (for 3×10^{14} W/cm^2 and 1-ns pulses of 1.06-μm light) indicate that large-angle scattering increases rapidly with angle of incidence relative to the specular and backscattered or small-angle backscattered flux, from about 10% at 0° to more than 80% at 30° for gold targets. Recent experiments at 0.53 μm, however, show a large-angle scattering increase of less than a factor of 2 for targets tilted at 30° compared to normal incidence.

Since other evidence shows less Brillouin backscattering at the shorter wavelength (see "Preliminary $2\omega_0$ Results" later in this section), it is tempting to attribute the observed increased flux at 1.06 μm to Brillouin sidescatter. This assumption is consistent with observed larger $3/2\omega$ emission out of the plane of polarization of the incident light than in the plane, which would otherwise be difficult to explain. Raman sidescatter is unlikely to contribute to the observed flux, since experiments[9] at 1 ns and 3×10^{14} W/cm^2 have shown it to be on the order of only 0.005% efficient. We note that the box calorimeter panels are capable of absorbing several harmonics of the incident light (including $\omega/2$). Finally, an instability which ripples the plasma density contour near the classical reflection point can also play a role.[10]

Theoretical studies of the large-angle enhancement in sidescatter normal to the plane of incidence of p-polarized light are in progress. We may speculate, however, that as the target is tilted Brillouin scattering occurs at lower densities where refraction is less severe. At normal incidence refraction would collimate the scattered radiation towards the small-angle backscattering direction ($\theta < 45°$ if scattering occurs at or above 0.5 n_c). The observed differences in large-angle sidescattering would then be related not only to actual differences

Fig. 6-8. Polar plot of 1.06-μm fluxes scattered both in and out of the place of polarization, as measured by PIN diodes; note the logarithmic scale. The target was a gold disk irradiated at 3×10^{14} W/cm^2 for a 200-ps pulse.

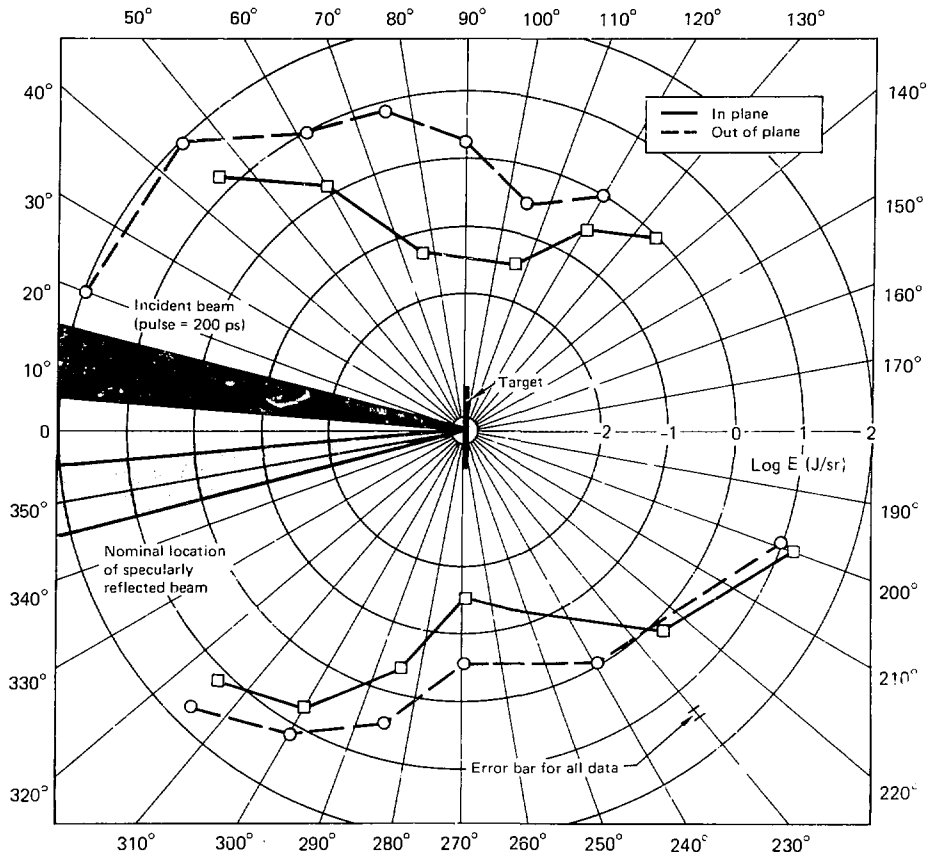

at the location where scattering occurs but also to the direction of propagation of the scattered wave as modified by refraction.

Authors: V. C. Rupert, W. L. Kruer, and D. W. Phillion

Major Contributors: E. M. Campbell, K. G. Estabrook, and the Argus Operating Staff

References

3. D. W. Phillion, W. L. Kruer, and V. C. Rupert, *Phys. Rev. Lett.* **39**, 24 (1977), p. 1529; B. H. Ripin, J. M. McMahon, E. A. McLean, W. M. Manheimer, and J. A. Stamper, *Phys. Rev. Lett.* **33**, 11 (1974), p. 634; B. Grek, H. Pepin, T. W. Johnston, J. N. Leboeuf, and H. A. B. Bo[illegible], *Nucl. Fusion* **17** (1977), p. 1165; and numerous others.
4. *Laser Program Annual Report—1976*, Lawrence Livermore Laboratory, Livermore, Calif., UCRL-50021-76 (1977), p. 5-156; D. W. Phillion, R. A. Lerche, V. C. Rupert, R. A. Haas, and M. J. Boyle, *Phys. Fluids* **20**, 11 (1977), p. 1892.
5. R. A. Haas, H. D. Shay, W. L. Kruer, M. J. Boyle, D. W. Phillion, F. Rainer, V. C. Rupert, and H. N. Kornblum, *Phys. Rev. Lett.* **39**, 24 (1977), p. 1533.
6. *Laser Program Annual Report—1975*, Lawrence Livermore Laboratory, Livermore, Calif., UCRL-50021-75 (1976), pp. 402 to 403.
7. *Laser Program Annual Report—1975*, Lawrence Livermore Laboratory, Livermore, Calif., UCRL-50021-75 (1976), pp. 404 to 405.

8. C. Gouedard, A. Saleres, and M. Decroisette, *Polarization and Angle-of-Incidence Dependence of Scattering and Absorption in Short Laser Pulse Interaction Experiments*, presented at the Fifth Workshop on Laser Interaction with Matter, Rochester, New York, 1979; R. Sigel, K. Eidmann, A. G. M. Maaswinkel, R. Petsh, G. Tsakiris and S. Witkowski, *Laser Plasma Interaction Studies of PLF Branching*, presented at the XIII European Conference on Laser Interaction with Matter, Leipzig, 1979.
9. D. W. Phillion, Lawrence Livermore Laboratory, Livermore, Calif., private communication (May 1979).
10. K. G. Estabrook, *Phys. Fluids* 19 (1976), p. 1733

Electron Transport Analysis Using Layered Slab Targets

Experiments using disk targets composed of layers of dissimilar materials have provided the most detailed information available on electron transport in laser-heated plasmas. The materials and layer thicknesses can be chosen so that their characteristic x-ray emissions indicate where, when, and by how much the plasma is heated.

Experiments employing varying thicknesses of one material covering a target substrate of another material have been reported by several workers.[11,12] Generally, the results have been interpreted as supporting the existence of some inhibition mechanism for electron thermal transport. In 1976 G. Dahlbacka performed LASNEX calculations[13] to model the experiments of Young et al.[11] that employed CH-coated Al disk targets; he found support for inhibited electron conduction. He further noted some differences between the model required to "fit" the experimental results and the usual LASNEX electron conduction model employed to simulate other experiments.

Our recent analysis using LASNEX has likewise shown that the usual electron conduction model simulates the CH-on-Al experiment poorly, and that very strong transport inhibition is indicated. We also find that even with revised transport modeling the calculations and experiment still show significant disagreement. We have thus performed similar experiments to further explore the nature of these differences.

We report here the results of our CH-on-Al disk irradiations using the Argus laser. Results of the experiments are presented first; these support and extend previous experimental results. Second, we analyze some of the surprising and interesting results from the viewpoint of LASNEX simulations.

Experimental Resuits

A series of twelve flat-disk experiments was conducted with the Argus laser to study electron transport at a nominal laser intensity of 10^{15} W/cm^2. The laser pulses were approximately Gaussian, with FWHM of ~100 ps and average energy of 122 (±23) J. Target irradiation was done with a p-polarized converging beam, focused through f/2.2 lenses; the target normals were rotated 30° relative to the incident laser pulse direction. The targets were aluminum disks 600 μm in diameter by 25 μm thick, coated with 0, 0.25, or 0.67 μm of parylene. We also irradiated pure parylene targets 600 μm in diameter and 25 μm thick.

From previous studies of the absorption of 1.06-μm laser light by low-Z planar plasmas,[14] we estimate that the absorbed energy was 30% (±10%) of the incident laser energy. The fraction of backscattered light was constant, within experimental error, at ~10% of the incident energy, independent of target material. The FWHM of the backscattered light was 65% (±6%) of the incident laser pulse FWHM.

Properties of the heated plasmas were inferred from various measurements of x-ray emissions from 150 eV to 50 keV. The array of x-ray diagnostics used for these experiments included a 10-channel

Fig. 6-9. Integrated soft x-ray emission into 2π, normalized by incident laser energy, vs CH thickness. Measurements were made with a flat calorimeter and a Dante spectrometer. The "attenuation" depth [see Eq. (3) and text] is 0.11 (±0.07) μm.

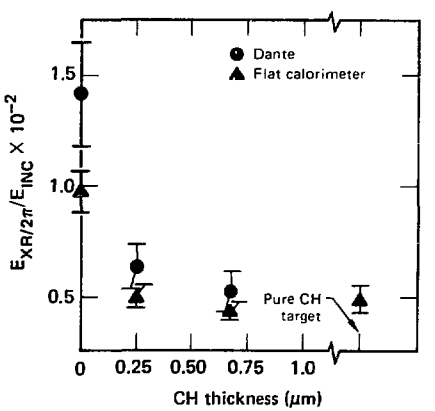

Fig. 6-10. Line emission spectra for a bare aluminum target and 0.25-μm CH target, detected by a crystal x-ray spectrograph.

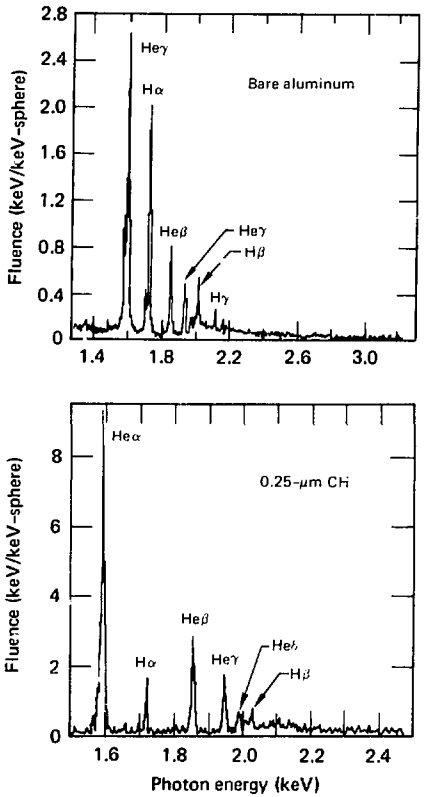

Fig. 6-11. Aluminum line radiation vs CH thickness; radiation was detected by the crystal spectrograph, integrated from 1.5 to 2.2 keV, and normalized by incident laser energy.

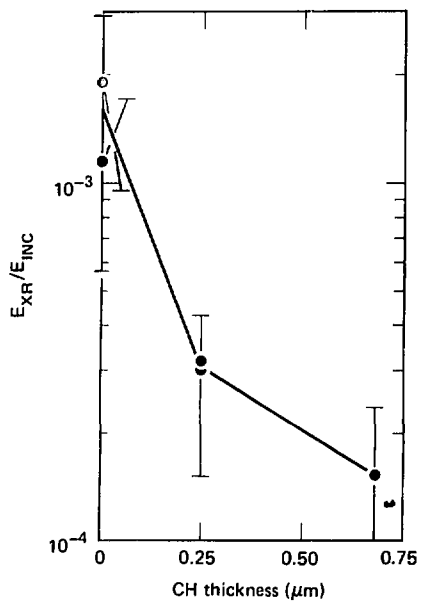

Dante spectrometer[15]; a fast, flat x-ray calorimeter[16]; a soft x-ray streak camera[17]; a 7-shooter (7 Si PIN K-edge filters); and an FFLEX (filter fluorescer) spectrometer.[18]

Figure 6-9 shows temporally and spectrally integrated emission energy ($0.15 \leq h\nu \leq 1.5$ keV) plotted against CH thickness, as measured by the fast, flat calorimeter and the Dante spectrometer, and normalized by the incident laser energy; the Dante and calorimeter data are plotted independently in the figure. (Though both sets of data indicate the same trends, the calorimeter data are lower than the Dante data; this relative difference between the two instruments is typical and so far is not explained.) Both detector systems, which were at 60° to the target normal, show that the soft x-ray emission drops off by a factor of 2.4 (±0.4) in going from bare Al to pure CH. It also appears that 0.25 μm of CH on Al behaves more nearly as pure CH than as Al. This indicates very steep thermal gradients and very shallow burn-through depths, consistent with previous measurements at NRL.[11]

If we describe the soft x-ray emission vs CH thickness by the relation

$$E_R = E_{Al}\, e^{\frac{-\Delta x}{L}} + E_{CH}\left(1 - e^{\frac{-\Delta x}{L}}\right), \qquad (3)$$

where $E_R \equiv (E_{XR}|_{2\pi})/E_{INC}$, E_{Al} and E_{CH} are the fraction of the total emission from the aluminum and parylene, respectively, Δx is the thickness of the CH, and L is an "attenuation" depth, then the data give the remarkably small value, L = 0.11 (±0.07) μm.

The soft x-ray streak camera recorded x-ray pulses whose duration was 2.0 (±0.2) times the

Fig. 6-12. High-energy x-ray fluence as measured with the FFLEX and 7-Shooter detector systems, normalized by incident laser energy.

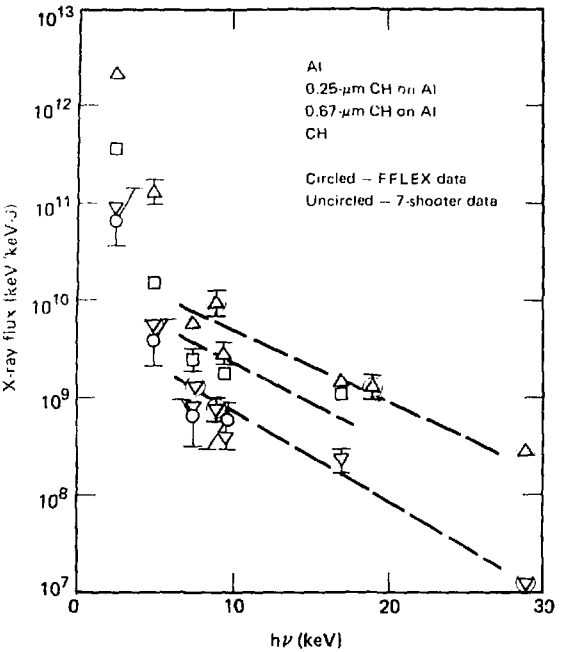

FWHM of the laser pulse, but the x-ray pulses were not a simple, standard (i.e., Gaussian) shape.

Figure 6-10 shows typical line emission spectra detected by an x-ray crystal spectrograph for a pure aluminum target and for a target coated with 0.25 μm of parylene. Hot aluminum He- and H-like lines are prominently visible. Though cold Al lines would have been detected if present, none were seen, which implies that energetic electrons capable of exciting these lines were not getting into cold Al to any appreciable degree. The Al He- and H-like lines occur above 1.5 and 1.7 keV, respectively, and below the respective series limits of 2.086 and 2.304 keV. The energy in the integrated spectrum from 1.5 to 2.2 keV, normalized by the incident laser energy and plotted in arbitrary units (Fig. 6-11), drops by a factor of 10 in going from bare Al to a 0.67-μm coating of CH.

The high-energy x-ray fluences shown in Fig. 6-12 follow the same trends, qualitatively, as the low-energy x-ray data. The spectrum for 0.67 μm of CH on Al is the same as for pure CH, while the spectrum for 0.25-μm CH on Al is intermediate between pure Al and pure CH.

The suprathermal x-ray spectrum implies a hot electron temperature of $T_h \simeq 4$ to 6 keV and a fraction of incident light converted into hot electron energy of $E_{HOT}/E_{INC} \approx 10$ to 15% for all targets. This, together with an assumed absorption of 30% (±10%), suggests that the suprathermal electron distribution contains ~1/3 to 1/2 of the energy absorbed by the targets. Corrections for hydrodynamic losses are small and are accounted for in the detailed calculations discussed below. Anisotropic x-ray emission[19] could also introduce an uncertainty of a factor of 2 or so.

Analysis and Simulations

We were surprised by the low measured flux and slope of the high-energy x rays in these measurements. Figure 6-13 compares the 10-to-50-keV x-ray fluence measurements obtained several years ago in CH disk irradiations near 10^{15} W/cm^2 on Janus[20] with those of the Argus experiment reported here. Each experimental point from Janus represents the average of three or more measurements, while only one CH disk shot was available from these Argus transport experiments. The Janus data have been corrected very slightly, using $T_{HOT} \propto I^{0.3}$ scaling to shift intensity by a factor of two to 10^{15} W/cm^2. Compared to the earlier Janus experiments, we find in these Argus experiments that the fluence of 10-to-50-keV x rays per incident joule is down by a factor of 4 to 10.

The simulation of hot electrons produced by resonance absoption in the LASNEX code is governed by the relation

$$T_{HOT} = \alpha \langle T_e \rangle + (I\lambda^2)^{\gamma} \langle T_e \rangle^{\delta} \left(1 + 3\frac{T_i}{ZT_e}\right)^{\epsilon} Z\phi, \qquad (4)$$

Fig. 6-13. Hot x-ray fluence comparison of current measurements on Argus with earlier results inferred from Janus disk experiments. A significant decrease in hot x-ray fluence and slope is indicated.

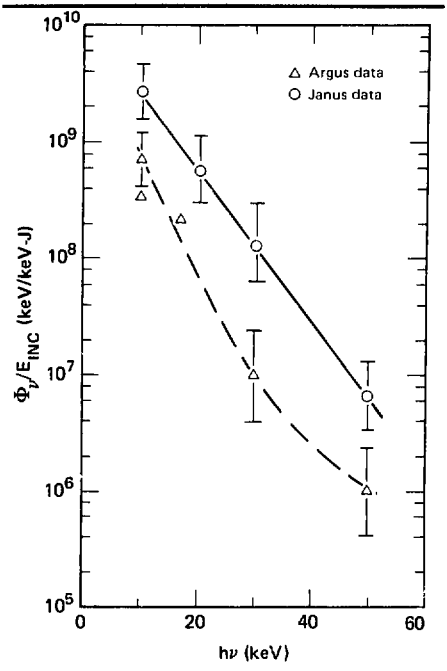

Fig. 6-14. Hot x-ray fluence comparison of various calculational absorption models (detailed in Table 6-5) with recent Argus measurements. To fit the Argus data, the spectral hardness parameter must be decreased by a factor of ~2 and the energy absorbed into hot electrons must be decreased by a factor of ~2 to 3.

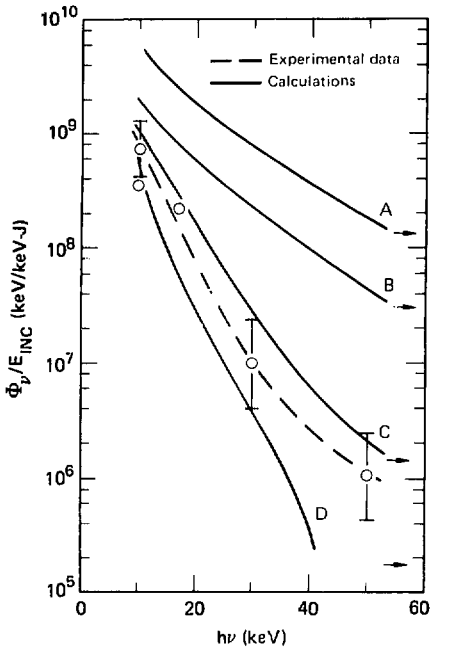

where T_e is the mean temperature in (keV) of all electrons, I is the laser intensity in units of 10^{17} W/cm^2, λ is the laser wavelength in units of 1.06 μm, T_e and T_i are the temperatures (in keV) of thermal electrons and ions, and Z is the nuclear Z of the plasma. From normalization to plasma simulation, and from recent high-Z disk experiments[21], the coefficients are determined to be $\alpha = 1$, $\beta = 50$, $\gamma = 0.42$, $\delta = 0.04$, $\epsilon = 0.25$ and $\varphi = 0.25$. Checking the model against the low-Z disk experiments on Janus, we find the calculated $T_{HOT}^{X} = 13$ keV, compared with the measured $T_{HOT}^{X} = 8.3$ (± 1.0) keV. Good agreement with the Janus data is obtained using $\beta = 30$, and depositing 20 to 30% of the incident energy into hot electrons.

The hot x-ray fluence calculated with LASNEX is plotted in Fig. 6-14, together with the Argus data for various absorption models; the four models plotted are summarized in Table 6-5. To fit the Argus data we were forced not only to reduce the spectral hardness of hot electrons by reducing β to 20, but also to reduce the hot electron energy to only ~10% of the incident energy, as indicated by the simple estimates above. This apparent decrease in the number and temperature of hot electrons is intriguing, and further verification of the data is clearly essential.

The information on electron transport is mainly contained in the absolute radiation emission levels for Al and CH, and in the rate of fall-off as increasing thicknesses of CH are applied to the Al. The data points in Fig. 6-15 show the absolute sub-keV emission determined experimentally; the curves show the same quantity calculated by LASNEX using various models (summarized in Table 6-6). The models are characterized by the values used for the "anomalous" flux-limit reduction of the thermal (f_t) and suprathermal (f_s) electrons, where, as usual, $\phi_{t,s}$

Table 6-5. Summary of various absorption models compared with high energy x-ray emission in Fig. 6-14. The parameters varied are f_D, the fractional dump of light at the critical surface (mocking up resonant absorption), and β, the coefficient of the $I\lambda^2$ term in the formula for T_{HOT} [see Eq. (4)]. The thermal and suprathermal flux limits have been reduced in all models by $f_e = f_s = 0.03$. Also given for the CH target are the energy absorbed by resonance absorption (E_{RA}) and the total absorption (E_{ABS}).

Model	f_D	β_D	E_{RA}(J)	E_{ABS}(J)
A	0.3	50	32	36
B	0.1	50	11	16
C	0.1	20	11	16
D	0.4[a]	20	11	14

[a]Model D utilized a preliminary treatment of Brillouin scattering, which reflected about 75% of the incoming light before it reached the critical surface.

$= f_{t,s}\, n_{t,s}\, mv^3_{t,s}$ is the saturated heat flux carried by either thermal or suprathermal electrons.

Many previous experiments have been adequately interpreted using $f_t = 0.03$, $f_s = 1$, and with absorptions into suprathermal electrons ~30%. As seen in Fig. 6-15, however, this model (E) does poorly when compared with the Argus experimental data; the absolute emission levels are too high and the scale-depth for emission fall-off is too great. Similar discrepancies had been seen in a comparison of LASNEX calculations with the NRL layered-slab experiments.

We have attempted several ways of varying the model's parameters to improve its correspondence to experimental values. Two obvious techniques are reducing the transport coefficients (Fig. 6-15, Table 6-6) and reducing the absorption (Fig. 6-16, Table 6-7). Either of these modifications can improve the agreement between calculated and measured attenuation depths. Using flux-limit reduction factors of $f_t = f_s = 0.01$ (Fig. 6-15) gives about the same results as reducing the absorption to 10% with $f_t = 0.03$, $f_s = 1$ (Fig. 6-16). Neither modification, however, produces an attenuation depth as small as that seen experimentally. Further, as some improvement is made in the calculation of the attenuation depth, the calculated ratio of emission from pure Al to emission of pure CH becomes discrepant with experimental results. Finally, either model alteration

Table 6-6. Summary of transport models compared with sub-keV x-ray data in Fig. 6-15. Parameters varied are the flux-limit multipliers for thermal and suprathermal electrons. These models have fixed absorption parameters: the resonance absorption dump fraction $f_D = 0.3$, and the suprathermal spectral hardness parameter $\beta = 20$. Energy deposited via resonant absorption was about 32 J throughout. The total absorbed energy E_{ABS} is tabulated for Al and CH disks, and varies weakly.

			E_{ABS}(J)	
Model	f_t	f_s	Al	CH
E	0.03	1.0	40.7	36.8
F	0.03	0.03	40.3	36.0
G	0.01	0.01	38.4	35.3
H	0.003	0.003	39.7	36.2

Table 6-7. Summary of absorption models compared with sub-keV x-ray data in Fig. 6-16. Parameters varied are the resonance absorption dump fraction f_D and the coefficient of the inverse bremsstrahlung absorption opacity K_{IB}. These models have fixed transport parameters: the thermal flux limit $f_t = 0.03$, and the suprathermal flux limit $f_s = 1.0$. The suprathermal spectral hardness parameter $\beta = 20$. Energy absorbed for Al and CH disks is tabulated separately for resonant absorption and total absorption.

			E_{RA}		E_{ABS}	
Model	f_D	K_{IB}	Al	CH	Al	CH
E	0.3	1.0	31.3	32.2	40.7	36.8
I	0.1	0.5	10.7	10.8	16.1	14.0
J	0.055	0.35	5.9	6.0	9.9	8.3
K	0.03	0.25	3.2	3.3	6.2	5.0

alone seems somewhat extreme from a theoretical point of view.

An intermediate model, involving some reduction in absorption and some reduction in transport, produces nearly equivalent results, and is perhaps more justifiable. Using a preliminary Brillouin scattering model,[22] we calculate 20% absorption. Combining this with $f_t = f_s = 0.03$ results in agreement as good as has been achieved to date. This LASNEX modeling is compared in Table 6-8 with the three roughly equivalent models discussed here; a comparison of the results obtained using each of these models with the results of the experiment is presented in Table 6-9. We have performed calculations using reduced electron conductivity (instead of reduced flux limit), and obtained results very similar to the experimental data reported here. Still another alternative is modifying the collisional coupling rate of suprathermal electrons, but this is not noticeably better.

Fig. 6-15. Comparison of models with varying transport coefficients with sub-keV emission measurements from Al targets with varying CH coating thickness; model details are given in Table 6-6. Best agreement for 35% absorption is obtained with flux-limit reduction by a factor of 0.01 for both thermal and suprathermal electrons.

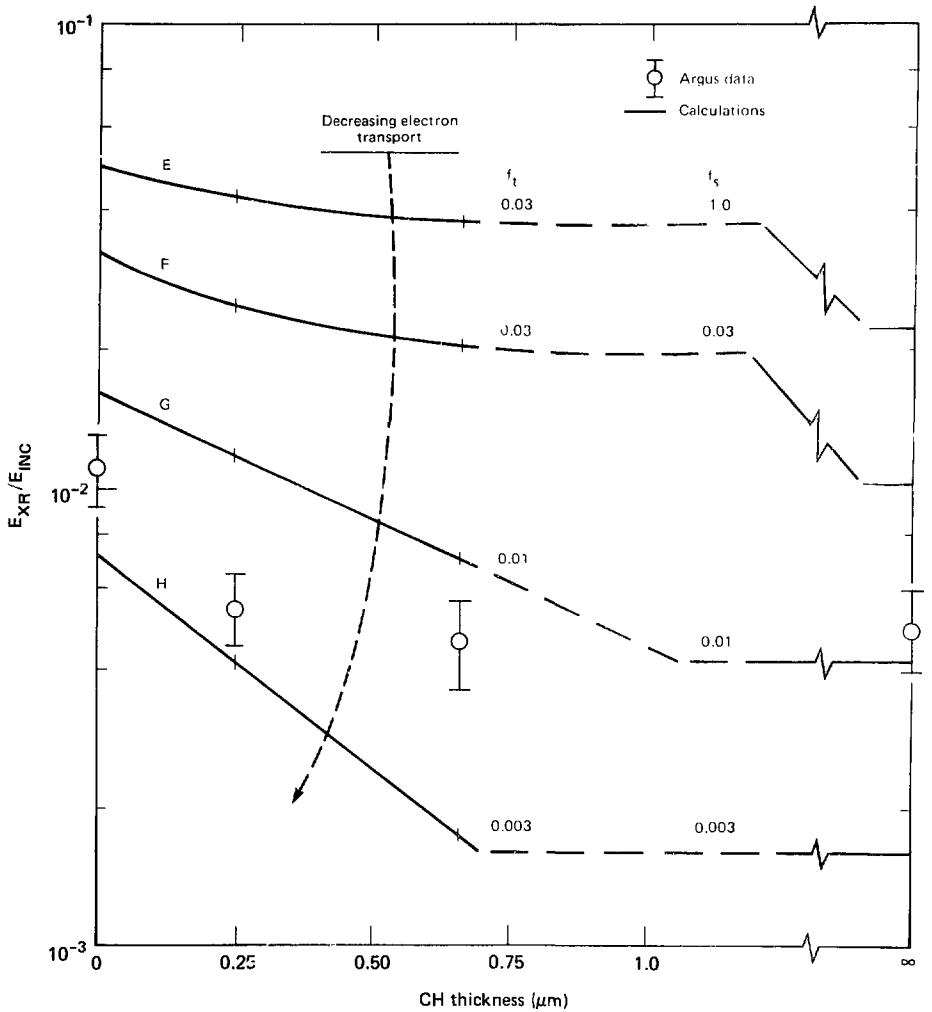

Summary

The recent layered-slab transport experiments have provided further, more quantitative evidence of strong transport inhibition in 100-ps, 10^{15} W/cm, 1.06-μm laser-produced plasmas. The experiments at Argus, under larger-spot irradiation conditions and using sub-keV x-ray diagnostics, have verified the attenuation depth measurement obtained at NRL. In addition, new high-energy x-ray measurements using the FFLEX and 7-shooter detector systems have raised intriguing questions about the

Fig. 6-16. Comparison of models with varying absorption with measured sub-keV emission from Al targets with varying CH coating thickness; model details are given in Table 6-7. Best agreement for 10% absorption is obtained with flux limit of 0.03 for thermal electrons and 1.0 for suprathermal electrons.

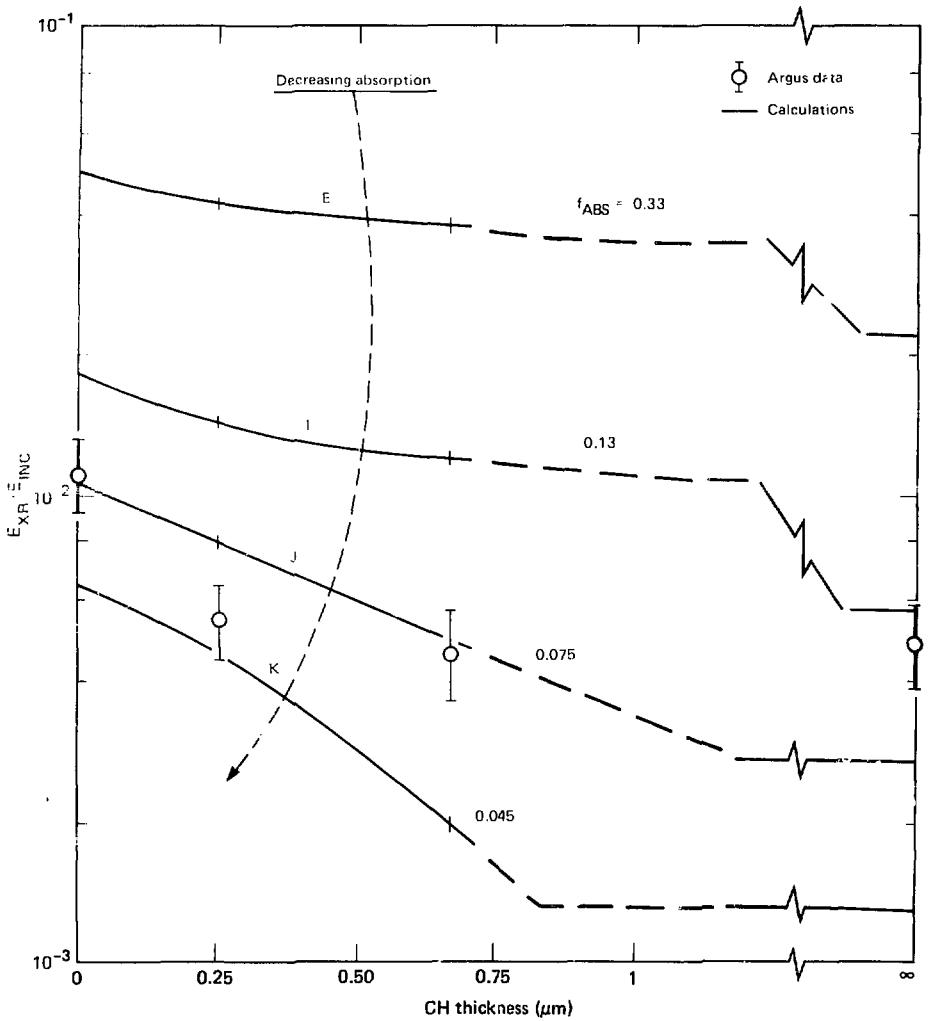

...gy-fraction and temperature of hot electrons. ... tional work is necessary, however, in order to ... both uncertainties in the experimental data ... discrepancies between the data and the results of LASNEX simulations.

LASNEX calculations of soft x-ray emission versus CH thickness that use standard model assumptions overestimate the attenuation depth by a factor of about 6, well outside the experimental uncertainties. Alternative assumptions can improve the attenuation-depth calculation somewhat, but

Table 6-8. Comparison of "standard" LASNEX model (A) used for previous interaction experiments with three alternative models which improve the modeling agreement with the Argus electron-transport experiment.

Model	f_D	β	K_{IB}	f_t	f_s	Comment
A	0.3	50	0.5-1.0	0.03	1.0	Previous work
G	0.3	20	1.0	0.01	0.01	Reduced transport
J	0.055	20	0.35	0.03	1.0	Reduced absorption
L	0.4[a]	20	1.0	0.03	0.03	Mixed, moderate changes

[a]This model utilized a preliminary treatment of Brillouin scattering, which reduces the energy incident on the critical surface by a factor of 1/3, thus reducing resonant absorption by 1/3 and inverse bremsstrahlung by 1/2.

Table 6-9. Summary of LASNEX model results and comparison with experiments. The models are described in Table 6-8 and the text. The attenuation depth measures the depth of a CH layer required over an Al target to make the sub-keV emission drop to CH-target levels [see Eq. (3)]. The emission ratio is the ratio of sub-keV emission energy from a pure Al target to the emission from a pure CH target.

Model	CH disk absorption fraction	Attenuation depth (μm)	Emission ratio
A	0.33	0.7	3.0
G	0.35	0.5	3.9
J	0.075	0.6	4.0
L	0.15	0.5	5.2
Experiment	0.15 to 0.35	0.11 ± 0.07	2.4 ± 0.4

overall agreement with the sub-keV x-ray measurements is not much improved.

Further work needs to be done in several areas: experimental checks of absorption and high-energy x-ray fluence are required; calculational checks and other models must be pursued; still other parameter regimes must be examined as well, to determine electron-transport properties in situations more relevant to future laser fusion targets.

Authors: D. L. Banner and W. C. Mead
Major Contributors: E. M. Campbell and W. L. Kruer

References

11. F. C. Young, R. R. Whitlock, R. Decoste, B. H. Ripin, D. J. Nagel, J. A. Stamper, J. M. McMahon, and S. E. Bodner, "Laser-Produced Plasma Energy Transport Through Plastic Films," *Appl. Phys. Lett.* **30**, 45 (1977).
12. B. Yaakobi and T. C. Bristow, "Measurement of Reduced Thermal Conduction in (Layered) Laser-Target Experiments," *Phys. Rev. Lett.* **38**, 350 (1977).
13. G.H. Dahlbacka, "Calculation of e⁻ Transport Coefficients in Layered Target Laser Plasmas," *Bull. Am. Phys. Soc.* **21**, 1028 (1976).
14. *Laser Program Annual Report—1977*, Lawrence Livermore Laboratory, Livermore, Calif., UCRL-50021-77 (1978), pp. 6-7 to 6-11.
15. *Laser Program Annual Report—1978*, Lawrence Livermore Laboratory, Livermore, Calif., UCRL-50021-78 (1979), pp. 6-5 to 6-7.
16. H. N. Kornblum and V. W. Slivinsky, *Rev. Sci. Instrum.* **49** 1204 (1978).
17. *Laser Program Annual Report—1978*, Lawrence Livermore Laboratory, Livermore, Calif., UCRL-50021-78 (1979), pp. 6-2 to 6-5.
18. *Laser Program Annual Report—1978*, Lawrence Livermore Laboratory, Livermore, Calif., UCRL-50021-78 (1979), pp. 6-8 to 6-12.
19. C. L. Wang, H. N. Kornblum, and V. W. Slivinsky, *Angular Distribution of Suprathermal X Rays from Laser Produced Plasma*, presented at the APS Plasma Physics Meeting, Boston, Mass., November 12 to 16, 1979.
20. R. A. Haas, W. C. Mead, W. L. Kruer, D. W. Phillion, H. N. Kornblum, J. D. Lindl, D. MacQuigg, V. C. Rupert, and K. G. Tirsell, "Irradiation of Parylene Disks with a 1.06 μm Laser," *Phys. Fluids* **20**, 322 (1977).
21. M. D. Rosen, D. W. Phillion, V. C. Rupert, W. C. Mead, W. L. Kruer, J. J. Thompson, H. N. Kornblum, V. W. Slivinsky, G. J. Caporaso, M. J. Boyle, and K. G. Tirsell, "The Interaction of 1.06 μm Laser Radiation with High Z Disk Targets," *Phys. Fluids* **22**, 2020 (1979).
22. K. G. Estabrook and J. V. Harte, "On Reducing Brillouin Scatter," Lawrence Livermore Laboratory, Livermore, Calif., UCRL-82620, 1979 (to be published).

Z-Dependence of Sub-keV X-Ray Emission and Laser Intensity Threshold for Inhibited Electron Thermal Conduction

Electron thermal conduction inhibition is a simple mechanism for regulating x-ray emission.[23] The laser light is absorbed at and below the critical density surface, which two-dimensional LASNEX[24] numerical simulations indicate is 50 to 100 μm from the original target surface at the time of peak laser intensity. On the other hand, most of the sub-keV x rays are emitted from the denser ablation layer

within 20 μm of the original disk-target surface. The absorbed laser energy must be transported by electron conduction from the underdense plasma to the overdense plasma. A decrease in electron thermal conductivity reduces the energy available for low-energy x-ray emission from the dense ablation layer.

Two-dimensional LASNEX simulations also indicate that when the heat flux is inhibited, the plasma corona becomes hotter by 50 to 100% compared to the uninhibited case; the corona temperature is 3 to 4 keV instead of ~2 keV. When inhibition occurs and the low-energy x-ray emission from the overdense region is therefore reduced, the rise in the corona temperature will result in additional x-ray emission in a higher energy range.

There is substantial experimental evidence (see Refs. 23, 25–33) that electron heat conduction is inhibited in plasmas produced by 1.06-μm laser intensities above 10^{14} W/cm^2. Discussions of mechanisms likely to inhibit electron thermal conduction in laser-irradiated targets have suggested self-generated magnetic fields,[34] ion acoustic turbulence,[35] and electrostatic fields set up by suprathermal electrons.[36] Data concerning the dependence of inhibition on parameters such as laser intensity, pulse width, wavelength, spot size, target material, and beam uniformity should contribute to a better theoretical understanding of conduction inhibition and help determine the dominant mechanism(s). Here we report our study of one such parameter, the dependence of inhibition on target Z.

Experimental Data

We have conducted a preliminary study of the Z-dependence of sub-keV x-ray production from laser-produced plasmas at Argus,[37] using one beam at a nominal laser pulse of 800 J for 1 ns FWHM; the typical intensity on the target was 5×10^{14} W/cm^2. The targets consisted of disks from 600 to 700 μm in diameter and from 12.7 to 25 μm thick. Target materials consisted of beryllium, aluminum, titanium, tin, gold, and uranium, with atomic numbers (Z) ranging from 4 to 92. The targets were irradiated with f/2.2 focusing optics; the incidence angle was 30°, and the incident beam was linearly polarized 12° out of the plane of incidence.

A 10-channel filtered x-ray detector system called Dante-T (Ref. 38) was used to record the sub-keV emission from the laser-irradiated targets. Dante-T viewed the x-ray emission at an angle of 60° from the target surface normal, in the plane of incidence away from the incident beam. The solid angle subtended by each detector channel was 2.11×10^{-5} steradians for the four lower energy channels and one flat response channel, and 4.36×10^{-5} steradians for the five higher energy channels.

One of the interesting results of this experimental series is the systematic Z-dependence of the time-resolved sub-keV x-ray emission, as shown in Fig. 6-17. The data were obtained for the 300-to-520-eV channel, with a time resolution of better than 190 ps. Note that as the target Z decreases (from uranium to beryllium, for example), for the same Gaussian laser pulse shape the x-ray pulse shape deviates from a smooth "Gaussian" to an irregular shape; the peak of the pulse becomes progressively

Fig. 6-17. Typical x-ray emission signals from disk targets ranging from Z = 4 to Z = 92, illuminated with 1.06-μm laser light at 5×10^{14} W/cm^2 with a pulse of 1 ns FWHM. A vanadium filter (L-edge at 520 eV) was used with an aluminum photocathode; time resolution is 190 ps.

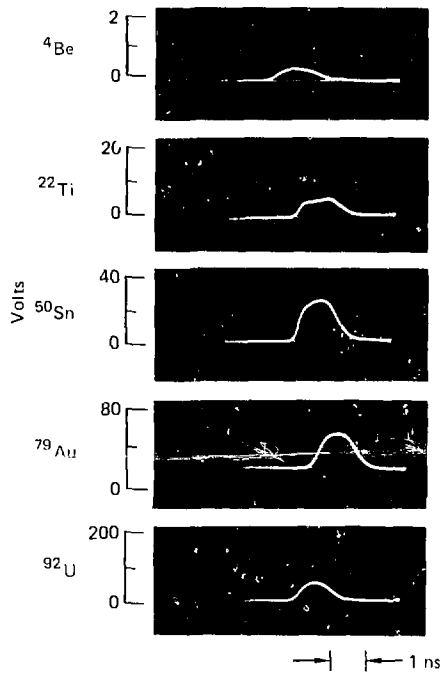

Fig. 6-18. The results of two Ti disk targets, for the same laser conditions as in Fig. 6-17. A copper filter (L-edge at 940 eV) was used with a chromium photocathode; time resolution is 170 ps. Note the oscillations in the "flattened" portion of the x-ray emission pulse.

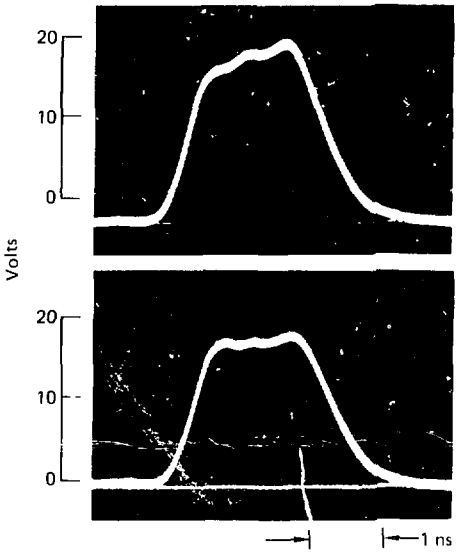

Fig. 6-19. X-ray emission signals from gold disks illuminated with 800 J for 1 ns with intensity of (a) 5×10^{14} W/cm^2 and (b) 3×10^{15} W/cm^2. A copper filter (L-edge at 940 eV) was used with a chromium photocathode; time resolution is 170 ps. The negative-going signal in each trace is a time fiducial.

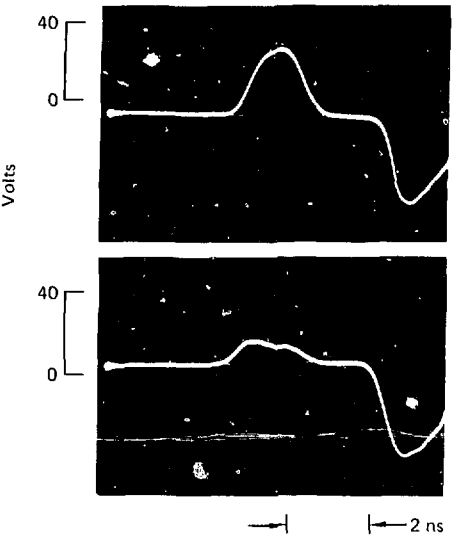

flattened as Z decreases. The transition is shown most clearly by a titanium target, whose x-ray emission starts to increase rapidly (presumably following the rise of the incident laser intensity), then at a well-defined point changes abruptly to a show "linear" rise, and then drops after 1 ns (a channel with higher resolution shows that there are oscillations in the "linear" rise region; see Fig. 6-18).

X-ray emission pulses for the same Z material can be quite different at different laser intensities; this is shown in Fig. 6-19 for gold disks. The data in this figure were obtained from the 650-to-940-eV channel, with a time resolution of better than 170 ps. Note that the x-ray emission pulse at the lower laser intensity (5×10^{14} W/cm^2) is fairly smooth, but at a higher laser intensity (3.3×10^{15} W/cm^2) the x-ray emission pulse rises normally at first, then breaks away abruptly.

A sample of some typical low-energy x-ray spectra is given in Fig. 6-20. The spectral shapes of different materials are quite distinct and can be readily reproduced by code calculations. The same is true for low-Z materials such as aluminum and beryllium, which latter material shows a much faster spectral decay with increasing x-ray energy. The titanium spectrum is quite different from the other spectra in the figure, in the sense that in the energy band from about 500 to 800 eV there are strong L-line emissions. On the other hand, the small bump near 700 eV in the aluminum spectrum is most probably due to an oxygen line, since an aluminum-oxide layer forms quite readily on an aluminum target.

Figure 6-21 shows how well code calculations are able to reproduce the features of the measured spectrum for a titanium target. Because of the presence of the L-lines of a titanium target, it was possible to use the data on relative line intensities of Kelly and Palumbo[39] to obtain a dominant charge state from the measured spectrum, which in this

Fig. 6-20. Sample low-energy x-ray spectra for U, Ti and Al disk targets, illuminated at 5×10^{14} W/cm^2 with a pulse of 1 ns FWHM. Note that the lowest energy channel has the largest error bar.

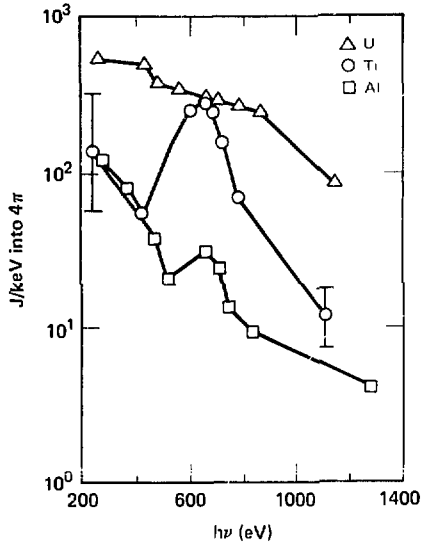

Fig. 6-21. Comparison of measured and code-calculated Ti spectrum. Z is the charge state of the Ti plasma; intensity and pulse length are same as in Fig. 6-20.

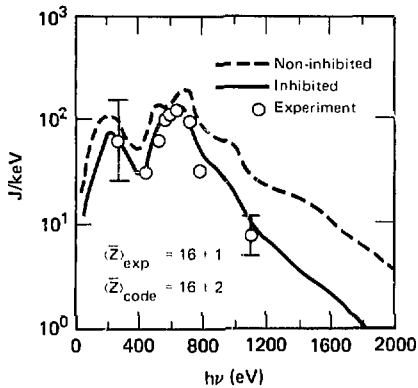

case was $Z_{exp} = 16 (\pm 1)$. Also, numerical simulations can obtain the average ionic charge in a computational zone with maximum x-ray emission power. The computed charge state was $Z_{code} = 16 (\pm 2)$; the ± 2 does not represent an error bar in the calculation, but indicates the variation in Z over the FWHM of the x-ray emission region.

The integrated x-ray energy from ~100 eV to 1.8 keV can be obtained from the Dante-T signals. The integrated x-ray energy normalized by the incident laser energy is plotted against target Z in Fig. 6-22. Since sub-keV x rays away from the energy regions dominated by line emission are presumably generated by bremsstrahlung of low-energy electrons, these low-energy electrons actually see a screened nucleus; therefore it would perhaps be more meaningful to plot the normalized x-ray energy as a function of Z, where Z is the code-calculated charge state. It is interesting to note that the normalized x-ray energy is almost linear with respect to Z. This result is quite similar to the bremsstrahlung data obtained with an ordinary thick-target x-ray tube with x-ray energy proportional to target Z,[40] the difference being that the x-ray energy produced per unit of incident laser energy is 1 to 2 orders of magnitude larger than the x-ray energy produced per unit of cathode-ray energy.[41]

Analysis

The existence of an intensity threshold for electron transport inhibition has been clearly demonstrated by Pearlman and Anthes,[27] with measurements of the front and rear plasma thermal expansion velocities from a thin polystyrene film. We extend the idea of an intensity threshold for inhibited conduction to include a Z-dependence of the threshold.

From the time-resolved x-ray data in Figs. 6-17, 6-18, and 6-19 we interpret the temporal behavior of the sub-keV x-ray emission as showing the onset of strongly inhibited electron thermal conduction during the rise of laser intensity. As the Z of the target material is reduced, this strong conduction inhibition occurs earlier, that is, at lower laser intensity.

The systematic variation of the x-ray pulse shape with Z (Fig. 6-17) indicates that the plasma process involved has a laser intensity threshold which increases with Z. Figure 6-19 can now be explained: initially the two pulses rise similarly, but the emission from the higher intensity shot abruptly

Fig. 6-22. X-ray energy for various targets as a function of target Z and charge state $\bar{Z}$, at incident intensity of 5×10^{14} W/cm^2. Error bars for values of $E_{x\text{-ray}}/E_{laser}$ are all ~±25%.

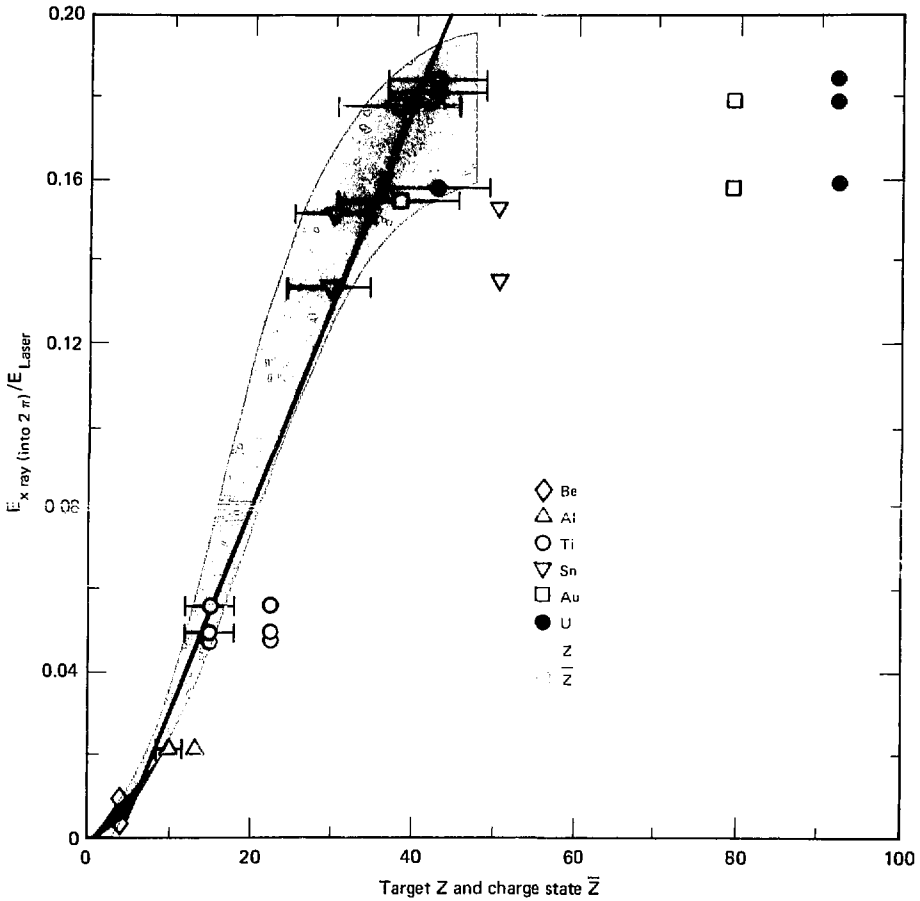

falls away as the threshold is crossed. This kind of behavior appears in all the Dante-T x-ray energy channels. Only a small part of this reduction in x-ray emission at the higher intensity is due to reduced absorption of the incident laser light, since the time-integrated x-ray emission drops by 60% while the time-integrated absorption[23] drops by only 25%. Of course a change in the absorption mechanism has not been ruled out. Anomalous absorption in the far underdense plasma would shift the energy flow away from the overdense plasma toward more energetic plasma blowoff: a buildup of ion acoustic turbulence with increased laser intensity, for example, might simultaneously increase inhibition and cause anomalous absorption.[42]

There are both theoretical and experimental reasons for believing that the variations in pulse shape shown in Fig. 6-17 are not a consequence of atomic structure differences of the targets. Numerical simulations with classical electron thermal conduction and non-LTE ionization physics

Fig. 6-23. Sub-keV x-ray emission spectra from gold disks at different intensities.

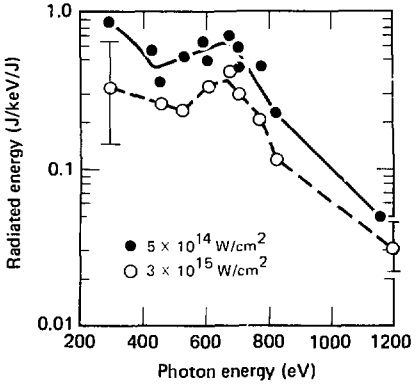

Fig. 6-24. Strongly inhibited electron thermal conduction threshold vs Z of the target material; solid data point in lower left is from Ref. 27.

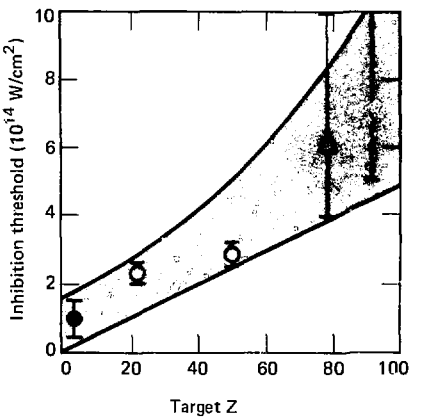

reproduce the qualitative features of the observed 0.2-to-1.5-keV x-ray spectra for all of the elements (see, for example, the Ti spectrum in Fig. 6-21), but show no deviations from a smooth, Gaussian-like time-dependence for the x-ray emission pulses.[24,42] Experimentally, the data for gold disks above and below the laser intensity threshold are decisive: in spite of a reduction in radiated energy by a factor of 2.5 for the higher intensity and a dramatic change in the x-ray emission pulse shape (Fig. 6-19), we observed only ±15% changes in the 0.2-to-1.5-keV spectral shape (Fig. 6-23). Thus, there is no correlation between atomic structure (as indicated by x-ray spectra) and the temporal behavior of the x-ray emission.

From the data of Fig. 6-19, the laser intensity threshold for gold is estimated to be $(6^{+4}_{-2}) \times 10^{14}$ W/cm^2. Even though the data of Fig. 6-17 lack time fiducials, it is clear that the threshold for uranium is greater than 5×10^{14} W/cm^2 and that rough estimates of the thresholds for titanium and tin may be made. These results, and the threshold for polystyrene from Ref. 27, are plotted in Fig. 6-24.

Effects such as Z-dependent absorption of laser light and angular distribution of x rays can influence the interpretation of experimental results; preliminary absorption measurements, however, indicate that absorption has a weak Z-dependence (Fig. 6-25). Also, code calculations seem to indicate that the Z-dependent angular distribution does not affect the data interpretation too much, because of the angle (60° with respect to target normal) at which the measurements were made. The numerical simulation result of 300-to-500-eV x-ray angular distributions is shown in Fig. 6-26.

Calculated x-ray emission pulses from Ti are shown in Fig. 6-27 for three models of the plasma electron thermal conductivity. Curves A and B are typical of standard models in that they produce Gaussian-like pulses only 10 or 20% wider than the incident laser pulse. Curve C was produced by applying a time-varying multiplier to the Spitzer conductivity chosen to reproduce the 1.8-ns FWHM and flat-topped shape of the x-ray data. Above threshold, the conductivity multiplier required by the simulation varied inversely with the 3/2 power of absorbed intensity for both the rising and falling parts of the laser pulse, with a value of about 0.2 at 10^{14} W/cm^2 absorbed intensity. This result is not unique, since the laser light absorption vs time has not been measured. It does show, however, that intensity-dependent conduction inhibition can produce the observed x-ray emission.

Since more than one inhibition mechanism may be operating, we do not rule out inhibition below the threshold of Fig. 6-19. In fact, the data presented here are consistent with previous results[23] which showed the need for some inhibition in gold even at 3×10^{14} W/cm^2.

Fig. 6-25. Plot of absorption fraction (at 5×10^{14} W/cm^2) vs Z; note that suprathermal electrons constitute only a few percent of the absorbed energy for 1-ns pulses.

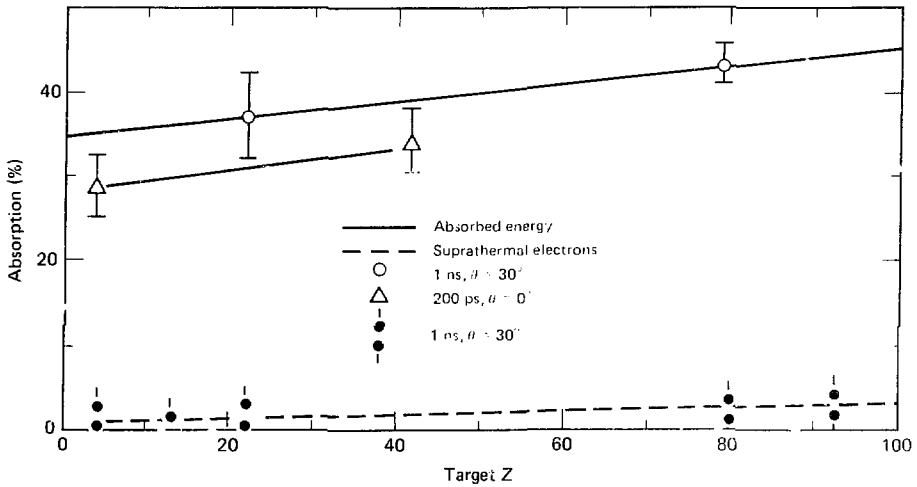

Fig. 6-26. Numerical simulations of the 300-to-500-eV x-ray angular distributions. The Dante-T value at $\theta = 60$ extrapolated to 2π sr gives total radiated energy within a few percent.

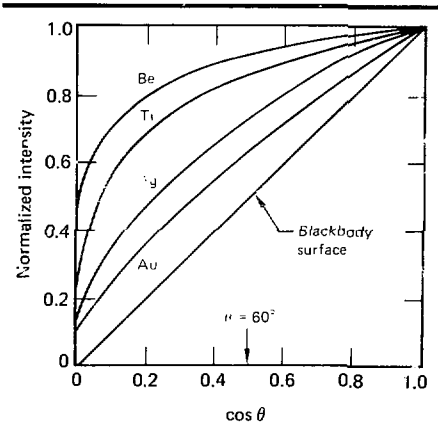

Fig. 6-27. X-ray emission vs time, taken from numerical simulations of a Ti disk illuminated with a 1-ns FWHM Gaussian pulse with peak intensity of 5×10^{14} W/cm^2 at time = 0. The three curves correspond to models of plasma electron thermal conductivity using (a) flux-limited diffusion with classical Spitzer conductivity, (b) a flux limit reduced by ion acoustic turbulence, and (c) a global conductivity multiplier varied in time to reproduce the experimentally observed x-ray emission.

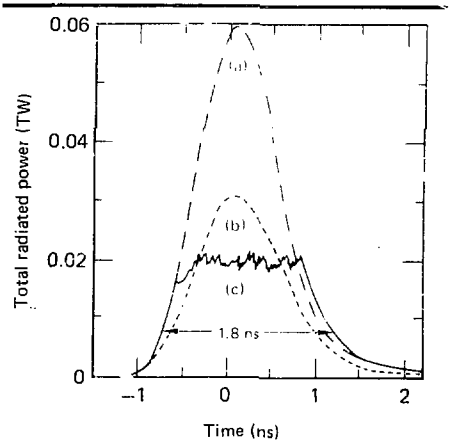

Conclusion

We have described the temporal behavior of the sub-keV x-ray emission from 1.06-μm laser-illuminated disk targets of fixed spot size at an in-

tensity of 5×10^{14} W/cm^2. Abrupt temporal variations in the radiated power as the laser intensity rises have been interpreted as showing the onset of strongly inhibited electron thermal conduction in the laser-produced plasma. The laser intensity threshold for this effect is shown to increase with the Z of the target. Consequently, for a fixed laser intensity of a few times 10^{14} W/cm^2, electron thermal conduction is more strongly inhibited for low-Z targets than for high-Z targets.

Authors: P. H. Y. Lee and G. E. McClellan
Major Contributors: K. G. Tirsell, E. M. Campbell, G. Caporaso, and M. D. Rosen

References

23. M. D. Rosen et al., *Phys. Fluids* **22**, 2020 (1979).
24. G. B. Zimmerman, *Numerical Simulations of the High Density Approach to Laser Fusion*, Lawrence Livermore Laboratory, Livermore, Calif., UCRL-74811 (1973).
25. R. C. Malone, R. L. McCrory, and R. L. Morse, *Phys. Rev. Lett.* **34**, 721 (1975).
26. B. H. Ripin et al., *Phys. Rev. Lett.* **34**, 1313 (1975).
27. J. S. Pearlman and J. P. Anthes, *Appl. Phys. Lett.* **27**, 581 (1975).
28. B. Yaakobi and A. Ne, *Phys. Rev. Lett.* **36**, 1077 (1976).
29. W. C. Mead et al., *Phys. Rev. Lett.* **37**, 489 (1976).
30. F. C. Young et al., *Appl. Phys. Lett.* **30**, 45 (1977).
31. B. Yaakobi and T. C. Bristow, *Phys. Rev. Lett.* **38**, 350 (1977).
32. P. M. Campbell, R. R. Johnson, F. J. Mayer, L. V. Powers, and D. C. Slater, *Phys. Rev. Lett.* **39**, 274 (1977).
33. R. Benattar, C. Popovics, R. Sigel, and J. Virmont, *Phys. Rev. Lett.* **42**, 766 (1979).
34. J. A. Stamper et al., *Phys. Rev. Lett.* **26**, 1012 (1971); for an extensive review see J. A. Stamper, *U.S. Naval Research Laboratory Report No. 3872*, 1978 (unpublished).
35. D. W. Forslund, *J. Geophys. Res.* **75**, 17 (1970); R. Bickerton, *Nucl. Fusion* **13**, 457 (1973).
36. F. J. Valeo and I. R. Bernstein, *Phys. Fluids* **19**, 1348 (1976).
37. W. W. Simmons et al., *Appl. Opt.* **17**, 999 (1978).
38. K. G. Tirsell, H. N. Kornblum, and V. W. Slivinsky, *Bull. Am. Phys. Soc.* **23**, 807 (1978).
39. R. L. Kelly and L. J. Palumbo, *U.S. Naval Research Laboratory Report No. 7599*, (June 1973).
40. E. U. Condon and H. Odishaw, eds., *Handbook of Physics* (McGraw Hill, New York, 1967), 2nd ed. p. 7-127.
41. A. H. Compton and S. K. Allison, *X RAYS in Theory and Experiment* (Van Nostrand Co., New York, 1957), p. 89.
42. R. J. Faehl and W. L. Kruer, *Phys. Fluids* **20**, 55 (1977); W. M. Manheimer, D. G. Colombant, and B. H. Ripin, *Phys. Rev. Lett.* **38**, 1135 (1977).

High-Energy X-Ray Measurements From Disks of Different Z

We have traditionally measured high-energy (20 keV $\lesssim h \lesssim$ 100 keV) x rays to gather information about suprathermal electrons produced in the laser-plasma interaction.[43] During the last year we have made such measurements at Argus, as part of the long-pulse ($t \sim 0.9$ ns), variable-Z disk experiments. The primary diagnostic was a 6-channel filter fluorescer (FFLEX) spectrometer located in the plane of incidence and 14.5° from the plane of polarization.[44] The six energy channels were located at 20, 29, 50, 54, 70, and 88 keV. Due to the low flux obtained from the majority of the targets, four of the six channels employed only K-edge filters; in view of the rapidly falling spectra that were recorded, however, there was little difficulty in assigning accurate energy bins to the different channels. The targets were rotated 30° with respect to the laser axis with the beam incident near p-polarization. The filter fluorescer viewed the targets at an angle of 25° to the disk normal. The geometry of the experiment is shown in Fig. 6-28.

Samples of the data collected for plasmas with low (Be), intermediate (Ti), and high (U) Z are shown in Fig. 6-29. The peak intensity incident on the targets ranged from 3 to 5×10^{14} W/cm^2. The

Fig. 6-28. Experimental geometry for long-pulse, high-energy x-ray measurements using a 6-channel filter fluorescer detector.

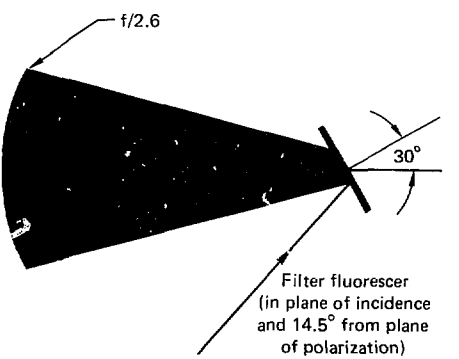

flux from these targets scales roughly linearly with nuclear charge Z, as we would expect for high-energy-electron, thick-target bremsstrahlung. Bremsstrahlung emission scales with Z^2 whereas stopping power scales with Z.[45] To illustrate this Z-dependent scaling, Fig. 6-29 gives the expected flux from Ti and U (dashed lines) based on the Be data (solid line), assuming identical electron spectra and absorption of light independent of target Z.

The data also suggest a hardening of the spectrum as the target Z increases (e.g., compare Be and U). This trend is in qualitative agreement with theoretical expectations based on recirculation of the hot electrons through the heating region at critical density, due to the target albedo increasing with Z (with a predicted scaling of $Z^{1/4}$).[46]

The experimental results for these long-pulse irradiations also show the difficulty in describing the spectrum as a simple exponential with a slope defined as θ_H^{-1}. This is most clearly evidenced by the titanium data, whose spectrum can be described as both a hot tail and a superhot tail. The latter component could possibly arise from processes such as Raman scattering and $2\omega_{pe}$ decay, occurring at one-quarter critical density.[47]

To unfold from the measured x-ray spectrum both the electron spectrum and the energy absorbed via collective processes requires the use of any assumptions which cannot be as yet verified experimentally. Interpretation of experimental results is affected, for example, by the shape of the electron distribution, by coronal losses, and by isotropy of the x-ray emission. Nonetheless, if we ignore coronal losses and assume both isotropy of x-ray emission and a Maxwellian electron distribution characterized by θ_H, the measured flux levels suggest that for all the Z materials only $\lesssim 1\%$ of the incident energy appears in suprathermal electrons for these moderate-intensity, long-pulse irradiations. Calculations indicate that coronal losses may account for 80% of the suprathermal energy, however, and thus the hot-electron fraction suggested by the x-ray flux should be viewed only as a lower bound.

A full understanding of suprathermal electron generation under these irradiation conditions will require more sophisticated experimentation, to measure the electron spectrum, determine coronal losses, examine the Raman and $2\omega_{pe}$ instabilities, and ascertain the isotropy of the x-ray emission.

Fig. 6-29. High-energy x-ray emission as a function of Z; Z scaling at flux normalized to Be. Curves for Ti and U (dashed lines) are expected fluxes, based on measured Be data (solid line).

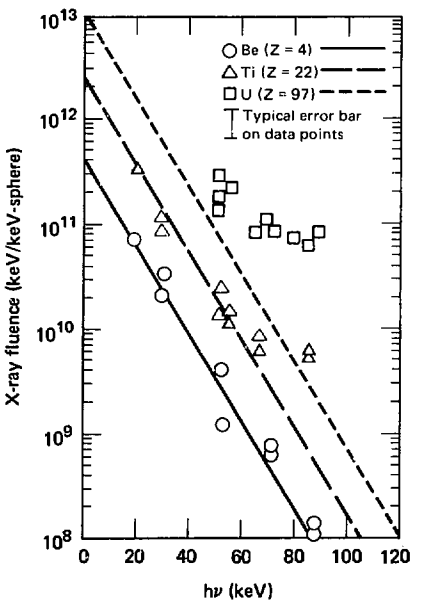

Author: E. M. Campbell
Major Contributors: S. M. Lane, B. L. Pruett, and H. N. Kornblum

References

43. P. A. Haas, W. C. Mead, W. L. Kruer, D. W. Phillion, N. H. Kornblum, J. D. Lindl, D. MacQuigg, V. C. Rupert, and K. G. Tirsell, *Phys. Fluids* **20**, 332 (1977).
44. H. N. Kornblum, B. L. Pruett, K. G. Tirsell, and V. W. Slivinsky, "Filter Fluorescer Experiments on Argus Laser," presented to the Division of Plasma Physics at the Meeting of the American Physical Society, Colorado Springs, Colo. (1978).
45. J. D. Jackson, *Classical Mechanics* (New York: Wiley & Sons, 1962), p. 513.
46. K. Estabrook, M. D. Rosen, *Bull. Am. Phys. Soc.* **24**, 8 (1979).
47. J. R. Albritton, *Bull. Am. Phys. Soc.* **24**, 8 (1979).

Angular Distribution of Suprathermal X Rays

The angular distribution of suprathermal x rays emitted from laser-produced plasmas has generally been assumed to be isotropic, except for thick targets; the total x-ray emission energy has usually been calculated simply by multiplying the energy-integrated spectrum by 4π. The angular distributions of low-energy x rays and ions from such plasmas are anisotropic,[48,49] however, and for some laser conditions the fast electrons produced in laser-gas interactions are also directional, due to the resonance absorption effect.[50] It is therefore both interesting and important to measure the angular distribution of high-energy x rays from laser-produced plasmas.

Some details of our measurement geometry are shown in Fig. 6-30. We placed eight x-ray detectors in Shiva target chamber ports located at an azimuthal angle $\phi = 126°$ and at polar angles ranging from $\phi = 45$ to 148°; the target is located at the origin of the coordinate system in the figure. The detectors consist of a Be-windowed NaI(Tl) crystal 50.8 mm in diameter and 32 mm thick, coupled to a photodiode with S-20 response. Behind the 0.64-mm Be window on the target chamber is a 0.1-mm Cu filter, followed by a Ta collimator 4.8 mm thick with an opening 36.1 mm in diameter (the collimeter is not shown in the figure). A typical response of the detector system is given for a flat x-ray spectrum in Fig. 6-31. The cutoff of the low-energy x rays is determined by the 50% transmission of the Cu filter, at 37 keV. The calibrated sensitivities of the eight detectors varied up to 40% for x-ray energies between 8 and 97 keV.

Fig. 6-30. Experimental geometry for measurements of high-energy x-ray angular distribution. Shiva laser beams are incident on the target (at the origin of the coordinate system) from above and below; only one of eight detectors is shown.

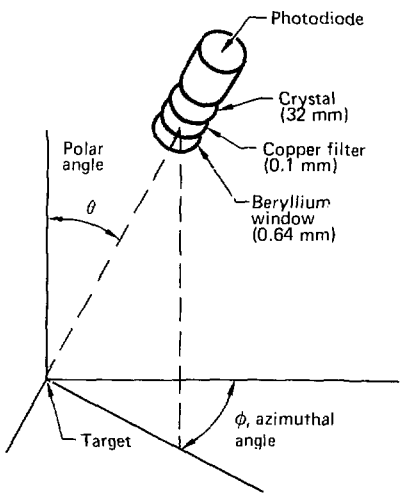

Fig. 6-31. Sample detector response to a flat x-ray spectrum.

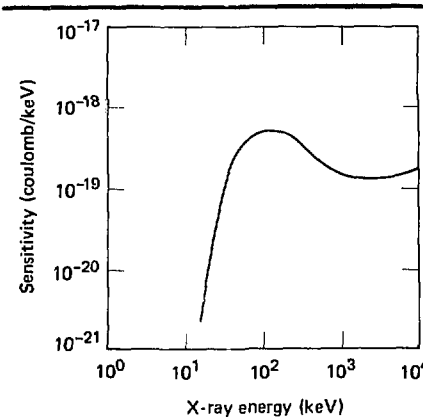

Figure 6-32 shows the measured suprathermal x-ray angular distribution normalized at 90°, from gold disks 600 μm in diameter and 15 μm thick, and from a glass microsphere 149 μm in diameter and 6.4 μm thick filled with D-T gas. The angular distribution shows two strong peaks, one at about 60° and the other at about 105°. That different targets gave similar angular distribution tends to suggest that the minimum at 90° is not due to absorption of x rays in the plane of the gold disks.

Any such unexpected result is initially suspect, however, and we tried many variations of the experiment to confirm the effect. We switched detectors, filters, cables, scopes, etc., to check any possible systematic errors, and added 0.813-mm Al filters behind the Cu filters to remove any possible K-edge effect from the Cu. Interposing Pb filters 0.5 mm

Fig. 6-32. Angular distribution of suprathermal x rays normalized at 90°, from gold disks and a D-T-filled glass microsphere. Note the uniform peak distribution at 60° and 105°.

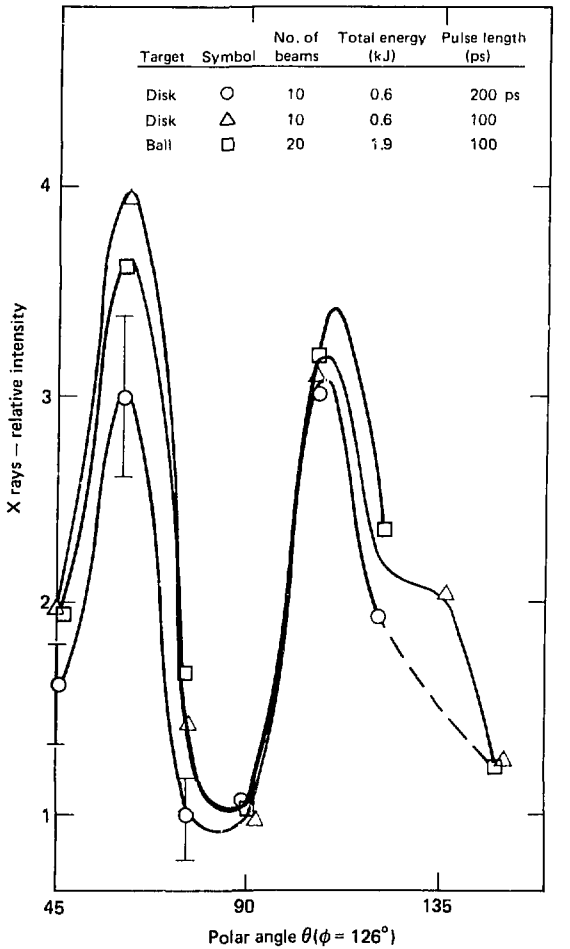

We next conducted a series of single-beam shots to study the possible dependence of the peaks on the polarization or electric vector of the laser light; no such dependence was observed. This result is shown in Fig. 6-33, in which $\Delta\phi°$ and $\Delta\theta°$ (E) refer respectively to the change in the polarization angle and the change in the electric vector direction of each beam with respect to beam 13. The detectors are located in the plane of polarization of beam 13. Generally the x-ray peak on the same side of the incident beams is stronger than the peak at the opposite side of the gold disk; i.e., the peak at 60° is stronger than at 105° for beams 13, 11 and 17, which are incident from θ near 0°.

In order to see the angular distribution visually, a stack of 50-mm-by-50-mm x-ray films behind a 0.1-mm Cu filter was placed 30 mm (at ϕ = 162°, θ = 105°) from a gold disk (Figs. 6-34 and 6-35). The orientation of the target and film pack is shown in Fig. 6-35. The target was irradiated at 2.8×10^{14} W/cm^2 with the upper 10 Shiva beams; sample results are given in Fig. 6-34, which shows (a) the density distribution of the x-ray deposition on R-type film, and (b) the density profile along a horizontal line at the center of the film image. The profile was not corrected for the varying distance and incident angle of x rays on the film from the target.

thick reduced the signal more than tenfold, but the peaks remained. In some experiments we used all 20 Shiva beams, in others we used only 10. We also varied the pulse length and beam energy. Installing powerful magnets capable of removing 30-MeV electrons from the paths to the x-ray detectors had no effect, indicating that the signal came from photons, not electrons.

In another shot, a stack of 18-mm-by-92-mm film strips was placed 50 mm (at ϕ = 198°, θ = 90°) from a gold disk target. The film strips were curved so that their surfaces were at equal distances from the target and covered 110° (θ = 35° to 145°).

Fig. 6-33. Angular distribution of suprathermal x-ray emission from single-beam shots on gold disks, again showing peak distributions at 60° and 105°.

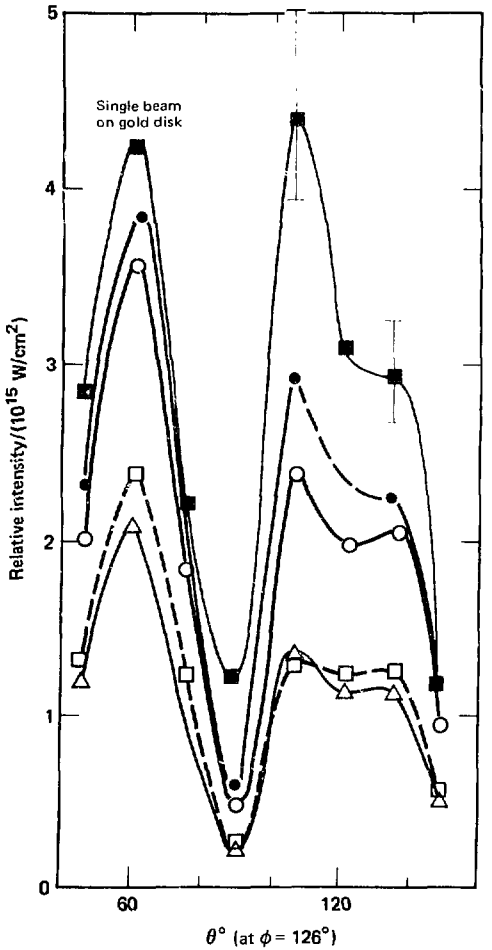

Beam	Energy (J)	Intensity (10^{15} W/cm^2)
13 □	207	2.11
13 ○	191	1.77
11 △	209	2.13
17 ●	247	2.52
3 ■	219	2.03

Beam	Δφ°	Δθ° (E)
13	0	0
11	72	7.7
17	36	17.4
3	0	0

Target normal was pointing at $\theta = 30°$ and $\phi = 90°$, and the target was irradiated at 10^{16} W/cm^2 with the lower 10 Shiva beams. The geometry of this configuration is shown in Fig. 6-36; results are given in Fig. 6-37. Note the strong peak at $\theta \approx 105°$. The shallow dip in the intensity profile is due to absorption of x rays in the target plane.

In conclusion, our film exposures indicate that there are definitely peak structures in the x-ray angular distribution, but exact correlation with the result of NaI detectors has yet to be established. It is not clear at present what mechanism may be responsible for generating the observed angular dis-

Fig. 6-34. (a) Density distribution of the x-ray deposition on R-type film, based on the target-film configuration in Fig. 6-34 with incident laser intensity of 2.8×10^{14} W/cm^2. (b) Density profile along a horizontal line at the center of the film image.

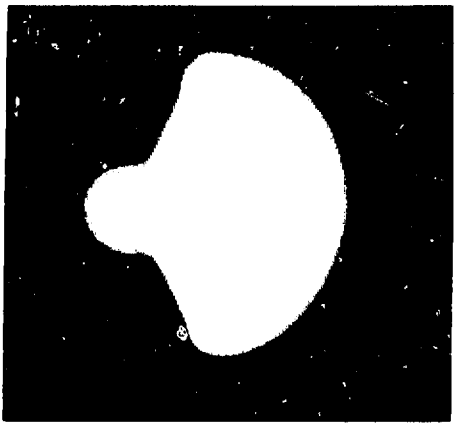

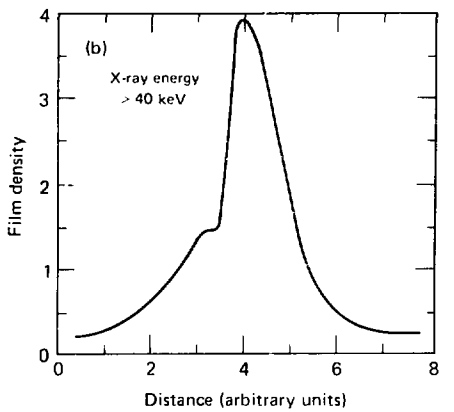

tribution. If our measurements are valid, however, then our previous estimate of the total energy in hot electrons (assuming isotropy) may be seriously in error. To explore this possibility we have now fabricated a film cylinder 230 mm in diameter and 305 mm long, which will enable us to cover a large solid angle and thus conduct a more systematic x-ray film study of x-ray angular distribution.

Author: C. L. Wang
Major Contributors: H. N. Kornblum, G. R. Liepelt, K. D. Poor, and V. W. Slivinsky

Fig. 6-35. Experimental orientation of a gold disk target and x-ray film pack.

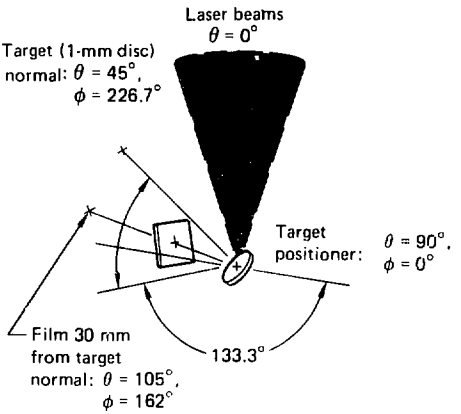

Fig. 6-36. Experimental orientation of a gold disk target and an x-ray film pack curved to expose the film surface at a uniform distance from the target.

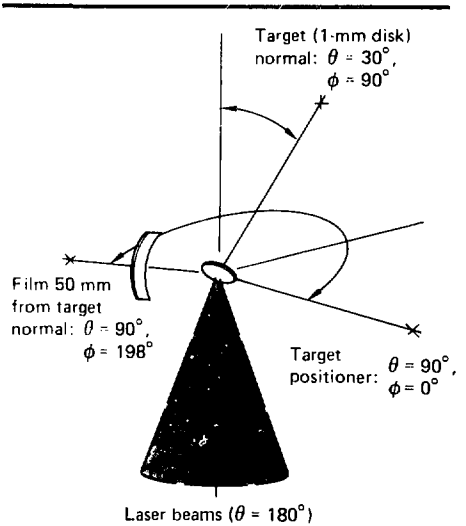

Fig. 6-37. (a) Density distribution of the x-ray deposition on R-type film, based on the target-film configuration in Fig. 6-36 with incident laser intensity of 10^{16} W/cm^2. (b) Density profile along a horizontal line at the center of the film image. Note the strong peak at $\theta \approx 105°$.

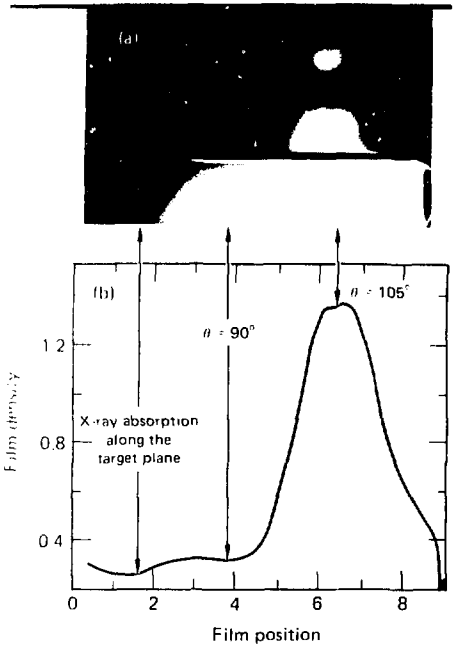

References

[ ] V. C. Rupert, M. J. Boyle, H. N. Kornblum, and K. G. Tirsell, *Angle-Dependent X-ray Measurements on Gold Disks Irradiated with Nanosecond, 1.06-μm Pulses*, Science Livermore Laboratory, Livermore, Calif., UCRL-51486 (1978).

[ ] Rupert, S. R. Gunn, and J. E. Holzrichter, *J. Appl. Phys.* 49, 132 (1978).

[ ] Kidder and I. Yablonovitch, *Phys. Rev. Lett.* 37, 1754 (1976).

Stimulated Raman Scattering Experiments

For high-intensity ($\gtrsim 5 \times 10^{14}$ W/cm^2 at 1 μm), long-pulse ($\gtrsim 1$ ns at 1 μm) irradiation of laser fusion targets, stimulated Raman scattering (SRS) may scatter several percent of the incident beam into lower-intensity light. SRS is a parametric instability in which an incident photon decays into an electron-plasma wave (epw) and a lower-frequency photon. This process can occur only at electron densities below quarter-critical density (0.25 n_c). The epw is usually collisionlessly damped by trapping, and creates suprathermal electrons which can preheat the pusher and D-T fuel. Even at modest intensities, laser beam filamentation in the plasma may create the high intensities needed for the Raman instability to become important. Thus, experiments are needed to explore and quantify this process in long-pulse irradiation of large targets at both moderate and high intensities.

We have made measurements which show that SRS is more significant at longer pulse lengths, and that at high intensities it occurs not only near 0.25 n_c (where the light is scattered with frequency $\omega_0/2$), but also at much lower densities. In this article we report the first observation of Raman scattering occurring in the very underdense plasma (at $n_e \approx 0.1$ n_c) for a solid target.

The earliest observation of $\omega_0/2$ light was reported by Bobin,[51] who reported a line spectrum centered at $2\lambda_0$ with a 60-Å width between half-intensity points, compared to 30-Å width for the incident laser light. This $\omega_0/2$ light can be attributed either to resonance Raman scattering or to linear-mode conversion of the epw's produced by the $2\omega_{pe}$ instability into light waves. Watt has seen Raman scattering of CO_2 laser light irradiating a 200-mm length of plasma formed in a solenoid.[52] Many 1-1 2-dimensional particle code simulations of SRS have been done by Estabrook.[53] In one simulation, 1.06-μm light at 3×10^{15} W/cm^2 was incident upon 10-keV plasma with its initial density rising linearly from zero to 0.4 n_c in $105\lambda_0$. Approximately 15% of the incident light was Raman-backscattered. Baldis[54] has directly observed $\omega_0/2$ epw's in a CO_2-irradiated plasma using Thompson scattering.

All our measurements were made (Fig. 6-38) with indium arsenide detectors cooled in Dewar flasks to liquid nitrogen temperature and reverse-biased by about one volt. A 1-mm-diam quartz optical fiber brought the light collected in the target chamber to the indium arsenide detector outside the target chamber vacuum. The 1.064-μm light and light of shorter wavelength was blocked by filters both at the light collector and at the detector; the 1.064-μm light was attenuated by a factor on the or-

Fig. 6-38. Experimental setup for measuring Raman-scattered light. The light collector is mounted at Argus on a theta arch which covers the angular range 25 °< θ < 155°. The visible-light-absorbing Corning 7-56 filters have a transmittance below 0.75 μm of $<10^{-4}$; the near-infrared-absorbing Corning 4-64 filters have a transmittance between 0.65 μm and 1.1 μm of $<10^{-3}$, and a 99.9% reflective coating at 1.064 μm. The band-pass interference filter has a nominal 800-Å half-width and is blocked to better than 10^{-3}.

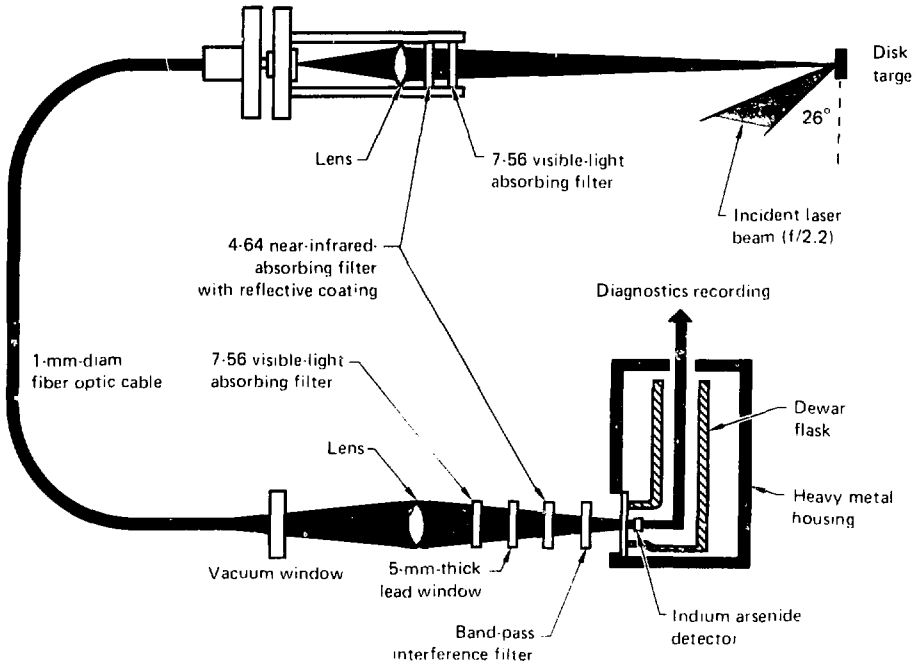

der of 10^{14}, while shorter-wavelength light saw a total attenuation of at least 10^{10}. Corning 7-56 visible-light-absorbing filters and Corning 4-64 near-infrared-absorbing filters with a dielectric coating highly reflective at 1.064 μm were placed both in the light collector and in the filter holder, which were light-tight except for light transmitted through the filters. X-ray shielding was provided by the W-Cu housing and a lead-glass window in the filter holder. The light brought by the fiber optic cable from the target chamber was focused by a lens onto the 2-mm-diam indium arsenide detector. Null experiments gave us confidence that we were actually looking at light from the target; when we blocked the light with a dark slide placed against the vacuum window, we observed no signal from a target shot. This eliminated other sources of the observed signal, such as electrical noise, flashlamp light, and high-energy x rays.

All the initial alignment and focusing was done by connecting one of the ends of the fiber optic cable to a visible light source. For most of the experiments, the focus of the collector was then moved a calculated distance from the best visible focus, so as to be in focus during the experiment at the wavelength of interest. If the light collector is in focus at a particular wavelength, all the light col-

lected by the lens at that wavelength will be focused into the fiber optic. For some of the experiments, however, we deliberately defocused to reduce the light intensity at the fiber optic. The calibration factor is, of course, then multiplied by the fraction of the light making it into the fiber optic. No correction for dispersion was made in focusing the light onto the In-As detector; rather, we always focused the light to a spot just a little larger than the detector area. Dispersion will make the spot larger at longer wavelengths, but so long as the procedure is repeatable, so that the setup can be exactly duplicated when the calibration is done, it makes no difference.

We used two different calibration techniques. The most accurate calibration method employed a blackbody source whose temperature was set (and checked with a calibrated thermocouple) to be 1200 K (±2 K), and whose emissivity was known to be 0.99 (±0.01). Except for the neutral-density filter attenuation, the calibration setup duplicated the experimental setup. A separate calibration was performed for each band-pass filter. The precision aperture of the blackbody source was placed at the same distance from the light collector as the target was in the experiments. The 1.27-mm-diam aperture chosen was imaged by the light collector as a 0.5-mm-diam spot on the 1-mm-diam fiber optic; thus all the light collected was focused into the optical fiber. The absolute spectral intensity of the apertured blackbody source in W/(sr-μm) is known to within 2%. The current was measured by a Keithley nanovoltmeter shunted by 1 kΩ. The internal impedance on the scales used (1 μV to 100 μV full scale) exceeds 100 kΩ and the In-As impedance at 77 K is also several hundred kΩ, so the current can be accurately measured. The rather large (≈100 nA) dc offset current was cancelled by sinking this current into an adjustable current source rather than the 1-kΩ resistor. There was no problem in making measurements to 0.05-nA accuracy if the input voltage was nulled just prior to each measurement. To ensure repeatability we made several measurements for each point.

The power per unit of emitting area per unit of wavelength interval radiated by a blackbody source into 2π steradians (one hemisphere) is given by

$$\frac{W(\lambda,T)}{W_{max}(T)} = \frac{0.2909}{(\lambda T)^5\left[\exp\left(\frac{c_2}{\lambda T}\right)-1\right]}, \qquad (5)$$

where λ is in μm, T is in K, and $c_2 = 1.4388$ cm-K is the second radiation constant. The maximum radiated power per unit wavelength for a fixed temperature is

$$W_{max}(T) = 1.286 \times 10^{-15}\, T^5 \quad W/(cm^2-\mu m)\ ; \qquad (6)$$

for T = 1200 K, $W_{max}(T) = 3.21$ W/(cm^2-μm). The on-axis maximum spectral intensity from an apertured blackbody source is

$$I_{max} = \frac{\eta A}{\pi} W_{max}(T)\ , \qquad (7)$$

where η is the emissivity (0.99) and A is the aperture area, 0.0127 cm^2. The units are power per unit solid angle per unit wavelength interval. Putting in the numbers, we find

$$I_{max} = 0.013 \quad W/(sr-\mu m)\ . \qquad (8)$$

The spectral intensity of the blackbody source at any other wavelength is given by

$$I(\lambda,T) = I_{max}(T)\left(\frac{W(\lambda,T)}{W_{max}(T)}\right)\ . \qquad (9)$$

A second, less accurate pulsed calibration method enabled us to calibrate the In-As detector at flux levels comparable to experimental ones, using a charge-integrating amplifier. The pulsed light source was a Q-switched Nd:Yag laser with λ = 1.064 μm. The spectral transmission curves for the filters and fiber optic cable were combined with the spectral response curve for the In-As detector to obtain the overall spectral response.

Low-intensity experiments were carried out on 600-μm-diam, 25-μm-thick gold disk targets irradiated by one beam of the Argus laser facility. The disks were irradiated by 800 J in 950 ps, focused to a spot of about 425 μm minor diameter, 500 μm major diameter. An exception was a $Ba(NO_3)_2$ disk target which was irradiated with about

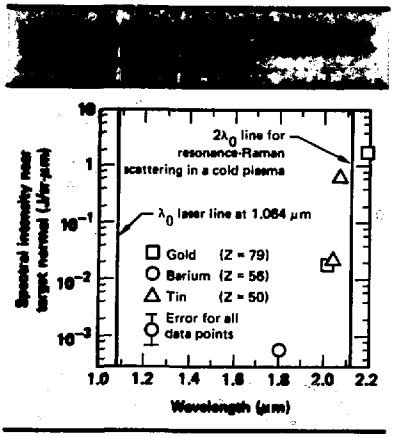

one third the energy focused to a correspondingly smaller spot size. The intensity was always about 5×10^{14} W/cm^2. The disks were tilted 30° in the plane of polarization and the light collector always looked within 11° of the target normal. This is necessary because the light at frequency $\omega_0/2$ is generated very near its critical density and refraction will cause it to emerge at an angle very near to the normal regardless of its direction when first generated in the plasma.

Each point in Fig. 6-39 represents the result of one target experiment. The band-pass interference filter in front of the In-As detector was changed between shots, so we could get the spectral shape from a set of otherwise identical experiments. The width of each point is given by the FWHM band-pass of the interference filter. Target materials differed because our Raman light measurements were secondary diagnostics in an experimental series on varied-Z disk targets designed to characterize x-radiography sources. Since all the target materials had at least a moderately high Z, however, we assumed that the Z variation was unimportant for our measurements. The spectrum is highly peaked and extends to the red beyond $2\lambda_0$. We did not make any measurement for wavelengths longer than 2.2 μm. The signals at 1.8 μm and 2.0 μm could be caused by leakages through the band-pass filters of the observed strong signal near $2\lambda_0$. If one conservatively assumes a solid angle of about 0.25 sr and a spectral width of about 1000 Å, these measurements imply a conversion efficiency into $\omega_0/2$ light of 5×10^{-5}, but this is only an order-of-magnitude estimate.

The $\omega_0/2$ light spectrum extends to the red beyond 2.128 μm ($2\lambda_0$) due to the Bohm–Gross shift, as first explained by Kruer.[55] If one solves the dispersion relations for the two light waves and the epw to find the density at which the Raman light wave is exactly at its critical density, one finds this density is below 0.25 n_c for a hot plasma and that the Raman light wave thus has a wavelength longer than $2\lambda_0$. These dispersion relations are

$$\omega_0^2 = \omega_{pe}^2 + c^2 k_0^2 \tag{10}$$

for the incident light wave,

$$\omega^{*2} = \omega_{pe}^2 + 3v_{te}^2 k^{*2} \tag{11}$$

for the electron-plasma wave, and

$$\omega_R^2 = \omega_{pe}^2 + c^2 k_R^2 \tag{12}$$

for a Raman light wave, where ω_{pe} is the electron plasma frequency, $v_{te} = \sqrt{kT_e/m_e}$ is the electron thermal velocity, and ω^* and k^* are the angular frequency and wave number of the epw, respectively. We set $\omega_R = \omega_{pe}$ and $\omega^* = \omega_0 - \omega_R$ to find

$$(\omega_0 - \omega_{pe}) = \sqrt{\omega_{pe}^2 + 3v_{te}^2 k^{*2}} \,. \tag{13}$$

Representing the square root by the first two terms in its binomial expansion, we get

$$\frac{\lambda_R - 2\lambda_0}{2\lambda_0} = \frac{\theta_e}{227\ \text{keV}} \,, \tag{14}$$

where θ_e is the electron temperature in keV. This shift is about 0.5% per keV electron temperature. Figure 6-40 plots the wavelength of the Raman light for backscatter as a function of electron density for $T_e = 0$ and $T_e = 10$ keV, again making the Bohm–Gross approximation given by Eq. (11).

Fig. 6-40. Dependence of Raman light wavelength on electron density at two electron temperatures, for backward scattering using the Bohm-Gross approximation.

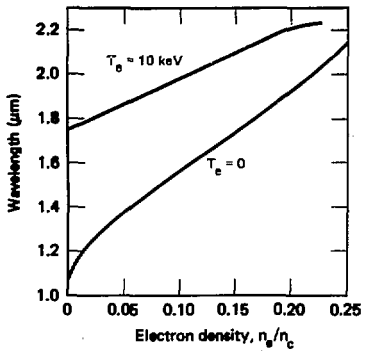

Fig. 6-41. Electron wave-breaking energy for SRS in a hot plasma, for several electron temperatures.

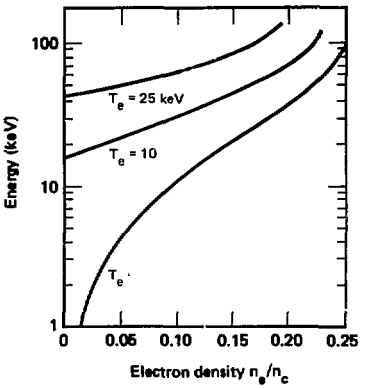

The threshold for SRS is expected to be lowest near quarter-critical density for two reasons:

- The group velocity of the Raman light wave is near zero at 0.25 n_c, so the instability can become absolute rather than convective.
- For backward scattering the phase velocity of the Raman light wave is highest at 0.25 n_c, resulting in the least Landau damping.

The phase velocity of the epw at 0.25 n_c is near $c/\sqrt{3}$: an electron moving at this speed has a kinetic energy of 115 keV. Thus Raman light generated near its critical density produces electrons with energies on the order of 100 keV. In Fig. 6-41 the wave-breaking energy (the kinetic energy of an electron moving at the epw phase velocity) is plotted against electron density at various electron temperatures, assuming direct backscatter. For a given electron density, the phase velocity increases with electron temperature. As n_e approaches zero, the phase velocity approaches $\sqrt{3}\, v_{te}$, but the Bohm-Gross approximation is not valid if $k\lambda_{De} \gtrsim 1$, where $\lambda_{De} \equiv v_{te}/\omega_{pe}$ is the electron Debye length. As electron temperature increases, the maximum electron density at which Raman scattering can occur decreases. This density is given by

electron density at which Raman scattering can occur decreases. This density is given by

$$\left(\frac{n_e}{n_c}\right)_{max} = \left(\frac{1-\xi}{1+\sqrt{1-\xi+\xi^2}}\right)^2, \qquad (15)$$

where $\xi = 3v_{te}^2/c^2$ is a dimensionless parameter proportional to the electron temperature. In Fig. 6-42 the wave-breaking energy is plotted for side- and forward-scatter as well as backscatter.

C. S. Liu[56] shows the condition for absolute instability in an inhomogeneous plasma to be

$$\left(\frac{v_0}{c}\right)^2 > \frac{4}{(k_0 L)^{4/3}}, \qquad (16)$$

where L is the local density gradient defined by

$$L^{-1} = \frac{d \ln n_e}{dx}. \qquad (17)$$

Here k_0 is the wave number of the incident light in vacuum, and v_0 is the peak oscillatory velocity of the electron in the incident light field. The threshold condition given here actually agrees with Liu's (given in Eq. 1-31 on page 133 of Ref. 56), despite a

Table 6-10. Summary of SRS spectral intensity measurements for two experimental setups.

Distance (μm)	Experiment: ~10^{16} W/cm^2, 100-μm-diam spot, 600 J in 600 ps; targets tilted 30° toward light collector.		Experiment: ~5×10^{16} W/cm^2 best-focus spot, 900 J in 1 ns; targets irradiated at normal incidence.	
	J/(sr-μm), in plane	Δθ	J/(sr-μm), in plane	Δθ
1.6	0.33	5.6°	1.3 to 1.7	25°
1.8	>0.26	7.2°	0.84	25°
2.0	No measurement made		1.2	25°
2.13	0.4 to 1.1	11.2°	No measurement made	

Fig. 6-42. Electron wave-breaking energy for SRS in a cold plasma, for side- and forward-scatter as well as backscatter.

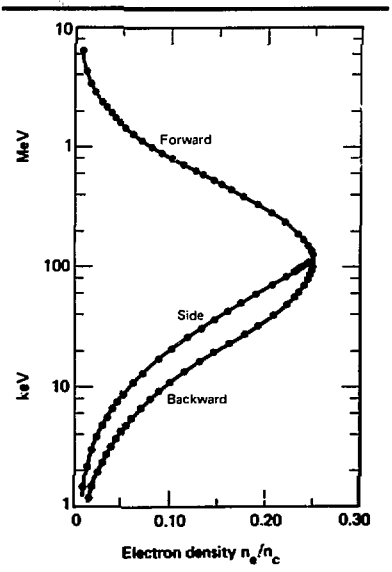

seeming discrepancy by a constant factor. Liu's v_0 is actually half the peak oscillatory velocity (see Eqs. I-13 and I-19 in Ref. 56), which for linearly polarized 1.064-μm light is given in term of the intensity I by:

$$\left(\frac{v_0}{c}\right)^2 = \frac{I}{1.21 \times 10^{18}\ \text{W/cm}^2}. \qquad (18)$$

Simulations indicate L ≈ 150 μm, so that we were close to threshold for $I = 5 \times 10^{14}$ W/cm^2. Of course, the peak intensity of the beam in hot spots may be higher than this average intensity by a factor of 2 or 3.

At light intensities of 10^{16} and 10^{17} W/cm^2, the *spectral intensity of the Raman-scattered light increased* not only near the degeneracy frequency $\omega_0/2$, but even more so at higher frequencies (Table 6-10). The Raman light intensity at 1.6 μm and 1.8 μm is comparable to that at 2.13 μm. All these measurements were made with the Raman light collector in the plane of polarization of the incident light. SRS, however, should have its maximum gain when the scattering plane is orthogonal to the plane of polarization: the electric vector of the Raman light would then be parallel to the electric vector of the incident light. The growth rate of the Raman instability is proportional to the dot product of the two electric vectors, so out-of-plane scattering (which we have not yet measured) is expected to occur preferentially.

For the experiments at 10^{16} W/cm^2, the gold disks were tilted 30° in the plane of polarization and toward the Raman light collectors, so that they *looked nearly normal to the target surface.* However, the shots at 5×10^{16} W/cm^2 were done at normal incidence, so the Raman light collectors were looking 25° away from the incident beam and in the plane of polarization: at this intensity the fraction of the incident light energy appearing as Raman-scattered light is at least 0.05%.

Raman-scattered light in the wavelength range from 1.6 to 1.8 μm probably originates around 0.1 n_c, although it is not possible to determine precisely at what density the Raman scattering occurs without knowing more than just the wavelength of the Raman-shifted light: one must also know the

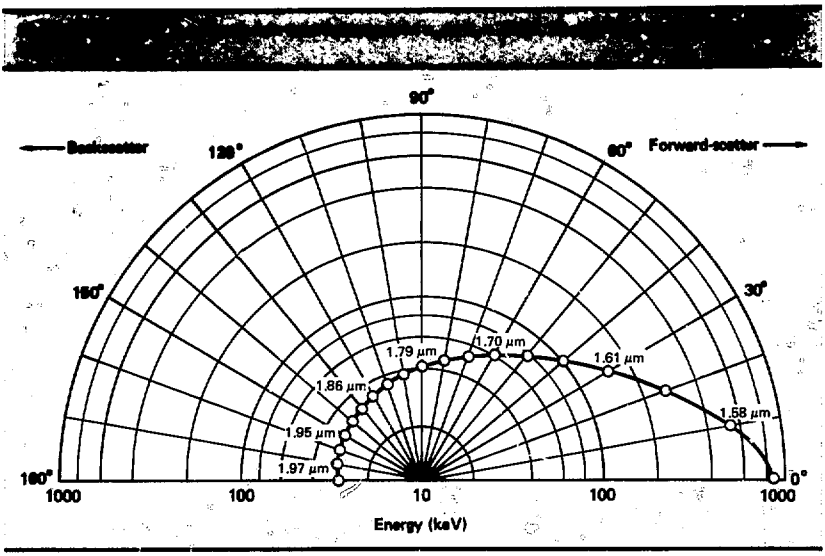

electron temperature and the scattering angle within the plasma. Backward Raman scattering has the highest growth rate, but also the highest Landau damping, since for backscatter the epw has the lowest phase velocity. The log-polar plot in Fig. 6-43, of the wave-breaking energy at density 0.1 n_c and temperature 10 keV, shows that the epw for backscattering has a wave-breaking energy of only 31 keV and thus will be highly Landau-damped. If the scattering direction is within 30 or 40° of the forward direction, the Landau damping will be extremely small, though the growth rate will also be much reduced because of the smaller wave number of the epw.

An estimate of when SRS is important can be made on the basis of a simple steady state model in which the epw is assumed to be strongly damped and the plasma to be planar with a linear density gradient (Fig. 6-44). The incident light (not shown in Fig. 6-44) is assumed to be a monochromatic plane wave normally incident upon the plasma, and while the Raman-scattered light wave can have any frequency and be incident at any angle, it will not see significant growth unless the beat term in the ponderomotive force drives the epw nearly resonantly along part of the ray path. If there is a ray which will be amplified ten or more e-foldings in intensity, Raman scattering can be expected to occur.

How strongly damped the epw needs to be before a strongly damped approximation is valid depends upon the scale length. At some point in the plasma, let the epw be driven nearly resonantly at angular frequency ω^* and wave vector k^*. If a noninteracting electron-plasma wave packet with the same center frequency ω^* and propagation direction (but with the wave number required by the dispersion relation) damps before it can fall out of phase with the ponderomotive-force driving term, then the epw is considered to be strongly damped. We are then justified in neglecting propagation in the model and can assume the epw amplitude at any point is determined by the ponderomotive-force driving term at that same point. We also make the slowly varying approximation and assume $\delta n/n$ small.

If the frequency of the Raman-scattered light wave is fixed and its angle of incidence allowed to vary, we find that the ray path which gives maximum growth is the one for which the epw is driven nearly resonantly at its turning point. This is physically reasonable since the interaction length is

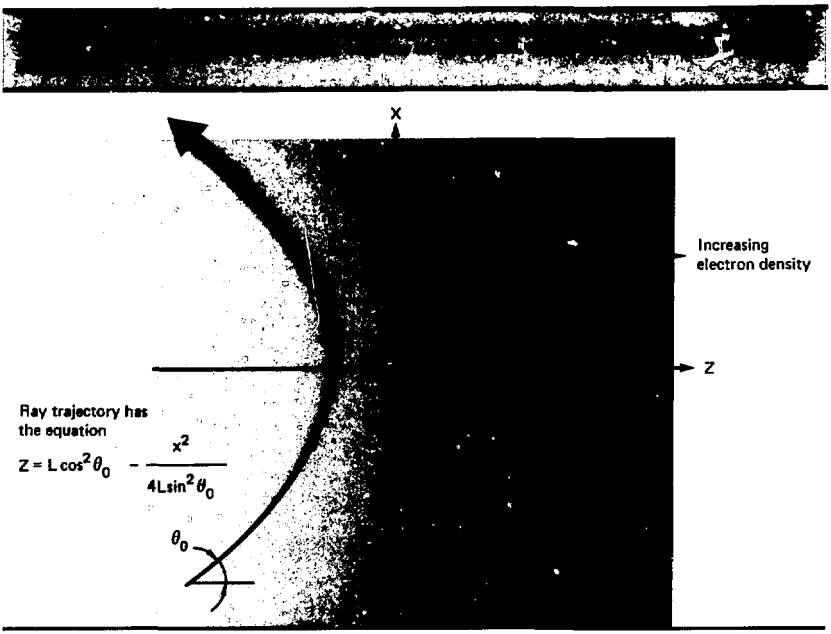

then maximum. Unrealistic results may be obtained for the growth seen by rays having turning points very far out in the underdense plasma, since in this model the interaction length increases without limit as the turning density goes to zero. The interaction length may be limited by the finite spot size or the curvature of the plasma density contours rather than by refraction.

The number of intensity e-foldings along the optimal path (λ_R fixed) is given by

$$K_{max} = \frac{3\sqrt{3}\pi}{4}\left|\vec{e}_R \cdot \vec{e}_O\right|^2 \left(\frac{k^{*2}}{k_0\left(\frac{\omega_R}{c}\right)}\right)\left(\frac{\omega^*}{\omega_R}\right) \times \left(\frac{v_0}{c}\right)^2 \left(\frac{L}{\lambda_0}\right)\sqrt{\frac{\omega^*}{\nu_L}}, \qquad (19)$$

where ν_L is the Landau damping rate, $\vec{e}_R$ and $\vec{e}_O$ are unit electric vectors, and L is the scale length, defined by

$$n_e = n_c\left(\frac{x}{L}\right). \qquad (20)$$

The subscript R refers to the Raman-scattered light wave, the subscript O to the incident light wave, and the superscript * to the epw.

Notice that as expected, K_{max} is proportional to the density scale length L and to the incident laser intensity, but, surprisingly, is proportional only to $\nu_L^{-1/2}$ rather than ν_L^{-1}, where ν_L is the Landau damping rate. This dependence is explained when we observe that the interaction length increases with $\nu_L^{-1/2}$ while the growth per unit distance varies with ν_L^{-1}. The Raman-shifted light wave will interact nearly resonantly with the other two waves only over a narrow electron-density interval whose width is proportional to ν_L. If the resonance point occurs near the turning point of the Raman-shifted light wave, the interaction length is then proportional to $L\nu_L^{1/2}$.

We can now evaluate K_{max} for $n_e = 0.1\ n_c$, $T_e = 10$ keV, to find

$$K_{max} = \frac{1}{22}\left(\frac{L}{\lambda_0}\right)\left(\frac{\omega^*}{\nu_L}\right)\left(\frac{I}{10^{16}}\right). \qquad (21)$$

A gold disk simulation[55] for $I = 10^{16}$ W/cm^2, spot size = 100 μm, and pulse length = 1 ns shows $T_e \approx 12$ keV and $L \approx 500$ μm, where $L^{-1} = d(n_e/n_c)/dx$. Equation (21) would give $K_{max} \approx 25$. In this case it is the radius of curvature of the plasma rather than refraction which limits the interaction length. Using a 250-μm radius of curvature at 0.1 n_c, we estimate $K_{max} \approx 12$.

In conclusion, Raman scattering is an instability which must be seriously considered in designing laser-heated ICF targets, especially at high intensity ($I\lambda^2 \lesssim 10^{15}$ W/cm^2-μm^2).

Author: D. W. Phillion

Major Contributors: D. L. Banner, K. G. Estabrook, and W. B. Laird

References

51. J. L. Bobin, M. Decroisett, B. Meyer, and Y. Vitel, *Phys. Rev. Lett.* **30**, 594 (1973).
52. R. G. Watt, R. D. Brooks, and Z. A. Pietrzyk, *Phys. Rev. Lett.* **41**, 271 (1978).
53. W. L. Kruer, K. Estabrook, B. F. Lasinsky, and A. B. Langdon, *Phys. Fluids* (to be published).
54. H. A. Baldis, J. C. Samson, and P. B. Corkum, *Phys. Rev. Lett.* **41**, 1719 (1979).
55. *Laser Program Annual Report—1978*, Lawrence Livermore Laboratory, Livermore, Calif., UCRL-50021-78 (1979), pp. 3-42 to 3-45.
56. *Advances In Plasma Physics*, Albert Simon and W. B. Thompson, eds. (Wiley & Sons, New York, 1976), vol. 6, p. 121.

Fig. 6-45. General experimental setup of the $2\omega_0$ experiments.

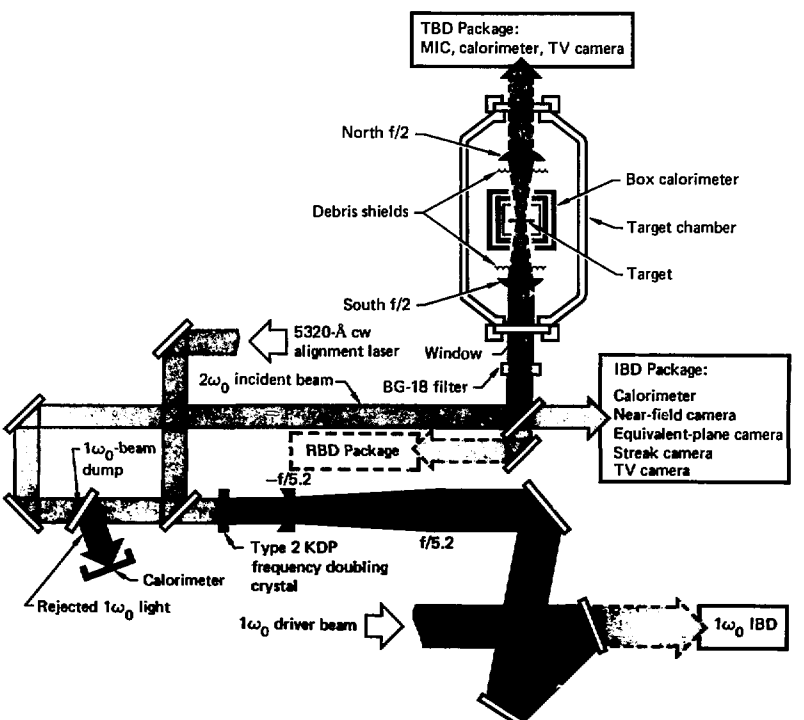

Experimental Configuration of the $2\omega_0$ Experiments

The experimental setup used at the Argus laser facility for target irradiation experiments at 0.532 μm (frequency-doubled 1.06 μm) is shown schematically in Fig. 6-45; since the basic design principles and calibration techniques of the various instruments employed in the $2\omega_0$ experiments are analogous to those described in detail in Refs. 57, 58, and 59, we will not repeat those descriptions here.

A system of three turning mirrors directs the 1.06-μm driver beam onto a lens assembly that demagnifies and recollimates the beam from about 280 mm to approximately 80 mm in diameter. This is done to reconcile the beam size with the clear aperture (90 mm) of the frequency-doubling crystal (KDP type II, with a thickness $\approx$13 mm). The unconverted 1.06-μm ($1\omega_0$) beam is eliminated from the frequency-doubled ($2\omega_0$) beam by reflection from a coated BK-7 glass slab (the "$1\omega_0$-beam dump" in Fig. 6-45); the $2\omega_0$ beam is then directed into the target chamber using an f/2 focusing lens (f/2.2 effective aperture). As discussed earlier in this report (see Section 2, "Argus Operations Summary"), frequency-doubling conversion efficiencies in excess of 55% were obtained at Argus at an incident-driver-beam radiation intensity of 1.5 GW/cm^2 or higher. In the experiments reported here, however, Fresnel reflection losses cut the actual $2\omega_0$-beam energy incident on the target to approximately 30% of the $1\omega_0$ driver-beam energy.

Beam Diagnostics Packages

Less than 3% of the incident $2\omega_0$ beam is directed into an incident-beam diagnostics (IBD) package (Fig. 6-46), which includes a near-field camera, an equivalent-plane (target-plane) camera, a streak camera,[57,58] a calorimeter,[59] and a monitoring TV camera. A representative near-field image of the $2\omega_0$ beam is shown in Fig. 6-47, together with a corresponding near-field image of the driver $1\omega_0$ beam. Comparison of the two pictures shows that the $2\omega_0$-beam amplitude modulation exceeds that of the $1\omega_0$ beam.

The equivalent-plane camera is used to obtain two-dimensional pictures of the incident $2\omega_0$ beam near best focus; these pictures are in turn used to characterize the beam spatial intensity distribution there. Figure 6-48 shows a representative equivalent-plane camera image taken near best focus. The presence of comatic aberrations made determination of the lens best-focus position very difficult.

We used rod shots to determine spot size and adjust the streak camera timing. Figure 6-49 shows

Fig. 6-46. Incident-beam diagnostics configuration for $2\omega_0$ measurements.

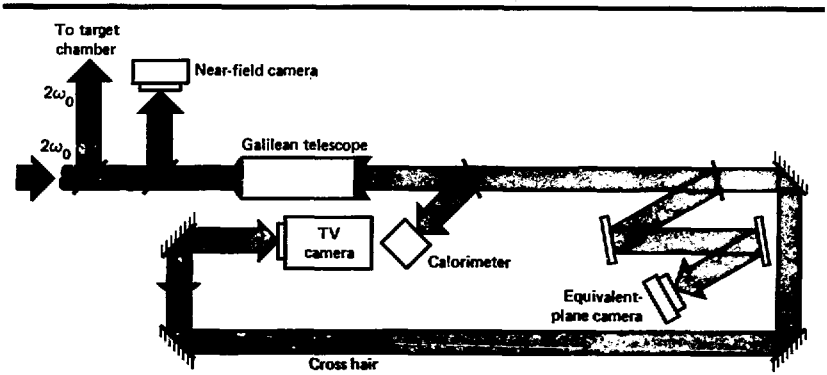

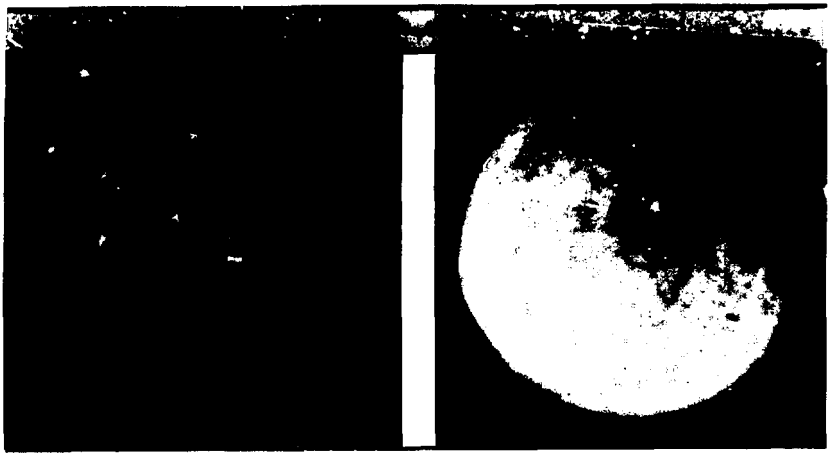

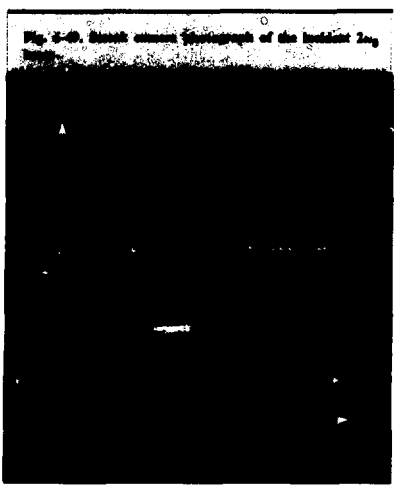

a sample $2\omega_0$-beam streak picture, in which time is measured horizontally and radial distance measured vertically; the pulse duration was about 600 ps. Digitized pictures similar to the one shown here were instrumental in the determination of the temporal $2\omega_0$ pulse widths discussed in Section 2 of this report.

We measured the incident $2\omega_0$-beam energy with a calibrated calorimeter. We calibrated the calorimeter with calorimetric readings taken of the transmitted beam (without target), taking into account the chamber lens transmission coefficients; the chamber single-lens transmission, including the

Fig. 6-50. Transmitted-beam diagnostics configuration.

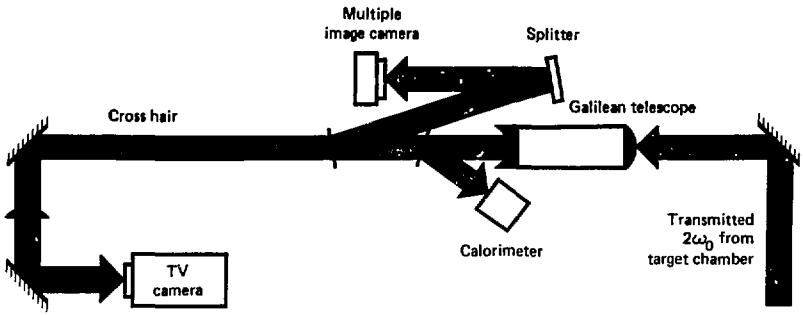

lens' protective debris shield, was found to be about 94%. By positioning a BG-18 glass filter across the $2\omega_0$ beam outside the target chamber, we determined that the level of residual 1.06-μm light that leaked through the coated BK-7 glass (the $1\omega_0$-beam dump) represented less than 1% of the total beam energy incident on the target.

The transmitted beam diagnostics (TBD) package (Fig. 6-50) included a calorimeter, a multiple image camera (MIC) similar to the one used for the equivalent-plane two-dimensional imaging of the incident beam, and a monitoring TV camera. Accurate irradiation spot sizes were determined from the MIC pictures of the transmitted beam. The monitoring TV camera was instrumental in target alignment and positioning.

Target Alignment and Spot Size Determination

Three steps were required for $2\omega_0$ beam alignment.

- The $1\omega_0$ beam was first made to properly point through the target chamber. This procedure involved replacing the 1.06-μm beam dump with an uncoated BK-7 glass slab of the same thickness. With the chamber lenses temporarily removed, we aligned an attenuated cw 1.06-μm beam through the chamber with the aid of reference crosshairs, turning mirrors, and infrared sensitive viewers.
- After replacing the simulated dump with the real one (but with the chamber lenses still out), we verified that the pulsed $2\omega_0$ beam also properly pointed through the target chamber. The final $2\omega_0$ pulsed-beam alignment was achieved by fine tuning crosshair positions and verifying the alignment with photographs of the transmitted pulsed beam on rod shots. In Fig. 6-51 we show a sample transmitted-beam picture displaying two correctly matched crosshairs (one placed in front of the final turning mirror, one placed beyond the exit window of the target chamber).
- After remounting the two chamber lenses, we used an auxiliary cw $2\omega_0$ alignment laser (whose optics were decoupled from those of the main beam;

Fig. 6-51. Crosshair alignment through the target chamber.

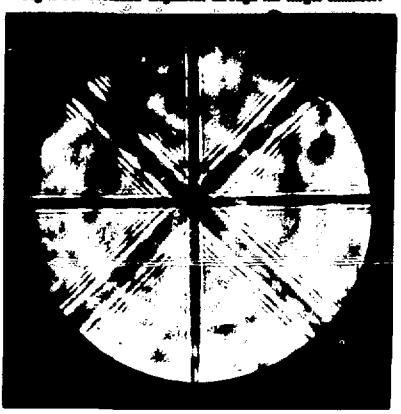

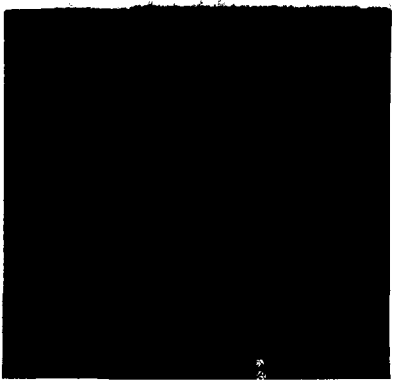

see Fig. 6-45) to check the orientation of the lenses. This was followed by another rod shot to recheck the $2\omega_0$ pulsed-beam alignment. Finally, the auxiliary cw $2\omega_0$ beam was used to monitor the alignment and to backlight the target after it had been aligned.

Before a target is inserted into the chamber, its orientation on the target holder is set on a specially built mounting table; in these experiments the table setup simulated the chamber geometrical configuration and was equipped with an angle-setting prealignment jig. The oriented target was then inserted into the chamber and exactly positioned at the center of the chamber, by adjusting its vertical position while viewing it through two perpendicular telescopic viewers that cross at the chamber center (TCO viewers). High-intensity white-light illuminators opposite the telescopes served to illuminate the target during this part of the procedure. Next, diffused cw $2\omega_0$ light was used to project the target image on a TBD monitoring TV camera screen while the position of the chamber North lens was adjusted until the image appeared sharpest.

The chamber South lens was focused in a somewhat similar manner. The lens position was varied until the sharpest, smallest image was ob-

tained in photographs of the transmitted pulsed beam on a rod shot. A calibration curve was then used to deduce the position of the chamber South lens that would give the desired beam spot size at the target plane. The chamber South lens was moved toward or away from the target plane until the desired converging or diverging spot size was obtained on a two-dimensional MIC image of the transmitted pulsed beam. In the representative image in Fig. 6-52, it is evident that the spot displays significant beam-amplitude modulation. Photographs of the transmitted beam used for spot size selection were also digitized to provide necessary information about the beam's physical qualities.

Figure 6-53 illustrates the success of the methods just described for target alignment and spot size selection. The film recorded both the pulsed beam and the image of the target, a plastic parylene disk oriented normal to the incident beam. The camera magnification was 38.2.

Diagnostics During Target Shots

The determination of energy balance during target shooting was made by calorimetric measurements. Target irradiation was done inside a box calorimeter that measured the scattered and refracted $2\omega_0$ energy. The box calorimeter incorporated a plasma shield (WG-280 glass) so that only scattered light could reach the energy-absorbing NG-1 glass panels. Because of its vital importance in the determination of light absorption by the target, the box calorimeter was designed for high sensitivities ($\gtrsim$3

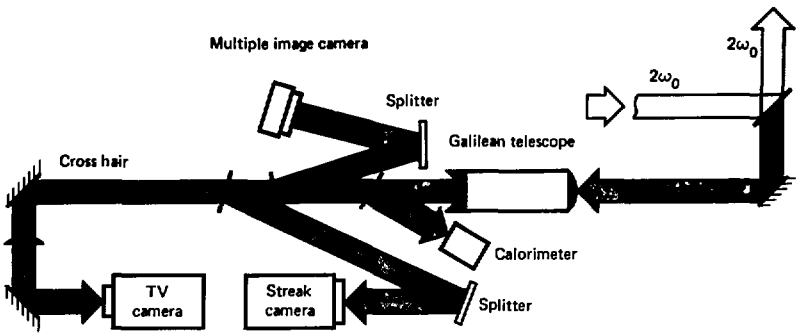

μV/J for the North and South panels and ~120 μV/J for the other four panels). The amplifier settings for the signals from the panels were closely monitored to prevent saturation. The plasma shield was replaced whenever there was evidence of excessive debris deposited on the WG-280 glass.

Corrections were made to account for losses through access and diagnostics holes in the box. The South and the North holes of the box subtended small solid angles of about 0.20 sr each. Fortunately, however, the effective f/2.2 optics (for a beam diameter of ~82 mm) and the chamber South lens ($ff \approx 180$ mm) subtend a solid angle of about 0.18 steradian. Therefore, all the light scattered back through the chamber South hole was collected by the backscattered-light diagnostics instruments. Similarly, any forward-scattered light going through the North f/2 lens was registered in the TBD package. Preliminary results revealed that during target experiments the amount of forward-scattered light was negligible, so that no calorimetric measurements of the transmitted beam were recorded.

The reflected-beam diagnostics (RBD) package (Fig. 6-54) consisted of a calorimeter, a two-dimensional MIC camera, two streak cameras (one for the spectrally analyzed light, the other for the nondispersed back-reflected light), an optical spectrometer, and a monitoring TV camera. An MIC image of back-reflected light taken during an experiment on a gold disk target is shown in Fig. 6-55. Figure 6-56 shows two streak pictures from the same shot, one (a) for the temporal behavior of the spectrally analyzed backscattered light, the other (b) giving the time history and one spatial dimension of the scattered light. Analysis of the spectrally resolved light provided insight for our laser-plasma coupling studies (discussed in the following article). Spectral data was gathered via a 1-m-grating spectrograph coupled to an optical multichannel

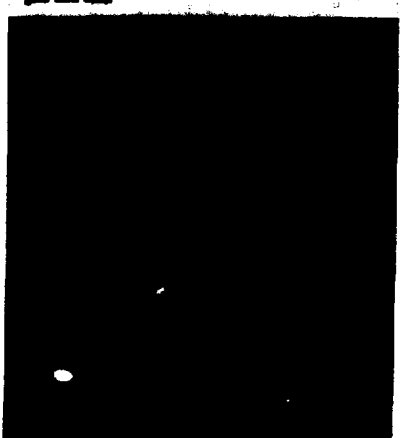

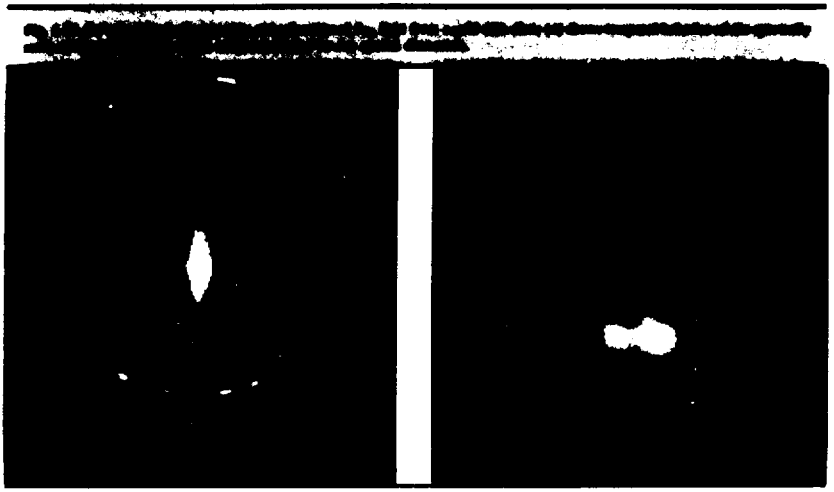

analyzer (a 1205E detector head provided by Princeton Applied Research Laboratory). The spectrograph angular dispersion was 2.80×10^{-4} rad/Å, which gave a dispersion of 8.82×10^{-2} Å/channel on the optical multichannel analyzer.

Author: F. Ze

Major Contributors: E. M. Campbell, V. C. Rupert, J. E. Swain, and D. W. Phillion

References

57. D. R. MacQuigg and D. R. Speck, *Beam Diagnostics on Argus*, Lawrence Livermore Laboratory, Livermore, Calif., UCRL-78447 (1976).
58. *Laser Program Annual Report—1975*, Lawrence Livermore Laboratory, Livermore, Calif., UCRL-50021-75 (1976), pp. 367 to 405.
59. *Laser Program Annual Report—1976*, Lawrence Livermore Laboratory, Livermore, Calif., UCRL-50021-76 (1977), pp. 3-55 to 3-60.

Preliminary $2\omega_0$ Results

We have initiated a series of experiments to study the wavelength scaling of physical processes such as absorption, stimulated scattering, energy transport, and suprathermal electron generation, which are important in laser-driven inertial confinement fusion. Our variable-wavelength source will be provided by nonlinear frequency conversion of the fundamental 1.064-μm output of Nd lasers into the 2nd, 3rd and possibly 4th harmonics (0.532 μm, 0.355 μm, and 0.266 μm respectively). As discussed in the previous article, we are presently utilizing a 90-mm-diam, 13-mm-thick KDP type II crystal to frequency-double one of the two Argus laser beams.

To date, we have used a box calorimeter[60] to measure the absorption and scattering of light from both Au and CH disk targets irradiated with green light at intensities in the range of 10^{14} to 10^{15} W/cm^2. Targets are typically 600 μm in diameter and 14 to 25 μm thick; pulse lengths ($2\omega_0$) are 600 ps (FWHM). The laser spot (containing 90% of the energy) is elliptical, with a major axis ranging from 50 to 160 μm and an eccentricity of 1.5 to 2. Peak-to-average intensity modulations within this spot are typically 3 or 4 to 1.

In Fig. 6-57, the absorption of Au targets at intensities of 2 to 4×10^{14} W/cm^2 is shown as a function of the angle of incidence between the disk normal and the laser propagation direction. The irradiations were done near p-polarization (E lies 14.5° out of the plane of incidence). At normal incidence, the laser-spot major axis was 110 μm; beam area was kept constant as the target was rotated through the various angles.

The angular variation was motivated by the following considerations:

Wavelength (μm)	Absorption	Backscatter	Intensity (W/cm²)	Pulse length (ps)	Spot size (μm)	Focusing optics
1.064	54%	11%	3×10^{14}	900	140	f/2.6
0.532	80%	5.6%	2 to 4×10^{14}	600	80(140)	f/2.2

Fig. 6-57. 2ω absorption of Au disks as a function of angle of incidence.

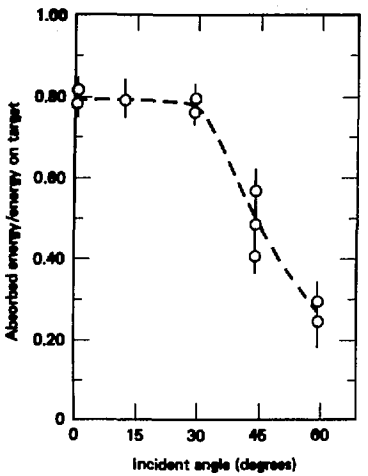

- Future measurements of low-energy ($h\nu \leq 1$ keV) x rays (which can provide information on thermal transport into the supercritical plasma) require a quantitative knowledge of the angular distribution of emission.[61] To map this out using immobile diagnostics (i.e., our Dante systems) requires incidence angles up to 30°.
- Examination of the spectrum of the backscattered light at different incidence angles allows the potential unfolding of Doppler and Brillouin components.
- The specular and backscatter components of the scattered light can be determined with the six discrete calorimeter modules of the cubical box calorimeter as the targets are rotated through the various angles. Analysis of this data in terms of absorption mechanism or scale length, however, is complicated by the fast optics (marginal rays are 12.8°) and possible two-dimensional expansion effects due to the relatively small laser spot and the long pulse length. This latter difficulty has arisen in the vast majority of long-pulse experiments performed to date.[62]

As shown in Fig. 6-57, the Au absorption is 80% at normal incidence and falls relatively slowly with angle of incidence. The weak dependence of absorption on the angle of incidence (roughly $\cos\theta^{1.4}$) simplifies future x-ray conversion efficiency measurements.

In Table 6-11 we compare the measured Au absorption and backscatter fraction obtained at normal incidence with 1.06-μm and 0.532-μm light under similar irradiation conditions.[64] The large absorption obtained at the shorter wavelength is primarily due to more effective inverse bremsstrahlung absorption, although this may also be in part due to a reduction in stimulated Brillouin backscatter.[63]

Independent monitoring of signals from the six panels of the cubic box calorimeter and the measurement of the direct backscatter energy allows a crude determination of the angular dependence of the scattered light. In particular it is possible, by rotating the target through large angles (45° and 60°) and using the responses of the individual panels in the box calorimeter, to separate specular reflection from the backscatter. The basic idea behind this is indicated in Fig. 6-58, which shows a top view of the calorimeter and the orientation of a target at a 45° incident angle. At incident angles of 45° and 60° (where target misalignment of ±3° does not influence the possible panel distribution), 36% and 55% (respectively) of the incident energy appears on the east panel (specular) of the box calorimeter, while only 6% and 10% (respectively) appear in the backscatter direction. Here we define backscatter to include light collected by both the focusing lens and the south panel (i.e., angles up to 45° from the laser axis).

In contrast, data obtained with Au disks oriented at 45° (s-polarization) and irradiated at 3 ×

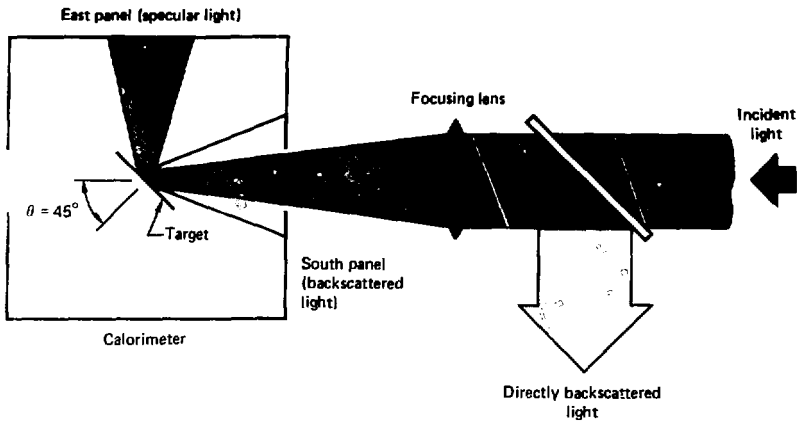

10^{14} W/cm^2 with s-polarized 1.064-μm light showed that 25% of the incident energy appeared in the backscatter direction.

For all of the target orientations, the amounts of energy collected by the top and bottom panels of the calorimeter [i.e., large-angle scattering ($\theta > 45°$) out of the plane of polarization] were negligible. This result is not surprising in view of the small laser spot (and hence the small number of growth lengths for stimulated Brillouin side-scatter), and the tendency of refraction to direct the light along the density gradient.[61,63] Though not conclusive and lacking quantitative data on refraction effects, our calorimeter results suggest that stimulated Brillouin scattering is reduced at the shorter wavelength (at least for densities less than 0.5 n_c).

Another interesting feature of the scattered-light distribution is found by plotting the energy directly backscattered through the f/2 lens as a function of angle of incidence. The results (Fig. 6-59) show an unexpected increase in the backscattered energy as the incidence angle is increased to 60°. This phenomenon is not yet understood.

Evidence that Brillouin scattering is still operative at these irradiation conditions (although at a reduced level) can be found by examining the

Fig. 6-59. Backscatter fraction from Au disks as a function of angle of incidence.

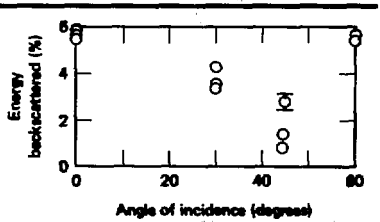

frequency spectrum of the backscattered light. One of the signatures of Brillouin scattering is the red shift of the scattered light.[64] In an expanding plasma, however, the Brillouin shift is reduced by the blue Doppler shift. Since the plasma nominally blows off normal to the disk plane, rotating the target diminishes the Doppler shift by reducing the velocity projection along the observation line of sight.

Figure 6-60(a) shows the time-integrated frequency spectra obtained in these experiments. As expected, the spectrum is increasingly red-shifted as the disk is rotated. From these data (summarized in Table 6-12) and from the dispersion relation for ion

Fig. 6-48. Normalized spectral intensity as a function of Doppler shift (in angstroms) from the 3508-Å laser line, for (a) Au and (b) CH disk targets.

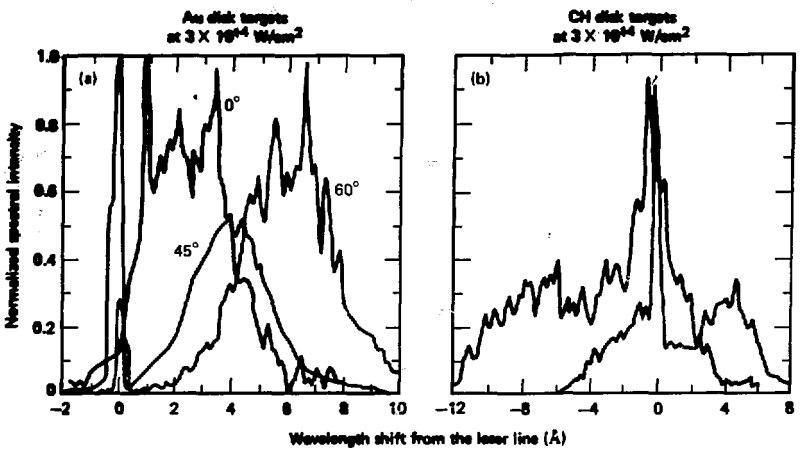

Table 6-12. Au backscatter characterization as a function of incident angle.

Angle	Centroid shift
0°	2.38 Å
30°	2.5 Å
45°	3.99 Å
60°	6.86 Å

Parameter	0° and 45° data	0° and 60° data
$\Delta\lambda_{FB}$	7.9 Å	11.3 Å
$\Delta\lambda_{SB}$	5.5 Å	8.8 Å
Matter speed	1.8×10^7 cm/s	2.9×10^7 cm/s
kT_e	2.7 keV	5.4 keV
Mach number	0.7	0.8

Table 6-13. Absorption from CH and Au disk shots, for incident intensity of 2 to 4×10^{14} W/cm^2 on a laser spot of 100 μm for a 600-ps pulse.

Material	θ	Absorption (%)	Backscatter (%)
CH	0°	71 ± 9	11 ± 4
Au	0°	80 ± 5	5.4 ± 0.5
CH	45°	34 ± 5	3 ± 2
Au	45°	49 ± 8	1.8 ± 1

acoustic waves, we can obtain estimates of both the matter velocity and coronal electron temperature. To derive the electron temperature T_e and matter velocity U, we have used the centroid of the spectrum and assumed

- A mean ionization state $\bar{Z}$ of ~50.
- $ZT_e \gg 3T_i$.
- That the scattering takes place at 0.25 n_c (turning density at 60°).
- That no quantities change significantly as the disk is rotated.

As can be seen from the inferred values, there is considerable scatter in the results, particularly in the electron temperature. This is not unexpected, since the electron temperature depends on the square of the Brillouin shift. Nonetheless it is interesting to note that the inferred quantities indicate that the flow is subsonic (*i.e.*, Mach numbers ~0.75) where the scattering occurs.

In addition to the Au discs, several CH targets have been irradiated under similar conditions at both normal incidence and at 45°. The preliminary CH results are compared with the Au data in Table 6-13. As expected, the lower-Z CH plasma absorbs less efficiently than the Au plasma, although the difference is not as large as might be suspected with the Z scaling of classical absorption. The CH plasma

Table 6-14. CH backscatter characterization.

Angle	Centroid shift
0°	−3.39 Å
45°	1.64 Å

Parameter	Value
λ_B	13.5 Å
λ_D	16.8 Å
Matter speed	5.5×10^7 cm/s
KT_e	4 keV
Mach number	1.2

also backscattered more energy through the focusing lens than did the Au plasma. In previous long-pulse (0.9 ns) 1.06-μm experiments conducted at Argus with similar intensity, the opposite result was obtained—the backscatter fraction increased with Z (Ref. 65).

The measured absorption of CH is consistent with the data obtained by Fabre,[62] although the irradiation conditions are not identical. For example, at similar intensities, Fabre measured 63% absorption with 80-ps pulses. In addition, at lower intensities ($\sim 6 \times 10^{13}$ W/cm^2) only a weak dependency on pulse width was observed (absorptions of 75% and 82% were observed at 80-ps and 2.5-ns pulses). This weak dependence, however, may be due in part to the small laser spot (50 ± 15 μm in diameter) used in the Fabre experiments.

In addition to calorimetry, we performed spectral analysis on the backscattered CH light [Fig. 6-60(b)]. As was observed with Au disks, the light is increasingly red-shifted as the target is rotated to 45°. In contrast to the Au results, however, the CH spectrum exhibits a net blue shift at normal incidence. Results of unfolding the Brillouin and Doppler shifts from the data are displayed in Table 6-14, which shows that the CH plasma expands more rapidly than the Au plasma. This is most likely due to both the lower Z/A (A is the atomic weight) and increased radiation loss of the Au plasma. Also, in contrast to the Au results, the CH plasma appears to be expanding supersonically (i.e., Mach number = 1.2).

Author: E. M. Campbell
Major Contributors: F. Ze, D. W. Phillion, and V. C. Rupert

References

60. *Laser Program Annual Report—1975*, Lawrence Livermore Laboratory, Livermore, Calif., UCRL-50021-75 (1976), p. 404.
61. M. D. Rosen et al., *Phys. Fluids* **22**, 10 (1979).
62. F. Amiranoff et al., presented to the Division of Plasma Physics at the 21st Meeting of the American Physical Society, Boston, MA (1979).
63. C. E. Max and K. Estabrook, Lawrence Livermore Laboratory, Livermore, Calif. (submitted to *Comments Plasma Phys. Cont. Fusion*).
64. D. W. Phillion, W. L. Kruer, and V. C. Rupert, *Phys. Rev. Lett.* **39**, 1529 (1974).
65. G. McClellan, P. H. Y. Lee, and G. Caporaso, Lawrence Livermore Laboratory, Livermore, Calif., UCRL-83044 (submitted to *Phys. Rev. Lett.*).

Summary of Disk Experiments

In the past year we have continued our attempts to understand laser-plasma interaction phenomena occurring in large-volume, long-scale-length plasmas. In particular we have extended our data base concerning pulse length, plasma composition, and wavelength, through a wide variety of disk-target irradiations at both the Shiva and Argus facilities.

In studies at Shiva we have measured the intensity-dependence of the absorption and the x-ray emission from CH and Au plasmas irradiated with 2-ns (FWHM) 1.06-μm pulses. The absorption results are surprisingly insensitive to ' in a parameter regime where inverse bremsstrah..ng absorption should be operative. At low intensities (5×10^{13} W/cm^2) we have obtained absorptions as large as 70 to 80%, although there is still evidence for low (~5%) levels of stimulated Brillouin backscatter. Low-energy ($h\nu \gtrsim 1.5$ keV) x-ray measurements from Au at low intensities also suggest that thermal transport inhibition may not be severe. At an intensity of 3×10^{14} W/cm^2, the behavior of plasma interactions with Au is very similar to that obtained with 1-ns irradiation, although we measured a slight increase in absorption, from 50% for 1 ns to 60% for 2 ns. At the highest intensity examined (3×10^{15} W/cm^2), Au absorption was observed to drop from 35% to 25% as the pulse length was increased from 1 to 2 ns. Such results may illustrate the competition between inverse bremsstrahlung and stimulated Brillouin scattering, and show the potential problems of high-intensity operation with large-volume plasmas.

Interesting scattered-light angular distributions were measured with a box calorimeter on long-pulse (0.9-ns FWHM) large-focal-spot (350-μm-diam) irradiations of Au disks. These experiments were conducted at Argus with 1.06-μm light at peak intensities of 3×10^{14} W/cm^2. We observed an increase in large-angle scattering ($\theta > 45°$) out of the plane of polarization as the disk targets were isolated from 0° to 30° (p-polarization) with respect to the laser axis. At normal incidence only 3% of the incident light suffered large-angle out-of-plane scattering, whereas up to 23% was observed at 30°. This scattered energy was comparable to the specular and backscatter components. We obtained similar results for intermediate-Z (Ti) disk targets oriented at 30°. These data, though complicated by refraction and the poor angular resolution of the box calorimeter, are suggestive of Brillouin sidescatter.

A large fraction of our experimental time at Argus was allocated to interaction physics. We repeated and extended short-pulse (0.1 ns), high-intensity (10^{15} W/cm^2) energy-transport experiments with CH-coated Al microdisks. Measurements of sub-kilovolt x rays and Al line radiation as a function of CH thickness indicated burn-through depths of ~0.1 μm; this result is consistent with data obtained at other laboratories. Simulations of these experiments, though compromised by the lack of absorption data, suggest transport inhibition for both the thermal and suprathermal electrons. Modeling of the suprathermal electrons was also complicated, however, by the low x-ray fluxes between 10 and 50 keV measured during these experiments (the levels were a factor of 4 to 10 times lower than 1.06-μm experiments conducted at other facilities). This result is not yet fully understood but may be due to better beam quality or a lower absorption level than we expected.

We also measured x-ray emission (0.1 keV $\lesssim h\nu \lesssim$ 80 keV) from disks of various Z irradiatiated with 0.9-ns (FWHM) pulses. The targets were Be, Ti, Au, and U disks with atomic numbers of 4, 22, 79, and 92 respectively. The peak intensity was held constant at 3 to 5×10^{14} W/cm^2. Several interesting features of the low-energy ($h\nu \gtrsim$ 1.5 keV) x-ray emission were observed in these experiments:

- The total x-ray emission and spectrum were strongly dependent on Z.
- The emitted energy initially increased rapidly with Z and then leveled off due to saturation of the plasma ionization level in the radiating region.
- The spectrum, measured with the broadband Dante system, displayed the presence of dominant line radiation in the intermediate-Z (Ti) plasmas.
- At a fixed peak laser intensity the temporal profile of subkilovolt emission was found to depend on the Z of the target material. We have interpreted this phenomenon as a signature of thermal transport inhibition with a Z-dependent intensity threshold.
- The flux of the high-energy ($h\nu \gtrsim$ 10 keV) x rays also was seen to scale with Z. It is difficult to assign an accurate value to the slope of the x-ray spectrum (θ_H), but the data do show a hardening of the spectrum as target Z increases. For example, the Be spectrum is best fit with a θ_H of ~10 keV whereas the uranium data suggest θ_H ~20 keV. As we have found in our previous long-pulse (1-ns) experiments, the level of the hard-x-ray flux indicates that only a small fraction ($\lesssim$5%) of the incident energy appears in suprathermal electrons; this suprathermal level appears to be only weakly dependent on Z.

We have also begun to examine the mechanisms for suprathermal-electron production in long-pulse ($\tau \sim$ 1 ns), high-intensity irradiations. We are particularly concerned with Raman and $2\omega_{pe}$ instabilities which are operative at densities $\leq 0.25\ n_c$. Measurement of the scattered light from high-Z disk targets at wavelengths between 1.8 and 2.2 μm has demonstrated that these processes occur not only at 0.25 n_c (resonant Raman scattering and $2\omega_{pe}$) but at densities as low as 0.1 n_c [nonresonant Raman (Compton) scattering]. The fraction of the light energy appearing as scattered light between 1.8 and 2.2 μm is estimated to be at least 5×10^{-5} at intensities of $\sim 5 \times 10^{14}$ W/cm^2. When the peak intensity is increased to $\sim 10^{17}$ W/cm^2 we estimate a lower bound of 5×10^{-4} for the conversion efficiency.

Recent experiments at Shiva have indicated an isotropy in the angular distribution of x rays with energy of $\gtrsim$40 keV. These x rays are produced by suprathermal electrons, as they interact with the dense target material. Our measurements have been made with arrays of calibrated detectors and an extended film pack. The two-lobed distribution we

have observed (see "Angular Distribution of Suprathermal X Rays" earlier in this section) is relatively insensitive to changes both in target material (Au disks and glass microballoons) and irradiation conditions. Additional experiments are required to explore and quantify the source of these energetic x rays.

Finally, recent modifications to the Argus facility have allowed us to begin to explore wavelength scaling of laser-plasma interaction physics. Experiments at 0.532 μm have demonstrated high absorption efficiency of both Au and CH plasmas irradiated at peak intensities of 3×10^{14} W/cm^2 with 600-ps (FWHM) pulses. As in our long-pulse (2 ns) 1.06-μm experiments, we found only a weak Z-dependence for absorption, from 80% for Au to 70% for CH. The angular dependence of the scattered light and frequency analysis of the direct backscatter indicate that stimulated Brillouin scattering is still operative, although at a reduced level compared to 1.06 μm.

Author: E. M. Campbell
Major Contributors: D. W. Phillion, V. C. Rupert, D. L. Banner, P. H. Y. Lee, and C. L. Wang

10× Liquid Density Target Experiments

The achievement of high-density, isentropic implosions is critically important for realizing high gain by means of laser-driven inertial confinement fusion.[66] Most experimental experience to date, however, has been obtained with high-entropy, low-density exploding-pusher targets.[67] While such targets have achieved high final D-T ion temperatures (2 to 8 keV), demonstrated thermonuclear burn,[68] and produced high (3×10^{10}) neutron yields,[69] they are not scalable to break-even conditions.

We have recently begun experiments on thick-walled capsules designed to achieve high-density implosions ($\rho_{D\text{-}T} \sim 2$ g/cm^3). Accurate diagnosis of targets used in such implosions is in an early stage, since the relatively cold, dense implosions preclude the use of many techniques that have been successfully employed in traditional exploding-pusher experiments.[70] Thus, as experiments evolve toward a more direct study of ablatively driven targets, it is important to examine transitional targets which combine features of both simple exploding pushers and more advanced isentropic implosions. Such experiments serve as valuable checks on our simulation codes by allowing the use of several independent diagnostics to study the implosion. In addition, new experimental techniques designed to study high-density targets can be developed and compared with established, well-understood diagnostics.

For the above reasons, thick-walled polymer-coated glass microspheres designed to reach D-T densities of ~2 g/cm^3 (10× liquid density) were irradiated at Shiva.[71] The basic 10× target capsule [*Fig. 6-61(a)*] is a 140-μm-i.d. silicate glass microsphere with a 5-μm-thick wall and 15-μm coating of $CF_{1.4}$. The targets are filled with 50 atmospheres of equimolar deuterium and tritium (10 mg/cm^3) and approximately 0.05 atmospheres of argon (as will be discussed below, the trace amount of argon is used for diagnostic purposes and does not effect the implosion dynamics).

The targets were irradiated with 4 kJ in a 200-ps FWHM Gaussian pulse. The radially polarized Shiva beams, interacting with the plasma predominantly in p-polarization, were offset so that the marginal rays were tangential to the target [Fig. 6-61(b)]. Peak calculated intensities on the target were $\sim 4 \times 10^{15}$ W/cm^2 at the equator and the poles (intersecting the beam cluster axis), and $\sim 2 \times 10^{16}$ W/cm^2 in two bands at intermediate latitude.

We fielded a large number of diagnostics during this experimental series:

- Target absorption was measured with arrays of both plasma and laser calorimeters[72] and with scattered-light photodiodes.[73]
- Thermonuclear yields were measured with both lead and copper activation systems.[74]
- A filter fluorescer recorded the flux of 20-to-80-keV-bremsstrahlung produced by suprathermal electrons.[75]
- Time-integrated x-ray imaging of the target was accomplished by two Kilpatrick–Baez microscopes (giving polar and equatorial views)[76] and a Fresnel zone plate camera (giving an equatorial view).[77] Each microscope recorded images in four broad-band channels (defined by K-edge filters, the reflector material, and the angle of incidence) near 1.6, 2, 2.9, and 3.5 keV. The zone

Fig. 6-61. (a) Schematic of target capsule design for the 10X liquid density experiment series; (b) tangential irradiation geometry at Nova.

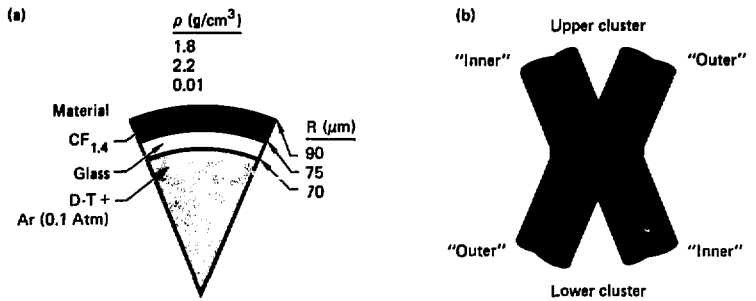

plate camera also had multi-image capability, through the use of 40-μm-thick Au zones and a film pack consisting of alternating layers of film and x-ray absorbers.[77] Though dependent on the x-ray spectrum, the broad zone-plate image channels were nominally centered on 5.9, 6.6, 10, 17, and 21 keV. This high-energy (≲4-keV) imaging capability is particularly important for viewing intermediate-density targets, as the large areal density of the stagnated pusher requires the imaging of multi-kilovolt x rays in order to view the pusher-fuel interface.[70] In addition, the large collection solid angle of the zone plate camera allows high sensitivity while still maintaining a resolution of 8 μm.

- Compressed-core conditions were also diagnosed with one-dimensional imaging spectroscopy of the argon seed gas in the fuel.[78] A low-dispersion PET crystal spectrograph, used in conjunction with a 20-μm slit aligned for a pole-to-pole view, imaged the 3.14-keV Hα [$1s2p(^1P_1) \rightarrow 1s^2(^1S_0)$] argon line emanating from the compressed-fuel region. The small amounts of argon led to a low signal-to-noise ratio and precluded any Stark analysis of the line radiation.
- The areal density, $\rho\Delta R$, of the compressed glass pusher, integrated over the burn time, was measured by counting ^{28}Al created by the $^{28}Si(n,p)\,^{28}Al$ reaction.[79] If we use the measured cross section for this reaction, the fractional concentration (25%) of ^{28}Si, and the measured 14.1-MeV neutron yield, Y_n, then measuring the number N* of activated ^{28}Al atoms yields the pusher areal density (in mg/cm²):

$$(\rho\Delta R)_{eff} \simeq 5 \times 10^5 \left(\frac{N^*}{Y_n}\right). \qquad (22)$$

It is possible to relate this measured quantity to the compressed-fuel conditions by both simple modeling and with detailed hydrodynamic simulations.

Experimental Results

We measured absorption on two shots for which the density-diagnostics instrumentation in the vicinity of the target was removed. Both the plasma calorimeters and Si PIN diodes indicated an absorption fraction of 23% (±5%). Previous experiments have shown that much of the light absorption at the high intensities and relatively short pulse lengths described above occurs via resonance absorption at the critical surface. Angle- and polarization-dependent absorption measurements have shown ~40% absorption at 1 to 3 × 10^{15} W/cm² for p-polarized light at incidence angles of 30° (Ref. 80). The reduction in absorption is most likely due both to irradiation geometry and to stimulated Brillouin scattering that scatters the light before it reaches the critical surface.[81]

In Fig. 6-62 the measured x-ray fluence at 20, 50, and 80 keV is compared with a LASNEX simulation in which resonance absorption accounts for 90% of the absorbed light. The effective slope of the x-ray tail is calculated to be ~21 keV. As shown

Fig. 6-62. Comparison of calculated and measured high-energy x-ray flux from 10X targets.

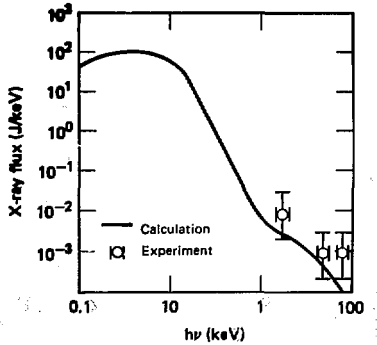

in the figure, the data agrees reasonably well with the simulation. Interpretation of the data is complicated, however, by recent experiments which suggest an apparent angular modulation of the high-energy ($h\nu \gtrsim 50$ keV) x rays[82]; the origin of this modulation (and the spectral dependencies) are not presently understood and will be explored in future experiments.

Thermonuclear yields between 10^8 and 10^9 were obtained in the 10X experiments. For seven shots with an average incident energy of 3.8 (±0.4) kJ the measured neutron yield was 3.1 (±0.5) × 10^8. These yields are consistent to within a factor of 3 with one-dimensional and two-dimensional LASNEX simulations,[83] using the modeling generally consistent with that used for previous interaction and implosion experiments. The predicted yields, however, are not sensitive to thermal-electron transport inhibition, however, and thus the

Fig. 6-63. Comparison of measured [(a) and (b)] and calculated [(c) and (d)] 3.5-keV x-ray images.

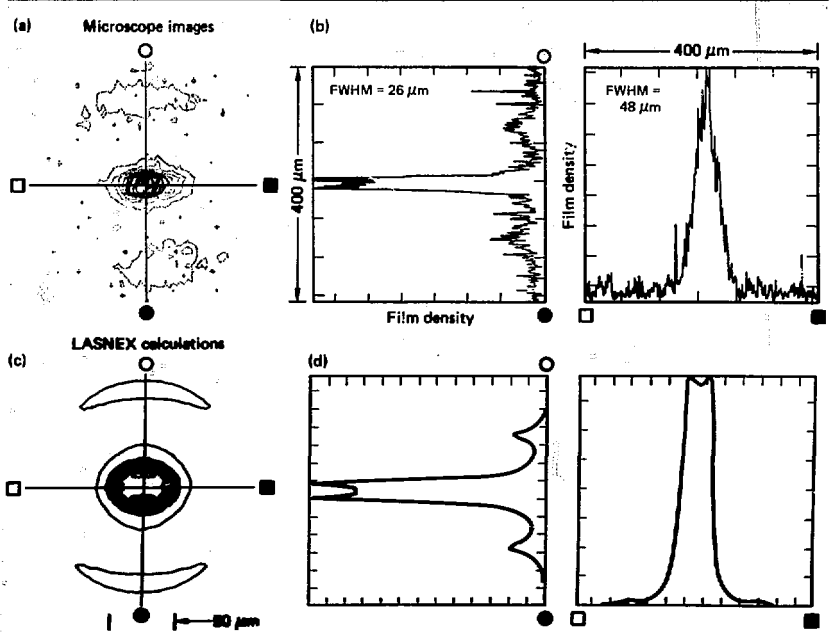

neutron measurement does not constrain this aspect of the modeling. Furthermore, neutron production is so strongly dependent on the fuel ion temperature and implosion dynamics of the target that additional details of the compression (such as symmetry and pusher fuel mixing) cannot be inferred from the TN-yield measurement.

Characteristics of the heating and stagnation symmetry of the target were obtained using two-dimensional continuum x-ray imaging. So many time-dependent factors are involved in producing the image, however, that deconvolution of quantitative physical information from the data, particularly in the imploded core, is impossible. The image is spatially integrated along a line of sight, spectrally integrated over broad channels, and temporally integrated over a complex, dynamic implosion. As implosions achieve higher final densities and correspondingly larger pusher areal densities, the additional complexity of x-ray transport arises. This results in the continuum images becoming increasingly determined by emission from the outer pusher material.

This problem is reduced by imaging x rays of sufficiently high energy, for which the pusher is essentially transparent. The targets used in these experiments had measured and calculated $\rho\Delta R$'s of $\sim$6 mg/cm^2, requiring x rays with energy $\gtrsim$5 keV to see into the pusher-fuel interface.[70] The ability to clearly see this interface is essential to ascertaining the fuel density, both for continuum and seed-gas imaging. This latter technique relies on information about symmetry to subsequently extrapolate from the one-dimensional image, obtained with a single slit-spectrograph combination, to a measurement of the x-ray emitting volume.

To illustrate these effects we show in Fig. 6-63(a) the image of the irradiated target recorded in the highest energy channel (3.5 keV) of the equatorial-viewing x-ray microscope. The asymmetry of the irradiation pattern is obvious from both the initial heating of the ablator and the oblate stagnated core. As can be seen from line scans through the digitized image along directions parallel and perpendicular to the laser axis [Fig. 6-63(b)], there is no clear delineation of the pusher-fuel interface. Thus we are unable to infer either the fuel density or the symmetry of the enclosed fuel volume from this experimental measurement.

Figures 6-63(c) and (d) show the corresponding x-ray image and line scans calculated in the two-dimensional modeling of the experiment using the appropriate filter functions of the microscope. In this simulation, in which we obtained a peak fuel density of 2 g/cm^3, the thermal electrons were inhibited by the 2-stream instability with an effective flux limiter of 0.03 (Ref. 77). The emission in this energy band is dominated by free-bound radiation from silicon in the pusher, although the calculation suggests that there may be an additional contribution from the high-Z argon fill mixed in with the fuel. The calculated images are in qualitative agreement with the overall shape of the measured emission region of the compressed core. The details of the modeling (and hence the calculated image), however, are extremely sensitive to illumination symmetry, absorption, transport, the mix of the pusher and fuel, and (in the case of the high-Z fill) to non-LTE ionization physics.

Figure 6-64(a) shows an x-ray image recorded in a broad energy bin near 6 keV, obtained with the multichannel zone plate, filter-film pack combination. A line scan along a direction colinear to the laser axis is shown in Fig. 6-64(b). Images recorded at this energy do not suffer from transport difficulties and are less affected by temporal smearing; at the implosion temperatures ($T_e \gtrsim 1$ keV) characteristic of these experiments, the emission time of the 6-keV x rays is only 10 to 20 ps. Since the x-ray emission is primarily free-bound radiation from silicon, however, the images are extremely sensitive to electron temperature gradients.

As shown in Fig. 6-64(a), the core region is considerably smaller than that measured by the x-ray microscope; the core also exhibits considerable structure in the emission pattern. This latter feature may suggest the existence of a pusher-fuel interface, although the region of enhanced x-ray emission does not totally encompass the central region of the core. This lack of emission could easily result from temperature gradients along the interface. Both high-energy ($h\nu \gtrsim 10$ keV) images where suprathermal bremsstrahlung emission dominates and two-dimensional simulations with thermal transport inhibition suggest that asymmetries in the high-energy core-ion emission can be correlated with regions of increased heating in a nonuniformly irradiated ablator.

The high-energy images did not reproduce from shot to shot during the experimental series, and in several of the experiments the presence of a

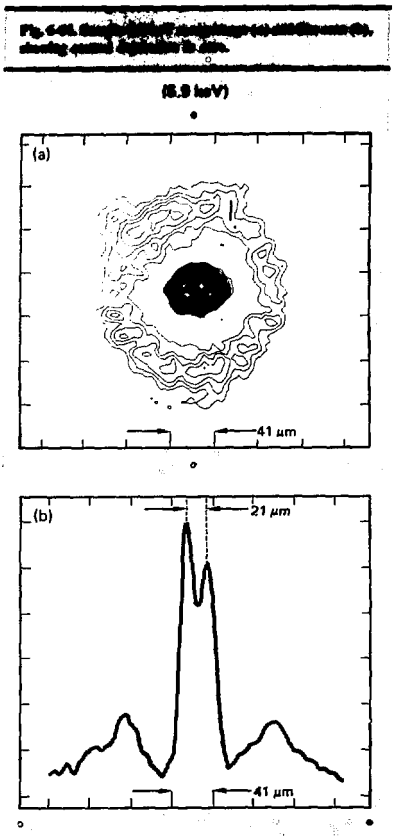

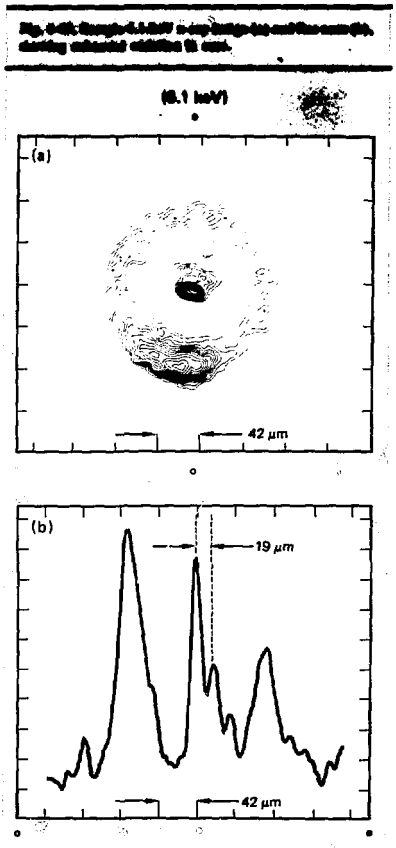

local minima is not obvious in the high-energy x-ray core emission. Nevertheless, despite a small data base, the performance of the capsules was nominally unchanged as measured by other experimental observables such as neutron yield, low-energy ($h\nu \gtrsim 3.5$ keV) x-ray images, $\rho\Delta R$ at burn time, and argon line imaging. A sample image and line scan are shown in Figs. 6-65(a) and (b); these should be compared with the corresponding zone-plate images in Fig. 6-64. It should be noted that dimensions of the core emission structure (i.e., two peaks separated by 21 μm) are similar in both images. The large difference in the asymmetries of the emission peaks may simply reflect the irreproducibility of the target irradiation.

Imaging of the line emission from a trace amount of argon mixed with the D-T ($n_{Ar} \sim 10^{-3}\, n_{D\text{-}T}$) provides information about fuel compression that is not available with x-ray continuum imaging. The combination of low fills of argon ($0.05 \gtrsim P_{Ar} \gtrsim 0.1$ Atm), transport losses through the pusher (survival fraction ~0.2), and background emission from

Fig. 6-66. Comparison of calculated and measured one-dimensional images of He-like argon resonance line.

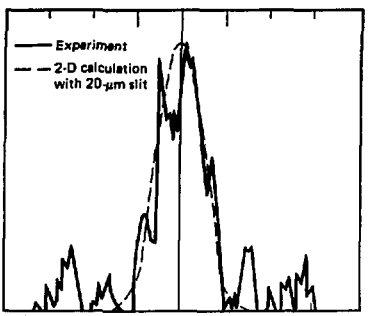

the silicon free-bound radiation from the pusher resulted in extremely poor signal-to-noise ratios (~1.5:1 to 2:1). The data reduction is further compromised by the need to unfold the effects of the 20-μm slit used in the experiment; this is particularly true when the slit is comparable to or larger than the source dimension to be imaged. To unfold the data we collapsed a uniformly emitting sphere or ellipsoid into one dimension, producing a parabolic radiance function. This profile is then convoluted with a slit response function and compared to the measured spatial profile.

Two experiments in which adequate data were obtained gave source dimensions of ~25 (±10) μm. The slit was aligned to provide a pole-to-pole view (i.e., the minimum core dimension, as indicated by the continuum x-ray imaging). Rough estimates of the fuel density can be obtained from this data if we assume instantaneous emission and equality of the x-ray emission volume and fuel burn volume:

- For a spherical core one obtains a fuel density of ~1.8 g/cm^3.
- For an oblate spheroid (with oblateness 2:1), as suggested by the two-dimensional modeling and continuum x-ray imaging, one obtains a density of ~0.4 to 0.5 g/cm^3.

In a more sophisticated analysis we compared the measured argon spatial profile with the profile predicted by two-dimensional simulations which calculate the non-LTE evolution of the argon He-like emission during the implosion.[71] Figure 6-66 shows the calculated profile (including effects of the 20-μm slit) and measured argon profiles. In this badly preheated implosion, mistiming of the argon emission relative to the peak compression results in a sampling of the fuel volume at about twice the minimum calculated value. Our observation is thus consistent with a two-dimensional simulation of the implosion which gives a D-T density of ~1 g/cm^3; if the implosion continues until maximum stagnation the calculation of peak fuel density is ~2 g/cm^3.

In the 10X series we measured effective pusher areal density $(\rho\Delta R)_{eff}$, averaged over the D-T burn duration, with neutron activation of ^{28}Si (see Ref. 79 and Section 5, "Implosion Measurements with Neutron Activation Techniques"). Excellent data was obtained on 3 target shots, giving a mean value of 5.8 (±1) mg/cm^2 (Ref. 84).

A simple model serves to illustrate the connection between $\rho\Delta R$ and D-T density. The model

- Assumes the final state is an isobaric and isothermal spherical core with instantaneous D-T burn.
- Incorporates the initial pellet geometry and a parameter ϵ, representing the fraction of the initial pusher mass which is stagnated around the fuel at burn.
- Uses an ideal gas equation of state to relate the densities of the stagnated glass and D-T.

Solving the equations for conservation of fuel and pusher mass gives the final fuel density as $\rho_f = G(\rho\Delta R)_{eff}^{3/2}$, where G is an algebraic expression containing the pellet parameters and ϵ.

We can use this simple model to estimate the fuel density attained experimentally. Setting $\epsilon = 0.5$, we obtain fuel densities of 1.5 to 2.5 g/cm^2 from the measured $(\rho\Delta R)_{eff}$ (Ref. 71). If all the pusher is assembled at high density about the fuel (i.e., if ϵ = 1), and no mixing occurs, then we obtain a lower limit of 0.8 to 1.4 g/cm^3.

More detailed modeling of the activation dynamics is possible with LASNEX simulations which take into account both the finite length of the D-T burn and the imploded-pusher density profile. The plot of Fig. 6-67 gives the relationship between D-T density and pusher areal density at peak burn.[71] Thus, the activation measurement implies

[illegible]

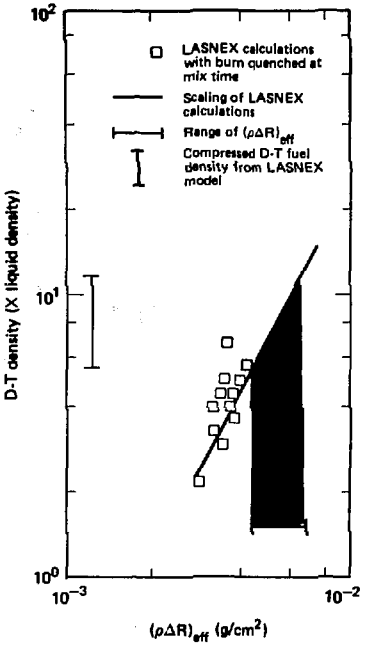

an average D-T density at burn time of ~1 to 2.4 g/cm^3 (5 to 12 times liquid density).

Two-dimensional effects (i.e., nonspherical implosions) modify the density that is attained but affect the ρ vs $(\rho\Delta R)_{eff}$ relationship only in pathological cases. This is particularly true for the implosions described here, for which core asymmetries of 1.5:1 to 2:1 are suggested by both calculations and experiments.

Mistiming of the implosion (i.e., burn time occurring before maximum compression) also affects the interpretation of the activation measurement, in terms of maximum fuel density achieved in the implosion. Figure 6-68 gives the timing of the late stages of the implosion and shows that the fuel density at the sample time of the neutron activation measurement is approximately half the peak calculated value.

Summary

The 10× experiments are among the first to examine targets whose performance deviates from that of the traditional thin-walled exploding pusher. Our measurements and calculations for this series indicate in particular the achievement of compression of the D-T fuel on the order of 5 to 12 times liquid density. Not all of our data is completely understood, but we have established the critical role of sophisticated two-dimensional simulations to describe asymmetric implosions.

A more quantitative understanding of the core conditions of high-density implosions requires an extension of our diagnostic capability:

- High-energy x-ray imaging where x-ray transport difficulties do not arise must be fully exploited in the future.
- The use of more than one imaging spectrometer will provide an accurate determination of the x-ray emitting volume.
- Increased seed-gas fills, allowing the use of narrower slits, will reduce the present image unfold difficulty and allow Stark broadening analysis.
- The addition of ~0.1 atmosphere of Br into the fuel will make possible neutron activation measurements of fuel areal density; simultaneous silicon activation measurements can be made in the pusher.

We have also derived several near-term improvements in design and diagnostics from the 10× experimental series. Several partially diagnosed experiments during this series showed more uniform ablator heating and increased core symmetry with a "ball in plate" target configuration (Fig. 6-69), thus making it possible to achieve more nearly spherical implosions.[85] The neutron yield obtained on one shot was consistent with that measured on bare ball targets, indicating that thermal losses to the plate were not excessive.

Besides providing more accurate data, these improvements and developments will constrain our simulation calculations and thus improve their credibility.

Authors: E. M. Campbell and W. C. Mead
Major Contributors: J. M. Auerbach, D. L. Matthews, S. M. Lane, N. M. Ceglio, D. T. Attwood, and K. R. Manes

Fig. 6-68. Calculated implosion history for a 10× target.

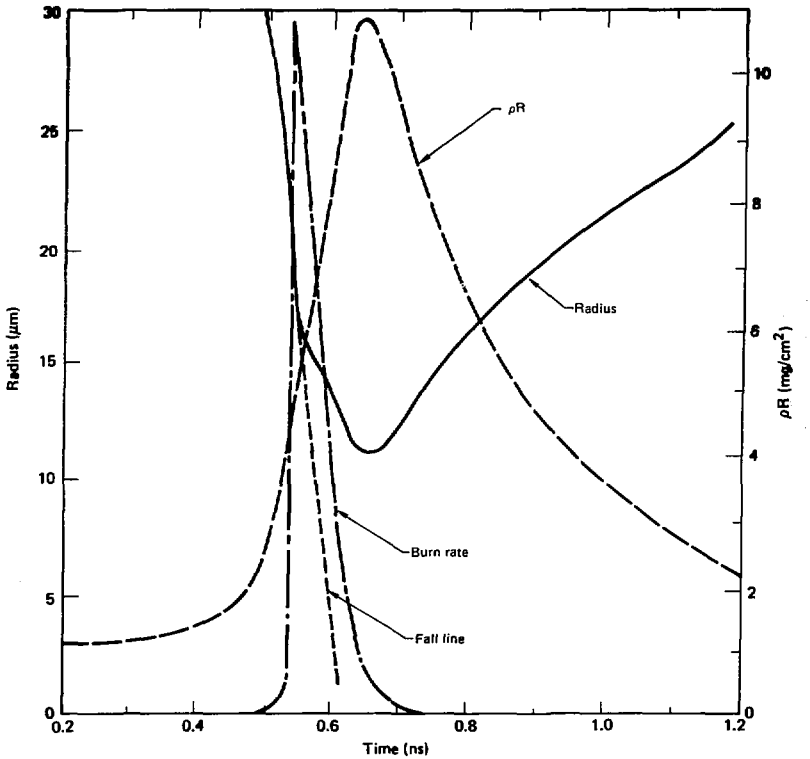

Fig. 6-69. "Ball in plate" target design for 10× experiments.

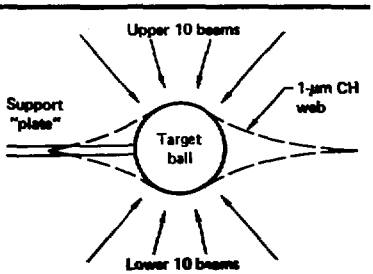

References

66. J. Nuckolls, L. Wood, A. Thiesson, and G. Zimmerman, *Nature* **239**, 139 (1972).
67. E. K. Storm et al., *Phys. Rev. Lett.* **40**, 1570 (1978).
68. V. W. Slivinsky et al., *Phys. Rev. Lett.* **35**, 1083 (1975).
69. D. R. Speck et al., Lawrence Livermore Laboratory, Livermore, Calif., UCRL-82117 (1979).
70. Y. L. Pan, and J. T. Larson, Lawrence Livermore Laboratory, Livermore, Calif., UCRL-79772 (1977); D. T. Attwood et al., Lawrence Livermore Laboratory, Livermore, Calif., UCRL-83541 (1979).
71. J. M. Auerbach, Lawrence Livermore Laboratory, Livermore, Calif., UCRL-83989 (1980) (submitted to *Phys. Rev. Lett.*).

72. *Laser Program Annual Report—1977*, Lawrence Livermore Laboratory, Livermore, Calif., UCRL-50021-77 (1978), p. 3-37.
73. *Laser Program Annual Report—1976*, Lawrence Livermore Laboratory, Livermore, Calif., UCRL-50021-76 (1977), p. 3-51.
74. *Laser Program Annual Report1976*, Lawrence Livermore Laboratory, Livermore, Calif., UCRL-50021-76 (1977), p. 3-105.
75. *Laser Program Annual Report—1977*, Lawrence Livermore Laboratory, Livermore, Calif., UCRL-50021-77 (1978), p. 3-64.
76. F. Seward et al., *Rev. Sci. Instrum.* **47**, 464 (1976).
77. N. M. Ceglio and J. T. Larson, *Phys. Rev. Lett.* **44**, 9 (1980).
78. J. N. Koppel et al., Lawrence Livermore Laboratory, Livermore, Calif., UCRL-81477 (1979).
79. E. M. Campbell et al., Lawrence Livermore Laboratory, Livermore, Calif., UCRL-83096 (1980) (to be published in *Phys. Rev. Lett.*).
80. K. R. Manes et al., *Phys Rev. Lett.* **39**, 281 (1977).
81. B. I. Cohen and C. E. Max, *Phys. Fluids* **22**, 1115 (1979).
82. C. Wang, H. Kornblum, and V. W. Slivinsky, *Bull. Am. Phys. Soc.* **24**, 1106 (1979).
83. *Laser Program Annual Report—1977*, Lawrence Livermore Laboratory, Livermore, Calif., UCRL-50021-77 (1978), p. 4-31.
84. S. M. Lane, E. M. Campbell, and C. K. Bennett, Lawrence Livermore Laboratory, Livermore, Calif., UCRL-83882 (1980) (to be published in *Appl. Phys. Lett.*).
85. W. C. Mead et al., Lawrence Livermore Laboratory, Livermore, Calif., UCRL-83163 (1979).

D-T Fuel Density Determination from Measurements of Pusher Areal Density ($\rho\Delta R$)

For near-term investigation of D-T fuel compression in the intermediate-density ICF targets (final fuel density $\rho_f \sim 2$ to 20 g/cm^3; neutron yield $N \sim 10^6$ to 10^9), we have chosen as our primary diagnostic the determination of pusher areal density, $\rho\Delta R$, by neutron activation.[86] This technique has recently been used to estimate the final compressed state for thin-walled, single-shell exploding pusher targets as well as thick-walled multilayered targets irradiated with pulses of 200 to 400 ps (Ref. 87 and the previous article).

With present-generation targets, the neutrons generated at peak D-T burn activate a measured fraction of ^{28}Si material in the glass pusher, transforming them to ^{28}Al by the ^{28}Si(n,p)^{28}Al reaction.[86,88] Assuming that the neutron yield occurs during a time period short compared with time scales of hydrodynamic motion, the number of activations are directly proportional to the product of the neutron yield N, and the pusher areal density $\rho\Delta R \equiv [\int \rho(R)dR]_{\text{pusher}}$ at the time of peak burn. The ^{28}Al atoms decay by β-emission (with a half-life of 2.24 minutes) to excited ^{28}Si, followed by a 1.78-MeV gamma deexcitation to the ground state of ^{28}Si. By measuring the β, γ coincidence decay rate from a known collected fraction of the pusher debris,[88] and taking the measured neutron yield, we can determine $\rho\Delta R$ at peak burn (that is, the peak neutron production rate).[89]

An exact determination of $\rho\Delta R$ from the number of pusher activations would require knowledge of the actual extended spatial distribution of neutron production. For spherically symmetric geometries, however, the assumption that the neutrons all originate at the center of the fuel produces the correct value for the determination of the number of activations (except for when the pusher and fuel are mixed at the time of peak burn). Consequently, except for analyzing the cases of pusher-fuel mix and nonspherical geometries, we will assume that the number of pusher activations is directly proportional to the product of the neutron yield and the pusher areal density. In this article we show how a simple, conservative estimate of the average fuel density at burn time, ρ_f, can be inferred from $\rho\Delta R$.

Target Geometry and Assumptions

The typical multilayered, ablatively driven target shown in Fig. 6-70(a) is designed to achieve 10 times the liquid density of D-T; although the figure shows the D-T fuel contained by a SiO_2 pusher, our analysis can be performed for pushers of different materials as well as for pushers containing neutron-activation trace materials. Figure 6-70(b) shows a typical one-dimensional computer calculation of the density distribution at peak burn. The density jump at the pusher-fuel interface is the result of the requirement of local pressure balance and the different atomic weights of SiO_2 and $CF_{1.4}$.

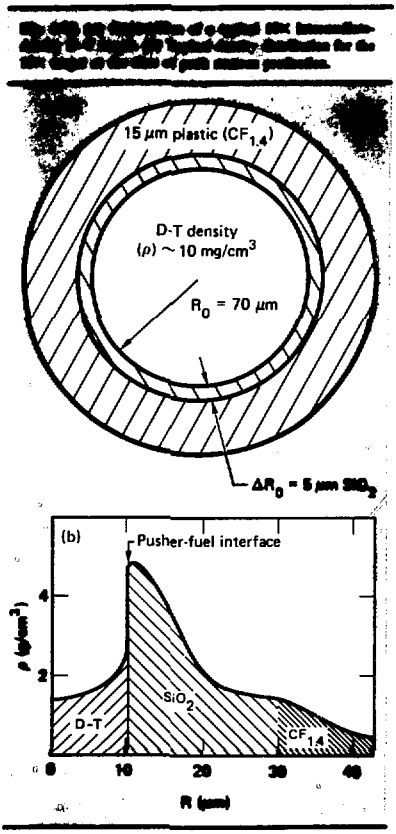

Computer code simulations show that the timing of peak compression and maximum neutron production in intermediate-density implosions depend on both the target design and irradiation conditions. For the targets discussed here, LASNEX calculations predict that peak burn occurs ~150 ps before maximum compression.[89] Thus, provided the pusher and fuel are not severely mixed at the time of peak neutron production, fuel densities determined from measurements of pusher areal density will in general be conservative (lower than the peak value).

To simplify the problem of determining the fuel density at peak burn, our simple model rests on four assumptions:

- Spherical symmetry.
- Conservation of both fuel and pusher mass.
- Uniform (though different) pusher and fuel densities.
- No mixing of pusher and fuel.

We will show later that relaxing the assumptions of mass conservation and uniform density distributions result in moderately higher calculated fuel densities for a given measured $\rho\Delta R$, while the effects of mixing and asymmetry produce reductions by (at most) a factor of about 2.

Thin-Walled Targets

Given the assumptions listed above it is straightforward to show that the statement of conservation of mass for the pusher and the fuel can be written

$$\left(\frac{\rho_f}{\rho_{f0}}\right)^{2/3} \approx \frac{\rho\Delta R}{\rho_0\Delta R_0}\,\frac{1+\frac{\Delta R}{R_f}+\frac{1}{3}\left(\frac{\Delta R}{R_f}\right)^2}{1+\frac{\Delta R_0}{R_{f0}}+\frac{1}{3}\left(\frac{\Delta R_0}{R_{f0}}\right)^2}, \qquad (23)$$

where ρ is pusher density, ρ_f is fuel density, R_f is fuel radius, and ΔR is pusher thickness; initial-state values are distinguished from final values by the subscript 0. If in addition we are dealing with thin-walled targets and final experimental conditions such that

$$\frac{\Delta R_0}{R_{f0}} \ll 1 \qquad \frac{\Delta R}{R_f} \ll 1, \qquad (24)$$

then Eq. (23) immediately simplifies to

$$\rho_f = G_0(\rho\Delta R)^{3/2}, \qquad (25)$$

where $G_0 = \rho_{f0}/(\rho_0\Delta R_0)^{3/2}$ is a parameter composed of measured intial quantities. We observe that given our initial assumptions, a measurement of $\rho\Delta R$ at the time of peak D-T burn allows a direct and simple calculation of the average fuel density without independent knowledge of the pusher density or thickness.

Thick-walled Targets in the Absence of Mixing

In most targets and final compressed-fuel conditions of interest, however, even if $\Delta R_0/R_0 \ll 1$, $\Delta R/R_f \lesssim 1$ (and may indeed be >1) and Eq. (25)

will significantly underestimate ρ_f. Yet it turns out that knowledge of the relationship between ρ_f and pusher density ρ at the time of peak burn is sufficient to establish the more general relationship, $\rho_f = f(\rho\Delta R)$. Still using the four assumptions outlined above, the conservation of pusher and fuel mass [Eq. (23)] can in this more general case be manipulated again to yield an expression between ρ_f and $\rho\Delta R$ of the form

$$\rho_f = G(\alpha, M_p, M_f)(\rho\Delta R)^{3/2} , \qquad (26)$$

where M_p is the pusher mass, M_f is the fuel mass, $\alpha = \rho/\rho_f$ (the ratio of pusher density to fuel density at the time of peak burn) and

$$G(\alpha, M_p, M_f) = \left[\alpha\left(\frac{3M_f}{4\pi}\right)^{1/3}\left[\left(1+\frac{M_p}{\alpha M_f}\right)^{1/3} - 1\right]\right]^{-3/2} . \qquad (27)$$

Thus, if α is relatively insensitive to variations in target parameters and performance, G will be (in the first approximation) a target-geometry-dependent constant given by the initial conditions, and we find that even in the more general case we have a very simple relationship between ρ_f and $\rho\Delta R$.

By invoking continuity of pressure and temperature across the pusher-fuel interface at the time of peak D-T burn, then for silicate glass pushers and equimolar D-T fuel we find that at the interface

$$\rho = \frac{16}{(Z)+1}\rho_f , \qquad (28)$$

where Z is the average charge state of the pusher. Here we assume that

- The pusher and D-T are perfect gases.
- At the interface, the D-T ion temperature is equal to the electron temperature; this assumption is satisfied except for transiently in the target center.
- The pusher is in thermal equilibrium with the fuel electrons; for target sizes used in current experiments this assumption is also satisfied.

For our first estimate of the functional relationship between ρ_f and $\rho\Delta R$, we will therefore assume that Eq. (28) is valid throughout the fuel and pusher, and use the D-T ion temperature at burn time, T, to evaluate Z. (We will later investigate the effect of fuel temperature equilibrium as well as nonuniform fuel and pusher density distributions.) We choose T to evaluate Z because:

- T, the spatially and temporally averaged D-T ion temperature at burn time, is the temperature most directly inferred from the target neutron yield.
- Almost 90% of the fuel mass lies beyond $R_f/2$, where the temperature ratio approaches 1.
- Even the transient ratio of electron to ion temperatures is much less than two.

Taking the specific case of SiO_2 pushers and using T ~ 0.4 keV as an approximate lower bound for the average D-T fuel temperature at peak burn, Eq. (28) becomes

$$\rho = \alpha\rho_f , \qquad (29)$$

where $1.5 \lesssim \alpha \lesssim 2.0$, and the upper and lower limits correspond to $Z \sim 7$ (T ~ 0.4 keV) and $Z = 10$ for fully ionized SiO_2 (T $\gtrsim$ 1 keV), respectively. The lower bound of T ~ 0.4 keV was chosen because temperatures much lower would result in neutron yields too low to allow determination of $\rho\Delta R$ by neutron activation. Thus, for target performance of interest (T $\gtrsim$ 0.4 keV) the total variation in α is relatively small, and we can ensure a conservative estimate of ρ_f by assuming $\alpha = 2$ throughout the experimental parameter range (T $\gtrsim$ 0.4 keV). Curve 1 in Fig. 6-71(a) is a plot of Eq. (26), assuming $\alpha = 2$, for a 10× target of the type shown in Fig. 6-70.

If a more accurate value of α is desired, however, we note that for T less than a few keV, neutron yield is a very sensitive function of the D-T ion temperature.[90,91] Assuming that the D-T fuel conditions do not vary significantly during the burn, that burn time (10% to 90%) is approximated by the final radius R_f divided by the D-T-ion sound speed, and given the D-T Maxwell-averaged cross section,[90] we can estimate the neutron yield as

$$N \simeq 2 \times 10^{27}\left(\rho_{f0}^{\,2} R_{f0}^{\,4}\right) C^{2/3} T_{exp}^{-2/3} \cdot \left(\frac{19}{T^{1/3}}\right), \qquad (30)$$

where T is in keV, R_{f0} and ρ_{f0} are in cgs units, and C is the fuel compression.

Figure 6-72 shows the result of solving Eq. (30) for the final D-T ion temperature as a function of neutron yield, for 10× targets as shown in Fig. 6-70(a); in experiments at Shiva (previous article) a fuel density for these targets of up to 10 times liquid D-T density was diagnosed using neutron activation. The curves show that for a given N, the final temperature is not a strong function of the final

Fig. 6-9L · (a) Average D-T fuel density at the time of peak neutron production as a function of pusher areal density; the four curves correspond to the four density-distribution models given in (b). Model fuel and pusher density distributions were used to calculate the curves in (a). The specific density distributions shown all correspond to a fuel average D-T fuel density of 2 g/cm^3, or 10 times the liquid density of D-T. For core-targets, with an initial inner diameter of 140 μm and an initial D-T density of 10 mg/cm^3, these compressed-fuel conditions also correspond to a final fuel radius of 12 μm. All curves assume σ, the ratio of pusher to fuel density, equal to 2.

(a)

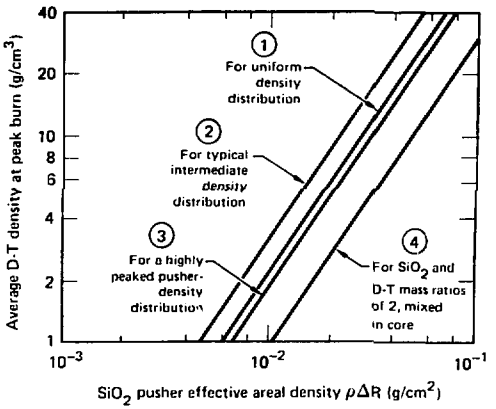

(b)

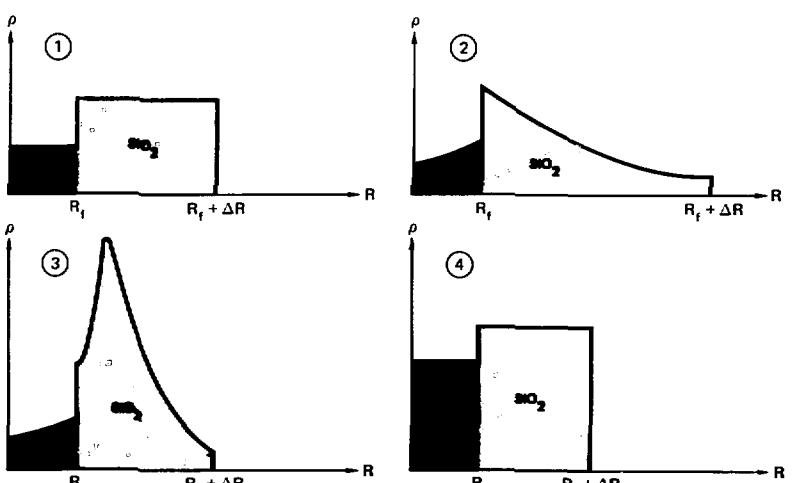

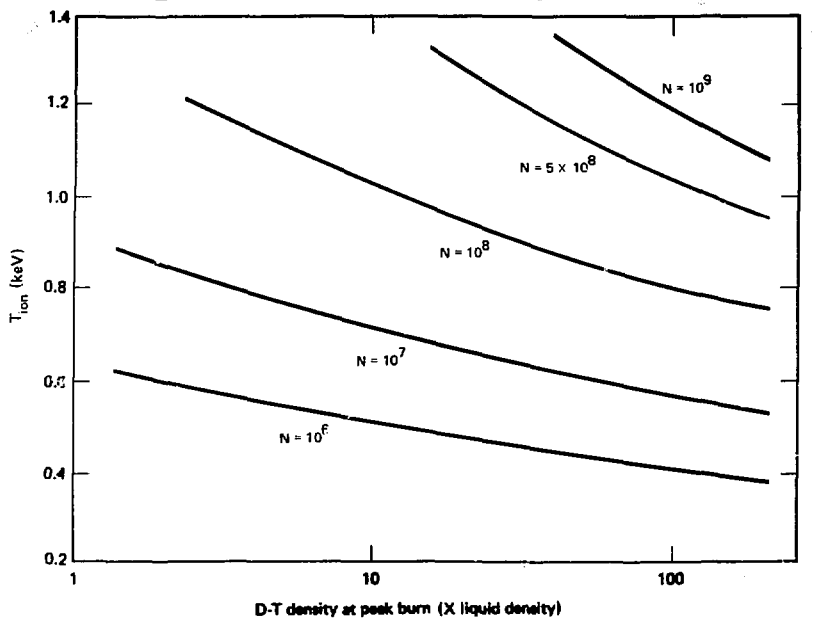

density. Thus a simple one-time iteration will suffice to give T sufficiently accurately to determine α.

Nonuniform Pusher Density Distributions

We can now investigate the effects of relaxing some of our earlier assumptions. In the above analysis we have assumed that while fuel and pusher density have different values, they were each uniform with radius. As mentioned previously, a fuel density variation with radius will not affect the activation of pusher material for any given value of $\rho\Delta R$, as long as the variation is spherically symmetric and no mixing has occurred. There are many reasonably possible pusher density distributions, however, that could greatly affect the pusher activation. If a portion of the pusher material is ablated during the implosion and thus significantly decompressed, then for a given average fuel density the pusher areal density will be less than in the case of uniform compression of all pusher material at burn time. In this case, curve 1 in Fig. 6-71(a) would underestimate the fuel density for a given (measured) $\rho\Delta R$ by approximately the amount of nonuniform compression; if 20% of the pusher mass of a 10× target is ablated away, ρ_f would be approximately 20% higher than is implied by curve 1.

While the effect of disequilibrium on fuel temperature conditions is a reduction in implied density, the result is relatively insensitive to the temperature ratio. Even assuming a D-T ion temperature that is twice the electron temperature throughout the fuel region, the relationship of ρ_f and $\rho\Delta R$ will see only a 25% reduction.

Fig. 6-73. Average D-T fuel density at peak burn for recent 20-TW, 200-ps experiments at Shiva, as inferred from neutron-activation measurements. Both the simple model and detailed one-dimensional calculations show reasonable agreement with measured fuel average fuel densities.

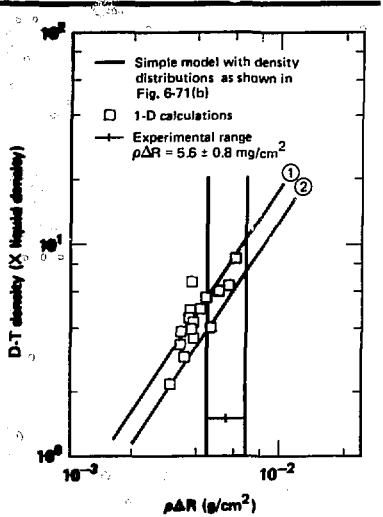

Nonuniform Radial Density

In investigating the effect of nonuniform radial density (and consequently pressure and temperature) distributions, we will still use $\bar{T}$ (the spatially and temporally averaged D-T fuel temperature) to evaluate $\langle Z \rangle$, and still consider Eq. (28) valid at the pusher-fuel interface. Simulations[89] indicate that for our 10× target the pusher is decelerating near peak neutron production, so the most realistic configurations give density distributions that are peaked at or near the pusher-fuel interface. With the tools developed above, it is thus relatively easy to evaluate the effect of such nonuniform density distributions.

Curves 2 and 3 in Fig. 6-71(a) show the result of determining ρ_f from the neutron-activation-determined $\rho\Delta R$, for two such peaked density distributions. The actual density-vs-radius distributions used in the computation are indicated (drawn to scale) in Fig. 6-73; rather than attempt to explore a variety of analytical expressions for $\rho(R)$, we have chosen these two generic distributions as examples. The numerical results quoted below are relatively insensitive to shape perturbations. For a given average fuel density, the effect of a nonuniform fuel distribution is to alter $\rho\Delta R$ from the value of the uniform density case.

We can now find $\rho\Delta R$ by evaluating the actual integral, $\int \rho(R) dR$. We note that the density distribution in model 2 in Fig. 6-71(b) (similar to that predicted by detailed computer simulations[91]) increases the implied average ρ_f for a given $\rho\Delta R$, and that moving the peak in the pusher density distribution away from the interface, as shown in model 3, brings the average ρ_f vs $\rho\Delta R$ back (approximately) towards the isodensity result. A pusher density distribution could be generated that would reduce the average ρ_f by a factor of 2 or 3 from the isodensity curve; this, however, would require a pusher density distribution similar to model 3 as shown, but with a peak pusher density of ~10 times the average fuel density at the time of peak neutron production. Such high densities do not occur because the adjacent SiO_2 glass and D-T are thermally coupled, and due to the finite time for the stagnation shock to propagate to the outer glass, the pressure on the outer glass is much less than the pressure on the D-T.

In the absence of mixing, the assumptions of conservation of mass and uniform density distribution in the pusher and fuel are thus seen to give a conservative estimate of average peak fuel density ρ_f as determined by $\rho\Delta R$. In our discussion of the effect of mixing, we will therefore limit ourselves to the case of uniform density distributions.

Effects of Mixing

During the final stages of implosion, the dense pusher will be decelerated by the lower-density D-T fuel. In this situation, the pusher-fuel interface can suffer significant growth of spatial perturbations via Rayleigh–Taylor instabilities. This instability can result in significant mixing of the pusher into the D-T fuel. The mixing process is thus dynamic rather than diffusive, driven by the density gradient at the interface, and can be visualized as the final breakup

of the wavy pusher-fuel interface and resultant intermixing of adjacent pusher and fuel "pockets." In addition, since adjacent layers of fuel and pusher mass are isobaric and isothermal, the ratio of pusher to fuel mass in the final mixed layer should be comparable to and probably no greater than the density ratio prior to mixing.

Simulations consider the upper unit of mix at burn time as when the pusher mix has affected approximately 2/3 of the fuel mass.[91] To ensure an even more conservative estimate on the effect of mixing, we will consider the situation when, at peak burn, the entire fuel region is involved in the mixing process; α, the ratio of pusher to fuel density at the interface, will be used for the ratio of pusher to fuel mass in the mix region. From the continuity of pressure and temperature at the boundary of the pusher-fuel mixture and the pusher we thus have

$$\rho = \frac{16}{\langle Z \rangle + 1}\,\rho_f + \rho_c = \alpha\rho_f + \rho_c = 2\alpha\rho_f \ , \qquad (31)$$

where ρ_c is the pusher density in the core (i.e., in the pusher-fuel mixture), and $1.5 \lesssim \alpha \lesssim 2.0$ as before. Invoking conservation of fuel and pusher mass, together with the assumption of uniform density distributions, we can proceed as in the no-mix example, and it is again straightforward to show that [see Eq. (26)]

$$\rho_f = G(\alpha, M_p, M_f)(\rho\Delta R)_{eff}^{3/2} \ ,$$

where

$$G(\alpha, M_p, M_f) = \sqrt{\frac{4\pi}{3M_f}}\left\{\frac{3}{4}\alpha + 2\alpha\left[\left(\frac{1}{2} + \frac{M_p}{2\alpha M_f}\right)^{1/3} - 1\right]\right\}^{-3/2} . \qquad (32)$$

Here $(\rho\Delta R)_{eff}$ is the *effective* $\int\rho dR$ as determined by the neutron activation diagnostic, and not simply $\int\rho dR$ as in the unmixed case. The factor of 3/4 in the expression for $G(\alpha, M_p, M_f)$ comes from the assumption [in computing the contribution to $(\rho\Delta R)_{eff}$] that the neutrons are produced throughout the mixed core.

Equation (26) is plotted as curve 4 in Fig. 6-71(a), again using the conservative value of $\alpha = 2$; the corresponding density-radius distribution (model 4) is shown in Fig. 6-71(b). We see that even with this severe degree of mix and with $\alpha = 2$, the implied ρ_f is reduced only by a factor of 2 over the unmixed case (curve and model 1).

Since in the actual situation the outer layers of the pusher are cooler than the hot central fuel region, mixing of the pusher and fuel involving any significant amount of pusher mass would result in a reduction of the fuel ion temperature and consequently a reduction of the burn rate in the mix region. Let us therefore analyze a more realistic case for which an inner region of the fuel (say, $R < R_f/2$) remains unmixed, and assume that the ion temperature in this region is ~2 times that of the mixed region, such that the neutrons are preferentially generated in this hot, unmixed region. In this case, the reduction in implied ρ_f for a given $(\rho\Delta R)_{eff}$ is only 35%. Relaxing the assumption of no pusher-mass ablation, setting $\langle Z \rangle > 7$, or relaxing the assumption of uniform density distributions will all again tend to increase the implied ρ_f. Hence the net error should be less than twofold, and curve 4 in Fig. 6-71(a) is clearly a conservative lower bound of the effect of mix.

Although we do not show the calculations here, it is easy to show that only extreme deviations from spherical symmetry produce reductions greater than 10 to 20%. Such large asymmetries would be readily observable in x-ray microscope images.

Comparison of Model with Experimental Results and One-Dimensional Simulation

We now use this simple model (based on the four assumptions) to predict the fuel densities obtained in the actual intermediate-density experiment series, and compare them with detailed one-dimensional computer modeling. As mentioned earlier, a series of 140-μm-i.d., 5-μm-thick SiO_2 microshells coated with 15 μm of $CF_{1.4}$ and filled with 10 mg/cc of D-T were irradiated at Shiva with 20 TW in a 200-ps (FWHM Gaussian) pulse.[88] The target-wall thickness in these experiments offers greater pusher preheat protection against suprathermal electrons than the thin-shelled exploding-pusher targets. And, as a first step towards the targets ultimately required for high-density implosions, these multilayered targets were expected to operate in a more ablatively driven mode,[97] and to reach final fuel densities of ~2 g/cm^3 (10× liquid D-T density). The target and laser parameters and experimental results are summarized in Table 6-15.

Table 6-15. Summary of results of these shots at Shiva, for intermediate-density targets.

Laser energy (kJ)	Pulse length (ps)	Neutron yield	$\rho\Delta R$ (mg/cm^2)
4.1	212	$6.7 (\pm 0.6) \times 10^8$	5.9 ± 1.5
3.5	210	$1.3 (\pm 0.14) \times 10^8$	4.7 ± 2.2
4.0	200	$3.5 (\pm 0.4) \times 10^8$	6.3 ± 1.8

Using neutron activation, the average, effective SiO_2 pusher areal density at peak burn was determined in these experiments to be 5.6 ($\pm$0.8) mg/cm^2. Using Fig. 6-72, we observe that even taking our lowest experimental value for neutron yield (1.3×10^8) and a most optimistic value for the fuel density (4 g/cm^3, or 20 times the liquid D-T density) we find that the minimum possible D-T ion temperature for these experiments is 1 keV; consequently, α is found to be ~1.5. Using this value for α in the uniform density distribution model, our experimental $\rho\Delta R$'s produce the range of ρf's plotted as curve 1 in Fig. 6-73, which also gives the one-dimensional calculations,[90] indicated by individual squares. Since the one-dimensional calculations imply that the actual density distribution is more like the one used for case 2 during the discussion of Fig. 6-71, however, we also show the fuel densities for this case (curve 2) in Fig. 6-73.

The one-dimensional calculations for this experiment show that peak neutron production occurs approximately 150 ps before stagnation (or peak compression). Thus we would not expect any appreciable mix of the fuel and pusher at the time the neutron activation measurement is made, and for these experimental conditions the two curves 1 and 2 should provide a good lower and upper bound for the fuel density at the time of peak burn. The relatively good agreement between the detailed computer calculations and the simple model gives us confidence that average fuel densities of 6 to 8 times liquid D-T densities were obtained at the time of peak burn. These results are also in good agreement with high-energy x-ray zone plate results and argon-imaging results from the same targets (reported in the preceding article).

The question of the final compressed density at stagnation is more complicated, as in this case the possibility of mix will have to be included. As we have no diagnostic measurement of $\rho\Delta R$ at this time, however, we can only use the densities found at peak burn as a lower, conservative estimate of the actual peak densities. For different targets and laser irradiation conditions under which peak burn and stagnation may occur simultaneously, although neutron activation will give us $\rho\Delta R$ at the time of peak compression, we will have to seriously consider the effects of pusher-fuel mix in order to infer final fuel density.

Conclusions

With only a few physically justifiable assumptions we have shown that neutron activation measurements of pusher areal density can be used to infer final fuel density with uncertainties of less than a factor of 2. Our simple modeling is in good agreement with complex simulation codes which include neutron production as well as all of the relevant hydrodynamics. Using this model we have found that pusher areal densities of 5.6 mg/cm^2, obtained in recent target experiments on the Shiva laser, imply a fuel density of 1 to 2 g/cm^3.

Authors: E. K. Storm, V. W. Slivinsky, and E. M. Campbell

References

86. E. M. Campbell, W. M. Ploeger, P. H. Lee, and S. M. Lane, Lawrence Livermore Laboratory, Livermore, Calif., UCRL-83096 (1979) (submitted to *Appl. Phys. Lett.*).
87. J. M. Auerbach, W. C. Mead, E. M. Campbell, D. L. Matthews, D. S. Bailey, N. M. Ceglio, C. W. Hatcher, L. N. Koppel, S. M. Lane, P. H. Lee, K. R. Manes, G. McClellan, D. W. Phillion, R. L. Price, V. C. Rupert, V. W. Slivinsky, and C. D. Swift, Lawrence Livermore Laboratory, Livermore, Calif., UCRL-83057; presented at the Meeting of the American Physical Society, Boston, Mass., November 1979.
88. E. M. Campbell, H. G. Hicks, W. C. Mead, L. W. Coleman, C. W. Hatcher, J. H. Dellis, M. J. Boyle, J. T. Larson, and S. M. Lane, Lawrence Livermore Laboratory, Livermore, Calif., UCRL-83072 (to be published in *J. Appl. Phys.*, April 1980).
89. W. C. Mead, C. D. Orth, D. S. Bailey, G. McClellan, and K. Estabrook, Lawrence Livermore Laboratory, Livermore, Calif., UCRL-83163 (1979).
90. S. L. Green, Lawrence Livermore Laboratory, Livermore, Calif., UCRL-70522 (1967).
91. E. K. Storm et al., *Phys. Rev. Lett.* **40**, 1570 (1978).